NASA-CR-194389

Annual Research Briefs – 1992

Center for Turbulence Research

January 1993

(NASA-CR-194389) ANNUAL RESEARCH BRIEFS, 1992 Progress Reports (Stanford Univ.) 449 p

N94-12284
--THRU--
N94-12320
Unclas

G3/34 0185260

NASA

Ames Research Center

Stanford University

CONTENTS

Preface

This report contains the 1992 annual progress reports of the Research Fellows and students of the Center for Turbulence Research. It is intended primarily as a contractor report to the National Aeronautics and Space Administration, Ames Research Center. Another report covering the proceedings and research activities of the 1992 Summer Program was distributed earlier this year. In addition to this and the Summer Program reports, each year several CTR manuscript reports are published to expedite the dissemination of research findings by the CTR Fellows.

The Fellows of the Center for Turbulence Research are engaged in fundamental studies of turbulent flows with the objective of advancing the physical understanding of turbulence which will help to improve turbulence models for engineering analysis and develop techniques for turbulence control. The CTR Fellows have a broad range of interests and expertise; together with the NASA-Ames scientific staff and Stanford faculty members, they form a stimulating environment devoted to the study of turbulence.

In its sixth year of operation, CTR hosted twenty-one resident Postdoctoral Fellows, three Research Associates, and four Senior Research Fellows, and it supported four doctoral students and nine short term visitors. The major portion of Stanford's doctoral program in turbulence is sponsored by the United States Air Force Office of Scientific Research and the Office of Naval Research. Many students supported by these programs also conduct their research at the CTR.

Last year considerable effort was focused on the large eddy simulation technique for computing turbulent flows. This increased activity has been inspired by the recent predictive successes of the dynamic subgrid scale modeling procedure which was introduced during the 1990 Summer Program. Several Research Fellows and students are presently engaged in both the development of subgrid scale models and their applications to complex flows. The first group of papers in this report contain the findings of these studies. They are followed by reports grouped in the general areas of modeling, turbulence physics, and turbulent reacting flows. The last contribution in this report outlines the progress made on the development of the CTR post-processing facility. The objective of this effort is to develop advanced software for access and processing of direct numerical simulation databases. Our aim is to facilitate data transfer to the research community outside the physical boundaries of the CTR as well as to largely circumvent the tedious aspects of data management and computer programming for our visitors.

The CTR roster for 1992 is provided in the Appendix. Also listed are the members of the Advisory Committee which meets annually to review the Center's program and the Steering Committee which acts on Fellowship applications.

It is a pleasure to thank Debra Spinks, the Center's Administrative Assistant, for her skillful compilation of this report.

Parviz Moin
William C. Reynolds
John Kim

A local dynamic model for large eddy simulation

By S. Ghosal, T. S. Lund AND P. Moin

1. Motivation and objectives

The dynamic model (Germano *et al.* 1991) is a method for computing the coefficient C in Smagorinsky's (1963) model for the subgrid-scale stress tensor as a function of position from the information already contained in the resolved velocity field rather than treating it as an adjustable parameter. There are two advantages to this. Firstly, it gives a systematic procedure for computing a flow about which we have no prior experience and, therefore, cannot properly adjust the parameter C. Secondly, in an inhomogeneous flow, the optimum choice of C may be different at different points in the flow, and one does not expect the entire flow to be represented by a single constant. The same consideration applies to flows undergoing a transition to turbulence or, more generally, to flows whose statistical properties are changing with time. In the traditional approach, one needs to introduce further *ad hoc* assumptions, such as wall damping functions or a prescription to reset the value of C from zero to a finite number as the flow undergoes a transition to turbulence. In contrast, inhomogeneous and statistically unsteady flows can be handled very naturally in the context of the dynamic model since C is now a function of position and time. Though the dynamic model lacked the full generality necessary to handle general turbulent flows with no homogeneous directions, the method had some important successes.

The basic formalism behind the method is summarized below following Germano *et al.* (1991). The equations of LES can be thought of as a filtered form of the Navier-Stokes equations where the filtering serves to remove fluctuations on length-scales smaller than the computational grid. The effect of the unresolved eddies on the large eddies is then manifested through the Reynolds stress term $\tau_{ij} = \overline{u_i u_j} - \overline{u}_i \overline{u}_j$ where the bar denotes some grid-level filtering operation on a given field $\psi(\mathbf{x})$;

$$\overline{\psi}(\mathbf{x}) = \int G_0(\mathbf{x},\mathbf{y})\psi(\mathbf{y})d\mathbf{y}.$$

The filtering kernel $G_0(\mathbf{x},\mathbf{y})$ has a 'filter width' equal to the grid spacing Δ of the LES. To compute C one first introduces a 'test' filtering operation on the large-eddy field that is denoted by the symbol ' $\widehat{\ }$ ';

$$\widehat{\psi}(\mathbf{x}) = \int G(\mathbf{x},\mathbf{y})\psi(\mathbf{y})d\mathbf{y},$$

where $G(\mathbf{x},\mathbf{y})$ is any kernel that serves to damp all spatial fluctuations shorter than some characteristic length $\widehat{\Delta} > \Delta$ and $\mathbf{x}$, $\mathbf{y}$ are position vectors. The equations for the test-filtered field contain the Reynolds stress term $T_{ij} = \widehat{\overline{u_i u_j}} - \widehat{\overline{u}}_i \widehat{\overline{u}}_j$. Both T_{ij}

and τ_{ij} are unknown in LES; however, the two are related by the identity (Germano 1992)

$$L_{ij} = T_{ij} - \widehat{\tau}_{ij}. \tag{1}$$

Here the Leonard term $L_{ij} = \widehat{\overline{u}_i\overline{u}_j} - \widehat{\overline{u}}_i\widehat{\overline{u}}_j$ is computable from the large-eddy field. Finally, it is assumed that a scaling law is operative and, therefore, the Reynolds stress at the grid and test levels may be written as

$$\tau_{ij} - \frac{1}{3}\tau_{kk}\delta_{ij} = -2C\Delta^2|\overline{S}|\overline{S}_{ij}. \tag{2}$$

and

$$T_{ij} - \frac{1}{3}T_{kk}\delta_{ij} = -2C\widehat{\Delta}^2|\widehat{\overline{S}}|\widehat{\overline{S}}_{ij}, \tag{3}$$

respectively. The model coefficient 'C' in (2) and (3) need not be the same. The prescription for determining C described below can be generalized to obtain both coefficients (Moin 1991). In what follows, 'C' is taken to be the same in (2) and (3) for simplicity. On substituting (2) and (3) in (1), an equation for determining C is obtained:

$$L_{ij} - \frac{1}{3}L_{kk}\delta_{ij} = \alpha_{ij}C - \widehat{\beta_{ij}C} \tag{4}$$

where

$$\alpha_{ij} = -2\widehat{\Delta}^2|\widehat{\overline{S}}|\widehat{\overline{S}}_{ij},$$

$$\beta_{ij} = -2\Delta^2|\overline{S}|\overline{S}_{ij}.$$

Since C appears inside the filtering operation, equation (4) is a system of five independent integral equations involving only one function C. In previous formulations (Germano *et al.* 1991, Moin *et al.* 1991, Lilly 1992), one simply ignored the fact that C is a function of position and took C out of the filtering operation as if it were a constant. This *ad hoc* procedure cannot even be justified *a posteriori* because the C field computed using this procedure is found to be a rapidly varying function of position (Moin 1991). One of the objectives of this research is to eliminate this mathematical inconsistency.

The C obtained from equation (4) can be either positive or negative. A negative value of C implies a locally negative eddy-viscosity, which in turn implies a flow of energy from the small scales to the resolved scales or back-scatter. It is known from direct numerical simulation (DNS) data (Piomelli *et al.* 1991) that the forward and reverse cascade of energy in a turbulent flow are typically of the same order of magnitude with a slight excess of the former accounting for the overall transfer of energy from large to small scales. The presence of back-scatter, therefore, is a desirable feature of a subgrid-scale model. However, when the C computed from (4) is used in a large-eddy simulation, the computation is found to become unstable. The instability can be traced to the fact that C has a large correlation time. Therefore, once it becomes negative in some region, it remains negative for excessively long periods of time during which the exponential growth of the local

velocity fields, associated with negative eddy-viscosity, causes a divergence of the total energy. Though this issue of stability remained unresolved, a way around the problem was found if the flow possessed at least one homogeneous direction. Previous authors (Germano *et al.* 1991, Moin *et al.* 1991, Cabot and Moin 1991) have used an *ad hoc* averaging prescription to stabilize the model. The disadvantages of this are: (a) It is based on an *ad hoc* procedure. (b) The prescription can only be applied to flows that have at least one homogeneous direction, thus excluding the more challenging flows of engineering interest. (c) The prescription for stabilizing the model makes it unable to represent back-scatter. The present research attempts to eliminate these deficiencies.

2. Accomplishments

In the next section, a variational formulation of the dynamic model is described that removes the inconsistency associated with taking C out of the filtering operation. This model, however, is still unstable due to the negative eddy-viscosity. Next, three models are presented that are mathematically consistent as well as numerically stable. The first two are applicable to homogeneous flows and flows with at least one homogeneous direction, respectively, and are, in fact, a rigorous derivation of the *ad hoc* expressions used by previous authors. The third model in this set can be applied to arbitrary flows, and it is stable because the C it predicts is always positive. Finally, a model involving the subgrid-scale kinetic energy is presented which attempts to model back-scatter. This last model has some desirable theoretical features. However, even though it gives results in LES that are qualitatively correct, it is outperformed by the simpler constrained variational models. It is suggested that one of the constrained variational models should be used for actual LES while theoretical investigation of the kinetic energy approach should be continued in an effort to improve its predictive power and to understand more about back-scatter.

2.1 A variational formulation

Equation (4) may be written as $E_{ij}(\mathbf{x}) = 0$, where

$$E_{ij}(\mathbf{x}) = L_{ij} - \frac{1}{3}L_{kk}\delta_{ij} - \alpha_{ij}C + \widehat{\beta_{ij}C}. \tag{5}$$

The residual $E_{ij}(\mathbf{x})$ at any given point depends on the value of the function C at neighboring points in the field. One cannot, therefore, minimize the sum of the squares of the residuals $E_{ij}E_{ij}$ locally (as in Lilly, 1992) since reducing the value of $E_{ij}E_{ij}$ at one point '$\mathbf{x}$' changes its values at neighboring points. However, the method of least squares has a natural generalization to the non-local case. The function C that "best satisfies" the system of integral equations (4) is the one that minimizes

$$\mathcal{F}[C] = \int E_{ij}(\mathbf{x})E_{ij}(\mathbf{x})d\mathbf{x}. \tag{6}$$

$\mathcal{F}[C]$ is a functional of C, and the integral extends over the entire domain. To find the Euler-Lagrange equation for this minimization problem, we set the variation of

$\mathcal{F}$ to zero:

$$\delta\mathcal{F} = 2\int E_{ij}(\mathbf{x})\delta E_{ij}(\mathbf{x})d\mathbf{x} = 0. \tag{7}$$

Using the definition of E_{ij}, we get

$$\int \left(-\alpha_{ij}E_{ij}\delta C + E_{ij}\widehat{\beta_{ij}\delta C}\right) d\mathbf{x} = 0 \tag{8}$$

which may be rearranged as

$$\int \left(-\alpha_{ij}E_{ij} + \beta_{ij}\int E_{ij}(\mathbf{y})\mathbf{G}(\mathbf{y},\mathbf{x})\mathbf{d}\mathbf{y}\right)\delta C(\mathbf{x})d\mathbf{x} = 0. \tag{9}$$

Thus, the Euler-Lagrange equation is

$$-\alpha_{ij}E_{ij} + \beta_{ij}\int E_{ij}(\mathbf{y})\mathbf{G}(\mathbf{y},\mathbf{x})\mathbf{d}\mathbf{y} = \mathbf{0} \tag{10}$$

which may be rewritten in terms of C as

$$f(\mathbf{x}) = C(\mathbf{x}) - \int \mathcal{K}(\mathbf{x},\mathbf{y})C(\mathbf{y})d\mathbf{y} \tag{11}$$

where

$$f(\mathbf{x}) = \frac{1}{\alpha_{kl}(\mathbf{x})\alpha_{kl}(\mathbf{x})}\left[\alpha_{ij}(\mathbf{x})L_{ij}(\mathbf{x}) - \beta_{ij}(\mathbf{x})\int L_{ij}(\mathbf{y})G(\mathbf{y},\mathbf{x})d\mathbf{y}\right],$$

$$\mathcal{K}(\mathbf{x},\mathbf{y}) = \frac{\mathcal{K}_{\mathcal{A}}(\mathbf{x},\mathbf{y}) + \mathcal{K}_{\mathcal{A}}(\mathbf{y},\mathbf{x}) - \mathcal{K}_{\mathcal{S}}(\mathbf{x},\mathbf{y})}{\alpha_{kl}(\mathbf{x})\alpha_{kl}(\mathbf{x})}$$

and

$$\mathcal{K}_{\mathcal{A}}(\mathbf{x},\mathbf{y}) = \alpha_{ij}(\mathbf{x})\beta_{ij}(\mathbf{y})G(\mathbf{x},\mathbf{y}),$$

$$\mathcal{K}_{\mathcal{S}}(\mathbf{x},\mathbf{y}) = \beta_{ij}(\mathbf{x})\beta_{ij}(\mathbf{y})\int d\mathbf{z}G(\mathbf{z},\mathbf{x})G(\mathbf{z},\mathbf{y}).$$

Equation (11) is readily recognized as Fredholm's integral equation of the second kind.

2.2. The constrained variational problem

In this section, we address the stability problem created by the negative eddy-viscosity by requiring that in addition to minimizing the functional (6), C satisfy some constraints designed to ensure the stability of the model. The choice of such constraints is clearly not unique. It is shown that the local least squares method (Lilly 1992) coupled with the volume averaging prescription (Germano *et al.* 1991) can actually be derived as a rigorous consequence of such a constrained variational problem for flows with at least one homogeneous direction. The method is then extended to general inhomogeneous flows.

2.2.1 Homogeneous turbulence

In the case of homogeneous turbulence, it is natural to assume that C can depend only on time. Let us, therefore, impose this as a constraint in the problem of minimizing the functional (6). The functional $\mathcal{F}[C]$ then reduces to the function

$$\mathcal{F}(C) = \langle \mathcal{L}_{ij}\mathcal{L}_{ij}\rangle - 2\langle \mathcal{L}_{ij}m_{ij}\rangle C + \langle m_{ij}m_{ij}\rangle C^2 \tag{12}$$

where $\mathcal{L}_{ij} = L_{ij} - (1/3)L_{kk}\delta_{ij}$ is the traceless part of L_{ij}, $m_{ij} = \alpha_{ij} - \widehat{\beta}_{ij}$ and $\langle\ \ \rangle$ denotes integral over the volume. The value of C that minimizes the function $\mathcal{F}(C)$ is easily found to be

$$C = \frac{\langle L_{ij}m_{ij}\rangle}{\langle m_{kl}m_{kl}\rangle} \tag{13}$$

where the isotropic part of $\mathcal{L}_{ij}$ has vanished on contracting with the traceless tensor m_{ij}. Equation (13) is precisely the result of Germano *et al.* and Lilly.

2.2.2 Flows with at least one homogeneous direction

As an example, we consider a channel flow with the y-axis along the cross-channel direction and periodic boundary conditions in the x and z directions. Since the flow is homogeneous in the x-z plane, we impose the constraint that C can depend only on time and the y co-ordinate. It is necessary to assume (as did Germano *et al.*) that the filtering kernel $G(\mathbf{x},\mathbf{y})$ is defined so as to be independent of the cross-channel direction, y. Therefore C may be taken out of the filtering operation and the functional (6) reduces to

$$\mathcal{F}[C] = \int dy \langle (\mathcal{L}_{ij} - m_{ij}C)(\mathcal{L}_{ij} - m_{ij}C)\rangle_{xz} \tag{14}$$

where $\langle\ \ \rangle_{xz}$ denotes integral over the x-z plane and $i = 1$, 2, and 3 represents the x, y, and z directions, respectively. The condition for an extremal of the functional (14) may be written as

$$\delta\mathcal{F} = 2\int dy \delta C(y)\langle m_{ij}m_{ij}C - m_{ij}\mathcal{L}_{ij}\rangle_{xz} = 0 \tag{15}$$

which implies

$$\langle m_{ij}\mathcal{L}_{ij} - m_{ij}m_{ij}C\rangle_{xz} = 0 \tag{16}$$

and since C is independent of x and z and m_{ij} is without trace,

$$C = \frac{\langle m_{ij}L_{ij}\rangle_{xz}}{\langle m_{kl}m_{kl}\rangle_{xz}}. \tag{17}$$

This is the same expression as that of Germano *et al.* and Lilly for flows homogeneous in the x-z plane.

2.2.3 Inhomogeneous flows

In this section, we will adopt the point of view that perhaps the eddy-viscosity describes only a mean flow of energy from large to small scales, and back-scatter needs to be modeled separately as a stochastic forcing (Chasnov 1990, Leith 1990, Mason *et al.* 1992). We shall, therefore, insist on the eddy-viscosity always being positive and for the time being disregard back-scatter. Accordingly, in the problem of minimizing the functional (6), we impose the constraint

$$C \geq 0. \tag{18}$$

It is convenient to write the variational problem in terms of a new variable ξ such that $C = \xi^2$. Then the constraint (18) is equivalent to the condition that ξ be real. In terms of the new variable ξ, equation (9) becomes

$$\int \left(-\alpha_{ij} E_{ij} + \beta_{ij} \int E_{ij}(\mathbf{y}) G(\mathbf{y}, \mathbf{x}) d\mathbf{y} \right) \xi(\mathbf{x}) \delta\xi(\mathbf{x}) d\mathbf{x} = 0, \tag{19}$$

which gives for the Euler-Lagrange equation

$$\left(-\alpha_{ij} E_{ij} + \beta_{ij} \int E_{ij}(\mathbf{y}) G(\mathbf{y}, \mathbf{x}) d\mathbf{y} \right) \xi(\mathbf{x}) = 0. \tag{20}$$

Therefore, at any point $\mathbf{x}$, either $\xi(\mathbf{x}) = 0$ or the first factor in (20) vanishes. That is, at some points of the field $C(\mathbf{x}) = 0$ and at the remaining points

$$C(\mathbf{x}) = \mathcal{G}[C(\mathbf{x})]$$

where

$$\mathcal{G}[C(\mathbf{x})] = f(\mathbf{x}) + \int \mathcal{K}(\mathbf{x}, \mathbf{y}) C(\mathbf{y}) d\mathbf{y}$$

with $f(\mathbf{x})$ and $\mathcal{K}(\mathbf{x}, \mathbf{y})$ as defined in section 2.1. Note, however, we do not know in advance on which part of the domain C vanishes; this information is part of the solution of the variational problem. Therefore, if a C can be found such that

$$C(\mathbf{x}) = \begin{cases} \mathcal{G}[C(\mathbf{x})], & \text{if } \mathcal{G}[C(\mathbf{x})] \geq 0; \\ 0, & \text{otherwise} \end{cases} \tag{21}$$

then it is a nontrivial solution of the Euler-Lagrange equation (20). Equation (21) may be written concisely as

$$C(\mathbf{x}) = \left[f(\mathbf{x}) + \int \mathcal{K}(\mathbf{x}, \mathbf{y}) C(\mathbf{y}) d\mathbf{y} \right]_+ \tag{22}$$

where the operation denoted by the suffix '+' is defined as $x_+ = \frac{1}{2}(x + |x|)$ for any real number x. It is clear that a solution of (22) satisfies the Euler-Lagrange equation (20), but it is not obvious whether this solution is unique (we exclude the trivial solution $C(\mathbf{x}) = 0$). Equation (22) is a nonlinear integral equation, and no rigorous results regarding the existence or uniqueness of its solutions are known to the authors. Nevertheless, we will assume that it has a unique solution in all cases of interest. Numerical experiments so far have given us no reason to question this assumption.

2.9. A model with back-scatter

The instability associated with the negative eddy-viscosity may be understood in the following way. The Smagorinsky eddy-viscosity model does not contain any information on the total amount of energy in the subgrid scales. Therefore, if the coefficient C becomes negative in any part of the domain, the model tends to remove more energy from the subgrid scales than is actually available, and the reverse transfer of energy does not saturate when the store of subgrid-scale energy is depleted. However, in a physical system, if all the energy available in the subgrid scales is removed, the Reynolds stress will go to zero, thus quenching the reverse flow of energy. Clearly, a more elaborate model that keeps track of the subgrid-scale kinetic energy is required. Such a model is described in this section. (The possibility of treating the dynamic model in conjunction with an equation for turbulent kinetic energy was considered by Wong (1992) in a different context.)

From dimensional analysis, the turbulent viscosity is the product of a velocity and a length-scale. We will take the square root of the subgrid-scale kinetic energy for the velocity scale and the grid spacing as the length scale. Thus,

$$\tau_{ij} - \frac{1}{3}\delta_{ij}\tau_{kk} = -2C\Delta k^{1/2}\overline{S}_{ij} \tag{23}$$

and

$$T_{ij} - \frac{1}{3}\delta_{ij}T_{kk} = -2C\widehat{\Delta}K^{1/2}\widehat{\overline{S}}_{ij} \tag{24}$$

where

$$k = \frac{1}{2}(\overline{u_i u_i} - \overline{u}_i\overline{u}_i) = \frac{1}{2}\tau_{ii}, \tag{25}$$

$$K = \frac{1}{2}(\widehat{\overline{u_i u_i}} - \widehat{\overline{u}}_i\widehat{\overline{u}}_i) = \frac{1}{2}T_{ii}. \tag{26}$$

On taking the trace of (1), we have

$$K = \widehat{k} + \frac{1}{2}L_{ii}. \tag{27}$$

Since the average of the square of any quantity is never less than the square of its average, it follows that L_{ii} is non-negative provided the filtering operation involves a non-negative weight $G(\mathbf{x},\mathbf{y})$. Therefore, K is never less than $\widehat{k}$, a result that might be anticipated since there are more modes below the test level cut-off than below the grid level. Substituting (23) and (24) in (1) and solving the corresponding variational problem, we get (11) with $\alpha_{ij} = -2\widehat{\Delta}K^{1/2}\widehat{\overline{S}}_{ij}$ and $\beta_{ij} = -2\Delta k^{1/2}\overline{S}_{ij}$ to determine $C(\mathbf{x})$.

To complete the model, it remains to give a method for determining k. For this we will use the well known model of the transport equation for k (e.g. Speziale 1991)

$$\partial_t k + \overline{u}_j\partial_j k = -\tau_{ij}\overline{S}_{ij} - C_*\frac{k^{3/2}}{\Delta} + \partial_j(D\Delta k^{1/2}\partial_j k) + Re^{-1}\partial_{jj}k \tag{28}$$

with the grid spacing Δ taken as the length-scale appropriate for the subgrid-scale eddies. Here C_* and D are non-negative dimensionless parameters, and Re is a Reynolds number based on molecular viscosity. The coefficients C_* and D can be determined dynamically. For this purpose, one writes down a model equation for K which is identical in form to (28) with test-level quantities replacing grid-level quantities. One then requires that K and k obtained by solving the corresponding evolution equations be consistent with (27). This gives the following integral equations for determining C_* and D:

$$C_*(\mathbf{x}) = \left[f_*(\mathbf{x}) + \int \mathcal{K}_*(\mathbf{x},\mathbf{y}) C_*(\mathbf{y}) d\mathbf{y} \right]_+ \tag{29}$$

and

$$D(\mathbf{x}) = \left[f_D(\mathbf{x}) + \int \mathcal{K}_D(\mathbf{x},\mathbf{y}) D(\mathbf{y}) d\mathbf{y} \right]_+ . \tag{30}$$

The derivation and notation are explained in the appendix.

2.3.1 Stability

It will be shown that the model described above is globally stable, that is, the total energy in the large-eddy field remains bounded in the absence of external forces and with boundary conditions consistent with no influx of energy from the boundaries. Using the continuity and momentum equations for the large-eddy fields and the sub-grid kinetic energy equation (28), we derive

$$\frac{d}{dt}\left(\frac{1}{2}\int \overline{u}_i \overline{u}_i dV + \int k dV \right) = -\int \frac{C_*}{\Delta} k^{3/2} dV - Re^{-1} \int (\partial_j \overline{u}_i)(\partial_j \overline{u}_i) dV \tag{31}$$

where the integral is over the region occupied by the fluid. Boundary conditions are assumed to be such that there is no net flux of energy from the boundaries of the domain so that the surface terms vanish. Note that the terms in $\tau_{ij}\overline{S}_{ij}$ which appear as a source term for k and a sink for the resolved scales (if $C > 0$ and vice versa when $C < 0$) have cancelled out in equation (31), and we are left with the result that in the absence of externally imposed forces and nontrivial boundary conditions, the total energy in the large and small scales taken together must monotonically decrease as a result of molecular viscosity. Using the notation

$$E(t) = \frac{1}{2}\int \overline{u}_i \overline{u}_i dV \tag{32}$$

and

$$e(t) = \int k dV, \tag{33}$$

we have by (31), $E(t) + e(t) \leq E(0) + e(0)$ and since $e(t) \geq 0$ (see next section), $E(t) \leq E(0) + e(0)$. Thus, the energy in the large-eddy field cannot diverge even though the eddy-viscosity is allowed to be negative.

2.3.2 Realizability

It is necessary to demonstrate that the k computed using (28) has the following property; $k(\mathbf{x},t) \geq 0$ at all points $\mathbf{x}$ at all times t if $k(\mathbf{x},0) \geq 0$. This condition is required because it is clear from its definition that k cannot be negative, and, indeed, the model cannot be implemented unless the non-negativeness of k can be guaranteed. This condition is part of and included in a more general condition of 'realizability' (Schumann 1977, Lumley 1978) required of subgrid-scale models to be discussed later. It must also be pointed out that L_{ii} is an intrinsically positive quantity only if the filtering kernel $G(\mathbf{x},\mathbf{y}) \geq 0$. The most commonly used filters in physical space such as the 'tophat' filter and the Gaussian filter do meet this requirement while the Fourier cut-off filter does not. Therefore, the Fourier cut-off filter may not be appropriate in this context.

Suppose that initially ($t = 0$), $k > 0$ at all points. Let $t = t_0$ be the earliest time for which k becomes zero at some point $\mathbf{x} = \mathbf{x}_0$ in the domain. It will be shown that $\partial_t k(\mathbf{x}_0, t_0) > 0$ which ensures that k can never decrease below zero. Integration of equation (28) over an infinitesimal sphere of radius ϵ centered around $\mathbf{x}_0$ gives after dividing by ϵ^3

$$\frac{\partial k}{\partial t} = -\frac{1}{\epsilon^3}\int \overline{u}_n k d\sigma + C\Delta k^{1/2}|\overline{S}|^2 - \frac{C_*}{\Delta}k^{3/2} + \frac{1}{\epsilon^3}\int \nu \frac{\partial k}{\partial n} d\sigma, \tag{34}$$

where $\nu = Re^{-1} + D\Delta\sqrt{k}$ and $d\sigma$ is an infinitesimal element of area on the surface of the sphere with $\hat{n}$ as the outward normal. Since k first becomes zero at $\mathbf{x} = \mathbf{x}_0$, $\mathbf{x}_0$ is a local minimum. Therefore, $k = \nabla k = 0$ at '$\mathbf{x}_0$', and hence $k \sim \epsilon^2$ and $\nabla k \sim \epsilon$ inside the sphere. Therefore, every term on the right side of (34) is of order ϵ or higher except for the last term which is of order one. Thus, on taking the limit $\epsilon \to 0$ in equation (34), we have

$$\frac{\partial k}{\partial t} = \lim_{\epsilon \to 0} \frac{1}{\epsilon^3}\int \nu \frac{\partial k}{\partial n} d\sigma. \tag{35}$$

Since k is a minimum at the point $\mathbf{x}_0$, the right-hand side is positive. Therefore, k can never decrease below zero. Note that we have assumed that C remains finite as $k \to 0$. Indeed, (27) implies α_{ij} remains finite as k (and hence β_{ij}) goes to zero. Thus, in this limit, (11) reduces to

$$C(\mathbf{x}) = \frac{\alpha_{ij}(\mathbf{x})L_{ij}(\mathbf{x})}{\alpha_{kl}(\mathbf{x})\alpha_{kl}(\mathbf{x})}$$

which is finite. Also, in this proof we assumed that the second derivatives of k at $\mathbf{x}_0$ are not all zero. The proof, however, can be easily extended to remove this restriction.

The requirement that k be non-negative is contained in a more general set of properties of the tensor τ_{ij}. They are called realizability conditions and may be stated in several equivalent forms (Schumann 1977). Since the Reynolds stress τ_{ij}

is a real symmetric tensor, it can be diagonalized where the diagonal elements τ_α, τ_β and τ_γ are real. The realizability conditions can be stated as

$$\tau_\alpha, \tau_\beta, \tau_\gamma \geq 0. \tag{36}$$

It will be noted that (36) implies

$$k = \frac{1}{2}\tau_{ii} = \frac{1}{2}(\tau_\alpha + \tau_\beta + \tau_\gamma) \geq 0. \tag{37}$$

Positivity of the turbulent kinetic energy is, therefore, a consequence of the more general conditions (36).

The modeled Reynolds stress (23) is diagonal in a co-ordinate system aligned to the principal axes of the rate of strain tensor, and the diagonal elements are

$$\tau_i = -2C\Delta k^{1/2} s_i + \frac{2}{3}k \tag{38}$$

where s_i ($i = \alpha, \beta, \gamma$) are eigenvalues of the rate of strain. The realizability conditions (36) are satisfied if

$$-\frac{k^{1/2}}{3\Delta|s_\gamma|} \leq C \leq \frac{k^{1/2}}{3\Delta s_\alpha} \tag{39}$$

at each point of the field. In writing (39), the eigenvalues of the strain rate tensor have been arranged so that $s_\alpha \geq s_\beta \geq s_\gamma$. The incompressibility condition implies $s_\alpha + s_\beta + s_\gamma = 0$ and, therefore, $s_\alpha \geq 0$, $s_\gamma \leq 0$ and s_β may be of either sign. Since C is obtained by solving the integral equation (11), it is difficult (perhaps impossible) to prove any general mathematical result on whether the realizability condition (39) is satisfied. Nevertheless, we offer the following estimates.

A reasonable estimate for k when the turbulence is locally in equilibrium is $k \approx \Delta^2|\bar{S}|^2$. (This gives Smagorinsky's formula on substitution in (23).) With this estimate for k, (39) may be written as $C_{min} \leq C \leq C_{max}$ where

$$C_{min} = -\frac{\sqrt{2}}{3}\frac{\sqrt{s_\alpha^2 + s_\beta^2 + s_\gamma^2}}{|s_\gamma|} \leq -\frac{\sqrt{2}}{3} \tag{40}$$

and

$$C_{max} = \frac{\sqrt{2}}{3}\frac{\sqrt{s_\alpha^2 + s_\beta^2 + s_\gamma^2}}{s_\alpha} \geq \frac{\sqrt{2}}{3}. \tag{41}$$

It is found from numerical experiments on LES of freely decaying homogeneous turbulence (section 2.5) that the distribution of values in the C field at any instant of time is approximately Gaussian with mean about 0.025 and standard deviation about 0.15. The precise values depend on the details of the simulation, but these numbers are representative. For such a field, the number of points falling inside the range $C_{min} \leq C \leq C_{max}$ exceeds 99.9 percent.

2.3.3 Galilean invariance

The Navier-Stokes equations are invariant with respect to the transformations

$$x_i^{'} = x_i - U_i t \tag{42}$$

$$t^{'} = t \tag{43}$$

$$u_i^{'} = u_i - U_i \tag{44}$$

where U_i is independent of space or time. It will be shown that the model described in this section as well as the constrained variational formulation lead to Galilean invariant equations for the large-eddy field.

Substituting (44) in the definition of the Leonard term, we derive $L_{ij}^{'} = L_{ij}$. Since U_i is constant, clearly the rate of strain tensors are invariant. It is shown in the appendix that equation (28) for the subgrid-scale kinetic energy is Galilean invariant. Therefore, $k^{'} = k$, and on using equation (27), $K^{'} = K$. Therefore, each term in the integral equation for C in both the constrained variational formulation and the subgrid-scale kinetic energy formulation are invariant, so that $C^{'} = C$. The invariance of the model now follows on using $\frac{\partial}{\partial x_i^{'}} = \frac{\partial}{\partial x_i}$ and $\frac{D}{Dt^{'}} = \frac{D}{Dt}$.

2.3.4 Behavior near solid walls

Consider a point near the wall with x_1, x_2, and x_3 in the streamwise, wall-normal, and spanwise directions, respectively. Then near the wall, $\overline{u}_1$, $\widehat{\overline{u}}_1$, $\overline{u}_3$, $\widehat{\overline{u}}_3 \sim x_2$, and hence, by the continuity equation, $\overline{u}_2$, $\widehat{\overline{u}}_2 \sim (x_2)^2$. The near wall behavior of the subgrid-scale kinetic energy k involves some subtle issues. From its definition $k = \overline{u_i u_i} - \overline{u}_i \overline{u}_i$, we must have $k \sim (x_2)^2$. In order to obtain such a behavior from (28), one needs to impose the boundary conditions that both k and $\partial k / \partial x_2$ vanish at the walls. However, since equation (28) is only second order in space, we cannot impose both these conditions. Thus, we are forced to choose only $k = 0$ at the wall and this, in general, will give a solution with the asymptotic behavior $k \sim x_2$. One possible remedy is to consider a two equation model (such as a k-ϵ model) in place of equation (28). This gives a system that is fourth order in spatial derivatives and can, therefore, support the additional boundary condition (Durbin 1990. Also see the report by Cabot in this volume). In this report, however, we restrict ourselves to the simpler one equation model (28), and, therefore, the k obtained by solving (28) will in general have the behavior $k \sim x_2$. Nevertheless, we will show that with the model coefficients computed dynamically, the eddy-viscosity is proportional to $(x_2)^3$ and the molecular diffusion of kinetic energy balances the viscous dissipation near the wall independent of whether $k \sim x_2$ or $k \sim (x_2)^2$. To stress this generality, we will write $k \sim (x_2)^{2m}$ where $m = 1/2$ or 1.

The strain rate is dominated by the component $\overline{S}_{12}$ and $\widehat{\overline{S}}_{12}$ which are finite at the wall. The trace of the Leonard term $L_{ii} \sim (x_2)^2$, hence by (27) $K \sim (x_2)^{2m}$. Thus α_{12}, $\beta_{12} \sim (x_2)^m$ are the only surviving terms of α_{ij} and β_{ij} near the wall. With these estimates, $\mathcal{K}(\mathbf{x}, \mathbf{y}) \sim 1$ so that

$$C(\mathbf{x}) \approx f(\mathbf{x}) \approx \frac{L_{12}}{\alpha_{12}} \sim (x_2)^{3-m}.$$

Therefore, the eddy-viscosity $\nu_t = C\Delta\sqrt{k} \sim (x_2)^3$, the well-known "$y$-cubed behavior at the wall".

We now consider the near wall behavior of the kinetic energy equation (28). Using the estimates given in the previous paragraph, $\mathcal{K}_D \sim 1$, so that $D \sim f_D \to 0$ at the wall. On using the expressions for $\mathcal{K}_*$ and f_* given in the appendix, it is again easily verified that near the wall $\mathcal{K}_* \sim 1$, and hence

$$C_* k^{3/2} \sim f_* k^{3/2} \sim |\Delta Re^{-1} \partial_{jj} L_{ii}|$$

which is finite. Hence,

$$\frac{C_* k^{3/2}/\Delta}{|Re^{-1}\partial_{jj}k|} \sim 1 \tag{45}$$

independent of Δ and Re. Thus, all terms in the kinetic energy equation go to zero at the wall except the viscous dissipation and diffusion terms. These are finite and are of the same order at all Reynolds number and at any grid-resolution. This is the correct near wall behavior of the turbulent kinetic energy equation (Mansour, Kim and Moin 1988).

2.4 Numerical methods

The simplest iteration scheme for solving the integral equation (11) is

$$C_{n+1}(\mathbf{x}) = C_n(\mathbf{x}) + \mu \left[f(\mathbf{x}) + \int \mathcal{K}(\mathbf{x},\mathbf{y}) C_n(\mathbf{y}) d\mathbf{y} - C_n(\mathbf{x}) \right], \tag{46}$$

where μ is a relaxation factor that is selected to optimize convergence and n is an iteration index. To solve equation (22), the term

$$f(\mathbf{x}) + \int \mathcal{K}(\mathbf{x},\mathbf{y}) C_n(\mathbf{y}) d\mathbf{y}$$

in (46) needs to be replaced by its positive part. Convergence can be achieved provided $|\mu| \leq \mu_0$ where μ_0 is a number typically of order 0.1 for the present simulation. When the $C(\mathbf{x})$ from the previous time-step was used to start the iteration, convergence at the level of one percent residual error took about twenty iterations. However, if a random velocity field is used in (46), values of μ as small as 10^{-3} are required for stability, which greatly increases the number of iterations required for convergence. It is, therefore, prudent to use a better scheme that converges faster and is less dependent on the nature of the given LES field. Such a scheme can be devised using preconditioning methods.

The integral equation (11) may be written in operator notation as

$$(\mathbf{I} - \mathbf{K})C = f. \tag{47}$$

On substituting $\mathbf{K} = \mathbf{E} + (\mathbf{K} - \mathbf{E})$ (where $\mathbf{E}$ is for the moment an arbitrary operator) in (47) we obtain

$$C = (\mathbf{I} - \mathbf{E})^{-1} f + (\mathbf{I} - \mathbf{E})^{-1}(\mathbf{K} - \mathbf{E})C. \tag{48}$$

If C is replaced by C_{n+1} on the left-hand side and C_n on the right-hand side we obtain the iteration scheme

$$C_{n+1} = (\mathbf{I} - \mathbf{E})^{-1} f + (\mathbf{I} - \mathbf{E})^{-1}(\mathbf{K} - \mathbf{E})C_n. \tag{49}$$

Equation (49) reduces to (46) if we choose $\mathbf{E}$ such that

$$\mathbf{E}\psi = \frac{\mu - 1}{\mu}\psi \tag{50}$$

where ψ is an arbitrary function of position. It is well known that the speed of convergence of the scheme (49) depends on the eigenvalue spectrum of the operator

$$\mathbf{B} = (\mathbf{I} - \mathbf{E})^{-1}(\mathbf{K} - \mathbf{E}). \tag{51}$$

The smaller the spectral radius of $\mathbf{B}$, the faster is the convergence. An efficient scheme is therefore obtained by choosing $\mathbf{E}$ such that '$\mathbf{E} \approx \mathbf{K}$', and yet $(\mathbf{I} - \mathbf{E})$ can be readily inverted. One possible choice is

$$\mathbf{E}\psi(\mathbf{x}) = \mu\widehat{\Delta}^3\mathcal{K}(\mathbf{x},\mathbf{x})\psi(\mathbf{x}) \tag{52}$$

where μ is a positive parameter. The motivation for (52) is the following;

$$\mathbf{K}\psi = \int \mathcal{K}(\mathbf{x},\mathbf{y})\psi(\mathbf{y})d\mathbf{y} = \mu(\mathbf{x})\widehat{\Delta}^3\mathcal{K}(\mathbf{x},\mathbf{x})\psi(\mathbf{x}) \tag{53}$$

where $\mu(\mathbf{x})$ is expected to be between zero and one (corresponding to the limiting cases where the integrand is a delta function centered on $\mathbf{x}$ and a constant respectively). Equation (53) is exact. Equation (52) is the approximation to $\mathbf{K}$ obtained on ignoring the position dependence of μ. On substituting (52) in (49), we obtain after some algebra

$$C_{n+1}(\mathbf{x}) = \frac{1}{1 - \mu g(\mathbf{x})}\left[f(\mathbf{x}) + \int \mathcal{K}(\mathbf{x},\mathbf{y})C_n(\mathbf{y})d\mathbf{y} - \mu g(\mathbf{x})C_n(\mathbf{x})\right] \tag{54}$$

where

$$g(\mathbf{x}) = \frac{\widehat{\Delta}^3}{\alpha_{mn}(\mathbf{x})\alpha_{mn}(\mathbf{x})}\left[2\alpha_{ij}(\mathbf{x})\beta_{ij}(\mathbf{x})G(\mathbf{x},\mathbf{x}) - \beta_{kl}(\mathbf{x})\beta_{kl}(\mathbf{x})\int [G(\mathbf{z},\mathbf{x})]^2 d\mathbf{z}\right]. \tag{55}$$

When $G(\mathbf{x},\mathbf{y})$ is a tophat filter (that is, $G(\mathbf{x},\mathbf{y})$ is constant inside the cube of edge $\widehat{\Delta}$ centered at $\mathbf{x}$ and zero outside), (55) reduces to

$$g_{\text{tophat}}(\mathbf{x}) = \frac{2\alpha_{ij}(\mathbf{x})\beta_{ij}(\mathbf{x}) - \beta_{kl}(\mathbf{x})\beta_{kl}(\mathbf{x})}{\alpha_{mn}(\mathbf{x})\alpha_{mn}(\mathbf{x})}. \tag{56}$$

The iteration scheme (54) can be modified to solve (22) on simply replacing

$$f(\mathbf{x}) + \int \mathcal{K}(\mathbf{x},\mathbf{y})C_n(\mathbf{y})d\mathbf{y}$$

by its positive part. The preconditioning scheme presented here is analogous to the point Jacobi scheme of inverting a matrix suitably generalized to the continuous case. Numerical tests indicate that (54) is considerably more robust than (46) and converges much faster. If μ is chosen between about 0.2 and 0.5, the scheme is found to be convergent for arbitrary velocity fields including fields of random numbers. With the C from the previous time step used as the initial guess, convergence at the level of 0.01 percent residual error never required more than three iterations for the LES of homogeneous isotropic turbulence described in the next section.

2.5 Results

In this section, results of LES of homogeneous isotropic freely decaying turbulence are presented using the constrained variational approach of section 2.2.3 (henceforth referred to as ieq+) and the kinetic energy approach of section 2.3. The results are compared to the results using the volume averaged (section 2.2.1) approach and to the grid-generated wind tunnel turbulence experiments of Comte-Bellot and Corrsin (1971). The Reynolds number based on the Taylor microscale and rms fluctuating velocity is in the range 40-70 in the experiment. The ratio of the integral to Kolmogorov scale is about 80. Therefore, even if the computational box is to be only three integral scales on a side, a DNS of the experiment will require at least $(512)^3$ grid points.

A pseudo-spectral code due to Rogallo (1981) for homogeneous turbulence is modified and used with a $(32)^3$ grid. The filtering kernel $G(\mathbf{x},\mathbf{y})$ is taken as a Gaussian function of width $\widehat{\Delta} = 2\Delta$, where Δ is the grid spacing. The results of the simulation are expected to be quite insensitive to the exact shape of the filtering kernel or of the ratio $\widehat{\Delta}/\Delta$ (Germano *et al.* 1991). However, the filtering kernel is restricted to be non-negative in the kinetic energy formulation because of considerations of realizability (section 2.3.2).

Figure 1 shows the resolved energy decay as a function of time computed using the volume averaged, ieq+, and kinetic energy versions of the variational method together with the experimental data of Comte-Bellot and Corrsin (1971). All variables are in non-dimensional units. The energy has been scaled with the mean square fluctuation velocity, $\langle u'^2 \rangle$ at the first measuring station. Time is in units of M/U where M is the grid size in the experiment and U is the free stream velocity. To facilitate comparison between computation and experiment, the experimental data has been filtered to remove spatial scales below the resolution of the computational grid. Further, measured data on the energy decay as a function of distance from the grid has been converted into energy decay as a function of time using the measured convective velocity in the flow and Taylor's hypothesis of 'frozen turbulence'. Both the volume averaged and constrained versions give results that are in good agreement with the experimental data. The result obtained using the kinetic

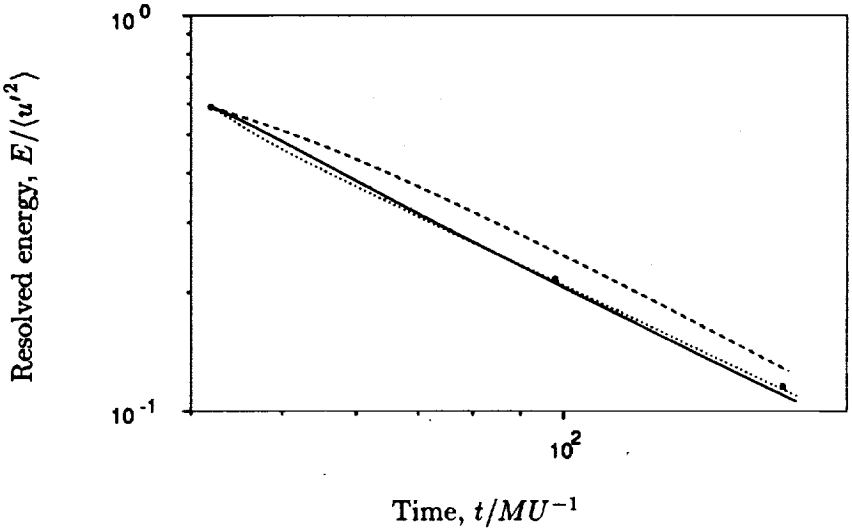

FIGURE 1. Decay of the resolved energy with time computed using the volume averaged (—), ieq+ (···) and kinetic energy (- - -) versions of the variational method.

energy method is seen to be not as good as the other two methods though it has the correct qualitative behavior.

Figure 2 (A), (B), and (C) show the energy spectra at the initial time and two subsequent times computed using the volume averaged, ieq+, and kinetic energy versions of the variational method, respectively, together with the experimental points. Distances have been scaled by $L/2\pi$ where L is length of the computational box which is about ten times the size of the grid generating the turbulence in the experiment. The initial velocity field is chosen to match the initial energy spectrum; therefore, only the last two curves on each figure are of significance.

It is rather surprising that the kinetic energy method which apparently is based on more detailed physical ideas is outperformed by the other two relatively simple models as far as practical LES is concerned. In an effort to understand the reason for this, the subgrid-scale kinetic energy computed using (28) is plotted against the subgrid-scale kinetic energy derived from the experimental data. The result is shown in figure 3. The agreement with the experiment is seen to be remarkably good. Thus, we conclude that the relatively poor performance of the kinetic energy version of the model is not due to errors in prediction of the subgrid-scale kinetic energy. Perhaps the attempt to represent back-scatter by a negative eddy-viscosity is the source of the problem. These issues are still under investigation by the authors.

A typical $C(\mathbf{x})$ field computed using the constrained variational approach is shown in figure 4 over a horizontal cross section of the computational box. The field is seen to be highly variable with C fluctuating by as much as an order of magnitude

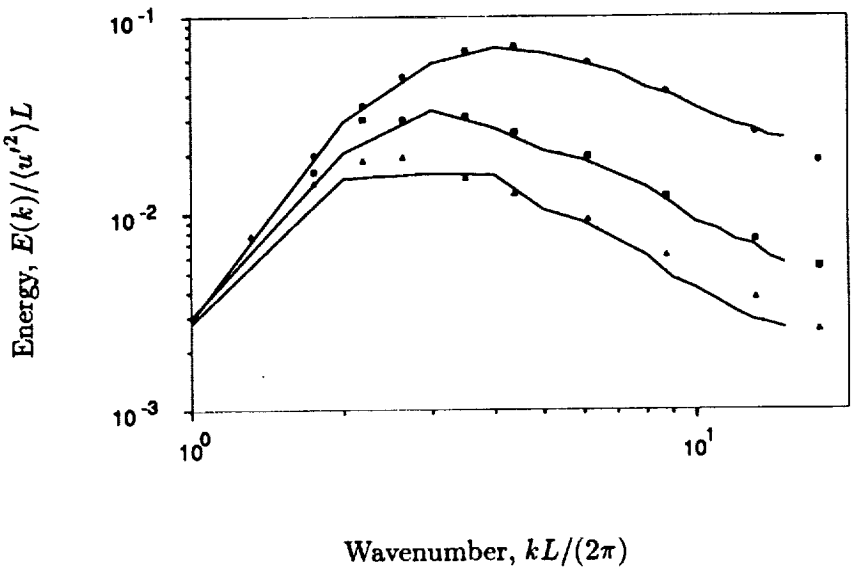

FIGURE 2(A). Energy spectra at $t\ (MU^{-1}) = 42$ (•), 98 (□), 171 (△) compared with the prediction (—) of the volume averaged model.

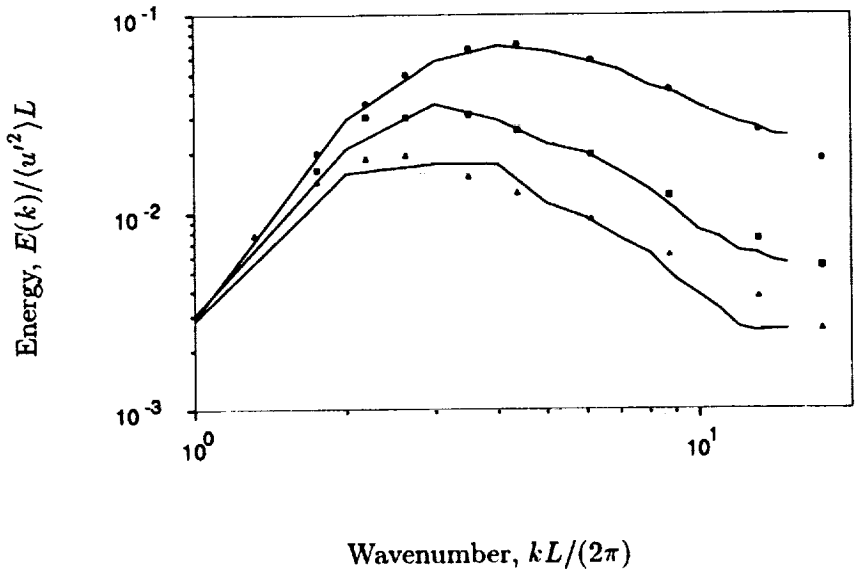

FIGURE 2(B). Same as in 2(A) with the ieq+ model.

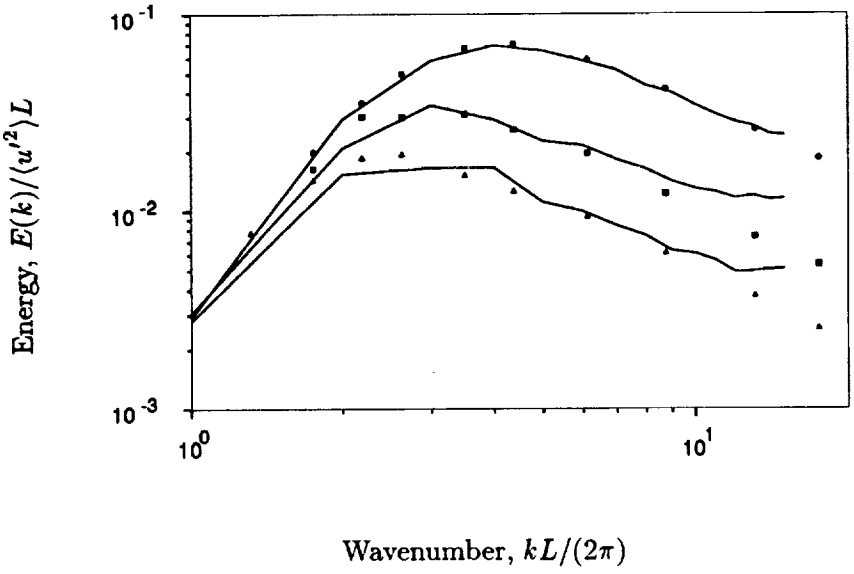

FIGURE 2(C). Same as in 2(A) with the kinetic energy model.

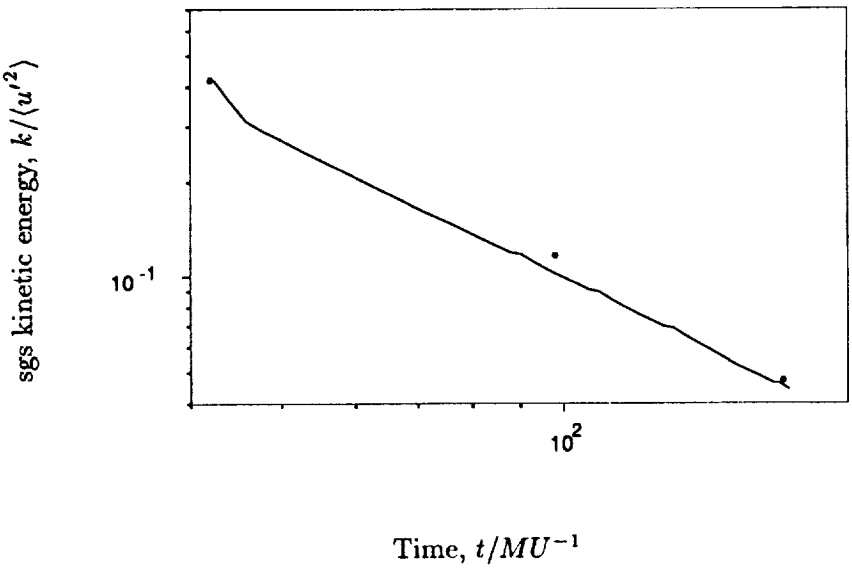

FIGURE 3. Decay of the subgrid-scale kinetic energy with time.

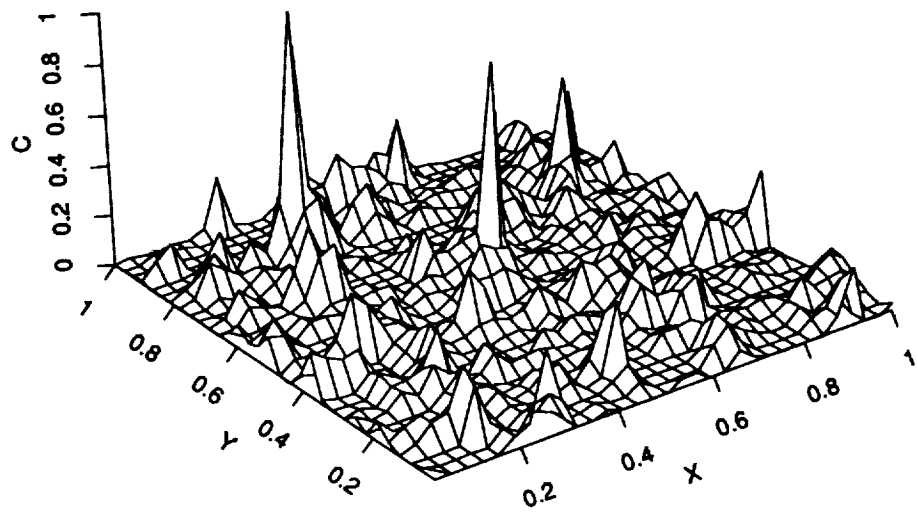

FIGURE 4. The C field over a horizontal cross section of the computational box.

over a few grid spacings. Similar plots of C obtained by solving the (unconstrained) variational problem show a similar qualitative structure.

3. Future plans

The methods for solving the integral equations presented here represent only a first step. A systematic study of the numerical methods available for solving such integral equations must be undertaken. The numerical codes used to conduct the tests presented here have not yet been optimized for performance. This must be done before computations of flows with complex geometry are undertaken. The application of the method in computations with nonuniform grids involve some subtle issues that are being analyzed. It is expected that the methods presented here will be tested in progressively more challenging flows and the outcome of these tests will be used to guide future improvements.

The kinetic energy version of the variational method is applicable to inhomogeneous flows and provides an interesting model of back-scatter. However, the performance of this model in practical LES was not as satisfactory as that of the constrained variational methods. An attempt to understand the reasons for this is likely to produce not only a better model for LES but also a better understanding of back-scatter. Research in this direction is continuing.

In conclusion, it must be stressed that the dynamic localization method is a very general idea and is not restricted in scope to Smagorinsky's model or even to algebraic closure models. Extension of the ideas presented here to improved subgrid-scale models and higher order closures are interesting possibilities.

Appendix. The dynamic determination of C_* and D.

The evolution of subgrid-scale kinetic energy is modeled by the equation

$$\partial_t k + \overline{u}_j \partial_j k = -\tau_{ij}\overline{S}_{ij} - C_* \frac{k^{3/2}}{\Delta} + \partial_j (D\Delta k^{1/2}\partial_j k) + (Re)^{-1}\partial_{jj} k \qquad (A.1)$$

where C_* and D are non-negative parameters. By analogy one can write down the corresponding evolution equation for the subtest-scale kinetic energy

$$\partial_t K + \widehat{\overline{u}}_j \partial_j K = -T_{ij}\widehat{\overline{S}}_{ij} - C_* \frac{K^{3/2}}{\widehat{\Delta}} + \partial_j (D\widehat{\Delta} K^{1/2}\partial_j K) + (Re)^{-1}\partial_{jj} K. \qquad (A.2)$$

Equations $(A.1)$ and $(A.2)$ must be consistent with the relation

$$K = \widehat{k} + \frac{1}{2} L_{ii} \qquad (A.3)$$

(equation (27) in the text). This fact can be exploited to determine C_* and D as shown below.

On substituting equation $(A.3)$ in $(A.2)$ one obtains after some algebraic manipulations

$$\partial_t \widehat{k} + \widehat{\overline{u}}_j \partial_j \widehat{k} = -e + \partial_j f_j + Re^{-1}\partial_{jj}\widehat{k} \qquad (A.4)$$

where

$$e = T_{ij}\widehat{\overline{S}}_{ij} + \frac{C_* K^{3/2}}{\widehat{\Delta}} - \frac{1}{2} Re^{-1}\partial_{jj} L_{ii} + \frac{1}{2}(\partial_t L_{ii} + \widehat{\overline{u}}_j \partial_j L_{ii}) \qquad (A.5)$$

and

$$f_j = D\widehat{\Delta} K^{1/2}\partial_j K. \qquad (A.6)$$

On applying the ' $\widehat{\ }$ ' operator to both sides of equation $(A.1)$ we obtain

$$\partial_t \widehat{k} + \widehat{\overline{u}}_j \partial_j \widehat{k} = -E + \partial_j F_j + Re^{-1}\partial_{jj}\widehat{k} \qquad (A.7)$$

where

$$E = \widehat{\tau_{ij}\overline{S}_{ij}} + \widehat{(C_* k^{3/2}/\Delta)} \qquad (A.8)$$

and

$$F_j = \widehat{k}\widehat{\overline{u}}_j - \widehat{k\overline{u}_j} + \widehat{D\Delta k^{1/2}\partial_j k}. \qquad (A.9)$$

Equations $(A.4)$ and $(A.7)$ are consistent only if

$$e = E \qquad (A.10)$$

and

$$f_j = F_j \qquad (A.11)$$

It may appear that the term $\frac{1}{2}Re^{-1}\partial_{jj}L_{ii}$ has been arbitrarily lumped with e while it might as well have been converted to a divergence term and made part of f_j. There is, however, no ambiguity as is evident from the following considerations. The coefficient D is a model for pressure diffusion and third order velocity correlation terms which do not depend explicitly on the Reynolds number. On the other hand, C_* models viscous dissipation which contains the Reynolds number explicitly. Thus, any term that contains the Reynolds number must appear in equation $(A.10)$ which determines C_* rather than in equation $(A.11)$ which determines D. A similar objection can be raised for the term $(1/2)\widehat{\bar{u}}_j\partial_j L_{ii}$ in equation $(A.5)$ which could have been written instead as $-(1/2)\widehat{\bar{u}}_j L_{ii}$ on the right hand side of equation $(A.6)$. The choice in this case is dictated by the requirement that both C_* and D must be Galilean invariant in order to be consistent with their physical interpretation. Since it is only the total time derivative $D_t = \partial_t + \widehat{\bar{u}}_j\partial_j$ appearing on the right hand side of equation $(A.5)$ and not ∂_t that is a Galilean invariant operator, the apparent ambiguity is removed. Finally, the purist might argue that the curl of an arbitrary vector can be added on the right hand side of equation $(A.11)$ since we only need to enforce $\partial_j f_j = \partial_j F_j$. This degree of freedom merely refers to the fact that the definition of flux is always ambiguous up to the curl of an arbitrary vector field. Since we assume that the flux is defined identically at both the test and grid levels, the arbitrary solenoidal vector on the right hand side of equation $(A.11)$ must, in fact, be zero.

Equations $(A.10)$ and $(A.11)$ can be rewritten in a more transparent form:

$$\chi = \phi C_* - \widehat{\psi C_*} \tag{A.12}$$

and

$$Z_j = X_j D - \widehat{Y_j D} \tag{A.13}$$

with the notation

$$\chi = \widehat{\tau_{ij}\bar{S}_{ij}} - T_{ij}\widehat{\bar{S}}_{ij} - \frac{1}{2}\partial_t L_{ii} - \frac{1}{2}\widehat{\bar{u}}_j\partial_j L_{ii} + \frac{1}{2}Re^{-1}\partial_{jj}L_{ii}$$

$$\phi = \frac{K^{3/2}}{\widehat{\Delta}}$$

$$\psi = \frac{k^{3/2}}{\Delta}$$

$$Z_j = \widehat{k}\widehat{\bar{u}}_j - \widehat{k\bar{u}_j}$$

$$X_j = \widehat{\Delta}K^{1/2}\partial_j K$$

$$Y_j = \Delta k^{1/2}\partial_j k.$$

Clearly χ, ϕ, ψ, Z_j, X_j, and Y_j are known fields at any given time step.

Since equation $(A.12)$ is a single integral equation for C_*, one might be tempted to solve it directly without first going through the variational formulation. However,

since viscous dissipation can only remove energy from the subgrid scales, C_* must be non-negative whereas the C_* obtained by solving (A.12) can have either sign. One must, therefore, try to "best satisfy" (A.12) subject to the constraint $C_* \geq 0$. That is, C_* must be chosen so as to minimize the functional

$$\int (\chi - \phi C_* + \widehat{\psi C_*})^2 d\mathbf{y}$$

with the constraint $C_* \geq 0$. Similarly, D is obtained on minimizing

$$\int (Z_j - X_j D + \widehat{Y_j D})(Z_j - X_j D + \widehat{Y_j D}) d\mathbf{y}$$

subject to the constraint $D \geq 0$. The solutions to these variational problems can be immediately written down in analogy to the solution (22) in the text if one notices the similarity in structure between equations (A.12), (A.13), and (4) in the text:

$$C_*(\mathbf{x}) = \left[f_*(\mathbf{x}) + \int \mathcal{K}_*(\mathbf{x},\mathbf{y}) C_*(\mathbf{y}) d\mathbf{y} \right]_+ \tag{A.14}$$

where

$$f_*(\mathbf{x}) = \frac{1}{\phi^2(\mathbf{x})} \left[\phi(\mathbf{x})\chi(\mathbf{x}) - \psi(\mathbf{x}) \int \chi(\mathbf{y}) G(\mathbf{y},\mathbf{x}) d\mathbf{y} \right],$$

$$\mathcal{K}_*(\mathbf{x},\mathbf{y}) = \frac{\mathcal{K}^*_{\mathcal{A}}(\mathbf{x},\mathbf{y}) + \mathcal{K}^*_{\mathcal{A}}(\mathbf{y},\mathbf{x}) - \mathcal{K}^*_{\mathcal{S}}(\mathbf{x},\mathbf{y})}{\phi(\mathbf{x})\phi(\mathbf{x})}$$

and

$$\mathcal{K}^*_{\mathcal{A}}(\mathbf{x},\mathbf{y}) = \phi(\mathbf{x})\psi(\mathbf{y}) G(\mathbf{x},\mathbf{y}),$$

$$\mathcal{K}^*_{\mathcal{S}}(\mathbf{x},\mathbf{y}) = \psi(\mathbf{x})\psi(\mathbf{y}) \int d\mathbf{z} G(\mathbf{z},\mathbf{x}) G(\mathbf{z},\mathbf{y}).$$

$$D(\mathbf{x}) = \left[f_D(\mathbf{x}) + \int \mathcal{K}_D(\mathbf{x},\mathbf{y}) D(\mathbf{y}) d\mathbf{y} \right]_+ \tag{A.15}$$

where

$$f_D(\mathbf{x}) = \frac{1}{X_j(\mathbf{x}) X_j(\mathbf{x})} \left[X_j(\mathbf{x}) Z_j(\mathbf{x}) - Y_j(\mathbf{x}) \int Z_j(\mathbf{y}) G(\mathbf{y},\mathbf{x}) d\mathbf{y} \right],$$

$$\mathcal{K}_D(\mathbf{x},\mathbf{y}) = \frac{\mathcal{K}^D_{\mathcal{A}}(\mathbf{x},\mathbf{y}) + \mathcal{K}^D_{\mathcal{A}}(\mathbf{y},\mathbf{x}) - \mathcal{K}^D_{\mathcal{S}}(\mathbf{x},\mathbf{y})}{X_j(\mathbf{x}) X_j(\mathbf{x})}$$

and

$$\mathcal{K}^D_{\mathcal{A}}(\mathbf{x},\mathbf{y}) = X_j(\mathbf{x}) Y_j(\mathbf{y}) G(\mathbf{x},\mathbf{y}),$$

$$\mathcal{K}^D_{\mathcal{S}}(\mathbf{x},\mathbf{y}) = Y_j(\mathbf{x}) Y_j(\mathbf{y}) \int d\mathbf{z} G(\mathbf{z},\mathbf{x}) G(\mathbf{z},\mathbf{y}).$$

It is readily verified that χ, ϕ, ψ, Z_j, X_j, and Y_j are all Galilean invariant. Thus C_* and D obtained by solving equations (A.14) and (A.15) are also Galilean invariant which, in turn, implies that the subgrid-scale kinetic energy equation (A.1) itself is Galilean invariant.

REFERENCES

CABOT W., & MOIN P. 1991 Large-eddy simulation of scalar transport with the dynamic subgrid-scale model. *CTR manuscript.* **128,** 1-19.

CHASNOV J. R. 1991 Simulation of the Kolmogorov inertial subrange using an improved subgrid model. *Phys. Fluids A.* **3(1),** 188-200.

COMTE-BELLOT G. & CORRSIN S. 1971 Simple eulerian time correlation of full and narrow-band velocity signals in grid-generated 'isotropic' turbulence. *J. Fluid Mech.* **48,** 273-337.

DURBIN P. A. 1990 Near wall turbulence closure modeling without 'damping functions'. *Theoret. Comput. Fluid Dynamics.* **3,** 1-13.

GERMANO M. 1992 Turbulence: the filtering approach. *J. Fluid Mech.* **238,** 325-336.

GERMANO M., PIOMELLI U., MOIN P. & CABOT W. 1991 A dynamic subgrid-scale eddy-viscosity model. *Phys. Fluids A.* **3 (7),** 1760-1765.

LEITH C. E. 1990 Stochastic backscatter in a subgrid-scale model: plane shear mixing layer. *Phys. Fluids A.* **2,** 297-299.

LILLY D. K. 1992 A proposed modification of the Germano subgrid-scale closure method. *Phys. Fluids A.* **4 (3),** 633-635.

LUMLEY J. L. 1978 Computational modeling of turbulent flows. *AIAM.* **18,** 123-176.

MANSOUR N. N., KIM J. & MOIN P. 1988 Reynolds-stress and dissipation-rate budgets in a turbulent channel flow. *J. Fluid Mech.* **194,** 15-44.

MASON P. J. & THOMSON D. J. 1992 Stochastic backscatter in large-eddy simulations of boundary layers. *J. Fluid Mech.* **242,** 51-78.

MOIN P. 1991 A new approach for large eddy simulation of turbulence and scalar transport. *Proc. Monte Verita coll. on turbulence. Birkhauser, Bale.*

MOIN P., SQUIRES K., CABOT W. & LEE S. 1991 A dynamic subgrid-scale model for compressible turbulence and scalar transport. *Phys. Fluids A.* **3 (11),** 2746-2757.

PIOMELLI U., CABOT W. H., MOIN P. & LEE S. 1991 Subgrid-scale back-scatter in turbulent & transitional flows. *Phys. Fluids A.* **3(7),** 1766-1771.

ROGALLO R. S. 1981 Numerical experiments in homogeneous turbulence. *NASA Tech. Mem.* **81315.**

SCHUMANN U. 1977 Realizability of Reynolds-stress turbulence models. *Phys. Fluids A.* **20(5),** 721-725.

SMAGORINSKY J. 1963 General circulation experiments with the primitive equations. I. The basic experiment. *Mon. Weather Rev.* **91**, 99-165.

SPEZIALE C. G. 1991 Analytic methods for the development of reynolds-stress closures in turbulence. *Ann. Rev. Fluid Mech.* **23**, 107-157.

WONG V. C. 1992 A proposed statistical-dynamic closure method for the linear or nonlinear subgrid-scale stresses. *Phys. Fluids A.* **4(5)**, 1080-1082.

Parameterization of subgrid-scale stress by the velocity gradient tensor

By T. S. Lund AND E. A. Novikov[1]

1. Motivation and objectives

In large eddy simulation (LES), the large scale motions are directly computed and the effects of the small scales are modeled. The term to be modeled is the subgrid-scale stress tensor,

$$\tau_{ij} = \overline{u_i u_j} - \bar{u}_i \bar{u}_j, \tag{1}$$

which arises when the Navier-Stokes equations are spatially filtered (denoted by overbar) to remove the small scale information. Most large eddy simulations make use of the Smagorinsky (1963) eddy-viscosity model,

$$\tau_{ij} - \frac{1}{3}\tau_{kk}\delta_{ij} = -2(C\Delta^2|\bar{S}|)\bar{S}_{ij}, \tag{2}$$

where C is a non-dimensional constant, Δ is the grid spacing, and $\bar{S}_{ij}$ is the resolved strain-rate.

Although the Smagorinsky model has been in use for nearly thirty years, for roughly half that period it has been known that the model provides only a crude estimate for the stresses. This fact was first demonstrated by Clark *et al.* (1979), where direct numerical simulation (DNS) data for homogeneous isotropic turbulence was used to evaluate model predictions. Clark *et al.* found a correlation coefficient of approximately 0.2 when comparing predictions of the Smagorinsky model with the exact stresses. McMillan *et al* (1979) found that the correlation coefficient was even lower in homogeneous shear flow, being close to 0.1. Later, Piomelli *et al.* (1988) found similar results in turbulent channel flow.

When contemplating these extremely low correlations, it may seem striking that the Smagorinsky model is successful when used in a large eddy simulation. The reason for the seemingly unwarranted accuracy is that, by construction, the Smagorinsky model insures a net drain of energy from the large scales to the subgrid-scale motions. This is the primary objective of the subgrid-scale model, and as long as this requirement is met, reasonable results are evidently obtained. On the other hand, the Smagorinsky model provides poor predictions of the individual elements of the stress tensor. It is natural to expect that superior results could be obtained with a model that predicts the stress tensor more accurately. The aim of this work is to seek out potentially more accurate models.

The Smagorinsky model is based on a molecular transport analogy where the stress is proportional to the rate of strain. The molecular analogy is a rather crude

1 Permanent address: Institute for Nonlinear Science, University of California, San Diego

model for turbulent transport, however, and it may be expected that a more accurate model for the subgrid-scale stress could be obtained if additional information were included. An obvious quantity to consider is the vorticity (or equivalently the rotation rate tensor). While molecular transport is unaffected by rotation, there is no reason to exclude rotation from a model for turbulent transport. Indeed, vortex stretching is believed to be the dominant mechanism by which turbulence transfers energy from large to smaller scales (Tennekes & Lumley 1971).

The objective of this work is to construct and evaluate subgrid-scale models that depend on both the strain rate and the vorticity. This will be accomplished by first assuming that the subgrid-scale stress is a function of the strain and rotation rate tensors. Extensions of the Caley-Hamilton theorem can then be used to write the assumed functional dependence explicitly in the form of a tensor polynomial involving products of the strain and rotation rates. Finally, use of this explicit expression as a subgrid-scale model will be evaluated using direct numerical simulation data for homogeneous, isotropic turbulence.

2. Accomplishments

2.1 Subgrid-scale stress as a tensor function of strain and rotation rates

It is assumed that the residual stress may be written as a function of the strain and rotation rate tensors, as well as the unit isotropic tensor, *viz.*

$$\tau_{ij} = f(S_{ij}, R_{ij}, \delta_{ij}), \tag{3}$$

where the strain and rotation rate tensors are defined as

$$S_{ij} = \frac{1}{2}\left(\frac{\partial \bar{u}_i}{\partial x_j} + \frac{\partial \bar{u}_j}{\partial x_i}\right), \tag{4a}$$

$$R_{ij} = \frac{1}{2}\left(\frac{\partial \bar{u}_i}{\partial x_j} - \frac{\partial \bar{u}_j}{\partial x_i}\right), \tag{4b}$$

and where $\bar{u}_i$ is the resolved velocity. Note that S and R are the symmetric and antisymmetric parts of the velocity gradient tensor. Thus Eq. (3) can be alternatively interpreted as a relationship between the subgrid-scale stress and the velocity gradient tensor.

For simplicity in the following development, a matrix notation is introduced. Let $\boldsymbol{\tau}$, $\mathbf{S}$, $\mathbf{R}$, and $\mathbf{I}$ be the matrices associated with the corresponding tensor quantities ($\mathbf{I}$ is the identity matrix associated with δ_{ij}). Tensor contractions correspond to matrix multiplications in the following way:

$$\mathbf{SR} = S_{ik}R_{kj}, \qquad \mathbf{R}^2 = R_{ik}R_{kj}, \quad \text{etc.}, \tag{5a}$$

$$\mathrm{tr}\left(\mathbf{SR}^2\right) = S_{ij}R_{jk}R_{ki}, \quad \text{etc.} \tag{5b}$$

The most general expression for Eq. (3) is an infinite tensor polynominal containing terms of the form $\mathbf{S}^{\alpha_1}\mathbf{R}^{\beta_1}\mathbf{S}^{\alpha_2}\mathbf{R}^{\beta_2}\ldots$, where α_i and β_i are positive integers.

Each term in the series is multiplied by a coefficient that may be a function of the simultaneous invariants of $\mathbf{S}$ and $\mathbf{R}$ (discussed below). The Caley-Hamilton theorem of matrix algebra (see Pipes & Hovanessian 1969) states that terms in the polynomial beyond a certain order are redundant, and thus the infinite polynomial is equivalent to one involving a finite number of terms. Spencer and Rivlin (1959) have determined the surviving terms when one tensor is expressed in terms of two others, as done here. Since the subgrid-scale stress is symmetric, only the symmetric tensors in this list need to be considered. When the Results of Spencer and Rivlin are applied to the present situation and the results properly symmetrized, the following tensors and associated invariants arise:

$$\begin{aligned}
\mathbf{m}_1 &= \mathbf{S}, & \mathbf{m}_2 &= \mathbf{S}^2, \\
\mathbf{m}_3 &= \mathbf{R}^2, & \mathbf{m}_4 &= \mathbf{SR} - \mathbf{RS}, \\
\mathbf{m}_5 &= \mathbf{S}^2\mathbf{R} - \mathbf{RS}^2, & \mathbf{m}_6 &= \mathbf{I}, \\
\mathbf{m}_7 &= \mathbf{SR}^2 + \mathbf{R}^2\mathbf{S}, & \mathbf{m}_8 &= \mathbf{RSR}^2 - \mathbf{R}^2\mathbf{SR}, \\
\mathbf{m}_9 &= \mathbf{SRS}^2 - \mathbf{S}^2\mathbf{RS}, & \mathbf{m}_{10} &= \mathbf{S}^2\mathbf{R}^2 + \mathbf{R}^2\mathbf{S}^2, \\
\mathbf{m}_{11} &= \mathbf{RS}^2\mathbf{R}^2 - \mathbf{R}^2\mathbf{S}^2\mathbf{R}, &&
\end{aligned} \tag{6}$$

$$\begin{aligned}
I_1 &= \mathrm{tr}\left(\mathbf{S}^2\right), & I_2 &= \mathrm{tr}\left(\mathbf{R}^2\right), \\
I_3 &= \mathrm{tr}\left(\mathbf{S}^3\right), & I_4 &= \mathrm{tr}\left(\mathbf{SR}^2\right), \\
I_5 &= \mathrm{tr}\left(\mathbf{S}^2\mathbf{R}^2\right), & I_6 &= \mathrm{tr}\left(\mathbf{S}^2\mathbf{R}^2\mathbf{SR}\right).
\end{aligned} \tag{7}$$

These results were presented earlier by Pope (1975) in connection with models for the Reynolds averaged Navier-Stokes equations. The invariant I_6, however, was not included in Pope's analysis. This invariant is anomalous in the sense that it is related to the other 5 but with an ambiguity in sign. The relationship is

$$\begin{aligned}
I_6 = \pm[\, &(4\hat{I}_1^3 + \hat{I}_3^2)\hat{I}_2^3 - \hat{I}_3 I_4^3 - I_5^3 + 4\hat{I}_1(\hat{I}_3 I_4 - 2\hat{I}_1 I_5)\hat{I}_2^2 + \\
&\hat{I}_1(I_5 - \hat{I}_1\hat{I}_2)I_4^2 + 5\hat{I}_1\hat{I}_2 I_5^2 - 3\hat{I}_2\hat{I}_3 I_4 I_5\,]^{1/2},
\end{aligned}$$

where $\hat{I}_1 = I_1/2$, $\hat{I}_2 = I_2/2$, and $\hat{I}_3 = I_3/3$. The sign ambiguity can be resolved by replacing the $\pm$ above by the multiplicative factor $\mathrm{sign}(\tilde{w}_1\tilde{w}_2\tilde{w}_3)$, where $\tilde{w}_1$, $\tilde{w}_2$, and $\tilde{w}_3$ are the vorticity components expressed in the principal coordinate system of the strain rate tensor. (The function $\mathrm{sign}(x)$ returns either -1 for $x < 0$ or 1 for $x > 0$.) Since resolution of the sign ambiguity requires information that is not contained in the invariants I_1, I_2, ... I_5, the invariant I_6 may be considered to be independent of the other 5. For this reason, we shall include I_6 in the subsequent analysis.

The set of tensors displayed in Eq. (6) are complete in the sense that any symmetric polynomial involving products of $\mathbf{S}$ and $\mathbf{R}$ can be written as a linear combination of the 11 tensors, with the scalar multipliers expressed as polynomials of the 6 invariants. The tensors are also independent in the sense that none of the 11 tensors

may be written as a linear combination of the other 10 if the scalar multipliers are restricted to be polynomials of the 6 invariants. If this restriction is relaxed slightly so that the scalar multipliers may be *ratios* of polynomials of the invariants, then under the conditions discussed below only 6 of the above 11 tensors are independent (see Rivlin and Ericksen (1955) for more details). To see this, consider expressing one of the 11 tensors as a linear combination of 6 others:

$$\mathbf{m}_k = C_i \mathbf{m}_i; \qquad i = 1, 2, \ldots 6, \quad k > 6, \tag{8}$$

where the tensors are ordered in any desired way, not necessarily as in Eq. (6). Due to symmetry, each of the tensors $\mathbf{m}_i$ have only 6 unique elements. Thus Eq. (8) represents 6 algebraic equations for the 6 unknown coefficients C_i. The solution can be written as

$$C_i = [\mathrm{tr}\,(\mathbf{m}_i \mathbf{m}_j)]^{-1} \mathrm{tr}\,(\mathbf{m}_k \mathbf{m}_j)\,. \tag{9}$$

A unique solution will exist provided the above matrix of traces is non-singular, that is

$$\det[\mathrm{tr}\,(\mathbf{m}_i \mathbf{m}_j)] \neq 0. \tag{10}$$

Note that if Eq. (9) is solved by Cramer's rule, the C_i will be expressed as a ratios of polynomials of the invariants listed in Eq. (7).

Equation (10) can be violated under two conditions: when $\mathbf{S}$ has a repeated eigenvalue, or when two components of the vorticity, expressed in the principal coordinates of $\mathbf{S}$, vanish. The first condition corresponds to an axisymmetric state of strain. The second corresponds to a situation where the rotation is confined to a single axis, and this axis is aligned with one of the principal directions of the strain rate. Although either of these conditions could be realized in a turbulent field, the probability of exactly satisfying either of them is rather remote. Indeed, when the tensor expansion was evaluated using direct numerical simulation data as described in the following section, the conditions for lack of independence were never satisfied exactly, even for 128^3 realizations.

Assuming that Eq. (10) is satisfied, only the first 6 terms in Eq. (6) need to be considered. For incompressible flows, it is customary to model only the deviatoric part of τ and combine the isotropic part with the pressure. We shall follow the precedent here and subtract the trace from each of the first 6 tensors in Eq. (6). The 6th term vanishes when this is done, leaving only the first 5 as a basis. This is consistent with the fact that a trace-free symmetric tensor has only 5 unique elements. This result could have been obtained equivalently by subtracting the trace from each of the 11 tensors at the outset and then showing that any tensor in the list can be written as a linear combination of the first 5. In any event, the stress can be written as

$$\begin{aligned} \tau^* =& C_1 \Delta^2 |\mathbf{S}| \mathbf{S} + C_2 \Delta^2 (\mathbf{S}^2)^* + C_3 \Delta^2 (\mathbf{R}^2)^* + \\ & C_4 \Delta^2 (\mathbf{SR} - \mathbf{RS}) + C_5 \Delta^2 \frac{1}{|\mathbf{S}|} (\mathbf{S}^2 \mathbf{R} - \mathbf{R} \mathbf{S}^2), \end{aligned} \tag{11}$$

where Δ is the grid spacing, $|\mathbf{S}| = \sqrt{\mathrm{tr}(\mathbf{S}^2)}$, and $()^*$ indicates the trace-free part. Use of the strain rate magnitude as a scaling factor was chosen somewhat arbitrarily. In theory, this is not an issue since the C_i can depend on all of the invariants in Eq. (7) and the correct scaling will be obtained if the C_i are written as functions of the invariants. In practice, it is difficult to find the dependence of the C_i on the invariants, and thus the choice of the scaling becomes relevant. Several alternate scalings were tested and the results appeared to be quite insensitive to the particular choice.

Since the expansion coefficients C_i are non-dimensional, they can depend only on non-dimensional groupings of the invariants listed in Eq. (7). These are taken to be

$$s_1 = \frac{\mathrm{tr}\,(\mathbf{S}^3)}{\mathrm{tr}\,(\mathbf{S}^2)^{3/2}}, \tag{12a}$$

$$s_2 = \frac{\mathrm{tr}\,(\mathbf{R}^2)}{\mathrm{tr}\,(\mathbf{S}^2)}, \tag{12b}$$

$$s_3 = \frac{\mathrm{tr}\,(\mathbf{S}\mathbf{R}^2)}{\mathrm{tr}\,(\mathbf{S}^2)^{1/2}\mathrm{tr}\,(\mathbf{R}^2)}, \tag{12c}$$

$$s_4 = \frac{\mathrm{tr}\,(\mathbf{S}^2\mathbf{R}^2)}{\mathrm{tr}\,(\mathbf{S}^2)\,\mathrm{tr}\,(\mathbf{R}^2)}. \tag{12d}$$

$$s_5 = \frac{\mathrm{tr}\,(\mathbf{S}^2\mathbf{R}^2\mathbf{S}\mathbf{R})}{[\mathrm{tr}\,(\mathbf{S}^2)\,\mathrm{tr}\,(\mathbf{R}^2)](3/2)}. \tag{12e}$$

2.2 Evaluation of the proposed model

Equation (11) is an exact result that will hold as long a the basic assumption that the stress is expressible solely as a function of the strain and rotation rates is correct(i.e. Eq. (3)). Thus under this assumption, the stress τ can be represented exactly in terms of the strain and rotation rate tensors, provided the coefficients C_i are known functions of the invariants listed in Eq. (12). The functional form of the dependence on the invariants is unknown, however, and can not be determined easily. If the assumption that the stress is expressible solely as a function of the strain and rotation rates is not correct, then the coefficients will be functions of the unknown quantities on which the stress really depends. In either case, it can be anticipated that it will be difficult to predict the spatial variation of the expansion coefficients.

In the context of modeling, the expansion coefficients would most likely be assigned constant values that reflect an overall "best-fit" for all points in the field. If the true coefficient values do not vary greatly in space, then taking them to be constant will be a reasonable approximation and a good representation of the stresses can be expected. On the other hand, if the coefficients vary greatly in space, then taking them to be constant would be a poor approximation and the model would be of little value. Thus, in practical terms, the utility of this approach depends on the

degree to which the expansion coefficients vary or, alternately, how well Eq. (11) is satisfied for fixed coefficients.

The issue of coefficient variability was investigated through the use of direct numerical simulation (DNS) data of homogeneous, isotropic turbulence. By filtering the DNS field with a spectral cutoff filter, the subgrid-scale stress, as well as the "resolved" strain and rotation rates were computed exactly. The accuracy of Eq. (11) was then measured in two alternate ways: (1) by determining the expansion coefficients exactly at each grid point and then measuring their spatial variation and (2) by measuring the degree to which Eq. (11) was satisfied when the coefficients were assigned constant values.

The homogeneous, isotropic data was generated with a pseudo-spectral code (Rogallo, (1981) on a 128^3 mesh. The energy spectrum was initialized according to

$$E(k) = \frac{1}{32}\left(\frac{k}{2}\right)^4 \exp\left(-\frac{k}{2}\right). \tag{13}$$

This spectrum has its energy peak at wavenumber 8. The initial phases were chosen randomly, but in such a way that the divergence-free condition was satisfied (see Rogallo, (1981) for more details on the initial conditions). The flow was allowed to evolve freely for 2.9 small scale eddy turnover times, $\frac{\lambda}{u'}$ where λ is the Taylor microscale and u' is the rms turbulence intensity, both based on the final field. Over this period of time, the total turbulent kinetic energy decayed by 33%. The final Taylor microscale Reynolds number $(u'\lambda/\nu)$ was 45.3, and the velocity derivative skewness was -0.32. The final energy spectrum, scaled in Kolmogorov units, is plotted in Figure 1.

Also shown in Figure 1 are the experimental data of Comte-Bellot and Corrsin (1971). The simulation results fit well with the experimental data. The tail-up in the simulated spectrum at high wavenumbers is a characteristic of spectral methods and is more pronounced when the dissipation range is not fully resolved, as in this case. It is generally felt (Rogallo, private communication) that the tail-up at high wavenumber will not adversely affect the data in the central portion of the spectrum used here.

Following the procedure of Clark *et al.*(1975), a synthetic LES velocity field was generated from the DNS data by filtering out the small scale motions. The filtering was achieved via spherical truncation in wave space where three quarters of the active high frequency modes were removed. The LES field thus corresponded to an isotropic simulation performed on a $128/4 = 32$ cubed mesh. Denoting the filtering operation with an overbar, the subgrid-scale stress was determined by performing the operations in the de-aliased definition commonly used in spectral calculations,

$$\tau_{ij} = \overline{u_i u_j} - \overline{\bar{u}_i \bar{u}_j}. \tag{14}$$

The large scale strain and rotation rate tensors defined in Eq. (4) were determined by applying spectral derivative operators to the LES velocity field.

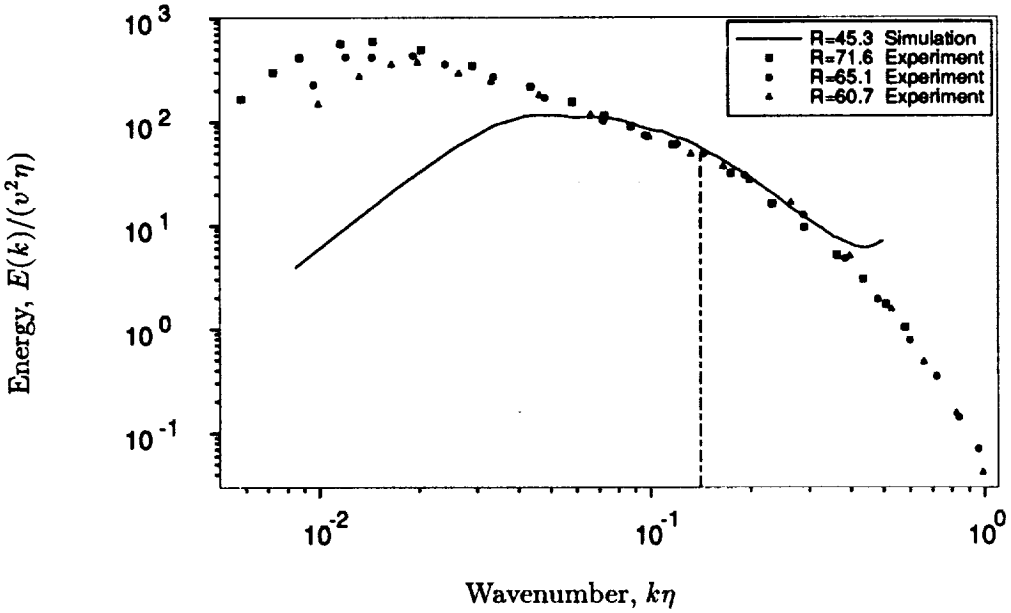

FIGURE 1. Energy spectrum from the DNS data base. The experimental data are taken from Comte-Bellot and Corrsin (1971). The vertical line corresponds to the scale at which the velocity field was filtered to generate the synthetic LES field.

2.3 Analysis for variable coefficients

With the subgrid-scale stress and the large scale strain and rotation rate tensors known, the expansion coefficients in Eq. (11) could be determined at each point in the field. This was done using a least-squares fitting procedure so that solutions could be obtained when less than all five of the tensors on the right hand side of Eq. (11) were used. To derive the least-squares expression, consider the error in satisfying Eq. (11) when an arbitrary number of tensors are used:

$$\mathbf{E} = C_i \mathbf{m}_i - \boldsymbol{\tau}, \tag{15}$$

where $\mathbf{m}_i$ are the model tensors on the right hand side of Eq. (11), and $i = 1, 2, ...n$; $1 \leq n \leq 5$. The square of the error will be minimized with respect to the C_i if the following condition is enforced

$$\frac{\partial}{\partial C_i} \mathrm{tr}\,(\mathbf{E}^2) = 0. \tag{16}$$

This condition leads to the following algebraic system for the coefficients:

$$C_i = [\mathrm{tr}\,(\mathbf{m}_i \mathbf{m}_j)]^{-1} \mathrm{tr}\,(\mathbf{m}_j \boldsymbol{\tau}). \tag{17}$$

If less than 5 model tensors are used, the subgrid-scale stress can not be represented exactly by Eq. (11). The following quantities are global measures of the error in this case:

$$\eta = \frac{< \mathrm{tr}\,(\boldsymbol{\tau}\mathbf{M}) >}{\sqrt{< \mathrm{tr}\,(\boldsymbol{\tau}^2) >< \mathrm{tr}\,(\mathbf{M}^2) >}}, \tag{18}$$

$$e_\tau = \sqrt{\frac{< \mathrm{tr}\left((\boldsymbol{\tau} - \mathbf{M})^2\right) >}{< \mathrm{tr}(\boldsymbol{\tau}^2) >}}, \tag{19}$$

where $\mathbf{M} = C_i \mathbf{m}_i$ is the composite model tensor and $<>$ denotes a volume average. The quantity η is the correlation coefficient between the exact and modeled stress, while e_τ is the rms error in the subgrid-scale stress. It is easy to show that η and e_τ are related via $e_\tau = \sqrt{1 - \eta^2}$. The variability of the coefficients themselves was measured in terms of the ratio of rms to mean value:

$$C_{rms} = \frac{\sqrt{< C^2 > - < C >^2}}{< C >}. \tag{20}$$

2.3.1 Results

As a first step, each of the 5 terms in Eq. (11) was considered separately. Measures of the error as well as coefficient variability were recorded for each term. Next, the 10 possible pairs of terms in Eq. (11) were investigated. The 10 possible triplets, the 5 possible quadruplets, and finally all 5 terms together were tested. For each of the groupings, the combinations that resulted in the highest as well as the lowest correlation coefficients were selected for further study. Figure 2 shows these correlation coefficients as a function of the number of terms in the group. As expected, the correlation coefficient rises as more terms are added and is unity if all five terms are present. The differences between the best and worst correlation coefficients are rather slight, indicating that none of the terms are neither far superior nor far inferior to the rest. The terms forming the best and worst subsets are listed in Table 1.

Number of terms	Best combination	Worst combination
1	1	3
2	1, 4	2, 3
3	1, 4, 5	3, 4, 5
4	1, 2, 4, 5	2, 3, 4, 5
5	1, 2, 3, 4, 5	1, 2, 3, 4, 5

TABLE 1. Best and worst subsets of the model terms in Eq. (11) - variable coefficients.

Although the differences between correlation coefficients obtained with the best and worst groupings are slight, there are some consistent trends if the terms are ranked by their relative importance. The best single term is term 1, which corresponds to the Smagorinsky model. This term is present in each of the optimal

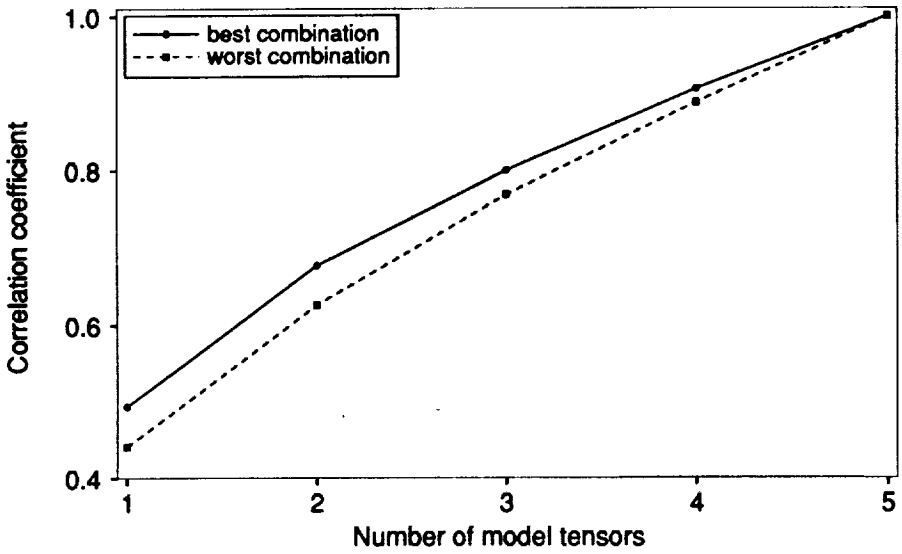

FIGURE 2. Correlation coefficients for the best and worst subsets of the terms in Eq. (11) - variable coefficients.

groupings. The worst single term is the rotation rate squared (term 3). This term is also the last one to enter in the optimal groupings. Most of the intermediate terms follow the general trend that if they enter the optimal groupings when n terms are present, then they enter the worst grouping when $5 - n$ terms are used.

Although ranking the various combinations of terms by their correlation coefficients is interesting, the more important issue is spatial variability of the corresponding expansion coefficients. The ratio of the coefficient rms to the coefficient mean for the optimal groupings of terms is shown in Figure 3. It is clear that a substantial variation in each coefficient is required to achieve the least-squares fit. If only one term is included, the coefficient variation is roughly three times the mean. As more terms are included, the variation rapidly increases. When all five terms are included, the coefficient variation is enormous, ranging from roughly 10 times the mean for C_1 to over 500 times the mean for C_3.

The rather large coefficient variation could in part be due to the the neglected dependence on the invariants listed in Eq. (12). It is conceivable that if this dependence were taken into account, the coefficient variability could be reduced. This issue is explored in the following section.

2.4 Dependence on the invariants

Each of the expansion coefficients in Eq. (11) can, in principal, depend of the five invariants listed in Eq. (12). Determining such a dependence in a five parameter space is a difficult task, however. One way to do this would be to divide the range of each invariant into m intervals, thereby partitioning the parameter space into m^5

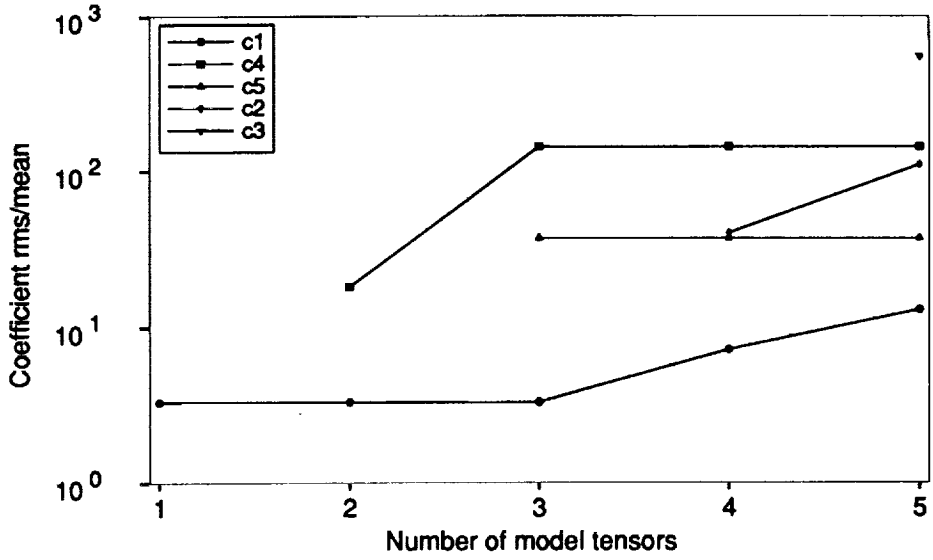

FIGURE 3. Coefficient variability for optimal subsets of the terms in Eq. (11).

hypercubes. Using the DNS data, the coefficients could then be sorted according to their associated invariant values and the resulting sample averaged over each hypercube. Unfortunately, this procedure requires an enormous amount of data if reliable statistics are to be obtained. As an illustration, consider the following example. If 16 intervals are chosen for the discretization and a 128^3 DNS data base is used, there will be on the average only $128^3/16^5 = 2$ samples within each hypercube. This sample is clearly too small to provide meaningful statistics. Furthermore, it may be anticipated that many of the cubes will contain no data at all. If a larger data base or more realizations are used and if the number of intervals is reduced, it may be possible to obtain reliable statistics. If this were done, the difficult task of fitting the statistical data with some sort of multidimensional function would still remain.

In view of these difficulties, two alternate approaches have been adopted here. In the first, the number of invariants was reduced to one by assuming that the stress depended only on the strain rate. The local smoothing procedure described above was used in this case since the sample size was large and the resulting one-dimensional function could be easily curve fit. In the second approach, the full problem was considered and a sophisticated regression algorithm was used to find any dependence as well as its associated functional form.

2.4.1 Dependence on a single invariant

The question of dependence on the invariants can be answered completely if it is first assumed that the stress depends only on the strain rate. In this case, the Caley-Hamilton theorem states that the stress can be explicitly written as a linear

combination of $\mathbf{S}$, $\mathbf{S}^2$, and $\mathbf{I}$ (all higher powers of $\mathbf{S}$ are related to these three terms). If only the deviatoric part of $\boldsymbol{\tau}$ is to be modeled, then only $\mathbf{S}$ and $(\mathbf{S}^2)^*$ are required. Thus Eq. (11) reduces to first two terms in this case. The corresponding coefficients, C_1 and C_2, could depend at most on the invariant s_1 listed in Eq. (12).

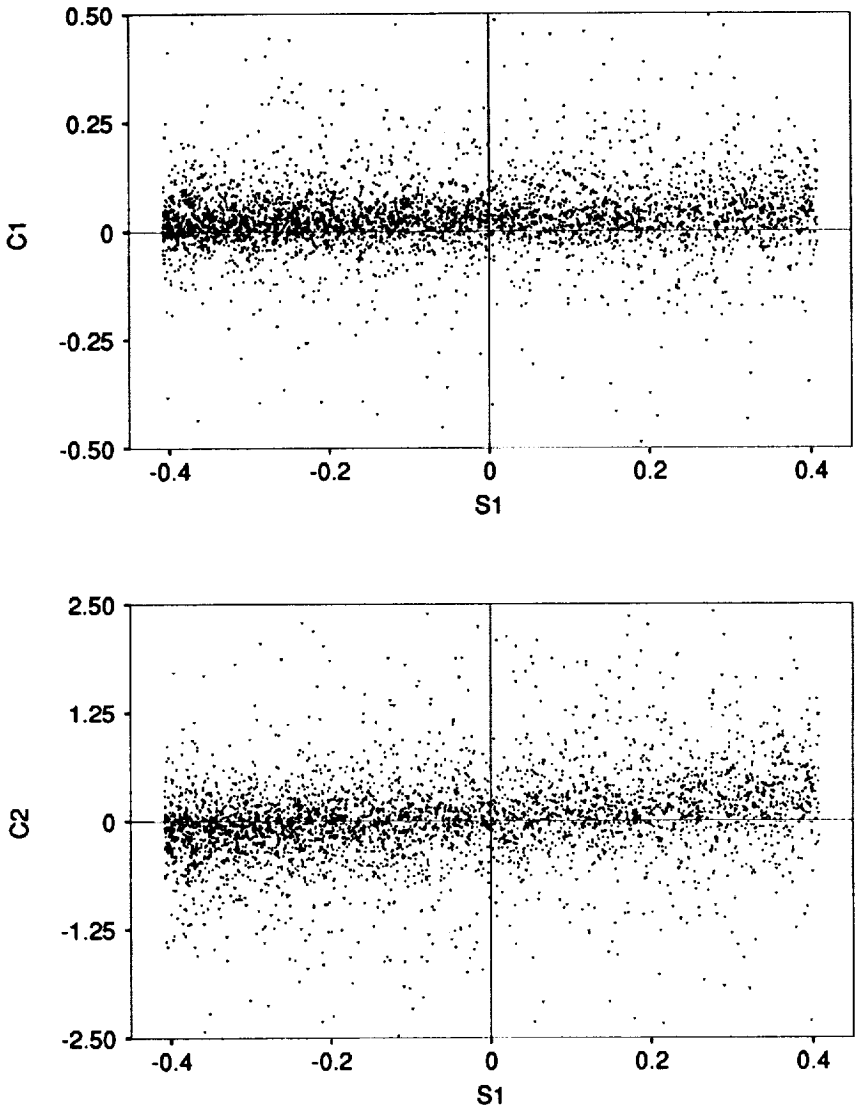

FIGURE 4. Scatter plot of model coefficients versus the invariant s_1. Only every 8^{th} data point in each direction is plotted.

This abbreviated model was tested as in section 2.3, with the coefficients determined locally. The resulting coefficients are plotted as a function of the associated

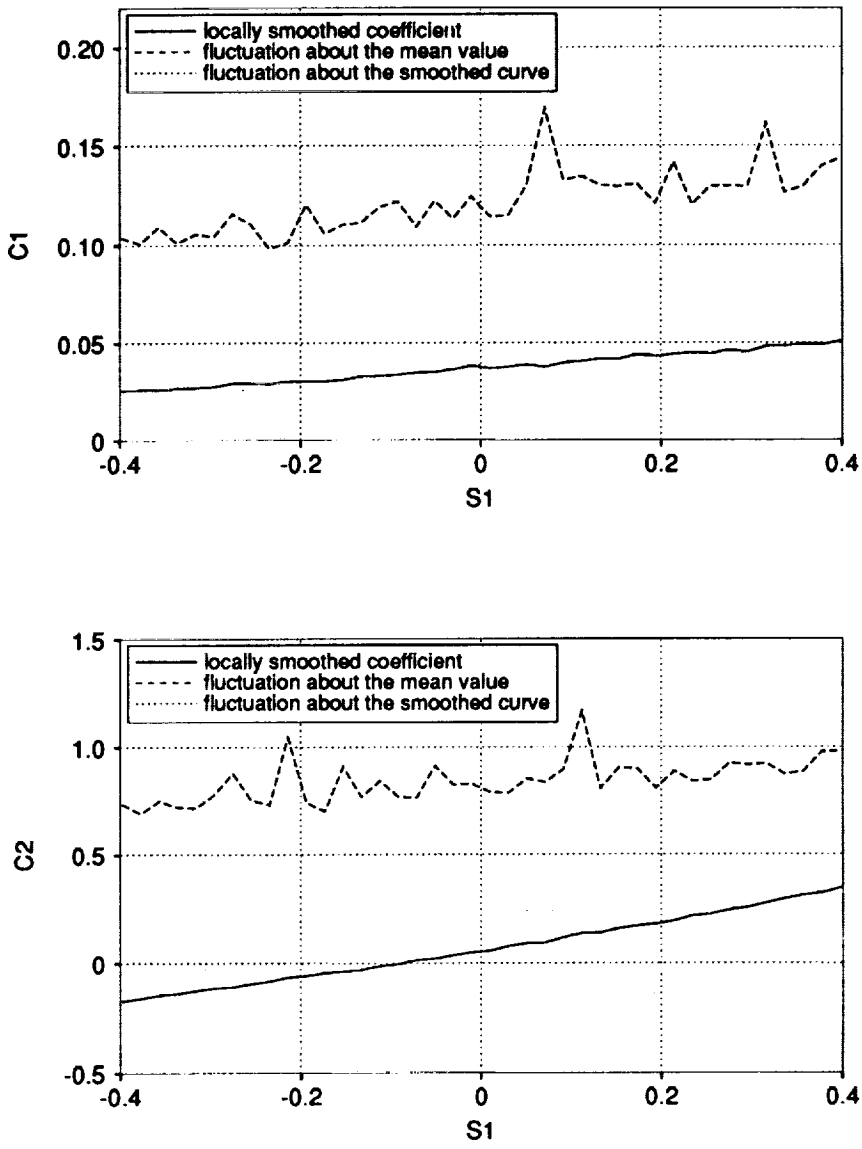

FIGURE 5. Model coefficient conditionally averaged on invariant s_1.

invariant value in Figure 4. There does not seem to be any strong dependence on the invariant in either case. If the raw data are averaged over narrow intervals in s_1, however, a weak trend emerges. The results of such an averaging are shown in Figure 5. It appears that both C_1 and C_2 depend linearly on the invariant s_1. Also shown in Figure 5 is the rms fluctuation of the data about the smoothed curve as

well as the rms fluctuation about the coefficient mean value. There is no visible reduction in the fluctuation level if the dependence on the invariant is accounted for. Thus while a clear dependence on the invariant was found, it accounts for vary little of the coefficient variation.

2.4.2 Dependence on all five invariants: Projection pursuit regression

Although the local smoothing procedure described in Section 2.4 does not seem suitable for this problem, there are other numerical methods that can perform multi-variable regression, even for a moderate sample size. Perhaps the best of these methods is the projection pursuit regression algorithm developed by Friedman and Stuetzle in 1981. The algorithm consists of a numerical optimization routine that finds one dimensional projections of the original independent variables for which the best correlations with the dependent variable can be obtained. The dependent variable is then written as a sum of empirically determined functions of these projections. The method is quite robust and has been able to determine nonlinear relationships within a 5 parameter space using only 213 realizations (see Friedman and Stuetzle (1982) for more details and examples). The method has also been used by Meneveau *et al.* (1992) to search DNS data for improved subgrid-scale model parameterizations.

The projection pursuit algorithm was used to search for coefficient dependence on the five invariants. The DNS data was used to determine the five expansion coefficients and five invariants at each point in the field. This data was then input to the projection pursuit algorithm and each coefficient was analyzed independently. For each coefficient, the numerical optimization routine was able to find projections for which the variance was minimized, but the reduction in variance never exceeded 2%. Furthermore, the empirically determined functions of the invariants did not appear to have recognizable structure and contained many oscillations. This type of behavior is often an indication that the algorithm has only found a local minimum in field of noise.

The results of the projection pursuit regression are consistent with the results presented in the previous section where the dependence on a single invariant was investigated. In both cases, the coefficients do appear to depend on the invariants, but that dependence is extremely weak. Accounting for this weak dependence on the invariants does not significantly reduce the coefficient spatial variation and thus is probably not worth pursuing further. More importantly, the large coefficient variation does not appear to be related to neglected dependence on the invariants, but rather to a weakness in the assumption that the subgrid-scale stress is solely a function of the velocity gradient.

2.5 Analysis for constant coefficients

In this section, we explore the accuracy of Eq. (11) when the coefficients are assumed to be constant in space. The constants are again determined through a least-squares procedure, this time minimizing the global error rather than the local error. The derivation of the global least-squares procedure is identical to that outlined in section 2.3, with the exception that the error is averaged over the domain

before it is differentiated with respect to the C_i. The end result is an expression analogous to Eq. (12):

$$C_i = < \mathrm{tr}(\mathbf{m}_i\mathbf{m}_j) >^{-1} < \mathrm{tr}(\mathbf{m}_j\boldsymbol{\tau}) >, \tag{21}$$

where <> indicates a spatial average. It is important to note that when the coefficients are determined globally, there will be non-zero error even when all five terms in Eq. (11) are used.

2.5.1 Results

As in section 2.3.1, all possible combinations of the various terms in Eq. (11) were tested. The correlation coefficients for the best and worst combinations of terms are shown in Figure 6. The actual terms corresponding to these groupings are listed in Table 2.

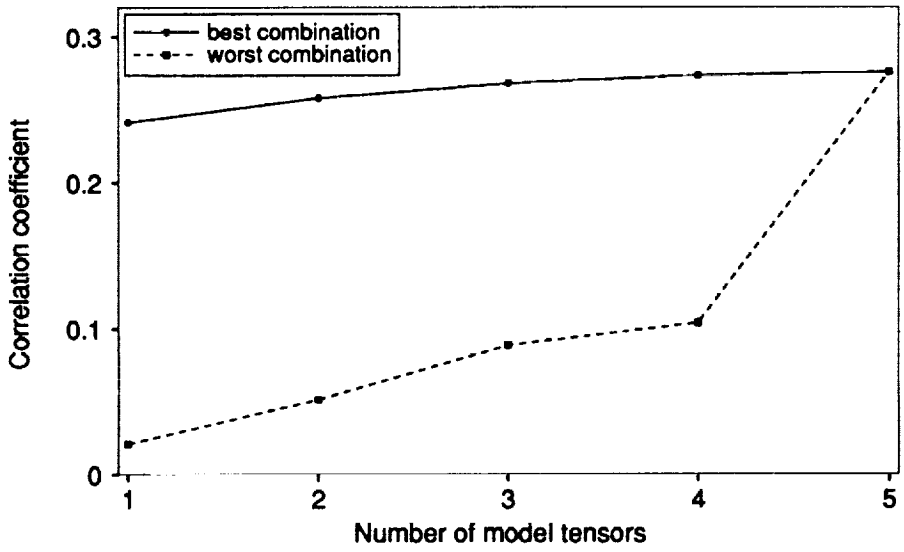

FIGURE 6. Correlation coefficients for the best and worst subsets of the terms in Eq. (11) - constant coefficients.

The best single term is again term 1, the Smagorinsky model. The correlation coefficient of the optimal groups increases as more terms are added, but the improvement is rather slight (15% increase from 1 to 5 terms). The optimal correlation coefficients also are rather low, never exceeding 0.28. In light of the slow increase with additional model terms, it appears that terms 2 through 5 are not nearly as important as the Smagorinsky model. This conclusion can also be drawn from the results for the worst groupings. The correlation coefficients for the worst groupings are far inferior to those of the best groupings, even when 4 terms are used. The Smagorinsky model is the last one to be added to the worst groupings, and the

Number of terms	Best combination	Worst combination
1	1	2
2	1, 2	2, 3
3	1, 2, 5	2, 3, 4
4	1, 2, 4, 5	2, 3, 4, 5
5	1, 2, 3, 4, 5	1, 2, 3, 4, 5

TABLE 2. Best and worst subsets of the model terms in Eq. (11) - constant coefficients.

correlation coefficient is seen to more double when this term is added (transition from 4 to 5 terms).

It is interesting to compare the results for variable and fixed coefficients (Figures 2 and 6). Several differences are readily apparent. The level of correlation is much lower in the case of fixed coefficients; if only a single term is used, the correlation coefficient for a constant coefficient is about one half the value obtained with a variable coefficient. As more terms are added, the correlation improves steadily when the coefficients are variable, but improves little if the coefficients are constant. In the variable coefficient case, there is little to choose between the best and worst groupings, whereas in the constant coefficient case, the differences are substantial. Overall, the variable coefficient results are much better than those for fixed coefficients.

The differences between the variable coefficient and constant coefficient results are due to differences in the scope of the minimization in the least-squares formulation. When the coefficients are allowed to vary in space, the error is minimized at each mesh point. This local minimization yields MN^3 degrees of freedom, where M is the number of model terms used and N^3 is the number of mesh points. When the coefficients are fixed in space, the error is minimized globally, and only M degrees of freedom are available. Evidently, the extra degrees of freedom are well utilized in the variable coefficient case, and superior correlations are obtained. At the same time, the additional degrees of freedom result in coefficients that vary greatly in space (recall Figure 3). This spatial dependence would be unknown in an actual LES, and thus the results of Figure 2 could not be realized in practice. The negative impact of the large coefficient variation is accounted for in Figure 6, and these results could be expected in practice.

The large coefficient variation also has an important physical implication. If it were true that the subgrid-scale stress depended *only* on the velocity gradient tensor, then the expansion given in Eq. (11) would be complete. The coefficients could vary in space, but this variance would have to result from dependence on the invariants listed in Eq. (11). Since the coefficients are observed to vary and this

variation does not appear to be connected with the invariants, it must be true that the subgrid-scale stress at one point in space depends on more than the velocity gradient at the same point. While this conclusion might have been anticipated, the more relevant issue is to what extent the expansion in Eq. (11) captures the dependence of the subgrid-scale stresses on the resolved variables. In view of Figure 6 and Table 2, it is clear that the dominant term is the Smagorinsky model. The remaining terms in Eq. (11) appear to be of lesser importance. In fact, if all of the terms are used, the correlation is only 15% higher than with the Smagorinsky model. Thus, at least for homogeneous isotropic flow, the expansion in Eq. (11) does not seem to contain much of the physical mechanisms by which the large scales influence the small scales.

2.6 Summary

A tensor relationship between subgrid-scale stress and the velocity gradient tensor has been developed. This relationship takes the form of a series expansion involving products of the strain and rotation rate tensors. The expansion was used as a modeling hypothesis, and the latter was evaluated using direct numerical simulation data for homogeneous isotropic turbulence. The Smagorinsky model, which is one of the terms in the expansion, was found to be the dominant term. The remaining terms were found to be of lesser importance and, when included, did not significantly improve upon the Smagorinsky model. These results suggest that while the expansion is exact, the inherent assumption that the subgrid-scale stress depends only on the velocity gradient tensor is not well supported by the numerical simulation data for homogeneous isotropic turbulence at low Reynolds number.

3. Future plans

The conclusions drawn in the previous section apply only to homogeneous isotropic turbulence at low Reynolds number. Both the success of the model and the coefficient values could be Reynolds number dependent. This issue will be addressed by repeating the tests with higher Reynolds number DNS data. For this purpose, forced homogeneous isotropic simulation data is available with Reynolds number roughly four times greater than that used in the present study. In addition to Reynolds number effects, the success of the proposed model may be related to the flow situation. For example, it is quite possible that the model would work better in a shear flow where the effects of rotation are more pronounced. This possibility will be explored by testing the model with DNS data for homogeneous turbulent shear flow and for turbulent channel flow. If these results are sufficiently encouraging, the model will be used in an actual large eddy simulation and the results compared with experimental or DNS data. For the purpose of simulation, the procedure of §2.5 will be used to assign constant values to the expansion coefficients.

A separate attempt will be made to use the model in conjunction with the dynamic procedure of Ghosal *et al.*(this volume). In this procedure, information contained in the resolved field will be used to estimate the value of the expansion coefficients as a function of space and time. This approach has the potential to recover the accuracy displayed in Figure 2 since the coefficients will be free do develop

any arbitrary degree of variability.

Acknowledgements

In addition to support from the Center for Turbulence Research, this work was supported in part by the Air Force Office of Scientific Research, the Office of Naval Research, and the Department of Energy. TSL acknowledges support from the ONR under grant N00014-91-J-4072 and from the AFOSR under grant F49620-92-J-0003. EAN acknowledges support from the CTR, ONR and DOE.

REFERENCES

CLARK, R. A., FERZIGER, J. H., & REYNOLDS, W. C. 1979 Evaluation of subgrid-scale models using an accurately simulated turbulent flow. *J. Fluid Mech.* **91,** 1-16.

COMTE-BELLOT, G., & CORRSIN, S. 1971 Simple Eulerian time correlation of full and narrow-band velocity signals in grid-generated 'isotropic' turbulence. *J Fluid Mech.* **48,** 273-337.

FRIEDMAN J. H. & STUETZLE W. 1981 Projection pursuit regression. *J. Amer. Stat. Assoc.* **76,** 817

MENEVEAU, C. LUND, T. S., & MOIN, P. 1992 Search for subgrid-scale parameterization by projection pursuit regression. *Proceedings of the 1992 summer program,* CTR, Stanford Univ, 61-80.

MCMILLAN O. J. & FERZIGER J. H 1979 Direct testing of subgrid-scale models. *AIAA J.* **17,** 1340

PIPES, L. A. & HOVANESSIAN, A. 1969 *Matrix-computer methods in engineering,* J. Wiley & Sons.

PIOMELLI U., MOIN P. & FERZIGER J.H. 1988 Model consistency in large eddy simulation of turbulent channel flows. *Phys. Fluids.* **31,** 1884

POPE, S. B. 1975 A more general effective-viscosity hypothesis. *J. Fluid Mech.* **72,** 331-340.

RIVLIN, R. S. & ERICKSEN, J. L. 1955 Stress-deformation rates for isotropic materials. *Journal of Rational Mechanics and Analysis.* **4,** 323-425.

ROGALLO R. 1981 Numerical experiments in homogeneous turbulence. *NASA Tech. Mem.*, 81315.

SPENCER, A. J. M & RIVLIN, R. S. 1959 The theory of matrix polynomials and its application to the mechanics of isotropic continua. *Archive for Rational Mechanics and Analysis.* **2,** 309-336.

SMAGORINSKY, J. 1963 General circulation experiments with the primitive equations. *Mon. Weather Rev.* **91,** 99-164.

TENNEKES, H. & LUMLEY, J. L. 1972 *A first course in turbulence,* MIT Press.

Large eddy simulations of time-dependent and buoyancy-driven channel flows

By W. Cabot

1. Motivations and objectives

The dynamic subgrid-scale (SGS) model (Germano *et al.*, 1991; Lilly, 1992) has proven successful in the large-eddy simulation (LES) of several simple turbulent flows, e.g., in homogeneous, incompressible flow with passive scalars and homogeneous, compressible flow (Moin *et al.*, 1991); in transitional and steady plane-Pouiseille channel flow (Germano *et al.*, 1991); and in passive scalar transport in channel flow (Cabot, 1991; Cabot & Moin, 1991). The dynamic SGS model, using eddy viscosity and diffusivity models as a basis, determines the spatially and temporally varying coefficients by effectively extrapolating the SGS stress and heat flux from the small, resolved scale structure, thus allowing the SGS model to adapt to temporally varying flow conditions and solid boundaries. In contrast, standard SGS models require tuning of model constants and *ad hoc* damping functions at walls. In order to apply the dynamic SGS model to more complicated turbulent flows that arise in geophysical and astrophysical situations, one needs to determine if the dynamic SGS model can accurately model the effects of subgrid scales in flows with, e.g., thermal convection, compressibility, and rapid uniform or differential rotation.

The primary goal of this work has been to assess the performance of the dynamic SGS model in the LES of channel flows in a variety of situations, viz., in temporal development of channel flow turned by a transverse pressure gradient and especially in buoyancy-driven turbulent flows such as Rayleigh-Bénard and internally heated channel convection. For buoyancy-driven flows, there are additional buoyant terms that are possible in the base models, and one objective has been to determine if the dynamic SGS model results are sensitive to such terms. The ultimate goal is to determine the minimal base model needed in the dynamic SGS model to provide accurate results in flows with more complicated physical features. In addition, a program of direct numerical simulation (DNS) of fully compressible channel convection has been undertaken to determine stratification and compressibility effects. These simulations are intended to provide a comparative base for performing the LES of compressible (or highly stratified, pseudo-compressible) convection at high Reynolds number in the future.

2. Accomplishments

2.1 Large eddy simulation of time-dependent channel flow

The dynamic SGS model was used in the LES of fully turbulent channel flow driven by a uniform streamwise (x) pressure gradient that is suddenly turned by a transverse (z) pressure gradient 10 times larger. The DNS of this case was performed by Moin *et al.* (1990). They found, counterintuitively but consistent with

experimental results of three dimensional boundary layers, that the turbulence kinetic energy and shear production rate initially decrease and later recover. Until Durbin (1992, and in this volume), no Reynolds averaged type model had been able to reproduce this behavior.

The LES was performed with a spectral-Chebyshev code (Kim *et al.*, 1987) on a $32 \times 65 \times 32$ mesh in a $4\pi \times 2 \times 4\pi/3$ box (in units of channel half-width δ). The dynamic SGS model used a ratio of test to grid filter widths of 2 in the horizontal directions (using a sharp spectral-cutoff filter) and 1 in the normal (y) direction (i.e., no explicit filtering in y). Defining the effective filter width as $\Delta = (\Delta_x \Delta_y \Delta_z)^{1/3}$ gives a test to grid effective filter width ratio $\widehat{\Delta}/\Delta = 2^{2/3}$. A Smagorinsky (1963) eddy viscosity base model was used whose coefficient, assumed to be a function of y and time, was calculated at each time step by averaging over horizontal planes (see Cabot, 1991). An ensemble of temporally developing flows was approximated by initially generating 15 fully developed turbulent channel flow fields separated in time by a sufficient amount to make them statistically independent. The initial channel flow fields were developed for a friction Reynolds number ($Re_\tau = u_{\tau o}\delta/\nu$, where $u_{\tau o}$ is the initial friction speed and ν is the molecular viscosity) of 180. The 15 fields were simultaneously advanced in time from $t = 0$ to 1.2 (in units of $\delta/u_{\tau o}$), and statistics were generated for each field every Δt of 0.15 and averaged together. The statistics from this LES were in good qualitative and quantitative agreement with those from the DNS (Moin *et al.*, 1990), although the recovery in the turbulence kinetic energy in the LES occurred at a slightly later time than in the DNS.

To test if it was the SGS model that was responsible for these good results in the LES or if it was due merely to an accurate portrayal of the large-scale interactions, a DNS was computed on the same coarse grid. The initial fields for the time-dependent calculation were first run to statistical equilibrium on the coarse grid, rather than simply turning off the SGS model in the LES initial fields, in order to avoid spurious transients due to the sudden drop in effective viscosity. The initial statistics for the coarse DNS and LES cases are thus not the same. The results of the coarse DNS were for the most part found to be in qualitative agreement with the well resolved DNS results of Moin *et al.* (1990), but the quantitative agreement was substantially poorer than was found using the dynamic SGS model. Thus much of the "three-dimensional" response of the turned channel flow is contained in the large-scale interactions, but the finer details require the SGS model. The greatest disagreement was found in the temporal behavior of the total (resolved and SGS) dissipation rate (Figure 1), which is to be expected since it depends to a larger extent on the different treatment of the small scales. In the DNS of Moin *et al.* (1990) and the LES, the dissipation rate has a complicated behavior near the wall, initially decreasing at the wall but increasing farther out in the near-wall region; the wall dissipation eventually begins to recover at $t = 1.2$. In the coarse DNS, however, the dissipation rate (which begins at a substantially higher level at the wall than in the LES) decreases both at the wall and in the near-wall region with no sign of recovery at $t = 1.2$. Such inaccuracies in the energy rates likely lead to the quantitative discrepancies in the velocity statistics.

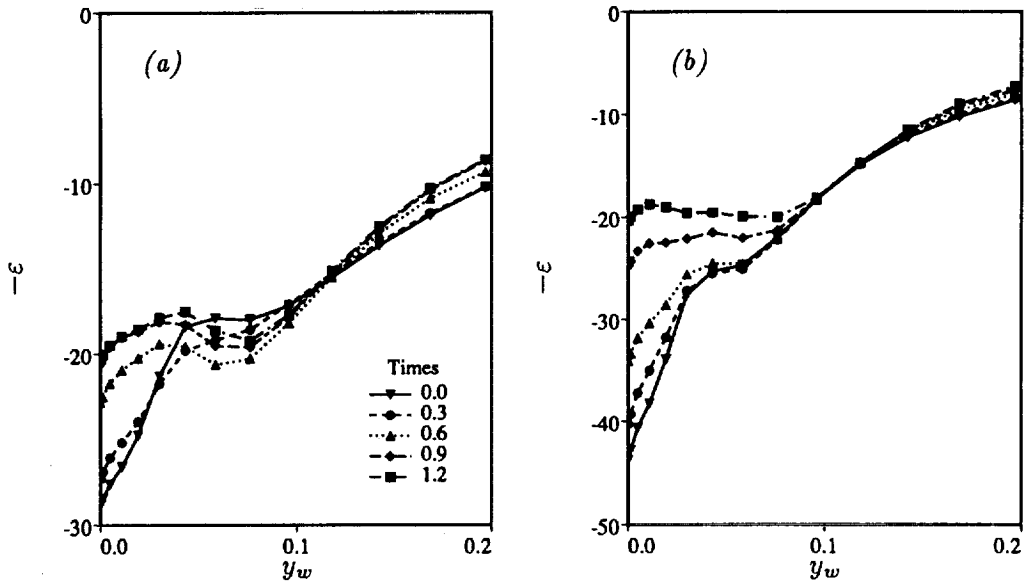

FIGURE 1. Total dissipation rates near the wall (plotted as the distance from the wall in units of δ) for channel flow turned by a transverse pressure gradient. (a) LES using the dynamic SGS model; (b) coarse DNS computed on the same grid.

2.2 Large eddy simulation of thermal convection

2.2.1 Base models

Simple eddy viscosity and diffusivity SGS models, with some near-wall corrections, are commonly used in the LES of thermal convection (see Nieuwstadt, 1990, for a recent review). Some modelers employ additional buoyancy corrections (e.g., Eidson, 1985; Mason, 1989; Schumann, 1991). The eddy viscosity and diffusivity models that I have used to date as the basis for the dynamic SGS procedure can be generalized in a form similar to Schumann's (1991) "first-order" SGS model, which is a vast simplification of more general, second-order, Reynolds-stress-like equations. The model for the residual SGS Reynolds stress at an arbitrary filter level is

$$\tau - \tfrac{1}{3}\mathrm{Tr}(\tau)\mathbf{I} = -2\nu_t \mathbf{S} = -2C_\nu \Delta^2 \sigma \mathbf{S}\,, \tag{1}$$

where $\mathbf{I}$ is the identity tensor, C_ν is the coefficient of the eddy viscosity ν_t, Δ is the effective filter width, and $\mathbf{S}$ is the strain rate tensor; σ is a scale rate defined below. The residual heat (or scalar) flux is modeled by

$$\mathbf{h} = -C_\alpha \Delta^2 \sigma \mathcal{B} \cdot \nabla\theta\,, \quad \mathcal{B} = \mathbf{I} + c_2 \boldsymbol{\beta}\nabla\theta/(\sigma^2 - c_2 N_c^2)\,, \tag{2}$$

where C_α is the eddy diffusivity coefficient, θ is the potential temperature, $\boldsymbol{\beta}$ is the buoyancy vector (gravity times thermal expansion coefficient), and $N_c^2 = \boldsymbol{\beta} \cdot \nabla\theta$. The scale rate σ is given, from SGS energy production = dissipation arguments, by

$$\sigma^2 = \tfrac{1}{2}\left[S^2 + (c_1 + c_2)N_c^2\right] + \left\{\tfrac{1}{4}\left[S^2 + (c_1 - c_2)N_c^2\right]^2 + c_1 c_2 N_m^4\right\}^{1/2}, \tag{3}$$

where $S^2 = 2\mathbf{S} : \mathbf{S}$ and $N_m^4 = (\boldsymbol{\beta} \cdot \boldsymbol{\beta})(\nabla\theta \cdot \nabla\theta)$. The constant or coefficient c_1 is, in principle, $C_\alpha/C_\nu = 1/\mathrm{Pr}_t$; c_2 is, in principle, related to the ratio of turbulent time scales of the velocity and potential temperature. Notice that (3) reduces to the normal Smagorinsky model scaling ($\sigma = S$) for no buoyancy ($\boldsymbol{\beta} = 0$) and that σ^2 and $\sigma^2 - c_2 N_c^2$ are positive semi-definite if $c_1 c_2 \geq 0$. Also notice that the residual heat flux in (2) is anisotropic with respect to $\nabla\theta$ for finite c_2 and $\boldsymbol{\beta}$, being enhanced in the direction of buoyancy forces. (Analogous anisotropic terms could be included in (1) by replacing $\mathbf{S}$ by $\boldsymbol{\mathcal{B}} \cdot \mathbf{S}$; but Schumann (1991) found that they led to realizability problems in his LES and so advocates dropping them.) For $c_2 = 0$, we can identify $\mathbf{h}$ with $-\alpha_t \nabla\theta$, where α_t is the eddy diffusivity.

The differences in the base models arise from different treatments of c_1 and c_2:

A. The "scalar" model has $c_1 = c_2 = 0$. C_ν and C_α are determined as functions of y and t by the dynamic test-filtering procedure. This is the model for the dynamic SGS model employed by Moin *et al.* (1991) and Cabot & Moin (1991). I have applied it to Rayleigh-Bénard convection.

B. The "buoyancy" model has c_1 as a coefficient equated consistently with $C_\alpha/C_\nu = 1/\mathrm{Pr}_t$ and $c_2 = 0$ (isotropic eddy diffusivity). This requires an iterative solution of the eddy coefficients (Cabot, 1991) with a Newton's (secant) method. It has been applied to Rayleigh-Bénard convection and low-Pr internally heated channel convection.

C. The "Eidson" model, after Eidson's (1985) SGS model, is the same as B but with c_1 taken as a constant (2.5) corresponding to his best value of $\mathrm{Pr}_t = 0.4$ for the LES of Rayleigh-Bénard convection. C_ν and C_α are determined, as in model A, with the dynamic procedure. I have applied this model to internally heated channel convection.

D. The "Schumann" model has c_1 and c_2 taken as constants (2.5 and 3.0, respectively, which are near Schumann's (1991) best values for the LES of planetary boundary layers). C_ν and C_α are determined, as in model A, with the dynamic procedure. This model has been applied to high-Pr internally heated channel convection.

2.2.2 LES of Rayleigh-Bénard convection

Large eddy simulations of Rayleigh-Bénard convection were performed with a spectral-finite difference code (Piomelli *et al.*, 1987) with the dynamic SGS model using base models A and B, the same filters as described in §2.1, and a mesh of $32 \times 63 \times 32$. The molecular Prandtl number Pr was taken as 0.71 (air), and Rayleigh numbers $\mathrm{Ra} = 8|\boldsymbol{\beta}\Delta\Theta|\delta^3/\nu\alpha$ (where $\Delta\Theta$ is the wall-to-wall mean potential temperature difference) of 6.25×10^5, 2.5×10^6, and 1×10^7 were considered with horizontal-to-vertical aspect ratios of 5, 6, and 7, respectively.

The buoyant (B) base model was found to give very similar results to the scalar (A) base model without buoyancy production terms. This probably happened because the buoyancy term is generally less than, or at best comparable, to the strain term in (3) for this flow and because even with a different scaling the dynamic eddy viscosities and diffusivities tend to adjust to a similar level. The dynamic SGS model with the buoyant base model typically required only 2 or 3 iterations to determine the eddy coefficients consistently; this still doubled the computational

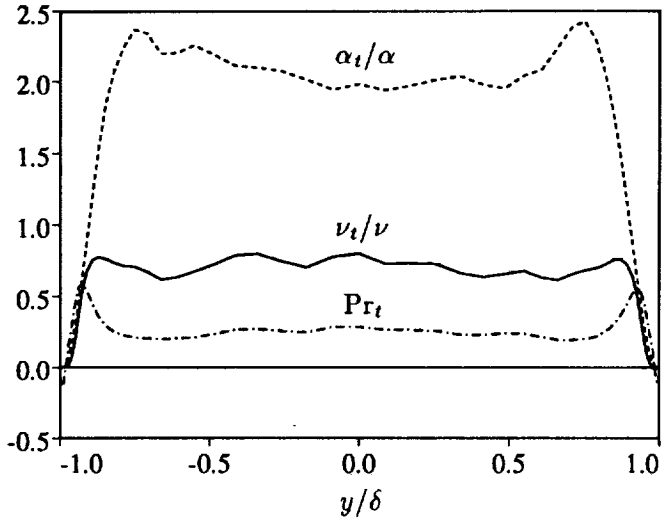

FIGURE 2. SGS eddy coefficients and Prandtl number from the LES of Rayleigh-Bénard convection with $\mathrm{Ra} = 1 \times 10^7$ and $\mathrm{Pr} = 0.71$ using the dynamic SGS model.

cost of the SGS model and, considering the little difference it made to the results, is probably not warranted. Occasionally the iteration scheme failed to find solutions at some planes, perhaps indicating that no real solutions existed. The scheme gave up after 10 iterations; but converged solutions were always found a few time steps later as flow conditions changed.

The SGS eddy viscosity and diffusivity using base model B are shown in Figure 2 with respect to their molecular values for the $\mathrm{Ra} = 1 \times 10^7$ case. Their fairly low values (of order 1 in the core) are a result of trying to resolve a reasonable amount of horizontal small scales near the wall. The dissipation due to the SGS model is comparable to that from the large scales in the core of the flow but becomes negligible near the wall. In fact, the eddy viscosity usually has small negative values in the viscous boundary layer though this has virtually no effect on the convective flow; it is not known if this is a real physical feature or an artifact of the poor horizontal resolution there. In contrast, the heat flux carried by the SGS model terms is negligible in the core of the flow but typically 20–30% of the total near the walls, which will affect the heat flux statistics. A concern is that the test filtering in the dynamic SGS model may not give accurate results near the wall since it usually samples in the energy-bearing part of the energy spectra there. The SGS Prandtl number is also shown in Figure 2. It is less than the standard value of about 0.4 (Eidson, 1985) in the core, where I find values of 0.20–0.25, but it becomes larger near the walls, reaching 0.6. Sullivan & Moeng (1992) found qualitatively similar results for Pr_t in an *a priori* test of a DNS field but at levels 3–4 times higher. They used, however, an effective filter width ratio of 4 (versus my $2^{2/3}$) and $\mathrm{Pr} = 1$; they also revamped the dynamic procedure in a way that gives only positive values of ν_t, so a direct comparison is difficult.

Large-scale statistics (such as rms velocity and potential temperature fluctuation intensities and velocity-temperature correlations) were found to be in good agreement with experimental measurements in air by Deardorff & Willis (1967) and Fitzjarrald (1976) and with previous LES results by Eidson (1985). The Nusselt numbers ($\mathrm{Nu} = 2\delta|\nabla\Theta|_w/\Delta\Theta$) of 7.7, 12.0, and 18.0 found for $\mathrm{Ra} = 6.25 \times 10^5$, 2.5×10^6, and 1×10^7 using the scalar (A) base model are about 5–10% higher than the experimental values reported by Fitzjarrald (1976) ($\mathrm{Nu} \approx 0.13\mathrm{Ra}^{0.30}$ in air) and Threlfall (1975) ($\mathrm{Nu} \approx 0.178\mathrm{Ra}^{0.280}$ in gaseous helium). A DNS for $\mathrm{Ra} = 6.25 \times 10^5$ with the same code gave $\mathrm{Nu} = 7.2$. A coarse DNS needs to be performed for one or more of these cases to determine the actual extent to which the SGS model improves the results.

2.2.3 LES of internally heated channel convection

Turbulent channel convection in water ($\mathrm{Pr} \approx 6$) with uniform volumetric heat sources and cooled, no-slip walls has been examined experimentally by Kulacki & Goldstein (1972) and numerically by Grötzbach (1982). This flow is asymmetric about the midchannel: the upper part of the channel is convectively unstable and the lower part is stable. The convective heat flux in the fully developed flow is typically downgradient in the exterior regions and countergradient in the interior. Because of this inherent asymmetry, the LES of this flow is expected to be more sensitive to the SGS model; it also allows us to test the behavior of the dynamic SGS model in transition from unstable to stable regions.

Large eddy simulations were performed with a spectral-Chebyshev code (Kim *et al.*, 1987) for $\mathrm{Pr} = 0.2$ at $\mathrm{Ra} = 1.25 \times 10^5$ on a $32 \times 65 \times 32$ mesh and at $\mathrm{Ra} = 1.25 \times 10^6$ on a $32 \times 129 \times 32$ mesh, and for $\mathrm{Pr} = 6.0$ at $\mathrm{Ra} = 1.25 \times 10^5$ on a $32 \times 65 \times 32$ mesh. Here $\mathrm{Ra} \equiv |\beta|\dot{q}\delta^5/\alpha^2\nu$, where $\dot{q}$ is the thermometric heating rate. All simulations used a horizontal-to-vertical aspect ratio of 4.

For the low-Pr runs, I used both the scalar (A) and buoyant (B) base models in the dynamic SGS model. Although there were some differences in the ν_t and α_t profiles for the low-Ra runs using different base models, the large-scale statistics were not particularly distinguishable. They shared the traits of having negative values of ν_t and/or α_t near the walls; and Pr_t had values of 0.1–0.2 in the upper convective region, growing to values near unity near the unstable upper wall and the lower, stable region. Nusselt numbers at the upper wall were found to be about 5% greater than in DNS results (O. Hubickyj & W. Cabot, unpublished). The profiles of ν_t and α_t with respect to molecular values and Pr_t are shown for the high-Ra case in Figure 3 using the buoyant (B) base model in the SGS model. Except in the narrow viscous boundary layers, ν_t and α_t are positive. In the core convective region ($y/\delta = -0.25$ to 0.75), Pr_t is about a constant 0.2 but grows to values of 1–2 in the near-upper-wall region and the stable lower channel. The eddy diffusivity remains positive throughout the center of the channel where the large-scale heat flux is countergradient; this means that the SGS heat flux is downgradient in this region, counter to the large-scale flow, and that α_t acts rather to dissipate thermal fluctuations. Since the vertical temperature gradient is small in the central region, however, the SGS heat flux is negligible there and only becomes significant in the

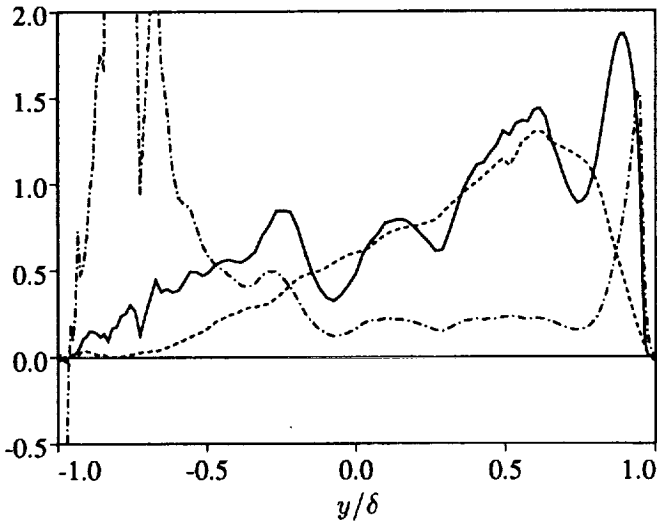

FIGURE 3. SGS eddy coefficients and Prandtl number from the LES of internally heated channel convection with Ra = 1.25×10^6 and Pr = 0.2 using the dynamic SGS model with the buoyancy base model. —— ν_t/ν, ---- α_t/α, —·— Pr_t.

near-upper-wall region, attaining 20-30% of the total heat flux as in the LES of Rayleigh-Bénard convection. The Nusselt numbers for this case are found to be about 10% higher than DNS results. (The large-scale statistics were again found to be fairly insensitive to the base model used.)

The LES with the buoyancy base model experienced significant iteration problems, most noticeable in the low-Pr, high-Ra run. Not only were there instances of failure to converge to a solution at some planes, more disturbingly there were clear instances when more than one solution existed and the values to which Pr_t converged depended on the initial guess. (I needed to average the initial guesses over adjacent planes to get reasonable answers.) On the other hand, the LES with the scalar base model gave a broad drop in ν_t in the upper convective region, in poor agreement with the previous model (see Figure 4). Better agreement was found using the Eidson (C) base model, which includes the buoyancy production term in a less consistent but cheaper way than the buoyancy base model. The choppiness in ν_t in Figure 4 may be due in part to some numerical instability from advancing the SGS terms explicitly in the code at too large a time step, but it may also stem from filtering only in planes and not in the vertical direction, which would probably smooth the results considerably.

For direct comparison with laboratory experiments, simulations with Pr = 6 have been recently undertaken. The eddy diffusivities from the Ra = 1.25×10^5 run using the Eidson (C) base model are shown in Figure 5a. The eddy viscosity and Pr_t are found to be negligible everywhere since the velocity in this case is almost completely resolved. However, near the upper wall I find $\mathrm{Pr}_t \approx 5$–7 (comparable to Pr). The eddy diffusivity in this case does have negative values in part of the

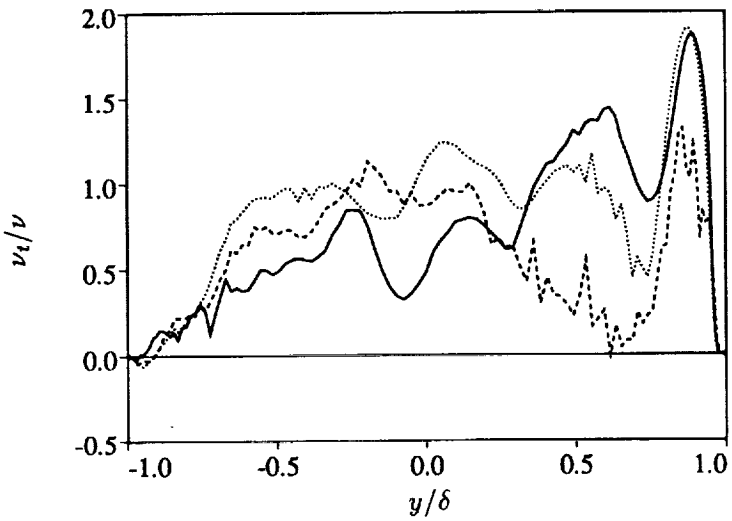

FIGURE 4. SGS eddy viscosity from the LES of internally heated channel convection with Ra = 1.25×10^6 and Pr = 0.2 using the dynamic SGS model with base model ---- A (scalar), —— B (buoyancy), and ····· C (Eidson).

central, countergradient region. Results using the Schumann (D) base model are also shown in Figure 5; α_t in this case is defined as $-\mathbf{h} \cdot \nabla\theta / \nabla\theta \cdot \nabla\theta$. Some minor differences in the central, countergradient region are noticeable. The residual heat flux resulting from these two models are shown in Figure 5b. It is seen that the Eidson base model only contributes to the heat flux in the upper convective region where the temperature gradient is appreciable while the Schumann base model contributes to the heat flux farther into the central region and gives comparatively more heat flux in the upper convective region due to the additional buoyancy term in Equation (2). Note that the SGS terms virtually vanish in the lower wall region where the flow becomes nearly laminar and that the dynamic SGS model allows a smooth transition between the turbulent and laminar regions. The LES results again tend to overestimate the Nusselt numbers by about 5% compared to DNS results; preliminary results indicate that coarse DNS computed on the same grid as LES overestimates Nu by more than twice as much. There is some discrepancy between experimental results (Kulacki & Goldstein, 1972) and numerical results (see Grötzbach, 1982), the former tending to give smaller Nusselt numbers and larger mean potential temperatures, the latter shown in Figure 6. The two different DNS results agree well but lie well below the experimental results; the LES results lie slightly below the DNS results (which make a fairer comparison).

2.2.4 Conclusions from LES results

The dynamic SGS model has been used in the LES of a number of buoyancy-driven flows with different eddy viscosity/diffusivity base models that do or do not include buoyancy terms. I tentatively conclude from the results so far that the

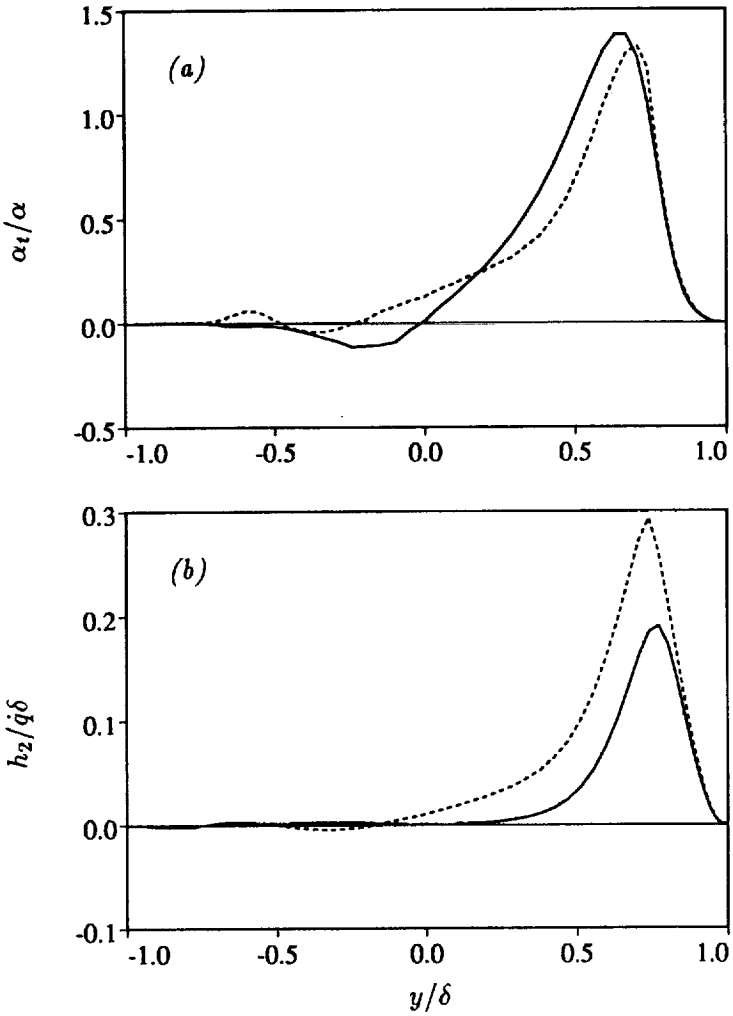

FIGURE 5. SGS (a) eddy diffusivity and (b) vertical heat flux from the LES of internally heated channel convection with Ra = 1.25×10^5 and Pr = 6 using the dynamic SGS model with base model —— C (Eidson) and ---- D (Schumann).

buoyancy base model, which requires the consistent (iterative) determination of Pr_t, is too computationally expensive and sometimes has either no real solution or multiple solutions. The "Eidson" base model, which simply sets Pr_t to a constant in the model scaling, seems to provide a cheaper alternative that generally reproduces the buoyancy model better than the scalar model. It is not clear yet that the "Schumann" base model confers any real advantage over the others although it can accommodate, in principle, the countergradient heat flux that occurs in internally heated channel convection.

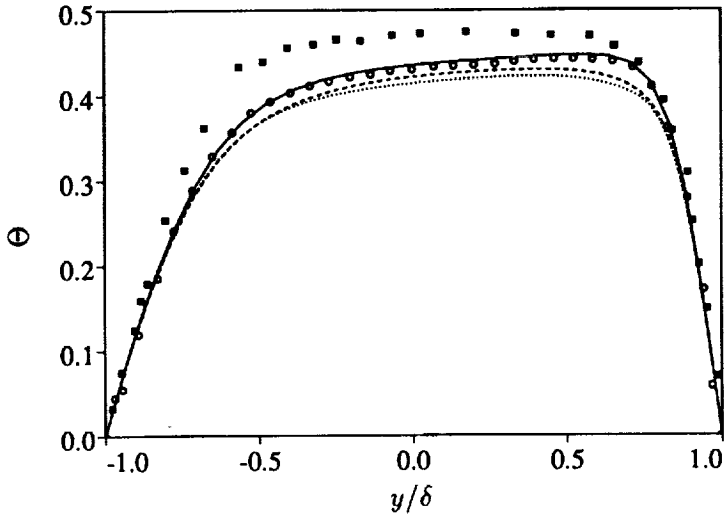

FIGURE 6. Mean potential temperature for internally heated channel convection with $\mathrm{Ra} = 1.25 \times 10^5$ and $\mathrm{Pr} = 6$. ■ experimental data (Kulacki & Goldstein, 1972), o DNS (Grötzbach, 1982), —— DNS (O. Hubickyj & W. Cabot, unpublished), ---- LES with base model C, and ····· LES with base model D.

2.3 DNS of fully compressible convection

Direct numerical simulations of fully compressible, internally heated channel convection were performed using a fourth-order, explicit, finite-difference code (Thompson, 1990, 1992a,b). Simulations were performed for several different density and temperature stratifications at $\mathrm{Ra} = 1.23 \times 10^5$ (defined at midchannel) and $\mathrm{Pr} = 0.2$ in a linearly varying gravity. Fixed temperature, no-stress (free-slip) boundary conditions are used at the walls. The no-stress, impermeable walls are meant to approximate free boundary conditions. For uniform volumetric heating rates, a mesh of $96 \times 33 \times 96$ and horizontal-to-vertical aspect ratios of 4 or 5 are used; for uniform specific heating rates, a mesh of $64 \times 65 \times 64$ and horizontal-to-vertical aspect ratios of 3 or 4 are used.

The mean potential temperature profile from a low stratification, low Mach number run was found to agree very well with the Boussinesq results of Cabot *et al.* (1990) for nearly the same values of Ra and Pr. For moderate to large density stratifications (central to wall ratios of a few to greater than 10) and moderate temperature stratification, the convection was found to be weaker due to the increase in viscosity and diffusivity (with inverse density) toward the walls; the Nusselt number was found to vary approximately as $\mathrm{Nu} - 1 \propto (\mathrm{Ra}^{1/4} - \mathrm{Ra}_c^{1/4})(\rho_w/\rho_c)^{3/4}$, where $\mathrm{Ra}_c \sim 1000$ is the critical Rayleigh number for the onset of convection. The interior rms Mach number was found to be typically 0.20–0.25, increasing to about 0.4 at the free-slip walls. Peak Mach numbers were found to be about 2.5 times the rms, and Mach numbers slightly in excess of unity were observed at the walls

in agreement with previous simulations by Malagoli *et al.* (1990). The compressible code did not require an additional high-order artificial damping built into it to compute these runs. Only weak shock features appeared to form because the high speed flows that form as the hot, rising interiors of convective cells expand horizontally along the walls tend to impinge on neighboring cells obliquely as the convergent flows plunge downward in cool, narrow downdrafts. Even a simulation with high temperature stratification (with central to wall ratio of ~ 30) with peak Mach numbers at the walls of 3.8 and occasional strong shock fronts was able to run a fair length of time without the artificial dissipation to damp two-delta waves, although it was eventually needed in this case.

The levels of fluctuations in thermodynamic quantities relative to their mean values are found to be consistent with those of Chan & Sofia (1989) for simulations of deep stellar convection. As in their work, the rms pressure fluctuations were found to be almost equal to the turbulence kinetic energy everywhere in the convective region so that the relative pressure fluctuations scale as rms Mach number squared. An examination of the terms in the equation governing the potential energy $P = \overline{p'^2}/2\gamma\bar{p}$ shows that they typically satisfy some of Zeman's (1991) assumptions for a compressible boundary layer. The steady-state equation for P gives

$$\underbrace{-(\bar{\mathbf{u}}\cdot\nabla P + 2\gamma P\nabla\cdot\bar{\mathbf{u}} + \frac{P}{\bar{p}}\bar{\mathbf{u}}\cdot\nabla\bar{p})}_{1} \underbrace{-\overline{p'\nabla\cdot\mathbf{u}'}}_{2} \underbrace{-\frac{1}{\gamma\bar{p}}\overline{p'\mathbf{u}'}\cdot\nabla\bar{p}}_{3}$$
$$\underbrace{-\frac{1}{\gamma\bar{p}}(\overline{p'\mathbf{u}'\cdot\nabla p'} + \gamma\overline{p'^2\nabla\cdot\mathbf{u}'})}_{4} + \underbrace{(\gamma-1)\frac{\overline{H'p'}}{\gamma\bar{p}}}_{5} = 0. \tag{4}$$

Here H is the net heating rate for the internal energy. As shown in Figure 7, term 3 is a production term due to the pressure flux, which is very nearly balanced by the pressure dilatation in term 2. The remaining terms are higher order in Mach number squared and are negligible in moderate Mach number flows. Even in the high Mach number case cited previously, term 2 cancelled 60% of term 3. The production in term 3 is controlled here primarily by buoyancy terms since the pressure flux is proportional to the convective heat (enthalpy) flux and the pressure gradient is proportional to gravity from hydrostatic equilibrium. For convection then, unlike Zeman's compressible boundary layer, the pressure flux should be modeled in terms of a thermal convection model, perhaps using the superadiabatic temperature gradient, rather than in terms of the normal density gradient.

Compressional effects only appear to be significant at the (artificial) walls in the fully convective channels. Simulations with uniform specific heating rates are currently under way that feature convectively stable exterior regions bounding a convective interior. These should provide a better basis for determining compressional effects in the freely bounded convection; it is likely that acoustic effects are more important in the convectively stable exterior. We are also currently exploring whether the use of soundproofed, pseudo-compressible governing equations (like

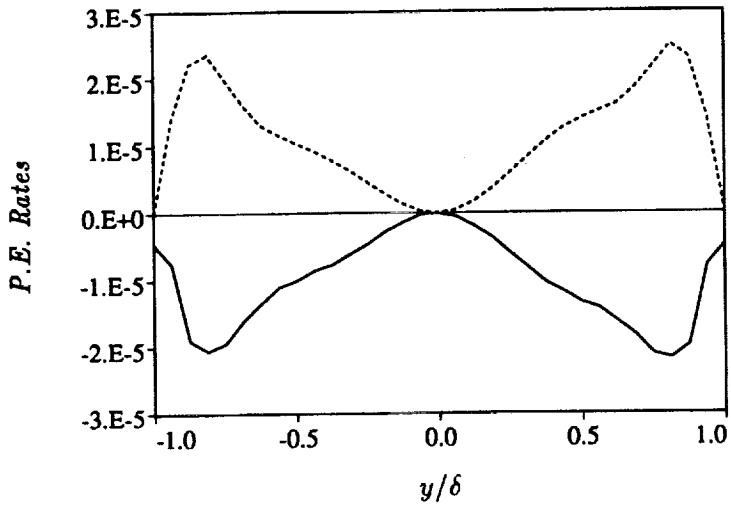

FIGURE 7. Potential energy rates from equation (4) in fully compressible channel convection with high density stratification: —— pressure dilatation (term 2) and ---- pressure flux production (term 3).

Durran, 1989) in the simulations of highly stratified convection would be acceptably accurate and more efficient than the fully compressible simulations.

3. Future plans

3.1 "One-equation" local dynamic subgrid-scale models in channel flow

Using locally defined coefficients from the dynamic SGS model has generally led to numerical instability due to persistent negative values of the SGS eddy viscosity. Ghosal, Lund & Moin in this volume (also see Wong, 1992) have proposed scaling the eddy viscosity with half of the trace of SGS residual stress ($k = \tau_{kk}/2$), which is evolved along with the flow. If the local k is driven to zero by negative eddy viscosities, the local eddy viscosity vanishes until k is replenished. This limits the duration of negative eddy viscosities and has been shown to stabilize calculations of homogeneous turbulence with local dynamic SGS modeling. We plan to implement this approach in channel flow. We also plan to implement Ghosal *et al.*'s variational approach to determine the local dynamic coefficients consistently.

An immediate problem arises in how to cast the k-equation to give proper behavior near and at the walls. Ghosal *et al.* use the form of a standard one-equation k-model with a SGS production term to evolve k at the grid-filter ($\bar{}$) level:

$$Dk/Dt = \nu_t \overline{S}^2 + \nabla \cdot [(\nu + \nu_D)\nabla k] - C_E k^{3/2}/\Delta\,, \tag{5}$$

where $\nu_t = C\Delta k^{1/2}$ is determined by the dynamic test-filtering procedure (in which C is determined locally) and $\nu_D = C_D \Delta k^{1/2}$ is the diffusive eddy viscosity. The constants or coefficients C_D and C_E remain to be specified; they could be preset

constants or be themselves determined by a dynamic fitting procedure. First, k properly goes to zero at a no-slip wall as y_w^2 (where y_w is the distance from the wall). Since (5) is a second-order equation, only two boundary conditions are needed, namely $k = 0$ at either wall, but this generally results in $k \propto y_w$ at the walls. Second, the $\nu\nabla^2 k$ term is generally finite at the wall, but it is difficult to make any other term in (5) balance it for plausible definitions of Δ, C_D, and C_E. (Note that ν_t in (5) always goes as y_w^3 from the dynamic model.) Both of these problems can be addressed (but not necessarily solved) if we consider evolving the equation for q (where $k = q^2/2$) and understand the last term in (5) to be the model for the reduced dissipation rate $\varepsilon'' = \varepsilon - \nu\nabla q \cdot \nabla q$, which goes as y_w^2 at the wall. The additional term $\nu\nabla q \cdot \nabla q$ must then be subtracted from $\nu\nabla^2 k$ in (5) to give $\nu q\nabla^2 q$, and the q-equation conveniently becomes

$$Dq/Dt = c\Delta\overline{S}^2 + \nabla \cdot [(\nu + c_d\Delta q)\nabla q] + c_d\Delta\nabla q \cdot \nabla q - c_e q^2/\Delta\,. \tag{6}$$

The lower case constants/coefficients in (6) differ from their upper case counterparts in (5) by various powers of $\sqrt{2}$. Note that there is an additional source term in (6) from the diffusion term in (5). But now the term $\nu\nabla^2 q$ is generally finite and unbalanced at the walls (unless, e.g., $c_d\Delta$ in the diffusive terms is made finite at the walls). However, even if this term is not balanced at the wall (in which case the numerical solution gives $q = \partial^2 q/\partial y^2 = 0$), one obtains the correct second-order asymptotic behavior for k at the wall ($k = \partial k/\partial y = 0$).

Tests of the sensitivity of the results to different treatments of the k- or q-equation will need to be made for the LES of channel flow. A further modification that has been made to the channel flow code is to use top-hat (real space averaging) filters in the horizontal directions to assure that the trace of the residual SGS stress at the test-filter level is positive definite (which is not necessarily the case for spectral-cutoff filters). Also, top-hat filtering will also eventually be implemented in the direction normal to the walls for consistency with simulations of homogeneous flows, albeit not strictly commutative with normal derivatives on the stretched grid used. It also appears that a scheme must be developed for treating points with vanishing or negative q since equation (6) may have realizability problems.

3.2 Further testing of the dynamic SGS model in thermal convection problems

More large eddy simulations of Rayleigh-Bénard and internally heated channel convection are needed to determine the optimal values of c_1 and c_2 in equations (1)–(3) for the base models of the dynamic SGS model with plane averaging. The computational expense of computing them consistently at each time step with the dynamic test-filtering procedure is prohibitive (and ill-defined at some points), but sample calculations might be used to establish reasonable constant or functional values. For example, the value of $\mathrm{Pr}_t = 1/c_1$ is found to about a constant 0.2 in the core of several convective flows when $c_2 = 0$ (although this may be a function of filter sizes and the molecular Prandtl number). Some corresponding coarse-grid direct numerical simulations are also needed to gauge the effect of the SGS models. Filtering in the vertical direction, not explicitly done heretofore in the channel codes,

will also be implemented. Results from these volume-filtered channel simulations will be compared with previous DNS and plane-filtered LES results. The effect of including Leonard stress terms, similar to the mixed Smagorinsky-Bardina model (Piomelli *et al.*, 1987), will also be tested; these terms are generally non-dissipative but provide a fairly realistic level of local forward and backward scatter.

More general base models for the subgrid scales are possible, especially in more complicated flows (e.g., with both buoyancy and rotation). Such models are being considered based on the governing equations for the residual Reynolds stress and heat flux, which closely resemble Reynolds stress equations for large-scale modeling (cf. Schumann, 1991). Dropping material derivative and diffusion terms, the governing equations for residual stress (τ), heat flux ($\mathbf{h}$), and temperature intensity squared (k_θ) are

$$\mathcal{A}\cdot\tau+\tau\cdot\mathcal{A}^\dagger+\beta\mathbf{h}+\mathbf{h}\beta=\Pi-2\epsilon, \tag{7}$$

$$\tau\cdot\nabla\theta+\mathcal{A}\cdot\mathbf{h}+\beta k_\theta=\Pi_\theta-2\epsilon_\theta, \tag{8}$$

$$\mathbf{h}\cdot\nabla\theta=-\varepsilon_{\theta\theta}, \tag{9}$$

where $\mathcal{A}$ comprises the velocity gradient tensor and the mean rotation tensor ($A_{ij}=u_{i,j}-2\Omega_\ell\epsilon_{ij\ell}$) and $\mathcal{A}^\dagger$ is its transpose. The right-hand sides of (7)–(9) involve pressure-strain terms (Π) and dissipation terms (ε) that must be modeled. A Smagorinsky model-like equation (1), for example, is recovered from (7) for standard return-to-isotropy models of Π and approximating the trace-free part of the left-hand side by $2\tau_{kk}\mathbf{S}/3$. The importance of the more general terms will be tested in *a priori* tests of DNS data. The need for explicit rotational terms in the dynamic SGS base model will be tested with the LES of some rotating flows. A base model with rotational effects might be based on the above equations with rotation entering through $\mathcal{A}$ and/or through the models for Π and ε.

The net amount of energy and dissipation that the dynamic SGS model can represent in channel flow has been limited due to the reduction of both normal and horizontal length scales near the no-slip walls, which causes the test filter to eliminate scales with a significant fraction of energy. Large eddy simulations for channel convection with no-stress walls will be performed in an attempt to improve on this situation. However, only flows with smaller scale disparity (freely bounded or with matching to near-wall solutions) will probably be able to use the dynamic SGS model efficiently at very high Reynolds numbers. Finally, we plan to implement the dynamic SGS model in our compressible convection simulations, starting with the form used in the LES of homogeneous compressible flow by Moin *et al.* (1991). The simulations now in progress with convectively stable exterior regions freely bounding the interior convective region should be more suitable for the dynamic SGS model by eliminating (or at least severely reducing) the amount of turbulence at the impermeable walls.

REFERENCES

CABOT, W. 1991 Large eddy simulations of passive and buoyant scalars with dynamic subgrid-scale models. In *CTR Annual Research Briefs 1991*, ed. P. Moin,

W. C. Reynolds, & J. Kim (Center for Turbulence Research, Stanford University/NASA Ames), pp. 191–205.

CABOT, W., & MOIN, P. 1991 Large eddy simulation of scalar transport with the dynamic subgrid-scale model. *CTR Manuscript 128,* (Center for Turbulence Research, Stanford University/NASA Ames). Also to appear (1992) in *Large Eddy Simulation of Complex Engineering and Geophysical Flows*, ed. B. Galperin & S. A. Orszag (Cambridge University Press).

CABOT, W., POLLACK, J. B., CASSEN, P., HUBICKYJ, O., & CANUTO, V. M. 1990 Direct numerical simulations of turbulent convection: I. Variable gravity and uniform rotation. *Geophys. Astrophys. Fluid Dyn.* **53,** 1–42.

CHAN, K. L., & SOFIA, S. 1989 Turbulent compressible convection in a deep atmosphere. IV. Results of three-dimensional computations. *Astrophys. J.* **336,** 1022–1040.

DEARDORFF, J. W., & WILLIS, G. E. 1967 Investigation of turbulent thermal convection between horizontal plates. *J. Fluid Mech.* **28,** 675–704.

DURBIN, P. A. 1992 On modeling three-dimensional wall layers. *CTR Manuscript 135,* (Center for Turbulence Research, Stanford University/NASA Ames).

DURRAN, D. R. 1989 Improving the anelastic approximation. *J. Atmos. Sci.* **46,** 1453–1461.

EIDSON, T. M. 1985 Numerical simulation of turbulent Rayleigh-Bénard convection using subgrid scale modeling. *J. Fluid Mech.* **158,** 245–268.

FITZJARRALD, D. E. 1976 An experimental study of turbulent convection in air. *J. Fluid Mech.* **73,** 693–719.

GERMANO, M., PIOMELLI, U., MOIN, P., & CABOT, W. H. 1991 A dynamic subgrid-scale eddy viscosity model. *Phys. Fluids A.* **3,** 1760–1765.

GRÖTZBACH, G. 1982 Direct numerical simulation of the turbulent momentum and heat transfer in an internally heated fluid layer. In *Heat Transfer 1982*, vol. 2, ed. U. Grigull, E. Hahne, K. Stephan & J. Straub (Hemisphere Publishing), pp. 141–146.

KIM, J., MOIN, P., & MOSER, R. 1987 Turbulence statistics in fully developed channel flow at low Reynolds number. *J. Fluid Mech.* **177,** 133–166.

KULACKI, F. A., & GOLDSTEIN, R. J. 1972 Thermal convection in a horizontal fluid layer with uniform volumetric energy sources. *J. Fluid Mech.* **55,** 271–287.

LILLY, D. 1992 A proposed modification of the Germano subgrid-scale closure method. *Phys. Fluids A.* **4,** 633–635.

MALAGOLI, A., CATTANEO, F., & BRUMMELL, N. H. 1990 Turbulent supersonic convection in three dimensions. *Astrophys. J.* **361,** L33–L36.

MASON, P. J. 1989 Large-eddy simulation of the convective atmospheric boundary layer. *J. Atmos. Sci.* **46,** 1492–1516.

MOIN, P., SHIH, T.-H., DRIVER, D., & MANSOUR, N. N. 1990 Direct numerical simulations of a three-dimensional turbulent boundary layer. *Phys. Fluids A.* **2,** 1846–1853.

MOIN, P., SQUIRES, K., CABOT, W., & LEE, S. 1991 A dynamic subgrid-scale model for compressible turbulence and scalar transport. *Phys. Fluids A.* **3,** 2746–2757.

NIEUWSTADT, F. T. M. 1990 Direct and large-eddy simulation of free convection. In *Heat Transfer 1990*, vol. 1, ed. G. Hetsroni (Hemisphere Publishing), pp. 37–47.

PIOMELLI, U., FERZIGER, J. H., & MOIN, P. 1987 Models for large eddy simulations of turbulent channel flows including transpiration. *Rep. TF-32, Dept. of Mech. Eng.* (Stanford University).

SCHUMANN, U. 1991 Subgrid length-scales for large-eddy simulation of stratified turbulence. *Theoret. Comput. Fluid Dyn.* **2,** 279–290.

SMAGORINSKY, J. 1963 General circulation experiments with the primitive equations. I. The basic experiment. *Mon. Weather Rev.* **91,** 99–164.

SULLIVAN, P. P., & MOENG, C.-H. 1992 An evaluation of the dynamic subgrid scale model in buoyancy driven flows (to be published).

THOMPSON, K. W. 1990 Turbulent transport in the solar nebula. In *CTR Annual Research Briefs 1989*, ed. P. Moin, W. C. Reynolds, & J. Kim (Center for Turbulence Research, Stanford University/NASA Ames), pp. 175–184.

THOMPSON, K. W. 1992a Numerical conservation properties of finite difference approximations. Submitted to *J. Comp. Phys.*

THOMPSON, K. W. 1992b High-order dissipation methods for the suppression of high-frequency numerical oscillations. Submitted to *J. Comp. Phys.*

THRELFALL, D. C. 1975 Free convection in low-temperature gaseous helium. *J. Fluid Mech.* **67,** 17–28.

WONG, V. C. 1992 A proposed statistical-dynamic closure method for the linear or nonlinear subgrid-scale stresses. *Phys. Fluids A.* **4,** 1080–1082.

ZEMAN, O. 1991 The role of pressure-dilatation correlation in rapidly compressed turbulence and in boundary layers. In *CTR Annual Research Briefs 1991*, ed. P. Moin, W. C. Reynolds, & J. Kim, (Center for Turbulence Research, Stanford University/NASA Ames), pp. 105–117.

A normal stress subgrid-scale eddy viscosity model in large eddy simulation

By K. Horiuti,[1] N. N. Mansour[2] AND J. Kim[2]

1. Motivation and objectives

The Smagorinsky subgrid-scale eddy viscosity model (SGS-EVM) is commonly used in large eddy simulations (LES) to represent the effects of the unresolved scales on the resolved scales. This model is known to be limited because its constant must be optimized in different flows, and it must be modified with a damping function to account for near-wall effects. The recent dynamic model (Germano *et al.* 1991) is designed to overcome these limitations but is compositionally intensive as compared to the traditional SGS-EVM. In a recent study using direct numerical simulation data, Horiuti (1993) has shown that these drawbacks are due mainly to the use of an improper velocity scale in the SGS-EVM. He also proposed the use of the subgrid-scale normal stress as a new velocity scale that was inspired by a high-order anisotropic representation model (Horiuti 1990). The testing of Horiuti (1993), however, was conducted using DNS data from a low Reynolds number channel flow simulation. It was felt that further testing at higher Reynolds numbers and also using different flows (other than wall-bounded shear flows) were necessary steps needed to establish the validity of the new model. This is the primary motivation of the present study. The objective is to test the new model using DNS databases of high Reynolds number channel and fully developed turbulent mixing layer flows. The use of both channel (wall-bounded) and mixing layer flows is important for the development of accurate LES models because these two flows encompass many characteristic features of complex turbulent flows.

2. Accomplishments

The subgrid-scale stress tensor, τ_{ij}, that results from filtering the Navier-Stokes equations consists of three terms (Bardina 1983):

$$\tau_{ij} = L_{ij} + C_{ij} + R_{ij}, \tag{1}$$

$$L_{ij} = \overline{\overline{u}_i \overline{u}_j} - \overline{u}_i \overline{u}_j, \qquad C_{ij} = \overline{\overline{u}_i u'_j + u'_i \overline{u}_j}, \qquad R_{ij} = \overline{u'_i u'_j}$$

where $overline{u}_i$ denotes the filtered velocity component and $u'_i = u_i - \overline{u}_i$ denotes the SGS component of u_i. L_{ij} is the Leonard term, C_{ij} is the cross term, and R_{ij} is the SGS Reynolds stress. The indices $i = 1, 2, 3$ correspond to the directions

1 Institute of Industrial Science, University of Tokyo
2 NASA Ames Research Center

x, y, and z, respectively, with x the streamwise ($u_1 = u$), y the "major-gradient" (wall-normal or cross-stream) ($u_2 = v$), and z the spanwise ($u_3 = w$) directions.

The Leonard term in eq. (1) is not modeled but is treated explicitly by applying the filter, while the other two terms (C_{ij} and R_{ij}) need to be modeled. A successful model for the cross term is a model suggested by Bardina (1983) where

$$C_{ij} = \overline{u'_i}\overline{\overline{u}}_j + \overline{\overline{u}}_i\overline{u'}_j$$

This model has been tested by Bardina (1983) for homogeneous flows and by Horiuti (1989) for the channel flow and was found to be a good model for the cross terms. This model will not be tested further in this work.

For the R_{ij} terms, the eddy viscosity model by Smagorinsky (Smagorinsky 1963):

$$R_{ij} \sim \frac{2}{3}\overline{E}_G\delta_{ij} - \nu_e\left(\frac{\partial \overline{u}_i}{\partial x_j} + \frac{\partial \overline{u}_j}{\partial x_i}\right), \tag{2}$$

$$\nu_e = (C_S\Delta)^2[\frac{1}{2}S_{ij}S_{ij}]^{1/2}, \qquad S_{ij} = \frac{\partial \overline{u}_i}{\partial x_j} + \frac{\partial \overline{u}_j}{\partial x_i},$$

and the Bardina model

$$R_{ij} \sim C(\overline{u}_i - \overline{\overline{u}}_i)(\overline{u}_j - \overline{\overline{u}}_j). \tag{3}$$

are two of several models which are used in LES computations. In these models, C_S and C are model constants, and $E_G = \overline{u'_l u'_l}/2$ and ν_e are, respectively, the SGS turbulent kinetic energy and SGS eddy viscosity coefficient. Δ is the characteristic SGS length scale whose value is defined as $(\Delta x \Delta y \Delta z)^{1/3}$; Δx, Δy, and Δz are the grid intervals in the x, y, and z directions, respectively. The Smagorinski model is a "Prandtl-type" mixing length model that can be derived by starting with the eddy viscosity approximation to the subgrid-scale Reynolds stresses and assuming production and dissipation are in balance. In an eddy viscosity approximation, ν_e is written as the product of a characteristic time scale τ and a velocity scale $E^{1/2}$,

$$\nu_e = C_\nu \tau E \tag{4}$$

where C_ν is a model constant. τ is then expressed as (Horiuti 1993)

$$\tau = \frac{\overline{E}_G}{\epsilon}, \qquad \epsilon = \nu\overline{\frac{\partial u'_i}{\partial x_l}\frac{\partial u'_i}{\partial x_l}} = C_\epsilon\frac{\overline{E}_G^{3/2}}{\Delta}, \tag{5}$$

where ϵ is the dissipation rate of $\overline{E}_G$ and C_ϵ is a model constant. The Smagorinsky model assumes that $E = \overline{E}_G$ in (4).

In the present study, we make use of the direct numerical simulation flow fields available at CTR to directly test the various approximations. The fields we consider are homogeneous in two-directions. To compute the large-eddy flow fields, we filter the DNS fields by applying a two-dimensional Gaussian filter in the $i = 1, 3$ directions. In the inhomogeneous direction ($i = 2$), a top-hat filter is applied to the

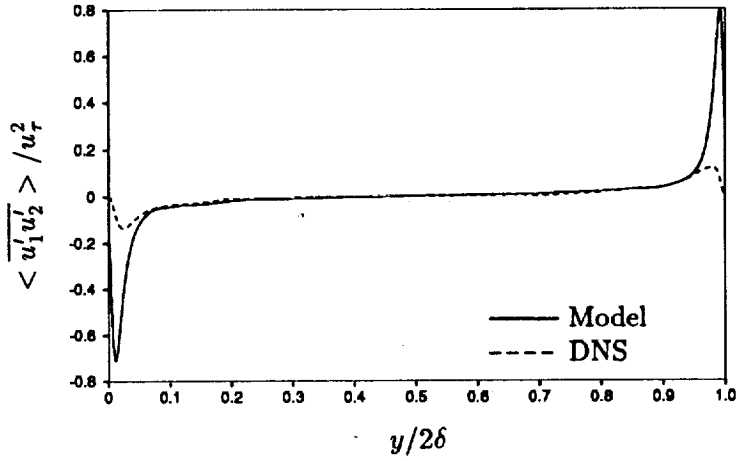

FIGURE 1. y-distribution of the SGS-Reynolds shear stress in turbulent channel at $Re_\tau = 790$. (Model with $E = \overline{E}_G/u_\tau^2$.)

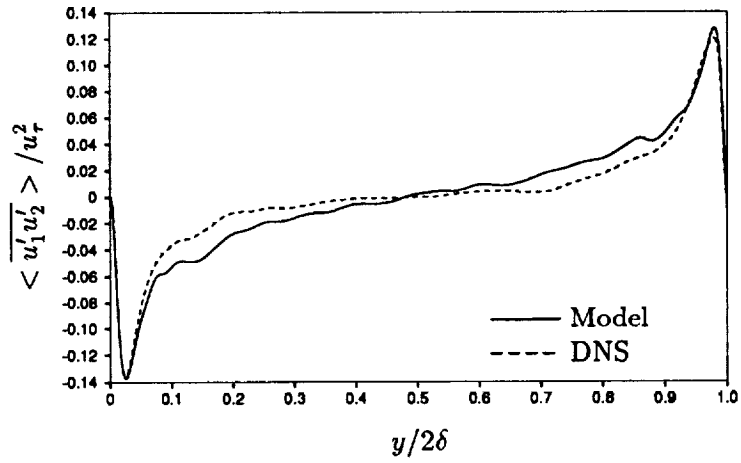

FIGURE 2. y-distribution of the SGS-Reynolds shear stress in turbulent channel at $Re_\tau = 790$. (Model with $E = \overline{u_2' u_2'}/u_\tau^2$.)

channel flow fields. No filter was applied in this direction ($i = 2$) to the mixing layer flow field. This is due to the fact that occasionally the doubly filtered ($\overline{\overline{[]}}$) grid-scale variables were larger than the singly filtered ones ($\overline{[]}$), owing to the inaccuracy of a top-hat filter in regions where grid spacing is coarse.

The DNS databases we used were the fully developed incompressible channel flows at Re_τ (Reynolds number based on the wall-friction velocity, u_τ, and the channel height, 2δ)= 360 (Kim *et al.* 1987) and 790 (Kim 1990), and the incompressible mixing layer at Re_θ (the Reynolds number based on the momentum thickness, δ_m,

and the velocity difference, ΔU)= 2400 (Moser and Rogers 1992). We started with the low Reynolds number channel flow data as a confidence test. We found that the results obtained in this case are consistent with the previous work of Horiuti (1993), who used a different set of DNS data but at the same Reynolds number. The details of this testing are not shown in the present report.

The high Reynolds number channel flow field (with $256 \times 193 \times 192$ grid points) was filtered to $64 \times 97 \times 48$ grid points. The mixing layer flow field (with $512 \times 210 \times 192$ grid points) was filtered to $64 \times 210 \times 48$ grid points. These LES grid point numbers were chosen so that the turbulent kinetic energy retained in the SGS components is large. This is needed to make a fair assessment of the SGS models. SGS model evaluations were conducted by comparing the y-distribution of the mean values averaged in the $x - z$ plane (denoted by $< () >$), and also by comparing the y-distribution of the root-mean-square (rms) values of the exact terms with the model predictions. Only the y-distribution of the mean values are shown in the present report because the rms values were found to give similar results.

2.1 A proper eddy viscosity velocity scale

2.1.1 Channel flow

The y-distribution of the SGS Reynolds shear stress $< \overline{u_1' u_2'} >$ obtained with $E = \overline{E}_G$ and $C_\nu = 0.1$ in (4) is compared with the DNS data in Fig. 1. While the agreement between the model and the term is good in the central portion of the channel, the agreement deteriorates near the wall where the model predicts a very large peak compared to the actual data. This overprediction of the shear stress near the wall when $\overline{E}_G$ is used for E in (4) implies that a damping function is needed to account for the presence of the wall. This near-wall overprediction of the stress is similar to the near-wall behavior of one-point closure models (see Rodi & Mansour 1991). This behavior of one-point closure models is attributed to the rapid reduction of the Reynolds shear stress (as the wall is approached) due to the preferential damping of the normal stress (Launder 1987, and Durbin 1992). Horiuti (1993) reasoned that the same wall damping effects should hold true for the SGS field. Indeed, when the SGS normal stress $\overline{u_2' u_2'}$ is used for E (with $C_\nu = 0.23$, see Fig. 2), the model agrees well with SGS Reynolds shear stress near the wall without an additional damping function. The model is, however, less effective as compared to using the total energy in the core region of the channel. The main deficiency in the core region is attributed to excessive grid stretching in the y-direction because of the mapping used in conjunction with Chebyshev expansions. In an actual LES computation, finite differences with a more uniform grid are used in the y direction and, therefore, a more isotropic energy distribution can be expected in this case.

The effects of the anisotropic grid can be evidenced by the y-distribution profile of the 'flatness parameter' A (Lumley 1978) averaged in the x-z plane. In this case A is defined as

$$A = [1 - \frac{9}{8}\{A_2 - A_3\}], A_2 = a_{ij}a_{ij}, A_3 = a_{ij}a_{jk}a_{ki}, \tag{6}$$

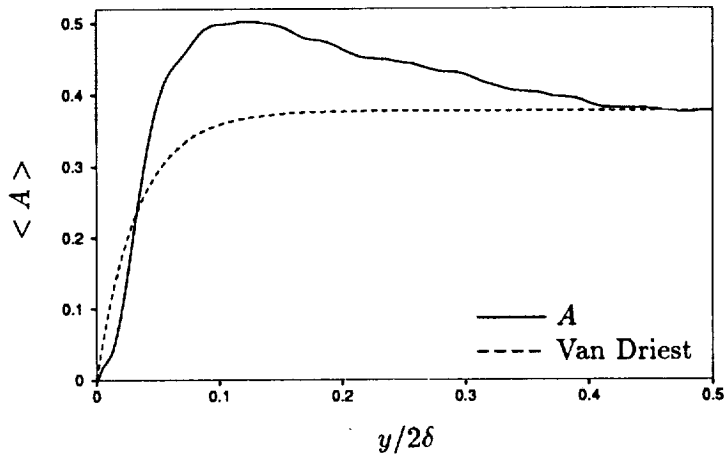

FIGURE 3. y-distribution of the flatness parameter A and the Van Driest function (channel at $Re_\tau = 790$).

$$a_{ij} = \{\overline{u_i' u_j'} - \frac{1}{3}\delta_{ij}\overline{u_k' u_k'}\}/k, k = \frac{1}{2}\overline{u_k' u_k'}$$

We find (see Fig. 3) that in the core region of the channel, $A \sim 0.35$, which is much smaller than the expected $A = 1$ when the small scale turbulence is isotropic. In the region around $y \sim 0.1$, A peaks around $A \sim 0.5$, and then gradually decreases to 0.35 at the channel center. The y-distribution of A for the unfiltered DNS data does not show this overshoot and is close to $A = 1$ around the centerline. The grid spacing in the central region of channel seems to be too coarse; therefore, a considerable anisotropy exists in the SGS turbulence fluctuations. In fact, when the SGS-EVM model with $E = \overline{u_2' u_2'}$ in (4) was used in an actual LES channel flow calculations using a more uniform grid at high Reynolds number ($Re_\tau = 1280$) (Horiuti 1993), a good agreement with experimental data was found. The present comparisons for the high Re channel flow confirm the conclusions of Horiuti (1993) based on the low Re channel flow fields.

For the record, the y-distribution of the conventional Van Driest damping function $((1 - exp(-y^+/26.0))$ (normalized with value of A at the channel center) is included in Fig. 3. It should be noted that the 'flatness parameter' A has a similar distribution across the channel as the Van Driest function, suggesting that A may be used as an alternative method to damp the eddy viscosity near the wall (Horiuti 1992).

2.1.2 Mixing layer

The y-distribution of $\overline{u_1' u_2'}$ obtained using $E = \overline{E}_G$ ($C_\nu = 0.20$) and $E = \overline{u_2' u_2'}$ ($C_\nu = 0.26$) in (4) are compared with the DNS data in Fig. 4 and 5, respectively. Both cases show a good agreement of the model with the DNS data, indicating that the two models are equivalent in this case. It should be noted that the optimized C_ν values obtained for the $\overline{u_2' u_2'}$ model in the channel flow at lower Re (0.22), at high Re

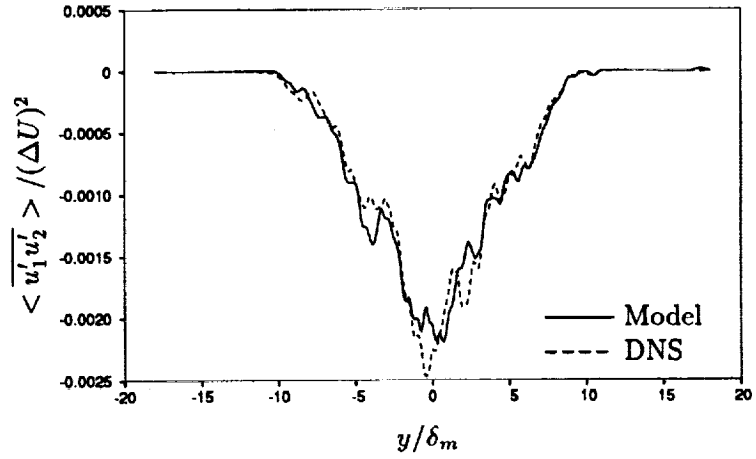

FIGURE 4. y-distribution of the SGS-Reynolds shear stress in turbulent mixing layer. (Model with $E = \overline{E}_G//(\Delta U)^2$.)

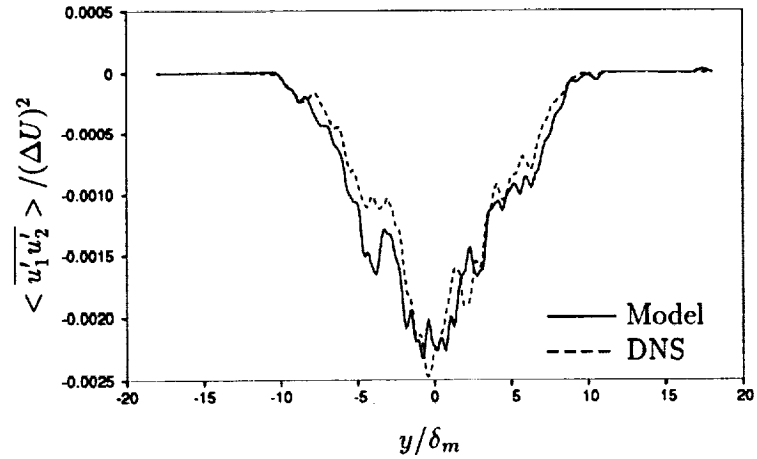

FIGURE 5. y-distribution of the SGS-Reynolds shear stress in turbulent mixing layer. (model with $E = \overline{u_2' u_2'}/(\Delta U)^2$)

(0.23), and in the mixing layer (0.26) are very close to each other. This implies that the model constant of the SGS normal stress model is rather universal independent of the type of flow, whereas the optimized C_ν values for the $E = \overline{E}_G$ model were 0.11, 0.10, 0.20, respectively. This is further indication of the potential strength of the normal-stress model. It is interesting to note that, particularly in the outer edge region of the mixing layer ($y \sim 10$ or ~ -10), the magnitude of normal component was the largest among the three components of the SGS turbulence fluctuations. A possible relationship of this phenomenon with the significant intermittency in these regions will be investigated in future work.

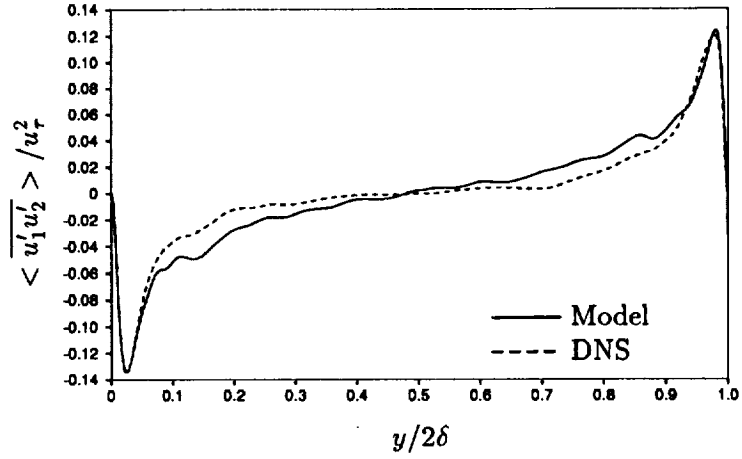

FIGURE 6. y-distribution of the SGS-Reynolds shear stress using Generalized normal stress model (Channel at $Re\tau = 790$)

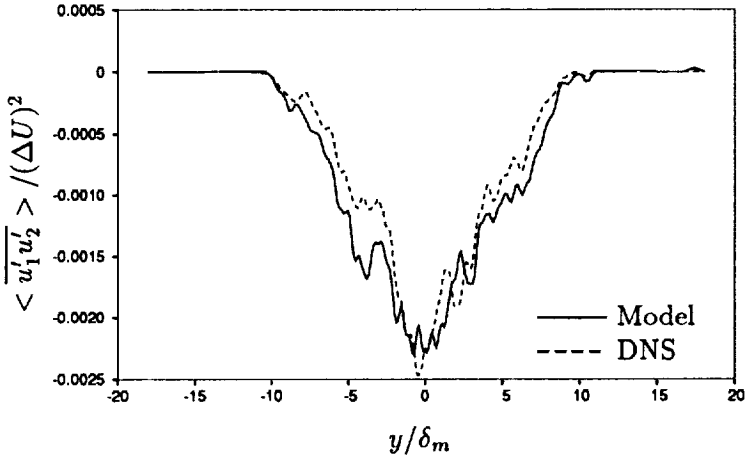

FIGURE 7. y-distribution of the SGS-Reynolds shear stress using Generalized normal stress model (Mixing layer)

2.2 Generalized SGS normal-stress model

Although it is shown that the SGS-EVM based on the 'major-gradient stress' model (Eq. (4) with $E = \overline{u_2' u_2'}$) shows a high correlation with the DNS data, this model does not preserve the tensoral invariance of the SGS Reynolds stresses. This drawback can be circumvented by generalizing this model as follows (Durbin 1991 and Horiuti 1993):

$$\overline{u_i' u_j'} = \delta_{ij}(\frac{2}{3}\overline{E}_G + \frac{2}{3}P) - \nu_{e_{il}}\frac{\partial \overline{u}_j}{\partial x_l} - \nu_{e_{jl}}\frac{\partial \overline{u}_i}{\partial x_l} \tag{7}$$

where

$$\nu_{e_{ij}} = C_\nu \frac{\Delta}{\overline{E}_G^{1/2}} \overline{u_i' u_j'}, \qquad P = \nu_{e_{ml}} \frac{\partial \overline{u}_m}{\partial x_l}.$$

This model is not identical to the conventional eddy viscosity model. In this model, the velocity scale is chosen as the component normal to the principal shear plane, for example, for $\overline{u_1' u_2'}$, the most dominant term in the RHS becomes $nu_{e_{22}} \partial \overline{u}_1 / x_2$.

The generalized normal stress model is tested in the same manner as in the last section. The results for the high-Re channel flow ($C_\nu = 0.23$) and the mixing layer ($C_\nu = 0.26$) are shown in Figs.6 and 7, respectively. It is evident that the generalized normal stress model shows a high correlation with the previous normal stress model.

It should be pointed out that the generalization of the normal stress model without losing the tensorial invariance is not unique, e.g. terms such as

$$-\nu_{e_{il}} \frac{\partial \overline{u}_l}{\partial x_j} - \nu_{e_{jl}} \frac{\partial \overline{u}_l}{\partial x_i} \tag{8}$$

can be added to Eq. (7). When these terms are included, however, the term $\nu_{e_{11}} \times \partial \overline{u}_1 / \partial x_2$ causes a large peak in the model for the $\overline{u_1' u_2'}$ profile in the channel flow. For this reason, the terms in Eq. (8) were excluded when generalizing the normal stress model.

2.3 Approximation method of the SGS turbulent energy

To effectively use the model advocated in the previous sections, a model for the normal stresses is needed. We can either carry equations for the normal stresses or estimate the energy in the subgrid-scales from the energy in the large scales. In testing the scale-similarity model of Bardina (1983), Horiuti (1993) found good correlation between the model and the data. The model reads,

$$\overline{\overline{E}}_G = C_K (\overline{u}_l - \overline{\overline{u}}_l)(\overline{u}_l - \overline{\overline{u}}_l), \tag{9}$$

$$\overline{u_2' u_2'} = C_N (\overline{u}_2 - \overline{\overline{u}}_2)(\overline{u}_2 - \overline{\overline{u}}_2),$$

where a constant different from unity was needed. It was pointed out that the optimized model constants C_K and C_N were not equal to unity because the scale-similarity model provides a partial estimate of the whole SGS fluctuations which resides in the vicinity of the cutoff-wave number ($= \pi/\Delta$). The poor performance of the model when these coefficients are set equal to unity can be evidenced by the fact that in this case the SGS flatness parameter A becomes identically zero (purely two-dimensional state). We have optimized C_K/C_N for the low-Re, the high-Re channel, and the mixing layer flows and found 7.0/12.0, 7.0/ 9.0, and 9.0/ 12.0 to be representative values for these flows. We note that they are slightly (but tolerably) sensitive to the type of flow fiel, and that they are generally close to each other. A representative comparison of the model prediction with the DNS data for $\overline{u_1' u_1'}$ is shown for the high-Re channel flow and the mixing layer in Figs. 8 and 9, respectively. We find a good agreement with the DNS data for both flows.

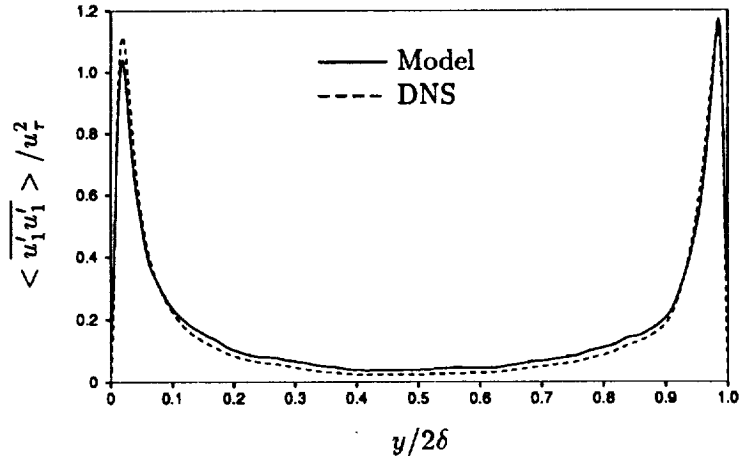

FIGURE 8. y-distribution of $\overline{u_1' u_1'}/u_\tau^2$ using the Bardina model (Channel at $Re_\tau = 790$)

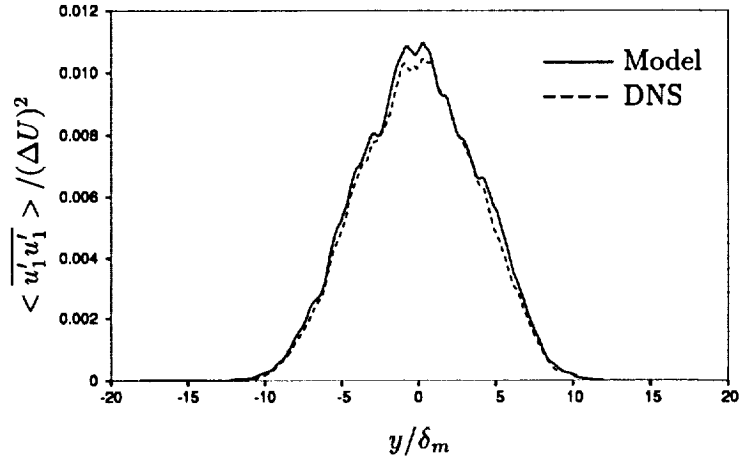

FIGURE 9. y-distribution of $\overline{u_1' u_1'}/(\Delta U)^2$ using the Bardina model (Mixing layer)

3. Future plans

An ultimate goal of the present study is to develop an SGS model which yields good predictions of turbulent flows in a complex geometry. Of particular interest is the flow over a backward-facing step. In this case, while the flow is bounded by the walls, the internal mixing layer present in this flow plays a major role in setting the turbulence levels. In this work, a proper velocity scale for the SGS-EVM viscosity was determined for the fully developed channel and the mixing layer flows. In the channel, a clear advantage over more conventional treatments was shown by using the normal stress. It was also shown that the SGS normal stress is equally

useful as the total SGS turbulent energy for modeling in mixing layers. The model constant in the normal-stress model was found to be fairly independent of the type of flow. It was demonstrated that a generalized normal stress model can be used as an alternative method for the normal-stress model, and the tensorial invariance which is violated in the normal-stress model can be recovered. This generalized normal-stress model will be tested in a backward-facing step flow in both 'a priori' and 'a posteriori' manner in the future. Although the Bardina model constants C_K and C_N in Eq. (9) are rather consistent in three different flow fields, some variance was noticed. An attempt to determine these coefficients more accurately using the Dynamic scale model approach is currently underway.

Acknowledgements

K. H. is grateful to the Center for Turbulence Research for providing the opportunity to access the DNS database located at CTR. We are grateful to Drs. P. Durbin, P. Moin, and J. H. Ferziger for stimulating discussions. Gratitude is also extended to Drs. R. D. Moser and M. M. Rogers for their kindness in providing the recent DNS data. This work was partially supported by the International Exchange Program, University of Tokyo.

REFERENCES

BARDINA, J. 1983 Improved turbulence models based on large eddy simulation of homogeneous, incompressible turbulent flows. *Ph.D. dissertation.* Stanford University, Stanford, California.

DURBIN, P. A. 1991 Near wall turbulence closure modelling without damping functions. *Theor. Comp. Fluid Dynamics.* **3,** 1.

GERMANO, M., PIOMELLI, U., MOIN, P. & CABOT, W.H. 1991 A dynamic subgrid-scale eddy viscosity model. *Phys. Fluids A.* **3,** 1760.

HORIUTI, K. 1989 The role of the Bardina model in large eddy simulation of turbulent channel flow. *Phys. Fluids A.* **1,** 426.

HORIUTI, K. 1990 Higher-order terms in the anisotropic representation of Reynolds stresses. *Phys. Fluids A.* **2,** 10.

HORIUTI, K. 1992 Damping effects in large eddy simulation subgrid-scale modeling. *In preparation.*

HORIUTI, K. 1993 A proper velocity scale for modeling subgrid-scale eddy viscosity in large eddy simulation. *Phys. Fluids A.* **(1).**

KIM, J., MOIN, P. & MOSER, R. D. 1987 Turbulent statistics in fully developed channel flow at low Reynolds number. *J. Fluid Mech.* **177,** 133.

KIM, J. 1990 unpublished data.

LAUNDER, B. E., REECE, G. J. & RODI, W. 1975 Progress in the development of a Reynolds-stress turbulence closure. *J. Fluid Mech.* **68,** 537.

LAUNDER, B. E. 1987 An introduction to single-point closure methodology. *Report No. TFD/97/7.* Mechanical Engineering Department, UMIST, Manchester.

LUMLEY, J. L. 1978 Computational modeling of turbulent flows. *Adv. in Appl. Mech.* **18,** 123.

MOIN, P. & KIM, J. 1982 Numerical investigation of turbulent channel flow. *J. Fluid Mech.* **118,** 341.

MOSER, R. D. & ROGERS, M. M. 1992 Coherent structures in a simulated turbulent mixing layer. *IUTAM Symposium on Eddy Structure Identification. Oct.12-14, Poitiers France.*

RODI, W. & MANSOUR, N. N. 1992 Low Reynolds number k-ϵ modeling with the aid of direct simulation data. *To appear in J. Fluid Mech.*

SMAGORINSKY, J. 1963 General circulation experiments with the primitive equations. I. The basic experiment. *Monthly Weather Review.* **91,** 99.

VAN DRIEST, E. R. 1956 On turbulent flow near a wall. *J. Aero. Sci.* **23,** 1007.

Large eddy simulation of shock turbulence interaction

By S. Lee

1. Motivations and objectives

The presence of shock waves is an important feature that distinguishes high-speed flows from low-speed ones. Understanding the mechanisms of turbulence interacting with a shock wave is not only of generic interest, but also of fundamental importance in predicting the interactions of turbulent boundary layers with shock waves which occur in many practical engineering applications. Many flows of interest have very high Reynolds numbers with large ranges of dynamic scales which cannot be captured by direct numerical simulation (DNS). Large eddy simulation (LES) is thus required where the large scale structures are resolved and the effects of the small, unresolved "subgrid" scales on the larger, resolved scales are modeled. The cost of resolving the shock wave structure is extremely prohibitive for a strong shock wave (Lee *et al.* 1992). Therefore, a numerical method is required which can predict changes of flow variables across the shock wave without resolving the structure. The method is required to have high order numerical accuracy in smooth regions of the flow domain to properly predict the evolution of turbulence.

A new subgrid-scale (SGS) model was developed by Germano *et al.* (1991) that augments the standard Smagorinsky (1963) eddy viscosity model by replacing the *ad hoc*, flow dependent constant with a coefficient determined by the resolved scales in the LES. The coefficient automatically adjusts to the flow conditions. This "dynamic" SGS model has been extended by Moin *et al.* (1991) to the simulation of compressible turbulence and passive scalar transport. Recently, Ghosal *et al.* (1992) developed SGS models which eliminate some inconsistencies in the previous dynamic models.

A shock capturing scheme developed by Harten *et al.* (1987) is essentially non-oscillatory (ENO), which can also be constructed to be high order accurate throughout the domain. The non-oscillatory nature of the scheme is achieved by choosing a interpolating stencil which gives the smoothest evaluation of the derivatives of the primitive variables. Shu and Osher (1989) extended the scheme to interpolate the fluxes instead of the primitive variables, which significantly simplifies the scheme.

The immediate goal of this work is two-folds: to test the performance of LES calculation performed with a conservative formulation, a formulation preferred in the shock-involved simulations, and to test the performance of the shock capturing scheme and validate the scheme against the DNS by Lee *et al.* (1992) for a weak shock wave.

An immediate extension of the present work is to perform DNS of low Reynolds number turbulence interacting with strong shock waves by using the shock capturing scheme. Understanding the interaction of high Reynolds number turbulence with shock waves through LES is the long range goal of this work.

2. Accomplishments

A nonconservative formulation of the energy equation (solving for internal energy) was used to perform large eddy simulations of compressible turbulence in Moin *et al.* (1991) due to its simplicity in implementing SGS models compared to the conservative formulation (solving for total energy). In problems with shocks in the domain, however, the total energy formulation is preferred due to its conservative nature. A conservative set of equations for the LES were derived from the nonconservative equations derived by Moin *et al.* (1991). Performance of the conservative formulation was compared with the experiment on decaying grid-generated turbulence as well as with the filtered DNS field, which is reported in §2.1. Various shock-capturing schemes were tested, and an ENO shock-capturing scheme of Shu and Osher (1989) was chosen for the simulation of shock/turbulence interaction. The scheme was tested and validated against the data base generated by DNS of weak shock waves, which is reported in §2.2. The results obtained with the ENO scheme were within 5% from the DNS results, and used less than 25% of the CPU time used in the DNS.

2.1 LES with a conservative formulation

In the LES of compressible simulation by Moin *et al.* (1991), nonconservative energy equation was used due to its simple form. The equations used are

$$\frac{\partial \overline{\rho}}{\partial t} + \frac{\partial \overline{\rho}\widetilde{u}_k}{\partial x_k} = 0,$$

$$\frac{\partial \overline{\rho}\widetilde{u}_i}{\partial t} + \frac{\partial \overline{\rho}\widetilde{u}_i\widetilde{u}_k}{\partial x_k} = -\frac{\partial \overline{p}}{\partial x_i} + \frac{\partial \sigma_{ik}}{\partial x_k} - \frac{\partial \tau_{ik}}{\partial x_k},$$

$$\frac{\partial \overline{\rho} c_v \widetilde{T}}{\partial t} + \frac{\partial \overline{\rho} c_v \widetilde{T}\widetilde{u}_k}{\partial x_k} = -\overline{p}\frac{\partial \widetilde{u}_k}{\partial x_k} + \sigma_{ik}\frac{\partial \widetilde{u}_k}{\partial x_i} - c_v\frac{\partial q_k}{\partial x_k},$$

where σ_{ik}, τ_{ik}, and q_k represent the resolved viscous stress, the subgrid-scale stress, and heat flux,

$$\sigma_{ik} = \overline{\mu}\left(\frac{\partial \widetilde{u}_i}{\partial x_k} + \frac{\partial \widetilde{u}_k}{\partial x_i} - \frac{2}{3}\frac{\partial \widetilde{u}_m}{\partial x_m}\delta_{ik}\right)$$

$$\tau_{ik} = \overline{\rho}(\widetilde{u_i u_k} - \widetilde{u}_i\widetilde{u}_k)$$

$$q_k = \overline{\rho}(\widetilde{u_k T} - \widetilde{u}_k\widetilde{T}),$$

respectively. The overbar denotes the filtering operation, and the tilde denotes the density-weighted filter. The filtering operations always refer to a sharp cutoff (or volume-weighted average) in the homogeneous direction of the flow. The subgrid scale stress τ_{ik} and heat flux q_k were determined through the dynamic procedure suggested by Germano *et al.* (1991). Derivation of the energy equation for the LES using the conservative formulation introduces terms which are complex to model, for example, the subgrid scale convection of the total energy (sum of thermal and kinetic energy) needs to be modeled.

However, if the resolved total energy ($\overline{E}_T$) is defined as

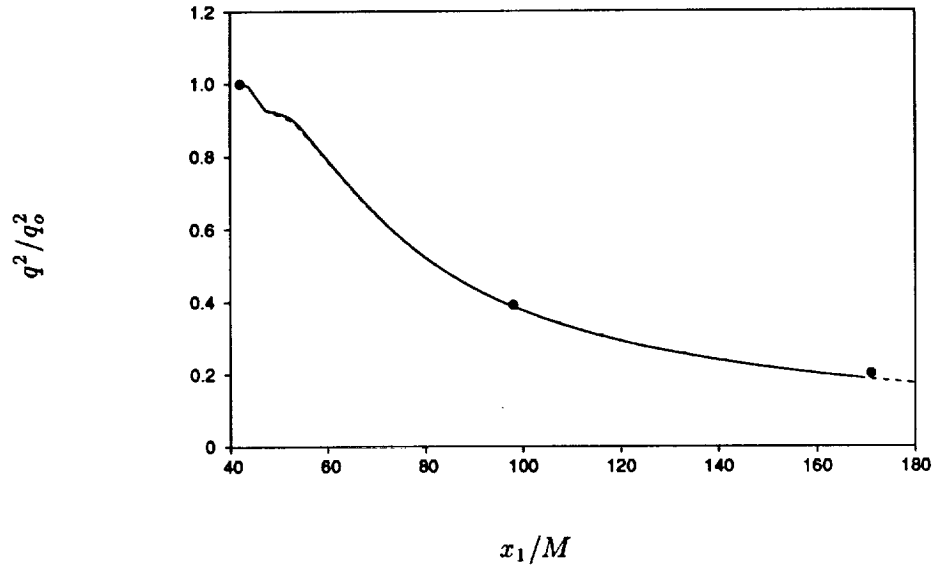

FIGURE 1. Evolution of resolved turbulent kinetic energy. • filtered experiment (Comte-Bellot & Corrsin 1971), —— LES with conservative formulation, ---- LES with nonconservative formulation.

$$\overline{E}_T = \overline{\rho}(c_v\widetilde{T} + \widetilde{u}_k\widetilde{u}_k/2)$$

rather than $\overline{\rho}(c_v\widetilde{T} + \widetilde{u_k u_k}/2)$, the conservative energy equation can be derived from the nonconservative equations presented above, and the extra complexities can be circumvented. The resulting energy equation becomes

$$\frac{\partial \overline{E}_T}{\partial t} + \frac{\partial \overline{E}_T \widetilde{u}_k}{\partial x_k} = -\frac{\partial \overline{p}\widetilde{u}_k}{\partial x_k} + \frac{\partial \sigma_{ik}\widetilde{u}_k}{\partial x_i} - \widetilde{u}_k\frac{\partial \tau_{ik}}{\partial x_i} - c_v\frac{\partial q_k}{\partial x_k},$$

The terms to be modeled remain the same and are parametrized as

$$\tau^*_{ik} = \overline{\rho}C_S\Delta^2|\widetilde{S}|\widetilde{S}^*_{ik},$$
$$q^2 = \overline{\rho}C_I\Delta^2|\widetilde{S}|^2,$$
$$q_k = \overline{\rho}D\Delta^2|\widetilde{S}|\widetilde{T}_{,k},$$

where $q^2 = \tau_{mm}$ and $\tau^*_{ik} = \tau_{ik} - q^2\delta_{ik}/3$. The detailed procedures of dynamically determining coefficients, C_S, C_I, and D, are described in Moin *et al.* (1991). The concept of least squares suggested by Lilly (1992) replaced the rather arbitrary procedure of determining scalar coefficients, C_S and D, from the tensor or vector relations.

The experiment on the decay of grid-generated turbulence with $Re_\lambda = 71.6$ (Comte-Bellot and Corrsin 1971) was simulated as a temporal decay with $32\times32\times32$

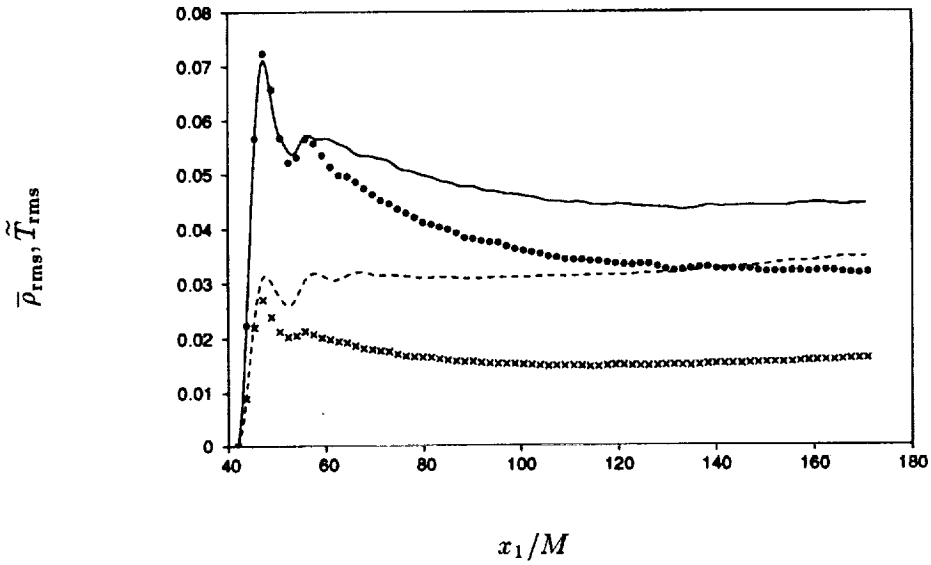

FIGURE 2. Evolution of resolved density and temperature fluctuations. Conservative formulation: —— density, ---- temperature, nonconservative formulation: • density, × temperature.

grid points with different formulations. Decay of the resolved scale TKE is compared in Figure 1. The evolution is insensitive to the choice of the formulation. Evolutions of *rms* density and temperature fluctuations are compared in Figure 2. (The fluctuations in thermodynamic quantities were initially set to zero.) Even though the evolution of velocity field does not depend significantly on the choice of the formulation, the evolution of density fluctuation depends on this choice.

To check if this dependence is due to the initial transient of the fluctuation density field, LES's of decaying compressible turbulence ($Re_\lambda = 35, M_t = 0.61$, where eddy-shocklets were found in DNS) were performed. Initial conditions of the simulation were taken as the Fourier filtered DNS field onto $32 \times 32 \times 32$ grids at $t/\tau_t \simeq 0.85$, when turbulence is fully developed in every respect. Figure 3 shows evolution of *rms* density fluctuation from the two formulations, which shows good agreement between the two and with the filtered DNS.

The reason for the different evolution of density field shown in Figure 2 is not yet fully understood. Some possible reasons are: (1) aliased evaluation of temperature in the conservative formulation ($\overline{\rho}\widetilde{u}_k\widetilde{u}_k$ is subtracted from $\overline{E}_T$), (2) different initial transient to set up temperature fluctuations. Before conducting the LES of shock/turbulence interaction, validity of the formulation and the SGS models should be established.

2.2 Development of an ENO scheme

For a strong shock wave, resolving the shock structure by solving Navier-Stokes equations is irrelevant because Navier-Stokes equations are no longer valid inside

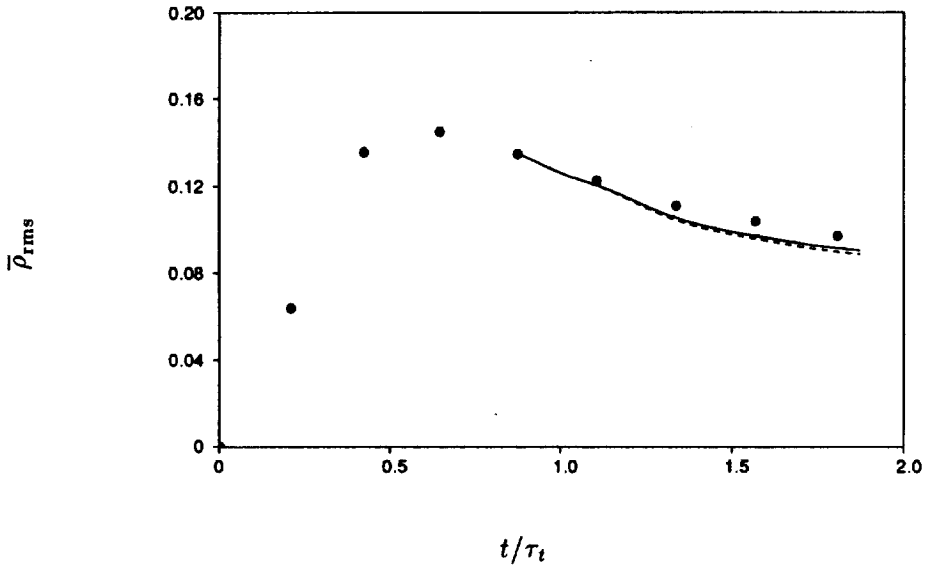

FIGURE 3. Evolution of resolved density fluctuation. • filtered DNS (Lee *et al.* 1992), ——— LES with conservative formulation, ---- LES with nonconservative formulation.

the shock wave with $M_1 > 2.0$. (Sherman 1955) Therefore, there is no point to resolving the structure of the strong shock wave with the expense of huge computational cost. A shock-capturing scheme is implemented for the simulation of strong shock wave/turbulence interaction. In simulations of shock/turbulence interaction, a shock capturing scheme is required to be high order accurate throughout the computational domain (to properly simulate the turbulence evolution) as well as to be able to give smooth and accurate transition across the shock wave. The shock-capturing scheme of the choice is the essentially non-oscillatory (ENO) scheme, which can be constructed up to any order of accuracy. The ENO scheme used in this work is based on the Lax-Friedrichs scheme with interpolation of fluxes (Shu and Osher, 1989). Some modifications are made to the basic scheme to improve the solution accuracy and to enhance the code performance.

For the sake of completeness, the *basic* ENO scheme is briefly described in the following. The three-dimensional, compressible Navier-Stokes equation can be written as

$$\mathbf{q}_t + \mathbf{f}(\mathbf{q})_x + \mathbf{g}(\mathbf{q})_y + \mathbf{h}(\mathbf{q})_z = \mathbf{V},$$

where,

$$\mathbf{q} = (\rho, \rho u_1, \rho u_2, \rho u_3, E_T)^T,$$
$$\mathbf{f}(\mathbf{q}) = u_1\mathbf{q} + p(0,1,0,0,u_1)^T,$$
$$\mathbf{g}(\mathbf{q}) = u_2\mathbf{q} + p(0,0,1,0,u_2)^T,$$
$$\mathbf{h}(\mathbf{q}) = u_3\mathbf{q} + p(0,0,0,1,u_3)^T,$$

and $\mathbf{V}$ is the molecular diffusion terms.

The ENO adaptive-stencil procedure is applied only to the convection terms (the left-hand side of the above equation). The diffusion terms are approximated by the sixth-order Pade scheme, which is the base scheme used in the shock-resolving direct numerical simulation (Lee *et al.* 1992). The time advancement is performed by a third order Runge-Kutta method. Three convection terms are approximated dimension-by-dimension: for example, when approximating $\mathbf{f}(\mathbf{q})_x$, y and z are fixed. The core algorithm is then a one-dimensional ENO approximation to $\mathbf{f}(\mathbf{q})_x$.

The flux vector $\mathbf{f}(\mathbf{q})_x$ can be approximated either by component by component or in characteristic directions, but for simplicity of implementation, the component treatment was chosen. To obtain nonlinear stability by upwinding, $\mathbf{f}(\mathbf{q})_x$ is decomposed into

$$\mathbf{f}(\mathbf{q})_x = \mathbf{f}^+(\mathbf{q})_x + \mathbf{f}^-(\mathbf{q})_x$$

with

$$\mathbf{f}^\pm(\mathbf{q})_x = (\mathbf{f}(\mathbf{q})_x \pm \alpha\mathbf{q})/2,$$

where $\alpha = \max(|u_1| + c)$ (c is the sound speed) is the largest eigenvalue in absolute value of the Jacobian $\partial\mathbf{f}/\partial\mathbf{q}$ along the relevant x-line. The decomposition guarantees that $\partial\mathbf{f}^\pm/\partial\mathbf{q}$ has positive/negative eigenvalues. Therefore, upwinding (to be discussed) is the same for all components of the flux.

Suppose f is a component of the flux $\mathbf{f}^\pm(\mathbf{q})$. $f(\mathbf{q})_x$ is written as a conserved flux difference

$$f_x\big|_{x=x_j} \simeq \frac{1}{\Delta x}(\hat{f}_{j+\frac{1}{2}} - \hat{f}_{j-\frac{1}{2}}),$$

where the numerical flux $\hat{f}_{j+1/2}$ approximates $h(x_{j+1/2})$ to a high order with $h(x)$ defined by

$$f(u(x)) = \frac{1}{\Delta x}\int_{x-\frac{\Delta x}{2}}^{x+\frac{\Delta x}{2}} h(\xi)d\xi.$$

In order to evaluate the numerical flux $\hat{f}_{j+1/2}$, $h(x)$ need not to be explicitly constructed. The numerical fluxes can be expressed in terms of the undivided differences of $f(u(x))$ as

$$\hat{f}_{j+1/2} = \sum_{m=0}^{r} c(i-j,m)f[i,m],$$

with i being the left-most point in the stencil used to approximate $\hat{f}_{j+1/2}$, and $c(s,m)$ and the undivided difference $f[j,k]$ being defined by

$$c(s,m) = \frac{1}{(m+1)!} \sum_{l=s}^{s+m} \prod_{\substack{p=s \\ p \neq l}}^{s+m} (-p)$$

and

$$f[j,0] = f(u_j),$$
$$f[j,k] = f[j+1,k-1] - f[j,k-1], \qquad k = 1,...,r$$

respectively.

The adaptive stencil (represented by i) is determined by the following procedure.
(1) Start with $i = j$ or $i = j+1$ according to the local upwinding direction.
(2) For k-th level of approximation,

$$i = i - 1 \text{ if } |f[i,k]| > |f[i-1,k]| \qquad \text{for } k = 1,...,r.$$

The ENO scheme was implemented in the code developed for the simulation of shock/turbulence interaction. Simulation of spatially decaying turbulence was performed (1) to validate the scheme and (2) to determine the required order of the ENO scheme to reproduce the quality of the corresponding DNS. In the validation procedure, a totally unexpected accuracy degeneracy was noticed with the increase of the ENO scheme's order. As the order of the ENO increases, the solution deviates further from the DNS solution. Similar accuracy degeneracy was reported by Rogerson and Meiburg (1990) while they were refining the grid. This degeneracy was due to the choice of linearly unstable stencils during the adaptive ENO procedure (Shu 1990). This phenomenon is more pronounced for the higher order scheme with more refined grid. A biasing toward the central difference stencil (Shu 1990) was implemented to avoid the accuracy degeneracy in smooth regions. With this fix, by raising the order of accuracy, more accurate results could be obtained. Results comparable to the corresponding DNS (with sixth-order Pade scheme) was obtained when the accuracy of the ENO scheme was sixth order. Beyond the sixth-order, the effect of the increased order was found negligible in this case.

The operation count and, accordingly, the CPU time are increased a few times compared to the standard DNS code when the ENO scheme is implemented throughout the domain. The region where the ENO scheme plays a significant role is quite localized, usually less than a tenth of the computational domain in DNS of weak shock waves, and is expected to be even smaller for stronger shock waves. The idea of applying the ENO scheme only where it plays an active role and switching elsewhere into the usual Pade central difference was tested in pursuit of saving unnecessary computer usage. The local region of ENO application can even be specified *a priori* to be a zone around the shock since the simulation is performed in a coordinate system fixed on the mean shock wave. The concept of local application of the ENO scheme was validated against fully resolved DNS results both for the case of two-dimensional shock/turbulence interaction with $M_1 = 1.2$, $M_t = 0.07$ and the case of three-dimensional spatially decaying turbulence with $M_t = 0.51$ and

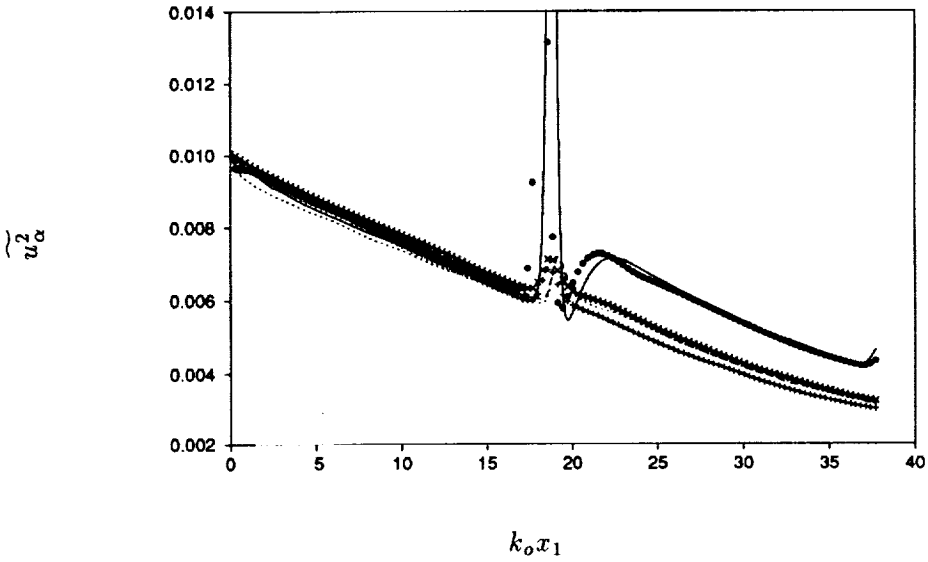

FIGURE 4. Evolution of velocity fluctuations in three-dimensional shock/turbulence interaction. Lines denote DNS results and symbols denote results using the ENO scheme. u_1 (——— , •), u_2 (---- , ×), u_3 (····· , +).

$Re_\lambda = 25$. For the two-dimensional shock/turbulence case with $M_1 = 1.2$, CPU time required was reduced to a third of the corresponding DNS and is expected to be larger for the stronger shock waves.

The next validation was to simulate the three-dimensional shock/turbulence interaction using the ENO scheme near the shock and the Pade scheme elsewhere. Significant additional decay of TKE was found in the shock vicinity where the ENO scheme is applied, which was not pronounced in two-dimensional shock/turbulence simulations. The excessive TKE dissipation in the ENO zone was suspected to be from the additional dimension (x_3-direction) for the ENO procedure. In order to investigate the effect of the dimensions, the ENO scheme was applied only in the shock-normal direction for the two-dimensional shock/turbulence simulation. More accurate results were obtained with less CPU time used. For $M_1 = 1.2$, the ENO scheme required only a quarter of the CPU time used in the corresponding DNS.

The final ENO scheme developed in this work interpolates (up to sixth-order) fluxes based on Lax-Friedrichs method with biasing the interpolation stencil toward the central differencing. The ENO procedure is applied only to the convection terms in the shock-normal direction. The ENO scheme is made only active near the shock wave and switched into the sixth-order Pade scheme elsewhere.

The final validations were made for two cases: (1) three-dimensional turbulence interacting with a weak shock wave ($M_1 = 1.2$) and (2) two-dimensional turbulence interacting with a relatively strong shock wave ($M_1 = 2.0$). The first case was chosen to check the performance of the ENO scheme in three-dimensional case, and

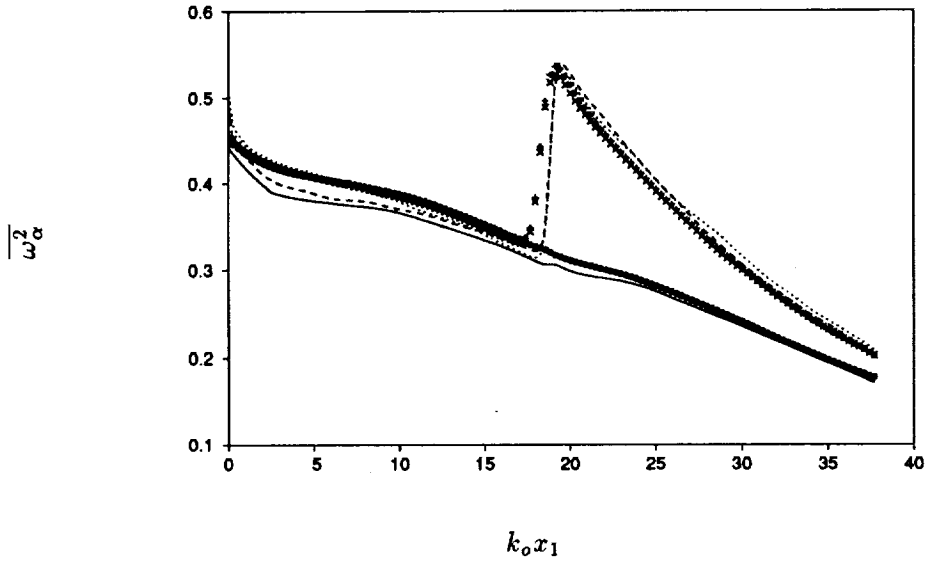

FIGURE 5. Evolution of vorticity fluctuations in three-dimensional shock/turbulence interaction. Lines denote DNS results and symbols denote results using the ENO scheme. ω_1 (——— , •), ω_2 (---- , ×), ω_3 (····· , +).

the result was compared with the corresponding DNS result (Lee *et al.* 1992). The second case was chosen to check the accuracy of the ENO scheme for strong shock waves. For the purpose of comparison, a shock-resolving DNS of two-dimensional shock/turbulence interaction was also performed.

As a validation of the ENO scheme for three-dimensional shock/turbulence interaction, reproduction of the DNS results of Case C in Lee *et al.* (1992) was tried where $M_1 = 1.2$, $M_t = 0.095$, and $Re_\lambda = 12$ just upstream of the shock. In the DNS, $193 \times 64 \times 64$ grids (with significant grid refinement near the shock) and 160 Cray/Y-MP CPU hours were used to give marginally converged statistics. In the ENO scheme, $129 \times 64 \times 64$ uniform grids and 40 Cray/Y-MP CPU hours were used for the same quality of statistics.

Figure 4 compares the evolution of velocity fluctuations obtained by DNS and ENO in three-dimensional shock/turbulence interaction. Except for the position of the mean shock wave, the amplification and free evolution of velocity from DNS are well reproduced by the ENO scheme. Since the ENO scheme is activated in the shocked zone, the peak *rms* fluctuations inside the shock wave due to the shock intermittency are not expected to agree with the DNS.

Figure 5 compares vorticity component evolution obtained by DNS and ENO. Once the shift of the mean shock position is considered, predictions by the ENO scheme are in excellent agreement with the DNS results. Other turbulence quantities, such as fluctuations in dilatation, density, and temperature, were in good agreement with the DNS results outside the zone occupied by the shock wave.

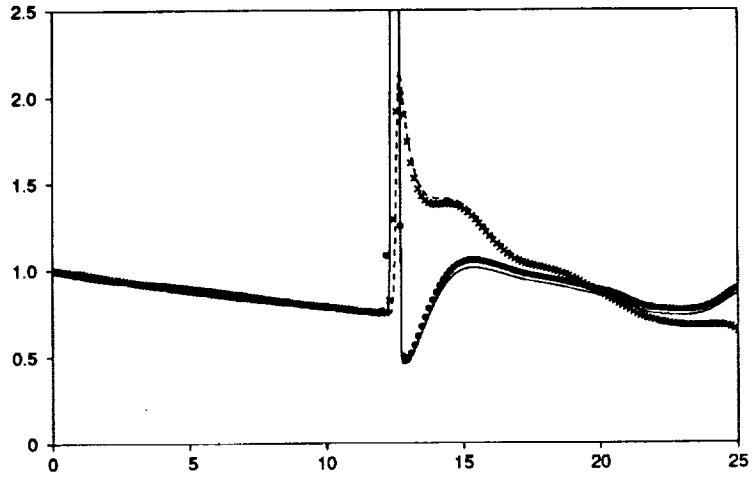

FIGURE 6(A). Evolution of velocity fluctuations in two-dimensional shock/turbulence interaction. Lines denote DNS results and symbols denote results using the ENO scheme. u_1 (——— , •), u_2 (---- , ×).

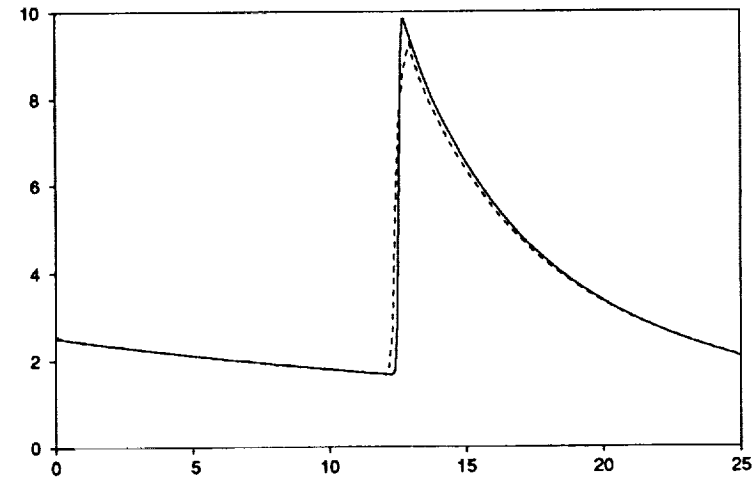

FIGURE 6(B). Evolution of vorticity fluctuations in two-dimensional shock/turbulence interaction. ——— DNS, ---- ENO.

As a validation of the ENO scheme for shock/turbulence interaction at high Mach numbers, results of the ENO scheme on two-dimensional shock/turbulence interaction was compared with the corresponding DNS, where $M_1 = 2.0$ and $M_t = 0.07$ at the inflow. The minimum grid spacing required by the ENO scheme was five times larger than that used in the DNS. Figure 6(a) and (b) compare velocity and vorticity fluctuations from the ENO scheme with those from the DNS. The jumps and evolutions behind the shock wave were reproduced by the ENO scheme with much less cost than the DNS. The results from the ENO scheme are indeed dependent on the resolution near the shock wave, and a grid-refinement test was performed before comparing the results. In order to accurately predict the interaction of turbulence with the stronger shock waves, where no DNS results are available, a grid in the shock vicinity should be refined until the result is no longer dependent on further grid refinement.

3. Future plans

Further tests of the LES with the conservative formulation against the filtered DNS and LES with the nonconservative formulation will continue. Extension of Ghosal *et al.*'s (1992) model (a constrained integral equation approach and a SGS model using transport equation for SGS turbulent kinetic energy) to compressible turbulence will also be performed.

In most DNS and LES of compressible turbulence, aliasing errors were controlled rather than clearly removed. In Lee *et al.* (1992), it was proposed to solve a continuity equation in terms of specific volume instead of density to completely remove aliasing errors. A simulation with this formulation will be executed. The simulation can be used as a reference to investigate the accuracy of the existing formulations.

Interaction of three-dimensional isotropic turbulence with strong shock waves will be performed to study the effect of the shock strength. Once SGS models and formulations are developed and validated, LES of turbulence interacting with shock waves of various strengths will also be performed.

REFERENCES

COMTE-BELLOT, G. & CORRSIN, S. 1971 Simple Eulerian time correlation of full and narrow band velocity signals in grid generated, isotropic turbulence. *J. Fluid Mech.* **48**, 273-337.

GERMANO, M., PIOMELLI, U., MOIN, P., & CABOT, W. 1991 A dynamic subgrid-scale eddy-viscosity model. *Phys. Fluids A.* **3**, 1760-1765.

GHOSAL, S., LUND, T. S., & MOIN, P. 1992 A dynamic localization model for large-eddy simulation of turbulent flows. *CTR Ann. Res. Brief-1992*, Stanford Univ./NASA Ames.

HARTEN, A., ENQUIST, B., OSHER, S., & CHAKRAVARTHY, S. R. 1987 Uniformly high order accurate essentially non-oscillatory schemes, III. *J. Comp. Phys.* **71**, 231-303.

LEE, S., LELE, S. K., & MOIN, P. 1991 Eddy shocklets in decaying compressible turbulence. *Phys. Fluids A.* **3,** 657-664.

LEE, S., MOIN, P., & LELE, S. K. 1992 Interaction of isotropic turbulence with a shock wave. *Report TF-52,* Department of Mechanical Engineering, Stanford University.

LILLY, D. K. 1992 A proposed modification of the Germano subgrid-scale closure method. *Phys. Fluids A.* **4,** 633-635.

MOIN, P., SQUIRES, K., CABOT, W., & LEE, S. 1991 A dynamic subgrid-scale model for compressible turbulence and scalar transport. *Phys. Fluids A.* **3,** 2746-2757.

ROGERSON, A. & MEIBURG, E. 1990 A numerical study of the convergence properties of ENO schemes. *J. Sci. Comp.* **5,** 151-167.

SHERMAN, F. S. 1955 A low-density wind-tunnel study of shock-wave structure and relaxation phenomena in gases. *NASA TN-3298.*

SHU, C.-W. 1990 Numerical experimentation on the accuracy of ENO and modified ENO schemes. *J. Sci. Comp.* **5,** 127-149.

SHU, C.-W., ERLEBACHER, G., ZANG, T. A., WHITAKER, D., & OSHER, S. 1992 High-order ENO schemes applied to two- and three-dimensional compressible flow. *Appl. Num. Math.* **9,** 45-71.

SHU, C.-W. & OSHER, S. 1989 Efficient implementation of Essentially Non-oscillatory shock-capturing schemes, II. *J. Comp. Phys.* **83,** 32-78.

SMAGORINSKY, J. 1963 General calculation experiments with the primitive equations. I. The basic experiment. *Mon. Weather Rev.* **91,** 99-164.

Application of a dynamic subgrid-scale model to turbulent recirculating flows

By Y. Zang[1], R. L. Street[1] AND J. R. Koseff[1]

The dynamic subgrid-scale model of Germano *et al.* (1991) is implemented in a finite volume formulation and applied to the simulation of turbulent flow in a three-dimensional lid-driven cavity at Reynolds number of 7500. The filtering operation is carried out in physical space, and the model coefficient is calculated locally. The computed mean and r.m.s. velocities as well as the Reynolds stress are compared with experimental data. It is shown that backscatter from small to large scales is necessary to sustain turbulent fluctuations. The model is being applied to the simulation of turbulent flows in stratified and rotating environment in complex geometries.

1. Motivations and objectives

Simulation of most engineering, environmental, or geophysical flows requires the use of turbulence model to represent unresolved small scale motions. Large eddy simulation (LES), which computes the motion of large spatial scales explicitly and models that of subgrid scales, proves to be an effective tool. During the last three decades, extensive effort has been put into developing subgrid-scale (SGS) turbulence models. Conventional SGS models such as the popular Smagorinsky (1963) model have several significant drawbacks. For example, they usually require model constants as input. These constants are not universal and have to be optimized to fit each type of flow. Although the Smagorinsky model has been successfully used in both homogeneous and wall-bounded turbulent flows (Bardina *et al.* 1983; Piomelli *et al.* 1988), it was found to be too dissipative in wall-bounded transitional flows (Piomelli *et al.* 1990), partly because the model does not account for the effect of energy backscatter from small to large scales. In addition, the Smagorinsky model gives a non-zero SGS stress in laminar flows.

Recently, Germano *et al.* (1991) developed a new SGS model which calculates the model coefficient dynamically using the smallest resolved scales. This dynamic SGS model (hereafter referred to as DSM) has many desirable features such as requiring only one input parameter, exhibiting the correct asymptotic behavior near solid walls and in laminar flow, and being capable of accounting for energy backscatter. Most of the studies so far using the dynamic model has coupled it with spectral methods and computed flows with one or more homogeneous directions (Germano *et. al.* 1991; Moin *et. al.* 1991).

The long-term goal of this project is to develop a numerical model to investigate environmental or geophysical flows in complex geometries. These flows are highly

1 Stanford University

inhomogeneous and may contain local regions of laminar, transitional, or turbulent flows of which successful simulations require a SGS model that can adjust itself to local flow dynamics – a quality which DSM possesses. The immediate objectives of the present work are to incorporate DSM into a finite volume Navier-Stokes code (Zang *et. al.* 1992) which is written in the general curvilinear coordinate system and to examine the model's applicability to turbulent recirculating flows. We performed large eddy simulations of flow in a lid-driven cavity at a Reynolds number of 7500. The computed mean and fluctuating profiles were compared with experimental data. Local averaging of the model coefficient was investigated. The model is being applied to the simulation of stratified rotating upwelling flows on a slopping bottom.

2. Accomplishments

2.1. The finite-volume implementation of DSM

The SGS Reynolds stress after applying the grid filtering operation represented by an overbar to the momentum equation is

$$\tau_{ij} = \overline{u_i u_j} - \overline{u}_i \overline{u}_j \tag{1}$$

The Smagorinsky model is employed as the base model for τ_{ij} as

$$\tau_{ij} - \frac{\delta_{ij}}{3}\tau_{kk} = -2\nu_T \overline{S}_{ij} \tag{2}$$

where the eddy viscosity

$$\nu_T = C\overline{\Delta}^2 |\overline{S}| \tag{3}$$

$\overline{\Delta}$ is the grid filter width, $|\overline{S}| = (2\overline{S}_{ij}\overline{S}_{ij})^{1/2}$ is the magnitude of the resolved large-scale strain rate tensor

$$\overline{S}_{ij} = \frac{1}{2}\left(\frac{\partial \overline{u}_i}{\partial x_j} + \frac{\partial \overline{u}_j}{\partial x_i}\right) \tag{4}$$

and C is the model coefficient which is to be computed dynamically using the procedure described below. We note that C is the square of the commonly used Smagorinsky constant C_S.

Following Germano *et al.* (1991), we introduce a test-scale filter represented by a tilde whose length scale $\widetilde{\overline{\Delta}}$ is larger than $\overline{\Delta}$. The purpose of doing this is to utilize the information between the grid-scale and the test-scale filters to determine the characteristics of the SGS motion. By applying Germano's algebraic identity (Germano 1991) relating the subgrid-scale stress and the test-scale stress and employing a least-square closure (Lilly 1992), we obtain an explicit expression for the model coefficient C based on the local flowfield as

$$C = -\frac{\mathcal{L}_{ij} M_{ij}}{2\overline{\Delta}^2 M_{ij} M_{ij}} \tag{5}$$

where

$$\mathcal{L}_{ij} = \widetilde{\overline{u}_i \overline{u}_j} - \widetilde{\overline{u}}_i \widetilde{\overline{u}}_j, \tag{6a}$$

$$M_{ij} = \alpha^2 |\widetilde{\overline{S}}| \widetilde{\overline{S}}_{ij} - \widetilde{|\overline{S}| \overline{S}_{ij}}, \tag{6b}$$

$$\alpha = \widetilde{\overline{\Delta}} / \overline{\Delta}. \tag{6c}$$

In the above model, α is the only input parameter.

The implementation of the SGS stress term '$-\partial \tau_{ij}/\partial x_j$' in the momentum equations needs some consideration. First the trace of τ_{ij} is combined with the pressure gradient. Then, if the time marching scheme is explicit, τ_{ij} can be calculated directly from equations (2), (3) and (4). However, if an implicit or semi-implicit time marching scheme is used, it is advantageous to advance the SGS stress term (or at least a part of it) implicitly. This requires us to express SGS stress term in terms of of the velocity as

$$-\frac{\partial \tau_{ij}}{\partial x_j} = \frac{\partial}{\partial x_j}(\nu_T \frac{\partial \overline{u}_i}{\partial x_j}) + \frac{\partial \nu_T}{\partial x_j} \frac{\partial \overline{u}_j}{\partial x_i} \tag{7}$$

In deriving the above equation, we have utilized the continuity equation. The first term on the right-hand-side of equation (7) can be combined with the viscous terms and be advanced in time implicitly. The second term, on the other hand, poses difficulty if treated implicitly because by doing so, the three momentum equations are coupled and the resulting matrix is more complicated. In the present work, this term is advanced explicitly as an extra source term. Numerical experiments showed that this treatment did not affect stability in the present case.

The governing equations are transformed into the computational space and discretized on a non-staggered grid using a finite volume approach (Zang *et al.* 1992). Cartesian velocity and volume fluxes are used as dependent variables. The solution method integrates the governing equations in time semi-implicitly by solving the viscous terms with the approximate factorization technique. The pressure Poisson equation is solved using a multigrid method. The overall accuracy is second-order in both space and time. The use of the non-staggered grid layout and Cartesian velocities as dependent variables makes the filtering operations very easy to carry out when the dynamic eddy viscosity is computed.

Most studies to date using DSM have carried out filter operations in wave space. Recently, effort has been made to evaluate the behavior of different kinds of filters in physical space (Lund 1991). In the present formulation, we employ a top-hat filter in physical space with the trapezoidal rule for the test-scale filter. Because of the non-staggered-grid layout, all the variables that are used in the calculation of C are defined at the center of a control volume, and thus the filtering operation is the same for every variable. The length scale of the test filter is twice of that of the grid cell resulting in an α of 2. This value of α has been shown to be the optimal choice in the simulation of a turbulent channel flow (Germano *et al.* 1991).

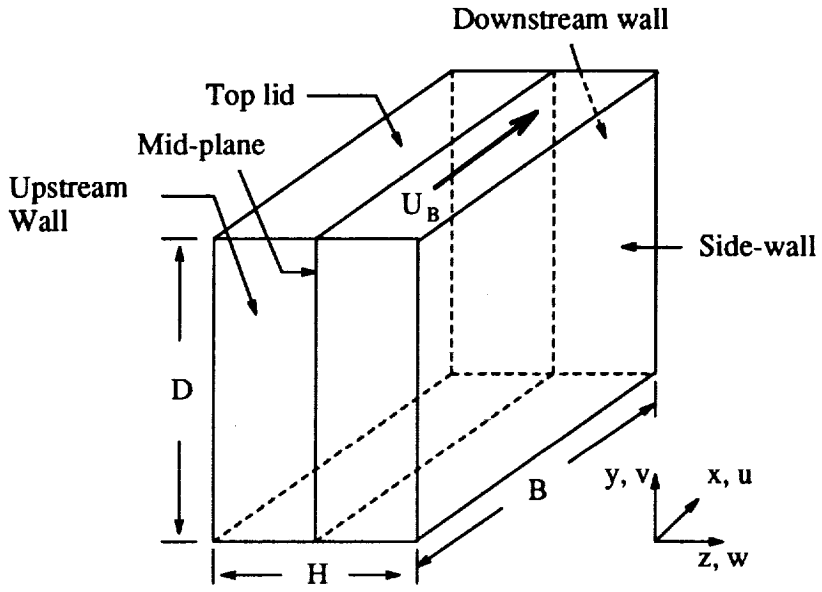

FIGURE 1. Geometry and boundary condition of the lid-driven cavity flow.

After the model coefficient C is computed from equation (4), it is averaged locally in space using the same scheme as that of the test filtering.

When local averaging of C alone was employed, numerical instability was experienced. This occurred because a large and negative C could lead to a negative eddy viscosity ν_T with a magnitude larger than the molecular viscosity, resulting in a negative total viscosity. Similar instability has been observed in previous simulations using the dynamic model and a local model coefficient $C(x, y, z, t)$ (Cabot 1991). When there are one or more homogeneous directions, a plane or line average in those directions could be used to stabilize the calculation (e.g., Germano *et al.* 1991). In the present wall-bounded flows, however, there is no homogeneous direction. Larger averaging volume and/or averaging in time could be employed to reduce the magnitude of negative Cs (Piomelli 1991), but they still do not generally guarantee stability. To overcome this difficulty, we set the total viscosity $\nu_T + \nu$ equal to zero wherever it becomes negative. This cutoff eliminates the negative total viscosity that causes the numerical instability and at the same time allows energy to backscatter from small to large scales. The local averaging before the cutoff serves to spread the effect of large negative values of C if they exist. For the case computed in this work, the cutoff does not affect the flow significantly as the magnitude of the negative ν_T is larger than ν only in a very localized region near the upper right corner of the cavity.

2.2. LES of flow in a lid-driven cavity

Lid-driven laminar flows in a cavity have long been used as a benchmark to test the accuracy of numerical methods (e.g., Ghia *et al.* 1982; Perng & Street

1989). Although extensive experimental measurements have been performed for transitional and turbulent flows in cavities (Koseff & Street 1984; Prasad & Koseff 1989), to the authors' knowledge, there have been no detailed direct or large-eddy simulations. Part of the difficulty lies in that in its temporal evolution the flow goes through the whole range of laminar, transitional, and turbulent stages. Moreover, even at the fully developed state, the flow is highly inhomogeneous and may have both laminar and turbulent regions. Successful simulation of this flow requires a SGS model which is capable of adjusting itself to the local flow dynamics.

We computed the lid-driven flow in a three-dimensional cavity with aspect ratios B:D:H of 1:1:0.5. A schematic of the cavity together with the notations are given in Figure 1. The Reynolds number based on the lid velocity U_B and the cavity length B is 7500. Past experiments (Koseff & Street 1984) have shown that at Reynolds numbers higher than about 6000, instabilities occur near the downstream eddy. As the Reynolds number increases, the flow becomes increasingly turbulent near walls, and at Reynolds numbers higher than 10,000, the flow near downstream eddy becomes fully turbulent. Thus, the present flow is in the transitional regime. In the simulation, we use a 64x64x32 grid, which is non-uniform in the streamwise and vertical directions but is spanwise uniform. Initially the fluid is at rest. Computation was first carried out in a half of the cavity with a 64x64x18 grid. A symmetry boundary condition was specified at the mid-plane. After the flow was fully developed, the half flowfield was mirrored onto the whole cavity. Simulation then continued and statistics were collected after a relaxation time of three turnaround time-scale T_a of the cavity. The value of T_a, which was about 1 minute in this case, was estimated as the time for a particle at the edge of the top boundary layer to travel back to its starting position in the cavity.

Figure 2 shows the computed mean center-line velocity profiles on the mid-plane. Measurements by Prasad and Koseff (1989) are also shown. The computed statistics were collected during a period of $5T_a$, while the experimental data was averaged over periods of $5T_a$ to $10T_a$. The computation slightly over-predicts the thickness of the boundary layer on the upstream wall but captures the thickness of the bottom boundary layer and the magnitude of the two peak velocities fairly accurately. The averaged relative error between the two data sets scaled by the lid velocity is less than 2 percent.

The r.m.s. of fluctuating velocities $\sqrt{< u'^2 >}/U_B$ and $\sqrt{< v'^2 >}/U_B$ and the Reynolds stress $< u'v' > /U_B^2$ on the center-lines in the mid-plane are shown in Figure 3, where $< \cdot >$ denotes time averaging. We note that in the figure, these two quantities are increased by a scale of 10 and 500, respectively. The computation slightly over-predicts the r.m.s. of u' near the bottom boundary layer and under-predicts the r.m.s. of v' near the upstream wall. There is a minimum in the r.m.s. profile of u velocity in the bottom boundary layer which is not evident in the experimental data. The magnitude of the Reynolds stresses near the bottom and the upstream boundary layers is well represented. A maximum of the Reynolds stress is observed above the bottom boundary layer which is not shown in the experimental profile.

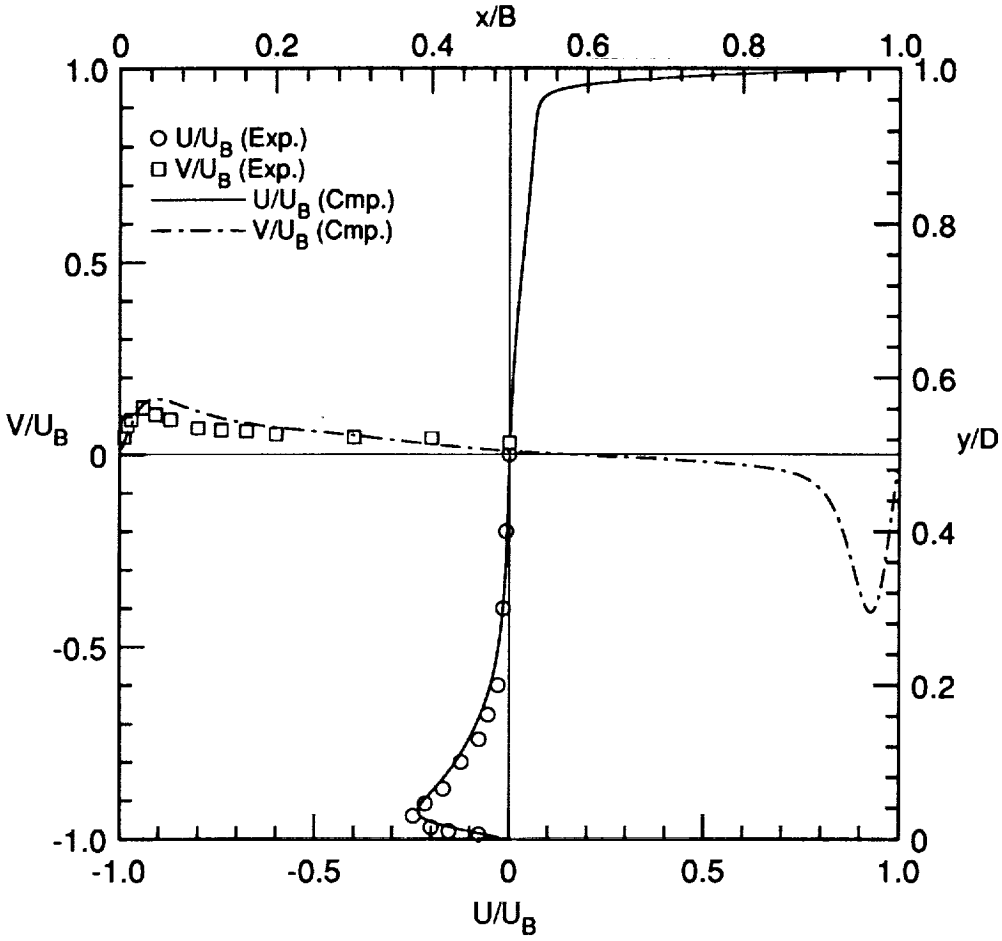

FIGURE 2. Mean centerline velocities on the mid-plane. Symbols are from Prasad and Koseff (1989). Lines are from the present computation.

The computed profiles in Figures 2 and 3 are the large-scale quantities resolved by the grid, while the experimental data contains contribution from both the large and small scales. The contribution of the SGS motion to the Reynolds stress $< u'v' >$ can be estimated using the time average of the SGS stress, $< \tau_{12} >$. In the present case, the value of $< \tau_{12} >$ is at least an order of magnitude smaller than $< \overline{u}'\overline{v}' >$ which is the large-scale contribution to the Reynolds stress. This indicates that the time-averaged statistics are well represented by the large-scale quantities. Two factors besides modeling error could have contributed to the above discrepancies. One is the experimental uncertainty, and the other is the effect of numerical resolution. However, at the present time, collecting statistics on a grid substantially finer than the one presently used is prohibitively expensive.

Figure 4a shows the dynamically computed C on the mid-plane of the cavity, and 4b displays C on a plane close to one of the side-walls. On the mid-plane,

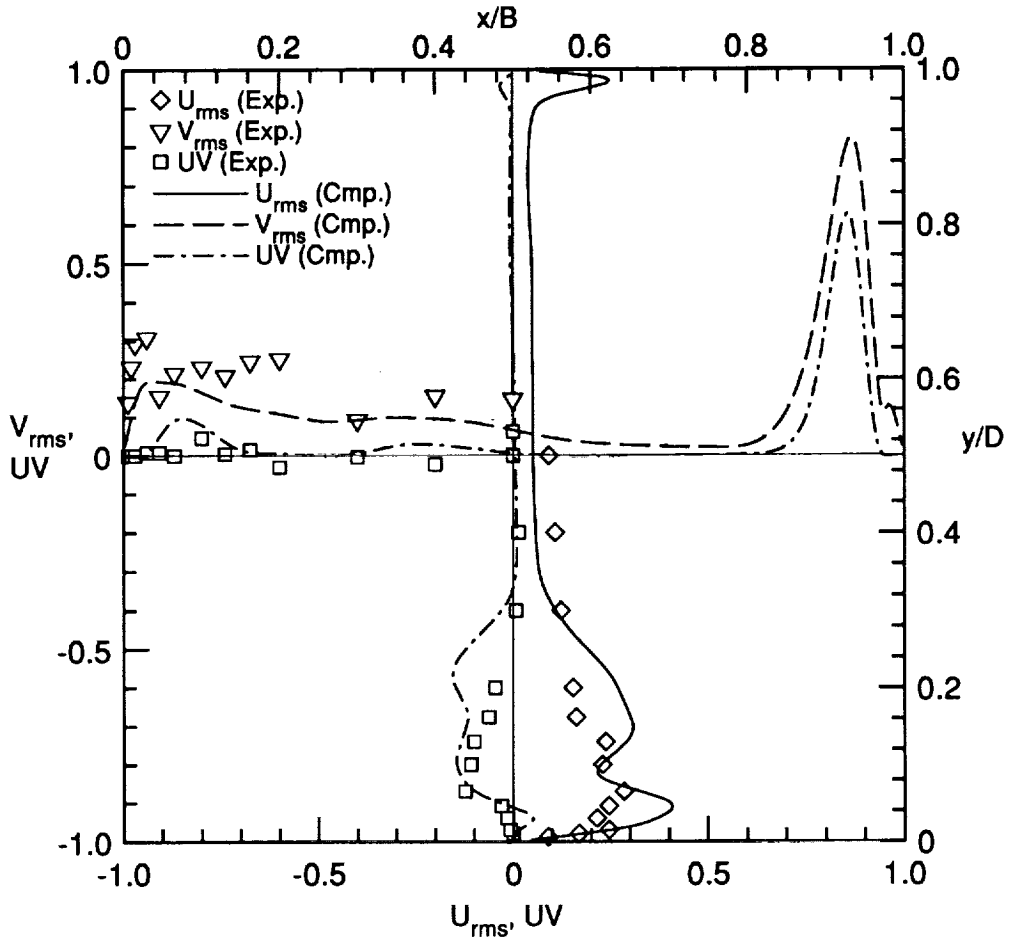

FIGURE 3. R.m.s. velocity and Reynolds stress at the centerlines on the mid-plane. $U_{rms} = 10\sqrt{< u'^2 >}/U_B$, $V_{rms} = 10\sqrt{< v'^2 >}/U_B$, $UV = 500 < u'v' > /U_B^2$. Symbols are from Prasad and Koseff (1989). Lines are from the present computation.

the range of C is from -0.12 to 0.1, while on the near-wall plane, the range is from -0.17 to 0.22. In the bulk region of the mid-plane, the magnitude of C is from 0.01 to 0.02, which is comparable to the square of the commonly used value of 0.1 for the Smagorinsky constant. On the other hand, near the side wall (Figure 4b), C is small except near the corners and in the corner boundary layers. This is consistent with the expected behavior of C near a solid wall. It is interesting to notice that C is small near the moving top lid in both planes.

There are localized regions in Figure 4 where C is negative, which results in negative eddy viscosity representing energy backscatter from small to large scales. The ability of the present model to backscatter energy to large scales is important in sustaining turbulent fluctuations in the simulation. The time history of the

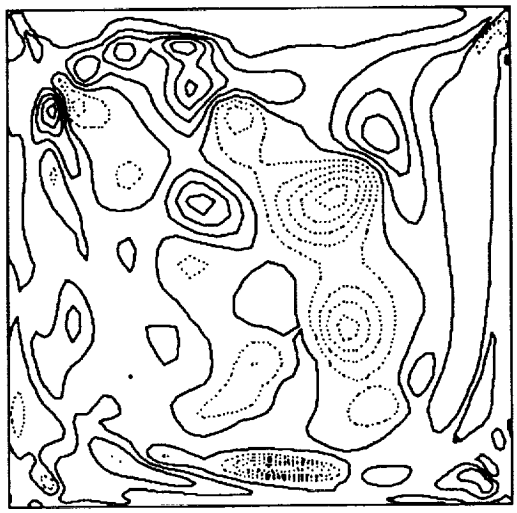

FIGURE 4A. Contours of computed C on the mid-plane. Dotted lines represent negative values.

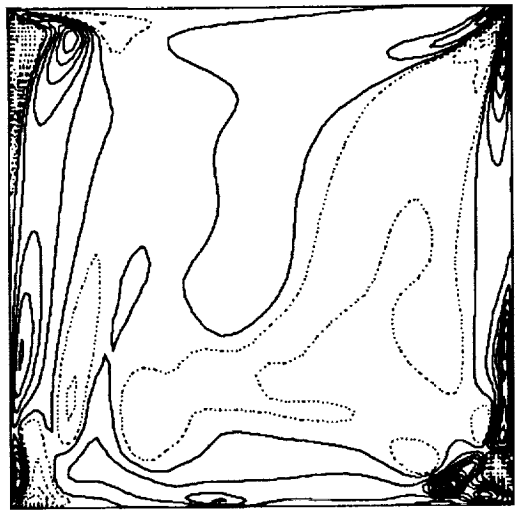

FIGURE 4B. Contours of computed C near one of the side walls. Dotted lines represent negative values.

large-scale streamwise velocity $\overline{u}(t)$ near the peak of the bottom boundary layer on the center-line of the mid-plane is shown in Figure 5a, where the flow was in its fully developed state. Figure 5b gives $\overline{u}(t)$ at the same location when no negative ν_T was allowed. The fluctuations in 5b were slowly damped out, indicating that backscatter from small to large scales is necessary to sustain turbulence. The low frequency oscillations with a period of about 1 minute in Figure 5a correspond

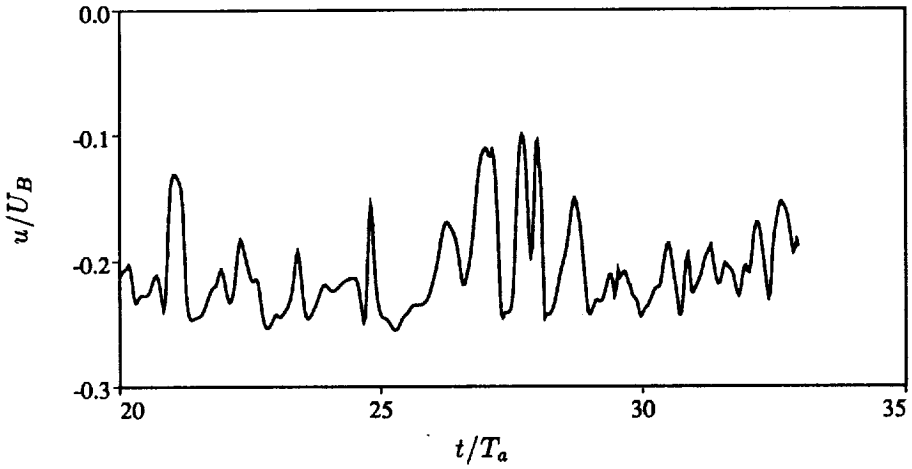

FIGURE 5A. Time history of u near the peak of the lower boundary layer on the vertical center-line in the mid-plane. Model with backscatter. Fully developed state.

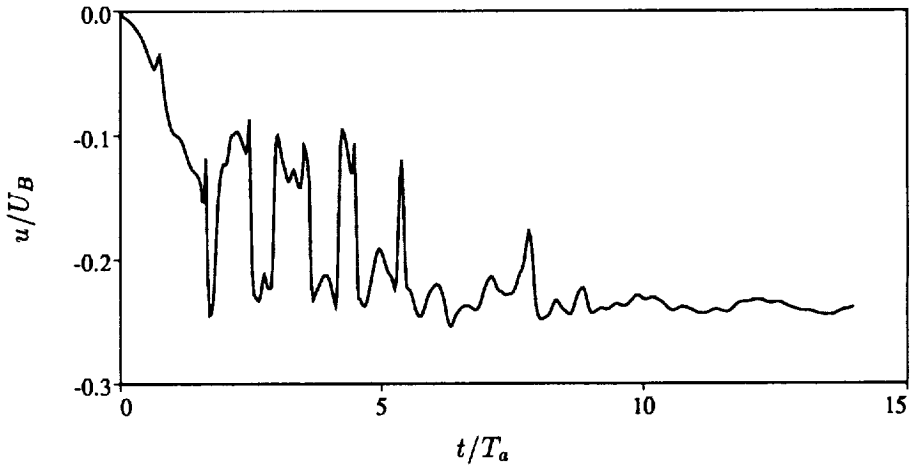

FIGURE 5B. Same as Figure 5a. Model without backscatter.

to the spanwise meandering of TGL vortices. Examination of the flow structures in the spanwise direction shows the appearance of one pair of TGL vortices near the downstream wall which is meandering spanwisely. This is consistent with past experimental results (Prasad 1989).

Previous simulations of cavity flows at lower Reynolds numbers have shown that the flows are essentially symmetric over the mid-plane (Perng & Street 1989). This is true when the flow is laminar since there is no non-symmetric forcing and any non-symmetric small disturbances are damped. However, in turbulent flows, small disturbances could be amplified and result in asymmetry. In the present case, it

was found that when the half-cavity domain was used and the symmetry boundary condition was imposed at the mid-plane, both the streamwise fluctuating velocity $< u'^2 >$ and the streamwise-vertical Reynolds stress $< u'v' >$ were unphysically large. On the other hand, the mean velocity profiles were barely changed. This was because the symmetry boundary condition eliminated the spanwise fluctuating velocity w' at the mid-plane and restricted the meandering of the TGL vortices which were responsible for the momentum and energy transfer in the spanwise direction near the mid-plane. These high frequency fluctuations are averaged out in the mean profiles but make significant contribution to the r.m.s. quantities and Reynolds stress.

3. Summaries and future plans

A dynamic SGS model is coupled with a finite volume solution method and employed in the large eddy simulation of turbulent flow in a lid-driven cavity. Local averaging together with a cutoff is employed to obtain the model coefficient. The mean and fluctuating quantities were compared with experimental data and good agreement was achieved. It was shown that backscatter is necessary to sustain fluctuations in the flow.

The model is being applied to the simulation of upwelling flows of a stratified rotating fluid on a slopping bottom. Baroclinic instability was observed at the surface density front and intensive mixing occurred on both sides of the front. Preliminary results have shown that the computed wave speed and wave size compare favorably with the experimental and theoretical values. The characteristics of the instabilities and the subsequent breakdown of the front are being investigated. The model is also being employed to investigate flows in more complex geometries.

Acknowledgement

The authors wish to thank Prof. J. H. Ferziger and Dr. T. S. Lund for many helpful suggestions. The Cray YMP allocation provided by NCAR Scientific Computing Division is gratefully appreciated. This research is supported by National Science Foundation through Grant CTS-8719509. T. Lin, who was supported by Center for Turbulence Research, made a significant contribution in the early stages of this work.

REFERENCES

BARDINA, J., FERZIGER, J. H., & REYNOLDS W. C. 1983 Improved turbulence models based on large eddy simulation of homogeneous, incompressible, turbulent flows. *Report No. TF-19.* Dept. Mech. Eng., Stanford University.

CABOT, W. 1991 Large eddy simulation of passive and buoyant scalars with dynamic subgrid-scale models. *Annual Research Briefs.* Center for Turbulence Research, Stanford U./NASA-Ames, 191-205.

GERMANO, M. 1991 Turbulence: the filtering approach. *J. Fluid Mech.* **238,** 325-336.

GERMANO, M., PIOMELLI, U., MOIN, P. & CABOT, W.H. 1991 A dynamic subgrid-scale eddy viscosity model. *Phys. Fluids A.* **3,** 1760-1765.

GHIA, U., GHIA, K. N. & SHIN, C. T. 1982 High-Re solutions for incompressible flow using the Navier-Stokes equations and a multigrid method. *J. Comp. Physics.* **48,** 387-411.

KOSEFF, J. R. & STREET, R. L. 1984 Visualization studies of a shear driven three-dimensional recirculating flow. *J. Fluids Eng.* **106,** 21-29.

LILLY, D. K. 1992 A proposed modification of the Germano subgrid scale closure method. *Phys. Fluids A.* **4,** 633-635.

LUND, T. S. 1991 Discrete filters for finite differenced large eddy simulation. Presentation at the 44th Annual Meeting of the American Physical Society, Division of Fluid Dynamics, Scottsdale, Arizona.

MOIN, P., SQUIRES, K., CABOT W. & LEE, S. 1991 A dynamic subgrid-scale model for compressible turbulence and scalar transport. *Phys. Fluids A.* **3,** 2746-2757.

PERNG, C. Y. & STREET, R. L. 1989 3-D unsteady flow simulation: alternative strategies for a volume-averaged calculation. *Int. J. Num. Meth. Fluids.* **9,** 341-362.

PIOMELLI, U. 1991 Local averaging of the dynamic subgrid-scale stress model. Presentation at the 44th Annual Meeting of the American Physical Society, Division of Fluid Dynamics, Scottsdale, Arizona.

PIOMELLI, U., MOIN, P. & FERZIGER, J. H. 1988 Model consistency in large eddy simulation of turbulent channel flows. *Phys. Fluids.* **31,** 1884-1891.

PIOMELLI, U., ZANG, T. A., SPEZIALE C. G. & HUSSAINI, M. Y. 1990 On the large-eddy simulation of transitional wall-bounded flows. *Phys. Fluids A.* **2,** 257-265.

PRASAD, A. K. 1989 Effects of variable geometry on momentum and heat transfer in a lid-driven cavity flow. Ph.D Dissertation, Dept. Mech. Eng., Stanford University.

PRASAD, A. K. & KOSEFF, J. R. 1989 Reynolds number and end-wall effects on a lid-driven cavity flow. *Phys. Fluids A.* **1,** 208-218.

SMAGORINSKY, J. 1963 General circulation experiments with the primitive equations. I. The basic experiment. *Mon. Weather Rev.* **91,** 99-164.

ZANG, Y., STREET, R. L. & KOSEFF, J. R. 1992 A non-staggered grid fractional step method for time-dependent incompressible Navier-Stokes equations in general curvilinear coordinate systems *submitted to J. Comp. Physics.*

Center for Turbulence Research
Annual Research Briefs 1992

Large-eddy simulation of turbulent flow with a surface-mounted two-dimensional obstacle

By Kyung-Soo Yang[1] AND Joel H. Ferziger[1]

1. Motivation and objectives

Large-eddy simulation (LES) is an accurate method of simulating complex turbulent flows in which the large flow structures are computed while small scales are modeled. The rationale behind this method is based on two observations: most of the turbulent energy is in the large structures, and the small scales are more isotropic and universal. Therefore, LES may be more general and less geometry-dependent than Reynolds-averaged modeling, although it comes at higher cost.

Even though LES has been used by many investigators, most research has been limited to flows with simple geometry. Here we shall consider a rectangular parallelopiped mounted on a flat surface. Related flows are those over surfaces protruding from submarines (conning towers or control fins), wind flows around buildings, and air flows over computer chips, among others. The most distinctive features associated with these flows are three dimensionality, flow separation due to protruding surfaces, and large scale unsteadiness. As a model flow, we consider a plane channel flow in which a two-dimensional obstacle is mounted on one surface (see Fig. 1). This relatively simple geometry contains flow separation and reattachment. Flow in this geometry has been studied by Tropea & Gackstatter (1985) for low Re and Werner & Wengle (1989) and Dimaczek, Kessler, Martinuzzi & Tropea (1989) for high Re, among others.

Recently, Germano, Piomelli, Moin & Cabot (1991) suggested a dynamic subgrid-scale model in which the model coefficient is dynamically computed as computation progresses rather than input *a priori*. This approach is based on an algebraic identity between the subgrid-scale stresses at two different filter levels and the resolved turbulent stresses. They applied the model to transitional and fully turbulent channel flows and showed that the model contributes nothing in laminar flow and exhibits the correct asymptotic behavior in the near-wall region of turbulent flows without an *ad hoc* damping function. This is a significant improvement over conventional subgrid-scale modeling.

Until very recently, use of the dynamic model in complex geometries has been difficult owing to the lack of homogeneous directions over which to average the model coefficient (see Ghosal *et al.* this volume for a dynamic model applicable to inhomogeneous flows). The present work was accomplished prior to the developments of Ghosal *et al.* and accordingly makes use of a combination of time and spatial averages in order to determine the model coefficient. The averaging scheme will be discussed in more detail in §3.

1 Stanford University

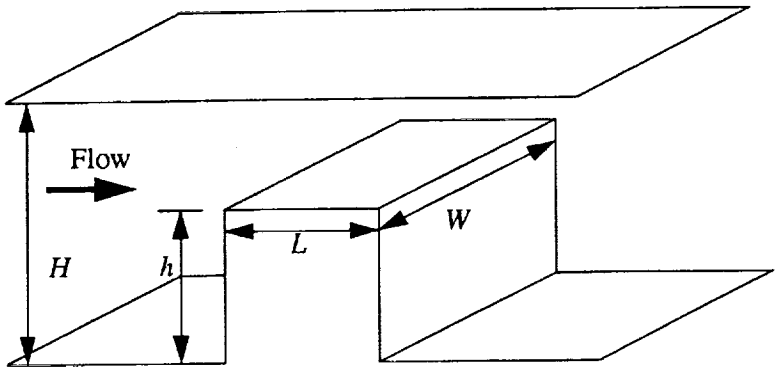

FIGURE 1. Physical configuration.

In this paper, we perform an LES of turbulent flow in a channel containing a two-dimensional obstacle on one wall using a dynamic subgrid-scale model (DSGSM) at Re=3210, based on bulk velocity above the obstacle (U_m) and obstacle height (h); the wall layers are fully resolved. The low Re enables us to perform a DNS (Case I) against which to validate the LES results. The LES with the DSGSM is designated Case II. In addition, an LES with the conventional fixed model constant (Case III) is conducted to allow identification of improvements due to the DSGSM.

We also include LES at Re=82,000 (Case IV) using conventional Smagorinsky subgrid-scale model and a wall-layer model. The results will be compared with the experiment of Dimaczek *et al.* (1989).

2. Formulation

All variables are nondimensionalized by U_m and h. The code uses a nonuniform Cartesian staggered grid in a finite-volume approach. The incompressible momentum equations filtered by a simple volume-average box filter are

$$\frac{\partial \overline{u}_i}{\partial t} + \frac{\partial}{\partial x_j}(\overline{u_i u_j}) = -\frac{\partial \overline{p}}{\partial x_i} + \frac{1}{Re}\frac{\partial^2 \overline{u}_i}{\partial x_j \partial x_j}, \tag{1}$$

where u_1, u_2, u_3 (or u, v, w) are velocities in x_1 (streamwise), x_2 (normal), x_3 (spanwise) directions (or x, y, z), respectively, and p is pressure. The volume-average box filter is defined by

$$\overline{u}_i(\vec{x},t) = \frac{1}{\Delta x_1 \Delta x_2 \Delta x_3}\int_{x_1-\frac{\Delta x_1}{2}}^{x_1+\frac{\Delta x_1}{2}}\int_{x_2-\frac{\Delta x_2}{2}}^{x_2+\frac{\Delta x_2}{2}}\int_{x_3-\frac{\Delta x_3}{2}}^{x_3+\frac{\Delta x_3}{2}} u_i(\vec{x'},t)d\vec{x'}, \tag{2}$$

where $\vec{x}=(x_1,x_2,x_3)$ and $d\vec{x'}=dx_1'dx_2'dx_3'$. The convective term can be rewritten as

$$\frac{\partial}{\partial x_j}(\overline{u_i u_j}) = \frac{\partial}{\partial x_j}(\overline{u}_i\overline{u}_j + L_{ij} + C_{ij} + R_{ij}), \tag{3}$$

where

$$\begin{cases} L_{ij} = \overline{\overline{u}_i \overline{u}_j} - \overline{u}_i \overline{u}_j \\ C_{ij} = \overline{\overline{u}_i u'_j} + \overline{\overline{u}_j u'_i} \\ R_{ij} = \overline{u'_i u'_j}. \end{cases} \tag{4}$$

L_{ij}, C_{ij}, R_{ij} represent Leonard stresses, cross terms, subgrid-scale Reynolds stresses, respectively. When a finite-difference scheme of second-order accuracy is used, the Leonard stresses are of the same order as the truncation error (Shaanan, Ferziger & Reynolds, 1975). The other terms have to be modeled.

The governing equations for LES become

$$\frac{\partial \overline{u}_i}{\partial x_i} = 0, \tag{5}$$

$$\frac{\partial \overline{u}_i}{\partial t} + \frac{\partial}{\partial x_j}(\overline{u}_i \overline{u}_j) = -\frac{\partial P}{\partial x_i} - \frac{\partial}{\partial x_j}\tau_{ij} + \frac{1}{Re}\frac{\partial^2 \overline{u}_i}{\partial x_j \partial x_j}, \tag{6}$$

where

$$\begin{cases} \tau_{ij} = Q_{ij} - \frac{1}{3}Q_{kk}\delta_{ij} \\ P = \overline{p} + \frac{1}{3}Q_{kk} \\ Q_{ij} = R_{ij} + C_{ij}. \end{cases} \tag{7}$$

Here, δ_{ij} is the Kronecker symbol. In the present simulation, the eddy viscosity model of Smagorinsky (1963) is used:

$$\tau_{ij} = -2\nu_T \overline{S}_{ij}, \tag{8}$$

where

$$\begin{cases} \overline{S}_{ij} = \frac{1}{2}\left(\frac{\partial \overline{u}_i}{\partial x_j} + \frac{\partial \overline{u}_j}{\partial x_i}\right) \\ \nu_T = l^2\sqrt{2\overline{S}_{ij}\overline{S}_{ij}}. \end{cases} \tag{9}$$

Here, l is a characteristic length scale of the small eddies. In Case III and IV, the smaller value of κd and $0.1\overline{\Delta}$ is used for l, where κ and d are von Karman's constant and the distance normal to a wall, respectively, and $\overline{\Delta} = (\Delta x \Delta y \Delta z)^{\frac{1}{3}}$. The particular form of τ_{ij} in (7) is chosen in order to make both (7) and (8) consistent on contraction ($i = j$).

In Case II, $l^2 = C_s\Delta^2$ is dynamically determined following the prescription of Germano *et al.* (1991) as modified by Lilly (1992). When the dynamic model is used, C_s is an instantaneous and local quantity that can vary wildly in time and space. This wide variation results in large negative values of C_s that lead to numerical instability. To avoid this difficulty, averaging is performed in space and time. (For an alternate approach see Ghosal *et al.*, this volume). Spatial averaging is done in the homogeneous (z) direction first. Then additional averaging is performed over nine neighboring grid points with the point for which the averaging is carried out at the center, using volume weighting, in order to obtain an averaged value of C_s at a given inner grid point. In the near-wall region, averaging is done only in the direction parallel to the solid wall, i.e. using three points. It is necessary to repeat this process to smooth C_s sufficiently. Germano *et al.* (1991) found the optimum value of the ratio, $\widetilde{\overline{\Delta}}/\overline{\Delta}$, to be two, a value we adopted.

3. Numerical method

To advance the solution in time, a fractional step method (Kim and Moin, 1985) is employed. The time-advancement of the momentum equation is hybrid; the convective terms are explicitly advanced by a third-order Runge-Kutta scheme and the viscous terms implicitly by Crank-Nicolson method:

$$\frac{\widehat{\overline{u}}_i^k - \overline{u}_i^{k-1}}{\Delta t} = (\alpha_k + \beta_k)L(\overline{u}_i^{k-1}) + \beta_k L(\widehat{\overline{u}}_i^k - \overline{u}_i^{k-1})$$

$$-\gamma_k N(\overline{u}_i^{k-1}) - \zeta_k N(\overline{u}_i^{k-2}) - (\alpha_k + \beta_k)\frac{\partial \overline{P}^{k-1}}{\partial x_i}, \tag{10}$$

$$\frac{\overline{u}_i^k - \widehat{\overline{u}}_i^k}{\Delta t} = -\frac{\partial \overline{\phi}^k}{\partial x_i} \quad (k = 1, 2, 3), \tag{11}$$

where

$$\frac{\partial \overline{P}^k}{\partial x_i} = \frac{\partial \overline{P}^{k-1}}{\partial x_i} + \left(\frac{1}{\alpha_k + \beta_k} - \frac{\beta_k \Delta t}{\alpha_k + \beta_k} L\right)\frac{\partial \overline{\phi}^k}{\partial x_i},$$

$$L = \frac{1}{Re}\frac{\partial^2}{\partial x_j \partial x_j} + \frac{\partial}{\partial x_j}\nu_T(1 + \delta_{ij})\frac{\partial}{\partial x_j},$$

$$N(\overline{u}_i) = \frac{\partial}{\partial x_j}(\overline{u}_i \overline{u}_j) - \frac{\partial}{\partial x_j}\nu_T(1 - \delta_{ij})\frac{\partial \overline{u}_j}{\partial x_i},$$

with

$$\gamma_1 = \frac{8}{15}, \quad \gamma_2 = \frac{5}{12}, \quad \gamma_3 = \frac{3}{4}, \quad \zeta_1 = 0, \quad \zeta_2 = -\frac{17}{60}, \quad \zeta_3 = -\frac{5}{12},$$

$$\alpha_1 = \beta_1 = \frac{4}{15}, \quad \alpha_2 = \beta_2 = \frac{1}{15}, \quad \alpha_3 = \beta_3 = \frac{1}{6},$$

$$\sum_{k=1}^{3}(\alpha_k + \beta_k) = \sum_{k=1}^{3}(\gamma_k + \zeta_k) = 1.$$

In the expressions for L and $N(\overline{u}_i)$, summation is performed on the index j only. The momentum equation is time-advanced without implicit pressure terms and then projected onto a divergence-free space by introducing $\overline{\phi}$ that obeys a Poisson equation. The latter is solved by a multigrid method which is very flexible and more efficient than a number of competitors. For spatial discretization, second-order accurate central differencing was used. All terms in the model except the cross derivatives are treated implicitly in all three directions to avoid restrictions on time steps. The code is well vectorized; a speed of 150 MFLOPS has been achieved on CRAY Y-MP/832.

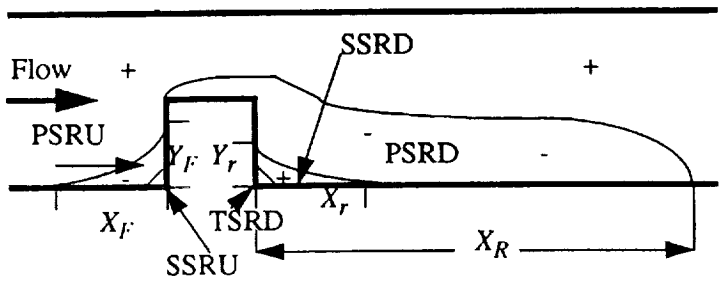

FIGURE 2. Schematic drawing of SR regions.

Case	Re	X_R	X_r	Y_r	X_F	Y_F
I	3310	6.42	1.21	0.35	1.51	0.28
II	3210	6.80	1.13	0.36	1.51	0.37
III	3330	7.01	1.76	0.28	1.35	0.40

Table 1. Comparison of various SR lengths.

4. Results and discussion

4.1 Choice of parameters and boundary conditions

The values of the geometric parameters in all four cases are h/H=0.5, W/h=2, and L/h=1, where H, W, and L are channel height, spanwise width of the obstacle and channel, and obstacle streamwise length, respectively (see Fig. 1). The inlet and the outlet are located at x=0 and x=31, respectively, and the obstacle is placed between x=10 and x=11.

In Cases II and III the center of the control volume adjacent to the wall was placed at Δy=0.0086 from horizontal walls except on the top of the obstacle where the nearest center was placed at Δy=0.0046. The corresponding distances for Case I and Case IV are 0.005 and 0.05 from horizontal walls and 0.0036 and 0.025 from the top of the obstacle. On the forward-facing wall, the first grid points are at Δx=0.0045 for Cases II and III and at 0.0033 and 0.025 for Cases I and IV respectively. On the backward-facing wall, the first grid points are at Δx=0.014 for Cases II and III and at 0.0045 and 0.025 for Cases I and IV respectively. The grid is densely packed around the obstacle and near the channel walls and geometrically stretched in the other regions. The number of control volumes in the x, y, and z directions are $112 \times 48 \times 40$ for Cases II and III, $272 \times 64 \times 64$ for Case I, and $96 \times 32 \times 32$ for Case IV. Grid refinement shows that the spatial resolution is adequate; using more control volumes shows improvement, but the difference is insignificant.

In all cases, periodic boundary conditions were employed in the homogeneous (z) direction. At the walls, no-slip boundary conditions were imposed except for Case IV where a wall-layer model was employed. We also apply periodic boundary conditions in the x direction in order to avoid any uncertainty related to outflow boundary condition which has been an area of controversy and to assure a reasonable

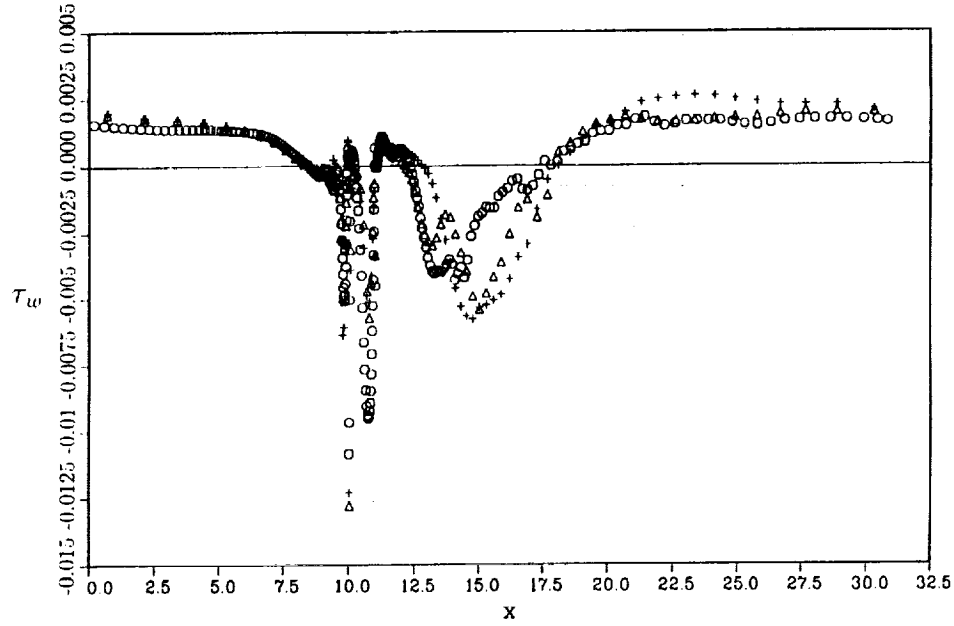

FIGURE 3(a). Averaged wall shear stress at the lower wall: o, DNS; $\triangle$, LES with DSGSM; +, LES with C_s=0.01.

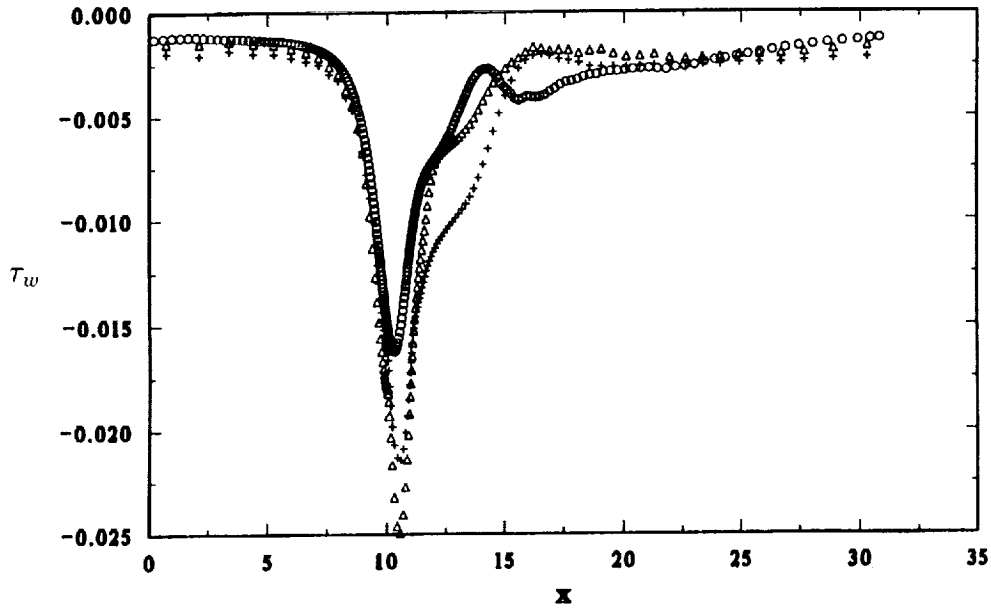

FIGURE 3(b). Averaged wall shear stress at the upper wall: o, DNS; $\triangle$, LES with DSGSM; +, LES with C_s=0.01.

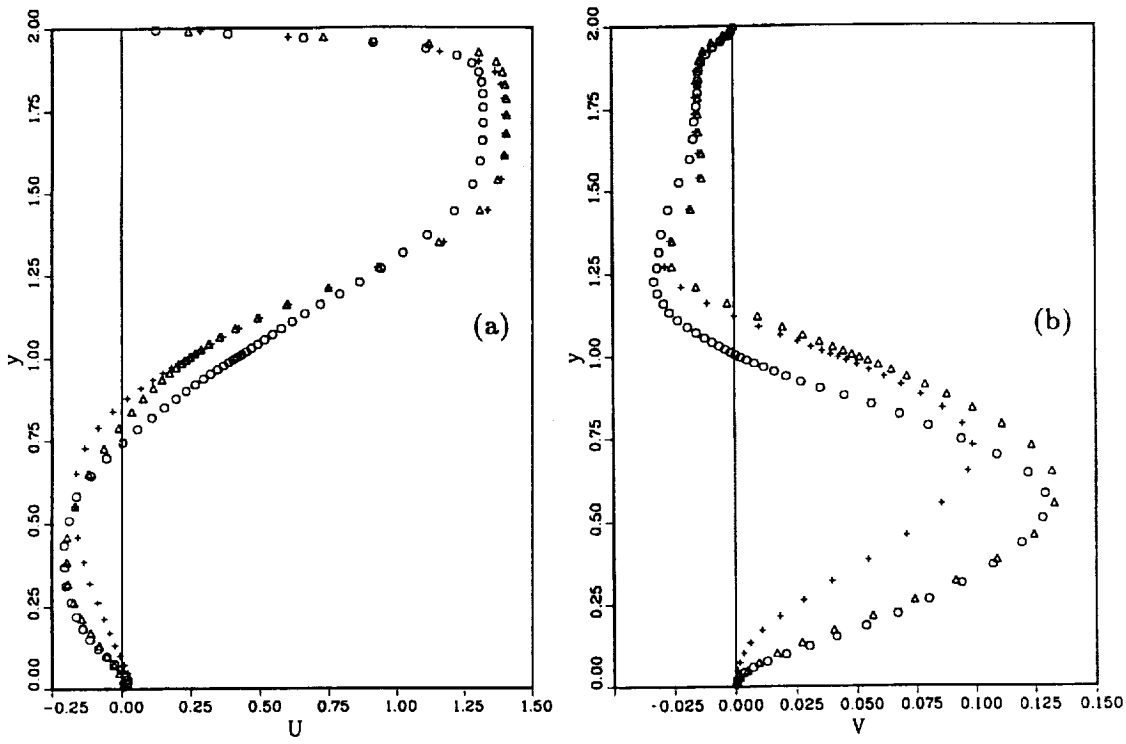

FIGURE 4. Averaged velocity profiles at x=12; (a) streamwise (U), (b) normal (V): o, DNS; $\triangle$, LES with DSGSM; +, LES with C_s=0.01.

flow approaching the obstacle. Therefore, we are actually simulating an infinitely-long channel flow with a periodic array of obstacles. To minimize the interaction between "neighboring" obstacles, the long streamwise computational domain ($31h$) is employed.

Since the pressure difference between the inlet and the outlet is fixed, Re is slightly different in each case. To match the Reynolds numbers of the various cases as closely as possible, we adjusted the pressure difference slightly. The second column of Table 1 shows Re for each low-Re case. The 3% variation in Re should be kept in mind in the comparisons below. The high-Re case will also be compared with the experiment of Dimaczek *et al.* (1989) at slightly different Re (Re=84,000). After an initial transient period, the flow becomes fully turbulent and sustained. Then, an averaging is performed in the homogeneous direction and in time in order to obtain averaged quantities. The time-averaging was taken over 27 characteristic time units (h/U_m) for low-Re cases and 38 units for Case IV.

4.2 Averaged flow field at Re=3210

The flow develops several separation and reattachment (SR) zones near the obstacle. Figure 2 shows schematic contours of U=0 (U and V represent averaged

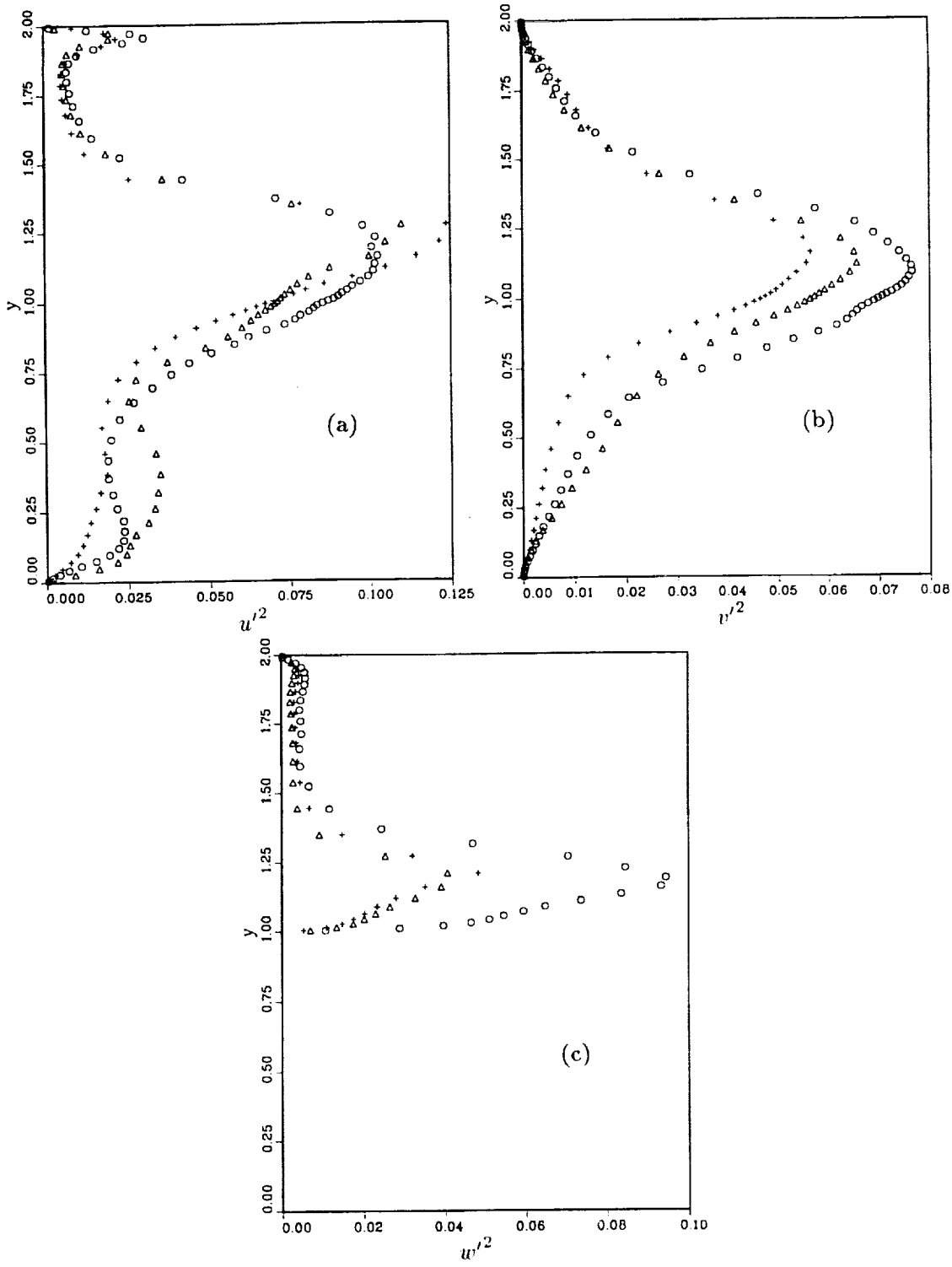

FIGURE 5. Averaged turbulent fluctuation profiles; (*a*) streamwise (u'^2) at x=12, (*b*) normal (v'^2) at x=12, (*c*) spanwise (w'^2) at x=11: ○, DNS; △ , LES with DSGSM; +, LES with C_s=0.01.

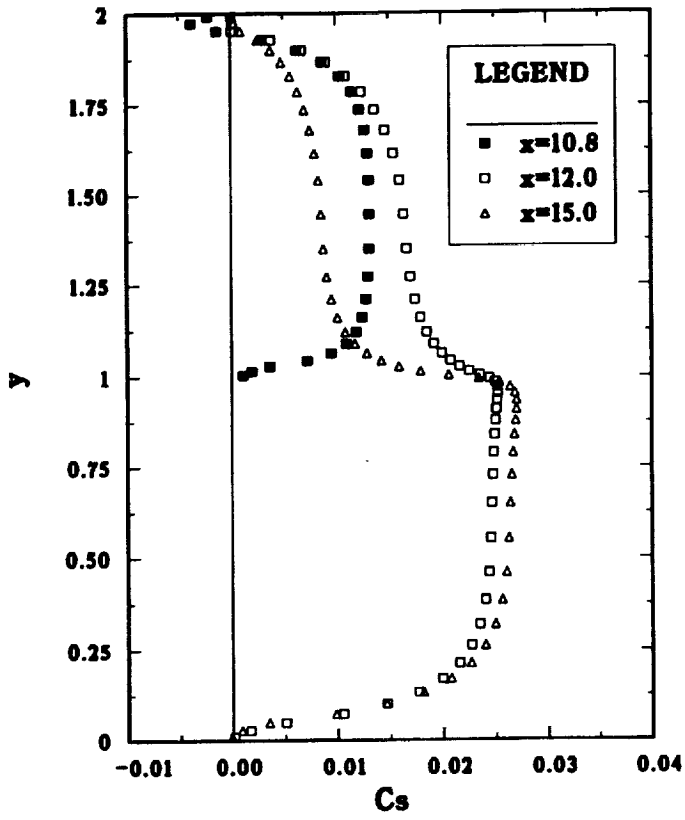

FIGURE 6. Profiles of C_s.

values of u and v, respectively). The + and - signs indicate regions of positive and negative U, respectively. In addition to the primary SR zones upstream (PSRU) and downstream (PSRD) of the obstacle, there are secondary SR zones upstream (SSRU, at the front corner), and downstream (SSRD, near the rear corner, bigger than SSRU) of the obstacle. A tertiary SR zone is discernible at the downstream corner of the obstacle (TSRD). For the given geometry and Re, reattachment does not occur on top of the obstacle in any of the three low-Re cases. The reattachment length of PSRD is denoted by X_R. The separation length and reattachment length of PSRU are represented by X_F and Y_F, respectively, and those of SSRD by X_r and Y_r, respectively. Table 1 gives computed values of those lengths in units of h for each case. Case I, the DNS, is the most accurate simulation. Its X_R differs by roughly 5% from the value of 6.1 determined in the experiment of Tropea & Gackstatter (1985). Although the aspect ratio (L/h) of the experimental obstruction is somewhat larger than in the simulation, the DNS value of X_R falls within the range of experimental error (quoted as 6%). Tropea & Gackstatter did not report other SR lengths. Case II is significantly more accurate than Case III for every length scale.

Figure 3 presents nondimensionalized shear stress (τ_w) on the lower (Fig. 3(a)) and upper walls (Fig. 3(b)). In Fig. 3(a), the values of τ_w between x=10 and x=11

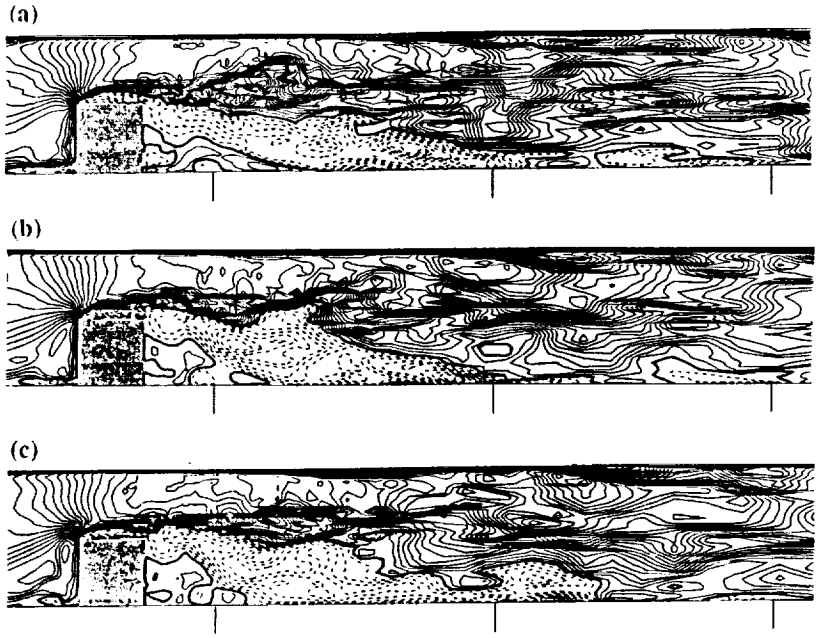

FIGURE 7. Regions of instantaneous negative u; solid, positive; dash, negative; thick solid, 0; increment, 0.016: (*a*) t=0; (*b*) t=Δt; (*c*) t=$2\Delta t$.

are for the top surface of the obstacle. The large variations in the values of τ_w on the top of the obstacle reflect the complexity of the flow in that region. The τ_w predicted by Case II agrees better with Case I in PSRD than does Case III, especially for $11 \leq x \leq 13$ and far downstream ($x \geq 20$). Case II also gives better results on the upper channel wall (Fig. 3(*b*)). The large $|\tau_w|$ near x=10 is caused by flow acceleration due to the sudden contraction in flow passage. Better agreement for $11 \leq x \leq 15$ and in the "channel region" ($x \leq 7.5$ or $x \geq 25$) are also noticeable.

Profiles of U and V at a selected streamwise location (x=12, just downstream of the obstacle) are shown in Figs. 4(*a*) and Fig. 4(*b*), respectively. In both figures, the DSGSM gives a significant improvement over the Smagorinsky model in the reversed flow region ($y \leq 0.75$).

Profiles of averaged turbulent fluctuations in the streamwise (u'^2), normal (v'^2), and spanwise (w'^2) directions at selected streamwise locations are presented in Figs. 5(*a*), 5(*b*), and Fig. 5(*c*), respectively. It should be noted that the LES results represent only the fluctuations in the resolved (grid-scale) velocity field. The subgrid-scale contribution is small at this low Re. The dynamic model gives an overall improvement for u'^2 and v'^2, but not for w'^2.

Figure 6 shows profiles of $C_s(x, y)$ at three different streamwise locations (x=10.8, 12, 15). Obviously, C_s depends upon grid used and the type of averaging in space and time. There is a sharp gradient near y=1 where the control volumes are densely clustered to resolve the flow above the obstacle. Without an arbitrary damping function, C_s vanishes at the walls and even takes some small negative values near

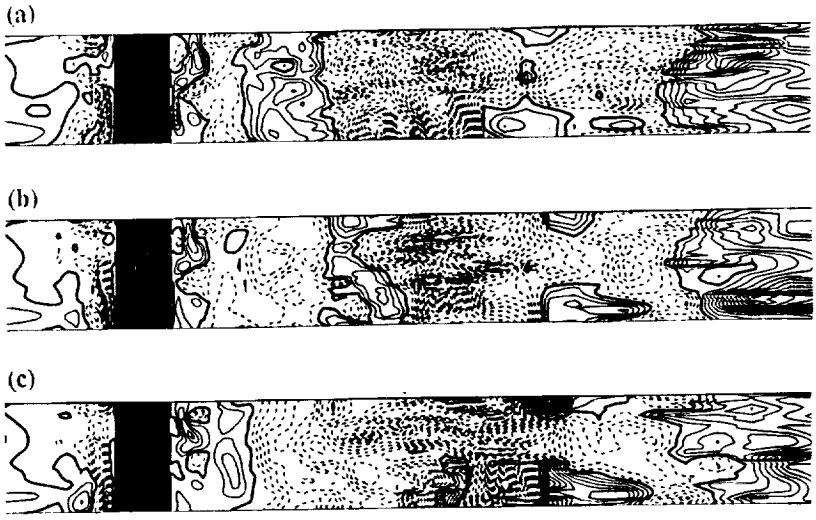

FIGURE 8. Regions of instantaneous negative u; solid, positive; dash, negative; thick solid, 0; increment, 0.016: (*a*) t=0; (*b*) t=Δt; (*c*) t=2Δt.

the upper wall.

4.3 Instantaneous flow field at Re=3210

4.3.1 Reversed flow regions

Figure 7 shows contours of u are presented at one x–y plane at three different times with a time interval of Δt=1.61. For convenience, the time for Fig. 7(*a*) is designated as t=0, and subsequent figures will be referred relative to that time. Figures 7(*a*)–(*c*) show how unsteady the flow is. Near the mean reattachment point of PSRD (6.8h downstream of the obstacle), u is small and oscillating in sign. Intense unsteady free-shear layers formed downstream of the obstacle are noticeable. Intermittent separation on the upper channel wall is observed near the streamwise location of mean reattachment (Fig. 7(*c*)).

Figures 8(*a*)–(*c*) show contours of u at the first grid point away from the lower channel wall at three different times. The instantaneous separation and reattachment lines are far from two-dimensional although the obstacle is geometrically two-dimensional. Secondary and tertiary flow regions are present near the obstacle at this *Re* and are highly unsteady.

Particle trace studies were also performed. A videotape displaying this data is available by request to the authors.

4.4 LES at Re=82,000

The wall-layer model we used is a variation of one proposed by Ciofalo and Collins (1989) for k–ϵ modeling of turbulent recirculating flows. It retains the form of the

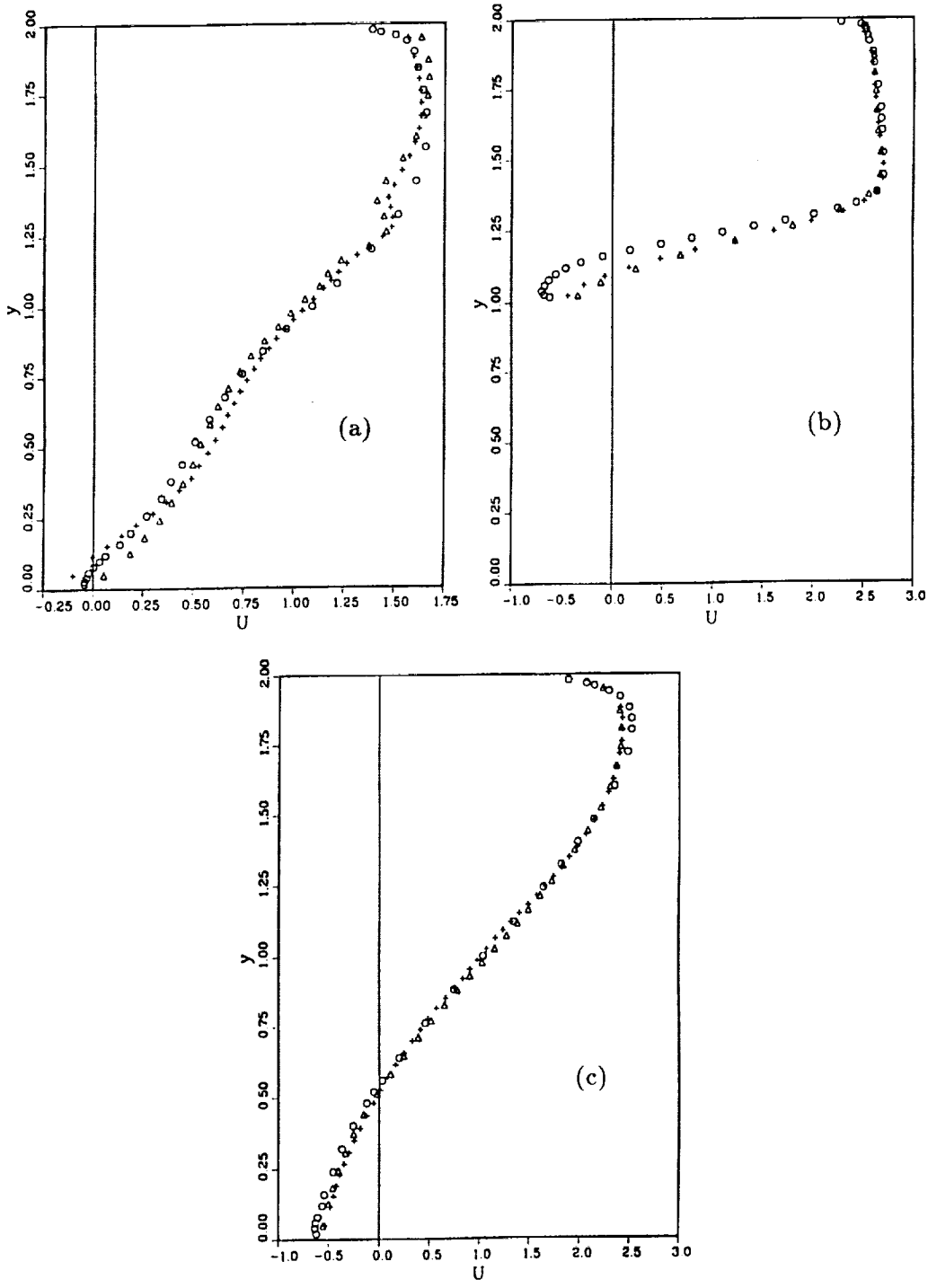

FIGURE 9. Streamwise velocity profiles: (*a*) x=9.6, (*b*) x=10.8, (*c*) x=15: o, exp.; △ , 96x32x32; +, 128x48x40.

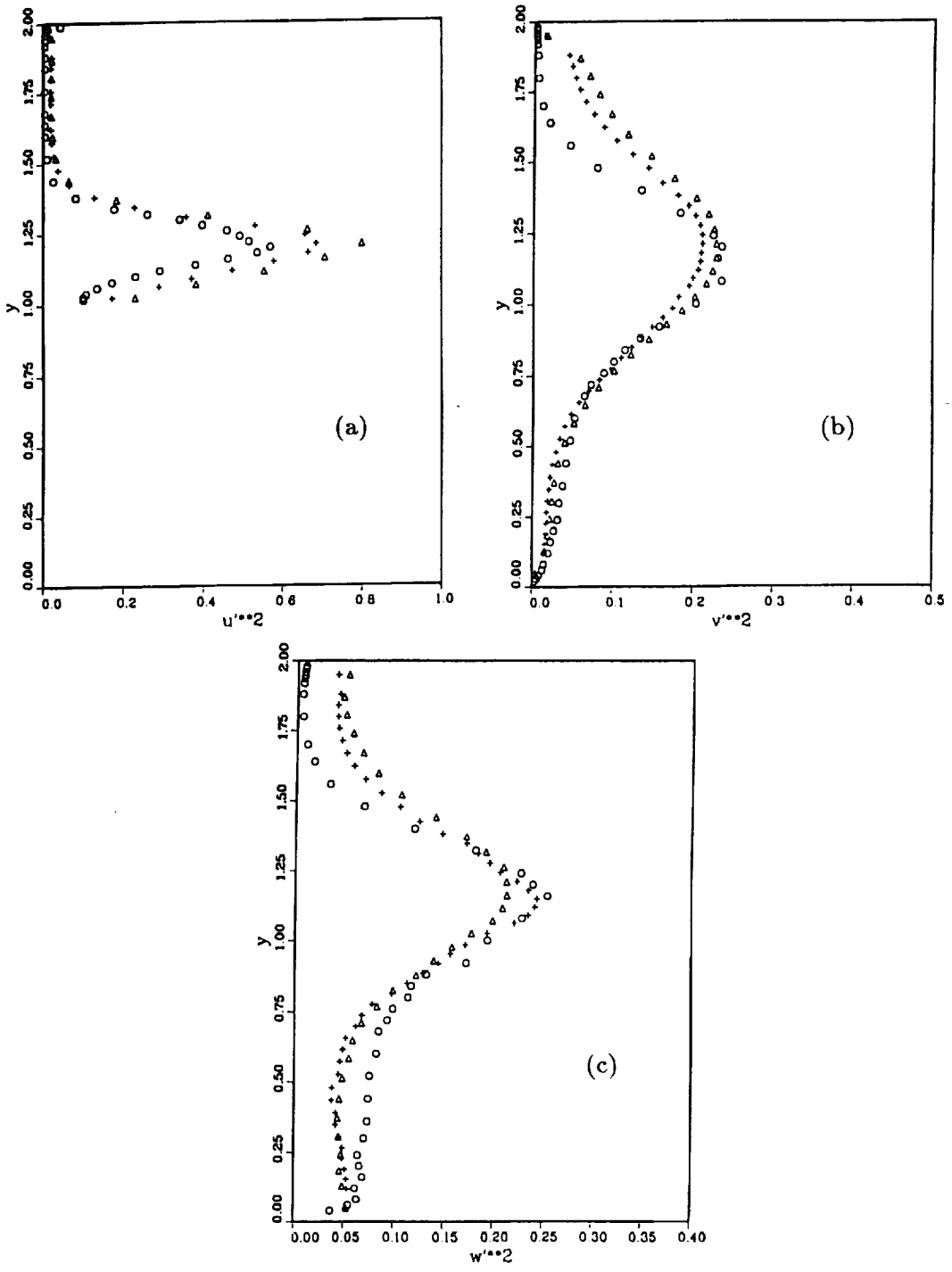

FIGURE 10. Turbulent fluctuation profiles: (*a*) u'^2 at x=10.8, (*b*) v'^2 at x=12, (*c*) w'^2 at x=12: : ○, exp.; △ , 96x32x32; +, 128x48x40.

wall function but allows the nondimensional thickness of the viscous sublayer to be a function of the local turbulence intensity.

Figure 9 presents streamwise velocity profiles normalized by $2U_m$ and averaged in z and t at three streamwise locations. Velocity profiles from coarse ($96 \times 32 \times 32$) and fine ($128 \times 48 \times 40$) grid simulations are shown along with the experimental one. The profiles are relatively well resolved. Only a slight improvement is obtained on the fine grid. The discrepancy near the top surface of the obstacle (Fig. 9(b)) is believed to be due to the wall-layer model. Averaged and normalized velocity fluctuations at selected x locations are shown in Fig. 10. Numerical results predicts higher values in the high speed regions near the upper wall.

5. Summary

A large-eddy simulation of low-Reynolds-number turbulent flow in a channel with a two-dimensional obstacle on one wall was presented with the wall layers fully resolved. The subgrid-scale model coefficient was computed dynamically. The results obtained were compared with a DNS and showed that the dynamic model yields better results than conventional LES with a fixed model constant. This demonstrates the value of the dynamic subgrid-scale model for computing complex flows. A high-Reynolds-number LES using a conventional Smagorinsky model with a fixed model constant was also included. The results are consistent with the experiment of Dimaczek *et al.* (1989). Application of the dynamic subgrid-scale model to high-Re flows is currently under investigation.

Acknowledgment

The authors gratefully acknowledge contributions from the following organizations. Financial support for the investigators was provided through the Office of Naval Research grant N00014-89J-1343 and the Stanford-NASA Center for Turbulence Research. The NASA–Ames Research Center has provided the computer time for this research.

REFERENCES

CIOFALO, M., & COLLINS, M. W. 1989 *Numerical Heat Transfer Part B.* **15,** 21-47.

DIMACZEK, G., KESSLER, R., MARTINUZZI, R., & TROPEA, C. 1989 The flow over two-dimensional, surface-mounted obstacles at high Reynolds numbers. *Proc. 7th Symposium on turbulent shear flows.* Stanford University, Aug. 21–23, 1989.

GERMANO, M., PIOMELLI, U., MOIN, P., & CABOT, W. H. 1991 A dynamic subgrid-scale eddy viscosity model. *Phys. Fluids A.* **3,** 1760-1765.

KIM, J., & MOIN, P. 1985 Application of a fractional-step method to incompressible Navier-Stokes equations. *J. Comp. Phys.* **59,** 308-323.

LILLY D. K. 1992 A proposed modification of the Germano subgrid-scale closure method. *Phys. Fluids A.* **4 (3),** 633-635.

ROBINSON, S. K., KLINE, S. J., & SPALART, P. R. 1988 Spatial character and time evolution of coherent structures in a numerically simulated boundary layer. *AIAA paper No. 88-3577.*

SHAANAN, S., FERZIGER, J., & REYNOLDS, W. 1975 Numerical simulation of turbulence in the presence of shear. *Report TF-6.* Thermosciences Division, Dept. of Mech. Eng., Stanford Univ., Stanford CA 94305, U.S.A.

SMAGORINSKY, J. 1963 General circulation experiments with the primitive equations. I. The basic experiment. *Monthly Weather Review.* **91,** 99-164.

TROPEA, C., & GACKSTATTER, R. 1985 The flow over two-dimensional surface-mounted obstacles at low Reynolds numbers. *J. Fluids Eng.* **107,** 489-494.

WERNER, H., & WENGLE, H. 1989 Large-eddy simulation of turbulent flow over a square rib in a channel. *Proc. 7th Symposium on turbulent shear flows.* Stanford University, Aug. 21–23, 1989.

Similarity states of homogeneous stably-stratified turbulence at infinite Froude number

By Jeffrey R. Chasnov

1. Motivation and objectives

Turbulent flow in stably-stratified fluids is commonly encountered in geophysical settings, and an improved understanding of these flows may result in better ocean and environmental turbulence models. Much of the fundamental physics of stably-stratified turbulence can be studied under the assumption of statistical homogeneity, leading to a considerable simplification of the problem. A study of homogeneous stably-stratified turbulence may also be useful as a vehicle for the more general study of turbulence in the presence of additional sources and sinks of energy.

Our main purpose here is to report on recent progress in an ongoing study of asymptotically long-time similarity states of stably-stratified homogeneous turbulence which may develop at high Reynolds numbers. A similarity state is characterized by the predictability of future flow statistics from current values by a simple rescaling of the statistics. The rescaling is typically based on a dimensional invariant of the flow. Knowledge of the existence of an asymptotic similarity state allows a prediction of the ultimate statistical evolution of a turbulent flow without detailed knowledge of the very complicated and not well-understood non-linear transfer processes.

We present in this report evidence of similarity states which may develop in homogeneous stably-stratified flows if a dimensionless group in addition to the Reynolds number, the so-called Froude number, is sufficiently large. Here, we define the Froude number as the ratio of the internal wave time-scale to the turbulence time-scale; its precise definition will be given below. In this report, we will examine three different similarity states which may develop depending on the initial conditions of the velocity and density fields. Theoretical arguments and results of large-eddy simulations will be presented. We will conclude this report with some speculative thoughts on similarity states which may develop in stably-stratified turbulence at arbitrary Froude number as well as our future research plans in this area.

2. The governing equations

Choosing our co-ordinate system such that the z-axis is pointed vertically upwards, we assume a stable density distribution

$$\rho = \rho_0 - \beta z + \rho',$$

where ρ_0 is a constant, uniform reference density, $\beta > 0$ is a constant, uniform density gradient along z, and ρ' is the density deviation from the horizontal average. The kinematic viscosity ν and molecular diffusivity D of the fluid are assumed

constant and uniform. After application of the Boussinesq approximation, the governing equations for the fluid velocity $\mathbf{u}$ and the density fluctuation ρ' are

$$\nabla \cdot \mathbf{u} = 0, \tag{2.1}$$

$$\frac{\partial \mathbf{u}}{\partial t} + \mathbf{u} \cdot \nabla \mathbf{u} = \frac{\rho' \mathbf{g}}{\rho_0} - \frac{\nabla(p + \rho_0 g z)}{\rho_0} + \nu \nabla^2 \mathbf{u}, \tag{2.2}$$

$$\frac{\partial \rho'}{\partial t} + \mathbf{u} \cdot \nabla \rho' = \beta u_3 + D \nabla^2 \rho', \tag{2.3}$$

where $\mathbf{g} = -\mathbf{j}g$ with $g > 0$, $\mathbf{j}$ is the vertical (upwards) unit vector, and p is the fluid pressure.

We will consider three limiting flows which may occur in a stably-stratified fluid. Firstly, we will consider decaying isotropic turbulence with an isotropic passive scalar, whose governing equations are obtained from (2.1) - (2.3) when $g, \beta = 0$. Secondly, we will consider decaying isotropic turbulence in a mean passive scalar gradient, obtained when $g = 0$ only, and; thirdly, we will consider buoyancy-generated turbulence (Batchelor, Canuto & Chasnov, 1992), obtained when $\beta = 0$ only. The conditions under which these limiting flows may develop in a stably-stratified fluid where both g and β are nonzero are most easily determined after a transformation of the equations to dimensionless variables. First, to make the equations more symmetric in the velocity and density fields, we define following Cambon (private communication) a normalized density fluctuation θ such that it has units of velocity,

$$\theta = \sqrt{\frac{g}{\rho_0 \beta}} \rho'. \tag{2.4}$$

Use of θ instead of ρ' in (2.2) - (2.3) modifies the terms proportional to g and β into terms proportional to N, where

$$N = \sqrt{\frac{g\beta}{\rho_0}} \tag{2.5}$$

is the Brunt-Vaisala frequency associated with the internal waves of the stably stratified flow. Furthermore, $\frac{1}{2}\langle \mathbf{u}^2 \rangle$ is the kinetic energy and $\frac{1}{2}\langle \theta^2 \rangle$ is the potential energy of the fluid per unit mass, and the equations of motion conserve the total energy (kinetic + potential) in the absence of viscous and diffusive dissipation.

Now, defining dimensionless variables as

$$T = t\frac{u_0}{l_0}, \quad X = \frac{x}{l_0}, \quad \mathbf{U} = \frac{\mathbf{u}}{u_0}, \quad P = \frac{(p + \rho_0 g z)}{\rho_0 {u_0}^2}, \quad \Theta = \frac{\theta}{\theta_0}, \tag{2.5}$$

where l_0, u_0, and θ_0, are as yet unspecified length, velocity, and normalized density scales, the equations of motion become

$$\nabla \cdot \mathbf{U} = 0, \tag{2.6}$$

$$\frac{\partial \mathbf{U}}{\partial T} + \mathbf{U} \cdot \nabla \mathbf{U} = -\mathbf{j} \frac{1}{F_0} \frac{\theta_0}{u_0} \Theta - \nabla P + \frac{1}{R_0} \nabla^2 \mathbf{U}, \tag{2.7}$$

$$\frac{\partial \Theta}{\partial T} + \mathbf{U} \cdot \nabla \Theta = \frac{1}{F_0} \frac{u_0}{\theta_0} U_3 + \frac{1}{\sigma R_0} \nabla^2 \Theta, \tag{2.8}$$

where

$$F_0 = \frac{u_0}{N l_0}, \quad R_0 = \frac{u_0 l_0}{\nu}, \quad \sigma = \frac{\nu}{D}. \tag{2.9}$$

F_0 and R_0 can be regarded as an initial Froude number and Reynolds number of the flow, respectively, although their precise definition is yet dependent on our specification of l_0, u_0, and θ_0; σ is the Schmidt (or Prandtl) number of the fluid.

2.1 Isotropic turbulence with an isotropic passive scalar

This limiting flow may be obtained by initializing the flow with an isotropic velocity and density field with given kinetic and potential energy spectrum of comparable integral scales. The unspecified dimensional parameter l_0 may be taken equal to the initial integral scale of the flow, and u_0 and θ_0 may be taken equal to the initial root-mean-square values of the velocity and normalized density fluctuations. The non-dimensional variables of (2.5) ensure that the maximum values of U and Θ and the non-dimensional integral length scale of the flow is of order unity at the initial instant, and, provided that u_0 is of order θ_0, implying comparable amounts of kinetic and potential energy in the initial flow field, and $F_0 \gg 1$, both of the terms multiplied by $1/F_0$ in (2.7) and (2.8) are small initially. Over times in which these terms remain small, the resulting equations govern the evolution of a decaying isotropic turbulence convecting a decaying isotropic passive scalar field.

2.2 Isotropic turbulence in a passive scalar gradient

Here, the flow is initialized with an isotropic velocity field with given kinetic energy spectrum and no initial density fluctuations. Again we take the dimensional parameter l_0 to be the initial integral scale of the flow and u_0 equal to the initial root-mean-square value of the velocity field. The maximum value of U and the non-dimensional integral length scale of the flow are then of order unity. However, the initial conditions introduce no intrinsic density scale, and such a scale needs to be constructed from other dimensional parameters in the problem. If at some time in the flow-evolution not too far from the initial instant the maximum of the dimensionless density fluctuation Θ is also to be of order unity, then the dimensionless group multiplying U_3 in equation (2.8) must necessarily be of order unity. Setting this group exactly equal to unity yields an equation for θ_0 with solution $\theta_0 = N l_0$. Thus defining θ_0, we find that the dimensionless group multiplying Θ in equation (2.7) is equal to $1/F_0^2$ so that, in the limit of $F_0 \gg 1$, this term is small at the initial instant and may be neglected for some as yet to be determined period of time. The resulting equations then govern the evolution of decaying isotropic turbulence in the presence of a mean passive scalar gradient over this period of time.

2.3 Buoyancy-generated turbulence

Here, the flow is initialized with an isotropic density field with given potential energy spectrum and no initial velocity fluctuations. Similarly as above, we take the dimensional parameter l_0 to be the initial integral scale of the density field and θ_0 to be equal to the initial root-mean-square value of the θ-field. The maximum value of Θ and the dimensionless integral scale of the flow is then of order unity. However, here the initial conditions introduce no intrinsic velocity scale. If at a time in the flow-evolution not too far from the initial instant we wish the maximum of the dimensionless velocity fluctuation U to also be of order unity, then the dimensionless group multiplying Θ in equation (2.7) must necessarily be of order unity. Setting this group exactly equal to unity yields a simple quadratic equation for u_0, with solution $u_0 = \sqrt{Nl_0\theta_0}$, or equivalently, $u_0 = \sqrt{gl_0\rho_0'/\rho_0}$, where ρ_0' is the value of $\langle\rho'^2\rangle^{1/2}$ at the initial instant. We note that this is the same velocity scale chosen previously by Batchelor *et al.* (1992) in their study of buoyancy-generated turbulence. Upon use of the identity $\theta_0 = u_0^2/Nl_0$, we find that the dimensionless group multiplying U_3 in (2.8) is exactly equal to $1/F_0^2$ so that, in the limit of $F_0 \gg 1$, this term is small at the initial instant. Using the definition of u_0, the initial Froude number here is seen to be equal to $F_0 = \rho_0'/\beta l_0$. For times over which the term multiplied by F_0^{-2} may be neglected, the resulting equations then govern the evolution of buoyancy-generated turbulence.

3. Asymptotic similarity states

3.1. Final period of decay

Exact analytical treatment of (2.1) - (2.3) is rendered difficult because of the quadratic terms. Under conditions of a final period of decay (Batchelor, 1948), these terms may be neglected and an exact analytical solution of (2.1)- (2.3) may be determined. Although most of the results concerning the final period are well-known or easily found, we recall them here since the ideas which arise in a consideration of the final period are relevant to our high Reynolds number analysis.

During the final period, viscous and diffusive effects dissipate the high wavenumber components of the energy and scalar-variance spectra, and, at late times, the only relevant part of the spectra are their forms at small wavenumbers at an earlier time. Defining the kinetic energy spectrum $E(k,t)$ and the density-variance spectrum $G(k,t)$ to be the spherically-integrated three dimensional Fourier transform of the co-variances $\frac{1}{2}\langle u_i(\mathbf{x},t)u_i(\mathbf{x}+\mathbf{r},t)\rangle$ and $\langle\rho'(\mathbf{x},t)\rho'(\mathbf{x}+\mathbf{r},t)\rangle$, an expansion of the spectra near $k = 0$ can be written as

$$E(k,t) = 2\pi k^2(B_0 + B_2k^2 + \ldots) \tag{3.1}$$

$$G(k,t) = 4\pi k^2(C_0 + C_2k^2 + \ldots), \tag{3.2}$$

where $B_0, B_2, \ldots$, and $C_0, C_2, \ldots$ are the Taylor series coefficients of the expansion. In a consideration of isotropic turbulence, Batchelor and Proudman (1956) assumed the spectral tensor of the velocity correlation $\langle u_i(\mathbf{x})u_j(\mathbf{x}+\mathbf{r})\rangle$ to be analytic at

$k = 0$ and determined that $B_0 = 0$ and that non-linear interactions (which are important during the initial period) necessarily result in a time-dependent non-zero value of B_2. Saffman (1967a) later showed that it is physically possible for turbulence to be initially created with a non-zero value of B_0 and that, for decaying isotropic turbulence, B_0 is invariant in time throughout the evolution of the flow. By analogous arguments, it can be shown that the spectrum of the density correlation is itself analytic at $k = 0$ when $C_0 \neq 0$, and, for an isotropic decaying density (scalar) field, C_0 is invariant in time (Corrsin, 1951).

Here, rather than present an exact derivation of the final period results, we will demonstrate how a simple dimensional analysis can recover the correct decay laws. We consider separately the three different limiting flows envisioned above.

Isotropic turbulence with an isotropic passive scalar

The evolution of the mean-square velocity may be found by dimensional analysis assuming the only relevant dimensional quantities are the low wavenumber invariant of the energy spectrum B_0, if non-zero initially, viscosity ν, and time t. The equations of motion are assumed to be linear in the velocity field during the final period so that $\langle \mathbf{u}^2 \rangle$ must linearly depend on B_0, and we find

$$\langle \mathbf{u}^2 \rangle \propto B_0 \nu^{-\frac{3}{2}} t^{-\frac{3}{2}}, \tag{3.3}$$

as determined by Saffman (1967a). If B_0 is initially zero, then B_2 is necessarily non-zero and is also invariant during the final period when nonlinear interactions are negligible. A corresponding dimensional analysis based on B_2 instead of B_0 yields

$$\langle \mathbf{u}^2 \rangle \propto B_2 \nu^{-\frac{5}{2}} t^{-\frac{5}{2}}, \tag{3.4}$$

as originally determined by Batchelor (1948). Analogous arguments applied to the isotropic passive density (scalar) field, which is seen to be uncoupled from the velocity field during the final period, implies a dependence on C_0, necessarily linear, the diffusivity D, and time t, yielding

$$\langle \rho'^2 \rangle \propto C_0 D^{-\frac{3}{2}} t^{-\frac{3}{2}}, \tag{3.5}$$

as originally determined by Corrsin (1951), and, if C_0 is initially zero,

$$\langle \rho'^2 \rangle \propto C_2 D^{-\frac{5}{2}} t^{-\frac{5}{2}}. \tag{3.6}$$

Isotropic turbulence with passive scalar gradient

The passive density (scalar) field for this flow is driven by velocity fluctuations, and the low wavenumber coefficient of the density-variance spectrum is no longer invariant in time. In fact, an exact relation, valid even when nonlinear terms are non-negligible, holds between C_0 and B_0 and is

$$C_0(t) = \frac{1}{3}\beta^2 B_0 t^2, \tag{3.7}$$

indicating that there is now only one invariant, namely B_0, which is relevant to our dimensional analysis. Making use of this invariant, we find in the final period the decay law

$$\langle \rho'^2 \rangle \propto \beta^2 B_0 \nu^{-\frac{3}{2}} t^{\frac{1}{2}}, \tag{3.8}$$

which is most simply found by substitution of (3.7) directly into (3.5). If B_0 is zero, then B_2 is invariant during the final period, and C_2 is related to B_2 (exact only when nonlinear terms are negligible) by

$$C_2(t) = \frac{1}{3}\beta^2 B_2 t^2. \tag{3.9}$$

The decay law in the final period is then

$$\langle \rho'^2 \rangle \propto \beta^2 B_2 \nu^{-\frac{5}{2}} t^{-\frac{1}{2}}. \tag{3.10}$$

We have thus found the interesting result that the density-variance may either increase or decrease during the final period depending on the form of the low-wavenumber energy spectrum. This result may be of use to researchers interested in determining the form of the low wavenumber energy spectrum in homogeneous turbulence under experimental conditions.

Buoyancy-driven flow

Here, it is the velocity field which is driven by density fluctuations, and the low wavenumber coefficient B_0 of the kinetic energy spectrum is no longer an invariant. The relevant invariant here is the low wavenumber coefficient C_0 of the density-variance spectrum. As before, an exact relation holds between B_0 and C_0, valid even when nonlinear terms are non-negligible, and is

$$B_0(t) = \frac{2}{3}\frac{g^2 C_0}{\rho_0^2} t^2. \tag{3.11}$$

Making use of the invariant C_0, we find another form for the mean-square velocity fluctuation under an assumption of a final period in which non-linear terms are negligible

$$\langle \mathbf{u}^2 \rangle \propto \frac{g^2 C_0}{\rho_0^2} \nu^{-\frac{3}{2}} t^{\frac{1}{2}}. \tag{3.12}$$

The mean-square density fluctuations decay as for the isotropic passive scalar flow. Clearly, an increase in $\langle \mathbf{u}^2 \rangle$ during a "final period" contradicts the very existence of a final period since the Reynolds number of the flow is increasing in time. If C_0 is initially zero, then C_2 is necessarily non-zero and is invariant when nonlinear terms are negligible. B_2 is now related to C_2 by

$$B_2(t) = \frac{2}{3}\frac{g^2 C_2}{\rho_0^2} t^2, \tag{3.13}$$

and the mean-square velocity follows

$$\langle \mathbf{u}^2 \rangle \propto \frac{g^2 C_2}{\rho_0^2} \nu^{-\frac{5}{2}} t^{-\frac{1}{2}}. \tag{3.14}$$

Although the mean-square velocity decays in this case, the integral scale grows like $t^{1/2}$ so that the Reynolds number increases in time, again contradicting the existence of a final period.

3.2. Exact high Reynolds number similarity states

At high Reynolds numbers, direct effects of viscosity and diffusivity occur at much larger wavenumber magnitudes than those scales which contain most of the energy and density-variance so that the asymptotic forms of $\langle \mathbf{u}^2 \rangle$ and $\langle \rho'^2 \rangle$ can be expected to be independent of ν and D. Viscous and diffusive smoothing of the energy and density-variance containing components of the spectra are now replaced by nonlinear transfer processes so that one can still reasonably expect the asymptotic scaling of $\langle \mathbf{u}^2 \rangle$ and $\langle \rho'^2 \rangle$ to be on the form of the spectra at low wavenumbers. The low wavenumber coefficient B_0 is an invariant, even at high Reynolds numbers, for decaying isotropic turbulence and so is C_0 for a decaying isotropic passive scalar. If there is a mean passive scalar gradient, then C_0 is asymptotically related to B_0 by (3.7). For buoyancy-driven flows, C_0 is an invariant and B_0 is asymptotically related to C_0 by (3.11).

Based on dimensional analysis, we can now determine the high Reynolds number, long-time evolution of the energy and density-variance when B_0 and C_0 are non-zero for our three limiting flows.

Isotropic turbulence with an isotropic passive scalar

The low wavenumber coefficients B_0 and C_0 are separately invariant and the high-Reynolds number asymptotic results are the Saffman (1967b) decay law

$$\langle \mathbf{u}^2 \rangle \propto B_0^{\frac{2}{5}} t^{-\frac{6}{5}}, \tag{3.15}$$

and its analogous law for the passive density-variance

$$\langle \rho'^2 \rangle \propto C_0 B_0^{-\frac{3}{5}} t^{-\frac{6}{5}}. \tag{3.16}$$

The nonlinearity of the governing equations is reflected by the nonlinear dependence of $\langle \mathbf{u}^2 \rangle$ and $\langle \rho'^2 \rangle$ on B_0, in contrast with the results of the final period. Note, however, that the linearity of the density equation in ρ' results in a linear dependence of $\langle \rho'^2 \rangle$ on C_0.

Dimensional arguments can also determine the asymptotic behavior of the velocity and density integral scales, and one finds

$$L_u, L_\theta \propto B_0^{\frac{1}{5}} t^{\frac{2}{5}}. \tag{3.17}$$

Isotropic turbulence with passive scalar gradient

Here C_0 is no longer invariant, but depends on B_0 asymptotically as (3.7) so that the density-variance now evolves as

$$\langle \rho'^2 \rangle \propto \beta^2 B_0^{\frac{2}{5}} t^{\frac{4}{5}}, \tag{3.18}$$

when B_0 is non-zero.

Buoyancy-driven flow

Here C_0 is invariant and B_0 is not, and B_0 depends on C_0 asymptotically as (3.11). By dimensional arguments (Batchelor *et al.*, 1992), the mean-square velocity and density-variance evolve as

$$\langle \mathbf{u}^2 \rangle \propto (g^2 C_0/\rho_0^2)^{\frac{2}{5}} t^{-\frac{2}{5}}, \tag{3.19}$$

$$g^2 \langle \rho'^2/\rho_0^2 \rangle \propto (g^2 C_0/\rho_0^2)^{\frac{2}{5}} t^{-\frac{12}{5}}, \tag{3.20}$$

and the integral scales evolve as

$$L_u, L_{\rho'} \propto (g^2 C_0/\rho_0^2)^{\frac{1}{5}} t^{\frac{4}{5}}. \tag{3.21}$$

A computation of a Reynolds number based on the root-mean square velocity fluctuation and the integral scale shows that $Re \propto t^{3/5}$ increases asymptotically, precluding the development of a final period in this flow.

3.3. Approximate high Reynolds number similarity states

When either B_0 or C_0 are zero, there are no longer strictly invariant quantities on which to base asymptotic similarity states. The coefficients B_2 and C_2 are affected by nonlinear transfer processes, and exact results as found above become unobtainable. Nevertheless, if we make an additional assumption, which needs to be verified by numerical or experimental data, that the time-variation of B_2 or C_2 due to nonlinear processes are small compared to the rate of change of the energy or density-variance, then approximate asymptotic similarity states may still be based on the nearly-invariant low wavenumber coefficients. The analysis proceeds in exact analogy to that above, and, for use in comparison to the numerical simulation data, we state the results below.

Isotropic turbulence with an isotropic passive scalar

For $B_0 = 0$, we have the Kolmogorov (1941) decay law

$$\langle \mathbf{u}^2 \rangle \propto B_2^{\frac{2}{7}} t^{-\frac{10}{7}}. \tag{3.22}$$

Three additional approximate similarity states exist for the decaying isotropic passive scalar depending on which of B_0 or C_0 are zero (Lesieur, 1990):

$$\langle \rho'^2 \rangle \propto C_2 B_0^{-1} t^{-2} \tag{3.23}$$

$$\langle \rho'^2 \rangle \propto C_0 B_2^{-\frac{3}{7}} t^{-\frac{6}{7}} \tag{3.24}$$

$$\langle \rho'^2 \rangle \propto C_2 B_2^{-\frac{5}{7}} t^{-\frac{10}{7}}, \tag{3.25}$$

Isotropic turbulence with passive scalar gradient

For $B_0 = 0$, we assume that B_2 is approximately invariant. The low wavenumber scalar-variance spectrum coefficient C_2 is approximately related to B_2 by (3.9). The density-variance is found to evolve as

$$\langle \rho'^2 \rangle \propto \beta^2 B_0^{\frac{2}{7}} t^{\frac{4}{7}}. \tag{3.26}$$

Buoyancy-driven flow

For $C_0 = 0$, we assume that C_2 is approximately invariant. The low wavenumber energy spectrum coefficient B_2 is approximately related to C_2 by (3.13). The mean-square velocity and density-variance evolve approximately as

$$\langle \mathbf{u}^2 \rangle \propto (g^2 C_0/\rho_0^2)^{\frac{6}{7}} t^{-\frac{6}{7}}, \tag{3.27}$$

$$g^2 \langle \rho'^2/\rho_0^2 \rangle \propto (g^2 C_0/\rho_0^2)^{\frac{6}{7}} t^{-\frac{20}{7}}, \tag{3.28}$$

and the integral scales evolve as

$$L_u, L_{\rho'} \propto (g^2 C_0/\rho_0^2)^{\frac{1}{7}} t^{\frac{4}{7}}. \tag{3.29}$$

A computation of a Reynolds number based on the root-mean square velocity fluctuation and the integral scale shows that Re again increases asymptotically, but now as $t^{1/7}$.

4. Large-eddy simulations

The high Reynolds numbers required to test the asymptotic scaling determined above may be obtained by a large-eddy simulation (LES) of Eqs. (2.1) - (2.3) using a pseudo-spectral code for homogeneous turbulence (Rogallo, 1981). For the subgrid scale model, we employ a spectral eddy-viscosity and eddy-diffusivity (Kraichnan 1976; Chollet and Lesieur 1981) parametrized by

$$\nu_e(k|k_m,t) = \left[0.145 + 5.01 \exp\left(\frac{-3.03 k_m}{k}\right)\right] \left[\frac{E(k_m,t)}{k_m}\right]^{1/2}, \tag{4.1}$$

and

$$D_e(k|k_m,t) = \frac{\nu_e(k|k_m,t)}{\sigma_e}, \tag{4.2}$$

where k_m is the maximum wavenumber magnitude of the simulation and σ_e is an eddy Schmidt number, assumed here to be constant and equal to 0.6. We take the initial energy spectrum to be

$$E(k,0) = A_n k_p^{-1} (k/k_p)^n \exp\left(-(n/2)(k/k_p)^2\right), \tag{4.3}$$

where n is equal to 2 or 4, A_n is chosen so that $\langle \mathbf{u}^2 \rangle = 1$, and k_p is the wavenumber at which the initial energy spectrum is maximum. The case $n = 2$ corresponds to $B_0 \neq 0$, and the case $n = 4$ corresponds to $B_0 = 0$. In the 256^3 numerical simulations presented here, the minimum computational wavenumber is 1, the maximum wavenumber is about 120, and we take $k_p = 100$. The initial energy spectrum is set to zero for wavenumbers greater than 118 to allow the subgrid scale eddy-viscosity and eddy-diffusivity to build up from zero values. The relatively large value of k_p chosen here allows an attainment of an asymptotic similarity state before the integral scales of the flow become comparable to the periodicity length. A velocity field with initial energy spectrum given by (4.3) is realized in the simulation by requiring the spectral energy content at each wavenumber to satisfy (4.3) but randomly generating the phase and velocity component distributions (Rogallo 1981).

In the simulations of decaying isotropic turbulence with a decaying isotropic passive scalar, the passive scalar-variance spectrum is also initialized with the spectrum given by (4.3) with A_n chosen so that $\langle \rho'^2 \rangle = 1$. We present the results of two simulations for this flow: the first with an initial energy spectrum with $n = 2$ convecting two passive scalar fields with initial spectra with $n = 2$ and $n = 4$, and the second with an energy spectrum with $n = 4$ convecting two passive scalar fields with $n = 2$ and $n = 4$. Computations of these two velocity fields and four scalar fields are sufficient to test the theoretical scaling discussed in §3.

In the simulations of decaying isotropic turbulence in a passive scalar gradient, the initial fluctuating passive density field is taken identically equal to zero, and two simulations are presented with an initial energy spectrum with $n = 2$ and $n = 4$. The exact value of β is inconsequential provided it is non-zero, and we choose $\beta = 1$.

In the simulations of buoyancy-generated turbulence, the initial fluctuating velocity field is taken identically equal to zero, and two simulations are presented with an initial density spectrum with $n = 2$ and $n = 4$. Here, the exact value of g is inconsequential provided it is non-zero, and we choose units such that $g/\rho_0 = 1$.

4.1. Results

In the interest of brevity, we present here only results from the large-eddy simulations pertaining to the power-law predictions of §3. More detailed results concerning decaying isotropic turbulence with and without a passive scalar gradient will be published in Chasnov (1993) and Chasnov & Lesieur (1993) - slightly lower-resolution simulations (128^3) of buoyancy-generated turbulence have already been published in Batchelor, Canuto & Chasnov (1992). In figures 1 and 2, we plot the instantaneous power-law exponents (logarithmic derivatives) versus time normalized by the initial large-eddy turnover time $\tau(0)$, of the mean-square velocity decay and the passive density-variance decay when $\beta, g = 0$ in (2.2) and (2.3), appropriate for the study of decaying isotropic turbulence with a decaying isotropic passive scalar. In figure 3, we plot the time-evolution of the power-law exponent of the passive density-variance when $\beta = 1$ and $g = 0$, appropriate for the study of decaying isotropic turbulence in the presence of a passive scalar gradient, and, in figures 4 and 5 we plot the time-evolution of the power-law exponent of the mean-square velocity and density-variance when $\beta = 0$ and $g/\rho_0 = 1$, appropriate for the study

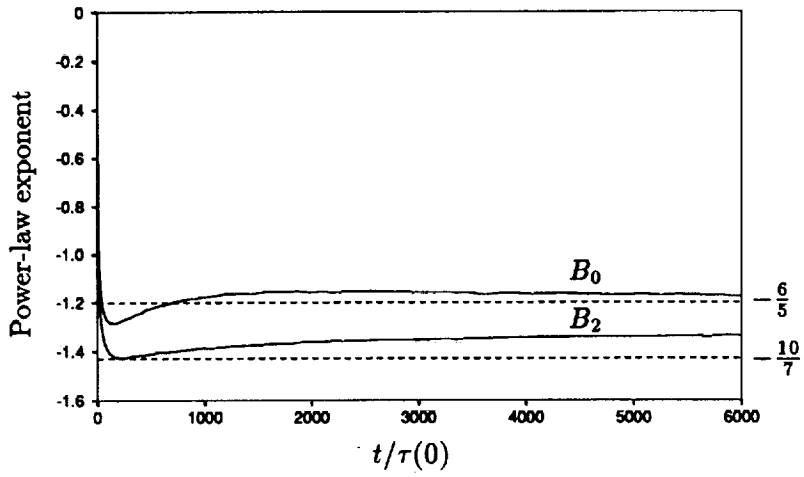

FIGURE 1. Time-evolution of the power-law exponent of $\langle \mathbf{u}^2 \rangle$ for decaying isotropic turbulence. The solid lines are the results of the large-eddy simulations and the dashed lines are the exact and approximate analytical results discussed in §3.

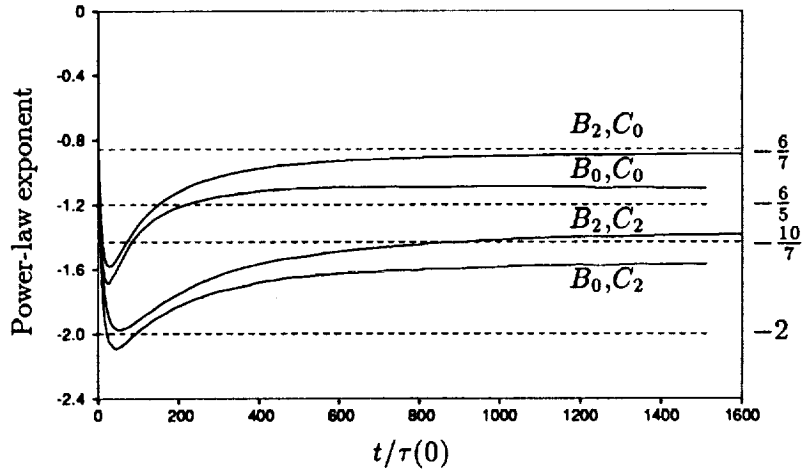

FIGURE 2. Time-evolution of the power-law exponent of $\langle \rho'^2 \rangle$ for a decaying isotropic passive density field.

of buoyancy-generated turbulence. The dashed lines in all of the figures correspond to the exact and approximate asymptotic similarity state results discussed in §3. The solid lines are the results of the large-eddy simulations and are labeled according to the low-wavenumber spectral coefficient which is non-zero and invariant, or postulated to be nearly-invariant.

Overall good agreement is observed between the analytical predictions and the numerical results, lending support to our simple analytical arguments.

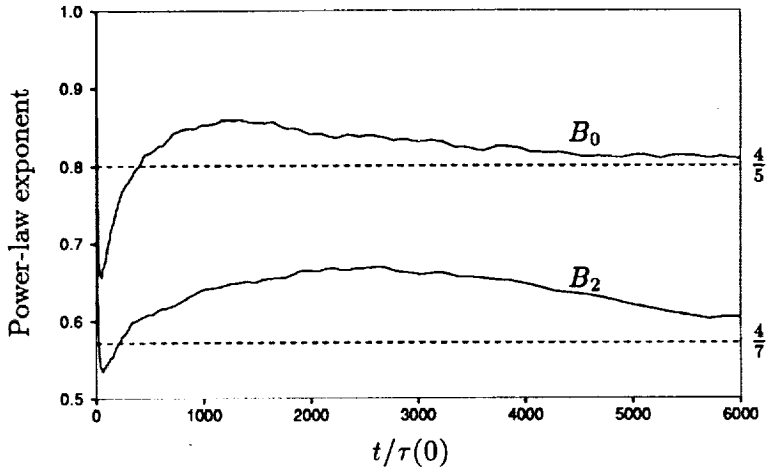

FIGURE 3. Time-evolution of the power-law exponent of $\langle \rho'^2 \rangle$ for decaying isotropic turbulence with a passive mean density gradient.

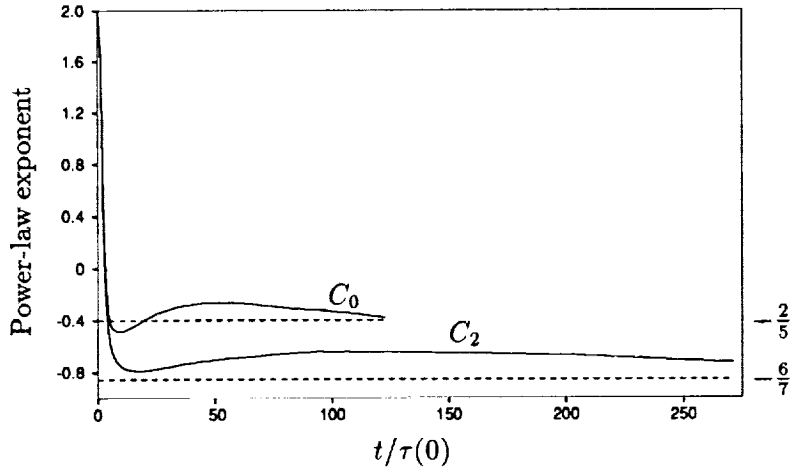

FIGURE 4. Time-evolution of the power-law exponent of $\langle \mathbf{u}^2 \rangle$ for buoyancy-generated turbulence.

Although the total evolution time of the simulations appears to be quite long, we note that the number of large-eddy turnover times undergone by the flow at time t is proportional to $log(t)$ so that the approach to asymptotic behavior may be quite slow. The small deviations from the analytical results which are thought to be exact observed in the simulations could very well be due to an insufficient time-evolution. Longer evolution times than presented here must await larger simulations.

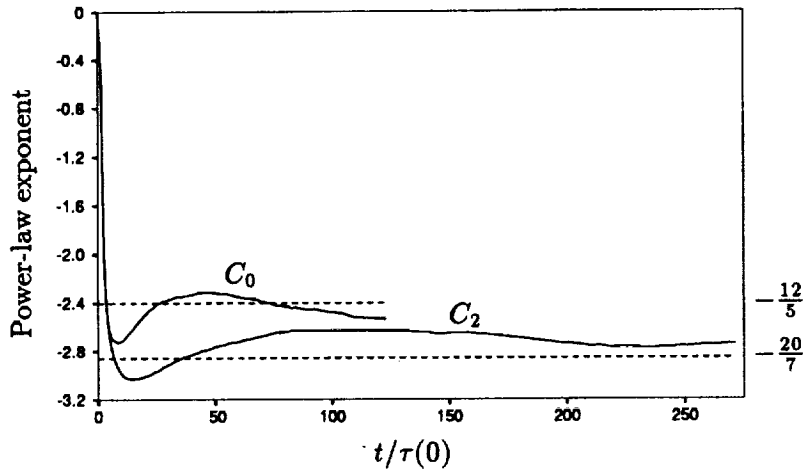

FIGURE 5. Time-evolution of the power-law exponent of $\langle \rho'^2 \rangle$ for buoyancy-generated turbulence.

5. Future plans

In this research brief, we have discussed results pertaining to three limiting flows possible in a stably-stratified fluid if the initial Reynolds number and Froude number is sufficiently large. The Froude number, measured at time t, can be shown to be proportional to $1/Nt$ in all of the above similarity states so that at times of order $1/N$ we expect the neglected terms in the equations of motion to become important. In particular, an internal wave field associated with the stable stratification will be generated. The main question which we are currently trying to answer is whether some new and different similarity state is developed asymptotically as the Froude number decreases. Here too, there is an invariant in the flow associated with the low wavenumber spectral coefficients, namely

$$B_0 + \frac{g}{\beta \rho_0} C_0,$$

which is the low wavenumber coefficient of the total (kinetic + potential) energy spectrum. We have tried to base a similarity state of the total energy on this invariant according to

$$\langle \mathbf{u}^2 \rangle + \frac{g}{\beta \rho_0} \langle \rho'^2 \rangle = (B_0 + \frac{g}{\beta \rho_0} C_0)^{\frac{2}{5}} t^{-\frac{6}{5}} \tag{5.1}$$

and to verify this power-law decay by large-eddy simulation. The results of the large-eddy simulations do indicate a possible similarity state but with a decay power-law exponent about a factor of two smaller than expected by (5.1). Another unusual feature of the simulation results was that the vertical integral scale associated with the total energy in this flow approaches a near-constant value while the horizontal integral scale continues to grow indefinitely. In a similarity state such as those presented

in this report, one would naively expect that all length scales would asymptotically behave in the same fashion. The difficulty in theoretically determining the correct similarity state (if one exists) which develops in the low Froude number flow lies with the additional non-dimensional parameter relevant to this flow, namely Nt, and a lack of intuition as to how this parameter should enter into the correct scaling laws. Work on this problem proceeds.

There is also some current interest in stably-stratified flows with regards to the formation of well-mixed layers separated by large density gradients. Such a flow is not statistically homogeneous, and there is some theoretical speculations, as well as experimental evidence, that under certain conditions an initially statistically homogeneous flow may in fact become unstable and form these layers. We wish to determine if such an effect may be observed and studied by numerical simulation.

While the physics behind the formation of these well-mixed layers requires further study, it is also of interest to see how the mixing process may proceed in each individual layer. To this end, it has been proposed (Batchelor, private communication) to study stably-stratified plane Couette flow in order to observe the competition between the generation of turbulence by the externally imposed shear and the stabilization of the flow by the stratification. Stably-stratified Couette flow can be simulated using a modified channel flow code (Lee & Kim, 1991). For high Reynolds numbers, use of a subgrid scale model would be required, and utilization of a modified version of the dynamic subgrid scale model (Cabot, this volume) might be appropriate for this purpose.

Acknowledgments

Extensive discussions with G. K. Batchelor, M. Lesieur, and R. S. Rogallo are gratefully acknowledged. Most of the simulations were performed on the Intel hypercube and I would like to thank R. S. Rogallo and A. Wray for the use of their software.

REFERENCES

BATCHELOR, G. K. 1948 Energy decay and self-preserving correlation functions in isotropic turbulence. *Quart. Applied Math.* **6,** 97-116.

BATCHELOR, G. K., CANUTO, V. M. & CHASNOV, J. R. 1992 Homogeneous buoyancy-generated turbulence. *J. Fluid Mech.* **235,** 349-378.

BATCHELOR, G. K. & PROUDMAN, I. 1956 The large-scale structure of homogeneous turbulence. *Phil. Trans. Roy. Soc.* **248,** 369-405.

CHASNOV, J. R. 1993 Decaying turbulence in a passive scalar gradient. To appear in *Proceedings of the Fourth European Turbulence Conference.*

CHASNOV, J. R. & LESIEUR, M. 1993 Decaying isotropic turbulence with passive scalars. In preparation.

CHOLLET, J. P. & LESIEUR, M. 1981 Parameterization of small scales of three-dimensional isotropic turbulence utilizing spectral closures. *J. Atmos. Sci.* **38,** 2747-2757.

CORRSIN, S. 1951 The decay of isotropic temperature fluctuations in an isotropic turbulence. *J. of the Aeronautical Sciences.* **18,** 417-423.

KOLMOGOROV, A. N. 1941 On degeneration of isotropic turbulence in an incompressible viscous liquid. *Dokl. Akad. Nauk. SSSR.* **31,** 538-541.

KRAICHNAN, R. H. 1976 Eddy viscosity in two and three dimensions.. *J. Atmos. Sci.* **33,** 1521-1536.

LEE, M. J. & KIM, J. 1991 The structure of turbulence in a simulated plane Couette flow. *Eighth Symposium on Turbulent Shear Flows.* Springer-Verlag.

LESIEUR, M. 1990 *Turbulence in Fluids.* Martinus Nijhoff Publishers.

ROGALLO, R. S. 1981 Numerical experiments in homogeneous turbulence. *NASA TM 81315.*

SAFFMAN, P. G. 1967a The large-scale structure of homogeneous turbulence. *J. Fluid Mech.* **27,** 581-593.

SAFFMAN, P. G. 1967b Note on decay of homogeneous turbulence. *Phys. Fluids.* **10,** 1349.

Application of incremental unknowns to the Burgers equation

By Haecheon Choi and Roger Temam[1]

In this article, we make a few remarks on the role that attractors and inertial manifolds play in fluid mechanics problems. We then describe the role of incremental unknowns for approximating attractors and inertial manifolds when finite difference multigrid discretizations are used. The relation with direct numerical simulation and large eddy simulation is also mentioned.

1. Motivations and objectives

At this time, there are two different methods for mathematically describing a turbulent flow when the permanent regime is established. The first one, more traditional, is related to the concept of ensemble averages and the idea that turbulent flows are statistically well defined and reproducible. The flow is described by a measure in the infinite dimensional function space, the statistics being, of course, that associated to the measure. Probabilities and statistical tools are essential in this approach.

Another more recent approach to turbulence stems from dynamical system theory in which the flow is described by an attractor which can be a complicated (fractal) set (see e.g. Constantin, Foias & Temam 1985). Furthermore, this attractor is expected to have in general a large dimension although some interesting turbulent flows with a low dimensional attractor have been produced in special cases. However, this low dimensional behavior is not likely to appear in general for flows of industrial interest (see Keefe, Moin & Kim 1992). Before making further remarks on the attractor point of view, let us observe that the statistical and attractor approaches are not inconsistent. A measure can be defined on the attractor. Furthermore, it was one of the main results of Constantin, Foias & Temam (1985, 1988) to show that certain segments of the Kolmogorov and Kraichnan theories of turbulence can be rigorously derived from the Navier-Stokes equations using the attractor point of view.

It may not seem practically useful to state that a turbulent flow is represented by a fractal attractor of large dimension. Fortunately, some useful information can be derived from the study of the attractor which sheds some new light on the numerical simulation of turbulence. The first information is that the attractor can be embedded approximately, or perhaps exactly, in smooth manifolds called inertial manifolds (Foias, Sell & Temam 1985, 1988; Foias, Manley & Temam 1987; see also Temam 1991a). These manifolds yield a slaving of the high frequency component of the flow by its low frequency component and reduce the number of modes needed to monitor a flow.

1 Permanent address: Université de Paris-Sud (France) and Indiana University (USA)

Incremental unknowns have been introduced in Temam (1990) as a means to approximate attractors and inertial manifolds in the context of finite difference multigrid approximations. Indeed, when spectral discretization is used, the separation between the small and large scale components of the flow occurs naturally in the spectral space. When finite differences are used, all mesh points play the same role however large is the number of mesh points, and there is no obvious way to distinguish between the small scales which carry little energy and the large scales which carry most of the energy. Incremental unknowns of various types have been introduced which produce the separation of scale which is needed (Chen & Temam 1993). The utilization of incremental unknowns for large scale computations of turbulent flows, for direct numerical simulation or large eddy simulation, remains to be done. As a first step towards this important task, we describe hereafter in section 2 the utilization of incremental unknowns for the solution of the Burgers equation with stochastic forces. Indeed, these equations are known to be a good model for turbulent flows (see e.g. Chambers *et al.* 1988; Choi *et al.* 1992).

These computations support two important observations:

—— The small scale component of the flow as defined in the context of incremental unknowns (IU) is indeed small. Its instantaneous variation is very fast while its averaged variation is very slow.

—— The IU method is numerically efficient. It produces an improvement of the CFL stability condition which has not been analytically fully explained, although there are already some partial theoretical justifications (Temam 1990, 1991b). Consequently, the same accuracy can be recovered with less calculations, the gain in computing time in the cases that we consider being a factor of 7.

2. Accomplishments

In this section, we describe the procedure for applying the IU method to the stochastic Burgers equation. This equation contains nonlinear convection and diffusion terms, and its solution exhibits a chaotic nature; these qualities make it a natural model for the more complicated Navier-Stokes equations. Section 2.1 describes the governing equation and boundary conditions. The mathematical and numerical procedures of applying the IU method to the stochastic Burgers equation are described in section 2.2. Numerical results are presented in section 2.3. Application of the IU method to the Navier-Stokes equations is considered in section 2.4.

2.1 The Burgers equation with random forcing

Consider the randomly forced non-dimensionalized Burgers equation with no-slip boundary conditions

$$\begin{aligned} &\frac{\partial u}{\partial t} + \frac{\partial}{\partial x}\frac{u^2}{2} = \frac{1}{Re}\frac{\partial^2 u}{\partial x^2} + \chi(x,t), \qquad 0 < x < 1, \\ &u(x=0,t) = u(x=1,t) = 0, \\ &u(x,t=0) = u_o, \end{aligned} \tag{2.1}$$

where u is the velocity, χ is the random forcing, and Re is the Reynolds number. The initial data u_o is an instantaneous solution of the Burgers equation with random forcing χ rather than an arbitrary function. The forcing function χ is a white noise random process in x with zero mean (see Chambers *et al.* 1988; Choi *et al.* 1992):

$$< \chi >_x = 0, \quad < \chi^2 >_x = 1.$$

Here $< \cdot >_x$ denotes the average value over space. In the absence of forcing ($\chi = 0$), the solutions of equation (2.1) decay to zero from any bounded initial data.

2.2 Description of the IU method for the Burgers solution

The discretized equations for the stochastic Burgers equation with no-slip boundary conditions are obtained using a semi-implicit method in time (Adams-Bashforth for the convection term and Crank-Nicholson for the diffusion term) and a second-order centered difference method in space:

$$\alpha u_i^n - \beta u_{i+1}^n - \beta u_{i-1}^n = g_i, \quad i = 1, \cdots, 2I-1, \tag{2.2}$$

$$u_0 = u_{2I} = 0,$$

where

$$\begin{aligned}
\alpha &= 1 + \frac{\Delta t}{Re \Delta x^2}, \\
\beta &= \frac{\Delta t}{2Re\Delta x^2}, \\
g_i &= u_i^{n-1} - \frac{\Delta t}{2Re\Delta x^2}\left(2u_i^{n-1} - u_{i+1}^{n-1} - u_{i-1}^{n-1}\right) \\
&\quad - \frac{\Delta t}{8\Delta x}\left[\, 3(u_{i+1}^{n-1\,2} - u_{i-1}^{n-1\,2}) - (u_{i+1}^{n-2\,2} - u_{i-1}^{n-2\,2})\right] + \Delta t\, \chi_i^{n-\frac{1}{2}},
\end{aligned} \tag{2.3}$$

where Δt is the computational time step and $\Delta x = 1/(2I)$ is the grid spacing.

The incremental unknowns for the present problem consist of the numbers ϕ_{2i} and ψ_{2i+1} (see figure 1):

$$\begin{aligned}
&\phi_{2i} = u_{2i}, \quad i = 0, \cdots, I, \\
&\psi_{2i+1} = u_{2i+1} - \frac{1}{2}(u_{2i} + u_{2i+2}), \quad i = 0, \cdots, I-1,
\end{aligned} \tag{2.4}$$

where ϕ_0 and ϕ_{2I} correspond to the velocities at the boundary points. Thus ψ_{2i+1} is the increment of u to the average of the values at the neighboring points, $2i$ and $2i+2$; hence by Taylor's formula, ψ_{2i+1} is small, of order Δx^2.

At points $2i+1$, equation (2.2) becomes

$$\alpha u_{2i+1}^n - \beta u_{2i+2}^n - \beta u_{2i}^n = g_{2i+1}.$$

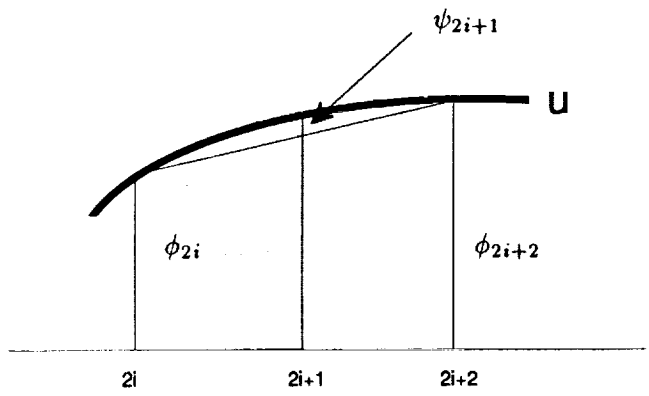

FIGURE 1. Incremental unknowns.

Using equation (2.4) gives

$$\alpha\psi^n_{2i+1} + \left(\frac{\alpha}{2} - \beta\right)\left(\phi^n_{2i} + \phi^n_{2i+2}\right) = g_{2i+1}, \tag{2.5}$$

where $i = 0, \cdots, I-1$. Similarly, at points $2i$, equation (2.2) becomes

$$\alpha u^n_{2i} - \beta u^n_{2i+1} - \beta u^n_{2i-1} = g_{2i}.$$

Substituting equations (2.4) and (2.5) into the above equation gives

$$\frac{1}{\alpha}\left(\alpha^2 - 2\beta^2\right)\phi^n_{2i} - \frac{\beta^2}{\alpha}\phi^n_{2i+2} - \frac{\beta^2}{\alpha}\phi^n_{2i-2} = g_{2i} + \frac{\beta}{\alpha}\left(g_{2i+1} + g_{2i-1}\right), \tag{2.6}$$

where $i = 1, \cdots, I-1$. The system consisting of equation (2.6) is similar to the system consisting of equation (2.2), but involves half as many unknowns.

We can, of course, repeat the procedure. If we start with $\Delta x = 1/(2^l I)$, then after l steps, we reduce the initial system involving $2^l I$ unknowns to a similar one involving I unknowns. Following the same procedure described above, one can get the discretized equations for multi-steps l:

$$\alpha^m \phi^{n,m}_{2i} - \beta^m \phi^{n,m}_{2i+2} - \beta^m \phi^{n,m}_{2i-2} = g^m_{2i}, \quad i = 1, \cdots, 2^{l-m} I - 1, \tag{2.7}$$

$$\psi^{n,m}_{2i+1} = \frac{1}{\alpha^m}\left[g^m_{2i+1} - \left(\frac{\alpha^m}{2} - \beta^m\right)\left(\phi^{n,m}_{2i} + \phi^{n,m}_{2i+2}\right)\right], \quad i = 0, \cdots, 2^{l-m} I - 1, \tag{2.8}$$

$$\begin{aligned}
\alpha^m &= \frac{1}{\alpha^{m-1}}\left(\alpha^{m-1^2} - 2\beta^{m-1^2}\right), \\
\beta^m &= \frac{\beta^{m-1^2}}{\alpha^{m-1}}, \\
g^m_i &= g^{m-1}_{2i} + \frac{\beta^{m-1}}{\alpha^{m-1}}\left(g^{m-1}_{2i+1} + g^{m-1}_{2i-1}\right), \quad i = 1, \cdots, 2^{l-m+1} I - 1,
\end{aligned} \tag{2.9}$$

where $m = 1, \cdots, l$ denotes the level of grids and $m = 1$ and l correspond to the finest and coarsest grids, respectively;

$\alpha^0 = \alpha$, $\beta^0 = \beta$ and $g_i^0 = g_i$, $i = 1, \cdots, 2^l I - 1$ (equation (2.3)).

Numerical procedure

The numerical procedure of applying the IU method to the stochastic Burgers equation can be written as follows:

Step 1: Start from an initial velocity field u_o, $u_i^{n-1} = u_{oi}$.
Step 2: Get α^m, β^m, and g_{2i}^m from equation (2.9) for $m = 1, \cdots, l$.
Step 3: Solve equation (2.7) for the coarsest grid ($m = l$) to obtain $\phi_{2i}^{n,l}$.
Step 4: Obtain $\psi_{2i+1}^{n,m}$ from equation (2.8) with $\phi_{2i}^{n,m}$.
Step 5: Obtain $u^{n,m}$; $u_{2i}^{n,m} = \phi_{2i}^{n,m}$ and $u_{2i+1}^{n,m} = \psi_{2i+1}^{n,m} + \frac{1}{2}\left(\phi_{2i}^{n,m} + \phi_{2i+2}^{n,m}\right)$.
Step 6: Obtain $\phi_{2i}^{n,m-1} = u_i^{n,m}$.
Step 7: Repeat Steps 4 and 6 until $u^{n,1}$ is obtained.

2.3 Numerical results using the IU method

In this section, we apply the numerical procedure described in the previous section to the Burgers equation. A uniform computational mesh of 2049 points is used in x ($\Delta x = 1/2048$) and $l = 4$ (number of the grid levels); therefore, the coarsest grid has 257 points.

2.3.1 Properties of the incremental unknowns

An initial velocity field u_o is obtained for $Re = 1500$ and $\Delta t_r = 0.01$, where Δt_r is the time scale of the random forcing (for more details see Choi *et al.* 1992). Figure 2 (a) shows the root-mean-square values of ϕ and ψ^m as a function of t, where $m = 1, 2, 3$; $m = 1, 2$, and 3 correspond to the grid points of 2049, 1025, and 513, respectively. It can be seen that the ψ^m's are several orders of magnitude smaller than ϕ. Also, note that the incremental unknowns ψ at the coarser grid level have larger magnitude as compared to those at the denser grid level.

The root-mean-square values of $\partial\phi/\partial t$ and $\partial\psi^m/\partial t$ as a function of t are shown in figure 2 (b). Contrary to the results of ϕ and ψ^m (figure 2 (a)), the magnitude of $\partial\psi^m/\partial t$ is comparable to that of $\partial\phi/\partial t$, indicating that $\partial\psi^m/\partial t$ cannot be neglected pointwise as compared to $\partial\phi/\partial t$ when there is a stochastic motion in flow. In case there is no small-scale motion in flow, however, the magnitude of $\partial\psi^m/\partial t$ is several orders of magnitude smaller than that of $\partial\phi/\partial t$: we have tested an initial velocity field, $\sin(2\pi x)$, without random forcing, and the result showed this is indeed the case. When a small-scale motion exists in the flow, we expect the derivatives $\partial\psi^m/\partial t$ to be small in average as evidenced in figure 3. This point will be discussed elsewhere.

Figure 4 shows $\partial\psi^1/\partial t$ at $x = 0.5$ as a function of t and $\partial\psi^1/\partial t$ at $t = 2$ as a function of x; $\partial\psi^1/\partial t(t)$ shows an intermittent behavior while a chaotic behavior is shown in $\partial\psi^1/\partial t(x)$. The power spectra of these $\partial\psi^1/\partial t$'s show that the incremental unknowns have nearly same power at all wavenumbers (a white noise) while they have higher power at the highest frequency.

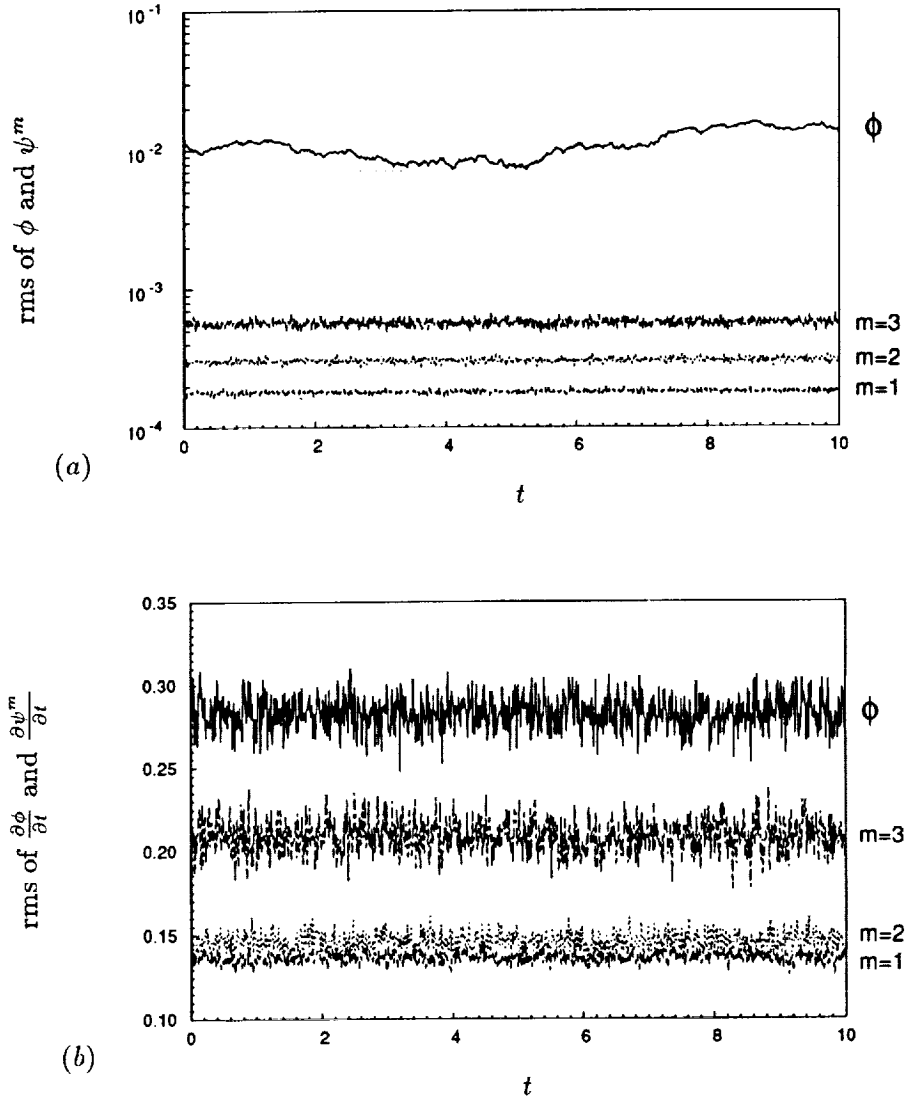

FIGURE 2. Root-mean-square values of the incremental unknowns as a function of t: (a) ——— , ϕ; ---- , ψ^1; ..... , ψ^2; — — — , ψ^3; (b) ——— , $\frac{\partial\phi}{\partial t}$; ---- , $\frac{\partial\psi^1}{\partial t}$; ..... , $\frac{\partial\psi^2}{\partial t}$; — — — , $\frac{\partial\psi^3}{\partial t}$. Note that $m = 1$ corresponds to the finest grid.

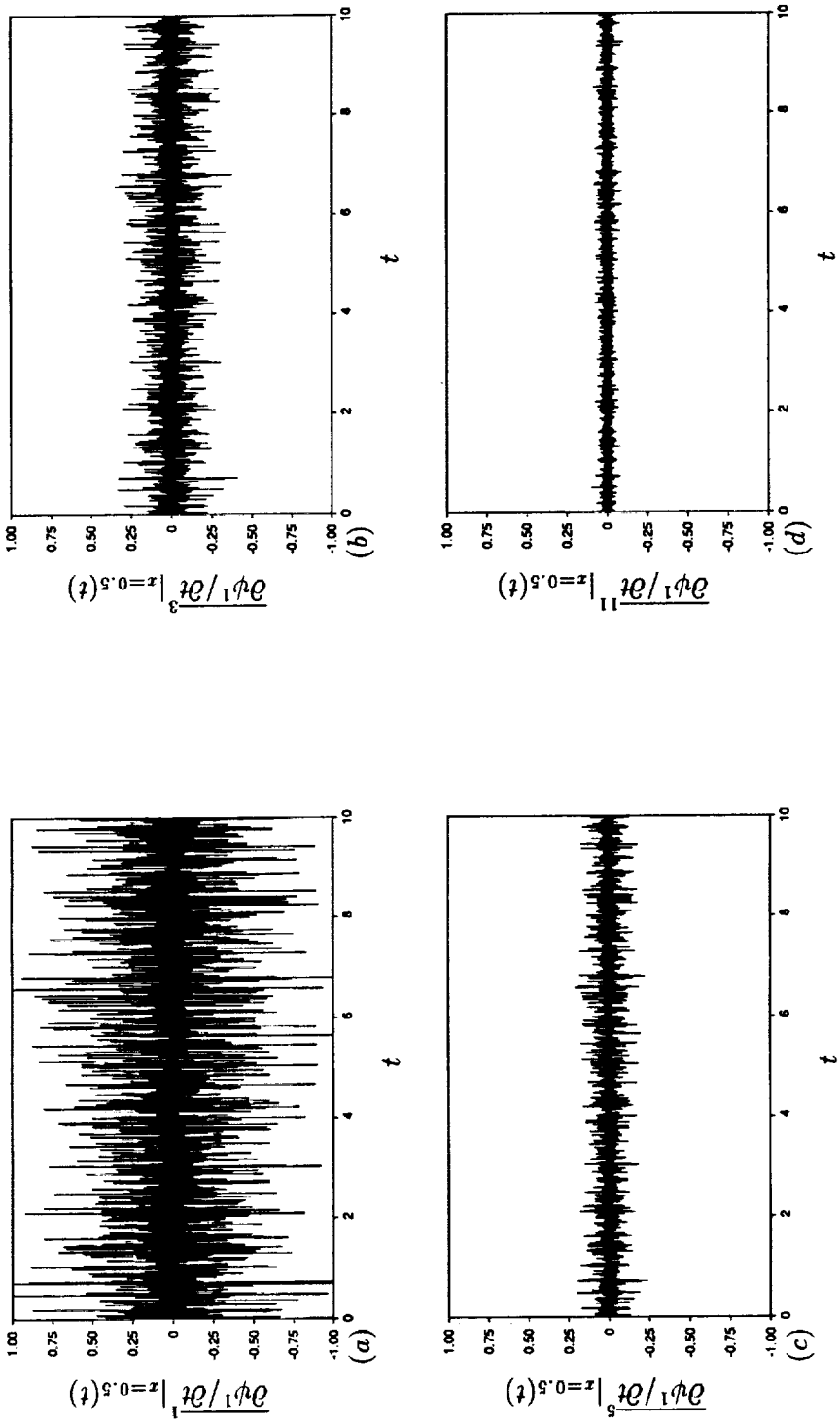

FIGURE 3. Time-averaged values of the incremental unknowns, $\overline{\partial\psi^1/\partial t}^k|_{x=0.5}(t)$: (*a*) $k = 1$; (*b*) $k = 3$; (*c*) $k = 5$; (*d*) $k = 11$, where $\overline{\frac{\partial\psi^1}{\partial t}}^k|_{x=0.5}(t) = \frac{1}{k\Delta t}\int_{t-\frac{k}{2}\Delta t}^{t+\frac{k}{2}\Delta t} \frac{\partial\psi^1}{\partial t}(\tau)\,d\tau$.

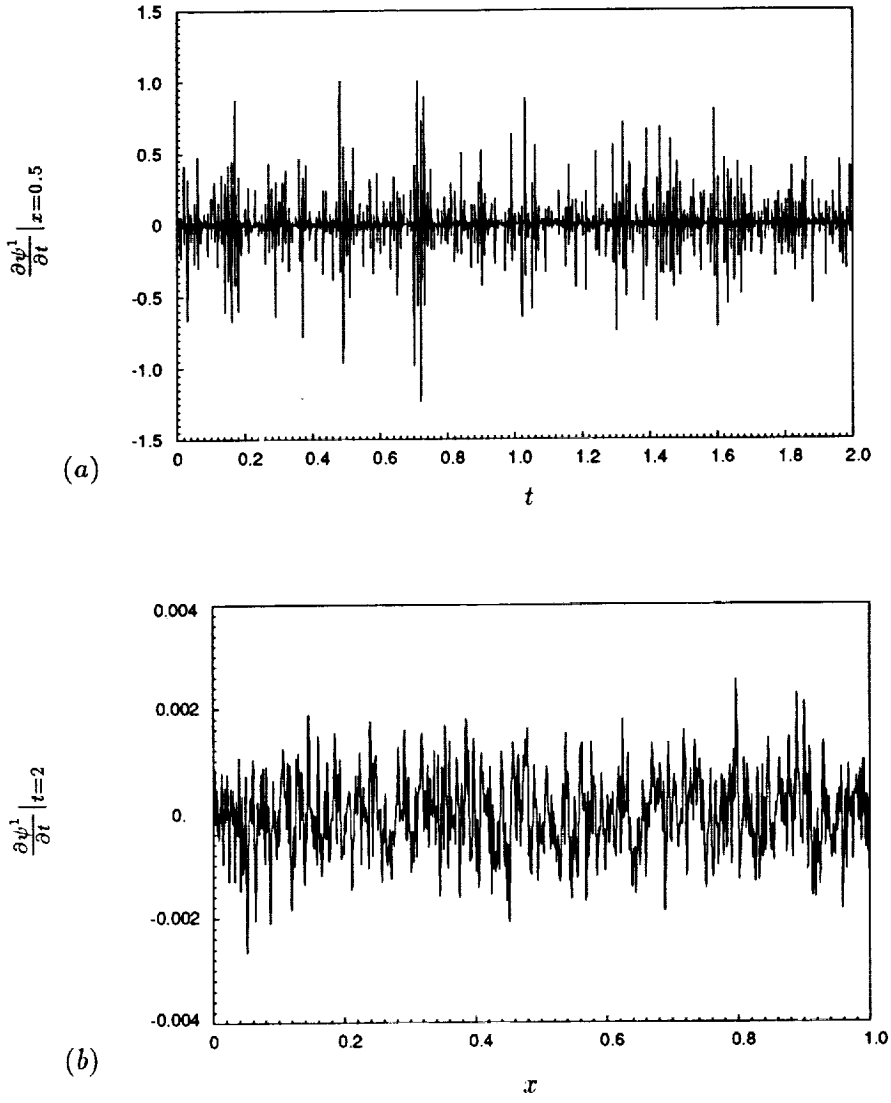

FIGURE 4. Instantaneous $\frac{\partial \psi^1}{\partial t}$ as a function of t or x.

2.3.2 Efficiency of the IU method

In this section, we investigate the effect of the IU method on the numerical stability. A classical semi-implicit method has a limit of the computational time step due to the explicit treatment of the nonlinear term. The maximum CFL (Courant-Friedrichs-Lewy) number is restricted to one with the present semi-implicit method (equation (2.2)). Hence, the maximum time step without the IU method is restricted

Case	$l=1$	$l=2$	$l=3$	$l=4$
Δt_{max}	0.0051	0.017	0.054	0.054
Total CPU (sec)	0.232	0.088	0.032	0.034

Table 1. Maximum computational time step and total CPU time using the IU method.

as

$$\Delta t \leq \frac{\Delta x}{u}. \tag{2.10}$$

Maximum computational time steps Δt_{max} using the IU method have been obtained for the initial value problem (2.1): $u_o = \sin(2\pi x)$, $Re = 100$, and $\chi = 0$ (no random forcing). Table 1 shows the maximum computational time step and total CPU time using the IU method, where l denotes the level of the coarsest grid. Note that the IU method is not used when $l = 1$. A maximum computational time step is clearly increased when $l > 1$, indicating that the numerical stability is enhanced using the IU method. However, there seems to exist a limit of level l of increasing Δt_{max}; for the present problem, $l = 3$ (see table 1).

The CPU time to advance one time step with the IU method is larger than that without the IU method due to the calculation procedure of α^m, β^m, and g^m, although the matrix size to be inverted is reduced from $2^l I$ to I. Total CPU times to reach $t = 1$ are shown in table 1. Computational cost is significantly reduced by a factor of 7 using the IU method. The mathematical analysis of the stability enhancement using the IU method for the Burgers equation is very complex and will be investigated in the future. Theoretical indications that the IU method produces stability enhancement appear in Temam (1990, 1991).

2.4 Application of the IU method to the unsteady Navier-Stokes equations

The IU method can be applied to the unsteady three-dimensional Navier-Stokes equations as follows: Firstly, the first step of the fractional-step method (Kim & Moin 1985) provides a second-order-accurate approximation of the three-dimensional Navier-Stokes equations with pressure term excluded. Secondly, an approximate factorization technique (Beam & Warming 1978) splits three-dimensional equations to three one-dimensional equations. Finally, the IU method as presented above is applied to each one-dimensional equation. This case will be addressed in the future.

REFERENCES

BEAM, R. M. & WARMING, R. F. 1978 An implicit factored scheme for the compressible Navier-Stokes equations. *AIAA J.* **16,** 393.

CHAMBERS, D. H., ADRIAN, R. J., MOIN, P., STEWART, D. S. & SUNG, H. J. 1988 Karhunen-Loéve expansion of Burgers' model of turbulence. *Phys. Fluids* **31**, 2573.

CHEN, M. & TEMAM, R. 1993 Nonlinear Galerkin method in finite difference case and wavelet-like incremental unknowns. *Numerische Math.* to appear.

CHOI, H., TEMAM, R., MOIN, P. & KIM, J. 1992 Feedback control for unsteady flow and its application to the stochastic Burgers equation. *CTR manuscript* **131**.

CONSTANTIN, P., FOIAS, C. & TEMAM, R. 1985 Attractors representing turbulent flows. *Memoirs of AMS* **53**, 67.

CONSTANTIN, P., FOIAS, C. & TEMAM, R. 1988 On the dimension of the attractors in two-dimensional turbulence. *Physica D* **30**, 284.

FOIAS, C., MANLEY, O. & TEMAM, R. 1988 Modelling of the interaction of small and large eddies in two-dimensional turbulent flows. *Math. Mod. and Num. Anal.* **22**, 93.

FOIAS, C., SELL, G. R. & TEMAM, R. 1985 Variétés inertielles des équations différentielles dissipative. *Comptes Rendus Ac. Sc. Paris* **301**, Série I, 139.

FOIAS, C., SELL, G. R. & TEMAM, R. 1988 Inertial manifolds for nonlinear evolutionary equations. *J. Diff. Equ.* **73**, 309.

KEEFE, L, MOIN, P. & KIM, J. 1992 The dimension of attractors underlying periodic turbulent Poiseuille flow. *J. Fluid Mech.* **242**, 1.

KIM, J. & MOIN, P. 1985 Application of a fractional-step method to incompressible Navier-Stokes equations. *J. Comput. Phys.* **59**, 308.

TEMAM, R. 1990 Inertial manifolds and multigrid methods. *SIAM J., Math. Anal.* **21**, 154.

TEMAM, R. 1991a Approximation of attractors, large eddies simulation and multiscale methods. *Proceedings of Royal Soc. A* **434**. 23.

TEMAM, R. 1991b Stability analysis of the nonlinear Galerkin method. *Math. of Comp.* **57**, 477.

Direct simulation of compressible wall-bounded turbulence

By Gary N. Coleman

1. Motivation and objectives

When analyzing many turbulent flows, the effects of compressibility can be neglected. Even some relatively high-speed flows, such as boundary layers generated by a supersonic aircraft, produce turbulent statistics (when scaled to account for mean density variations) that are similar to those found for the incompressible case (Bradshaw 1977). There are other situations, however, in which the nonzero divergence of the turbulence leads to behavior that is fundamentally different from that found at constant density (Speziale & Sarkar 1991). Examples include flows created by internal combustion engines, hypersonic flight, and supersonic combustion. It is with instances such as these that this project is concerned. In particular, we are interested in the effects of compressibility on turbulence near a smooth solid constant-temperature surface; our primary objective is an increased physical understanding that can be used to improve turbulence models of wall-bounded compressible flows.

With this in mind, we have begun a direct numerical simulation (DNS) study of turbulence in a plane channel. Because all of the relevant spatial and temporal scales are to be resolved, the simulations require no subgrid scale parameterization. The DNS code developed by Buell (1990, 1991) to study compressible plane Couette flow has been modified to solve the compressible Navier-Stokes equations in the plane channel. The channel was chosen over the Couette flow for two reasons: the first was to avoid using the very large streamwise domains needed to adequately capture the large Couette vortical structures (Lee 1990, Buell 1991); the second was to make use of previous experience by considering the compressible version of a well established case and isolate finite Mach number effects by comparing to the incompressible channel (Kim *et al.* 1987).

The code utilizes a Fourier-Legendre spatial discretization along with a hybrid third-order time advance algorithm developed to optimize the range of Mach numbers that may be considered (Buell 1991). The fluid is assumed to be an ideal gas, with constant specific heats and constant Prandtl number, and a (power-law) temperature dependent viscosity. Isothermal boundary conditions are used so that statistically stationary solutions may be obtained. The flow is driven by a body force rather than a mean pressure gradient to preserve streamwise homogeneity, with the body force f_i^* defined so that the bulk mass flux, $Q_* = \int_{-b_*}^{+b_*} \overline{\rho_* u_1^*} dy_*$, is constant ($y_*$ is the wall-normal coordinate, b_* the channel halfwidth, ρ_* the density, and u_1^* the streamwise velocity; "starred" quantities represent dimensional variables, and an overbar denotes an average over time and the streamwise and spanwise directions). Nondimensionalized by b_*, the bulk-averaged density $\Theta_* \equiv \frac{1}{2b_*} \int_{-b_*}^{+b_*} \bar{\rho}_* dy_*$,

the bulk velocity $\mathcal{U}_* \equiv Q_*/2b_*\Theta_*$, and the wall temperature T_w^*, the governing equations become:

$$\frac{\partial \rho}{\partial t} + \rho\frac{\partial u_j}{\partial x_j} + u_j\frac{\partial \rho}{\partial x_j} = 0, \tag{1}$$

$$\frac{\partial u_i}{\partial t} + u_j\frac{\partial u_i}{\partial x_j} + \frac{1}{\gamma M^2}\frac{\partial T}{\partial x_i} + \frac{T}{\gamma M^2 \rho}\frac{\partial \rho}{\partial x_i} - \frac{1}{Re\ \rho}\frac{\partial \tau_{ij}}{\partial x_j} - \Phi_i = 0, \tag{2}$$

$$\frac{\partial T}{\partial t} + u_j\frac{\partial T}{\partial x_j} + (\gamma-1)T\frac{\partial u_j}{\partial x_j} - \frac{\gamma(\gamma-1)M_d^2}{Re}\frac{\tau_{ij}}{\rho}\frac{\partial u_i}{\partial x_j} + \frac{\gamma}{Re\ Pr\ \rho}\frac{\partial q_j}{\partial x_j} = 0, \tag{3}$$

$$p = \rho T/\gamma M^2, \tag{4}$$

where

$$\tau_{ij} = \mu\left(\frac{\partial u_i}{\partial x_j} + \frac{\partial u_j}{\partial x_i} - \tfrac{2}{3}\delta_{ij}\frac{\partial u_l}{\partial x_l}\right) \qquad \text{and} \qquad q_j = -\mu\frac{\partial T}{\partial x_j}.$$

The relevant nondimensional parameters are thus (a) a Mach number, $M^2 = \mathcal{U}_*^2/\gamma R_* T_w^*$; (b) a Reynolds number, $Re = \Theta_*\mathcal{U}_* b_*/\mu_w^*$; (c) the Prandtl number, $Pr = C_p^*\mu_*/k_*$; (d) the ratio of specific heats, $\gamma = C_p^*/C_v^*$; and (e) the viscosity exponent, n, where $\mu = T^n$. In the above, $\mu = \mu_*/\mu_w^*$ is the dynamic viscosity, R_* the gas constant, k_* the thermal conductivity, and the w-subscript indicates a value at the wall. Equations (1) – (4) are identical to those used by Buell (1991) except for the presence of the nondimensional forcing, $\Phi_i = b_* f_i^*/\mathcal{U}_*^2$, in (2) and the use of $\mathcal{U}_*$ in the Mach and Reynolds numbers. Another parallel to Buell (1991) is the separate Mach numbers in the momentum and energy equations, M and M_d ("d" for "dissipation"), respectively. When $M = M_d$, a "physical" simulation is obtained; when they are not equal, the results can be used to differentiate between compressibility effects associated with the pressure gradient terms in (2) and the dissipation term in (3) and thus determine the relative importance of "acoustic" and "variable-property" influences at a given Mach number. This procedure will be followed in future simulations. In the next section, preliminary results from two $M = M_d$ runs are presented.

2. Accomplishments

Two cases have been simulated, one with $M = M_d = 1.5$, the other with $M = M_d = 3$; both use $Re = 3000$, $Pr = 0.7$, $\gamma = 1.4$, and $n = 0.7$. The $M = 1.5$ run begins by superimposing small random numbers on the laminar plane-Poiseuille velocity profile and uniform density and temperature fields, while the $M = 3$ case uses a mature $M = 1.5$ field as initial conditions. (An attempt to also begin the high Mach number simulation with random numbers and laminar profiles was unsuccessful since, during the initial transient, the temperature field becomes negative and the code stops. Lower level random disturbances could be used to avoid this problem but would significantly increase the time required to obtain fully developed turbulence — and if the disturbances are too small, there is no guarantee that a turbulent state will appear. To avoid a similar high-M initialization problem, Buell

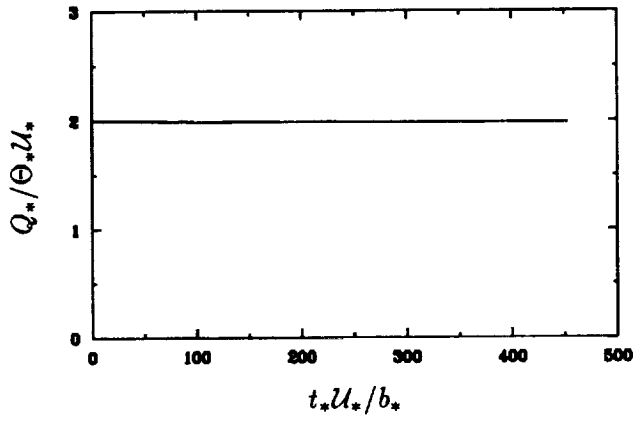

FIGURE 1. Mass flux history, $M = 1.5$ (Run m01x5g).

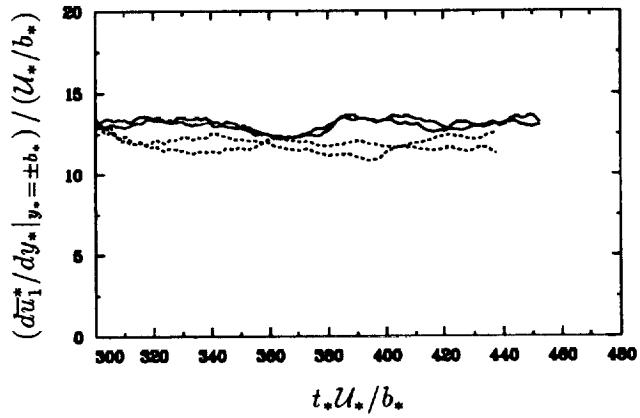

FIGURE 2. Wall shear histories at $y = \pm 1$: ——$M = 1.5$; ----$M = 3$; (Runs m01x5g and m03x0c).

(private communication) used eigenfunctions from a linear stability analysis of the Couette flow to begin his simulations.) The streamwise and spanwise domain sizes for both cases (in units of b_*) are 4π and $4\pi/3$, values that are chosen to correspond to a DNS run for the incompressible channel. The number of collocation points in the streamwise x, wall-normal y, and spanwise z directions are respectively 70, 90, and 40, which leads to the fully developed but marginally resolved turbulence desired to begin the simulations. After they have equilibrated to statistically stationary states, the flows represented by the figures below will in the future be fully resolved and studied in detail.

The $M = 1.5$ mass flux history is shown in Figure 1. To maintain the constant flux, the code adjusts the body force at each time step so that $\int_{-1}^{+1}(\partial\overline{\rho u}_1/\partial t)dy \approx \overline{\rho}\int_{-1}^{+1}(\partial\overline{u}_1/\partial t)dy = 0$ by using the Legendre quadrature routine to integrate all but

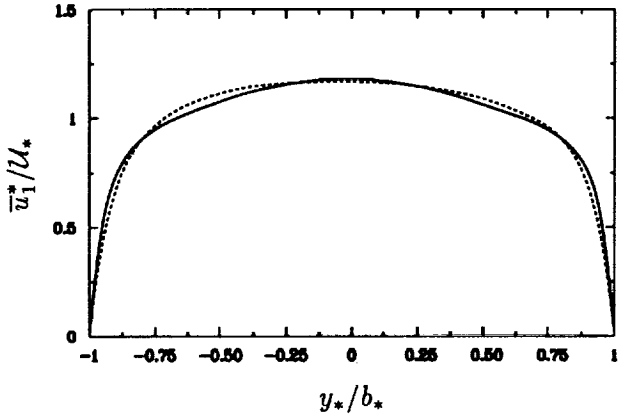

FIGURE 3. Mean streamwise velocity profiles: —— $M = 1.5$; ---- $M = 3$. Means in Figures 3–6 are the result of averaging over streamwise and spanwise directions and time; sampling period is from $t_*\mathcal{U}_*/b_* = 438$ to 448 for $M = 1.5$ and from 419 to 429 for $M = 3$.

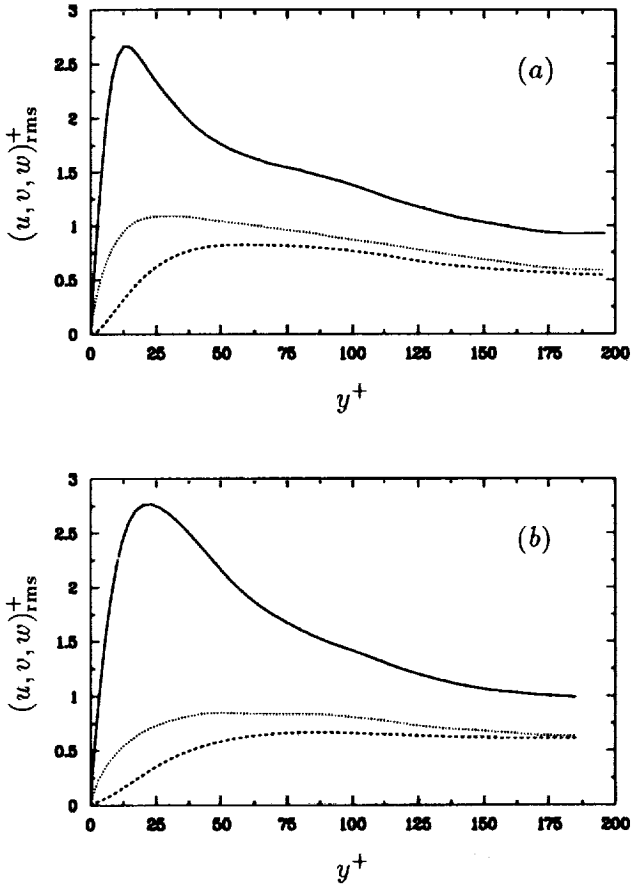

FIGURE 4. RMS velocity fluctuation profiles for (*a*) $M = 1.5$ and (*b*) $M = 3$ runs: —— streamwise; ---- wall-normal; and ····· spanwise components normalized by $(u_\tau^*)_{\rm w}$ and $\mu_{\rm w}^*/\rho_{\rm w}^*$.

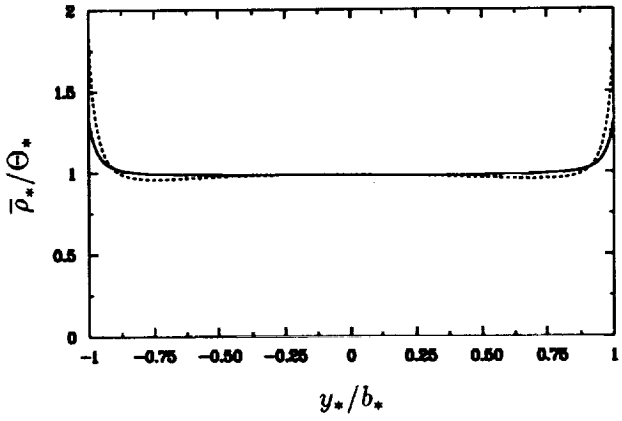

FIGURE 5. Mean density profiles: —— $M = 1.5$; ---- $M = 3$.

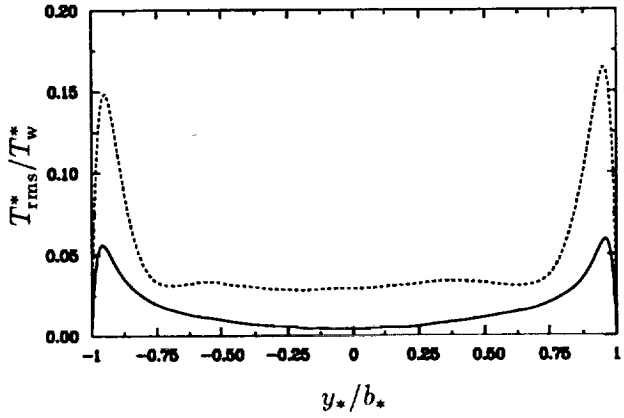

FIGURE 6. RMS temperature fluctuation profiles: —— $M = 1.5$; ---- $M = 3$.

the first and last terms in (2). Note that while this method is sufficiently accurate in practice (the value at $t = 450$ is within 1% of the initial flux), since we solve for u_i and not ρu_i, the constant-flux constraint cannot be enforced exactly.

Histories of the wall shear for the $M = 1.5$ and $M = 3$ cases are contrasted in Figure 2. As was true for the Couette DNS (Buell 1991), an increase in M leads to a drop in $|d\overline{u}_1/dy|$ at the walls. The higher Mach number is also responsible for a more pronounced flattening of the mean streamwise velocity profile as shown in Figure 3. Another similarity to the Couette results (cf. Figure 6 of Buell 1991) is revealed in Figure 4 where the near-wall maxima in the rms velocity fluctuations are observed to be less distinct at larger M. The mean density variation and temperature fluctuations are illustrated in figures 5 and 6; the large gradients of mean density (and therefore temperature) near the walls produce peaks in the rms temperature profiles, with both the density gradient and temperature fluctuations increasing with Mach number.

3. Future plans

Having modified the code and obtained preliminary results, we now intend to perform a number of case studies designed to quantify the compressibility effects. Our immediate task is to continue the $M = 1.5$ and $M = 3$ runs on a fully resolved grid and to begin new simulations for which M and M_d are not the same, as discussed above. Since there is a significant difference between the $M = 1.5$ and $M = 3$ data presented here, for the "unphysical" $M_d \neq M$ runs we will first choose $M = 3$ and $M_d = 1.5$ and then $M = 1.5$ and $M_d = 3$. Using the "$M_d \neq M$" scheme for the Couette flow, Buell (1991) found that "pure acoustic" (nonzero turbulent dilatation) effects and those due to variations of mean density are both important, with the former influencing the wall shear and the latter the large scale structures. We will determine if the same is also true for the present flow and attempt to incorporate the findings into compressible turbulence models.

REFERENCES

BRADSHAW, P. 1977 Compressible turbulent shear layers. *Ann. Rev. Fluid Mech.* **9**, 33–54.

BUELL, J. C. 1990 Direct simulations of wall-bounded compressible turbulence. In *Annual Research Briefs - 1989*. Center for Turbulence Research, Stanford Univ./NASA-Ames.

BUELL, J. C. 1991 Direct simulations of compressible wall-bounded turbulence. In *Annual Research Briefs - 1990*. Center for Turbulence Research, Stanford Univ./NASA-Ames.

KIM, J., MOIN, P. & MOSER, R. 1987 Turbulence statistics in fully developed channel flow at low Reynolds number. *J. Fluid Mech.* **177**, 133–166.

LEE, M. J. 1990 The large-scale structures in turbulent plane Couette flow. In *Annual Research Briefs - 1989*. Center for Turbulence Research, Stanford Univ./NASA-Ames.

SPEZIALE, C. G. & SARKAR, S. 1991 Second-order closure models for supersonic turbulent flows. *AIAA Paper No. 91-0212*.

Direct numerical simulation of hot jets

By M. C. Jacob[1]

1. Motivation and objectives

1.1 Background

The ultimate motivation of this work is to investigate the stability of two dimensional heated jets and its implications on aerodynamic sound generation from data obtained with direct numerical simulations (DNS). As pointed out in our last report, these flows undergo two types of instabilities, convective or absolute, depending on their temperature. We also described the limits of earlier experimental and theoretical studies (*e.g* Yu & Monkewitz (1989) and Huerre & Monkewitz (1990)) and explained why a numerical investigation could give us new insight into the physics of these instabilities. The aeroacoustical interest of these flows was also underlined.

In order to reach this goal, we first need to succeed in the DNS of heated jets. Our past efforts have been focused on this issue which encountered several difficulties. Our numerical difficulties are directly related to the physical problem we want to investigate since these absolutely or almost absolutely unstable flows are by definition very sensitive to the smallest disturbances and are very likely to reach non-linear saturation through a numerical feed-back mechanism. As a result, it is very difficult to compute a steady laminar solution using a spatial DNS. A steady state was reached only for strongly co-flowed jets (Jacob (1991)), but these flows are almost equivalent to two independent mixing layers. Thus they are far from absolute instability and have much lower growth rates.

1.2 Preliminary simulations

Nevertheless, DNS of convectively and absolutely unstable jets show some interesting features which qualitatively indicate that these two types of flows respond differently to the transient waves generated at the beginning of the simulations. Two cases were initially computed with the Poinsot-Lele code (Lele (1992), Poinsot & Lele (1992)): for both cases, the inflow jet-diameter $D = 10\delta_\omega$, where δ_ω is the vorticity thickness, the inlet U-velocity uses a top-hat profile given by Yu & Monkewitz (1989) to which a co-flow $U_2 = 0.05U_1$ has been added, the inlet V-velocity is zero, and the inlet temperature profile is given by the Crocco-Buseman relation (Sandham & Reynolds (1989)). For numerical reasons, the computation is carried out at a low Reynolds number ($Re_D = 2000$), which is still high enough to avoid significant viscous effects. The dimensions of the computational domain are: $L_x = 60\delta_\omega$ and $L_y = 40\delta_\omega$. Time is scaled by δ_ω/c, c being the speed of sound outside the flow. The centerline Mach number has been set to $M_1 = 0.4$ in order to

1 Currently at Ecole Centrale de Lyon, France

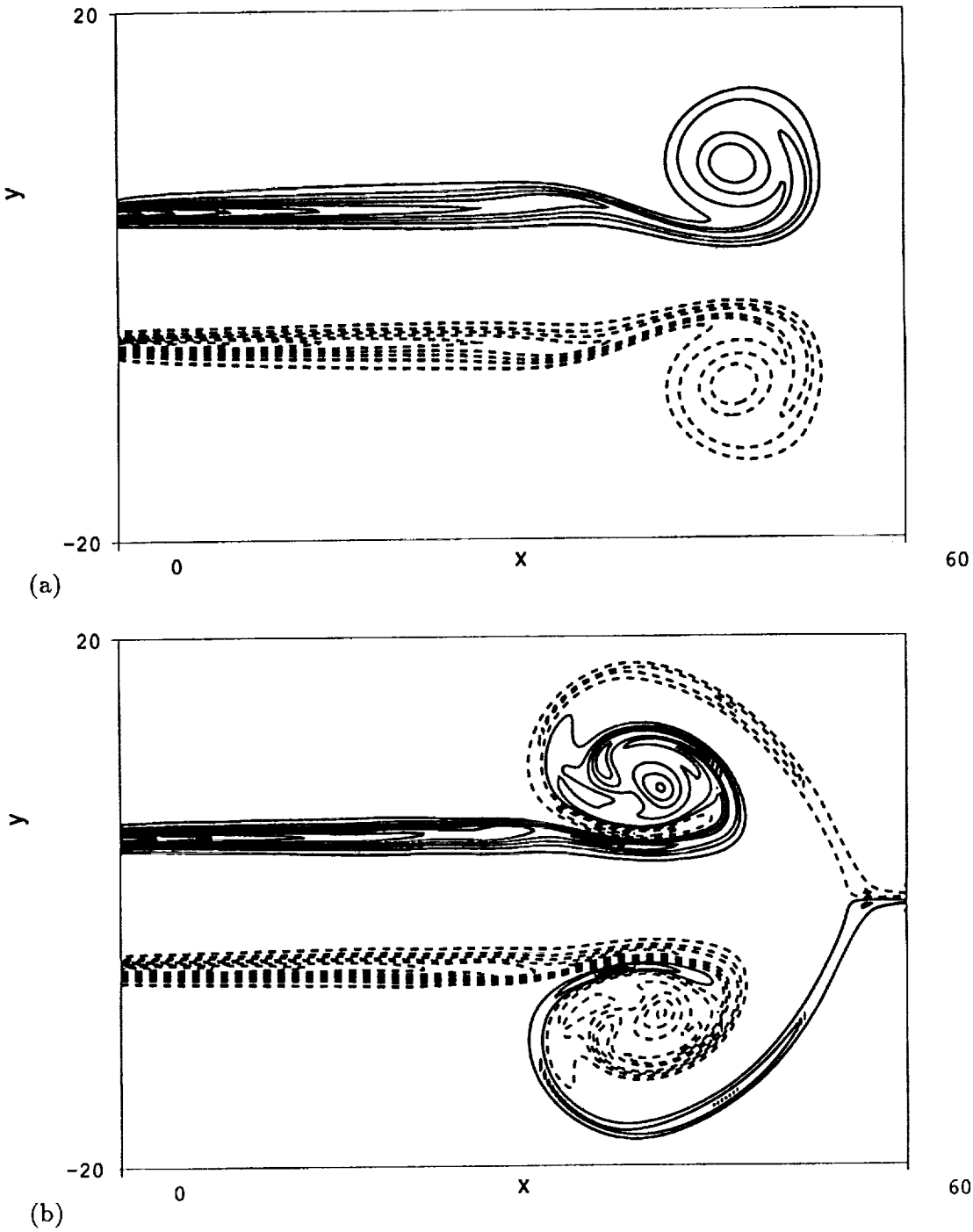

FIGURE 1. Vorticity contours. (a): Convectively unstable jet ($S = 1.0$) at time= 288 with 10 contours levels : min= -0.3799 , max= 0.3799; (b): Absolutely unstable jet ($S = 0.5$) at time= 314 with 10 contour levels : min= -0.3772 max= 0.3772. Dashed lines are used for negative values in both plots.

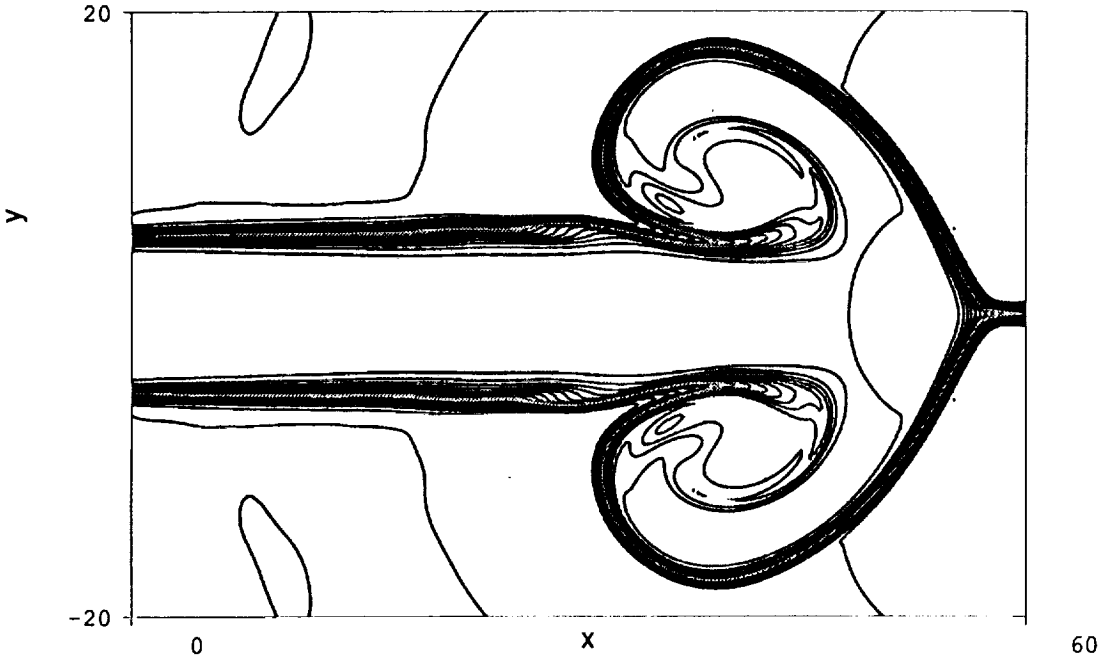

FIGURE 2. Density contours of the absolutely unstable jet ($S = 0.5$) at Time= 314 with 10 contour levels : min= 0.9697 , max= 2.0624 :the two shear layers are interacting.

limit compressibility effects. The two cases differ only by their temperature profiles: one is a cold (convectively unstable) jet, and the other is a heated absolutely unstable jet which has a temperature ratio $S = 0.5$ between the external temperature (T_2) and the centerline temperature (T_1). In both cases, the transient generates a pair of vortices on each shear layer. Figure 1 shows a typical vorticity field for each case. The snapshots are taken just after the first vortex leaves the domain and shortly before the largest structure of the transient reaches the outflow. It is clear that the vortices of the two mixing layers interact for the absolutely unstable case, whereas they seem to evolve independently in the cold jet. The corresponding density contour plot of the hot jet shows how the two shear layers interact in the transient perturbation (see Figure 2).

A theoretical explanation of this may be given in terms of vorticity dynamics: in the cold jet, pressure and density gradients are primarily created by the vortices. They are both predominately radial and, therefore, parallel. Thus the baroclinic term of the vorticity equation is negligible for a cold jet, and the evolution of the instability depends mainly on the velocity shear. In the hot jet, however, the baroclinic term is no longer negligible because the temperature stratification results in a cross-stream density gradient which combines with streamwise components of the pressure gradient and redistributes vorticity. According to this interpretation, vorticity should be decreased on the downstream side of a vortex and increased on the upstream side. This would explain qualitatively the difference between the vortical structures of Figures 1(a) and 1(b) which correspond to the upstream end of

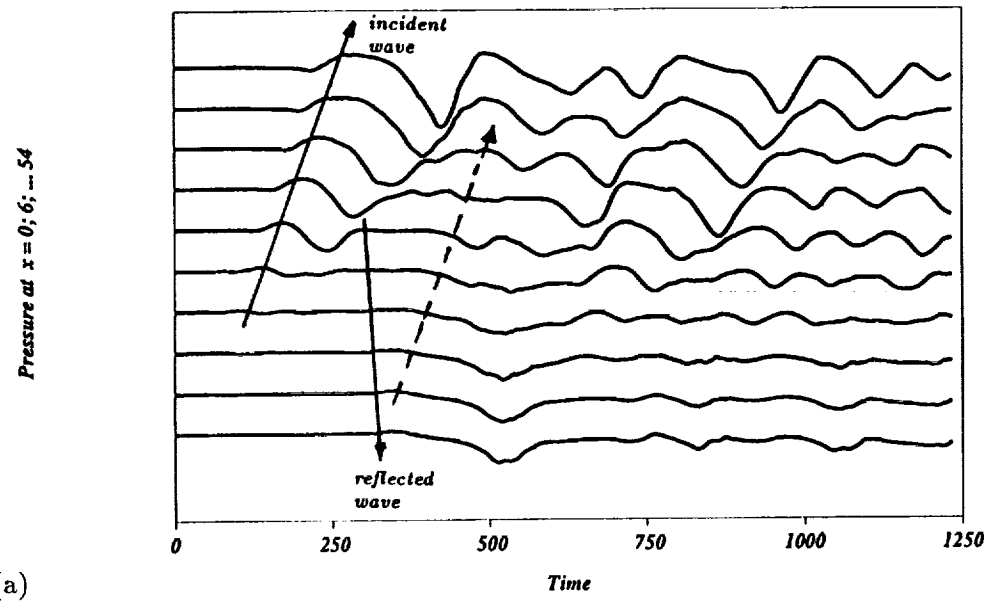

(a)

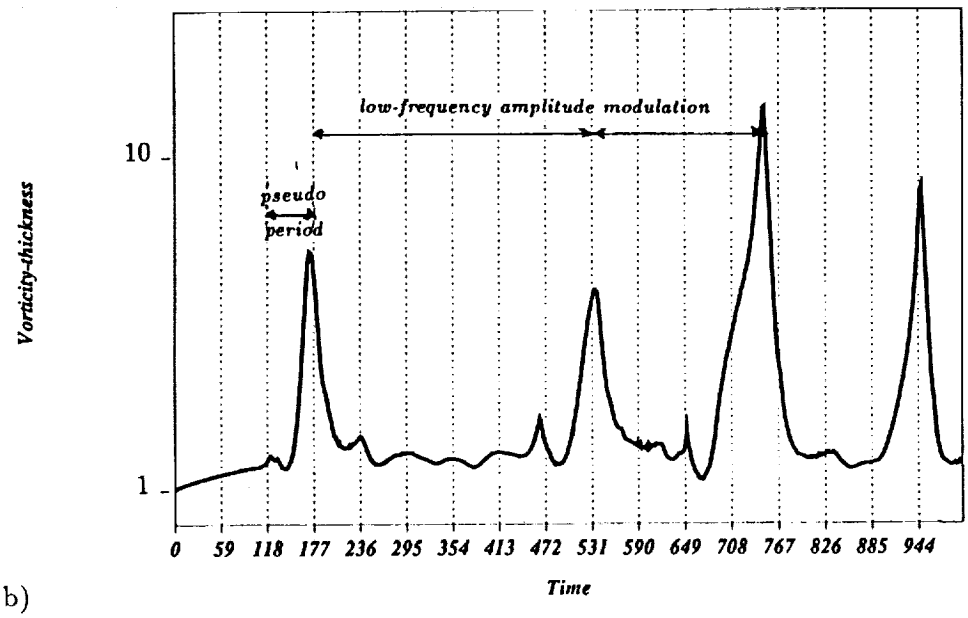

(b)

FIGURE 3. Flow history of the absolutely unstable jet ($S = 0.5$). (a): Pressure outside the jet at different x-locations; (b):Vorticity thickness history at x= 30.

the initial (vortical) disturbances for each case. Near the outflow the corresponding boundary conditions generate a strong pressure perturbation (see Figure 3(a)) which further modifies the baroclinic term.

In both cases, the disturbances are so strong that they reflect strong waves at the outflow which generate new, stronger perturbations at the inflow. Hints to this numerical feedback mechanism can be seen for the hot jet in Figure 3(a), although the upstream traveling waves are interfering with the continuously generated downstream traveling waves. This mechanism appears more strikingly in more stable flows in which fewer waves are propagating simultaneously (mixing layers, strongly co-flowed jets *etc.*).

We choose not to report this case since this feedback is already well documented elsewhere(*e.g.* Poinsot & Lele (1992)). The amplitude of the disturbances eventually saturates, and the flow reaches a pseudo-periodic state as shown in Figure 3(b). Furthermore, by comparing the two jets, we found that the pseudo-period (≈ 60 normalized time units) is roughly the same for both flows. It is also invariant to doubling the domain length which means that it is not due to a resonance of the computational domain. The low-frequency amplitude modulation is related to the biggest structures (as the one shown in Figure 1).

1.3 Objectives of the current research

Several questions arise from these results:

- What other physical conclusions can be drawn from these preliminary calculations?
- Does the observed pseudo-frequency correspond to a jet mode which is excited by ambient (numerical) noise or to a purely numerical artifact?
- Is there any possibility of controlling this frequency?
- Is there any hope of controlling the transient and thus the resulting feedback?
- Could the transient be reduced in order to reach a steady state, or are the self-sustained instabilities inherent to the jet dynamics?

In order to answer these questions, we have carried out various tests concerning both the numerics (boundary conditions, initial conditions) and the physics (stability analysis, forcing at eigen-frequencies, co-flow). In the following section, we shall give a summary of this investigation which was performed between November 1991 and June 1992.

2. Accomplishments and current work

2.1 Co-flowed jets

As previously mentioned, a steady laminar solution has been found for jets with a significant co-flow (see Figure 4). Figure 4(b) shows slight disturbances at the inlet which are due to an unrealistic V-velocity estimate ($V = 0$) at the inflow. In §2.4.1, we will see how this can be improved. For such a strongly co-flowed jet, several codes available at CTR (the Poinsot-Lele code with one dimensional boundary conditions and the Colonius code with obliquely non-reflecting first order

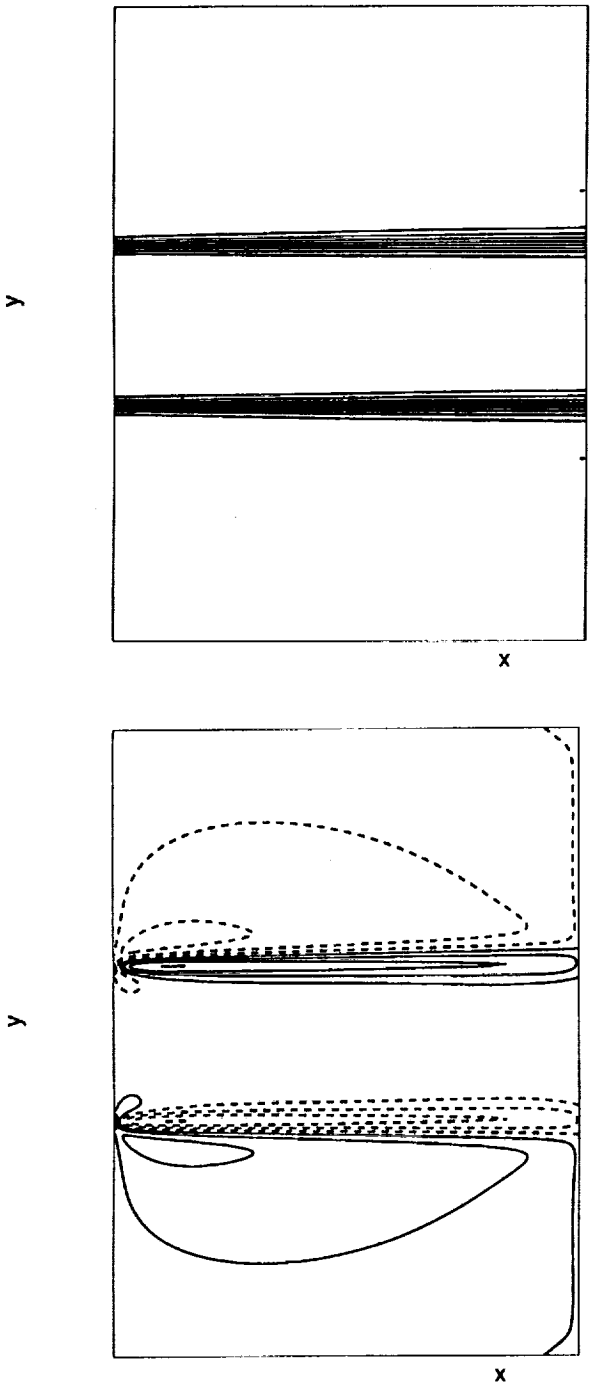

FIGURE 4. Co-flowed cold jet ($U_2 = 0.5U_1$; $L_x = 30$). Contour plots of: (a): U-velocity at time= 308 10 contour levels : min= 0.18 , max= 0.4; (b): V-velocity at time= 308. 10 contour levels : min= −0.001019 , max= 0.001019; Dashed lines are used for negative values in (b) only.

Giles boundary conditions (Colonius *et al.* (1991), Giles (1990)) converge with a comparable accuracy to the steady-state. This is not surprising since the co-flow reduces the relative shear with respect to the convection velocity and thus stabilizes the jet. Therefore, the transient is less amplified by the flow and possibly less intense initially. We found that the minimal co-flow required to reach a steady laminar state is at least $U_2 = 0.25U_1$ for cold jets and increases significantly along with the jet temperature. It is therefore legitimate to examine if absolute instabilities might still be observed given such constraints.

2.2 Linear Inviscid Incompressible Stability Analysis(LIISA)

In order to determine the specific impact of co-flows on the instability, a LIISA was carried out for 2D heated co-flowed jets. The restriction to inviscid incompressible flows is justified by the fact that the mechanism of the Kelvin-Helmholtz instability is inviscid and that compressibility effects are not significant for low Mach numbers. (We have verified that the results of our DNS code remain of the same type at lower Mach numbers and for inviscid flows.)

2.2.1 Absolute instability limit

The (complex) absolute frequency ω_0 (this is a freqency for which there exists a complex wavenumber k_0 such that : $[\partial\omega_0/\partial k](k_0) = 0$) has been determined by solving the complex dispersion relation $D(k_0, \omega_0) = 0$ of the linear stability problem. The dispersion relation is solved numerically *via* the Rayleigh equation for stratified flows using a finite difference scheme along with a minimization technique (Trouvé (1988)). The strategy for determining the zero group-velocity solution is described by Monkewitz & Sohn (1986). The values of ω_0 for various co-flows (U_2) and temperature ratios ($S = T_2/T_1$) are plotted in the (ω_r, ω_i) plane in Figure 5.

According to the linear stability theory, the absolutely unstable flows correspond to the cases where the imaginary part ω_i^0 of ω_0 is positive. It is also interesting to point out the shape of the spatial amplification in the vicinity of the absolute frequency for the case S = 0.5 (see Figure 6). According to Bers (1983), this might be due to an interchange between the two branches of the dispersion relation.

The important conclusion from this study is that absolute instability occurs only if the co-flow remains less than 1/10 of the centerline velocity. Thus the cases for which a steady laminar solution can be obtained *via* DNS correspond precisely to flows which are not likely to become absolutely unstable even by strong heating. Hence we must look for another way to reach a steady state or at least to control the transient generated when the DNS is started.

2.2.2 Forcing

One possible way to control the transient in the DNS of convectively unstable jets is to force the flow at its most unstable frequency; indeed, if the forcing level is comparable to the ambient noise, the flow will lock on the forcing frequency. This can, of course, only be achieved if the transient is not so intense that the non-linear saturation of the jet is reached. The LIISA is used to determine the spatial amplification curves: $-\alpha_i = f(\omega_r)$ for different co-flows (see Figure 6) and

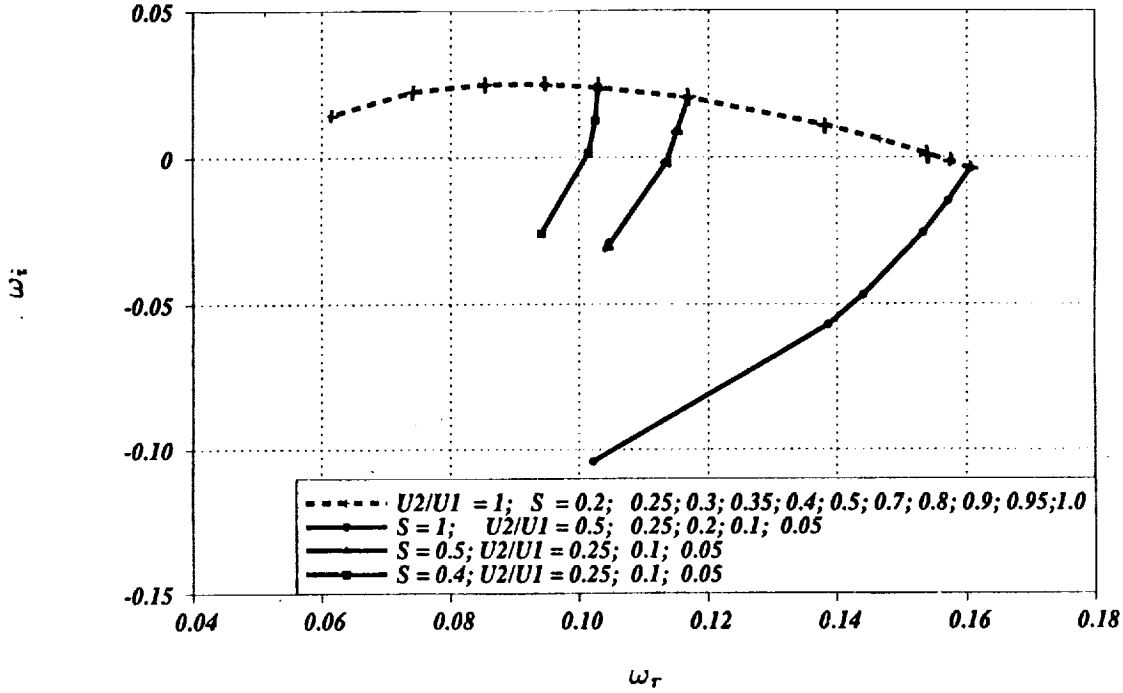

FIGURE 5. Absolute frequency for various co-flows (U_2) and temperature ratios(S).

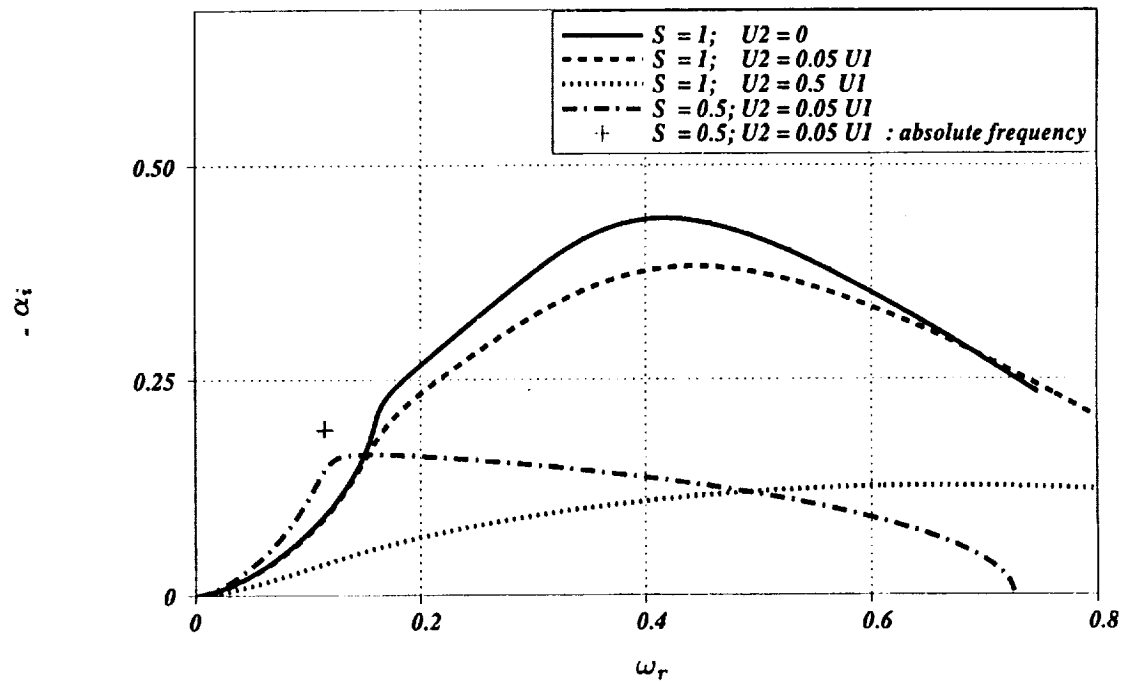

FIGURE 6. Spatial amplification $-\alpha_i$ *versus* real frequency (ω_r) for various co-flows (U_2/U_1) and temperature ratios (S).

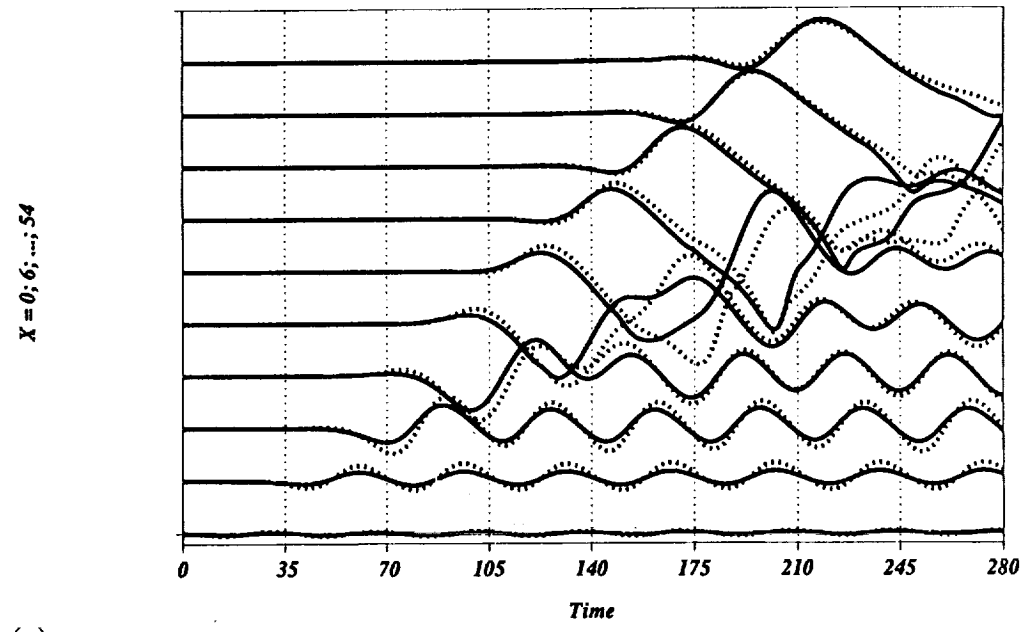

(a)

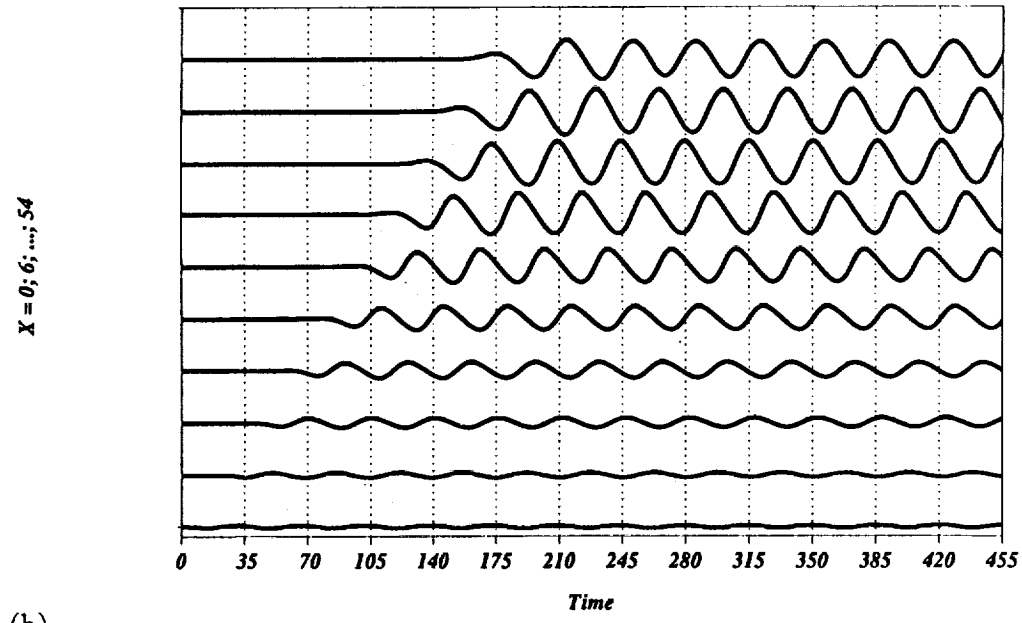

(b)

FIGURE 7. Cold jet ($L_x = 60$): V-velocity history in the shear layer at different x-locations.(a): $A_0 = 5\%$ (solid line) and 10% (dashed line), co-flow: $U_2 = 0.05U_1$; (b): $A_0 = 1\%$, co-flow $U_2 = 0.5U_1$.

to specify the incompressible eigenfunctions which are used as forcing functions. These are:

$$u(y,t) = A(t)\{U_c(y)\cos(\omega_r t) + U_s(y)\sin(\omega_r t)\}$$
$$v(y,t) = A(t)\{V_c(y)\cos(\omega_r t) + V_s(y)\sin(\omega_r t)\}$$

where:

$$A(t) = A_0(1 - e^{-(t/\tau)^2})$$
$$\tau = 10$$

and ω_r is the forcing frequency: $2\pi/\omega_r \approx 35$

The functions U_c, U_s, V_c, V_s which are given by the LIISA are normalized in order to obtain: $A_0 = u_{rms}/U_1$, and u_{rms} is evaluated by averaging over both the cross stream direction and time. These forcing functions are added to the steady inflow profiles. The results of the LIISA and the forcing provide useful information about the simulations which were described in §1.2:

1. The frequency which is observed in the DNS is slightly more than half the most amplified frequency, which means that it lies in the amplified part of the eigenvalue spectrum of the cold jet (see Figure 6). This result supports the idea that the simulated flows amplify physically the numerical noise generated at inflow in a similar way than jets amplify ambient noise in experimental facilities.
2. Forcing the jet at the most unstable frequency does not have any significant effect on the jet if the co-flow is small since the frequency which has been observed without forcing seems to reappear in the downstream half of the box. Furthermore, this tendency remains even at high forcing levels ($A_0 = 5\%$ and 10%) (see Figure 7(a)). Moreover, the level of the perturbations is only controlled in the vicinity of the inflow. If the co-flow is significant ($U_2 = 0.5U_1$), the frequency can be controlled in the whole domain (see Figure 7(b)) even with small forcing levels ($A_0 = 1\%$). This improvement is due to the fact that the stability increases along with the co-flow: thus the flow is not so sensitive to numerical disturbances. Nevertheless, these results prove that the feedback mechanism generates such strong perturbations that there is little hope of controlling them by forcing the inflow in the absolutely and almost absolutely unstable jets. Non-linear saturation occurs less than two diameters downstream.

2.3 Initial conditions

Another natural approach to control the transient is to reduce it by improving the initial conditions (the default initial conditions are obtained by translating the inflow profile through the computational domain). This seems to be a promising idea since we have no possibility of determining the jet entrainment velocity ($V_\infty = V(y_\infty)$) without knowing *a priori* the streamwise evolution of the axial velocity $U_1(x)$ (so far, the initial flows fields have no streamwise evolution). Thus a better estimate of the entrainment velocity than $V_\infty = 0$ could indeed be obtained from an initial flow field which would estimate the evolution of $U_1(x)$. We have examined several ways to achieve this goal.

2.3.1 Analytical or self-similar steady state solution

In the case of mixing layers, transients can be significantly reduced by computing numerically the self-similar steady state which is the solution of the Blasius boundary-layer equation. This has been done successfully for compressible unity-Prandtl number viscous flows by Sandham & Reynolds (1989) and Colonius (1992). For incompressible 2D-jets, a well-known analytic solution has been found by Schlichting (1933), but its validity is restricted to the region where the jet is fully developed. This solution can easily be generalized to compressible jets by using the Howarth (or Illingworth-Stewartson) transform of the cross stream variable:

$$Y_H = \int_0^T \frac{dy}{T}$$

in a similar manner as Sandham & Reynolds (1989) proceeded for 2D compressible mixing layers. Unfortunately, this solution can not be extended to the regions with strong shear (top-hat U-velocity profiles) because the dynamics are governed by two independent spatial scales, the jet diameter and the shear layer thickness. The resulting profile can't be self-similar unless the two spatial scales are identical (this is precisely the case of a fully developed jet which has a Gaussian U-velocity profile) or one of them is disappearing (this is the case of a no co-flowed mixing layer). For similar reasons, the analytic solution can not be extended to co-flowed jets for which U_1 and U_2 are two conflicting velocity scales unless they reduce to a single one. This happens for very small co-flows where the flow differs only slightly from the non-co-flowed case and also for $U_2 \approx U_1$ where the solution should be wake-like. This is in contradiction with Abramovich (1963), who found self-similarity in experimental results.

At any rate, there is neither an analytical nor a self-similar solution for the jet flows which meet the requirements of both the instability issue (top-hat profiles and small co-flows) and the DNS codes ($U_2 > 0$).

2.3.2 Numerical steady-state solution

Since analytical and semi-analytical tools fail to provide the desired steady-state solution, we drew our attention towards purely numerical solutions obtained from a less accurate but more robust code than the ones used so far for DNS. The feasibility of this approach for generation of initial conditions was tested by computing the steady state of strongly co-flowed jets with the Colonius code and zeroth order Giles boundary conditions. Once the steady state was reached, we switched to the more accurate first order boundary conditions. Figure 8 shows that even with a co-flow $U_2 = 0.5\ U_1$, the simple switch to first order boundary conditions generates a new transient which is as intense as the first one. By comparing this figure to Figure 2(a) of our previous report (Jacob (1991)), it turns out that this new transient is as strong as if the first order boundary conditions had been applied directly to the default initial condition.

Since the two codes differ only by their boundary conditions, the steady states reached with each of them are almost identical inside the computational domain.

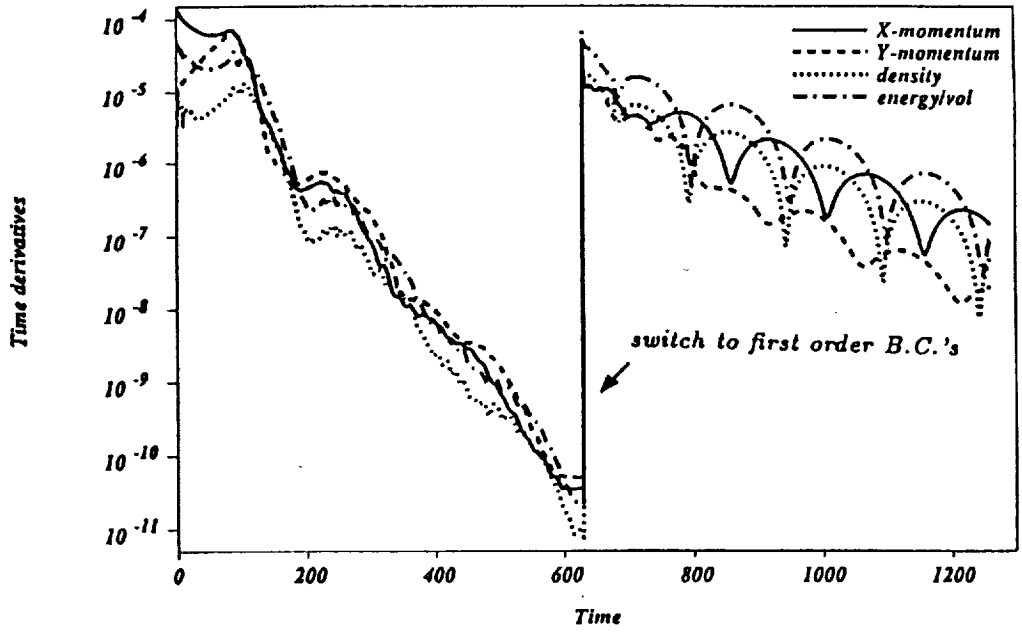

FIGURE 8. Cold jet: History of space averaged time derivatives with switch from zeroth order to first order BC's.

This means that the initial condition is unimportant inside the domain (with respect to the transient) and that the only really important feature is the initial field at the boundaries. This conclusion is consistent with the evolution plots of the field variables (*e.g.* see Figure 3 or 7) because these figures show that the transient originates from the inflow boundary. The switch of boundary conditions has been tested for various co-flows and temperature ratios and always leads to the same conclusions.

2.4 Towards DNS of a two dimensional jet

From the last section, it can be seen that a necessary condition to reduce the transient is to find a better formulation for the inflow boundary condition.

2.4.1 Improved one dimensional inflow boundary conditions

We started with the initial inflow boundary condition from the Poinsot-Lele code. It consists of enforcing the profiles of $U(y)$, $V(y)$ and $T(y)$ only in order to determine the transverse gradients and computing the density from the mass conservation equation *via* the interior variables. The remaining terms (normal gradients) are obtained by the one dimensional boundary conditions on the characteristic variables. They are equivalent to setting:

$$\partial \tilde{U}/\partial t = 0$$

$$\partial \tilde{V}/\partial t = 0$$

$$\partial \tilde{T}/\partial t = 0$$

where : $\widetilde{U}$, $\widetilde{V}$, and $\widetilde{T}$ are one-dimensional variables which are locally tangent to the inflow field. With this formulation, the fields at the boundary differ from the Navier-Stokes solution to which the interior fields tend. Thus strong gradients are generated at the inflow.

In order to smooth the transient, we sought a softer formulation in the spirit of that developed for the outflow in earlier studies (Poinsot & Lele (1992)). Instead of imposing the field variables and setting the time derivatives of their one-dimensional approximation to zero, these quantities are determined by a system of first order differential equations:

$$\partial\widetilde{U}/\partial t = \alpha(\widetilde{U} - U_\infty)$$

$$\partial\widetilde{V}/\partial t = \alpha(\widetilde{V} - V_\infty)$$

$$\partial\widetilde{T}/\partial t = \alpha(\widetilde{T} - T_\infty)$$

This is equivalent to enforcing the profiles of U,V,T upstream of the inflow at a typical distance $L(y) \sim U(y)/\alpha$ and letting them evolve exponentially to the interior fields. Thus the fields at the inflow boundary are less constrained and allow for more continuity in the inflow. A typical magnitude of α is $1/\alpha \sim 10$ time steps. The implementation of these boundary conditions gave promising results (particularly for strongly co-flowed cases, the noise was reduced in the converged state) but would not remove the switch-on transient.

2.4.2 Variable co-flow

Since with these improved boundary conditions the code gives very "clean" solutions for strong co-flows but does not converge to a steady state if the co-flow is small (giving the same type of results as those shown in Figure 1), it seems straightforward to start from a steady strongly co-flowed jet and to gradually reduce the co-flow down to a small value. Thus, the transient leaves the domain when the co-flow is still strong, and the small co-flow is reached with a quiet flow. Such a strategy is possible with our new boundary conditions since they allow for a time-fluctuating inlet profile. First tests indicate that steady states are likely to be reached if the time variation of the co-flow $U_2(t)$ is slow enough (ten to fifteen flow-trough times are necessary) to reduce the co-flow by a factor 2 and if $U_2(t)$ is smooth enough. Even though slight fluctuations remain in the flow, they now appear as perturbations of the mean flow whereas they dominated the flow in earlier simulations. Although they show the flow at different times Figure 9 and Figure 1 may be compared because the magnitude of the perturbations shown on Figure 1 does not change significantly over time as discussed in section 1.2. These tests have to be continued with smaller co-flows in order to determine whether this approach is suitable for the study of jets near the absolute instability limit.

2.4.3 Sponge outflow

In addition to the previously described efforts, we also tried a new version of the Colonius code: the outflow has been considerably improved by inserting between the physical domain and the outflow an exit zone or "sponge" in which disturbances

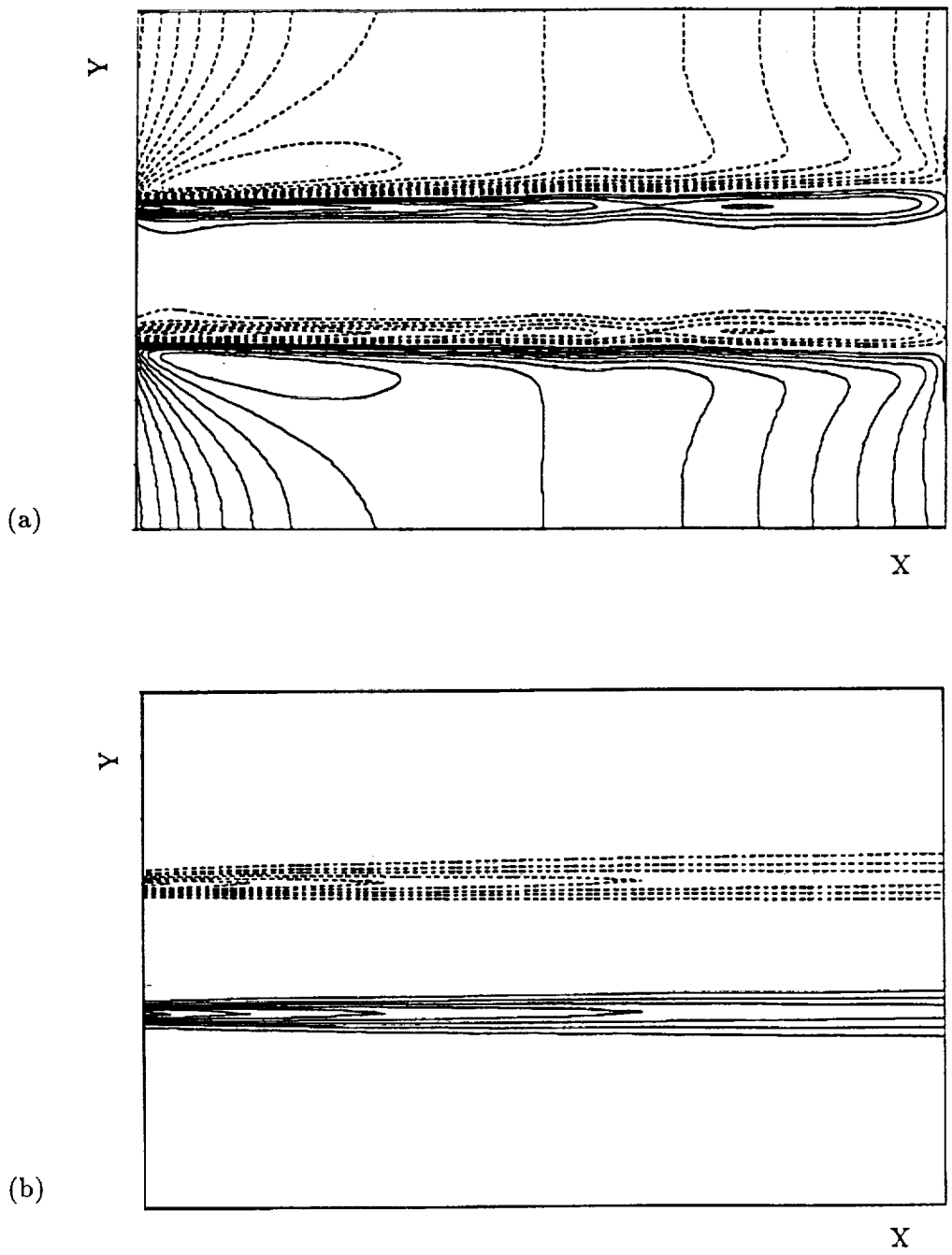

FIGURE 9. Laminar state with reduced co-flow : $U_2 = 0.25U_1$. Contour plots at time= 3000. (a): V-velocity : 10 contour levels : min= −0.00153 , max= 0.00153; (b) : vorticity : 10 contour levels : min= −0.242 , max= 0.0242. Dashed lines are used for negative values in both plots.

are attenuated by grid stretching and filtering (Colonius *et al* (1992)) (as we pointed out in our last year's report the initial two-dimensional first-order Giles boundary conditions were not suited for DNS of slightly co-flowed jets). We tested the case of a cold jet with a co-flow: $U_2 = 0.05U_1$. Even though we extended the domain laterally to a total width of fourteen diameters, the code still blows up as the transient leaves the physical domain since the V-velocity changes its sign on the lateral boundaries when the transient grows. This change from inflow to outflow is not tolerated by the lateral boundary conditions although the amplitude of the disturbance at the lateral boundaries remains small ($< 1\%$ of U_1). In this computation, we started directly with the small co-flow and the default initial conditions for which no entrainment velocity is computed at the lateral boundaries. These remarks already suggest some possible improvements of this simulation.

3. Conclusions

At the present state of this work, there seem to be several ways to obtain a steady state with small co-flows. The first one is to further reduce the co-flow in the Poinsot-Lele code with improved boundary conditions. This might eventually lead to the desired steady state and allow us to examine the issue of absolute instability. However, accurate acoustic fields will not be obtained with that formulation of the boundary conditions. The second choice is to combine some advantages of the two codes: for instance, one could apply the method of co-flow variation to the Colonius code in order to reduce the transient and its effects on the lateral boundaries. One could also reset the reference field for the linearization of the boundary equations once the strongly-coflowed jet has reached its steady state; thus the reference normal V-velocity at the lateral boundaries would be non zero and make these boundary conditions more stable (an increase of the domain width seems not to be a promising approach since this lateral dimension was already considerabely increased in the simulation described in section 2.4.3). The combination of these techniques in the Colonius code seems to be the most promising approach for both an aerodynamical and an aeroacoustical investigation of heated jets (this code already provides good hydrodynamical and aeroacoustical results for spatial mixing layers).

Acknowledgement

I wish to thank Profs. S. K. Lele and P. Moin for their comments and suggestions throughout this work. I am also indebted to Dr. A. Trouvé for the time he spent on this study providing interesting ideas and the LIISA codes which helped me in the ongoing research. Finally I would like to thank Mr. T. Colonius for helping me to test his new code on the jet flow.

REFERENCES

ABRAMOVICH, G. N. 1963 The theory of turbulent jets. *MIT Press Cambridge Massachusetts.*

BERS, A. 1983 Space-time evolution of plasma instabilities - absolute and convective. *In Handbook of Plasma Physics, ed. M. N. Rosenbluth, R. Z. Sagdeev, Amsterdam: North Holland.* **1,** 451-517.

COLONIUS, T., LELE, S. K. & MOIN, P. 1991 Scattering of sound waves by a compressible vortex. *AIAA Paper 91-0494.*

COLONIUS, T., LELE, S. K. & MOIN, P. 1992 Boundary conditions for direct computation of aerodynamic sound. Presented at *DGLR/AIAA 14th aeroacoustic conference, may 11-14, 1992, Aachen, Germany*; also to appear in *AIAA Journal 1993.*

GILES, M. B. 1990 Non reflecting boundary conditions for Euler equation calculations. *AIAA J.* **12,** 2050-2058.

JACOB, M. C. 1991 Direct numerical simulation of instability and noise generation of hot jets *Ann. Res. Briefs,* Center for Turbulence Research, Stanford Univ/NASA Ames.

HUERRE, P., & MONKEWITZ, P. A. 1990 Local and global instabilities in spatially developing flows. *Ann. Rev. Fluid Mech.* **22,** 473-537.

LELE, S. K. 1992 Compact finite difference schemes with spectral-like resolution. *J. Comp. Phys.* **103,** 16-42.

MONKEWITZ, P. A. & SOHN, K. D. 1986 Absolute instability in hot jets and their control . *AIAA Paper 86-1882.*

POINSOT, T. J. & LELE, S. K. 1992 Boundary conditions for direct simulations of compressible viscous reacting flows. *J. Comp. Phys.* **101,** 104.

SANDHAM N. D. & REYNOLDS, W. C. 1989 A numerical investigation of the compressible mixing layer. *Report TF-45,* Thermosciences Division, Department of Mechanical Engineering, Stanford University.

SCHLICHTING,H. 1933 Laminar spread of a jet. *Z. Angew. Math. Mech.* **13,** 260-263.

THOMPSON, K. W. 1989 Time dependant boundary conditions for hyperbolic systems. *J. Comp. Phys.* **68,** 1-24.

TROUVÉ, A. 1988 Instabilités hydrodynamiques et instabilités de combustion de flammes turbulentes, *Thèse de Docteur-ingénieur, Ecole Centrale de Paris.*

YU, M. H. & MONKEWITZ, P. A. 1989 Local and global resonances in heated 2-D jets. *Report for AFOSR grant No. 87-0329.*

Direct numerical simulation of turbulent flow over a backward-facing step

By H. Le AND P. Moin

1. Objectives

The objectives of this study are: (a) to conduct a direct numerical simulation of turbulent backward facing step flow using inflow and outflow conditions and (b) to provide data in the form of Reynolds stress budgets for Reynolds averaged modeling. The report presents the basic statistical data and comparisons with the concurrent experiments of Jovic and Driver (1991, 1992) and budgets of turbulent kinetic energy.

2. Accomplishments

2.1 Method

The Navier-Stokes equations are discretized using a finite difference method on a staggered mesh. Uniform mesh spacing is applied in the streamwise (x) and spanwise (z) directions. In the vertical (y) direction, non-uniform mesh is employed with mesh refinement at the wall and near the step. The fractional step method from Le and Moin (1990) is used for time advancement. The Navier-Stokes equations are first advanced using a second-order semi-implicit method without the pressure terms. The pressure is calculated by solving the Poisson equation, and the velocities are then corrected to satisfy the continuity equation.

The mean velocity profile obtained from a boundary layer simulation by Spalart (1986) is imposed at the inlet at $Re_\theta = 667$. Random velocity fluctuations u', v', and w' are superimposed on this profile according to a variant of the method of Lee *et al.* (1992). The fluctuations are prescribed such that, at the inlet, the turbulence intensities and Reynolds shear stress of Spalart's data are also duplicated. A convective boundary condition (Pauley *et al.*, 1988) is imposed at the exit.

The streamwise domain consists of an entry section of length $10h$ prior to the step and a $20h$ post-expansion section, where h is the step height. The vertical dimensions before and after the expansion are $W_1 = 5h$ and $W_2 = 6h$ which give an expansion ratio ER of 1.20. The spanwise dimension is $4h$ where periodic boundary conditions are imposed. The simulation uses $770 \times 194 \times 66$ grid points in the streamwise, wall normal, and spanwise directions, respectively. The Reynolds number, based on h and the mean inlet free stream velocity U_0, is $Re_h = 5100$. The computation uses 13 megawords of memory and requires approximately 55 CPU seconds per time step on a single processor CRAY Y-MP at a rate of 186 mflops. Statistical quantities are averaged over the spanwise direction and time. About 1100 CPU hours were required to obtain an adequate statistical sample. The total computational time corresponds to approximately 4.5 flow-through times.

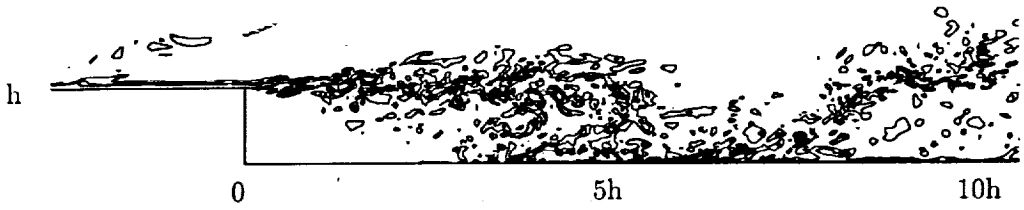

FIGURE 1. Instantaneous spanwise vorticity contours, ω_z; min = -7, max = 4.95, increment = 1.3.

2.2 Results

Figure 1 shows contour plots of the instantaneous spanwise vorticity ω_z on a typical vertical plane. The vorticity is normalized by U_0/h. A free-shear layer spreading from the step and interacting with the lower wall near the mean reattachment location, $x_R = 6h$, is discernible.

The basic statistical quantities are compared to results from concurrent experiments by Jovic and Driver. In 1991, they conducted a backward facing step experiment at $Re_h = 6800$ and $ER = 1.09$, herein referred as "JD1". However, the results indicated that these parameters are not sufficiently close to those used in simulations. Thus, Jovic and Driver in 1992 conducted a second experiment with $Re_h = 4950$ and $ER = 1.20$ ("JD2"). In the following sections, JD2 results will be used for comparison with numerical simulations.

2.2.1 Reattachment length

The instantaneous velocity fields indicate that the reattachment location oscillates in the streamwise direction and time and also varies in the spanwise direction. Several methods were used to determine the mean reattachment location, x_R: (a) by the location at which the mean velocity $U = 0$ at the first grid point away from the wall, (b) by the location of zero wall-shear stress ($\tau_w = 0$), and (c) by the location of the mean dividing streamline ($\psi = 0$). A *pdf* method was also used in which the mean reattachment point is indicated by the location of 50% forward flow fraction. The pdf method was also used experimentally by Westphal *et al.* (1984) and Adams *et al.* (1984). The results of the first three methods are within 0.1% of each other and about 4% from the pdf result. The calculated mean reattachment length is $6.0h$ compared to $6.1h$ measured in JD2 experiment.

2.2.2 Pressure distribution

The streamwise pressure coefficient at the step-wall is compared with the JD2 results in Fig. 2. The pressure coefficient is normalized by the mean inlet free-stream velocity. The two symbols in Fig. 2 are for the two walls of the double-sided expansion in the JD2 experiment. The comparison shows an excellent agreement between computation and experiment.

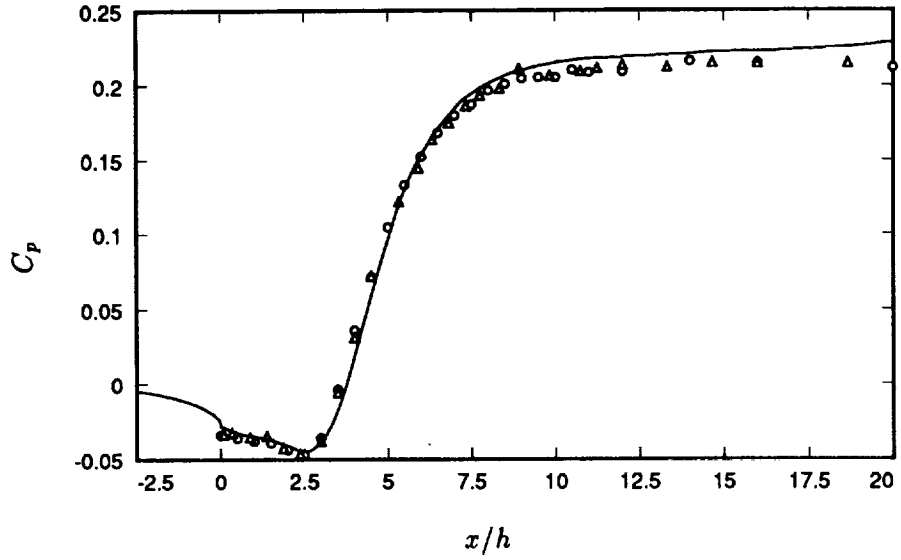

FIGURE 2. Step-Wall pressure coefficient as a function of x. ——— , computation; o , Jovic & Driver (1992), bottom wall; △ , Jovic & Driver (1992), top wall.

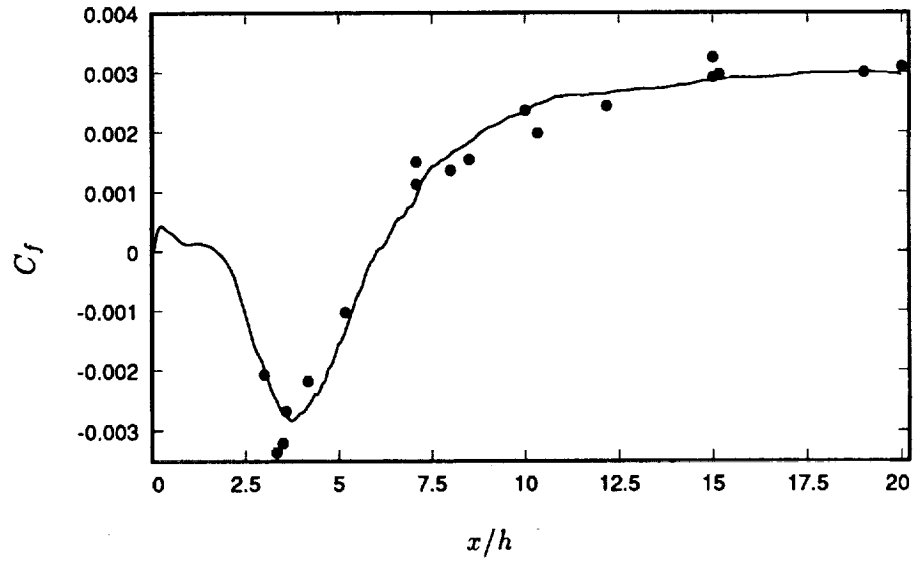

FIGURE 3. Step-wall coefficient of friction. ——— , computation; • , Jovic & Driver (1992).

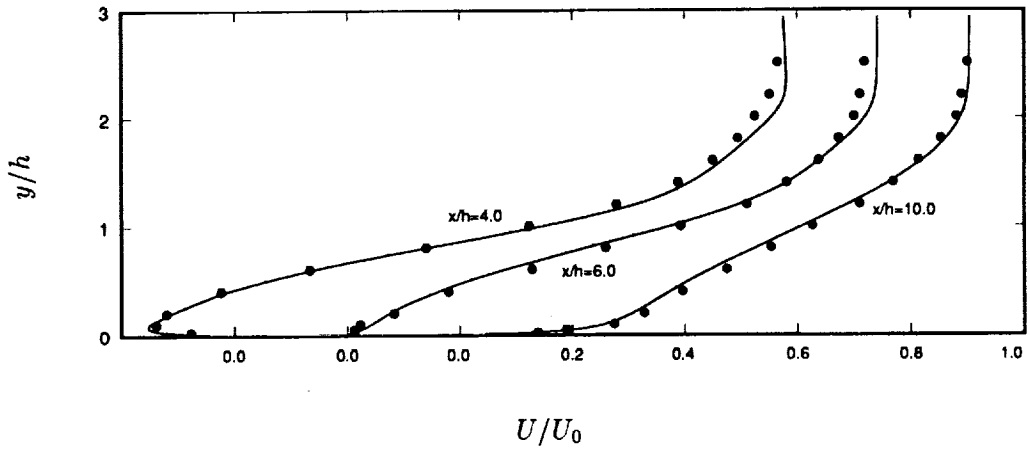

FIGURE 4. Mean velocity profiles. ——— , computation; • , Jovic & Driver (1992).

2.2.3 Skin friction coefficient

The skin friction coefficient C_f is computed from the mean velocity profile and shown in Fig. 3. Also plotted are the C_f data from the JD2 experiment. The large peak negative skin friction in the recirculation region ($\approx -3 \times 10^{-3}$), seen in both computation and experiment, is nearly 3 times larger than previous experimental findings, e.g. Adams *et al.* (1984). Jovic and Driver (1991) also measured the skin friction in the reverse flow region for a wide range of Reynolds numbers. Their results show that the recirculation C_f decreases with increasing Reynolds number. The peak negative C_f reaches a value of approximately -1.0×10^{-3} as $Re_h \approx 40000$ which is the Reynolds number range used in many experiments. Thus the large skin friction in the current study is due to low Reynolds number effects.

2.2.4 Mean velocity profiles

Figure 4 shows the mean velocity profiles compared with JD2 experimental results at three x-locations: $x/h = 4$ (recirculation region), $x/h = 6$ (reattachment location), and $x/h = 10$. Again, excellent agreement is obtained between computation and JD2 experiment.

The near-wall mean velocity profile in the recovery region at $x/h = 19$ is compared to experimental data in Fig. 5. The shear velocity u_τ of the JD2 experiment is calculated from the skin friction coefficient of Fig. 3. Above $y^+ = 10$, both profiles show a noticeable shift below the log-law, indicating that the turbulent boundary layer has not fully recovered. Previous studies, however, reported a recovery of the log-law profile even as early as $x - x_R = 6h$, e.g. Westphal *et al.* (1984). The apparent discrepancy is attributed to the method of obtaining the wall-shear velocity u_τ. In these experiments, the wall-shear velocity was calculated using the Clauser chart with the inherent assumption that the log-law of the zero-pressure gradient turbulent boundary layer is applicable. The result was lower values of u_τ.

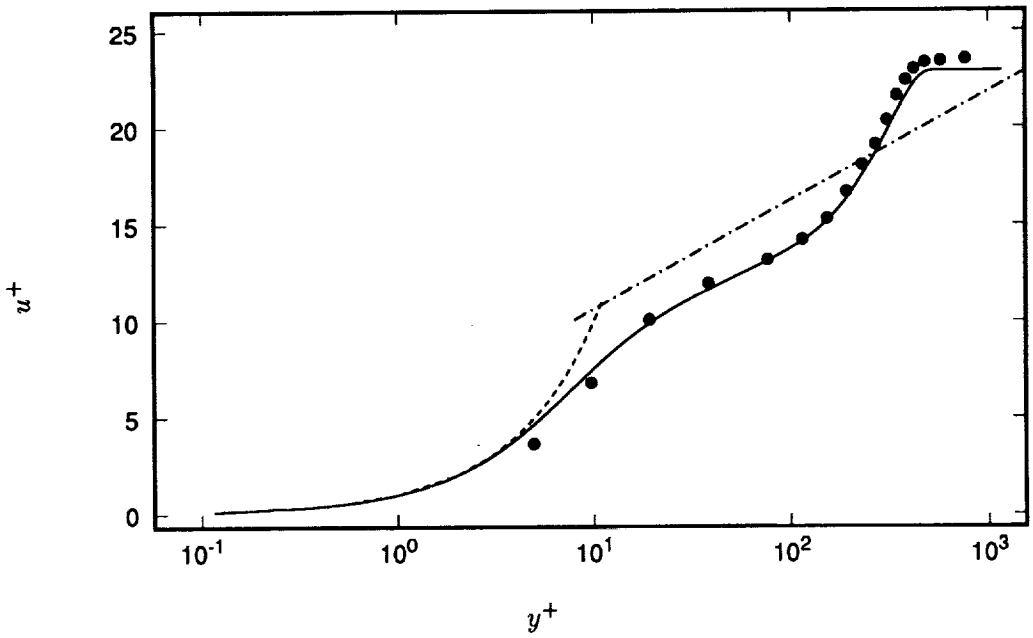

FIGURE 5. Mean velocity profile at $x/h = 19$. ---- , $u^+ = y^+$; —·— , $u^+ = (1/.41)\log(y^+) + 5.0$; ——— , computation; • , Jovic & Driver (1992).

Direct C_f measurements using a pulsed wall probe by Westphal *et al.* confirm that the correct shear velocity in this flow region is indeed higher than that predicted by the Clauser chart. In the present configuration, this discrepancy is as high as 17%, i.e., $u_\tau/u_{\tau_c} \approx 1.17$, where the subscript c denotes the value obtained using the Clauser chart. The deviation of the velocity profile from the log-law may be due to the effect of the strong streamwise adverse pressure gradient which is experienced by the flow following the sudden expansion (Nagano *et al.*, 1991). It may also be due to non-equilibrium effects which are persistent after reattachment.

2.2.5 Turbulence intensities and Reynolds stress

The turbulence intensity and Reynolds shear stress profiles, normalized by the inlet free-stream velocity U_0, are shown in Figs. 6–8. They are compared with those from JD2 experiment data at streamwise locations, $x/h = 4$, 6, 10. The overall agreement is good.

2.2.6 Turbulent kinetic energy budget

The terms of the turbulent kinetic energy transport equation are evaluated from the equation

$$\frac{\partial q^2}{\partial t} = \underbrace{-U_k\overline{(u_l'u_l')}_{,k}}_{C_k} \underbrace{-2\overline{u_l'u_k'}U_{l,k}}_{P_k} \underbrace{-\overline{(u_l'u_l'u_k')}_{,k}}_{T_k} \underbrace{+\frac{1}{Re}\overline{(u_l'u_l')}_{,kk}}_{D_k} \underbrace{-\frac{2}{Re}\overline{u_{l,k}'u_{l,k}'}}_{\epsilon_k} \underbrace{-2\overline{u_l'p_{,l}'}}_{\Pi_k}.$$

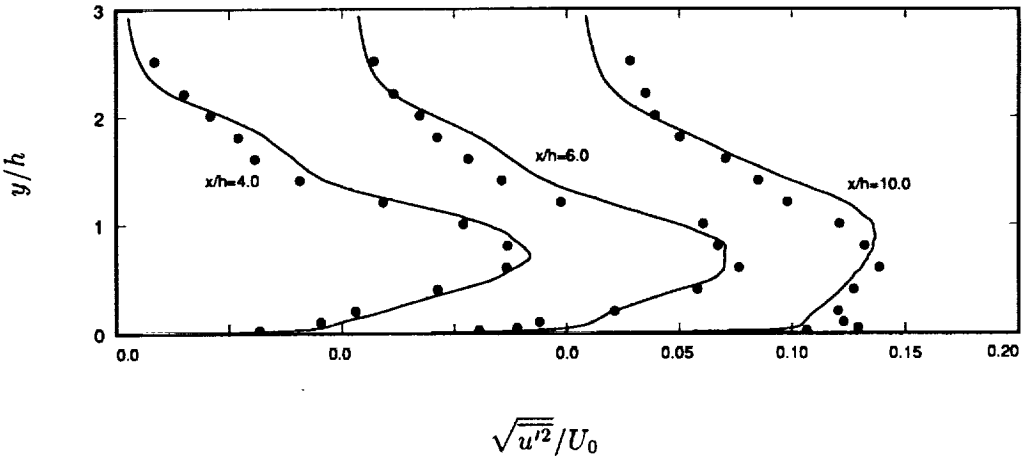

FIGURE 6. Turbulence intensity $\sqrt{\overline{u'^2}}$, normalized to inlet mean velocity U_0. ——— , computation; • , Jovic & Driver (1992).

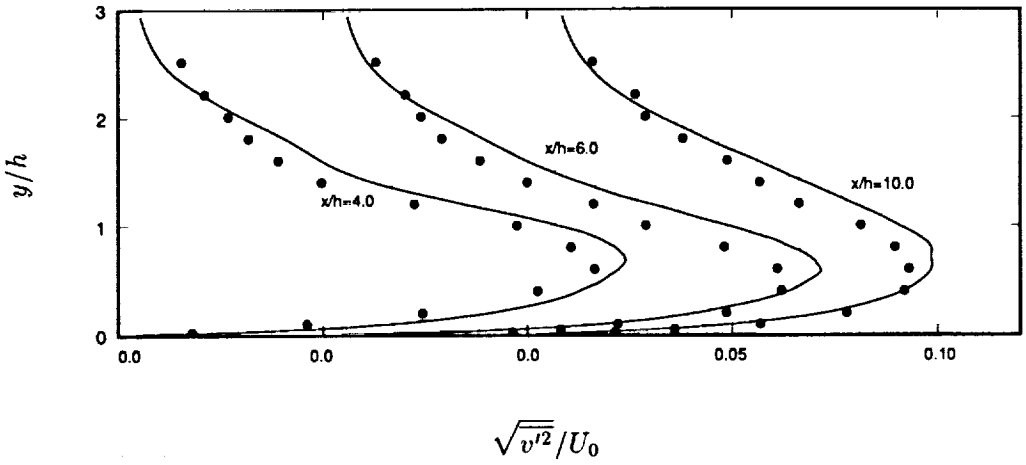

FIGURE 7. Turbulence intensity $\sqrt{\overline{v'^2}}$, normalized to inlet mean velocity U_0. ——— , computation; • , Jovic & Driver (1992).

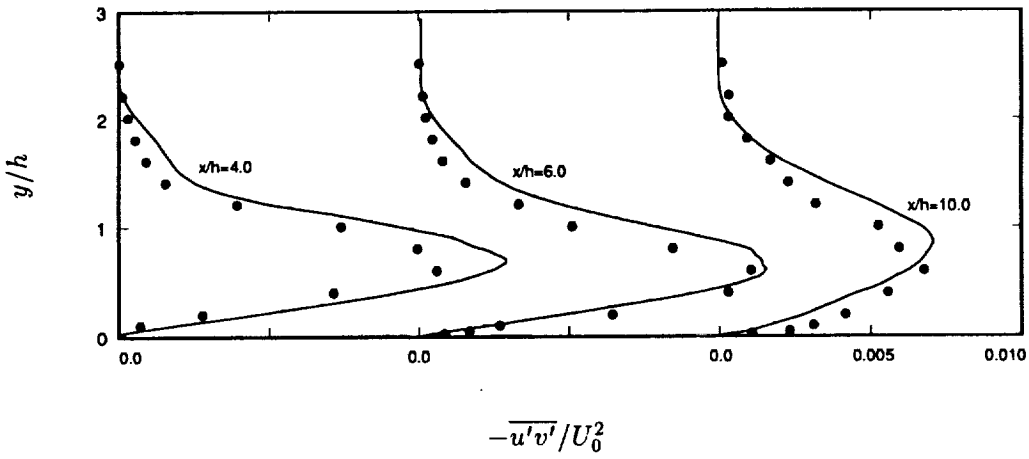

FIGURE 8. Reynolds shear stress $-\overline{u'v'}$, normalized to inlet mean velocity U_0^2. ——— , computation; • , Jovic & Driver (1992).

The terms on the right hand side are identified as follows:
C_k = Convection,
P_k = Production,
T_k = Turbulence Diffusion,
D_k = Viscous Diffusion,
ϵ_k = Viscous Dissipation,
Π_k = Velocity Pressure-Gradient.

The budget for the turbulent kinetic energy, $\frac{q^2}{2} = \frac{1}{2}(\overline{u_i' u_i'})$, is shown in Figs. 9 and 10.

At two step heights before the separation, the energy budget (Figs. 9(a) and 10(a)) is similar to that of a turbulent boundary layer (Spalart, 1988) although there is an enhancement of the viscous terms near the wall. The budget for the recirculation region is shown in Fig. 9(b). This energy budget is very similar to that of a plane mixing layer (Bradshaw and Ferriss, 1965). This budget also agrees qualitatively with the measurement by Chandrsuda and Bradshaw (1981) for a backward facing step flow. Both production P_k and viscous dissipation ϵ_k have maximum values at the same point in the free-shear layer. The peak ϵ_k is approximately 60% of the production peak. The other 40% is balanced by the turbulence transport T_k. Far from the wall, P_k is the only major gain term. T_k is a consuming term for $0.3 < y/h < 1$, but a gain term outside of this range. Above the step ($y/h > 1$), T_k is in balance with C_k, the turbulence convection by the mean flow. As one approaches the wall, the production becomes a consuming term because of the negative gradient of the mean reverse flow (Fig. 10(b)) although its magnitude is relatively small. Very close to the wall, the two viscous terms, D_k and

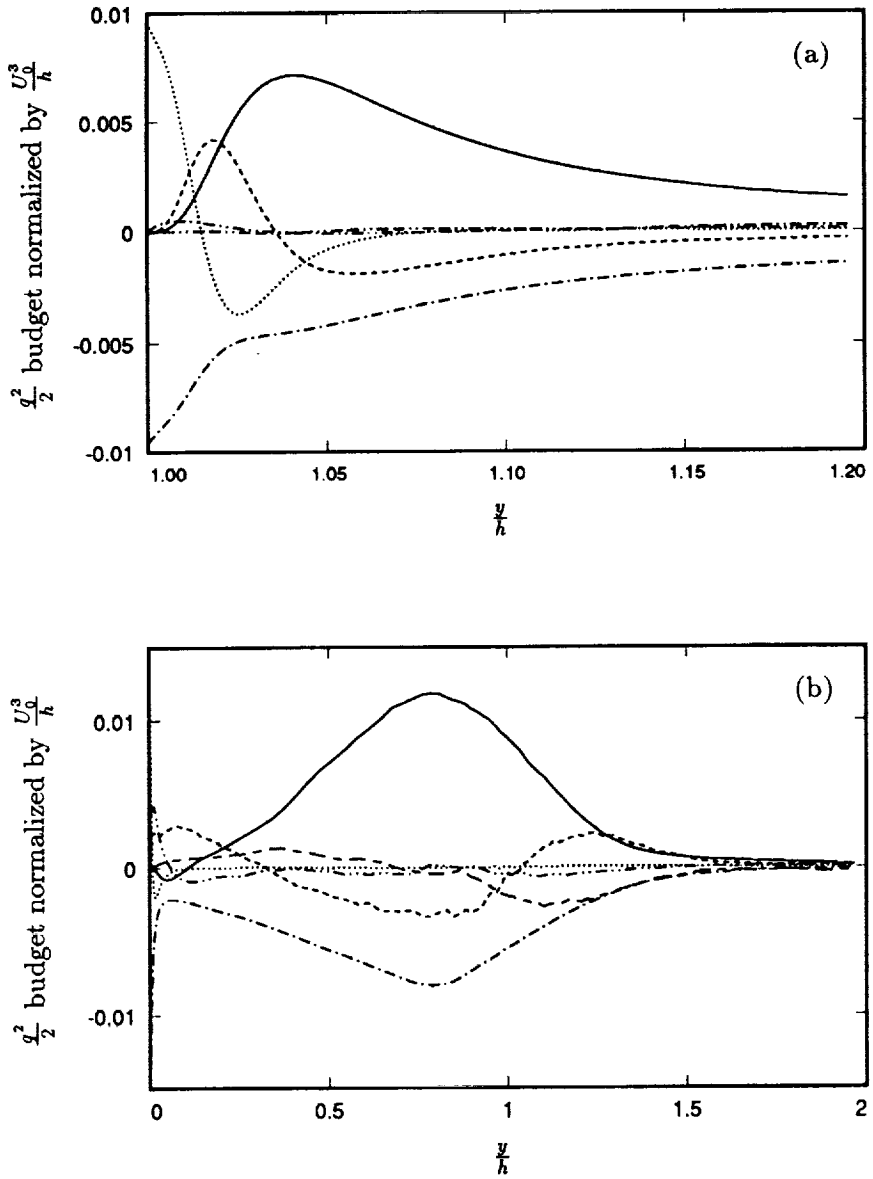

FIGURE 9. Budget terms for turbulent kinetic energy, $\frac{q^2}{2} = \frac{1}{2}(\overline{u_i' u_i'})$, away from the wall, normalized by U_0^3/h. (a) $x/h = -2.0$; (b) $x/h = 4$. ——— , production; - - - - , turbulence transport; ····· , viscous diffusion; —·— , viscous dissipation; —··— , velocity pressure-gradient; —— — , convection.

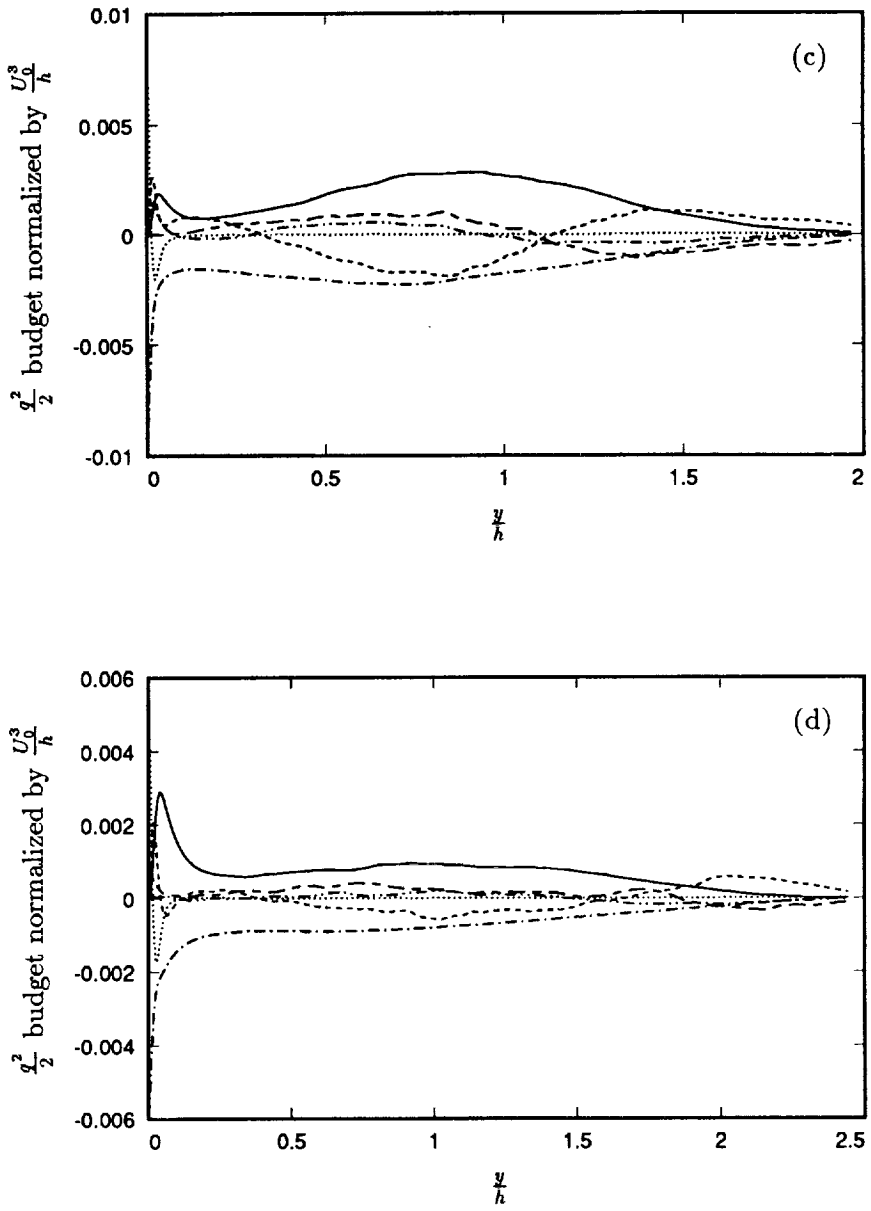

FIGURE 9. (cont.) Turbulent kinetic energy budget away from the wall, normalized by U_0^3/h. (c) $x/h = 10$; (d) $x/h = 18$. For caption see previous page.

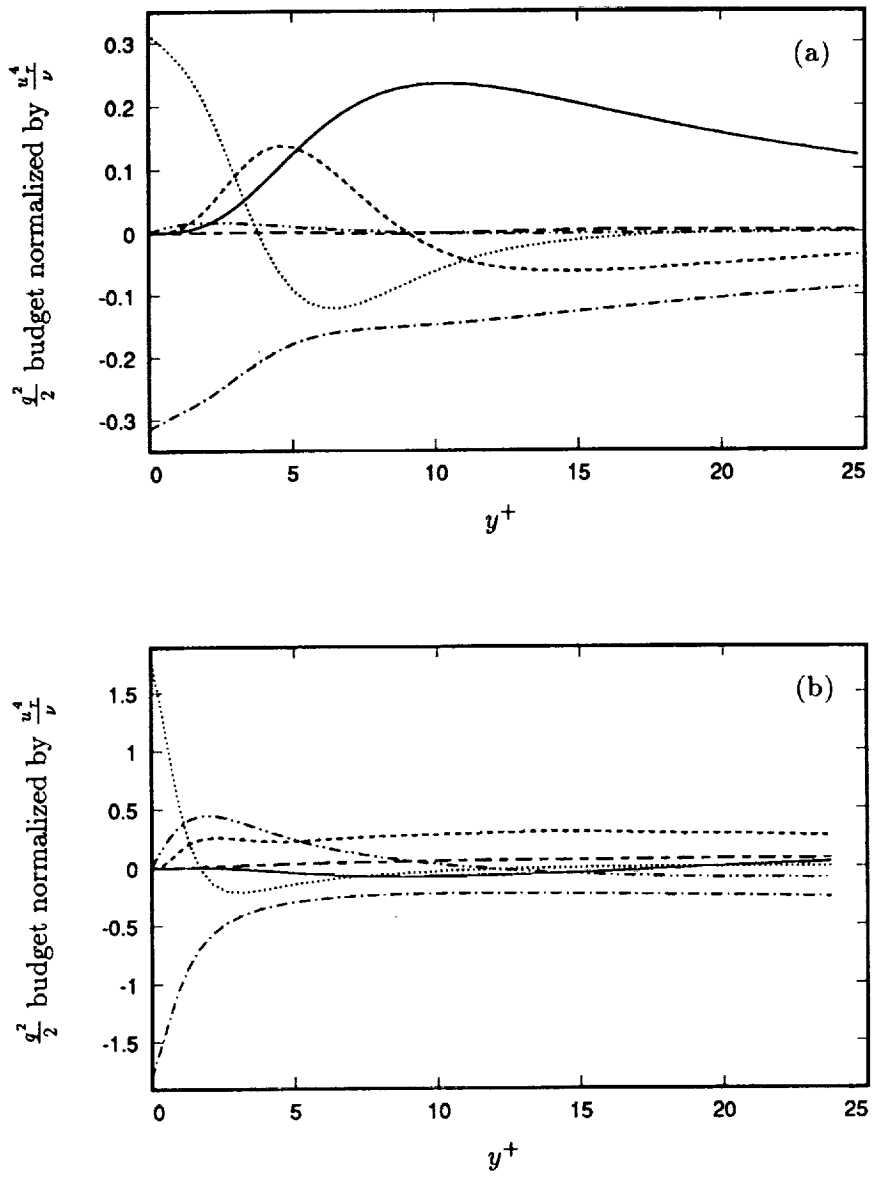

FIGURE 10. Budget terms for turbulent kinetic energy, $\frac{q^2}{2} = \frac{1}{2}(\overline{u_i' u_i'})$, normalized by local u_τ^4/ν. (a) $x/h = -2.0$; (b) $x/h = 4$. ——— , production; - - - - , turbulence transport; ····· , viscous diffusion; —·— , viscous dissipation; —··— , velocity pressure-gradient; — - — , convection.

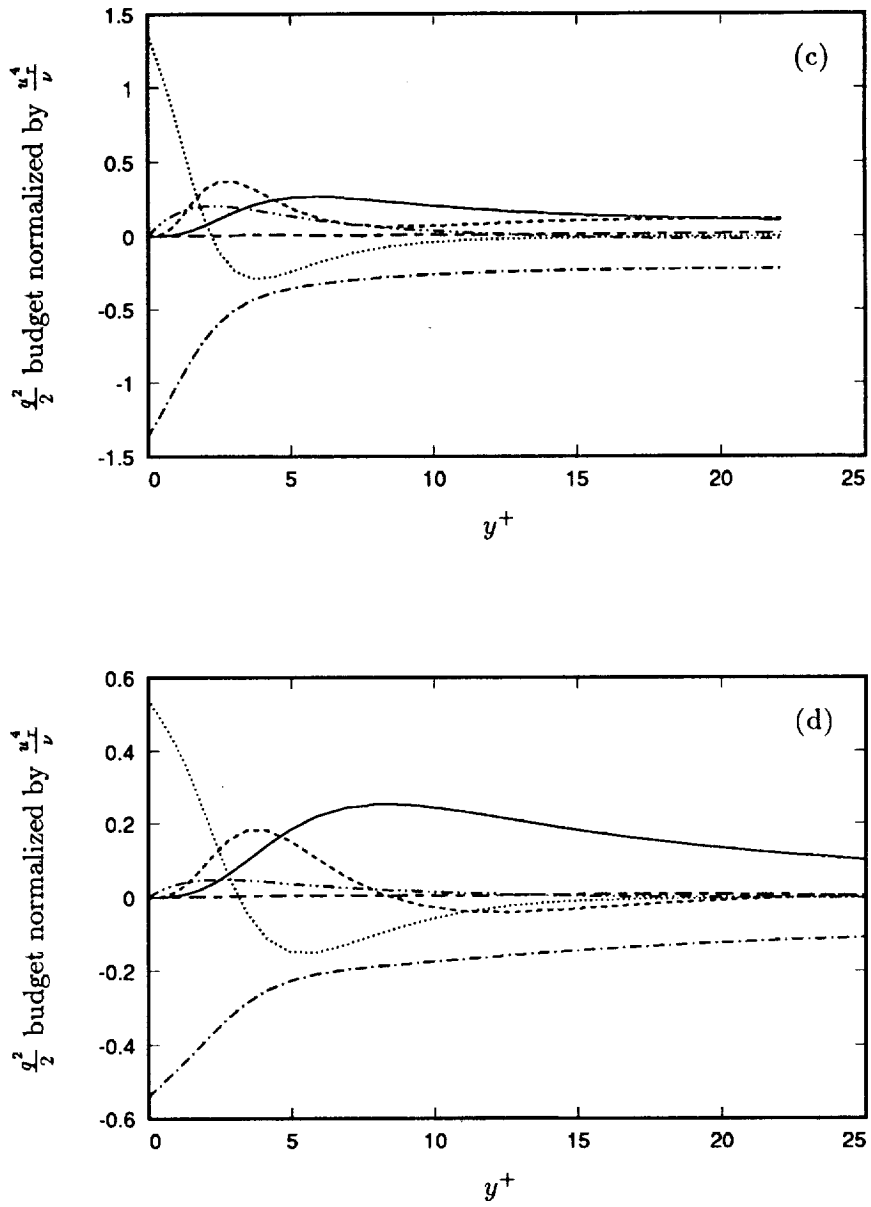

FIGURE 10. (cont.) Budget terms for turbulent kinetic energy near wall, normalized by u_τ^4/ν. (c) $x/h = 10$; (d) $x/h = 18$. For caption see previous page.

ϵ_k, grow rapidly due the high intensities in all three directions (their value at the wall is about 40% higher than the peak production in the shear layer). The velocity pressure-gradient term becomes significant only at $y^+ < 8$ where it balances the viscous terms plus T_k. The profiles have similar shapes through the reattachment point.

All terms decay with x; however, the energy in the shear layer decays much faster than at the wall (the streamwise decay of the budget terms are not apparent in Fig. 10 because they are normalized with the local u_τ). By $x/h = 10$, the value of D_k at the wall is about 3 times the peak production value. Near the flow exit, $y/h = 18$, the turbulent kinetic energy budget resembles that of a boundary layer. However, the effects of the free-shear layer is still apparent, e.g., T_k is still large at $y/h = 1$ and the peak ϵ_k is only $\approx 85\%$ of the peak P_k.

3. Conclusions

A direct numerical simulation of turbulent flow over a backward facing step at $Re_h = 5100$ was successfully completed. There is good agreement in turbulence statistics deduced from simulations and concurrent experiments of Jovic and Driver. Of interest are two observations not previously reported for the backward-facing step flow: (a) at the relatively low Reynolds number considered, large negative skin friction is seen in the recirculation region; the peak $|C_f|$ is about three times the value reported at high Reynolds numbers; (b) the velocity profiles in the recovery region fall below the universal log-law.

A large data base from this recently completed simulation has been archived. It contains up to third-order statistics at all locations in the recirculation, reattachment, and recovery zones and the budgets of all components of the Reynolds stress tensor.

Acknowledgements

This research was funded by the National Science Foundation (NSF) and the Center for Turbulence Research (CTR). We are grateful to Dr. J. Kim for very insightful discussions throughout the course of this study. The authors are also specially grateful to Drs. D. Driver and S. Jovic for their collaboration and performing the concurrent experiments.

REFERENCES

ADAMS, E. W., JOHNSTON, J. P. & EATON, J. K. 1984 Experiments on the structure of turbulent reattaching flow, Report MD-43, Department of Mechanical Engineering, Stanford University.

BRADSHAW, P. & FERRISS, D. H. 1965 The spectral energy balance in a turbulent mixing layer, AERO Report 1144, National Physical Laboratory, England, 6.

CHANDRSUDA, C. & BRADSHAW, P. 1981 Turbulence structure of a reattaching mixing layer. *J. Fluids Mech.* **110**, 171–194.

JOVIC, S. & DRIVER, D. 1991, 1992 private communication.

LE, H. & MOIN, P. 1991 An improvement of fractional step methods for the incompressible Navier-Stokes equations. *J. Comp. Physics.* **92,** 369–379.

LEE, S., LELE, S. K. & MOIN, P. 1992 Simulation of spatially evolving turbulence and the applicability of Taylor's hypothesis in compressible flow. *Phys. of Fluids A.* **4,** 1521–1530.

NAGANO, Y., TAGAWA, M. & TSUJI, T. 1991 Effects of adverse pressure gradients on mean flows and turbulence statistics in a boundary layer, Proceedings of the Eighth Symposium on Turbulent Shear Flows, Technical Univ. of Munich, 2-3-1–2-3-6.

PAULEY, L. L., MOIN, P. & REYNOLDS, W. C. 1988 A numerical study of unsteady laminar boundary layer separation, Report TF-34, Department of Mechanical Engineering, Stanford University.

SPALART, P. R. 1988 Direct simulation of a turbulent boundary layer up to $R_\theta = 1410$. *J. Fluids Mech.* **187,** 61–98.

WESTPHAL, R. V., JOHNSTON, J. P. & EATON, J. K. 1984 Experimental study of flow reattachment in a single-sided sudden expansion, Report MD-41, Department of Mechanical Engineering, Stanford University.

Numerical simulation using vorticity-vector potential formulation

By H. Tokunaga

1. Motivation and objectives

An accurate and efficient computational method is needed for three-dimensional incompressible viscous flows in engineering applications. On solving the turbulent shear flows directly or using the subgrid scale model, it is indispensable to resolve the small scale fluid motions as well as the large scale motions. From this point of view, the pseudo-spectral method is used so far as the computational method. However, the finite difference or the finite element methods are widely applied for computing the flow with practical importance since these methods are easily applied to the flows with complex geometric configurations. However, there exist several problems on applying the finite difference method to direct and large eddy simulations.

Accuracy is one of most important problems. This point has been already addressed by the present author on the direct simulations on the instability of the plane Poiseuille flow and also on the transition to turbulence (Tokunaga, Ichinose & Satofuka, 1991a, b). In order to obtain high efficiency, the multi-grid Poisson solver is combined with the higher order accurate finite difference method (Tokunaga, Satofuka & Miyagawa, 1986).

The formulation method is also one of the most important problems in applying the finite difference method to the incompressible turbulent flows. The three-dimensional Navier-Stokes equations have been solved so far in the primitive variables formulation. One of the major difficulties of this method is the rigorous satisfaction of the equation of continuity. In general, the staggered grid is used for the satisfaction of the solenoidal condition for the velocity field at the wall boundary. However, the velocity field satisfies the equation of continuity automatically in the vorticity-vector potential formulation. From this point of view, the vorticity-vector potential method was extended to the generalized coordinate system (Tokunaga, Yoyeda & Satofuka, 1991). In the present article, we adopt the vorticity-vector potential formulation, the generalized coordinate system, and the 4th-order accurate difference method as the computational method. At first, we present the computational method and apply the present method to computations of flows in a square cavity at large Reynolds number in order to investigate its effectiveness.

As is well known, the major drawback of the vorticity vector potential formulation is in the difficulty of specifying the boundary condition in the multiply connected domain. In applying the vorticity vector potential formulation to the flow with the complex geometric configuration, for example the flow along the multi-airfoil, we have to clear this hurdle. As the next step, therefore, we extend the present computational method to calculate the flow in a multiply connected domain. Lastly, the formulation of LES is dealt with in the framework of the present computational method.

2. Accomplishments

2.1 Vorticity vector potential formulation

Three-dimensional motions of fluid are governed by the Navier-Stokes equations and the equation of continuity

$$\frac{\partial u_i}{\partial t} + (\mathbf{u} \bullet \nabla) u_i = -\nabla p + \frac{1}{Re} \triangle u_i, (i = x, y, z) \tag{1}$$

$$\nabla \bullet \mathbf{u} = 0. \tag{2}$$

where $\mathbf{u} = (u_x, u_y, u_z)$ denotes the velocity, p the pressure, Re the Reynolds number, ∇ the gradient operator, and $\triangle$ the Laplacian operator. Now we introduce the vorticity ω, the vector potential ψ, and the scalar potential ϕ as

$$\mathbf{u} = \nabla \times \psi + \nabla \phi \tag{3}$$

$$\omega = \nabla \times \mathbf{u} \tag{4}$$

Then, the Laplace equation for the scalar potential, the vorticity transport equations, and the Poisson equations for the vector potential are derived:

$$\triangle \phi = 0 \tag{5}$$

$$\frac{\partial \omega_i}{\partial t} + \frac{\partial}{\partial x_j}(u_j \omega_i) = \omega_j \frac{\partial u_i}{\partial x_j} + \frac{1}{Re} \frac{\partial^2 \omega_i}{\partial x_j^2} \tag{6}$$

$$\triangle \psi_i = -\omega_i \tag{7}$$

We introduce the generalized coordinate as

$$x = x(\xi, \eta), y = y(\xi, \eta), z = z(\zeta) \tag{8}$$

The partial differentiation operator is then transformed into

$$\begin{aligned} \frac{\partial}{\partial x} &= \frac{1}{J}\left(\frac{\partial y}{\partial \eta}\frac{\partial}{\partial \xi} - \frac{\partial y}{\partial \xi}\frac{\partial}{\partial \eta}\right) \\ \frac{\partial}{\partial y} &= \frac{1}{J}\left(\frac{\partial x}{\partial \xi}\frac{\partial}{\partial \eta} - \frac{\partial x}{\partial \eta}\frac{\partial}{\partial \xi}\right) \\ J &= \frac{\partial x}{\partial \xi}\frac{\partial y}{\partial \eta} - \frac{\partial x}{\partial \eta}\frac{\partial y}{\partial \xi} \end{aligned} \tag{9}$$

In order to specify the wall boundary condition, we define the the normal and the tangential component of ψ as

$$\psi_n = \mathbf{n} \bullet \psi, \psi_{\tau_1} = \tau_1 \bullet \psi, \psi_{\tau_2} = \tau_2 \bullet \psi \tag{10}$$

where $\mathbf{n}$, τ_1, and τ_2 denote the normal and the tangential unit vector on the wall. Then, the wall boundary conditions for the vector potential are given as

$$\frac{\partial \psi_n}{\partial n} = \psi_{\tau_1} = \psi_{\tau_2} = 0 \tag{11}$$

On the other hand, the boundary vorticity is calculated from its definition

$$\omega = \nabla \times \mathbf{u} \tag{12}$$

2.2 Computational method

The explicit method of lines is adopted as the computational method. In this method, spatial discretizations and the time integration are treated separately. For spatial discretization, the 2nd- and 4th-order accurate modified differential quadrature (MDQ) method is used. Partial derivatives of ω, for example, are approximated as

$$\left.\frac{\partial \omega}{\partial \xi}\right|_{i,j,k} = \sum_{l=-L}^{L} a_{i,l}\omega_{i+l,j,k} \tag{13}$$

$$\left.\frac{\partial^2 \omega}{\partial \xi^2}\right|_{i,j,k} = \sum_{l=-L}^{L} b_{i,l}\omega_{i+l,j,k}, \; b_{i,l} = \sum_{m=-L}^{L} a_{i,m}a_{m,l} \tag{14}$$

The 2nd-order accuracy is obtained by $L = 1$ and the 4th-order accuracy by $L = 2$. Derivatives in the η- and ζ-direction are approximated in the same manner. After the above spatial discretization, the vorticity transport equations are reduced to a set of ordinary differential equations (ODEs)

$$\frac{\mathrm{d}\vec{\omega}}{\mathrm{d}t} = \vec{F}(\vec{\omega}) \tag{15}$$

$$\vec{\omega} = (\omega_{x,2,2,2}, \omega_{x,3,2,2}, \cdots, \omega_{x,I-1,J-1,K-1})^T \tag{16}$$

where I, J, and K represent the grid number in the ξ-, η-, and ζ-direction, respectively. As a time integration scheme of a set of ODEs, we apply the Runge-Kutta-Gill method.

2.3 Computation of flows in a square cavity

In order to confirm effectivity of the present computational method, we first carry out simulations of flows in a square cavity at Reynolds numbers $Re = 10^3$ and 10^4. Figure 1 shows the velocity distribution on centerlines of the cavity. It is shown

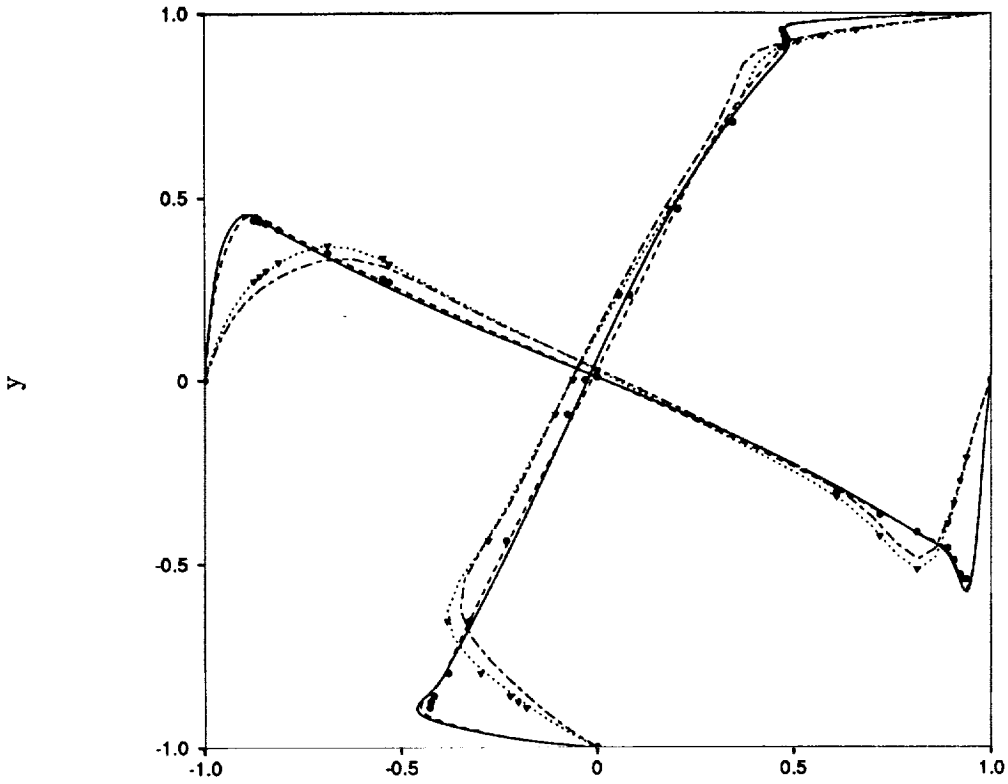

FIGURE 1. Velocity distribution of the flow in a square cavity at $Re = 10^3$ and 10^4. Chain dot and chain dash line depict the result by the 4th- and 2nd-order method at $Re = 10^3$ respectively; solid and dash line represent the result by the 4th- and 2nd-order method at $Re = 10^4$ respectively. Triangle and circle depict the results by Ghia *et al.*

that the result of the 4th-order accurate method with the less grid points (65×65 at $Re = 10^3$) is in good agreement with that of Ghia et al.(1982).

In computation of the cavity flow at $Re = 10^4$, we need the grid points 129×129 in order to make the grid sufficiently dense in the vicinity of the wall. Figure 2 shows the convergence history of these computations with 2nd- and 4th-order accuracy. We needed 75000 time steps with $\Delta t = 1/125$ in order to obtain the converged solution when we used the 2nd-order accurate method. It is shown that the residual

oscillates drastically in time, and a great number of time steps are needed to attain the converged solution even for the 2nd-order method. However, the result with the 4th-order accuracy shows that the L_2 residual preserves the constant level even at $t = 900$, and, therefore, it is concluded that the flow is unsteady.

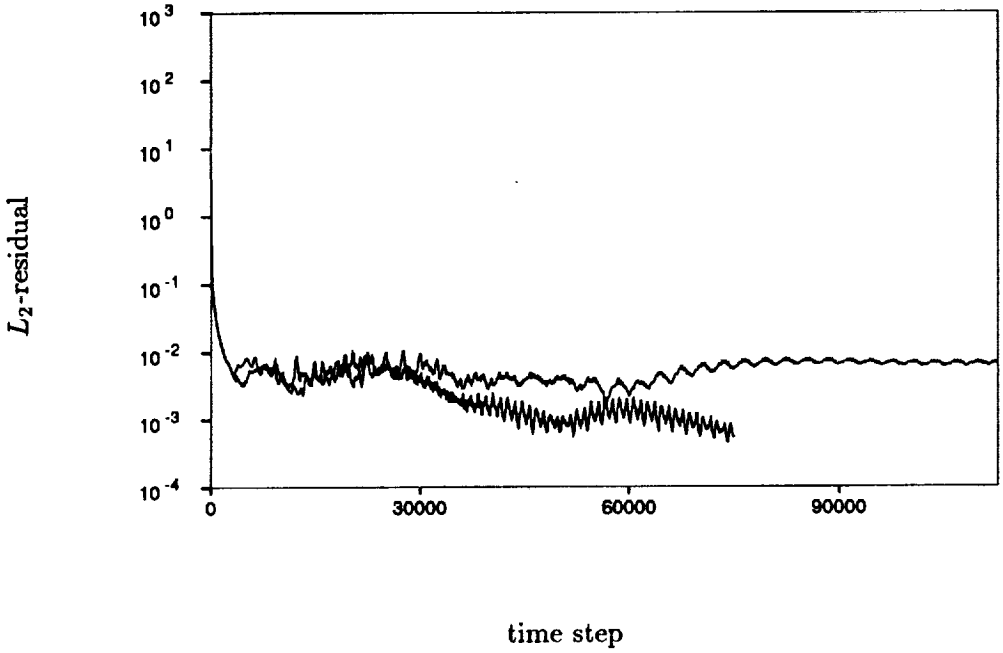

FIGURE 2. Convergence history of the cavity flow at $Re = 10^4$.

In order to investigate the temporal behavior of the flow, we show the vorticity contours at the early stage $t = 50$, 60, and 70, the middle stage $t = 140$, 150, and 160, and the later stage $t = 240$, 250, and 260. Since the present result has a fourth-order accuracy not only for the spatial discretization but also for time discretization, we can see the actual development of the cavity flow from the initial state in which the fluid is at rest.

At an early stage, we find that there exists a number of vortices and that they are stretched in the course of time. The main vortex grows near the center of the cavity, and the other vortices are moved by rotation of the main flow. The stretching is caused by this main flow. However, the center of the main vortex is displaced by the mutual interaction of vortices.

In the middle stage, we find that the main vortex is enclosed by the additional elongated vortex with the same sign. It is well known that a pair of vortices with the same sign rotate around each other along the weighting center of the pair. Thus, the unsteady motion of fluid is sustained. The center of the main vortex moves rapidly.

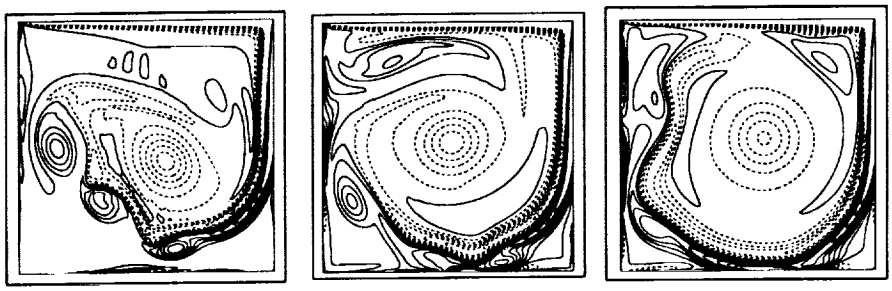

FIGURE 3. Vorticity contours of the cavity flow at $Re = 10^4$ at early time stage.

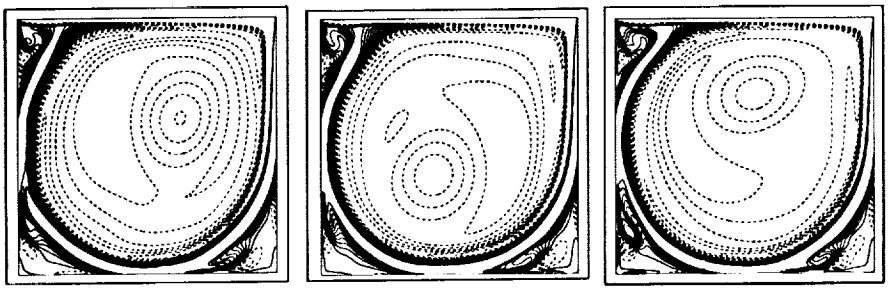

FIGURE 4. Vorticity contours of the cavity flow at $Re = 10^4$ at middle time stage.

The Biot-Savart velocity induced by the vortex is long-range, so the structure of small vortices in the corners of the cavity changes significantly in the course of time.

The pair of vortices persist even at the later stage. However, at $t = 260$, the neighboring vortex is absorbed by the main vortex. Figure 6 shows the vorticity contours at $t = 840$ and 850. The vortex sheets are extremely stretched, and one of them is cut. The vortex generated by this mechanism interacts with other vortices, which explains the unsteadiness of the flow in a cavity at high Reynolds number.

2.4 Computation of flows in a multiply connected domain

In general, the stream function value on the multiply connected domain is not known *a priori*. In order to resolve this problem, we apply the constraint proposed by Girault and Rivart (1979)

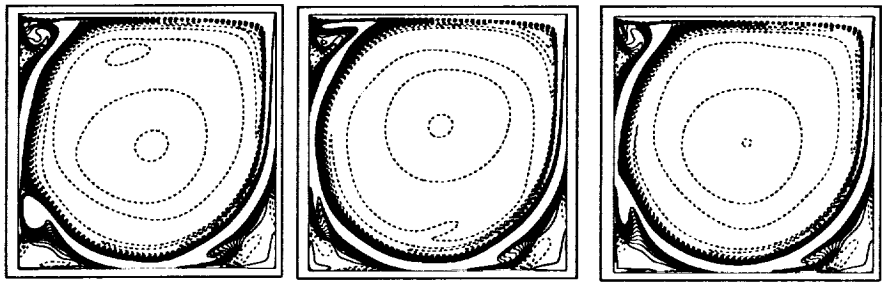

FIGURE 5. Vorticity contours of the cavity flow at $Re = 10^4$ at later time stage.

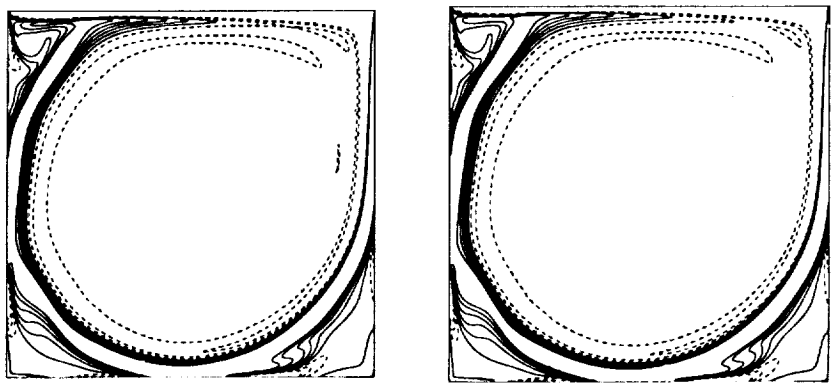

FIGURE 6. Vorticity contours of the cavity flow at $Re = 10^4$ at the latest time stage.

$$\oint_{\Gamma} \frac{\partial \omega}{\partial n} \mathrm{d}s = 0 \tag{17}$$

where Γ denotes the surface of the body placed in the flow. In the present computation, the integral constraint is applied when the Poisson equation on the stream function is solved. We depict the stream line in Figure 7. The stream function value is specified to 1 on the upper wall and 0 on the lower wall. We ultimately obtained the stream function value -0.11375 on the square, which shows a good agreement with the result of Lippke and Wagner (1991).

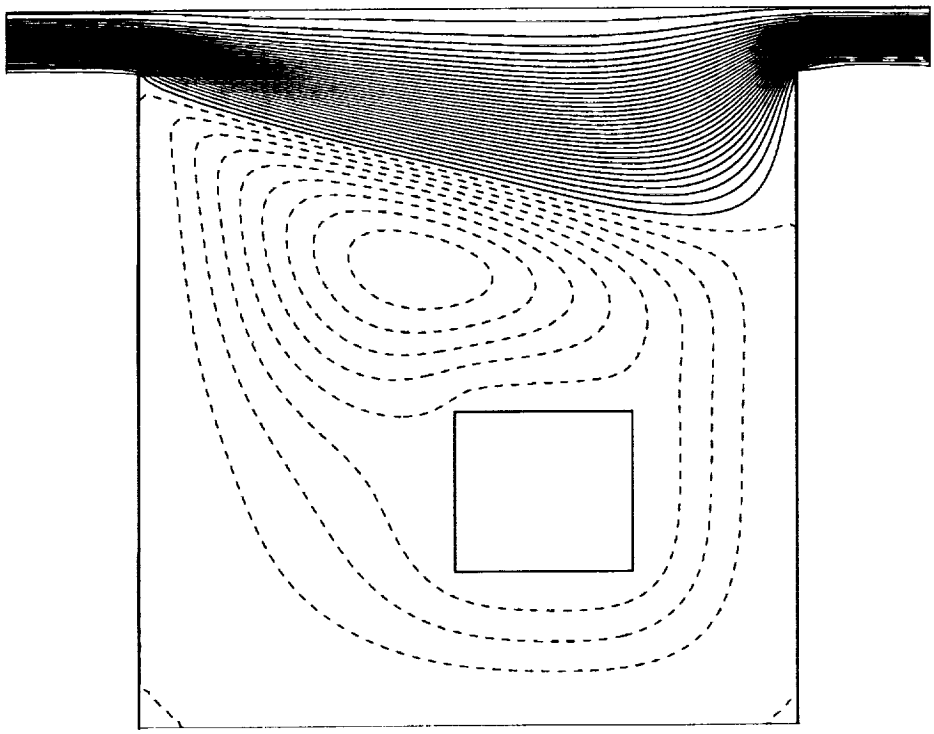

FIGURE 7. Streamline lines of the flow in a multiply connected domain at $Re = 20$.

2.5 Computation of transition of channel flow using LES

For the subgrid-scale model, we choose the dynamical model proposed by Germano *et al.* (1991). Then, the basic equation of LES is obtained in the vorticity vector potential formulation as

$$\frac{\partial \bar{\omega}_1}{\partial t} + \frac{\partial}{\partial x_j}(\bar{u}_j \bar{\omega}_1) = \bar{\omega}_j \frac{\partial \bar{u}_1}{\partial x_j} + \left(\frac{\partial^2 \nu_t}{\partial x_2 \partial x_j} \bar{S}_{3j} - \frac{\partial^2 \nu_t}{\partial x_3 \partial x_j} \bar{S}_{2j} \right) + \frac{1}{2}\left(\frac{\partial \nu_t}{\partial x_2} \frac{\partial^2 \bar{u}_3}{\partial x_j^2} - \frac{\partial \nu_t}{\partial x_3} \frac{\partial^2 \bar{u}_2}{\partial x_j^2} \right) + \frac{1}{2} \frac{\partial \nu_t}{\partial x_j} \frac{\partial \bar{\omega}_1}{\partial x_j} + \left(\frac{1}{2}\nu_t + \frac{1}{Re}\right) \frac{\partial^2 \bar{\omega}_1}{\partial x_j^2}$$

$$\frac{\partial\bar{\omega}_2}{\partial t}+\frac{\partial}{\partial x_j}(\bar{u}_j\bar{\omega}_2)=\bar{\omega}_j\frac{\partial\bar{u}_2}{\partial x_j}+\left(\frac{\partial^2\nu_t}{\partial x_3\partial x_j}\bar{S}_{1j}-\frac{\partial^2\nu_t}{\partial x_1\partial x_j}\bar{S}_{3j}\right)+$$
$$\frac{1}{2}\left(\frac{\partial\nu_t}{\partial x_3}\frac{\partial^2\bar{u}_1}{\partial x_j^2}-\frac{\partial\nu_t}{\partial x_1}\frac{\partial^2\bar{u}_3}{\partial x_j^2}\right)+\frac{1}{2}\frac{\partial\nu_t}{\partial x_j}\frac{\partial\bar{\omega}_2}{\partial x_j}+(\frac{1}{2}\nu_t+\frac{1}{Re})\frac{\partial^2\bar{\omega}_i}{\partial x_j^2} \tag{18}$$

$$\frac{\partial\bar{\omega}_3}{\partial t}+\frac{\partial}{\partial x_j}(\bar{u}_j\bar{\omega}_3)=\bar{\omega}_j\frac{\partial\bar{u}_3}{\partial x_j}+\left(\frac{\partial^2\nu_t}{\partial x_1\partial x_j}\bar{S}_{2j}-\frac{\partial^2\nu_t}{\partial x_2\partial x_j}\bar{S}_{1j}\right)+$$
$$\frac{1}{2}\left(\frac{\partial\nu_t}{\partial x_1}\frac{\partial^2\bar{u}_2}{\partial x_j^2}-\frac{\partial\nu_t}{\partial x_2}\frac{\partial^2\bar{u}_1}{\partial x_j^2}\right)+\frac{1}{2}\frac{\partial\nu_t}{\partial x_j}\frac{\partial\bar{\omega}_3}{\partial x_j}+(\frac{1}{2}\nu_t+\frac{1}{Re})\frac{\partial^2\bar{\omega}_3}{\partial x_j^2}$$

where ν_t denotes the dynamical subgrid scale turbulent viscosity and $\bar{S}_{i,j}$ the strain tensor. The generalized coordinate transformation is applied to this equation.

At first we will carry out LES of a transition of plane channel flow in order to investigate the validity of the present method. The initial condition is created by using the result of the direct simulation of 2-D and 3-D linear instability (Tokunaga, Satofuka & Miyagawa, 1986)

3. Summary and future plans

An accurate and efficient computational method is presented for incompressible viscous flows. It is shown that the present method well predicts the flow in multiply connected domain. The 4th-order accurate method shows that the square cavity flow can be calculated accurately by less grid points in comparison with the 2nd-order method at $Re = 10^3$. Further, it is shown that the cavity flow is unsteady at $Re = 10^4$, and actual process of the flow development is cleared by using the 4th-order accurate method.

The next step in this work will be to test the large eddy simulation of transition in a plane channel dealt with by Germano *et al.* (1991), and this study is under way. The ultimate goal of this work is direct and large eddy simulation of the flows in a multiply connected domain, which is of practical importance in aerodynamics.

REFERENCES

GERMANO, G., PIOMELLI, U., MOIN, P. & CABOT, W. H. 1991 A dynamical subgrid-scale eddy viscosity model. *Phys. Fluids.* **A3,** 1760-1765.

GIRAULT, V. & RAVIART, P. A. 1979 Finite element approximation of Navier-Stokes equations. *Lecture Notes in Mathematics.* **749,** Springer-Verlag.

GHIA, U., GHIA, K. N. & SHIN, T. 1982 High-Re solutions for incompressible flow using the Navier-Stokes equations and a multi-grid method. *J. Comp. Phys.* **48,** 387-411.

LIPPKE, A. & WAGNER, H. 1991 Numerical solution of the Navier-Stokes equation in multiply connected domains. *Computers & Fluids.* **20,** 19-28.

TOKUNAGA, H., ICHINOSE, K. & SATOFUKA, N. 1991a Numerical simulation of transient turbulent flows by the vorticity-vector potential formulation. *Computers & Fluids.* **19,** 413-420.

TOKUNAGA, H., ICHINOSE, K. & SATOFUKA, N. 1991b Direct simulation of transient turbulent flows using generalized method of lines. *Advances in Numerical Simulation of Turbulent Flows, ASME FED.* **117,** 57-82.

TOKUNAGA, H., SATOFUKA, N. & MIYAGAWA, H. 1986 Direct simulations of shear flow turbulence in a plane channel by sixth order accurate method of lines with new sixth order accurate multi-grid Poisson solver. *Lecture Notes in Physics.* **264,** Springer-Verlag.

TOKUNAGA, H., SATOFUKA, N. & MIYAGAWA, H. 1986 Direct simulation on instability of the plane Poiseuille flow. *Memoirs of Faculty of Engineering and Design, Kyoto Institute of Technology.* **34,** 72.

TOKUNAGA, H., SATOFUKA, N. & YOSHIKAWA, T. 1987 Direct simulation of high Reynolds number flows using a new integer-differential solver. *AIAA-87-1175-CP.*

TOKUNAGA, H., YOYEDA, K. & SATOFUKA, N. 1991 Direct simulation of three-dimensional flows using generalized vector potential method. *AIAA-91-1610-CP.*

Reynolds stress closure modeling in wall-bounded flows

By P. A. Durbin

This report describes two projects. Firstly, a Reynolds stress closure for near-wall turbulence is described. It was motivated by the simpler $k-\varepsilon-\overline{v^2}$ model described in last year's annual research brief.

DNS of three-dimensional channel flow show a curious decrease of the turbulent kinetic energy. The second topic of this report is a model which reproduces this effect. That model is described and used to discuss the relevance of the three-dimensional channel flow simulation to swept wing boundary layers.

1. Motivation and objectives

The region of a flow very near to a surface exerts a disproportionate control on transport of momentum and heat between surface and fluid. The turbulence in this region is strongly inhomogeneous and highly anisotropic. The anisotropy is particularly important: the normal component of turbulent intensity ($\overline{v^2}$) is responsible for transport to and from the surface; this component is suppressed by the proximate surface. The behavior of $\overline{v^2}$ was the focus of attention in our previous work on near-wall modeling (Durbin 1991). An elliptic relaxation equation was formulated to describe the suppression of $\overline{v^2}$ and to allow appropriate boundary conditions to be satisfied. Last year's report described an application of the $k-\varepsilon-\overline{v^2}$ model to boundary layers and heat transfer.

During the period covered by the present report the near-wall formulation was extended to a full Reynolds stress closure. This formulation is tensorally invariant: $\overline{v^2}$ is not singled out as the normal component; the full Reynolds stress model is applicable to general geometries. The application of this model to separated flows is described in the article by S. Ko in the present volume. The model and an assessment of its predictive potential are described in section 2.1.

Moin *et al.* (1990) performed a DNS of three-dimensional channel flow in order to provide detailed data for use in modeling. This flow was meant as an idealization of the swept-wing boundary layer. We have attempted to model three-dimensional channel flow and to assess the relevance of this flow to the infinite swept wing boundary layer. The most peculiar feature observed in the DNS was a *decrease* of the turbulent intensity when the cross-stream pressure gradient was applied. One would expect the cross-stream flow to add a new contribution to turbulence production and to *increase* the turbulence intensity; indeed, this is what existing turbulence models predict. To account for the reduction in intensity, we have assumed that the streamwise vorticity produced by the cross-flow enhances the cascade of energy to small scales. The mechanism might involve breakup of large, streamwise eddies. The present model consists simply of a parameterization of

three-dimensionality and an *ad hoc* modification to the ε-equation. With only this modification, the Reynolds stress model reproduces many of the features observed in the DNS. Three-dimensional shear flow is discussed in section 2.2.

2. Accomplishments

2.1 The Reynolds stress model

A detailed description of the Reynolds stress model is provided in Durbin (1992a); the following is a brief summary.

The exact Reynolds stress transport equation can be written

$$D_t\overline{u_iu_j} = \varphi_{ij} + P_{ij} - \frac{\overline{u_iu_j}}{k}\varepsilon - \partial_k\overline{u_ku_iu_j} + \nu\nabla^2\overline{u_iu_j} \tag{1}$$

where $D_t(\bullet)$ is the convective derivative following the mean flow;

$$P_{ij} = -\overline{u_iu_k}\partial_kU_j - \overline{u_ju_k}\partial_kU_i \tag{2}$$

is the rate of turbulence production by mean velocity gradients, and

$$\varphi_{ij} = -\frac{1}{\rho}\overline{u_i\partial_jp} - \frac{1}{\rho}\overline{u_j\partial_ip} - \varepsilon_{ij} + \frac{\overline{u_iu_j}}{k}\varepsilon \tag{3}$$

is the redistribution tensor. (The trace of (3) is not equal to zero, but it is common practice to ignore the trace of φ_{ij} on the grounds either that it is negligible or that it is a 'pressure diffusion' term that can be absorbed in the self-transport model.) The Rotta model for anisotropic dissipation, $-\overline{u_iu_j}\varepsilon/k$, has been added to (1) and subtracted from (3): among other virtues, this has the effect of making φ_{ij} vanish at rigid, no-slip boundaries. By definition, $\varepsilon = \varepsilon_{ii}/2$ is the rate of dissipation of turbulent kinetic energy (k).

In the notation of equation (3), all unclosed terms have been incorporated into φ_{ij} except for the transport terms. We follow the usual practice of modeling turbulent self- transport by gradient diffusion:

$$-\partial_l\overline{u_lu_iu_j} = \partial_l\left(\frac{\nu_{T_{lm}}}{\sigma_k}\partial_m\overline{u_iu_j}\right). \tag{4}$$

This amounts to regarding u_iu_j as a 'substance' being transported by the turbulent velocity u_l. The diffusional model is as much a representation of the smoothing effect of ensemble averaging as of convective transport *per se*: this is why the model is parabolic rather than hyperbolic. For the eddy viscosity,

$$\nu_{T_{ij}} = C_\mu\overline{u_iu_j}\,T \tag{5}$$

will be used. For the time scale T, we adopt

$$T = \max\left(\frac{k}{\varepsilon},\ C_T\left(\frac{\nu}{\varepsilon}\right)^{1/2}\right). \tag{6}$$

This becomes k/ε far from boundaries. Near a surface where $k \to 0$, it becomes the Kolmogorov time-scale $C_T(\nu/\varepsilon)^{1/2}$, which is a suitable lower bound on T.

A second order closure for φ_{ij} is simply a proposed relationship between this unknown and the dependent variable of equation (1), $\overline{u_i u_j}$. In all closures to date, this relationship has consisted of algebraic formulae. However, those formulae are based on quasi-homogeneous assumptions—most notably in the rapid pressure strain term—which are incorrect in the strongly inhomogeneous near wall region. I have proposed in previous reports that elliptic effects within the flow that are caused by the proximity of a boundary might be included by formulating an elliptic relaxation model for φ_{ij}. Because the exact elliptic effects are inherently non-local, they cannot appear explicitly in a *single* point model; they are represented quite indirectly by the present model.

The elliptic relaxation model can be put into coordinate independent form and written

$$\varphi_{ij} = k f_{ij} \tag{7}$$

$$L^2 \nabla^2 f_{ij} - f_{ij} = -\Pi_{ij}. \tag{8}$$

The length scale L is formulated by analogy to (6):

$$L = C_L \max\left(\frac{k^{3/2}}{\varepsilon}, C_\eta \left(\frac{\nu^3}{\varepsilon}\right)^{1/4}\right). \tag{9}$$

Boundary conditions influence the solution in the interior of the flow through the homogeneous solutions to (8) (Durbin 1992a). Far from the surface, these solutions decay, and the f_{ij} relax to quasi-homogeneity, as represented by a balance of the second term on the left side of (8) with its right side.

Any quasi-homogeneous model can be used for Π_{ij}. Here we adopt the simple model recommended by Launder (1989). This consists of a sum of Rotta's return to-isotropy and the isotropization-of-production models:

$$\Pi_{ij} = \frac{1 - C_1}{kT}\left(\overline{u_i u_j} - \frac{2}{3}k\delta_{ij}\right) - \frac{C_2}{k}\left(P_{ij} - \frac{2}{3}P\delta_{ij}\right) \tag{10}$$

where $2P = P_{ii}$, and P_{ij} is given by (2). C_1 is the usual Rotta constant, and $C_2 = 3/5$ is found by the method of perturbation of isotropy.

2.1.1 Assessment of the model

The viability of the present Reynolds stress closure was assessed by computing various boundary layer flows. An initial, detailed evaluation of the approach consisted of comparing the model solution to DNS data on channel flow; this comparison is provided in Figure 1. The near wall behavior of the components of the Reynolds stress tensor is captured very well by the model.

Durbin (1992a) contains further comparisons to data in zero pressure gradient, adverse pressure gradient, and curved wall boundary layers. I will not repeat all of those comparisons here, but simply provide a few representative figures. I will

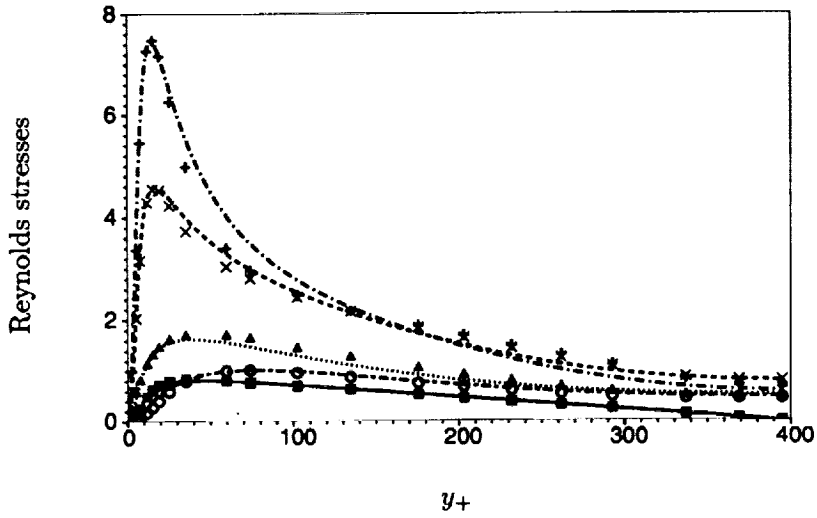

FIGURE 1. Comparison of model (lines) to DNS (symbols) profiles of Reynolds stresses in channel flow at $R_\tau = 395$. +, $\overline{u^2}$; ×, k; △, $\overline{w^2}$; ○, $\overline{v^2}$; ■, $-\overline{uv}$.

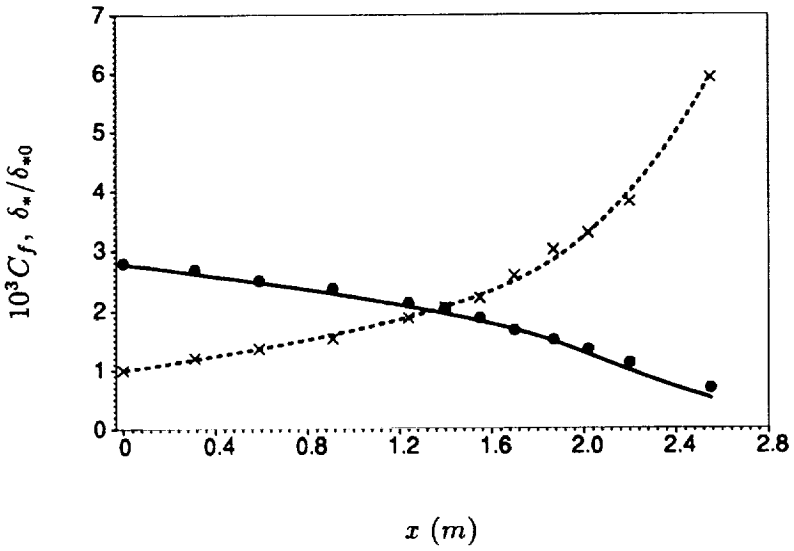

FIGURE 2. Friction coefficient (•) and displacement thickness (×) versus downstream distance for the Samuel and Joubert experiment. Curves are solution of model, symbols experimental data.

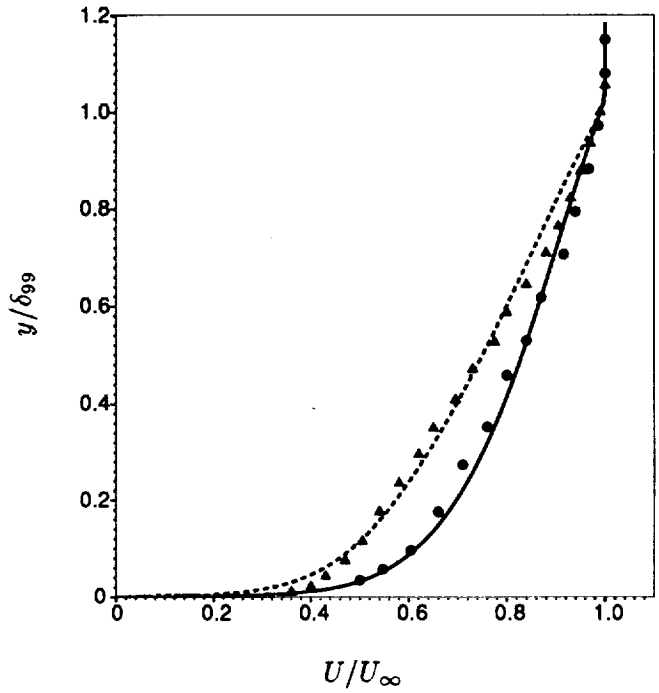

FIGURE 3. Mean velocity profiles at stations 9 ($x = 1.87\,m$, •) and 12 ($x = 2.55\,m$, △) of the Samuel and Joubert adverse pressure gradient boundary layer. Lines are model, symbols experiment.

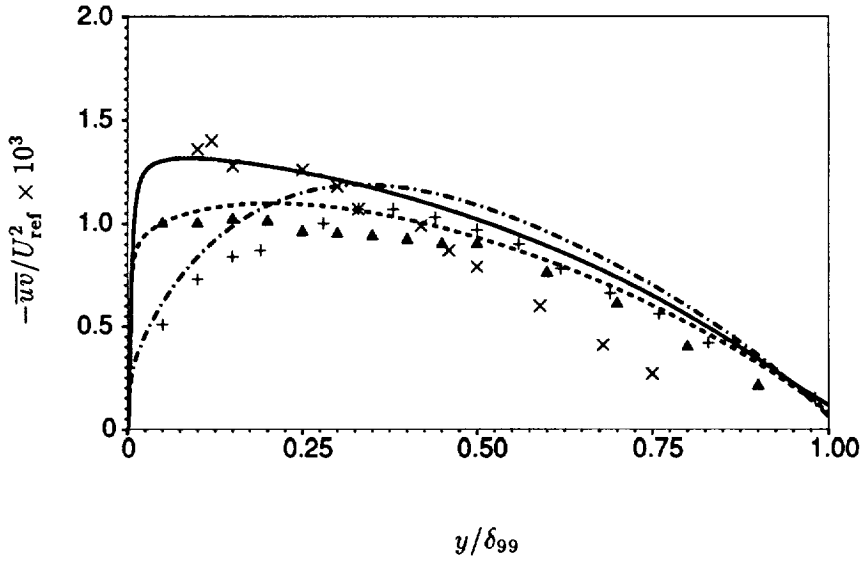

FIGURE 4. Reynolds shear stress profiles at stations T1 ($x = 0.19\,m$, ×, ——), T4 ($x = 1.53\,m$, △, - - -) and T6 ($x = 2.54\,m$, +, — · —) of Samuel and Joubert (1974). Curves are model, symbols experimental data.

skip the zero pressure gradient case. It provides a necessary prerequisite for any near wall turbulence model. The present model gives an excellent solution for the dependence of skin friction on Reynolds number and quite satisfactory profiles of mean velocity and turbulent Reynolds stresses.

The Samuel and Joubert (1974) experiment on a boundary layer progressing into a region of increasingly adverse pressure gradient is a good test of the response of a model to pressure gradients. Solutions for skin friction and displacement thickness versus downstream distance are shown in Figure 2 along with experimental data. Profiles of mean velocity and Reynolds shear stress are contained in figures 3 and 4. Agreement between the model and data is quite reasonable, although discrepancies clearly can be seen. It is encouraging that the model is able to describe the departure from equilibrium observed in the experiment; in particular, Figure 4 shows how the pressure gradient causes a change of the near wall region from a constant stress layer to a layer of increasing stress. The log-layer theory invokes a constant stress layer.

A nice illustration of the capability of the Reynolds stress model is provided by the boundary layer on a convex curved surface. A tensorially consistent model is formally independent of coordinate system. This means that the model equations can be projected onto curvilinear coordinates by the methods of differential geometry. Upon doing so, metric terms arise. The stabilizing effect of convex curvature can be attributed to those metric terms. Thus, much of the important physics are retained by the coordinate invariant Reynolds stress model. By contrast, noninvariant models (*e. g.*, mixing length) can not account for curvature effects, nor can quasi-isotropic, scalar models (*e. g.*, $k - \varepsilon$).

Figure 5 shows the downstream evolution of the skin friction coefficient in a boundary layer that starts on a flat plate, then flows around a 90° convex, circular arc, and then continues along another flat section. This boundary layer was studied experimentally by Simon *et al.* (1982). In the experiment, the wind tunnel wall opposite to the test surface was contoured to maintain a constant surface pressure beneath the boundary layer. A pressure gradient normal to the curved wall exists to balance the centrifugal acceleration.

The dashed line in Figure 5 shows the downstream evolution of C_f on a flat plate. Convex curvature begins at $x = 0$; the skin friction drops abruptly. In Figure 5, C_f has been normalized by its value at the start of curvature. This normalization enables one to invoke Reynolds analogy and include data on heat transfer coefficients in the figure. The heat transfer data are more comprehensive than the skin friction data and they were measured directly; the skin friction had to be inferred by assuming that the mean velocity profiles conformed to the universal, constant stress log-law.

In fact, in the curved section the Reynolds shear stress profile does not show a constant stress layer near the surface. Figure 6 shows how the centrifugal stabilization suppresses $-\overline{uv}$ in the outer region of the boundary layer. Indeed, $-\overline{uv}$ becomes slightly negative in the data denoted by $\times$ when $y/\delta_{99} > 0.4$. After the curved section, $-\overline{uv}$ initially recovers near the surface, and the region of increased

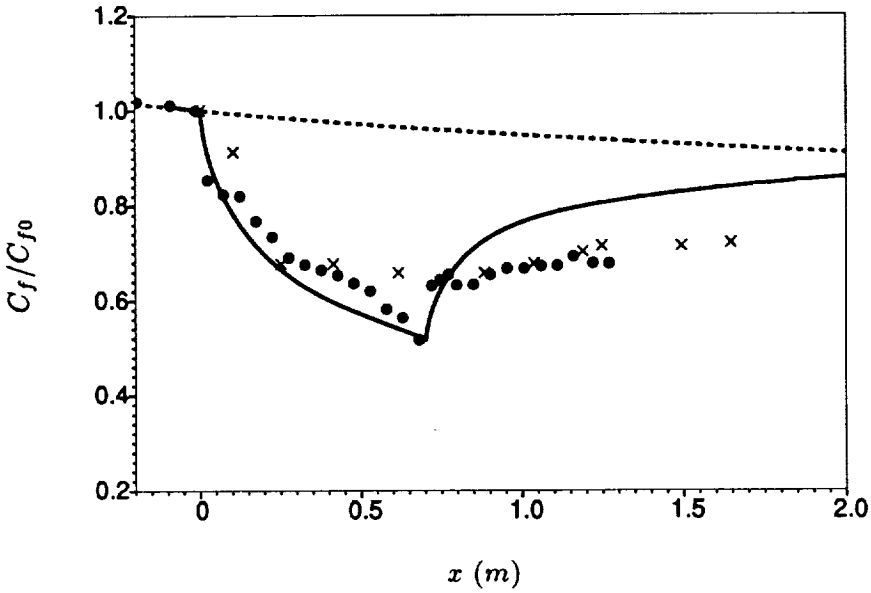

FIGURE 5. Solid line is computed skin friction, normalized on its value at the start of curvature; dashed line is normalized skin friction computed for a flat plate boundary layer. Experimental data on skin friction (×) surface heat flux (•) from Simon *et al.* (1982).

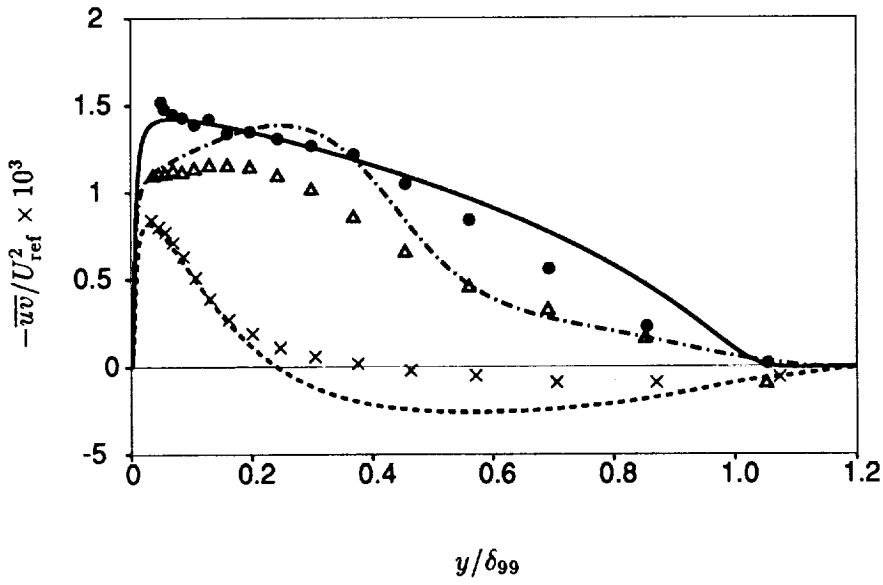

FIGURE 6. Model solutions and experimental data on Reynolds shear stress. The profiles are at $x = -0.062m$ (•, ——), $x = 0.162m$ (×, - - -) and $x = 1.124m$ (△, —·—). These stations are upstream of the bend, 20.6° around the bend and in the downstream recovery region.

stress then propagates across the boundary layer. The model shows some discrepancies with the data. These are most significant in the recovery region downstream of the bend. The model recovers to the flat plate skin friction too rapidly (Figure 5).

2.2 Effects of three-dimensionality

The work described in this section is presented at greater length in Durbin (1992b).

The most clear-cut feature of a three-dimensional boundary layer is the skewing of the direction of the mean velocity vector with height. This may alternatively be described as a presence of mean vorticity in the streamwise direction: in the boundary layer approximation, the vorticity vector is $\mathbf{\Omega} = (\partial_y W, 0, -\partial_y U)$; the projection of the vorticity onto the mean velocity is

$$\mathbf{\Omega} \cdot \mathbf{U} = U^2 \partial_y \left[\frac{W}{U}\right] = U^2 \partial_y \tan(\beta) \tag{11}$$

where β is the direction of the mean velocity relative to the x-axis. In a three-dimensional boundary layer, the quantities in (11) are non-zero; hence, the vorticity and velocity are not orthogonal, and the direction of the mean flow skews with height.

An additional feature of a three-dimensional turbulent shear layer is that the Reynolds stress is not collinear with the mean shear:

$$\frac{\partial_y W}{\partial_y U} \neq \frac{\overline{vw}}{\overline{uv}}$$

or

$$\partial_y U \overline{vw} - \partial_y W \overline{uv} \neq 0. \tag{12}$$

This is the most obvious feature of the turbulence, and has been demonstrated in numerous experiments.

Other effects of three-dimensionality on the turbulence are less clear cut. Many experiments on three-dimensional boundary layers use strong adverse pressure gradients to turn the flow. The role of three dimensionality in this type of experiment is clouded by the presence of the adverse pressure gradient. In order to isolate three- dimensional effects, and to provide comprehensive, accurate data, Moin *et al.* (1990) performed a DNS of pressure driven three-dimensional channel flow. This is a horizontally homogeneous flow produced by subjecting a fully developed two-dimensional channel flow to an accelerating spanwise pressure gradient.

Perhaps the most curious feature of this flow is that the turbulent intensity initially *decreases*. The cross-stream acceleration adds a cross-stream component of mean shear, increasing the magnitude of shear, so one would anticipate an *increase* in the turbulent intensity. Indeed, this flow will ultimately evolve into a two-dimensional channel flow, at an angle to the original flow, with a higher mean velocity and higher turbulent intensity. The initial evolution—which is all that could be numerically simulated—is counter intuitive.

The objective of the present study is to model the behavior of three-dimensional channel flow and then to assess its relevance to the swept wing boundary layer. I considered the possibility that the decrease of the turbulent intensity was due to a suppression of energy redistribution into $\overline{v^2}$, as proposed by Moin *et al.* This was unable to explain the effect. The most direct mechanism, and that which I modeled, is to suppose that the three-dimensionality increases the rate of the energy cascade to small scales.

A parameter is needed to characterize three-dimensionality. This ought to be related to the presence of streamwise vorticity (11) and to the misalignment of stress and shear (12). Consider projection of the production tensor on the direction of the mean vorticity: in a two-dimensional shear layer, $P_{ij}\Omega_i/|\Omega|$ is zero, but not in a three-dimensional layer. This suggests that the invariant $\Omega_i P_{ij}\Omega_j/|\Omega|^2$ might characterize three-dimensionality. Unfortunately, this quantity is identically zero in parallel shear flow. A non-vanishing invariant is $P_{3D}^2 \equiv \Omega_i P_{ij}^2 \Omega_j/|\Omega|^2$, where $P_{ij}^2 = P_{ik}P_{kj}$; this will be used to characterize the effect of three- dimensionality on ε. In parallel shear flow,

$$\Omega_i P_{ij}^2 \Omega_j/|\Omega|^2 = (\partial_y U\overline{vw} - \partial_y W\overline{uv})^2$$

so P_{3D} is related to (12), as required.

The ε-equation both closes the turbulent kinetic energy (k) budget and provides a time-scale for use in modeling: $T = k/\varepsilon$; or in viscous regions, $T = (\nu/\varepsilon)^{1/2}$. The exact equation for ε is of little value to modeling; the usual model equation is based on an *ad hoc* notion that the production and dissipation of ε can be represented by a function of the production and dissipation of energy. Thus, the evolution equation for homogeneous turbulence is assumed to be of the form

$$\dot{\varepsilon} = \frac{\varepsilon}{T} F(P/\varepsilon) \tag{13}$$

where $P = P_{ii}/2$ is the rate of energy production and $F(\bullet)$ is some function. (13) is simply a dimensionally consistent form for expressing the assumed dependence on production and dissipation of energy. The standard ε-equation is obtained by letting $F(\bullet)$ be linear:

$$F(P/\varepsilon) = C_{\varepsilon_1} P/\varepsilon - C_{\varepsilon_2} \tag{14}$$

where the C_ε's are empirical constants. Here we simply extend the argument list to include P_{3D}^2:

$$\dot{\varepsilon} = \frac{\varepsilon}{T} F(P/\varepsilon, P_{3D}^2/\varepsilon^2). \tag{15}$$

Again, we adopt a linear model

$$\dot{\varepsilon} = \frac{C_{\varepsilon_1} P - C_{\varepsilon_2}\varepsilon + C_{\varepsilon_3} P_{3D}^2/\varepsilon}{T}. \tag{16}$$

The value of $C_{\varepsilon 3} = 4$ was chosen.

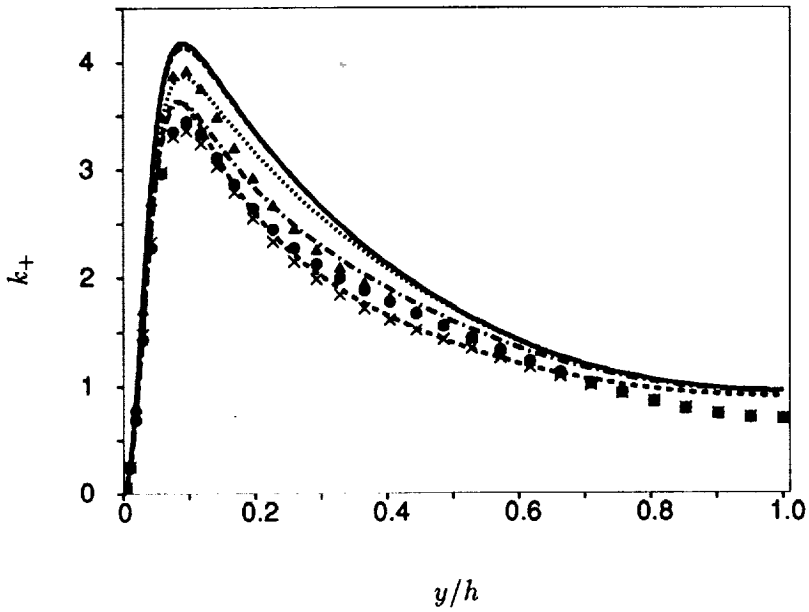

FIGURE 7. Turbulent kinetic energy in 3-D channel flow ($R_\tau = 180$), showing the initial decrease with time. The curves are solutions to the model and symbols DNS data. —— (△), $t = 0$; — - —, $t = 0.3$; ··· (•), $t = 0.6$; — · — (×), $t = 0.9$; - - -, t=1.2.

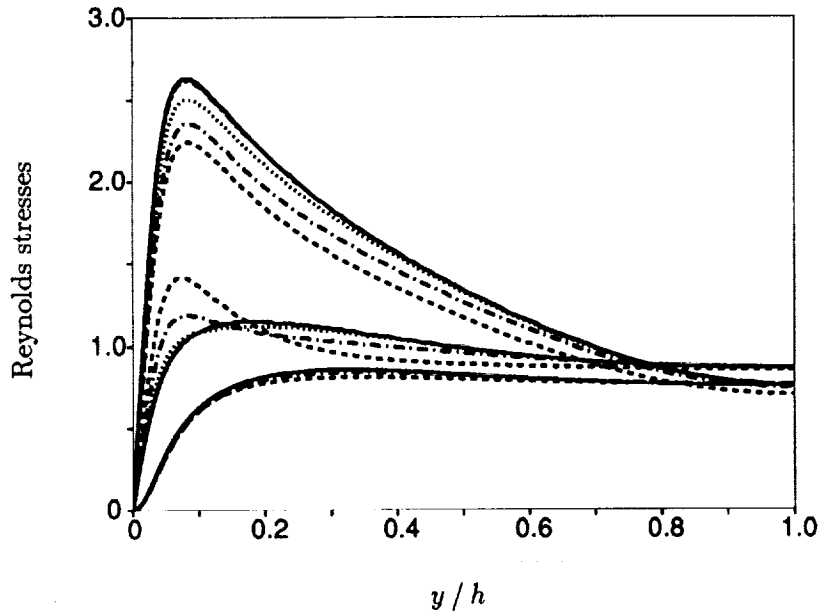

FIGURE 8. Components of turbulent intensity in channel flow. Curves as in Figure 7.

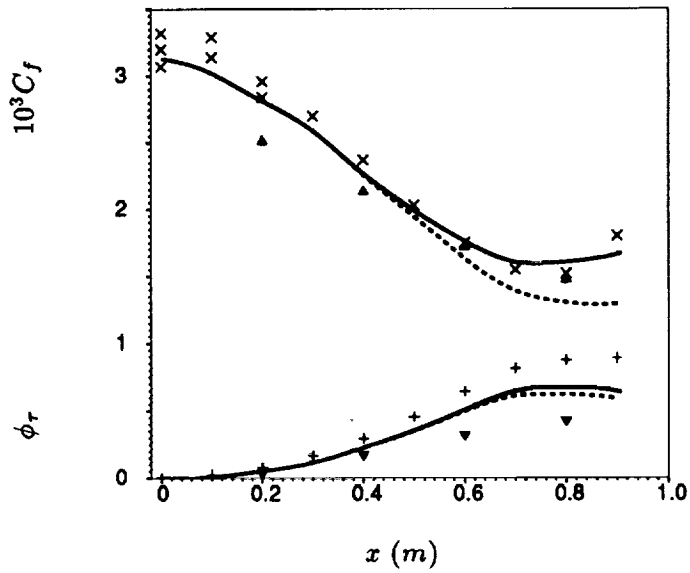

FIGURE 9. Skin friction coefficient and direction of surface stress, in radians, for infinite swept wing boundary layer. Data of Elsenaar and Boelsma (1974): ×, +; data of Pontikos and Bradshaw(1985): △, ▽. Model: ——, $C_{\epsilon_3} = 4.0$; - - -, $C_{\epsilon_3} = 0$.

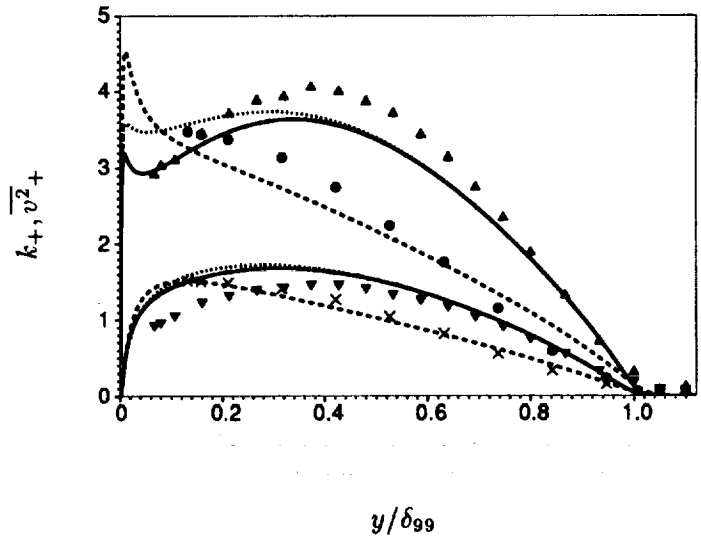

FIGURE 10. Kinetic energy (upper curves) and $\overline{v^2}$ for infinite swept wing; data from Elsenaar and Boelsma (1974). - - - (•, ×), $x = 0.3m$; —— (△, ▽), $x = 0.6m$; · · ·, $x = 0.6m$, $C_{\epsilon_3} = 0$. Normalization is by friction velocity at $x = 0$ and by 99% boundary layer thickness.

The model described in §2.1 was solved in conjunction with (16). The evolution of the turbulent kinetic energy with time is displayed in Figure 7 along with DNS data. It is seen that the model produces the initial drop of kinetic energy. Figure 8 shows the behavior of individual components of the Reynolds stress tensor. They evolve with time in much the same manner as observed in the Moin *et al.* DNS.

The model was solved for the infinite swept wing flow studied by Elsenaar and Boelsma (1974) and by Bradshaw and Pontikos (1985). This flow was produced by subjecting a boundary layer to a pressure gradient directed at 35° the initial flow direction. The boundary layer originated either at a swept leading edge (Elsenaar and Boelsma) or at a swept suction slot (Bradshaw and Pontikos) so that the whole flow was invariant with respect to translation along lines of constant pressure (ignoring end walls).

The upper curves in Figure 9 show the skin friction coefficient versus downstream distance and the lower curves show the angle of the surface stress to its upstream direction. The solid lines are a solution with $C_{\varepsilon_3} = 4$. The dashed lines are a solution with $C_{\varepsilon_3} = 0$, so that the 3D effect found in the channel flow simulations can be assessed. The two sets of experimental data show how poorly reproducible this experiment is. Given this ambiguity and an ambiguity in the pressure gradient prescribed in the present computation, it cannot be concluded that the three-dimensional effect shown by Figure 9 is significant.

Figure 10 shows profiles of k and $\overline{v^2}$ at two downstream locations. The first is near the beginning of the pressure gradient and the second is well into the three-dimensional region. The sets of curves at $x = 0.6\,m$ show how the model predicts that the 3D effect occurs near to the surface, where it causes a reduction of k. The experimental data suggest that this effect might be present in the flow.

My conclusion is that the three-dimensional effects uncovered in the channel flow DNS have only a minimal influence on the swept wing boundary layer. This is probably because the cross-stream pressure gradient in the DNS was quite large (10 times that of the initial equilibrium flow). In the swept wing experiments the perturbation to the boundary layer was not so abrupt.

3. Future plans

The Reynolds stress model is being solved in increasingly complex flows. The article by S. Ko in this volume describes computations of separated boundary layers. This work on complex flows will continue. A code for computing flow in curvilinear geometries is being developed (with N. Mansour). This will be used to compute turbulent flow on aerofoils.

The possibility of formulating an eddy viscosity transport model for use in complex flows is being explored. Although this is far less satisfactory than Reynolds stress modeling, simple models are preferred by those concerned with complex aerodynamic flows.

REFERENCES

BRADSHAW, P. & PONTIKOS, N. 1985 Measurements in the turbulent boundary

layer on an infinite swept wing. *J. Fluid Mech.* **159,** 105-130.

DURBIN, P. A. 1991 Analyses and modeling of evolving turbulent flow. *CTR Annual Research Briefs.* Stanford Univ./NASA Ames.

DURBIN, P. A. 1992a A Reynolds stress model for near-wall turbulence. *to appear in J. Fluid Mech.*

DURBIN, P. A. 1992b On modeling 3-dimensional wall layers. *CTR manuscript.* **135.**

ELSENAAR, A. & BOELSMA, S.H. 1974 Measurements of the Reynolds stress tensor in a three-dimensional turbulent boundary layer under infinite swept wing conditions. *NLR TR.* **74095 U.**

LAUNDER, B. E. 1989 Second-moment closure: present...and future. *Int. J. Heat and Fluid Flow.* **10,** 282-300.

MOIN, P., SHIH, T. H., DRIVER, D. & MANSOUR, N. 1990 Direct numerical simulation of a three-dimensional turbulent boundary layer. *Phys. Fluids A.* **2,** 1846-1856.

SAMUEL, A. E. & JOUBERT, P. N. 1974 A boundary layer developing in an increasingly adverse pressure gradient. *J. Fluid Mech.* **66,** 481-505.

SIMON, T. W., MOFFATT, R. J., JOHNSTON, J. P. & KAYS, W. M. 1982 Turbulent boundary layer heat transfer experiments: curvature effects including introduction and recovery. *NASA CR.* **3510.**

Application of a Reynolds stress model to separating boundary layers

By S. H. Ko

1. Motivation and objectives

Separating turbulent boundary layers occur in many practical engineering applications, yet the physics of separation/reattachment of the flows is poorly understood. During the past decade, various turbulence models have been proposed and their ability to successfully predict some types of flows has been shown. However, prediction of separating/reattaching flows is still a formidable task for model developers.

The present study is concerned with separation process from a smooth surface. Features of turbulent separating boundary layers that are relevant to modeling include: the occurrence of zero wall shear stress, which causes breakdown of the boundary layer approximation; the law of the wall not being satisfied in the mean backflow region; high turbulence levels in the separated region (Simpson *et al.* 1981); a significant low-frequency motion in the separation bubble (Dianat & Castro 1991); and the turbulence structure of the separated shear layer being quite different from that of either mixing layers or boundary layers (Dianat & Castro 1991). These special characteristics of separating boundary layers make it difficult for simple turbulence models to correctly predict their behavior.

Some researchers (De Henau *et al.* 1990, Atkinson & Castro 1991) have reported poor performance of existing turbulence models when the models were applied to the Simpson *et al.* (1981) separated flow experiment. They have found that a Reynolds stress model similar to Launder *et al.* (1975) and the standard k-ϵ model gave no separation — they could achieve separation only after an arbitrary increase of a coefficient in the ϵ equation. Menter (1991) evaluated various turbulence models ranging from algebraic to two-equation turbulence models for the marginal separated flow experiment of Driver (1991). He found that most mixing length models performed poorly, except for the Johnson-King model, and that the $k-\omega$ model predicted too high Reynolds shear stress.

An elliptic relaxation model, the $k-\epsilon-v$ model, was proposed by Durbin (1991) to treat the strongly non-homogeneous and anisotropic near-wall layer. This model eliminates the need for semi-empirical wall functions or *ad hoc* damping functions. Those functions assume universality of the near-wall flow, which is unwarranted in strongly adverse pressure gradients. After showing that the elliptic relaxation approach was successful in simple flows such as channel flow and flat plate, attached boundary layers, the model was extended to a full Reynolds stress model (RSM) (Durbin 1992) for more complicated near-wall problems. The primary objective of the present study is to apply the $k-\epsilon-v$ model and the full RSM to two-dimensional turbulent separating boundary layers.

2. Accomplishments

2.1 Turbulence model

The governing equations of the $k-\epsilon-v$ model can be found in last year's report (Ko, 1991). This section concerns only the equations of the RSM. The major difference between the $k-\epsilon-v$ model and the RSM is that the $k-\epsilon-v$ model uses an algebraic eddy viscosity expression, whereas the RSM uses differential equations for calculating Reynolds stresses in the time-averaged Navier-Stokes equations. It also has to be noted that the $k-\epsilon-v$ model can only be applied to thin shear layers while the RSM can be used for any complex flows.

The Reynolds stress transport equation is

$$\frac{D\overline{u_iu_j}}{Dt} = \mathcal{P}_{ij} + F_{ij} - \frac{\overline{u_iu_j}}{k}\epsilon + \frac{\partial}{\partial x_m}\left[(\nu + \frac{\nu_{ml}}{\sigma_k})\frac{\partial \overline{u_iu_j}}{\partial x_l}\right] \tag{1}$$

where

$$\mathcal{P}_{ij} = -\left(\overline{u_iu_k}\frac{\partial U_j}{\partial x_k} + \overline{u_ju_k}\frac{\partial U_i}{\partial x_k}\right) \tag{2}$$

is the rate of turbulence production by mean velocity gradients. In Eq. (1), the triple velocity correlation is modeled by the simple gradient-diffusion hypothesis of Daly & Harlow (1970):

$$\frac{\partial}{\partial x_m}(-\overline{u_mu_iu_j}) = \frac{\partial}{\partial x_m}\left(\frac{\nu_{ml}}{\sigma_k}\frac{\partial \overline{u_iu_j}}{\partial x_l}\right). \tag{3}$$

The tensorial eddy viscosity in Eq. (3) is

$$\nu_{ml} = C_\mu \overline{u_mu_l}\, T \tag{4}$$

where the time-scale T is

$$T = \max\left(\frac{k}{\epsilon}, C_T\left(\frac{\nu}{\epsilon}\right)^{1/2}\right). \tag{5}$$

The second term in Eq. (5) introduces the Komogorov time-scale as a lower bound.

The term F_{ij} in Eq. (1) includes the rest of the unclosed terms such as pressure gradient-velocity correlations and anisotropic dissipation ϵ_{ij}:

$$F_{ij} = -\frac{1}{\rho}\left(\overline{u_i\frac{\partial p}{\partial x_j}} + \overline{u_j\frac{\partial p}{\partial x_i}}\right) - \epsilon_{ij} + \frac{\overline{u_iu_j}}{k}\epsilon. \tag{6}$$

The elliptic relaxation model (Durbin 1992) for F_{ij} is

$$F_{ij} = k f_{ij} \tag{7}$$

$$L^2\nabla^2 f_{ij} - f_{ij} = \frac{(C_1 - 1)}{T}\left(\frac{\overline{u_i u_j}}{k} - \frac{2}{3}\delta_{ij}\right) + \frac{C_2}{k}\left(\mathcal{P}_{ij} - \frac{2}{3}\mathcal{P}\delta_{ij}\right) \tag{8}$$

where the length-scale L in Eq. (8) is expressed as

$$L = C_L \max\left(\frac{k^{3/2}}{\epsilon}, C_\eta\left(\frac{\nu^3}{\epsilon}\right)^{1/4}\right) \tag{9}$$

and $\mathcal{P} \equiv \mathcal{P}_{ii}/2$. The right side of Eq. (8) is simply the 'basic' model of Launder *et al.* (1975). Any other quasi-homogeneous Reynolds stress model could be used as the source term in this equation. Thus, the elliptic relaxation formulation primarily provides a framework for extending a quasi-homogeneous model to a model for near-wall turbulence.

The above RSM equations are coupled with transport equations for turbulent kinetic energy k and its rate of dissipation ϵ:

$$\underbrace{\frac{Dk}{Dt}}_{advection} = \underbrace{\mathcal{P}}_{production} \underbrace{-\epsilon}_{dissipation} + \underbrace{\frac{\partial}{\partial x_m}\left\{\left(\nu + \frac{\nu_{ml}}{\sigma_k}\right)\frac{\partial k}{\partial x_l}\right\}}_{diffusion} \tag{10}$$

$$\frac{D\epsilon}{Dt} = C_{\epsilon 1}\left(1 + 0.1\frac{\mathcal{P}}{\epsilon}\right)\frac{\mathcal{P}}{T} - C_{\epsilon 2}\frac{\epsilon}{T} + \frac{\partial}{\partial x_m}\left\{\left(\nu + \frac{\nu_{ml}}{\sigma_\epsilon}\right)\frac{\partial \epsilon}{\partial x_l}\right\}. \tag{11}$$

The model coefficients in Eqs. (4-11) are as follows

C_μ	C_T	C_1	C_2	C_L	C_η	$C_{\epsilon 1}$	$C_{\epsilon 2}$	σ_k	σ_ϵ
0.23	6.0	1.22	0.6	0.2	80.0	1.44	1.9	1.2	1.65

Detailed discussion of the RSM and its boundary conditions can be found in Durbin (1992).

2.2 Computational method

The $k - \epsilon - v$ model and the RSM were implemented into a finite difference computer code developed for solving 2-D, incompressible, steady-state turbulent flows. This program is based on finite difference procedures used in the TEACH computer program of Gosman and Pun (1974). The primitive variable equations are solved on a system of staggered grids. The discretization is based in all cases on the control volume approach.

The convective derivatives are approximated by the QUICK differencing scheme of Leonard (1979) in order to reduce the error due to the artificial viscosity. An iterative method for solving the algebraic finite-difference equations is employed. The SIMPLER algorithm of Patankar (1980) is used to obtain the pressure field from the continuity and momentum equations. The discretized equations are linear and are solved line-by-line using a tri-diagonal matrix algorithm applied in an alternating direction implicit manner. The accuracy of the present numerical methods has been tested by computing laminar flow in a driven cavity and laminar flow over a backward-facing step (Ko 1991).

2.3 Computation of separating boundary layer

The massive separating boundary layer of Simpson *et al.* (1981) was chosen as a test case. This flow is a two-dimensional, airfoil-type flow which was accelerated in a contraction and then decelerated until separation. It should be noted that the experimental data ended well before reattachment because the flow became increasingly three-dimensional downstream of separation.

Computations will be compared with experimental data for turbulence quantities as well as for the mean flow. The rectangular computational domain starts at the throat ($x = 1.6\,m$) of the wind tunnel where the flow is assumed to be a zero pressure gradient boundary layer. Reynolds number based on the momentum thickness and the free-stream velocity is 2800 at the inlet of the domain. A solution for a zero pressure gradient boundary layer is utilized to specify inlet conditions. The exit of the domain is located at $x = 8.6\,m$ which is sufficiently far downstream to permit reattachment of the flow and to allow zero-normal-gradient outflow conditions for all variables. In the vertical direction, the domain extends from the bottom wall to $y = 0.5\,m$.

Along the top boundary, the normal velocity V was specified to produce appropriate pressure gradients and the flow is assumed to be irrotational: $\partial U/\partial y = \partial V/\partial x$. A zero normal-gradient condition was applied to the other variables. On the solid wall, flow variables are specified as follows :

$$U = V = k = \overline{u_1{}^2} = \overline{u_2{}^2} = \overline{u_1 u_2} = f_{11} = 0,$$

$$\frac{d\overline{u_1{}^2}}{dy} = \frac{dk}{dy} = 0, \qquad \overline{u_2{}^2} = O(y^4), \qquad \overline{u_1 u_2} = O(y^4)$$

After grid independence testing, an 80 × 120 grid was selected for final computations. This had 80 uniformly-spaced lines in the streamwise direction and 120 uniformly-expanding lines in the transverse direction.

The prescribed V distribution at the top boundary is displayed in figure 1 along with the computed surface pressure coefficient, C_p. The inlet free-stream velocity U_{∞_0} ($= 21.7\ m/s$) was used to normalize the V velocity. Since the V profile at the top boundary could not be obtained from the experimental data, it was selected by matching the U-velocity of the experiments at the 99% boundary layer thickness. The experimental data only cover the region $x < 4.34\ m$. The V distribution downstream of this was arbitrarily chosen to close the separation bubble. Regrettably, this arbitrariness, stemming from the incompleteness of the data, makes the present comparison to experiment somewhat ambiguous. It should be mentioned that this V-profile matching was done only for computations of the $k-\epsilon-v$ model, and then the same V profile was used for computations of the RSM without adjustment. This adds additional ambiguity to the comparison of results of the RSM to experiment. The computed C_p profiles show good agreement with experimental data until the flow separates at $x = 3.45\ m$. In the separated region, the RSM overpredicts C_p whereas the $k-\epsilon-v$ model underpredicts C_p. Since C_p is a measure of the magnitude of mean velocity in the near-wall region, the C_p profiles in the figure could

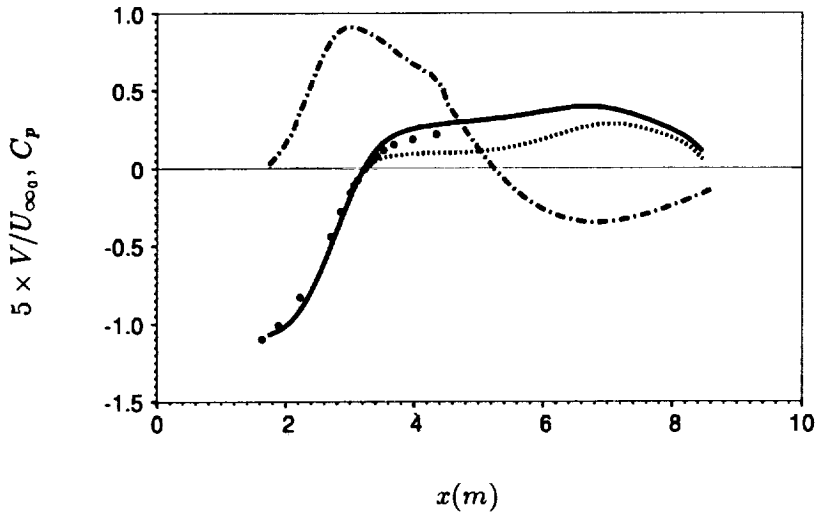

FIGURE 1. Prescribed V distribution at top of computational domain (—·—) and surface pressure coefficient C_p computed by the RSM (———) and the $k-\epsilon-v$ model (·····). • data (Simpson *et al.* 1981).

be interpreted as follows: the separation predicted by the RSM is weaker than that predicted by the $k-\epsilon-v$ model.

Figure 2 shows the computed streamline patterns and the computational domain. As suggested by figure 1, the $k-\epsilon-v$ model gives earlier separation and larger separation bubble compared to the RSM for the same V profile along the top boundary.

(a) the k-ε-v model

(b) the RSM

FIGURE 2. Predicted streamline patterns, showing computational domain.

Computed skin friction coefficients C_f are compared to measurements in figure 3. The agreement between model calculations and experimental results is reasonable in the region upstream of separation. In the separation region, the two models show

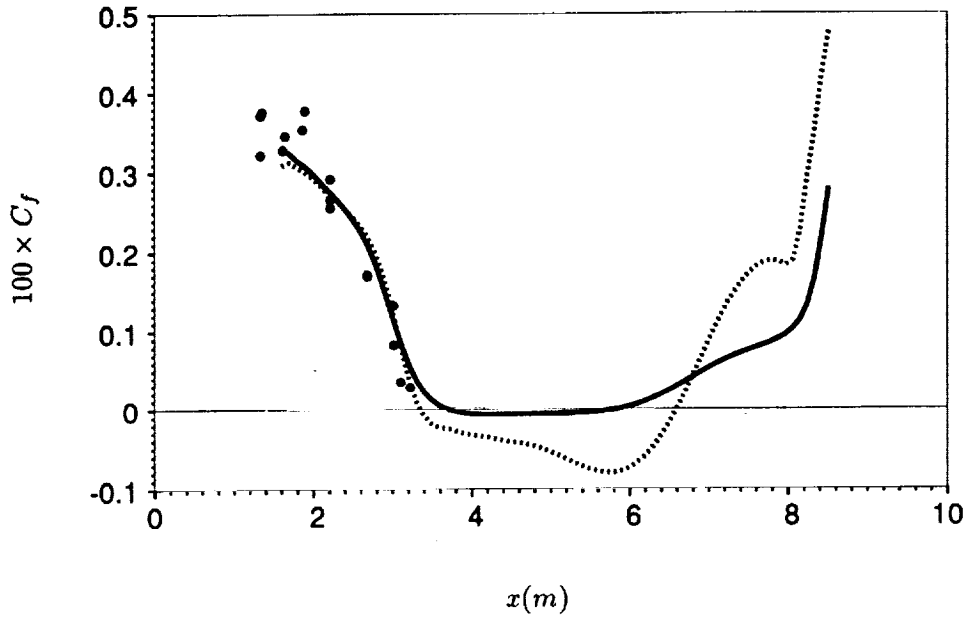

FIGURE 3. Skin friction coefficient C_f computed by the RSM (———) and the $k-\epsilon-v$ model (·····). • data (Simpson *et al.* 1981).

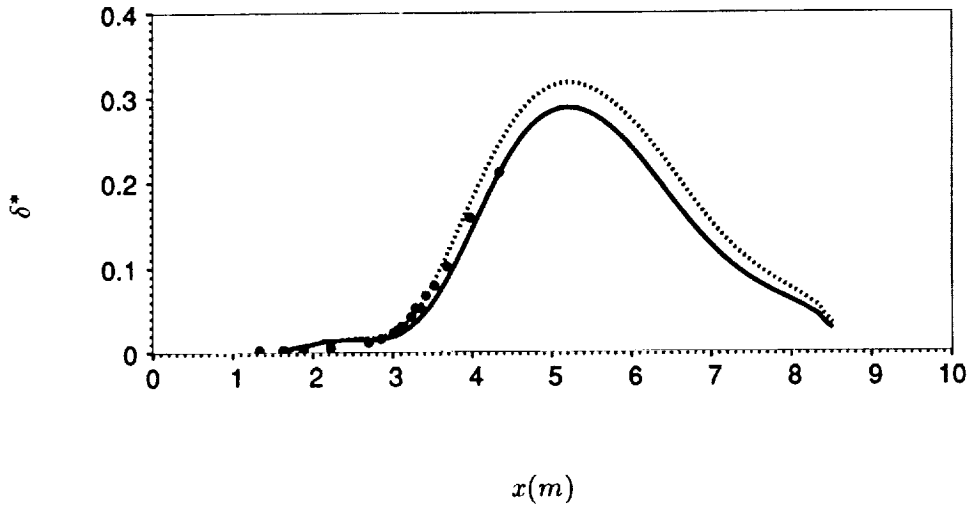

FIGURE 4. Displacement thickness δ^* computed by the RSM (———) and the $k-\epsilon-v$ model (·····). • data (Simpson *et al.* 1981).

a substantial difference; this is expected from the previous figures. The computed C_f's become negative at $x = 3.72\,m$ for the RSM and at $x = 3.35\,m$ for the $k - \epsilon - v$ model, while the measured separation was at $x = 3.45\,m$. However, this discrepancy is not very significant because of the ambiguity in prescribing V, alluded to previously. Celenligil & Mellor (1985) found that their results were very sensitive to the prescribed external pressure gradient. Figure 4 shows a reasonable agreement between the computed displacement thickness δ^* and measurements. It should be noted that as the flow separates, the δ^* grows drastically due to the reverse flow in the separated region. Once again, the $k - \epsilon - v$ model shows stronger displacement effects than the RSM in the separated region. Figures 5 – 9 show more detailed results. In these figures, the x-coordinate is measured relative to the separation point, which is equated to the experimental value of $3.45\,m$. In this way, comparison at various positions will give fair insight on how the model solutions evolve in space upstream and downstream of separation.

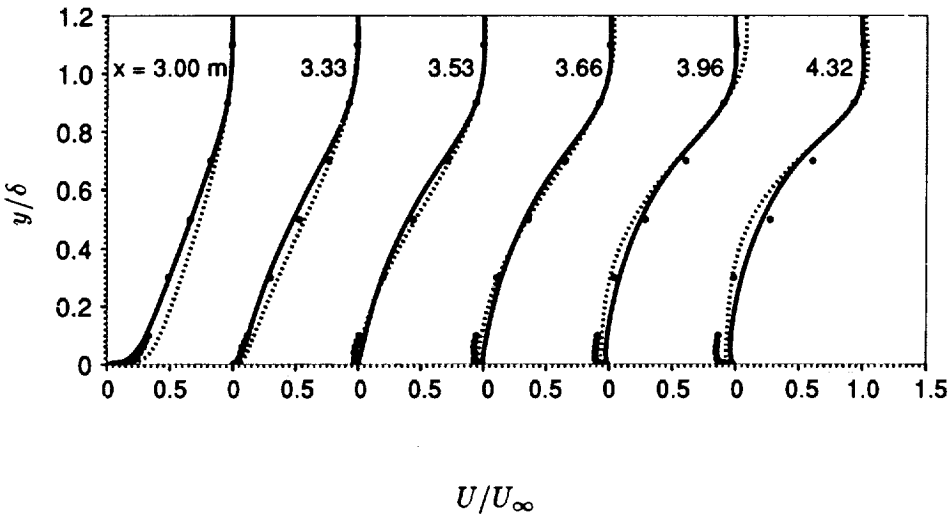

FIGURE 5. Mean flow profiles upstream and in the separated region. • data (Simpson *et al.* 1981).

Figure 5 shows the x-component of the mean velocity at various positions upstream and within the separated region. In the separated region, the $k - \epsilon - v$ model calculation shows closer agreement with measurements than the RSM calculation. However, this is mainly because the V profile along the top boundary was obtained for the $k - \epsilon - v$ model. Generally, the models predict the U-velocity profiles in the outer region reasonably well, but they underpredict mean backflow in the separated region. This underprediction of backflow is probably due to the Reynolds stress gradient being too large near the wall, hence transferring too much forward momentum from the outer flow.

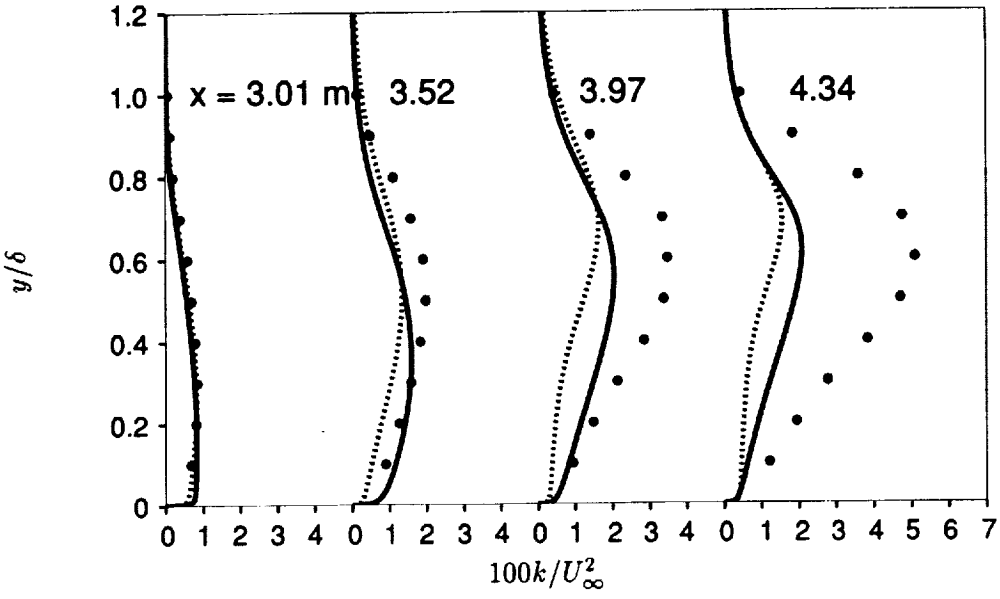

FIGURE 6. Profiles of turbulent kinetic energy computed by the RSM (———) and the $k-\epsilon-v$ model (·····). • data (Simpson *et al.* 1981).

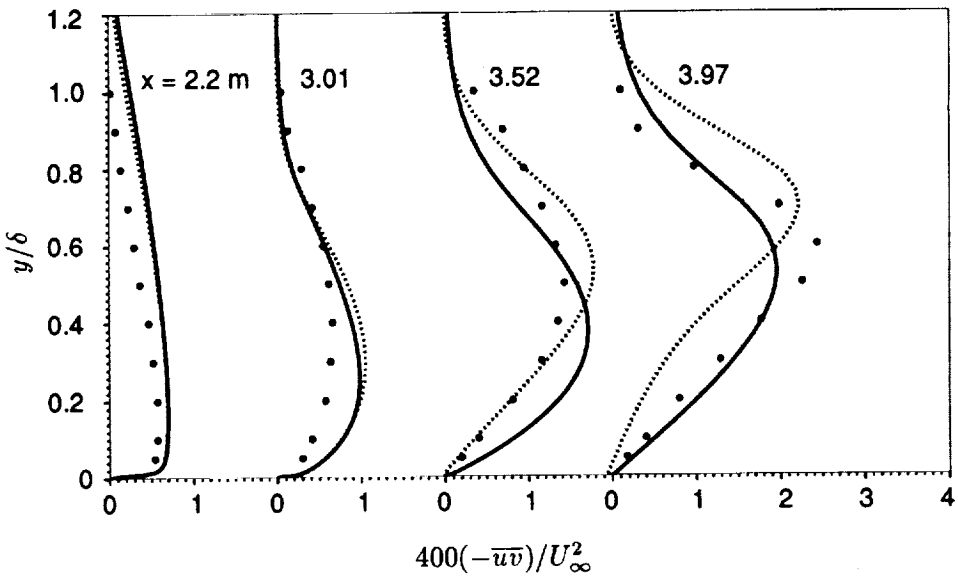

FIGURE 7. Profiles of Reynolds shear stress computed by the RSM (———) and the $k-\epsilon-v$ model (·····). • data (Simpson *et al.* 1981).

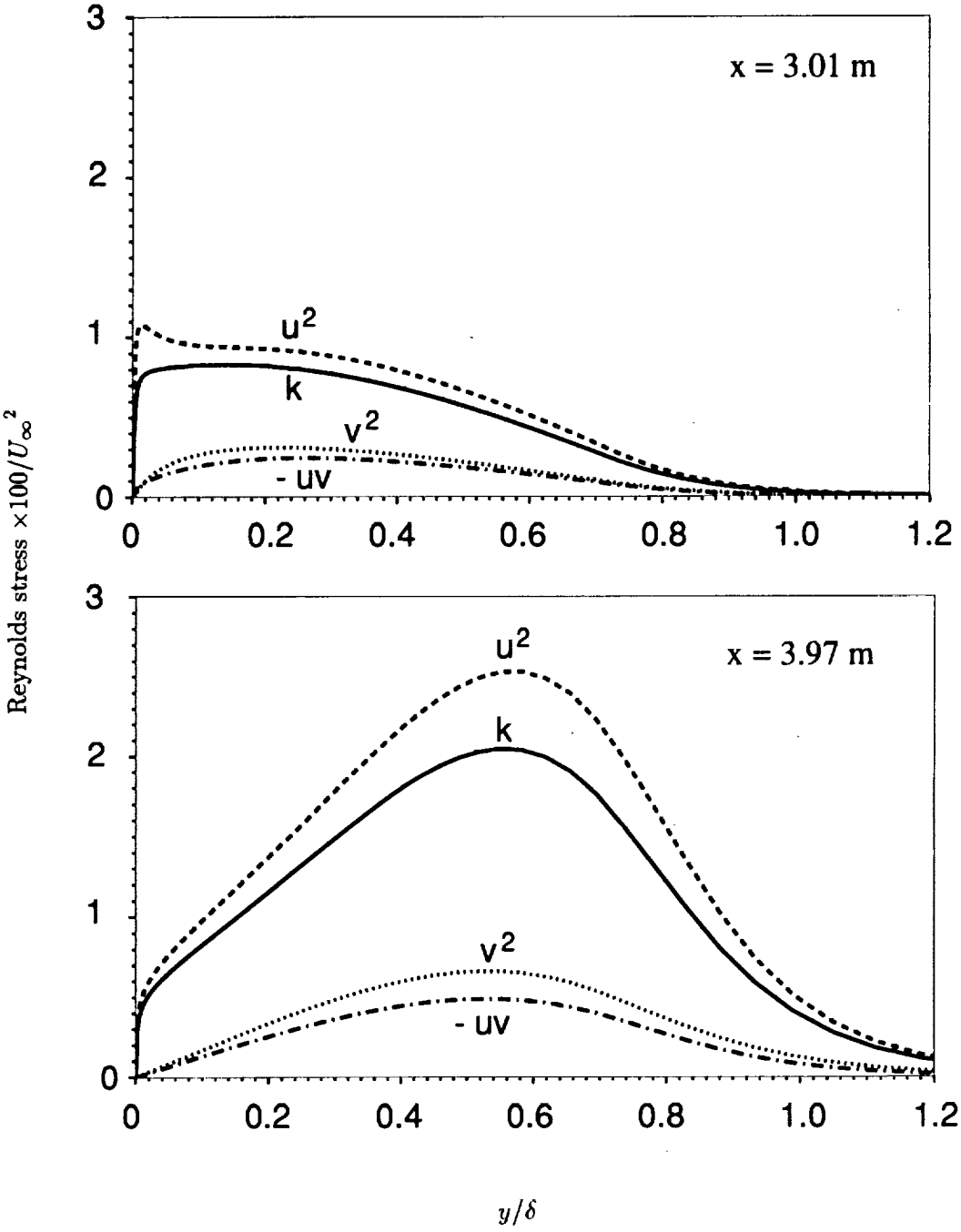

FIGURE 8. Profiles of Reynolds stresses.

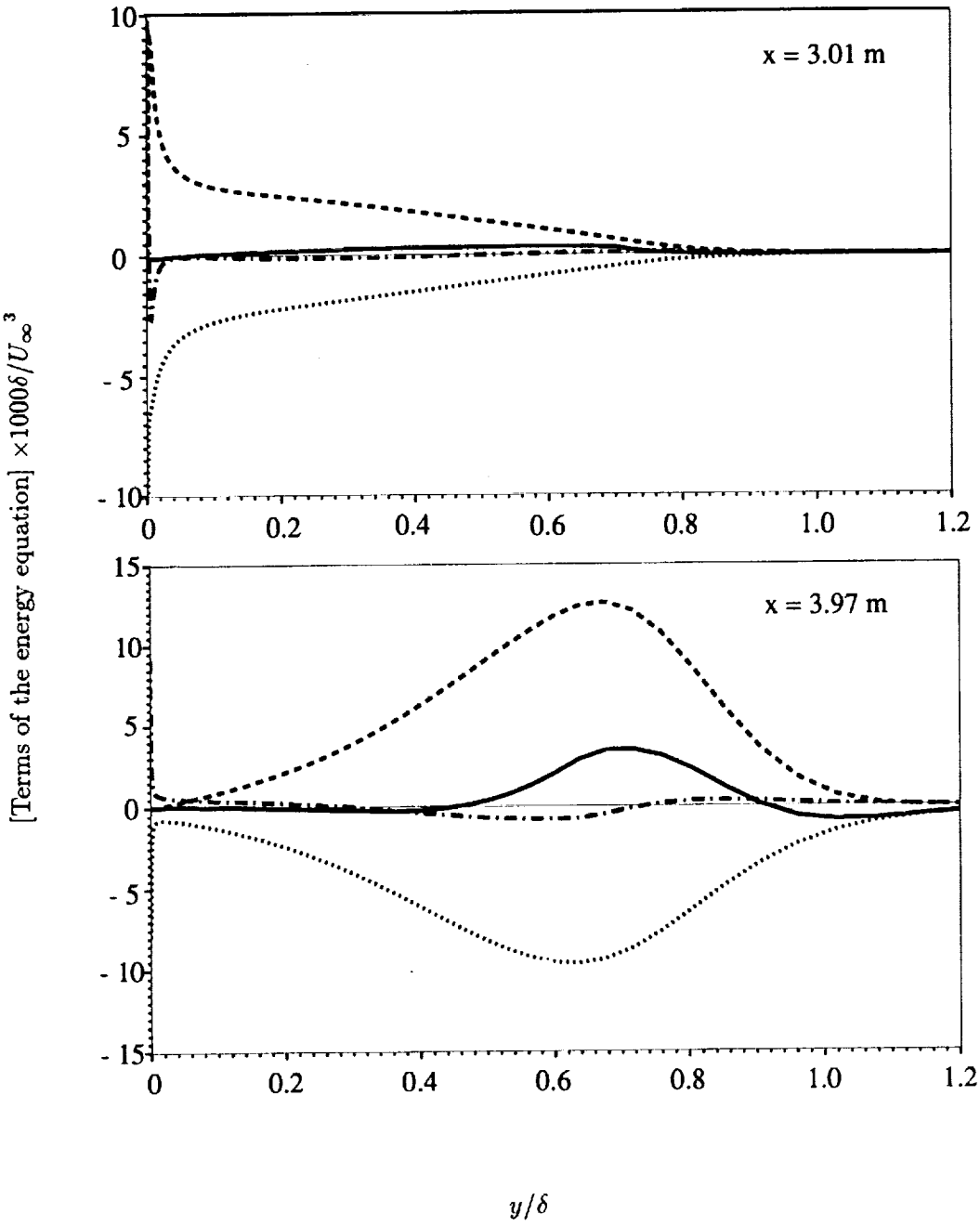

FIGURE 9. Turbulence energy balance : ——— , advection; - - - - , production; ····· , dissipation; —·— , diffusion.

Figures 6 and 7 show turbulent kinetic energy and Reynolds shear stress profiles at various positions. The turbulent kinetic energy predictions by both the $k-\epsilon-v$ model and the RSM are significantly too low in the separated shear layer. Low predictions of k were similarly found by De Henau *et al.* (1990) and Atkinson & Castro (1991). In figure 7, the level of $-\overline{uv}$ is in general agreement with experiments, but discrepancies exist in the shapes of the profiles. The models of Celenligil & Mellor (1985) and Atkinson & Castro (1991) severely underpredicted the Reynolds shear stress in the separated region.

In figure 8, profiles of Reynolds stresses computed by the RSM are plotted at $x = 3.01\,m$, and $3.97\,m$ upstream and downstream of the separation, respectively. As expected, Reynolds stresses at $x = 3.01\,m$ have profiles typical of an adverse-pressure-gradient boundary layer. At $x = 3.97\,m$ the maxima of Reynolds stresses occur at $y/\delta \approx 0.55$. Profiles of $\overline{w^2}$ can be deduced from the figure using the relationship $\overline{w^2} = 2k - (\overline{u^2} + \overline{v^2})$, which yields $\overline{w^2} \approx \overline{v^2}$ over a wide range. Overall, one can say that $\overline{u^2}$ is the largest and $\overline{uv}$ is the smallest of Reynolds stress components everywhere.

Figure 9 shows balances of the turbulence kinetic energy equation. Terms in Eq. (10) were normalized by the boundary layer thickness and local free-stream velocity. The production is mainly balanced by the dissipation while the advection and the diffusion are relatively small.

In conclusion, predictions of skin friction and displacement thickness for the pressure-induced separating boundary layer are in agreement with experimental measurements, but both the $k-\epsilon-v$ model and the RSM show insufficient backflow in the separated region. The models also underestimate the turbulent kinetic energy in the separated shear layer; the Reynolds shear stress is more accurately predicted. Overall, the separated flow computation was a bit unsatisfactory because suction and blowing at the upper boundary had to be imposed to simulate the experimental conditions. However, it is significant that the $k-\epsilon-v$ model and the RSM are able to produce a reasonable separated flow.

3. Future plans

Further assessment and improvement of the RSM for separated flows will continue in the future. Due to the ambiguity of the imposed flow conditions for the pressure-driven separated boundary layer computation, it is difficult to draw any conclusion on the model performance. Therefore, it is necessary to have a well-defined test case with clear-cut boundary conditions in order to isolate phenomena which are directly related to the turbulence model. With this consideration, turbulent flow over a backward-facing step is chosen as the next test case. The backward-facing step flow is an excellent case not only for studying the flow physics of separated and reattaching turbulent shear layers, but also for developing turbulence models. Numerical results will be compared with DNS (Direct Numerical Simulation) as well as experimental data.

As discussed in §2.1, a possible model improvement can be achieved simply by substituting a new quasi-homogeneous Reynolds stress model for the source term

in Eq. (8). The present RSM uses the basic version of the LRR model (Launder *et al.* 1975) in which the modeled rapid pressure-strain correlation is linear in the anisotropy tensor. Following the LRR model, many new ideas have been employed to develop more elaborate models for the last decade. Recently, Speziale *et al.* (1991) introduced a new second-order closure model - the SSG model - which is based on invariant dynamical systems analysis coupled with some additional constrains. This model is quadratically nonlinear in the anisotropy tensor and shows improvement over the LRR model for a variety of homogeneous turbulent flows. After investigating the performance of the RSM for the backward-facing step flow, the feasibility of the SSG model as the source term for the elliptic relaxation formulation will be studied.

REFERENCES

ATKINSON, K. N. & CASTRO, I. P. 1991 Computations of a separated turbulent boundary layer, Turbulent Shear Flows Conference, 20-2.

CELENLIGIL, M. C.& MELLOR, G. L. 1985 Numerical solution of two-dimensional turbulent separated flows using a Reynolds stress closure model. *J. Fluids Engr.* **107,** 467-476.

DALY, B. J. & HARLOW, F. H. 1970 Transport equations of turbulence. *Phys. Fluids.* **13,** 2634-2649.

DE HENAU, V., RAITHBY, G. D. & THOMPSON, B. E. 1990 Prediction of flows with strong curvature and pressure gradient using the k-ϵ turbulence model. *J. Fluids Engr.* **112,** 40-47.

DIANAT, M. & CASTRO, I. P. 1991 Turbulence in a separated boundary layer. *J. Fluid Mech.* **226,** 91-123.

DRIVER, D. M. 1991 Reynolds shear stress measurements in a separated boundary layer flow, AIAA paper 91-1787.

DURBIN, P. A. 1991 Near-wall turbulence closure modeling without "damping functions". *Theoretical and Computational Fluid Dynamics.* **3,** 1-13.

DURBIN, P. A. 1992 Near wall turbulence closure modeling without 'damping functions'. *CTR Manuscript 113,* Stanford Univ./NASA Ames (to appear in *J. Fluid Mech.*).

GOSMAN, A. D.& PUN, W. M. 1974 Calculation of recirculating flows. Research Report No. HTS/74/2., Dept. Mech. Engr. Imperial College, London, England.

KO, S. 1991 Near-wall turbulence modeling for boundary layers with separation. *Annual Research Briefs.* Center for Turbulence Research, Stanford Univ./NASA Ames, 137-146.

LAUNDER, B. E., REECE, G. J. & RODI, W. 1975 Progress in the development of a Reynolds-stress turbulence closure. *J. Fluid Mech.* **68,** 537-566.

LEONARD, B. P. 1979 A stable and accurate convective modelling procedure based on quadratic upstream interpolation. *Computer Methods in Applied Mechanics and Engr.* **19,** 59-98.

MENTER, F. R. Performance of popular turbulence models for attached and separated adverse pressure gradient flows, AIAA paper 91-1784.

PATANKAR, S. V. 1980 Numerical Heat Transfer and Fluid Flow. McGraw-Hill, New York.

SIMPSON, R. L., CHEW, Y. -T. & SHIVAPRASAD, B. G. 1981 The structure of a separating turbulent boundary layer. Part 1. Mean flow and Reynolds stresses. *J. Fluid Mech.* **113,** 23-51.

SPEZIALE, C. G., SARKAR, S.& GATSKI, T.B. 1991 Modelling the pressure-strain correlation of turbulence: an invariant dynamical systems approach. *J. Fluid Mech.* **277,** 245-272.

Progress in modeling hypersonic turbulent boundary layers

By O. Zeman

1. Motivations and objectives

A good knowledge of the turbulence structure, wall heat transfer, and friction in turbulent boundary layers (TBL) at high speeds is required for the design of hypersonic airbreathing airplanes and reentry space vehicles. This work reports on recent progress in modeling of high speed TBL flows. The specific research goal described here is the development of a second order closure model for zero pressure gradient TBL's for the range of Mach numbers up to hypersonic speeds with arbitrary wall cooling requirement.

2. Accomplishments

In this report, new compressible models and theories that lead to their development are reviewed with the focus on compressibility effects in quasi-equilibrium turbulent boundary layers. The primary purposes are to report on a new second order closure model (SOC) developed for hypersonic TBL's and to present comparison of model results with experiments in zero pressure gradient TBL's up to freestream Mach number $M_e = 10.3$. The following section is a modified and abbreviated version of the paper of Zeman (1993). The model described in subsection 2.2.2 is a new contribution.

2.1 Introduction

Recent renewed interest in high speed aerodynamics has led to new developments in theory, simulation, and modeling of compressible turbulence. Availability of direct numerical simulations (DNS) of basic homogeneous compressible flows has greatly facilitated the development of new models for compressible turbulent flows. In view of the recent DNS results and experiments, it now appears that in many flows of practical interest, the turbulence cannot be treated by the so-called anelastic models, where the variation of *averaged* density and pressure are accounted for but not their fluctuating fields. In the past three years, this realization has lead to development of a variety of new models which account for the effect of fluctuating divergence (dilatation) on turbulence. In this paper, we shall focus mainly on the compressibility effects pertaining to TBL's with zero pressure gradients (ZPG). The paper is organized as follows: in the following section, we present the background and review of the current representation of the dilatational terms in the modeling equations. The subsequent sections highlight the new SOC model for super/hypersonic TBL's, make comparisons with experiments, and conclude with a discussion of compressibility effects in high speed TBL's and their consequences for the turbulence models.

2.2 Background, review

As shown first in Zeman[1], the Favre-averaged energy governing equations for homogeneous compressible turbulence, in the absence of any forcing, can be written as

$$\frac{1}{2}\frac{Dq^2}{Dt} = -(\epsilon_s + \epsilon_d - \Pi_d) \tag{1}$$

$$\frac{D\widetilde{T}}{Dt} = (\epsilon_s + \epsilon_d - \Pi_d)c_p^{-1}, \tag{2}$$

where $q^2/2 = \widetilde{u_j u_j}/2$ is the turbulence kinetic energy and $c_p\widetilde{T}$ is the mean enthalpy (Favre and Reynolds averages are denoted by tilde and overbar, respectively) and $\epsilon_s = \nu\overline{\omega_j\omega_j}$ is the solenoidal dissipation associated solely with the enstrophy $\overline{\omega_j\omega_j}$ (of the solenoidal velocity field). The compressibility effects are contained in two terms labeled ϵ_d and Π_d. These are associated with the dilatational (or compressive) velocity field which has nonzero dilatation $u_{j,j}$ (denoted hereafter by θ). Thus, the dilatation dissipation $\epsilon_d = \frac{4}{3}\nu\overline{\theta^2}$ and $\Pi_d = \overline{p\theta}/\overline{p}$ is the pressure-dilatation correlation (per unit mass). The compressive and solenoidal fields are strictly separable only in homogeneous turbulent flows; in TBL's, the treatment of ϵ_d and ϵ_s as two distinct contributions to total dissipation is valid only approximately.

2.2.1 Dilatation dissipation

The need for a representation in turbulence models of dilatational dissipation ϵ_d associated with fluctuating Mach number has been now recognized by many authors (see e.g. Viegas and Rubesin 1991; Wilcox 1991). Computational results indicate that in TBL's over insulated walls for $M_e \leq 9$, the maximum values of M_t are below 0.3, and hence ϵ_d due to shocklet dissipation is insignificant. However, in hypersonic TBL's with increasing wall cooling, the sonic speed a near the wall decreases and the M_t levels grow larger. The shocklet dissipation then assumes a controlling role: it maintains M_t below a certain threshold level, which according to the computations is always below $M_t = 1$; we find this aspect of the dissipation physically appealing. The basic expression for the shocklet dissipation given in Zeman (1990) is

$$\epsilon_d \propto \frac{q^3}{\ell}F(M_t^*, K) \tag{3}$$

where ℓ is a suitably defined turbulence lengthscale and $F(M_t^*, K)$ is a function of the r.m.s. Mach number. M_t^* is related to the *principal* r.m.s. Mach number $M_t = q/\sqrt{\gamma R\widetilde{T}}$ through $M_t^* = \sqrt{\frac{2}{\gamma+1}}M_t$. The parameter K is the kurtosis of the fluctuating speed $\sqrt{u_j u_j}$ intended to characterize intermittency of a particular turbulent flow. The computed curves $F(M_t^*, K)$ vs M_t^* for different K have been given in Fig. 2 of Zeman (1990). It is of note that the dependence of ϵ_d on the specific heat ratio γ (through M_t^*) improves the correlation of mixing layer growth rate with M_c, when the layer streams are gases with different values of γ (Viegas and Rubesin 1991).

In modeling (3D) turbulence, the quantities q^3/ℓ and ϵ_s are considered interchangeable; however, it should be emphasized that (3) is valid also in 2D turbulence (DNS only) where typically $q^3/\ell >> \epsilon_s$. We also point out that no near-wall correction is necessary in the expression for ϵ_d since F approaches zero at a much faster rate than the turbulent Reynolds number R_t (defined hereafter as $R_t = q^4/9\epsilon_s\nu$). As in high speed mixing layers, $F(M_t^*, K)$ for TBL's is approximated by an exponential function

$$F(M_t^*, K)) = \frac{\epsilon_d}{\epsilon_s} = c_d(1 - \exp\{-(\frac{M_t^* - M_{to}}{\sigma_M})^2\}). \tag{4}$$

The parameters c_d, M_{to}, and σ_M are functions of the kurtosis K to approximate the shape of the F-curves for a specified K (see Zeman 1993 for details).

2.2.2 Pressure-dilatation correlation in ZPG TBL's

In inhomogeneous flows, nontrivial contributions to the pressure-dilatation term arise from the interaction between the mean density gradient $\nabla\overline{\rho}$ and fluctuating pressure field. The derivation of the density-gradient contribution $(\overline{p\theta})_\rho$ to the pressure dilatation has been presented in Zeman (1991, 1993). The form of the model for flat plate TBL's (ZPG) is

$$(\overline{p\theta})_\rho = \tau q^2 \widetilde{u_2^2}(\overline{\rho}_{,2})^2 \frac{1}{\overline{\rho}} \tag{5}$$

In the SOC model, the contribution (5) is indispensable for assuring a proper (Van Driest) scaling of mean and fluctuating velocities in the inertial sublayer as shown in Zeman (1991, 1993). However, in the presence of wall heat transfer (cooling), the model (5) has proved to be ineffective in enforcing the correct scaling, and it had to be modified (as discussed briefly at the end of the following section).

2.3 Closure of the compressible TBL equations

In the boundary-layer approximation, the principal equations governing the mean flow field are the mass, momentum, and enthalpy conservation Favre-averaged equations

$$\frac{D\overline{\rho}}{Dt} = 0 \tag{6}$$

$$\overline{\rho}\frac{D\widetilde{U}_i}{Dt} = -\overline{p}_{,i} - (\overline{\rho}\widetilde{u_i u_j} - 2\mu S_{ij}^*)_{,j} \tag{7}$$

$$\overline{\rho}\frac{D\widetilde{T}}{Dt} = -(\overline{\rho}\widetilde{T'u_j}(1 - F_p) - \kappa\widetilde{T}_{,j})_{,j} + \overline{\rho}(\epsilon_s + \epsilon_d - \Pi_d)c_p^{-1}, \tag{8}$$

and the density is obtained from the equation of state $\overline{\rho} = p_e/(R\widetilde{T} + \widetilde{u_2^2})$ where p_e is the freestream (constant) pressure. F_p in (8) denotes the ratio of pressure to enthalpy fluxes $F_p = \overline{pu_i}/(\overline{\rho}c_p\widetilde{T'u_i})$. In compressible TBL's, F_p is expected to be non zero, and Zeman (1993) proposed an expression

$$F_p = 0.3(1 - exp\{-(\frac{M_t}{0.4})^2\}). \tag{9}$$

The coefficient (0.3) in (9) was chosen to recover the correct adiabatic wall temperature for the range $0 < M_e < 11$. The small M_t limit, $F_p \to M_t^2$ is required by scaling arguments.

It is of interest to note that if the turbulent fluctuations follow an adiabatic relation $p \propto \frac{\gamma}{\gamma-1}T'$, then F_p would be unity, and no heat would be transferred by turbulence. In the presence of heat sources, the compressive turbulence field is ineffective in transferring heat since it is virtually adiabatic; hence, the heat is transferred by the solenoidal turbulence only. In this sense, $1 - F_p$ in (8) reflects the reduced mixing efficiency due to turbulence of acoustic origin.

The remaining quantities needed to close the mean momentum and enthalpy equations (7) and (8) are the Reynolds stresses $\widetilde{u_i u_j}$ and the heat fluxes $\widetilde{T' u_i}$. General conservation equations for these quantities are shown in Zeman (1993). These equations contain the following terms requiring closure: pressure gradient-velocity and pressure gradient-temperature correlations denoted respectively by Π_{ij} and Π_i, the triple-moment (transport) terms, the solenoidal dissipation ϵ_s, and the compressibility terms ϵ_d and $\Pi_d \equiv \overline{p\theta}/\overline{\rho}$.

The pressure and transport terms are modeled in the same manner as their incompressible (Reynolds averaged) counterparts and developed previously by Zeman and Jensen (1987) for atmospheric TBL's (rough walls) and by Zeman (1990) for free compressible flows. Zeman (1993) modified the rapid part of Π_{ij} to account for the Reynolds number effects near smooth walls. This has been accomplished by making the coefficients associated with rapid terms, functions of the Reynolds number R_t. For the asymptotically large values of R_t, the rapid term coefficients converge to the values for the rough wall TBL as discussed above.

The effect of the rapid pressure terms Π_i and Π_{ij} is best illustrated by writing closure equations for the shear stress $\widetilde{u_1 u_2}$ and heat flux $\widetilde{T' u_2}$ in 2D flat plate TBL. With x_1 in streamwise and x_2 in wall-normal direction, one obtains

$$\frac{D\widetilde{u_1 u_2}}{Dt} = -C_m \frac{\widetilde{u_1 u_2}}{\tau} - 0.4(\widetilde{u_2^2} - 5\triangle\alpha b_{11} q^2)\widetilde{U}_{1,2} + \quad T.T. \tag{10}$$

$$\frac{D\widetilde{T' u_2}}{Dt} = -C_\theta \frac{\widetilde{T' u_2}}{\tau} - (\widetilde{u_2^2} - 5\triangle\alpha b_{11} q^2)\widetilde{T}_{,2} + \quad T.T. \tag{11}$$

We can immediately see that apart from the transport terms ($T.T.$), (10) and (11) have a similar form which also suggests that $|T'| \propto |u_1|$. The similarity has been achieved by the novel formulation of the rapid part of Π_i. By neglecting the advection and transport terms, (10) and (11) reduce to algebraic relations $\widetilde{u_1 u_2} = -\nu_T U_{1,2}$, and $\widetilde{T' u_2} = -\alpha_T \widetilde{T}_{,2}$ with the eddy viscosity and diffusivity ν_T and α_T being proportional, i.e.

$$\nu_T \propto \alpha_T \propto \tau \widetilde{u_2^2}[1 - 5\triangle\alpha \frac{b_{11}}{b_{22} + 1/3}]. \tag{12}$$

Hence, in the algebraic approximation, the model yields a constant turbulent Prandtl number $Pr_t = \nu_T/\alpha_T$; the model constants were chosen so that $Pr_t = 0.9$,

the value which is supported by the DNS data in a channel flow, and by experiments in TBL's. In (12), b_{ij} is the anisotropy tensor and $\Delta\alpha$ is a R_t-dependent coefficient in the rapid pressure model (described in Zeman 1993).

The model equation for ϵ_s has a conventional form independent of M_t, except for the wall treatment. The wall boundary value $\epsilon_s(y=0)$ is determined from the approximate integral balance of the kinetic energy equation

$$\int_0^\infty \{P_s - \epsilon_s - \epsilon_d + \Pi_d\} dy = 0$$

where mean convection is ignored and the no-slip condition has been used. Furthermore, to eliminate the unphysical wall singularity in the ϵ_s-equation and in the return-to-isotropy pressure terms (due to $\tau = q^2/\epsilon_s \to 0$), the minimum τ is set by the Kolmogorov time scale

$$\tau \geq 5\sqrt{\frac{\nu}{\epsilon_s}}, \tag{13}$$

as suggested by Durbin (1991).

2.3.1 Modification of $\overline{p\theta}$ in the presence of wall heat flux

As mentioned earlier, in the presence of wall heat transfer, the model $(\overline{p\theta})_\rho$ in (5) has to be modified since the wall heat flux induces an entropic temperature field, giving spurious contributions to $\overline{p\theta}_\rho$. Zeman (1993) proposed to decompose the temperature field on the adiabatic contributions $T_a(\mathbf{x},t)$ (corresponding to an insulated wall TBL) and on the entropic contributions $T_s(\mathbf{x},t)$ which arise due to the surface heat flux alone (no dynamic heating); the actual temperature field is the sum $T = T_s + T_a$. The appropriate density gradient to be applied in (5) must be based on T_a, i.e. $\overline{\rho}_{,2}/\overline{\rho} \approx -(\widetilde{T}_a)_{,2}/\widetilde{T}$. The details of the determination of the entropic and adiabatic temperatures are presented in Zeman (1993).

2.4 Comparison with boundary layer experiments

The TBL computations are made by forward integration of the model equations starting with some initially thin TBL with the momentum thickness Reynolds number $Re_\theta = U_e\theta/\nu_e = 200-500$. The numerical scheme utilizes the compressible von Mises' transformation (Liepmann & Roshko 1967) in the inertial and outer region of the TBL where $y^+ \geq 30$, and, in the region below $y^+ = 30$ (where advection terms are negligible), the TBL is solved as a parallel flow. The vertical velocity in this region is nonzero (due to density variation) and is eliminated by the transformation to $\eta = \int_0^y \overline{\rho}/\rho_w dy$. This computational method is effective and accurate.

Fig. 1 is a sample of the model-experiment comparison: the streamwise r.m.s. fluctuations are plotted in a similarity form $(\overline{\rho}\widetilde{u_1''^2}/\tau_w)^{1/2}$ vs. y/δ for a variety of Mach numbers and cooling rates. The universal behavior of the computed profiles is quite surprising; the cross-hatched area represents the measurements as compiled by Dussauge and Gaviglio (1987) (the first of these authors has pointed out to me that the low hot-wire value of u-fluctuations near the wall are likely due to errors associated with the transonic flow regime).

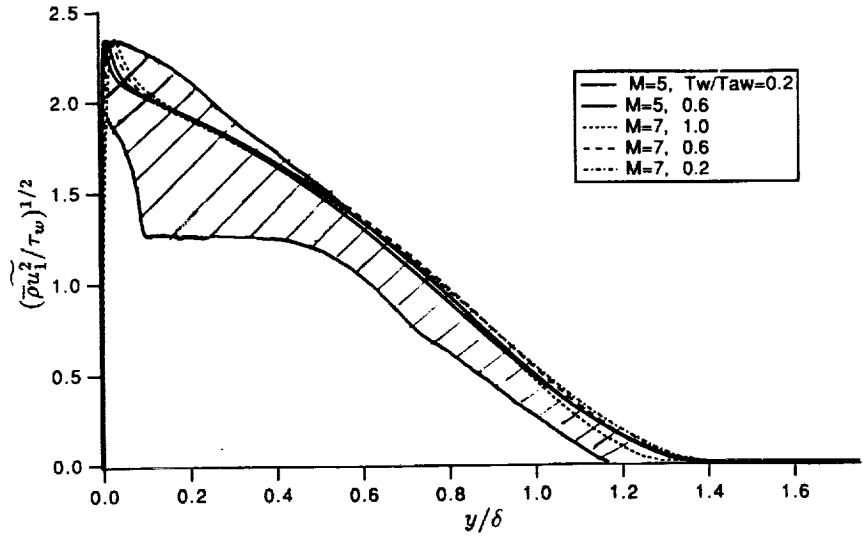

FIGURE 1. Similarity profiles of the streamwise r.m.s. fluctuations; cross-hatched area represents the scatter of experimental data compiled by Dussauge and Gaviglio (1986).

From a practical viewpoint, the most important test of a TBL model is its capability to predict the friction coefficient C_f and the Stanton number St, defined as

$$C_f = 2\frac{\tau_w}{\rho_e U_e^2} \quad St = \frac{q_w}{c_p \rho_e U_e (T_w - T_{aw})},$$

where q_w is the wall heat flux and T_{aw}, T_w are the adiabatic recovery and actual wall temperatures.

Fig. 2 shows standard plots of the ratio C_f/C_{fo} as a function of M_e and T_w/T_{aw} where C_{fo} is the low-speed value of $C_f(M_e \approx 0)$ corresponding to the same Re_θ. Fig. 2a shows the model-computed values of C_f/C_{fo} *vs* M_e, for an insulated-wall TBL for $Re_\theta \approx 10^4$ and the Van-Driest II curve; a few data points are shown in the hypersonic range. Fig. 2b shows C_f/C_{fo} *vs* T_w/T_{aw} for different M_e. The unknown value of C_{fo} is assumed $C_{fo} = 0.02632 Re_\theta^{-0.25}$. The model-computed values of C_f are in good agreement with theory and the data.

The model-experiment comparisons of St *vs* C_f is shown in Fig. 3. The model values (for the range $T_w/T_{aw} = 0.2-0.6$) indicate the Reynolds analogy factor $F_R = 2St/C_f \approx 1.2$; the displayed experimental values are in the range $F_R = 0.9 - 1.2$. In his review of experiments, Bradshaw (1977) suggests F_R be in the range $1.1 - 1.2$. In view of the likely experimental errors, the model predictions of the principal parameters C_f and St are consistent with the data and theory.

Fig. 4 consists of examples of the temperature profiles in the hypersonic range of Mach numbers. Fig. 4a shows model-experiment comparison of $\widetilde{T}/T_e(y/\delta)$ for an insulated-wall TBL in helium with $M_e = 10.3$; Fig. 4b is for $M = 8.2$ in air and with significant wall cooling ($T_w/T_{aw} = 0.28$). The computed temperature

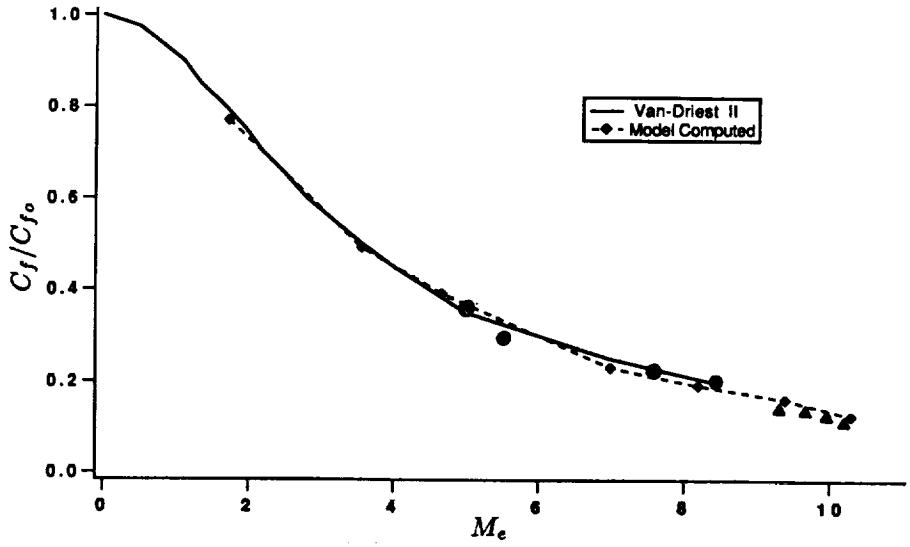

FIGURE 2. Variation of friction coefficient C_f/C_{fo} vs. M_e at $R_\theta \approx 10^4$. Solid line is the Van-Driest II, data points labeled ▲ are from Watson (1978), and • are from Lobb *et al.* (shown in Liepmann and Roshko (1967).

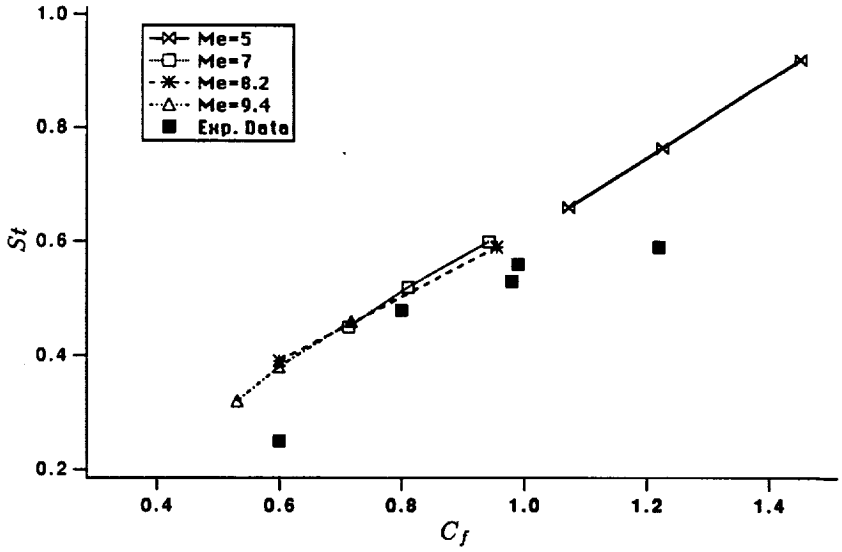

FIGURE 3. Variation of Stanton number St with C_f for $T_w/T_{aw} = 0.2 - 0.6$. Experimental data are from Laderman and Demetriades (1974), Kussoy and Horstman (1992), and Marvin and Coakley (1989).

profiles compare well with experiments (conducted on a sharp-edge flat plate). Of particular note is the prediction of the recovery temperature in the adiabatic TBL and of the temperature maximum near the wall in the cooled TBL.

To demonstrate the model performance at low speeds, in Fig. 5 the modeled velocity profile $U^+(y^+)$ is compared with the DNS results of Spalart (1988). Although Spalart's TBL Reynolds number, $Re_\theta = 1410$, is below what is considered a minimum self-similarity value, $Re_\theta = 3000$, the model prediction is evidently in good agreement with the DNS.

2.5 Model transition-to-turbulence prediction

There are two kinds of transition to turbulence, what F. T. Smith calls the civilized and the savage. In the civilized transition, small disturbances grow in accordance with the appropriate instability mechanisms, eventually reaching a point where transition to turbulence is initiated by strong nonlinearities and formation of turbulent spots in the flow. In the savage, or by-pass transition, the stage of the orderly disturbance growth is bypassed, and turbulence is directly initiated by a nonlinear process.

A fair indicator of the tendency to transition is the momentum Reynolds number Re_θ of the pre-transition, laminar boundary layer. Re_θ accounts for the flow history, and the transition Reynolds number $Re_{\theta t}$ correlates well with the transition onset on flat plates. Typically, turbulence models use transition formulas which inform the model, on the basis of values of Re_θ, pressure gradient, and freestream turbulence intensity, when to turn on the eddy viscosity. Wilcox (1992) mentions the remarkable property of his k-ω model "to describe the nonlinear growth of flow instabilities from laminar flow into the turbulent flow regime." In order to recover the appropriate transition Reynolds number for the Blasius profile, Wilcox modified the model parameters (as functions of turbulent Reynolds number R_t). Hence again, a correction has been provided to inform the model when to begin to amplify turbulence.

A remarkable property of the present model is its capability to mimic transition without any specific corrections added. This capability was tested only for high Mach numbers, and the results for two freestream Mach numbers are depicted in Fig. 6. The computations started with a thin TBL with a relatively small $Re_\theta \leq 200$. As seen in Fig. 6, the turbulence is initially attenuated and the TBL laminarizes. Only when Re_θ reached a certain (transition) value do the residual fluctuations within the boundary layer begin to rapidly grow until an equilibrium TBL is attained. More detailed investigations showed that $(Re_\theta)_t$ increased with M_e in a manner reminiscent of observed experimental transition (assuming $(Re_\theta)_t \propto \sqrt{Re_x t}$).

It is of note that the transitional growth of turbulent energy first occurred in the upper part of the layer in the vicinity of the maximum of the mass vorticity $\overline{\rho}U_{,y}$ (generalized inflection point). It is known from the stability theory that $(\overline{\rho}U_{,y})_{max}$ is potentially a point of maximum instability growth. In the model, the coincidence between the maxima of q^2 and $\overline{\rho}U_{,y}$ is a combined effect of the pressure-dilatation term $\overline{p\theta}$ in (5) and of strong viscous damping near the wall. At $M_e \geq 5$, the

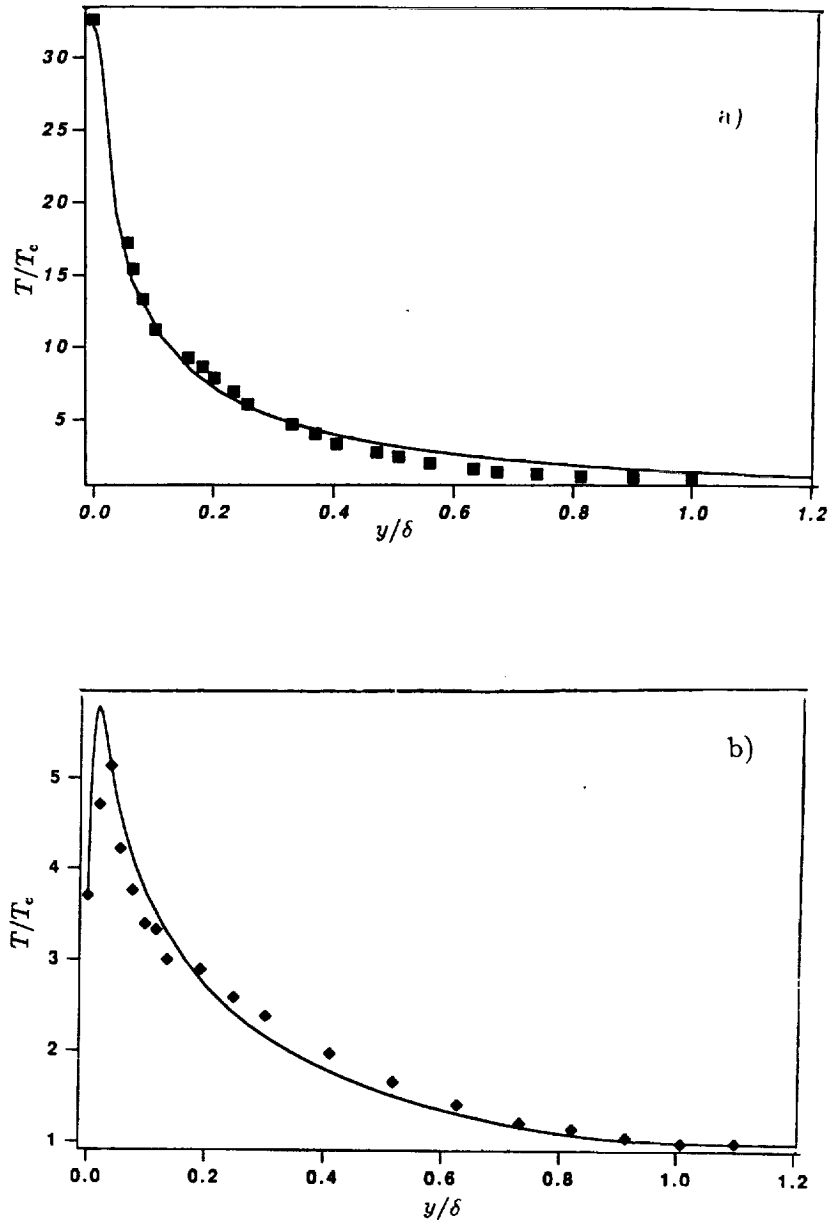

FIGURE 4 A& B. Model-experiment comparison of temperature profiles: a) data of Watson et. al. compiled in Fernholz and Finley (1977) under no. 73050504; $M_e = 10.31$, $R_\theta = 1.5 \times 10^4$, in helium. b) data from Kussoy and Horstman (1992) with $M_e = 8.2$, $T_w/T_{wa} = 0.28$, $R_\theta = 4.6 \times 10^3$.

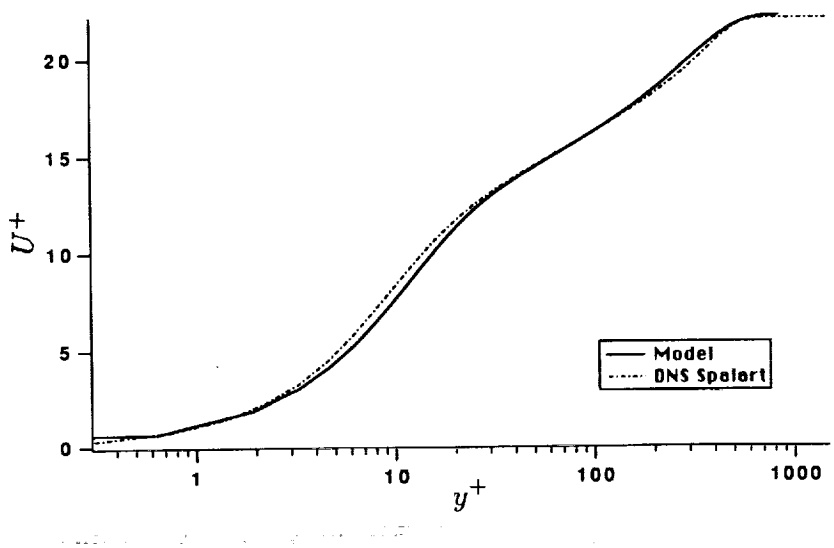

FIGURE 5. Model-DNS comparison of the velocity profiles $U^+(y^+)$. The DNS data are from Spalart (1988).

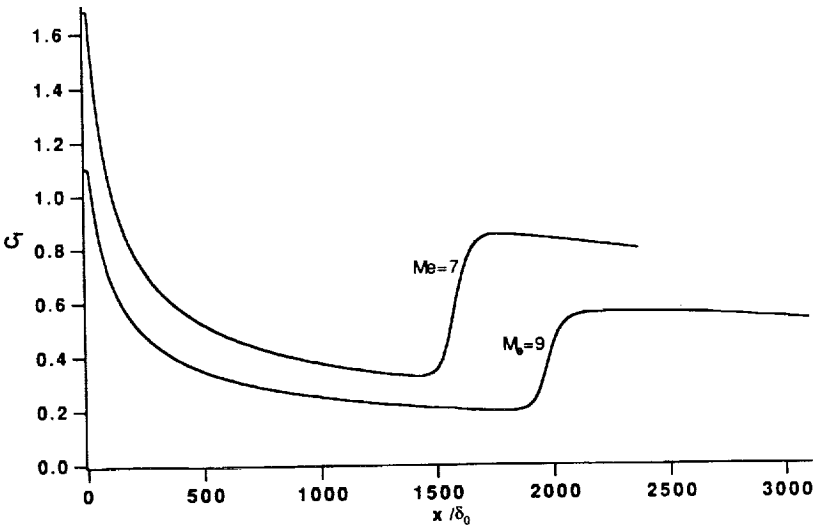

FIGURE 6. Laminarization and transition of a boundary layer at two different Mach numbers: SOC model results. The transition R_θ values are: for $M_e = 7$, $R_{\theta t} = 1100$; for $M_e = 9$, $R_{\theta t} = 1700$

incipient maximum production of q^2 is always in the upper part of the layer near the generalized inflection point; after the transition, the point of maximum q^2 moves towards the wall.

2.6 Discussion, Conclusions

We have developed a new SOC model intended for general applications in high-speed turbulent flows. It incorporates the latest advances in compressible turbulence theories and modeling. The explicit compressibility effect on turbulence is represented by models for the dilatation dissipation ϵ_d and pressure dilatation term $\overline{p\theta}$. Both ϵ_d and $\overline{p\theta}$ depend on the r.m.s. Mach number (M_t) and other structural parameters of the mean and fluctuating flow fields but not on the mean flow Mach number. The model predictions compare well with experiments for a wide range of Mach and Reynolds numbers. The importance of their contributions vary depending on flow speed and configuration.

In some recently published work, the importance of explicit compressibility corrections in TBL models has been questioned. It is indeed possible to adjust incompressible models to perform well in compressible regime without compressibility terms. However, ours is a more fundamental question: are the compressibility effects significant in reality, and can they be isolated in experiments and verified? If we consider DNS "experiments", then the answer is obviously yes. Both the dilatation dissipation and pressure dilatation terms have been identified in DNS of shear-generated and rapidly compressed turbulence. Their seeming unimportance in TBL's is only a question of degree. We find that as M_e and wall cooling increases, ϵ_d becomes increasingly important. In the hypersonic regime with $M_e > 7$ and sufficiently strong wall cooling, the standard k-ϵ models (without some form of dilatation dissipation) are likely to yield supersonic r.m.s. Mach number $M_t > 1$. This is obviously unrealistic; experimental evidence and DNS results suggest that M_t saturates well below unity.

Concerning the importance of the pressure dilatation $\overline{p\theta}$: the density-gradient contribution to $\overline{p\theta}$ constitutes a localized turbulence energy source which preserves the proper Van Driest scaling in the modeled TBL. The present results also suggest that $\overline{p\theta}$ counteracts the damping, viscous effects which have a tendency to laminarize the boundary layer at high values of M_e. The $\overline{p\theta}$-contributions are also related to the ability of the SOC model to mimic transition to turbulence. We intend to address these matters and the plausibility of modeling transitional (high-speed) flows in future investigations.

3. Future work

We shall continue to refine the new SOC model and search out more data for model-experiment comparison. We also hope to apply the model in nonequilibrium situations such as a compression corner flow.

In view of the ability of the SOC model to mimic transition, we shall attempt to investigate the connection between stability theory and model physics and to explore the potential of the SOC models to handle laminar and transitional regimes.

A major effort is going to be directed towards modeling nonequilibrium (incompressible) turbulence, such as in separated flows.

REFERENCES

BLAISDELL, G. A., MANSOUR, N. N.,& REYNOLDS, W.C. 1991 Numerical simulations of compressible homogeneous turbulence. *Ph. D. Thesis.* Mechanical Engineering Dept., Stanford University.

BLAISDELL, G. A. & ZEMAN, O. 1992 Investigation of the dilatation dissipation in compressible homogeneous shear flow. *Proceedings of the 1992 CTR Summer Program.* Stanford Univ./NASA Ames.

BRADSHAW, P. 1977 Compressible turbulent shear layers. *Annual Rev. Fluid Mech.* **9,** 33-54.

DURBIN, P. 1991 Near-wall turbulence closure modeling without "damping functions". *Theoret. Comput. Fluid Dyn.* **3,** 1-13.

FERNHOLZ, H. H., & FINLEY, P. J. 1977 A critical compilation of compressible turbulent boundary layer data. *AGARDograph No. 223.*

DUSSAUGE, J. P. & GAVIGLIO, J. 1987 The rapid expansion of a supersonic turbulent flow: the role of bulk dilatation. *J. Fluid Mech.* **174,** 81.

HORSTMAN, C. C. & OWEN, F. K. 1972 Turbulent properties of a compressible boundary layer. *AIAA J.* **10,** 1418.

KUSSOY, M. I. & HORSTMAN, K. C. 1992 Intersecting shock-wave/turbulent boundary layer interactions at Mach 8.3. *NASA Tech Memo 103909.*

LADERMAN, A. L. & DEMETRIADES, A. 1974 Mean and fluctuating flow measurements in the hypersonic boundary layer over a cooled wall. *J. Fluid Mech.* **63,** 121.

LIEPMANN, H. W. & ROSHKO, A. 1967 *Elements of Gas Dynamics.* John Wiley & Sons, pp 439.

MARVIN, J. G & COAKLEY, T. J. 1989 Turbulence modeling for hypersonic flows. 2nd Joint Europe/US Course in Hypersonics, 1989.

SARKAR, S., ERLEBACHER, G., HUSSAINI, M. Y. & KREISS, H. O. 1991 The analysis and modeling of dilatational terms in compressible turbulence. *J. Fluid Mech.* **227,** 473.

SPALART, P. R. 1988 Direct simulation of a turbulent boundary layer up to $R_\theta =$ 1410. *J. Fluid Mech.* **187,** 61-98.

VIEGAS, J. R., & RUBESI, M. W. 1991 A comparative study of several compressible models applied to high speed shear layers. AIAA paper 91-1783, June 1991, Honolulu, Hawaii.

WILCOX, D. C. 1991 Progress in hypersonic turbulence modeling. AIAA Paper 91-1785, 22nd Fluid Dynamics Conference, Honolulu, Hawaii.

WILCOX, D. C. 1992 The remarkable ability of turbulence model equations to describe transition. 5th Symposium on Numerical and Physical Aspects of Aerodynamic Flows, Long Beach, Florida, Jan. 1992.

WATSON, R. D. 1978 Characteristic of Mach 10 transitional and turbulent boundary layer. NASA Tech Paper 1243.

ZEMAN, O., & JENSEN, N. O. 1987 Modification of turbulence characteristics in flows over hills. *Q. J. Roy. Meteorol. Soc.* **113,** 5.

ZEMAN, O. 1990 Dilatation dissipation: The concept and application in modeling compressible mixing layers. *Phys. Fluids.* **A 2,** 178.

ZEMAN, O. 1991 The role of pressure-dilatation correlation in rapidly compressed turbulence. *CTR Annual Research Briefs 1991.* Stanford University/NASA Ames, 105-117.

ZEMAN, O. 1993 A new model for super/hypersonic turbulent boundary layers. *AIAA Paper 93-0897.* 31st Aerospace Science Meeting, Reno, Nevada, Jan. 1993.

Receptivity in parallel flows: an adjoint approach

By D. C. Hill

1. Motivation and objectives

Linear receptivity studies in parallel flows are aimed at understanding how external forcing couples to the natural unstable motions which a flow can support. The vibrating ribbon problem (Gaster (1965)) models the original Schubauer and Skramstad (1947) boundary layer experiment and represents the classic boundary layer receptivity problem. The process by which disturbances are initiated in convectively-unstable jets and shear layers has also received attention (Balsa (1988), Huerre and Monkewitz (1985), Tam (1978)).

Gaster (1965) was the first to handle the boundary layer analysis with the recognition that spatial modes, rather than temporal modes, were relevant when studying convectively-unstable flows that are driven by a time-harmonic source. The amplitude of the least stable spatial mode, far downstream of the source, is related to the source strength by a coupling coefficient. The determination of this coefficient is at the heart of this type of linear receptivity study.

Traditionally, the Briggs method is applied to Fourier-inversion integrals to find the asymptotic temporal and spatial behavior after a time-harmonic source has been switched on. Ashpis and Reshotko (1990) give a detailed description of this procedure for the vibrating ribbon problem. Unfortunately, the coupling coefficient, which gives a measure of the amplitude of the asymptotic response relative to the amplitude of the source, does not have a very convenient form, either from the point of view of interpretation or of computation. The expression involves derivatives with respect to wavenumber of either a flow quantity or the dispersion relation (Ashpis and Reshotko (1990), Kozlov and Ryzhov (1990), Balsa (1988), Huerre and Monkewitz (1985), Gaster (1965)).

Earlier work (Hill (1992)) indicates that adjoint eigensolutions for the global temporal modes of a cylinder wake characterize rather simply how receptive the wake is to control forces. Can this approach be adapted for the spatial instabilities that occur in boundary layers, jets, and shear layers? The first objective of the present study was to determine whether the various wavenumber derivative factors, appearing in the coupling coefficients for linear receptivity problems, could be re-expressed in a simpler form involving adjoint eigensolutions. Secondly, it was hoped that the general nature of this simplification could be shown; indeed, a rather elegant characterization of the receptivity properties of spatial instabilities does emerge. The analysis is quite distinct from the usual Fourier-inversion procedures, although a detailed knowledge of the spectrum of the Orr-Sommerfeld equation is still required. Since the cylinder wake analysis proved very useful in addressing control considerations, the final objective was to provide a foundation upon which boundary layer control theory may be developed.

2. Background

2.1 The Lagrange identity

The cornerstone of this work is the *Lagrange identity* (Ince (1944)), from which the adjoint equations are extracted. This remarkably powerful relation is implicit in the work of Salwen and Grosch (1981) (here onwards referred to as SG), and Salwen (1979), although it is never stated explicitly. As has already been intimated, the origins of the adjoint analysis can be traced back to work of Lagrange in the late 18th century (See Lagrange's collected works (1867)). Although Fuchs (1858) wrote in German, Ince (1944) credits the use of the word 'adjoint' to him. Adjoint eigensolutions play a key role in the imposition of solvability conditions (the Fredholm alternative) and as such are indispensable to researchers studying nonlinear phenomena using bifurcation theory (Iooss and Joseph (1980)).

The Lagrange identity is developed with reference to the linearized Navier- Stokes equations. If $\underline{V}(\underline{r})$ is a steady incompressible viscous flow field, then linear velocity disturbances $\underline{v}(\underline{r},t)$ and pressure disturbances $p(\underline{r},t)$ upon this flow satisfy

$$\frac{\partial \underline{v}}{\partial t} + \underline{L}(\underline{V};R)\,\underline{v} + \nabla p = \underline{0}, \tag{1}$$

$$\nabla.\underline{v} = 0, \tag{2}$$

where the ith component of the linear operator $\underline{L}(\underline{V};R)$ is

$$\left(\underline{L}(\underline{V};R)\,\underline{v}\right)_i = V_j\frac{\partial v_i}{\partial x_j} + v_j\frac{\partial V_i}{\partial x_j} - \frac{1}{R}\frac{\partial^2 v_i}{\partial x_j^2}. \tag{3}$$

For *any* pair of fields $(\underline{v},p)$ and $(\tilde{\underline{v}},\tilde{p})$, ($(\underline{v},p)$ does not have to satisfy (1) and (2)), defined over the flow domain, the following Lagrange identity is satisfied:

$$\left[\left(\frac{\partial \underline{v}}{\partial t} + \underline{L}(\underline{V};R)\,\underline{v} + \nabla p\right).\tilde{\underline{v}} + \nabla.\underline{v}\;\tilde{p}\;\right] + \left[\underline{v}.\left(\frac{\partial \tilde{\underline{v}}}{\partial t} + \underline{\tilde{L}}(\underline{V};R)\,\tilde{\underline{v}} + \nabla\tilde{p}\right) + p\nabla.\tilde{\underline{v}}\right]$$

$$= \frac{\partial}{\partial t}(\underline{v}.\tilde{\underline{v}}) + \nabla.\underline{J}\big((\underline{v},p),(\tilde{\underline{v}},\tilde{p})\big), \tag{4}$$

where $\underline{\tilde{L}}(\underline{V};R)$ is the adjoint linearized Navier-Stokes operator with components

$$\left(\underline{\tilde{L}}(\underline{V};R)\,\tilde{\underline{v}}\right)_i = V_j\frac{\partial \tilde{v}_i}{\partial x_j} - \tilde{v}_j\frac{\partial V_j}{\partial x_i} + \frac{1}{R}\frac{\partial^2 \tilde{v}_i}{\partial x_j^2}. \tag{5}$$

The vector $\underline{J}\big((\underline{v},p),(\tilde{\underline{v}},\tilde{p})\big)$ is the *bilinear concomitant* with components

$$\Big(\underline{J}\big((\underline{v},p),(\tilde{\underline{v}},\tilde{p})\big)\Big)_j = v_i\tilde{\sigma}_{ij} + \sigma_{ij}\tilde{v}_i, \tag{6}$$

where

$$\sigma_{ij} = p\delta_{ij} - \frac{1}{R}\frac{\partial v_i}{\partial x_j} + V_j v_i, \tag{7}$$

$$\tilde{\sigma}_{ij} = \tilde{p}\delta_{ij} + \frac{1}{R}\frac{\partial \tilde{v}_i}{\partial x_j}. \tag{8}$$

Examining the second term in square brackets on the left hand side of the Lagrange identity (4), we define the adjoint equations

$$\frac{\partial \tilde{\underline{v}}}{\partial t} + \tilde{\underline{L}}(\underline{V}; R)\,\tilde{\underline{v}} + \nabla\tilde{p} = \underline{0}, \tag{9}$$

$$\nabla.\tilde{\underline{v}} = 0. \tag{10}$$

2.2 Bi-orthogonality

A brief summary will be given in this section of the procedure by which bi-orthogonal spatial-eigensolution sets can be constructed for the Orr-Sommerfeld equation. This is essentially a review of the work of SG.

Schensted (1960), and Drazin and Reid (1981) show how general disturbances in spanwise-bounded plane parallel flows can be expanded as a sum of temporal eigensolutions of the Orr-Sommerfeld equation. These eigensolutions together with a set of eigensolutions of the corresponding adjoint equation form a bi-orthogonal set, under the action of an appropriate inner product. SG develop this further and demonstrate how expansion of arbitrary disturbances as a sum of temporal or spatial eigensolutions may be carried out in unbounded flows where, in fact, a continuum of eigensolutions forms part of the spectrum.

Following SG, let $\underline{V}(\underline{r}) = U(y)\hat{x}$ define a two-dimensional parallel flow in the xy-plane, for $y_1 < y < y_2$. For a boundary layer we may have $y_1 \equiv 0$ and $y_2 \equiv \infty$, whereas for a shear layer $y_1 \equiv -\infty$, and $y_2 \equiv \infty$. Writing $\underline{v} = \nabla \times (\psi(x,y,t)\hat{z})$ for some stream function $\psi(x,y,t)$, $\hat{z}$ being the unit vector normal to the plane of the flow, the governing equation is given by the z-component of the curl of (1)

$$\Big(\frac{\partial}{\partial t} + U\frac{\partial}{\partial x}\Big)\nabla^2\psi - \frac{d^2U}{dy^2}\frac{\partial\psi}{\partial x} - \frac{1}{R}\nabla^4\psi = 0. \tag{11}$$

Similarly, writing $\tilde{\underline{v}} = \nabla \times (\tilde{\psi}(x,y,t)\hat{z})$, the adjoint equation is

$$\Big(\frac{\partial}{\partial t} + U\frac{\partial}{\partial x}\Big)\nabla^2\tilde{\psi} + 2\frac{dU}{dy}\frac{\partial^2\tilde{\psi}}{\partial x\partial y} + \frac{1}{R}\nabla^4\tilde{\psi} = 0. \tag{12}$$

No-slip boundary conditions

$$\psi = \frac{\partial\psi}{\partial y} = 0, \text{ and } \tilde{\psi} = \frac{\partial\tilde{\psi}}{\partial y} = 0 \tag{13}$$

are imposed on any walls. As $|y| \to \infty$, disturbances are required to decay to zero. As a direct consequence, the y-component of $\underline{J}$ approaches zero as y approaches the limits of the flow domain.

With $\alpha, \tilde{\alpha}$ being wavenumbers and $\omega, \tilde{\omega}$ being frequencies, let

$$\psi(x,y,t) = \phi_{\alpha\omega}(y)e^{i(\omega t+\alpha x)}, \quad \tilde{\psi}(x,y,t) = \tilde{\phi}_{\tilde{\alpha}\tilde{\omega}}(y)e^{-i(\tilde{\omega}t+\tilde{\alpha}x)} \tag{14}$$

be solutions of equation (11) and the adjoint (12), respectively (i.e. $\phi_{\alpha\omega}(y)$ satisfies the Orr-Sommerfeld equation, and $\tilde{\phi}_{\tilde{\alpha}\tilde{\omega}}(y)$ an adjoint Orr- Sommerfeld equation). An auxiliary problem can then be solved to obtain the pressure eigensolution and the adjoint

$$p(x,y,t) = p_{\alpha\omega}(y)e^{i(\omega t+\alpha x)}, \quad \tilde{p}(x,y,t) = \tilde{p}_{\tilde{\alpha}\tilde{\omega}}(y)e^{-i(\tilde{\omega}t+\tilde{\alpha}x)}. \tag{15}$$

Substituting these velocity and pressure fields into the Lagrange identity (with $\underline{V}(\underline{r}) = U(y)\hat{x}$), the entire left hand side is zero, from which it follows (SG, Salwen (1979)) that

$$(\omega - \tilde{\omega})\langle\phi_{\alpha\omega}, \tilde{\phi}_{\tilde{\alpha}\tilde{\omega}}\rangle + (\alpha - \tilde{\alpha})[\phi_{\alpha\omega}, \tilde{\phi}_{\tilde{\alpha}\tilde{\omega}}] = 0, \tag{16}$$

with

$$\langle\phi_{\alpha\omega}, \tilde{\phi}_{\tilde{\alpha}\tilde{\omega}}\rangle = \int_{y_1}^{y_2} \left\{ \frac{\partial\phi_{\alpha\omega}}{\partial y}\frac{\partial\tilde{\phi}_{\tilde{\alpha}\tilde{\omega}}}{\partial y} + \alpha\tilde{\alpha}\phi_{\alpha\omega}\tilde{\phi}_{\tilde{\alpha}\tilde{\omega}} \right\} dy, \tag{17}$$

$$\begin{aligned}[\phi_{\alpha\omega}, \tilde{\phi}_{\tilde{\alpha}\tilde{\omega}}] = \int_{y_1}^{y_2} \Big\{ & (\omega\alpha + \tilde{\omega}\tilde{\alpha})\phi_{\alpha\omega}\tilde{\phi}_{\tilde{\alpha}\tilde{\omega}} \\ & + U\Big((\alpha^2 + \alpha\tilde{\alpha} + \tilde{\alpha}^2)\phi_{\alpha\omega}\tilde{\phi}_{\tilde{\alpha}\tilde{\omega}} + \phi_{\alpha\omega}\frac{\partial^2\tilde{\phi}_{\tilde{\alpha}\tilde{\omega}}}{\partial y^2} + 2\frac{\partial\phi_{\alpha\omega}}{\partial y}\frac{\partial\tilde{\phi}_{\tilde{\alpha}\tilde{\omega}}}{\partial y}\Big) \\ & - \frac{i(\alpha+\tilde{\alpha})}{R}\Big((\alpha^2 + \tilde{\alpha}^2)\phi_{\alpha\omega}\tilde{\phi}_{\tilde{\alpha}\tilde{\omega}} + 2\frac{\partial\phi_{\alpha\omega}}{\partial y}\frac{\partial\tilde{\phi}_{\tilde{\alpha}\tilde{\omega}}}{\partial y}\Big)\Big\} dy. \end{aligned} \tag{18}$$

When considering the spatial stability problem, ω is chosen to be purely real, and from the Orr-Sommerfeld equation, a set of characteristic values for α can then be found. This set can consist of discrete and continuum modes. For the adjoint problem, likewise selecting $\tilde{\omega} = \omega$, a set of possible values for $\tilde{\alpha}$ may be obtained. From (16), we have

$$(\alpha - \tilde{\alpha})[\phi_{\alpha\omega}, \tilde{\phi}_{\tilde{\alpha}\omega}] = 0, \tag{19}$$

from which it follows that

$$\text{if } [\phi_{\alpha\omega}, \tilde{\phi}_{\tilde{\alpha}\omega}] \neq 0 \text{ , then } \alpha = \tilde{\alpha}. \tag{20}$$

With appropriate care taken in handling the continuum modes, SG proceed to construct a bi-orthogonal eigensolution set in which for every solution $\phi_{\alpha\omega}(y)e^{i(\omega t+\alpha x)}$ to (11), there corresponds a normalized adjoint solution $\tilde{\phi}_{\alpha\omega}(y)e^{-i(\omega t+\alpha x)}$ to (12) such that, for example, for discrete modes with wavenumbers α_i,

$$[\phi_{\alpha_i\omega}, \tilde{\phi}_{\alpha_j\omega}] = \delta_{ij}. \tag{21}$$

A similar result is quoted by SG for the case of temporal modes, based on the inner product $\langle \cdot, \cdot \rangle$.

For an arbitrary solution $\underline{s} = (\underline{v}(x,y), p(x,y))e^{i\omega t}$ of the linearized equations, the adjoint solutions can be used to decompose the disturbance field. For a chosen eigenmode, if $\tilde{\underline{s}} = (\tilde{\underline{v}}_{\alpha\omega}(y), \tilde{p}_{\alpha\omega}(y))e^{-i(\omega t+\alpha x)}$ is the adjoint eigenmode, the filtering operation

$$\int_{y_1}^{y_2} \hat{x}.\underline{J}(\underline{s}, \tilde{\underline{s}})dy \tag{22}$$

returns the modal amplitude.

3. Accomplishments

In this section I will give examples of how the adjoint problem provides a reformulation of various aspects of the receptivity problem.

3.1 Failure of bi-orthogonality

It can be demonstrated that

$$\frac{d\omega}{d\alpha} = -\frac{[\phi_{\alpha\omega}, \tilde{\phi}_{\alpha\omega}]}{\langle \phi_{\alpha\omega}, \tilde{\phi}_{\alpha\omega} \rangle}, \tag{23}$$

which I believe to be a previously-unknown form for the group velocity of Orr-Sommerfeld eigenmodes. This form has implications for the formation of orthogonal solution sets. In the event that the chosen eigensolution is at a branch point singularity, for which $d\omega/d\alpha = 0$, then clearly

$$[\phi_{\alpha\omega}, \tilde{\phi}_{\alpha\omega}] = 0, \tag{24}$$

(the denominator in (23) is always bounded). The normalization condition (21) would require that the bilinear operation (24) take the value 1. The failure of (21) is connected to degeneracy of the wavenumber eigenvalues as the branch point is approached in the complex-ω plane.

3.2 The vibrating ribbon problem

The classical vibrating ribbon problem was discussed in some detail recently by Ashpis and Reshotko (1990). A vibrating ribbon is placed at the wall beneath a parallel boundary layer flow, and, after $t = 0$, it oscillates with velocity

$$\underline{v}_b(x,t) = \delta(x)e^{i\omega t}\hat{y}. \tag{25}$$

The classical result indicates that a long time after the initiation of the excitation and far downstream of the ribbon, the y-velocity of disturbances is

$$v(x,y,t) = i\frac{v(y;\alpha,\omega)}{\frac{\partial v}{\partial \alpha}(0;\alpha,\omega)}e^{i(\omega t+\alpha x)}, \tag{26}$$

where $\alpha(\omega)$ is wavenumber of the fastest growing discrete spatial mode of the Orr-Sommerfeld equation at frequency ω. The field $v(y;\alpha,\omega)$ is the y- velocity field of the mode. The factor $\partial v/\partial\alpha$ arises from contour integration around a pole in the complex wavenumber plane.

Beginning with (26), by differentiating the linearized equations of motion with respect to α and making use of the Lagrange identity, I have shown that

$$v(x,y,t) = \tilde{p}_{\alpha\omega}(0)\, v(y;\alpha,\omega)e^{i(\omega t+\alpha x)}. \tag{27}$$

Details of the analysis are not given here. The adjoint pressure at the wall, $\tilde{p}_{\alpha\omega}(0)$, gives the amplitude of the response to the ribbon oscillation.

3.3 Excitation of a free shear layer

Huerre and Monkewitz (1985) consider the response of an inviscid incompressible free shear layer ($U(y)$ defined for $-\infty < y < \infty$) to excitation by a point vorticity source positioned at $x = 0, y = y_0$,

$$\Omega(x,y,t) = \delta(x)\delta(y-y_0)e^{i\omega t}. \tag{28}$$

Quoting their result, far downstream the stream function behaves as

$$\psi(x,y,t) = \frac{\phi_{\alpha\omega}(y_0)\phi_{\alpha\omega}(y)}{(\alpha U(y_0)+\omega)\frac{\partial D}{\partial\alpha}(y_0;\alpha,\omega)}e^{i(\omega t+\alpha x)}, \tag{29}$$

where $\phi_{\alpha\omega}(y)$ is the least stable spatial eigensolution of the Rayleigh equation, and

$$D(y_0;\alpha,\omega) = \left(\Phi^+\frac{\partial\Phi^-}{\partial y} - \Phi^-\frac{\partial\Phi^+}{\partial y}\right)_{y=y_0}. \tag{30}$$

Here $\Phi^+(y;\alpha,\omega)$ and $\Phi^-(y;\alpha,\omega)$ are the upper ($y \geq y_0$) and lower ($y \leq y_0$) eigensolutions of the Rayleigh equation, which decay as $|y| \to \infty$.

I have taken (29) and simplified it to obtain

$$\psi(x,y,t) = \tilde{\phi}_{\alpha\omega}(y_0)\, \phi(y)e^{i(\omega t+\alpha x)}. \tag{31}$$

In this case, the modal amplitude is simply the value of the adjoint stream function, $\tilde{\phi}_{\alpha\omega}(y_0)$, at the source location.

3.4 Response to a general harmonic source distribution

Consider a source distribution oscillating harmonically at real frequency ω, including sources of momenta of strength $\underline{q}(\underline{r};\omega)$, and mass sources $\varphi(\underline{r};\omega)$. To keep the analysis as general as possible, we consider a boundary layer flow in the region $y > 0$ so that boundary velocities $\underline{v}_b(x;\omega)$ can be specified at $y = 0$. The governing equations are then

$$i\omega\underline{v} + \underline{L}(\underline{V};R)\,\underline{v} + \nabla p = \underline{q}(\underline{r};\omega), \tag{32}$$

$$\nabla.\underline{v} = \varphi(\underline{r};\omega), \tag{33}$$

with

$$\underline{v} = \underline{v}_b(x;\omega) \text{ on } y = 0. \tag{34}$$

The sources are assumed to be localized in so far as they disappear for $|x|$ larger than some value, say $X > 0$.

Let the discrete spatial mode of interest have stream function $\phi_{\alpha\omega}(y)e^{i(\omega t+\alpha x)}$. Typically the mode with largest value of $-Im(\alpha(\omega))$ would be considered. We wish to determine the amplitude of this mode far downstream as a result of the excitation by the various sources.

For a convectively-unstable mode which is traveling downstream, the stream function behaves as

$$a\ \phi_{\alpha\omega}(y)e^{i(\omega t+\alpha x)} \tag{35}$$

in the region downstream of all sources. The amplitude a is given explicitly by

$$\begin{aligned} a = \int_{x_1}^{x_2}\int_0^\infty \underline{q}(\underline{r};\omega).\tilde{\underline{v}}_{\alpha\omega}(y)e^{-i\alpha x}dydx + \int_{x_1}^{x_2}\int_0^\infty \varphi(\underline{r};\omega)\tilde{p}_{\alpha\omega}(y)e^{-i\alpha x}dydx \\ + \int_{x_1}^{x_2} \underline{v}_b(x;\omega).\tilde{\underline{S}}_{\alpha\omega}e^{-i\alpha x}dx, \end{aligned} \tag{36}$$

where $x_1 < -X, x_2 > X$. Clearly, if there are no sources, then $a = 0$. The field

$$\tilde{\underline{v}}_{\alpha\omega}(y) = \left(\frac{\partial\tilde{\phi}_{\alpha\omega}}{\partial y}, i\alpha\tilde{\phi}_{\alpha\omega}\right) \tag{37}$$

is the adjoint velocity field, $\tilde{p}_{\alpha\omega}(y)$ is the corresponding adjoint pressure, and the complex vector

$$\tilde{\underline{S}}_{\alpha\omega} = \left(\tilde{p}_{\alpha\omega}\hat{y} + \frac{1}{R}\frac{\partial\tilde{u}_{\alpha\omega}}{\partial y}\hat{x}\right)_{y=0} \tag{38}$$

is the *adjoint stress.*

The effect of some other types of sources can also be deduced. For sources of vorticity, the term involving $\underline{q}(\underline{r};\omega)$ is rewritten as

$$\int_{x_1}^{x_2}\int_0^\infty \underline{q}(\underline{r};\omega).\nabla\times(\tilde{\psi}\hat{z})dydx = \int_{x_1}^{x_2}\int_0^\infty \Omega(\underline{r};\omega)\tilde{\phi}_{\alpha\omega}(y)e^{-i\alpha x}dydx \tag{39}$$

where $\Omega(\underline{r};\omega) = \hat{z}.(\nabla\times\underline{q}(\underline{r};\omega))$ is the vorticity source distribution which would appear, for example, on the right-hand side of the Orr-Sommerfeld equation. Vorticity sources in the flow are weighted by the adjoint stream function.

Rather than specify a velocity at the wall (i.e. at $y = 0$), suppose that the wall is in motion, oscillating about its mean position with a small velocity $\underline{v}_d(x;\omega)$. Linearizing this boundary condition, it follows that the boundary integral in (36) can be re-expressed as

$$\int_{x_1}^{x_2} \underline{v}_d(x;\omega).\tilde{\underline{S}}'_{\alpha\omega}e^{-i\alpha x}dx \tag{40}$$

where

$$\underline{\tilde{S}}'_{\alpha\omega} = \left(\left(\tilde{p}_{\alpha\omega} + \frac{i}{\omega R}\frac{dU}{dy}\frac{\partial \tilde{u}_{\alpha\omega}}{\partial y}\right)\hat{y} + \frac{1}{R}\frac{\partial \tilde{u}_{\alpha\omega}}{\partial y}\hat{x}\right)_{y=0} \tag{41}$$

we will call the *modified adjoint stress.*

In each instance, the streamwise integration is weighted by $e^{-i\alpha x}$. Since, typically, $e^{i\alpha x}$ grows downstream, $e^{-i\alpha x}$ will grow *upstream.* There is no surprise here since sources further upstream will have a greater contribution to the far field disturbance amplitude; the response to such sources has convected further and hence has grown more.

The deductions made in sections 3.2 and 3.3 can now be reconfirmed. For the vibrating ribbon problem, the response to boundary motion (25) ($x_1 < 0, x_2 > 0$) predicted by (36) is

$$\int_{x_1}^{x_2} \delta(x)\hat{y}.\underline{\tilde{S}}_{\alpha\omega}e^{-i\alpha x}dx = \tilde{p}_{\alpha\omega}(0). \tag{42}$$

For excitation of a free shear layer by a vorticity source (28) with the y integration in (39) now extending from $-\infty$ to ∞, the amplitude of the response is

$$\int_{x_1}^{x_2}\int_{-\infty}^{\infty} \delta(x)\delta(y-y_0)\tilde{\phi}_{\alpha\omega}(y)e^{-i\alpha x}dydx = \tilde{\phi}_{\alpha\omega}(y_0). \tag{43}$$

The amplitude of a particular spatial eigensolution generated by an upstream time-harmonic source distribution can be expressed as a weighted integral of the sources whether they are within the flow or upon a flow boundary. The weighting functions are simply different field quantities of the adjoint eigensolution corresponding to the mode being considered. The field quantity which is appropriate depends upon the nature of the source. The following table summarizes the cases considered in this section.

Source type		*Adjoint weighting factor*		
description	*symbol*	*symbol*	*description*	*integrand*
momentum	$\underline{q}(\underline{r};\omega)$	$\underline{\tilde{v}}_{\alpha\omega}(y)e^{-i\alpha x}$	velocity	$\underline{q}(\underline{r};\omega).\underline{\tilde{v}}_{\alpha\omega}(y)e^{-i\alpha x}$
mass	$\varphi(\underline{r};\omega)$	$\tilde{p}_{\alpha\omega}(y)e^{-i\alpha x}$	pressure	$\varphi(\underline{r};\omega)\tilde{p}_{\alpha\omega}(y)e^{-i\alpha x}$
vorticity	$\Omega(\underline{r};\omega)$	$\tilde{\phi}_{\alpha\omega}(y)e^{-i\alpha x}$	stream function	$\Omega(\underline{r};\omega)\tilde{\phi}_{\alpha\omega}(y)e^{-i\alpha x}$
velocity at boundary	$\underline{v}_b(x;\omega)$	$\underline{\tilde{S}}_{\alpha\omega}e^{-i\alpha x}$	adjoint stress	$\underline{v}_b(x;\omega).\underline{\tilde{S}}_{\alpha\omega}e^{-i\alpha x}$
velocity of boundary	$\underline{v}_d(x;\omega)$	$\underline{\tilde{S}}'_{\alpha\omega}e^{-i\alpha x}$	modified adjoint stress	$\underline{v}_d(x;\omega).\underline{\tilde{S}}'_{\alpha\omega}e^{-i\alpha x}$

For momentum, mass, and vorticity sources, the integration is made over the entire flow domain in which sources are present. The resulting value gives the amplitude of the mode far downstream. For boundary sources, the integration is made over the boundary.

4. Future plans

The next step in this work will be to obtain simple numerical solutions of the adjoint fields in flows such as the Blasius boundary layer. A map of the receptivity characteristics for these flows can then be found. This will supplement analytical studies of boundary layer receptivity (Goldstein (1983), Goldstein *et al.* (1983)).

The coupling of free stream disturbances to boundary layer motions as a consequence of surface roughness is an important receptivity path (Goldstein (1985)). This has not yet been considered in the present work, and efforts will be made to extend the analysis to handle this scenario.

In the area of control, a means of analyzing boundary layer control strategies will be pursued. Suppression of a global (temporal) instability, such as occurs in a cylinder wake, can be achieved by a small permanent alteration of the flow field. The corresponding spatial problem is more complex since the control forces in practice are localized in space (for example, a region of suction in a boundary layer (Saric and Nayfeh (1977)), with their effect being felt both upstream and downstream.

Although reduction of the spatial growth rate of instabilities may be important, consideration will also be given to the alteration in the receptivity characteristics as a consequence of the presence of the control system. This can be quantified by examining changes in the adjoint field as a result of the control.

The global instability problem for strongly non-parallel flow has already been handled successfully (Hill (1992)). After the control of spatial instabilities in parallel flows has been fully investigated here, it will remain to consider the spatial problem in non-parallel flows.

It would seem inevitable that a connection will be established with the work of Herbert and Bertolotti (1987) on the Parabolised Stability Equations. Their studies on the evolution of a disturbance amplitude in a slowly evolving non-parallel flow would appear to be intimately connected to the present work, though they do not consider the receptivity problem explicitly.

In the longer term, a study will be carried out of the crossflow instability on an infinite swept airfoil leading edge. This is a phenomenon of major technological importance, and it is hoped that a systematic means of analyzing control possibilities may be found. Providing the ability to analyze how secondary instabilities and turbulent flows respond to control forces also remains a long term goal.

REFERENCES

ASHPIS, D. E. & RESHOTKO, E. 1990 The vibrating ribbon problem revisited. *J. Fluid Mech.* **213**, 531-547.

BALSA, T. F. 1988 On the receptivity of free shear layers to two-dimensional external excitation. *J. Fluid Mech.* **187**, 155-177.

DRAZIN, P. G. & REID, W. H. 1981 Hydrodynamic Stability. *Cambridge University Press.*

FUCHS, L. 1858-1875 Gessammelte Mathematische Werke I.

GASTER, M. 1965 On the generation of spatially growing waves in a boundary layer. *J. Fluid Mech.* **22,** 433-441.

GOLDSTEIN, M. E. 1983 The evolution of Tollmien-Schlichting waves near a leading edge. *J.Fluid Mech.* **127,** 59-81.

GOLDSTEIN,M. E. 1985 Scattering of acoustic waves into Tollmien-Schlichting waves by small streamwise variations in surface geometry. *J. Fluid Mech.* **154,** 509-529.

GOLDSTEIN, M. E., SOCKOL, P. M. & SANZ, J. 1983 The evolution of Tollmien-Schlichting waves near a leading edge. Part 2. Numerical determination of amplitudes. *J.Fluid Mech.* **129,** 443-453.

HERBERT, TH. & BERTOLOTTI, F. P. 1987 Stability analysis of non-parallel boundary layers. *Bull. Am. Phys. Soc.* **32,** 2079.

HILL, D. C. 1992 A theoretical approach for analyzing the restabilization of wakes. *AIAA paper No. 92-0067.*

HUERRE, P. & MONKEWITZ, P. A. 1985 Absolute and convective instabilities in free shear layers. *J. Fluid Mech.* **159,** 151-168.

INCE, E. L. 1944 Ordinary differential equations. *Dover Publications.*

IOOSS, G. & JOSEPH, D. D. 1980 Elementary stability and bifurcation theory. Springer-Verlag.

KOZLOV, V. V. & RYZHOV, O. S. 1990 Receptivity of boundary layers : asymptotic theory and experiment. *Proc. Roy. Soc. Lond. A.* **429,** 341-373.

LAGRANGE, J. L. 1867 Oeuvres de Lagrange. p.471. Gauthier-Villars, Paris. Originally in *Miscellanea Taurinensia, t. III,* 1762-1765.

SALWEN, H. 1979 Expansions in spatial or temporal eigenmodes of the linearized Navier-Stokes equations. *Bull. Am. Phys. Soc.* **24,** 74.

SALWEN, H. & GROSCH, C. E. 1981 The continuous spectrum of the Orr-Sommerfeld equation. Part 2. Eigenfunction expansions. *J. Fluid Mech.* **104,** 445-465.

SARIC, W. S. & NAYFEH, A. H. 1977 Nonparallel stability of boundary layers with pressure gradients and suction. *AGARD- CP-224.* **6:1-21.**

SCHENSTED, I. V. 1960 Contributions to the theory of hydrodynamic stability. Ph.D. dissertation. University of Michigan.

SCHUBAUER, G. B. & SKRAMSTAD, H. K. 1947 Laminar boundary layer oscillations and transition on a flat plate. *J. Aero. Sci.* **14,** 69-76 (Also NACA Rep. 909, 1948).

TAM, C. K. W. 1978 Excitation of instability waves in a two-dimensional shear layer by sound. *J. Fluid Mech.* **89(2),** 357-371.

Local isotropy in high Reynolds number turbulent shear flows

By Seyed G. Saddoughi

1. Motivation and background

This is a report on the continuation of the experiments, which Dr. Srinivas Veeravalli and the present author started in 1991, to investigate the hypothesis of local isotropy in shear flows. This hypothesis, which states that at sufficiently high Reynolds numbers the small-scale structures of turbulent motions are independent of large-scale structures and mean deformations (Kolmogorov 1941, 1962), has been used in theoretical studies of turbulence and computational methods like large-eddy simulation. The importance of Kolmogorov's ideas arises from the fact that they create a foundation for turbulence theory.

Local isotropy greatly simplifies the problem of turbulence. The total average turbulent energy dissipation ϵ, which in the usual tensor notation is given by

$$\epsilon = \nu\overline{\left(\frac{\partial u_i}{\partial x_j} + \frac{\partial u_j}{\partial x_i}\right)\frac{\partial u_j}{\partial x_i}}, \tag{1}$$

(summation on repeated indices) reduces to $\epsilon = 15\nu\overline{(\partial u/\partial x)^2}$, in locally isotropic turbulence (see Taylor 1935).

In the high-wavenumber region of the spectrum, Kolmogorov's universal equilibrium hypothesis implies that $E_{11}(k_1)/(\varepsilon\nu^5)^{\frac{1}{4}}$ is a universal function of $(k_1\eta)$, where $\int_0^\infty E_{11}(k_1)\,dk_1 = \overline{u^2}$, k_1 is the longitudinal wavenumber and $\eta = (\nu^3/\varepsilon)^{\frac{1}{4}}$ is the Kolmogorov length scale.

If the motion is isotropic, the transverse spectra $E_{22}(k_1)$ (for the velocity component normal to the wall) and $E_{33}(k_1)$ (for the spanwise component) are uniquely determined by the longitudinal spectrum (Batchelor 1953):

$$E_{22}(k_1) = E_{33}(k_1) = \frac{1}{2}(1 - k_1\frac{\partial}{\partial k_1})E_{11}(k_1). \tag{2}$$

In the inertial subrange, the 3D spectrum takes the form (Kolmogorov 1941)

$$E(k) = C\varepsilon^{2/3}k^{-5/3}, \tag{3}$$

where k is the wavenumber magnitude, and, assuming isotropy, the one-dimensional longitudinal and transverse spectra are

$$E_{11}(k_1) = C_1\varepsilon^{2/3}k_1^{-5/3} \tag{4}$$

and

$$E_{22}(k_1) = E_{33}(k_1) = C_1'\varepsilon^{2/3}k_1^{-5/3} \tag{5}$$

respectively. The Kolmogorov constant C is equal to $\frac{55}{18}C_1$, and equation (2) evaluated in the inertial subrange gives $C_1'/C_1 = 4/3$.

In isotropic flow the shear-stress co-spectrum, $E_{12}(k_1)$, defined by $\int_0^\infty E_{12}(k_1)\,dk_1 = -\overline{uv}$, is equal to zero. This indicates that for local isotropy to be satisfied, the normalized shear-stress co-spectrum,

$$R_{12}(k_1) = -E_{12}(k_1)[E_{11}(k_1)E_{22}(k_1)]^{-1/2}, \tag{6}$$

should roll-off at high wavenumbers.

Kolmogorov (1941) proposed scaling laws in the inertial subrange region for structure functions, which are moments of the velocity differences evaluated at points separated by longitudinal distances r. The second order longitudinal and transverse structure functions are given by

$$D_{11}(r) = \overline{[u(x+r) - u(x)]^2} = C_2\varepsilon^{2/3}r^{2/3} \tag{7}$$

and

$$D_{33}(r) = D_{22}(r) = \overline{[v(x+r) - v(x)]^2} = C_2'\varepsilon^{2/3}r^{2/3} \tag{8}$$

respectively, where $C_2 \approx 4C_1$ and $C_2'/C_2 = 4/3$. These are also known as Kolmogorov's 2/3 law. The third order longitudinal structure function was derived from the Navier-Stokes equations by Kolmogorov, without any appeal to self-similarity (Landau & Lifshitz 1987, p 140). In the inertial sub-range, this takes the following form;

$$D_{111}(r) = \overline{[u(x+r) - u(x)]^3} = -\frac{4}{5}\varepsilon r. \tag{9}$$

Our previous report (Veeravalli & Saddoughi 1991, hereinafter referred to as I), presented some spectral results taken at a single location in the boundary layer of the 80′ by 120′ wind tunnel at a freestream velocity of 40 m/s. These data indicated that the w-spectrum followed, but the v-spectrum deviated from (by a large amount) the isotropic relation in the inertial subrange region. No definite statement could be made for the dissipating eddies because our measurements were contaminated by high-frequency electrical noise. Some of the shortcomings of those measurements and their eventual improvement for the present experiments are discussed below in section 2.1.

In I, we also presented a short review of the work on local isotropy. Further, George & Hussein (1991) and Antonia, Kim & Browne (1991) have proposed that in shear flows the local-isotropy assumption should be relaxed to one of local axisymmetry (invariance with respect to rotation about the streamwise direction) and showed that the derivative moments obtained by experiments and by DNS in low-Reynolds-number flows supported the local-axisymmetry assumption. In I, it was concluded that, despite the many experiments conducted in a variety of flows to examine the validity of the local-isotropy hypothesis in shear flows, it appeared that there was no consensus regarding this concept in the scientific community. This conclusion still holds today. While the measurements in I were mainly intended as a *feasibility* study, it is hoped that the results presented here will enhance our understanding of the local-isotropy hypothesis.

2. Accomplishments

2.1. Apparatus and measurement techniques

The experiments described here were conducted at nominal freestream velocities (U_e) of 10 and 50 m/s in the boundary layer on the test-section ceiling of the full scale aerodynamics facility at NASA Ames. The test section is 80′ high, 120′ wide, and approximately 155′ long. All four walls of the test section are lined with acoustic paneling, yielding a rough-wall boundary layer. The measurement station was located towards the end of the test section on the centerline of the tunnel. The data recording equipment and a small calibration wind tunnel were installed in an attic above the ceiling.

Here we will highlight the modifications to the equipment used in I and only give a very brief description of the instrumentation and techniques for the present measurements. The full details are given by Saddoughi & Veeravalli (1992, hereinafter referred to as II). One of the major alterations was done to the traversing mechanism. In I, the hot-wire probe holders were permanently fixed to the traversing rod, and it was necessary to calibrate the hot-wires using a different set of probe holders and cables than those connected to the traverse. The hot-wires were disconnected from the bridges after the calibration and reconnected to the anemometers via the traverse cables and probe holders for the actual measurements. This can result in a change in the hot-wire characteristics and a deviation from the calibration (Perry 1982). For the present experiments, this problem was avoided by redesigning some parts of the traverse such that the same cables and probe holders were used during both the calibration and actual measurements, without disconnecting the hot-wires.

For I, the measurements were conducted during the NASA Ames "swing-shift" period from mid-afternoon to midnight. We found that during that shift the temperature in the calibration tunnel was about 8°C higher than the temperature inside the 80′ by 120′ wind tunnel. In I the intake of the blower of the calibration tunnel was packed with ice to overcome this problem. To ensure a uniform distribution of mean temperature at the exit of the calibration tunnel, copper wool was placed in the pipe which connected the output of the blower to the intake of the calibration tunnel. This method reduced the temperature difference between the calibration and the actual measurements but it did not give us a good control over the amount of temperature reduction. Furthermore, the calibration temperature rose as the ice melted. The present measurements were performed during the "graveyard" shift from midnight to mid-morning during which the difference between the temperatures in the attic and inside the tunnel is smaller. To allow a fairly good temperature adjustment for the calibration, the intake of the blower of the calibration tunnel was connected to an air-conditioner via pipes having valves for controlling the intake of cold air. While for I the hot-wires were operated with an overheat ratio of 1.8, for the present measurements this was set at 2.0, which further reduced the possibility of drift due temperature changes.

For the present experiments, we acquired the latest instruments, which have lower background noise than those used for I. In addition, all of our electronic equipment was connected to an Oneac Power Conditioner (CB 1115) and Uninterruptible Power

System (UPS Clary PC 1.25K), which supplied clean power and prevented loss of data due to power failure. We also expanded our data acquisition capability from simultaneous sampling of two to sampling of six time-series.

At this stage, it is important to elaborate on another major difficulty encountered during I. Figure 1(a) shows the longitudinal spectrum obtained in I at $y/\delta \approx 1.4$ at a nominal freestream velocity of 40 m/s. Note, apart from the apparent spikes, the rise in the tail of the spectrum with frequency before the final roll-off due to the low-pass filtering (cut-off set at 100 kHz). This rise, which apparently has a slope of 2, was of great concern since it took place in the same region as that of the expected Kolmogorov frequency for that speed.

To ensure that this was not peculiar to the flow inside the 80′ by 120′ wind tunnel, spectra were taken, both in the attic of the 80′ by 120′ tunnel and at the Stanford laboratory, in the freestream of our calibration tunnel at the same velocity and filter cut-off frequency as those above. These spectra, Figure 1(b), clearly show the same problem being present in both the experimental facilities. Furthermore, to isolate the source of this problem, the spectra were measured in the freestream of the calibration tunnel at the Stanford laboratory using hot-wire bridges manufactured by different companies (TSI, Dantec, and one designed by Dr. Watmuff of the Fluid Mechanics Laboratory at NASA Ames). These results are shown in Figure 1(c). Again it appears that, as far as this phenomenon is concerned, the responses of all three bridges are similar. Finally, with a TSI IFA-100 bridge, spectra were taken in still air with 2.5 μm Tungsten wires and also with a standard fuse wire. These data are compared in Figure 1(d), where the same trend is clearly present.

The conclusion drawn from these tests is that when the turbulent energy of the flow is very small, the performance of the hot-wire bridges at high frequencies is limited by this phenomenon. This means that at the freestream velocity of 50 m/s, where the Kolmogorov frequency near the mid-layer of the boundary layer is of the order of 60 kHz, this rise in the tail of the spectrum is inevitable. In I it was suggested that, to allow accurate measurement of the dissipation range of the spectrum in this facility, experiments ought to be conducted at a nominal freestream velocity of 10 m/s, where the expected Kolmogorov frequency would be of the order of 5 kHz and this phenomenon could be avoided. As will be shown later, this aim has been accomplished.

Unlike the experiments in I, where data were obtained while NASA engineers were investigating the flow around an F-18 fighter aircraft in the central region of the working section, the present experiments were performed in an empty tunnel fully dedicated to our experiment.

The hot-wire instrumentation consisted of Dantec models 55P01 single wire and 55P51 cross-wire probes, modified to support 2.5 μm Platinum plated Tungsten wires with an etched length of approximately 0.5 mm, TSI IFA-100 model 150 hot-wire bridges, and model 157 signal conditioners. The high-pass and low-pass filters were Frequency Devices model 9016 (Butterworth, 48dB/octave). The hot-wire output voltages were digitized on a micro computer equipped with two Adtek AD830 12-bit analog-to-digital converters. To improve the frequency bandwidth of

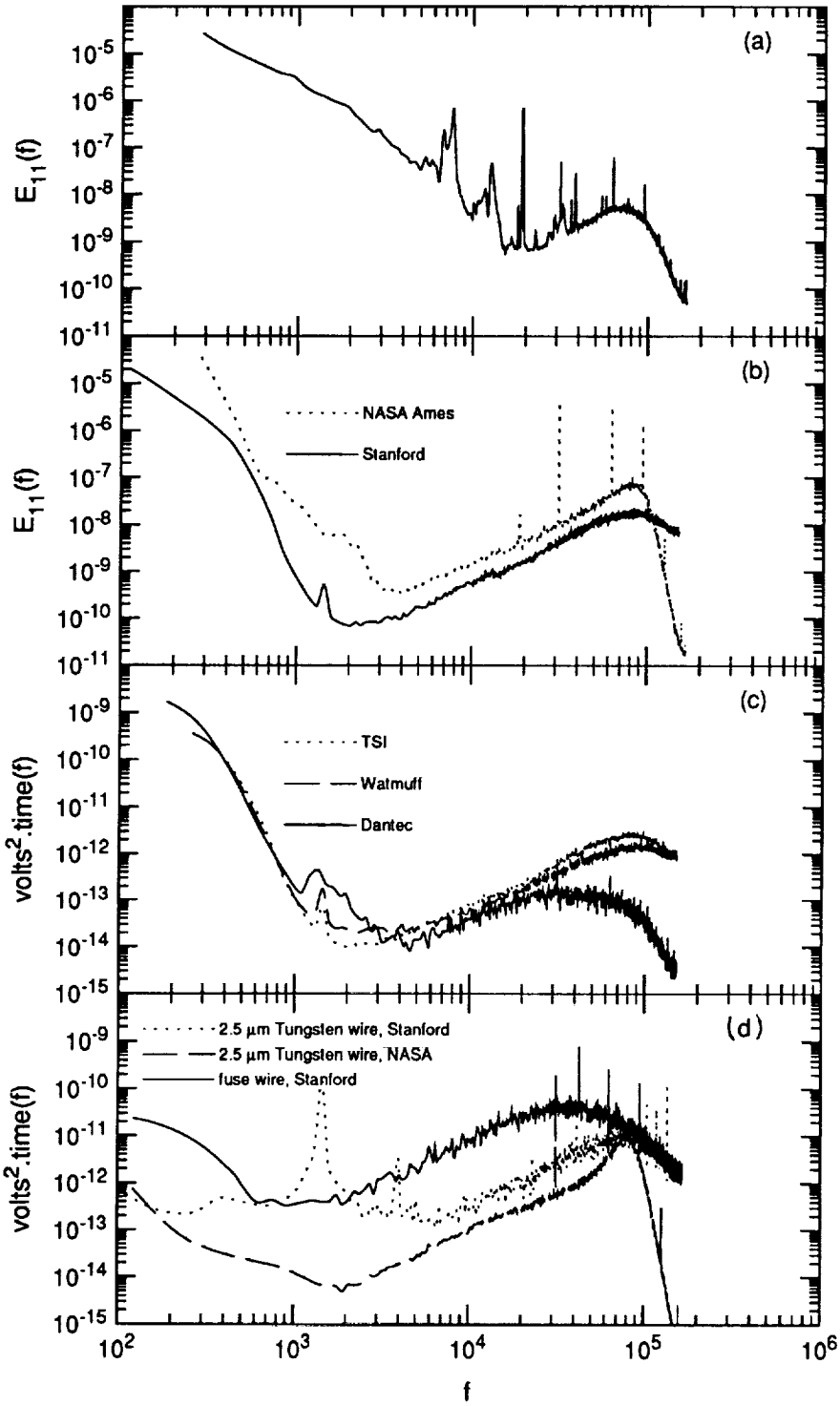

FIGURE 1. Comparison of noise spectra measured under different experimental conditions. (a) NASA 80- by 120-foot wind tunnel at freestream velocity of 40 m/s from I. (b) Calibration tunnel freestream at NASA and Stanford. (c) Calibration tunnel freestream at Stanford with different bridges. (d) TSI IFA-100 bridges with different wires in still air.

the spectrum at low frequencies, the data were obtained in three spectral bands. For the low-speed measurements around the mid-layer, these three bands were 0.1 Hz to 100 Hz, 0.1 Hz to 1 kHz, and 0.1 Hz to 10 kHz, which were chosen to resolve the large scales, inertial range, and the dissipation region respectively. The corresponding bands for the high-speed case were 0.1 Hz to 1 kHz, 0.1 Hz to 20 kHz, and 0.1 Hz to 100 kHz. In I, for each spectral segment, the high-pass filter-cutoff frequency was increased. The advantage of this method was that it permitted us to change the dynamic range of the analog-to-digital convertor to match that expected in a given band. However, recall from Figure 1 that a good resolution of the high-frequency end of the spectrum at high-speeds was not necessary since that part of the spectrum was contaminated by the f^2 behavior. It will be shown in section 2.2 that as expected, keeping all the other parameters the same, this change in the high-pass cutoff frequency did not affect our results.

In general, for spectral measurements, 200 records of 4096 samples each were recorded in the low-frequency band and 400 such records in the higher-frequency bands. In each case, the sampling frequency was three to four times larger than the low-pass filter cut-off frequency in order to avoid aliasing errors. The spectral density of each band was computed by a fast-Fourier-transform algorithm. To convert frequencies to wavenumbers, Taylor's hypothesis was used. The time series for both the X-wires (UV- and UW-mode) and the single wire were obtained simultaneously. For the low-speed experiment the measurement positions were at $y/\delta \approx 0.025$, 0.1, 0.3, 0.5, 0.9 and for the high-speed case they were at $y/\delta \approx 0.1$, 0.4, 0.8. Here we only present the data taken around mid-layer at both freestream velocities. These, as well as the results taken at other y/δ positions, are given in II.

2.2. Results and discussion

It is shown in II that the large-scale characteristics of the boundary layer followed the standard behavior in the outer part of the layer at both nominal freestream velocities of 10 m/s and 50 m/s. Also, it appeared that the thickness of the boundary layer, δ, in both cases was about the same ($\approx 1m$) at this measurement location. It is important to emphasize that the objective of the present experiments is not to investigate the concept of local isotropy in a canonical boundary layer. However, if it so happens that the boundary layer behaved reasonably close to the canonical form, this would be considered a bonus.

The mid-layer position is perhaps the best point at which to analyze the spectral results because of its following advantages: (a) the rms longitudinal velocity fluctuation normalized by the local mean velocity, $\sqrt{\overline{u^2}}/U$, is less than 0.1, so that errors arising from the use of Taylor's hypothesis will be small (Lumley 1965); (b) the Reynolds number R_λ ($\equiv \sqrt{\overline{u^2}}\lambda/\nu$), based on the Taylor microscale λ [$\equiv \sqrt{\overline{u^2}/\overline{(\partial u/\partial x)^2}}$] is close to its maximum value, and (c) it is well inside the layer so that boundary-layer edge intermittency effects are not present.

The main aim of the present study has been to investigate the effects of mean-strain rate ($S = \partial U/\partial y$) on local isotropy. The non-dimensional quantity

$$S^* = \frac{Sq^2}{\varepsilon}, \tag{10}$$

the shear-rate parameter, which is the ratio of the eddy turnover time (q^2/ε) to the timescale of mean deformation (S^{-1}), characterizes the effects of mean-strain rate on the turbulence (Moin 1990; Lee, Kim & Moin 1990). Durbin & Speziale (1991) examined the equation for the dissipation rate tensor and showed that local isotropy is inconsistent with the presence of mean-strain rate. The profile of shear-rate parameter for a turbulent channel flow (Lee, Kim & Moin 1990), reached its maximum value of about 35 at y^+ ($= yU_\tau/\nu$, where U_τ is the friction velocity) ≈ 10 in the viscous sublayer and decreased to a value of about 6 for $y^+ > 50$.

On the other hand, Corrsin (1958) proposed that local isotropy in shear flows can exist when

$$S_c^* = \frac{(\frac{\nu}{\varepsilon})^{1/2}}{S^{-1}} \ll 1. \tag{11}$$

This is the ratio of the Kolmogorov and mean-shear timescales. The channel-flow profile of S_c^*, presented by Antonia & Kim (1992), indicates a constant value of about 2.5 in the viscous sublayer and a reduction to a very small values for $y^+ > 60$. These authors suggested that the Corrsin criterion is too restrictive and may be relaxed to $S_c^* \leq 0.2$ for the small scales to be isotropic.

Table 1. shows the flow parameters for spectral measurements at mid-layer location. In general, there is some degree of uncertainty associated with the estimation of S^* and S_c^* because they involve gradients at data points that are widely spaced, and, as will be shown later, the dissipation values are accurate to 20%. In Table 1, it can be seen that the value of $S^*/\sqrt{R_\lambda}$ becomes independent of freestream velocity. It is shown in II that as the wall is approached the values of these two parameters increase, and, at a given y/δ, the trend seen in Table 1 prevails.

Freestream velocity, U_e (m/s)	≈ 50	≈ 10
Boundary layer thickness, δ (m)	≈ 1.0	≈ 1.0
Measurement location, y/δ	≈ 0.4	≈ 0.5
Local mean velocity, U (m/s)	$= 43.2$	$= 8.95$
Local turbulence intensity, $\sqrt{\overline{u^2}}/U$	$= 0.07$	$= 0.065$
Microscale Reynolds number, R_λ	≈ 1500	≈ 600
Ratio of hot-wire length, l to η	≈ 5	≈ 1.5
Shear-rate parameter, S^*	≈ 8	≈ 5
$S^*/\sqrt{R_\lambda}$	≈ 0.21	≈ 0.21
Corrsin parameter, S_c^*	≈ 0.0107	≈ 0.016

TABLE 1: Flow parameters for spectral measurements around mid-layer.

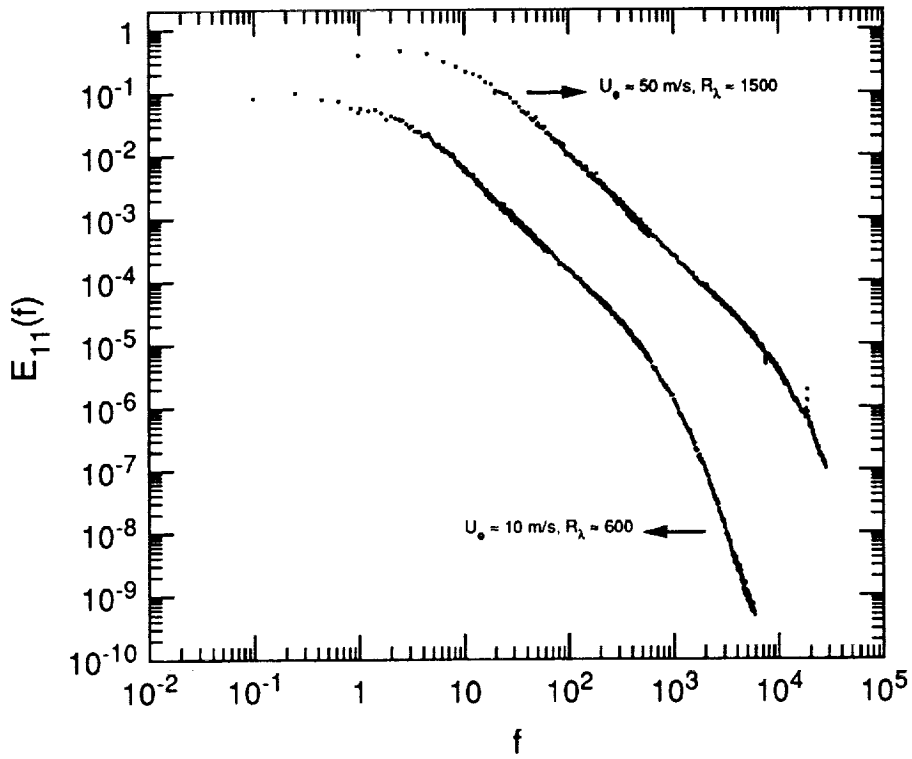

FIGURE 2. Longitudinal power spectra measured around mid-layer at different freestream velocities.

Figure 2 shows $E_{11}(f)$ for both freestream velocities, obtained in the three measurement bands given in section 2.1. Clearly, in each case, the agreement between the three segments of the spectrum is very good. The collapse for the transverse spectra was equally good. The Kolmogorov frequencies, $f_\eta (= U/2\pi\eta$, where η was calculated by using the isotropic relation) were about 69 kHz and 4.5 kHz for the high- and low-speed measurements respectively. To avoid the f^2 behavior of the tail of the spectrum (section 2.1), and also due to lack of sufficient spatial resolution (Wyngaard 1968; Ewing & George 1992), only frequencies up to about 30 kHz could be resolved for the high-speed case. However, for the low-speed measurements, five-decades of frequency were obtained with no contamination from electronics noise and with good spatial resolution. As explained in section 2.1, the low-speed measurements were required mainly to resolve the dissipation range of the spectrum, but it is important to bear in mind that the high-speed results are more appropriate for the investigation of inertial-subrange scaling because they are at a much higher R_λ. It will become clear in the following sections that without the measurements at 50 m/s in the inertial range, one may reach erroneous conclusions.

Figure 3, which is plotted with Kolmogorov scaling, shows a comparison between the present data and a compilation of some experimental work taken from Chapman (1979) with later additions. The agreement is good. With this type of scaling, the

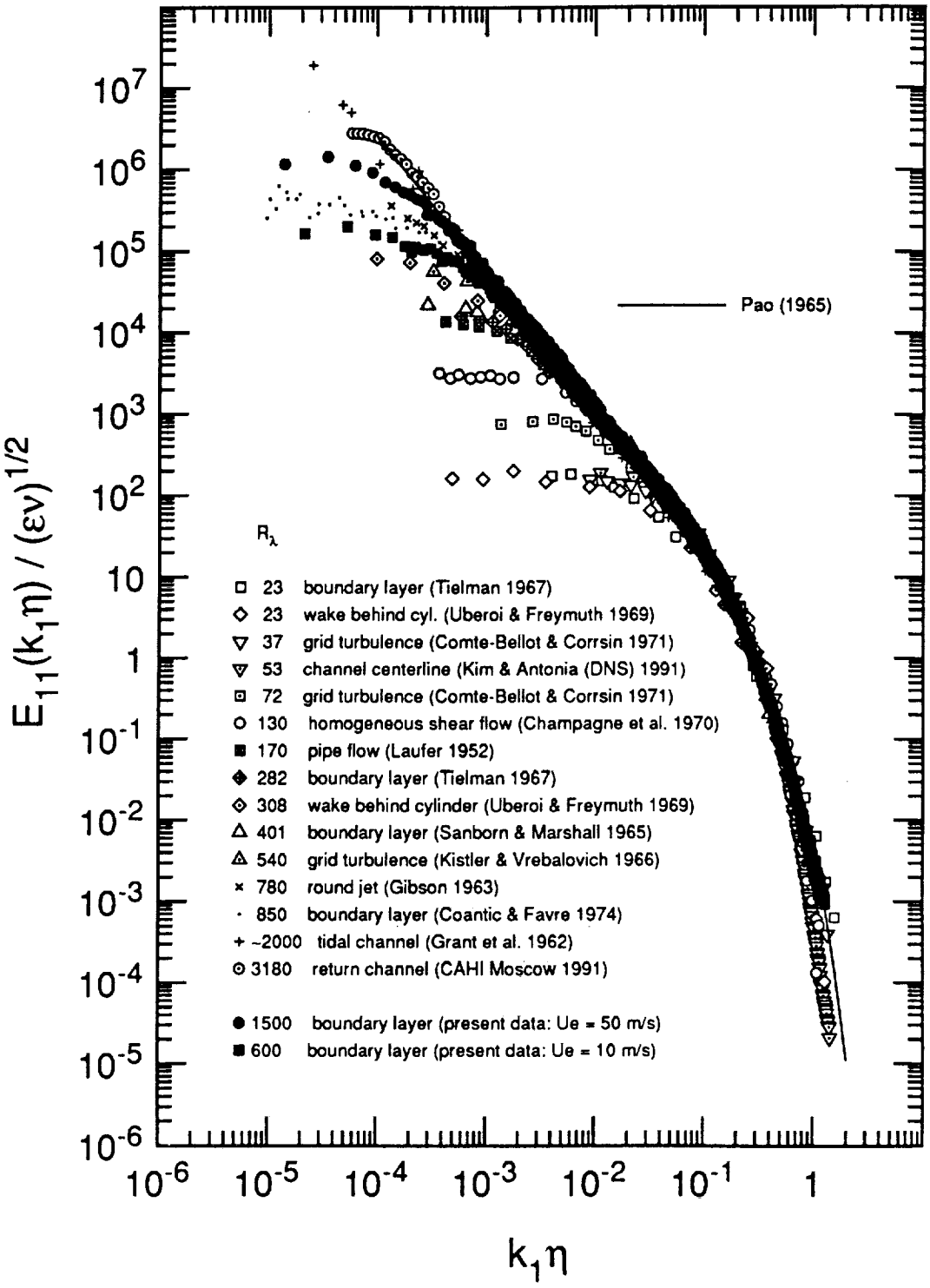

FIGURE 3. Kolmogorov scaling for the longitudinal spectra compared with data from other experiments. This compilation is from Chapman (1979) with later additions.

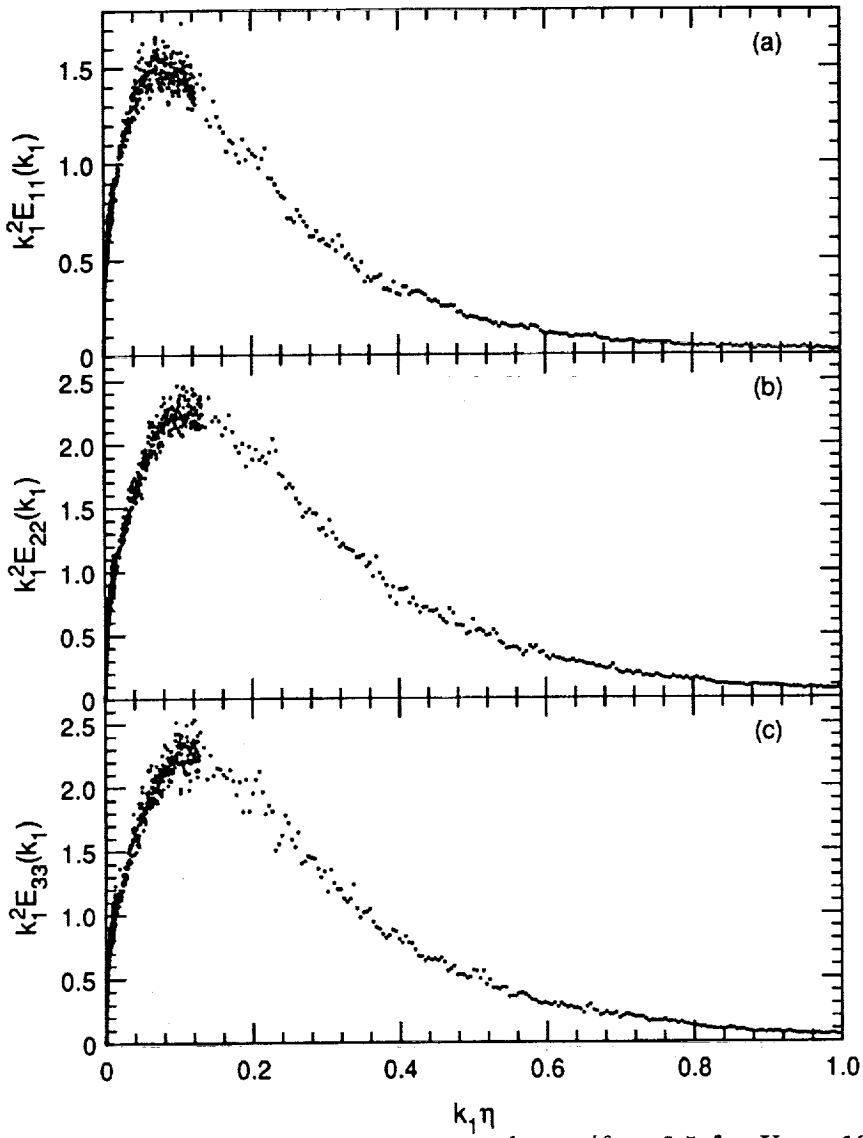

FIGURE 4. Dissipation spectra measured at $y/\delta \approx 0.5$ for $U_e \approx 10\ m/s$ and $R_\lambda \approx 600$. (a) u-spectrum; (b) v-spectrum; (c) w-spectrum.

spectra peel off from the $-5/3$ law at the low-wavenumber end in order of increasing Reynolds number. The present spectrum for $R_\lambda \approx 1500$ has a $-5/3$ slope over approximately two decades in wavenumber; one of the longest $-5/3$ ranges seen in laboratory flows.

For $U_e \approx 10\ m/s$ and $R_\lambda \approx 600$, dissipation spectra defined by the isotropic relation, $\varepsilon = 15\nu \int_0^\infty k_1^2 E_{11}(k_1)dk_1 = 7.5\nu \int_0^\infty k_1^2 E_{22}(k_1)dk_1 = 7.5\nu \int_0^\infty k_1^2 E_{33}(k_1)dk_1$, are plotted in Figure 4. For $R_\lambda \approx 1500$, a similar plot for only the u-spectrum is shown in Figure 5. These figures show that in the high-speed case, it is only possible to take measurements up to $k_1\eta \approx 0.4$, but for the low-speed experiments,

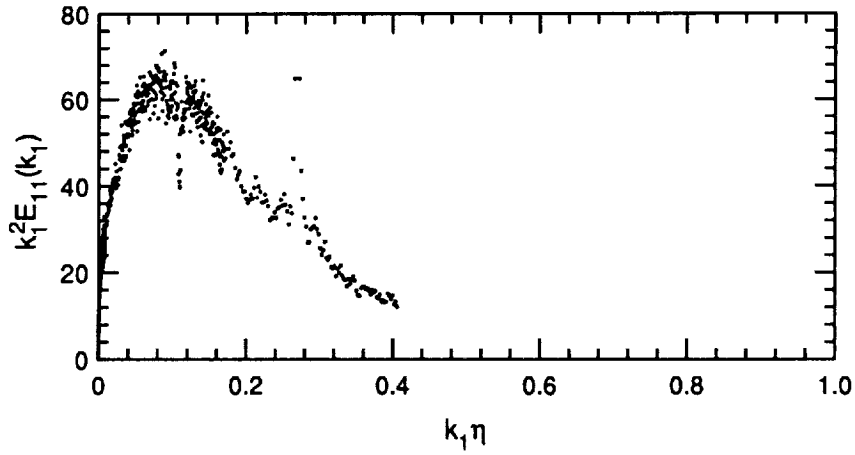

FIGURE 5. Dissipation spectrum measured at $y/\delta \approx 0.4$ for $U_e \approx 50\ m/s$ and $R_\lambda \approx 1500$.

the entire dissipation spectrum is obtained. However, for $R_\lambda \approx 600$ the scatter of the data around the peak is about $\pm 10\%$, and, as will be shown later, the data for $k_1\eta > 0.9$ may not be reliable. The integrations of these data satisfy the above isotropic relation to within 10%.

To investigate the isotropy of scales within the inertial subrange, we use equations (4) and (5) and analyze the compensated spectra $k_1^{5/3}E_{ii}(k_1)$, where $i = 1, 2$ or 3 (no summation over i) corresponds to u, v, or w respectively. In the inertial subrange, these compensated spectra should be independent of wavenumber, and the v- and w-spectra should be equal to each other and larger than the u-spectrum by a factor 4/3.

In Figure 6, the compensated spectra for $U_e \approx 10\ m/s$, $R_\lambda \approx 600$ are plotted against $k_1\eta$. The 9^{th}-order, least-square polynomial fit to these data presented in Figure 7 prove to be very instructive in analyzing the data. Using the dissipation value ($\epsilon \approx 0.33\ m^2/s^3$) obtained by integrating over the third-spectral band, which covered the entire frequency range of interest in Figure 4(a), and taking the classical value for the Kolmogorov constant, $C = 1.5$ (i.e. $C_1 \approx 0.5$), the isotropic values in the inertial subrange for the compensated spectra were calculated. These are shown as straight lines in Figures 6 and 7. For the u-spectrum, shown in Figure 7, there is slightly less than one decade of $-5/3$ region, and in that region $C = 1.5$ agrees well with the present data. Noting that our dissipation accuracy was to $\pm 10\%$, this gives $C = 1.5 \pm 0.1$. The w-spectrum shows more than half a decade of $-5/3$ region, with an amplitude equal to 4/3 times that of the u-spectrum (the difference between the flat region of the w-spectrum and the isotropic line is about 5%). However, it appears that in the region under consideration, the v-spectrum does not show a perfectly flat portion. It will be shown later that this is a Reynolds number effect. All three spectra have a "bump" between the inertial subrange and the dissipation range. These "bumps" have also been observed in other experiments (Williams & Paulson 1978 and Champagne, Friehe, LaRue & Wyngaard 1977 for temperature variance spectra; Mestayer 1982 for velocity spectra) and theoretical predictions

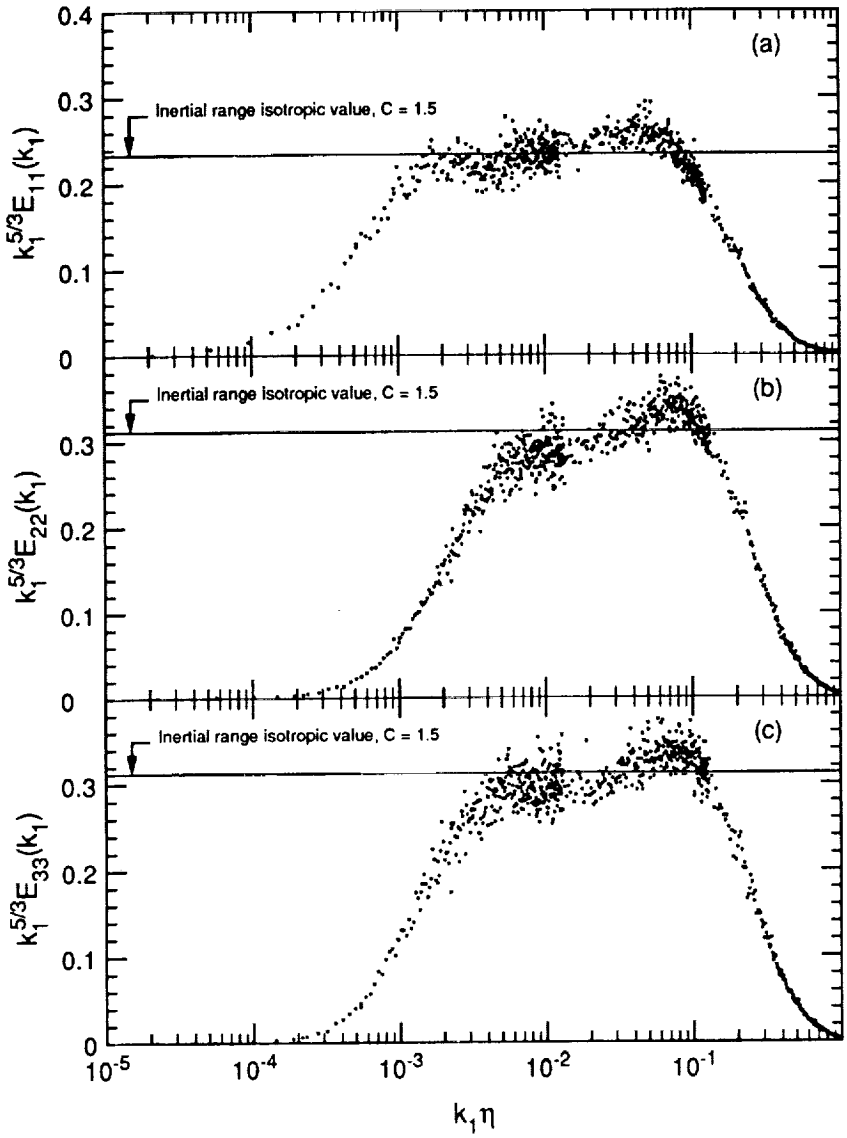

FIGURE 6. Compensated longitudinal and transverse spectra measured around mid-layer for $U_e \approx 10\ m/s$ and $R_\lambda \approx 600$. (a) u-spectrum; (b) v-spectrum; (c) w-spectrum.

such as Eddy-Damped Quasi-Normal Markovian (EDQNM), as discussed by Mestayer, Chollet & Lesieur (1984). Also, in his review talk, Saffman (1992) mentioned the existence of this "bump" in the 3D-spectrum.

The compensated spectra and their corresponding 9^{th}-order polynomial fits for $U_e \approx 50\ m/s$, $R_\lambda \approx 1500$, are shown in Figures 8 and 9 respectively. It is clear that for these high-speed data, a good estimate for dissipation is not possible (see Figure 5). However, since our low-speed data indicates that $C = 1.5 \pm 0.1$, we will use this value and the fitted isotropic lines shown in Figures 8 and 9, to calculate $\epsilon \approx 49$

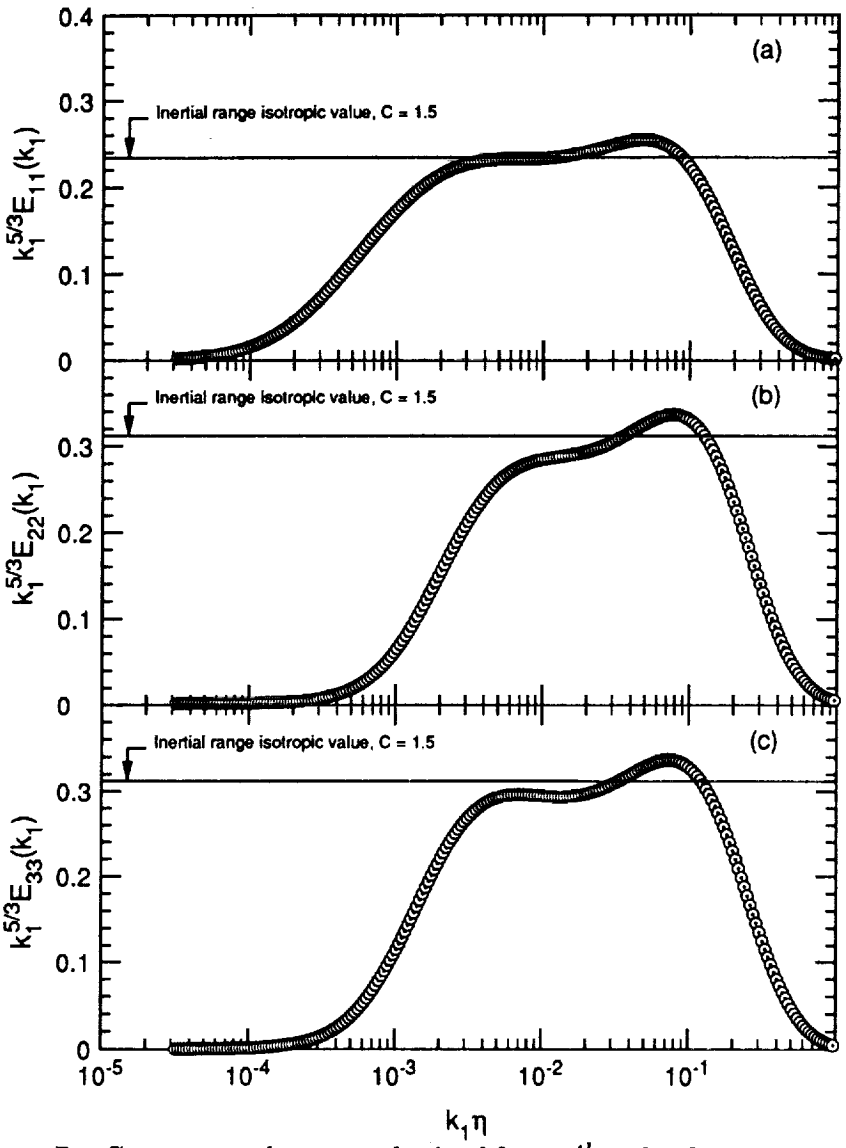

FIGURE 7. Compensated spectra obtained from 9^{th}-order, least-square polynomial fits to the data presented in Figure 6.

m^2/s^3. We will show later in the discussion of the third-order structure functions that this estimation is within the 20% uncertainty associated with our dissipation calculations. It can be seen from Figure 9 that for the higher R_λ, the compensated u-spectrum exhibits more than one decade of $-5/3$ region, but less than the log-log plot (Figure 3) suggested. Here the v-spectrum, as well as the w-spectrum contain well defined $-5/3$ inertial-subrange regions. They are, as predicted, equal to each other and are larger than the u-spectrum by the 4/3 factor. The "bumps" again appear on all the three spectra at almost the same $k_1\eta$ as for the low-speed case. There is no indication that the amplitude of the "bump" reduces with increasing

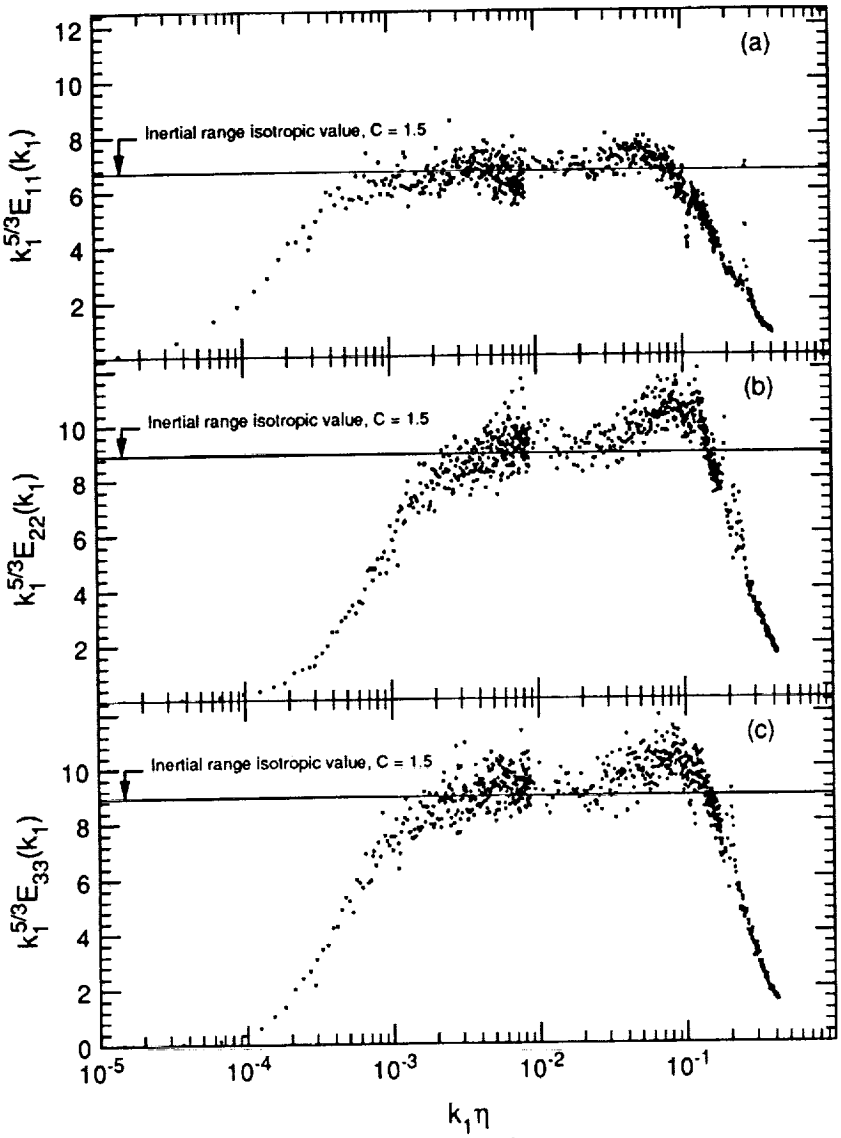

FIGURE 8. Compensated longitudinal and transverse spectra measured around mid-layer for $U_e \approx 50\ m/s$ and $R_\lambda \approx 1500$. (a) u-spectrum; (b) v-spectrum; (c) w-spectrum.

Reynolds number once a well-defined inertial subrange is present.

The above observations suggest that only the linear-log plot of compensated spectra can clearly show these intricate behaviors in the inertial-subrange region. Any claim for the existence of an inertial subrange should be substantiated with this kind of plot. Recall from Table 1 that the high-speed S^* value was larger than that of the low-speed case, which apparently indicates that here the deviation from the isotropic relations of the v-spectrum is mainly a function of the Reynolds number. Mestayer (1982), who presented u- and v-spectra (no w-spectrum was measured)

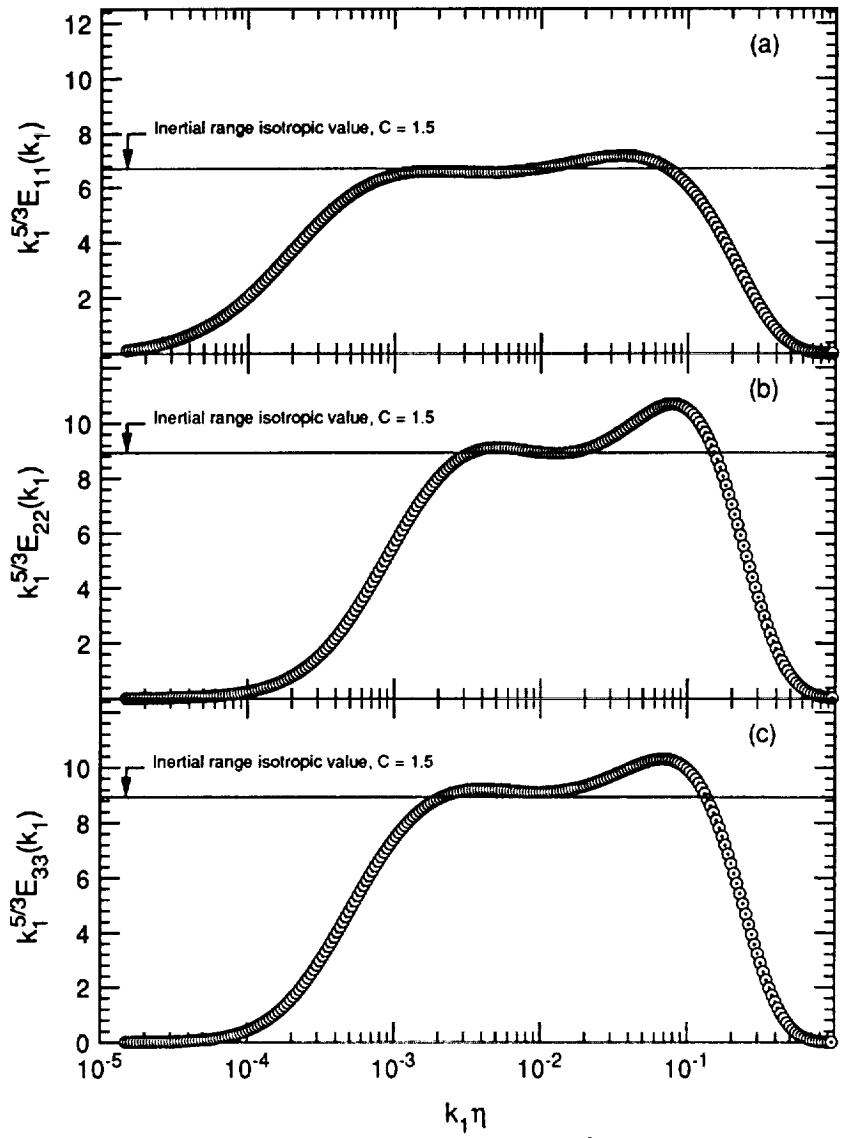

FIGURE 9. Compensated spectra obtained from 9^{th}-order, least-square polynomial fits to the data presented in Figure 8.

for only one position ($y/\delta = 0.33$) in a boundary layer at $R_\lambda \approx 616$ and $S_c^* = 0.02$, concluded that the local-isotropy criterion was not satisfied in the inertial-subrange region. Our measurements indicate that in his flow the Reynolds number was not large enough to produce $-5/3$ regions in the spectra.

The ratio of the measured w-spectrum to v-spectrum, $E_{33}^{meas}(k_1)/E_{22}^{meas}(k_1)$, in the inertial and the dissipation ranges should be equal to 1.0 if the turbulence is isotropic. As mentioned earlier, in I, for measurements at $y/\delta \approx 0.4$, $U_e \approx 40\ m/s$ and $R_\lambda \approx 1450$, this ratio deviated substantially from unity. Figure 10 shows the ratio of these spectra from I. The present measurements of this ratio at $y/\delta \approx 0.4$

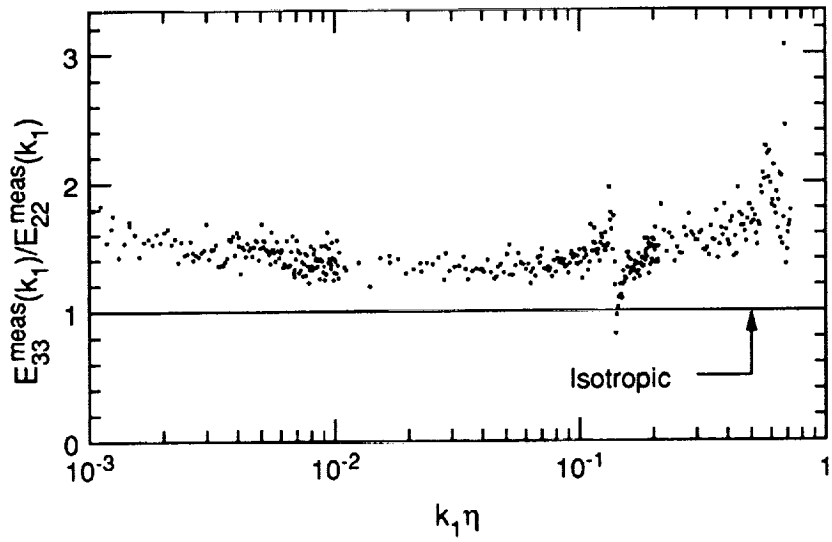

FIGURE 10. Ratio of the measured w-spectrum to v-spectrum at $y/\delta \approx 0.4$ for $U_e \approx 40\ m/s$ and $R_\lambda \approx 1450$ obtained in I.

for $R_\lambda \approx 1500$ are shown in Figure 11. The three plots of Figure 11 present data taken with different sets of X-wires having different calibrations. The data in Figure 11(c) were measured with the same high-pass filter-cutoff frequencies as in I (see section 2.1). As can be seen, the day-to-day variation among the present data is $\pm 10\%$, a fairly good repeatability. The present data are quite different from I, and, in view of all the measurement problems encountered during I (see section 2.1), we have greater confidence in the present data.

The ratio of the spectra measured around mid-layer in the present experiments for both the freestream velocities are shown in Figure 12. For $R_\lambda \approx 600$ and $R_\lambda \approx 1500$, the w-spectrum becomes equal to v-spectrum, to $\pm 10\%$, for $k_1\eta > 2 \times 10^{-2}$ and $k_1\eta > 3 \times 10^{-3}$ respectively.

The transverse spectra, $E_{22}^{calc}(k_1)$ and $E_{33}^{calc}(k_1)$ can be calculated from the measured longitudinal spectrum, $E_{11}^{meas}(k_1)$ using equation (2). An anisotropy measure may be defined as $E_{ii}^{calc}(k_1)/E_{ii}^{meas}(k_1)$, where $i = 2$ or 3 corresponds to v or w respectively. These anisotropy measures should be equal to 1.0 in an isotropic flow. We have used least-square fit data that were shown in Figures 7 and 9 to calculate these measures, which are shown in Figure 13. It appears that in both cases the isotropic value (to $\pm 10\%$) is obtained for the dissipation regions, and for $R_\lambda \approx 1500$, local isotropy is indicated for the entire inertial subrange of the transverse spectra. For $R_\lambda \approx 600$, the anisotropy coefficients for v and w become equal to $1.0 \pm 10\%$ at about $k_1\eta > 8 \times 10^{-3}$ and $k_1\eta > 4 \times 10^{-3}$ respectively. Comparison of the low- and high-Reynolds-number cases suggests that for the latter case, the rise in the anisotropy coefficients at the high-wavenumber end is not real, but rather an artifact of extending the polynomial fit to a region where no data was available.

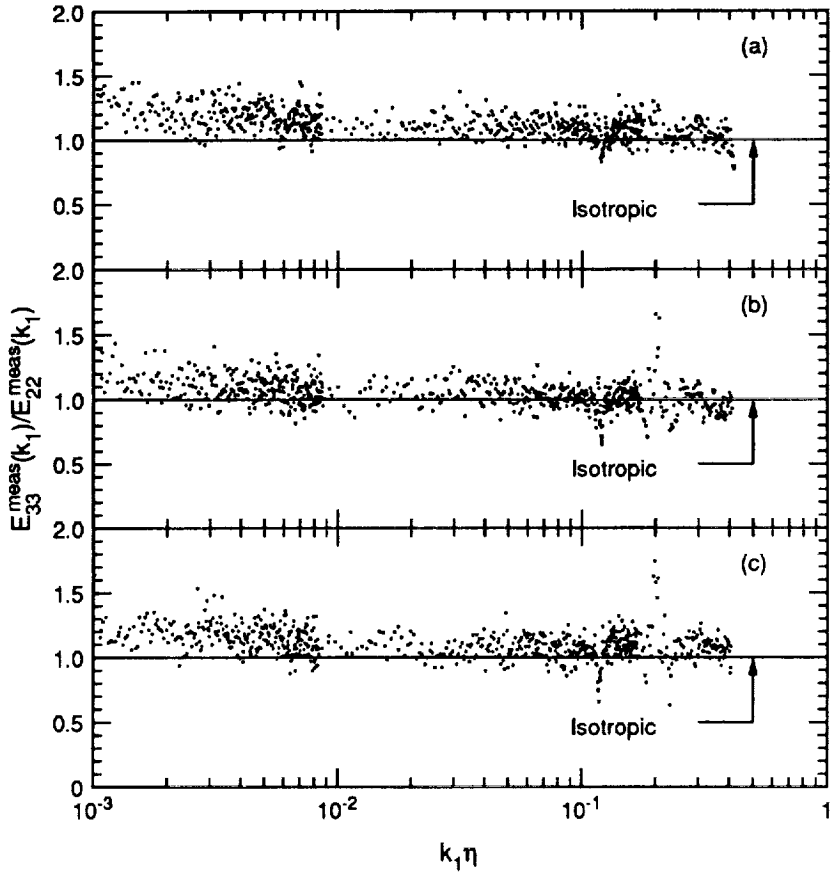

FIGURE 11. Ratios of the measured w-spectrum to v-spectrum at $y/\delta \approx 0.4$ for $U_e \approx 50\ m/s$ and $R_\lambda \approx 1500$ obtained under different experimental conditions.

For both Reynolds numbers under consideration, the normalized shear-stress co-spectrum, defined by equation (6), are shown in Figure 14. As expected (e.g. Mestayer 1982; Nelkin & Nakano 1983), these spectra roll-off to zero at high wavenumbers after showing initial values of about 0.6 to 0.7 in the low-wavenumber region. However, for $R_\lambda \approx 1500$, this coefficient reaches the zero value about half a decade later than the start of the $-5/3$ region.

Kraichnan (1959) proposed that the dissipation region of the 3D energy spectrum has a simple exponential decay with an algebraic prefactor of the form,

$$E(k) = A(k\eta)^{\alpha} exp[-\beta(k\eta)]. \tag{12}$$

Since then, his form has also been found in numerical simulations (DNS), but necessarily at very low Reynolds numbers, by other researchers who have proposed that for $0.5 \leq k\eta \leq 3$, $\beta \approx 5.2$ (Kida & Murakami 1987; Kerr 1990; Sanda 1992; Kida *et al.* 1992). It can be readily seen that for a locally-isotropic turbulence, the form of equation (12) and the numerical value of β, what ever it may be, should

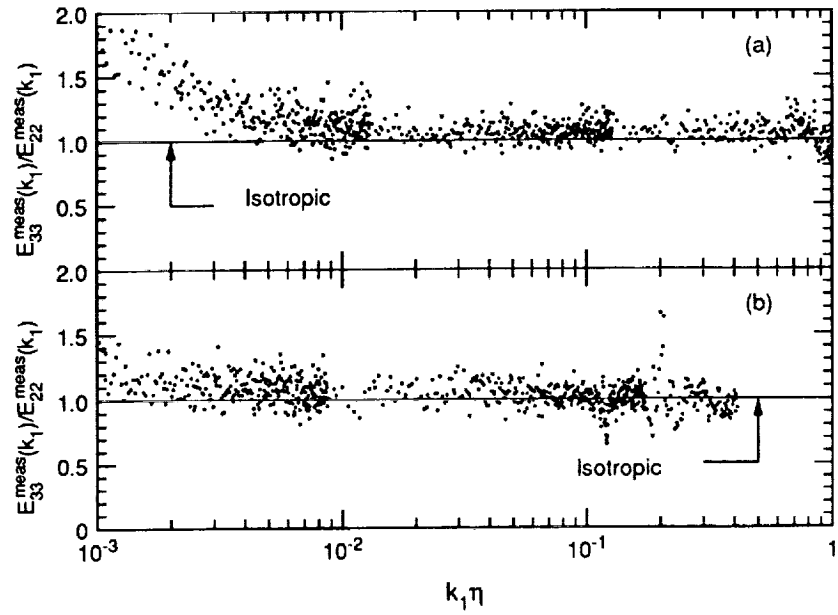

FIGURE 12. Ratios of the measured w-spectrum to v-spectrum obtained around mid-layer. (a) $U_e \approx 10\ m/s$, $R_\lambda \approx 600$; (b) $U_e \approx 50\ m/s$, $R_\lambda \approx 1500$.

be preserved for all three one-dimensional spectra. The exponential form for the u-spectrum in the far-dissipation region was observed in experiments by Sreenivasan (1985), but he proposed $\beta = 8.8$ for $0.5 \leq k_1\eta \leq 1.5$.

The compensated spectra can also be presented (see e.g. Smith & Reynolds 1991) as $\epsilon^{-2/3}k_1^{5/3}E_{ii}(k_1)$, where $i = 1$, 2 or 3 (no summation over i) corresponds to u, v or w respectively. Log-linear plots of these spectra at mid-layer for $R_\lambda \approx 600$ are shown in Figure 15. This figure also contains the low-speed spectra measured close to the wall at $y/\delta \approx 0.025$. It appears that in the dissipation region, all three components of spectra show an essentially exponential decay and follow reasonably well the straight lines with $\beta = 5.2$ for $0.5 \leq k_1\eta \leq 1$. Note that for the u-spectrum, the flat region for $k_1\eta \geq 0.9$ is perhaps due to noise and/or lack of resolution.

Local isotropy in the inertial subrange was also investigated, for consistency, with Kolmogorov's scaling laws for the structure functions, given by equations (7), (8), and (9). For both freestream velocities, the compensated third-order structure functions for the longitudinal velocity fluctuations, $(-5/4)r^{-1}D_{111}(r)$, are plotted versus (r/η) in Figure 16. With this scaling, the compensated third-order structure functions should become independent of r in the inertial subrange at a value equal to the dissipation. This is a good way to estimate ε if an inertial subrange exists. In each section of this figure, as explained in section 2.1, there are three different data sets corresponding to the three measurement bands used for resolving the large scales, inertial subrange, and the dissipation region. For $R_\lambda \approx 600$ and $R_\lambda \approx 1500$, about one-and-a-half and two decades of relatively flat regions can be seen respectively. The corresponding dissipation values taken from these plots were

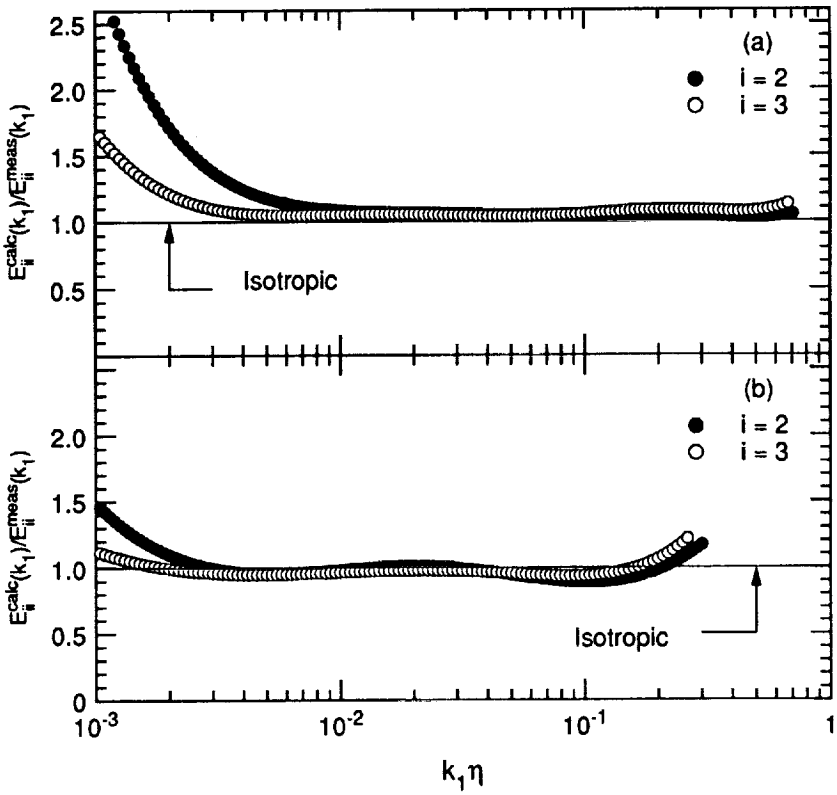

FIGURE 13. Anisotropy coefficients obtained around mid-layer. (a) $U_e \approx 10\ m/s$, $R_\lambda \approx 600$; (b) $U_e \approx 50\ m/s$, $R_\lambda \approx 1500$.

$\epsilon \approx 0.26\ m^2/s^3$ and $\approx 40\ m^2/s^3$, which are about 20% lower than those estimated from the spectra.

For $R_\lambda \approx 600$, the second-order compensated structure functions, $r^{-2/3}D_{ii}(r)$, where $i = 1$, 2, or 3 correspond to u, v, or w respectively, are plotted in Figure 17. For $R_\lambda \approx 1500$, a similar plot is shown in II. The three components of the second-order structure functions showed inertial-subrange regions, albeit the v-component for the low-speed case shows the least extent. For each Reynolds number considered independently, the v- and w-structure functions in the inertial subrange are equal to each other and are larger than the u-structure function by the factor 4/3, to within the measurement accuracy. Taking the Kolmogorov constant $C_2 \approx 2$ and for each Reynolds number using the dissipation obtained from its respective third-order structure function, the isotropic values of the second-order structure functions can be calculated. For the low speed case, these are shown as straight lines in Figure 17. For the high-Reynolds-number case, the deviation of the straight lines from the plateau regions was equivalent to a 10% change in the dissipation; better agreement was obtained if the ϵ estimated from spectra was used (see II). Therefore, here $C_2 = 2.0 \pm 0.1$.

Overall, as the above tests show, it is important that the concept of local isotropy be investigated by different means. The linear-log plot of compensated spectra

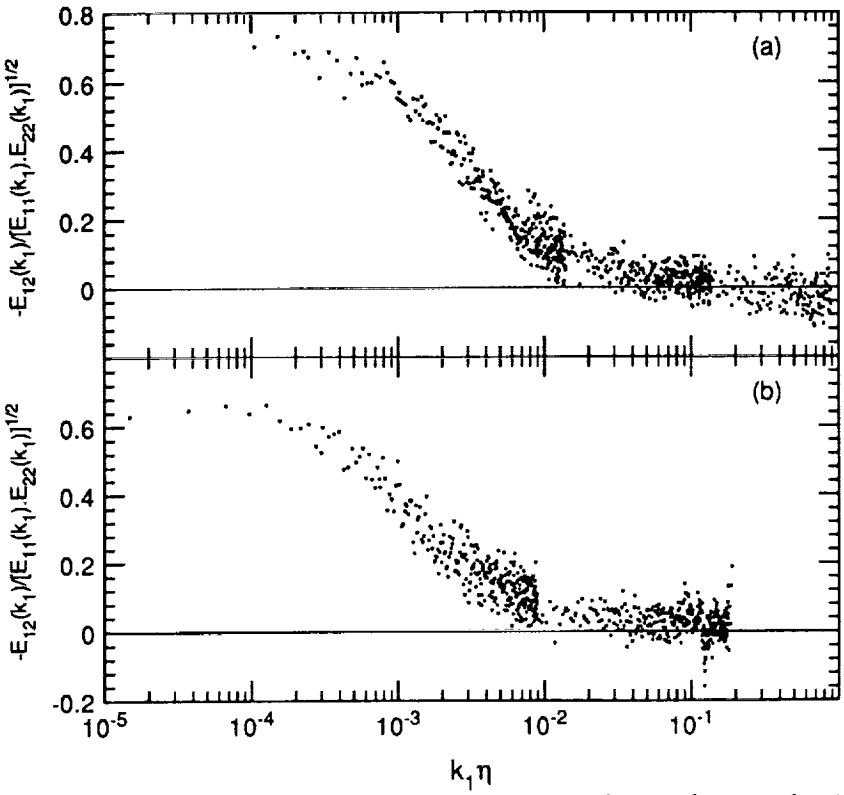

FIGURE 14. Normalized shear-stress co-spectra obtained around mid-layer. (a) $U_e \approx 10\ m/s$, $R_\lambda \approx 600$; (b) $U_e \approx 50\ m/s$, $R_\lambda \approx 1500$.

proved to be a very important test in the inertial-subrange region. The different sets of data taken around the mid-layer of the boundary layer at the two Reynolds numbers, $R_\lambda \approx 600$ and ≈ 1500, were complementary to each other. It appeared that the determining factor for the existence of a well-defined $-5/3$ region on all the three components of spectra was the Reynolds number: the v-spectrum appeared to be the most sensitive indicator of low R_λ effects. Spectral "bumps" between the inertial subrange and the dissipative region were observed on all the spectra. One may obtain an anomalously large Kolmogorov constant if these "bumps" are not identified. For the present experiments, we obtain $C = 1.5 \pm 0.1$ from the spectra and $C_2 = 2 \pm 0.1$ from the second-order structure functions. While in both high- and low-speed cases local isotropy is found (to $\pm 10\%$) in the dissipation regions, for $R_\lambda \approx 1500$, it was also found over the entire inertial subrange of the transverse spectra. However, the normalized shear-stress co-spectra reached the zero value about half of a decade later than the start of the $-5/3$ region. It was observed that in the dissipation region, all three components of spectra had an exponential decay and $\beta = 5.2$ for $0.5 \leq k_1\eta \leq 1$ agreed reasonably well with the present data.

In II we have analyzed the results taken in the log-layer at both nominal freestream velocities of $\approx 10\ m/s$ and $\approx 50\ m/s$. When the wall is approached, as expected, the shear-rate parameter increases and the Reynolds number decreases. In the

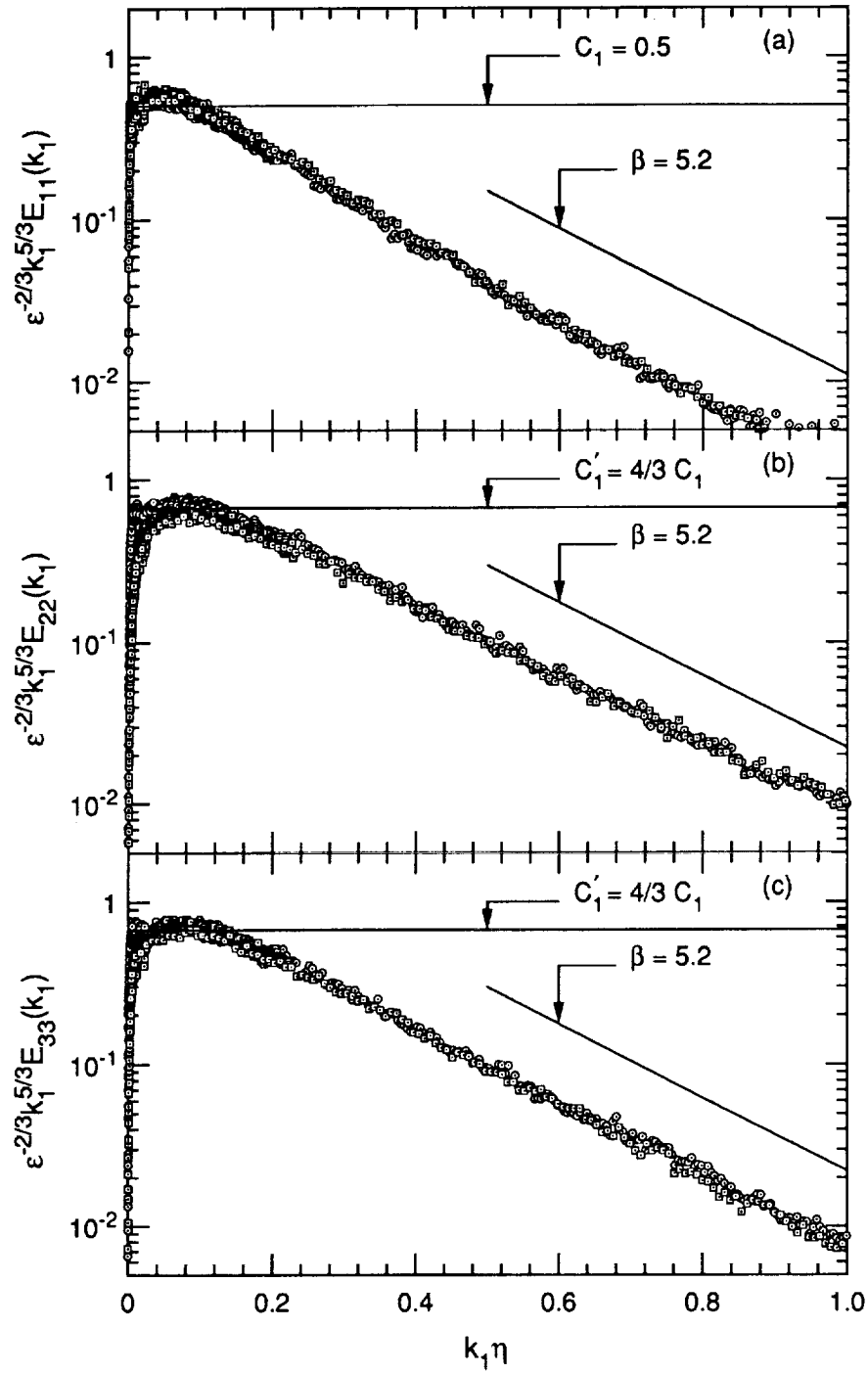

FIGURE 15. Log-linear plot of compensated spectra measured for $U_e \approx 10\ m/s$ at different locations in the boundary layer. (a) u-spectrum; (b) v-spectrum; (c) w-spectrum. □ ; $y/\delta \approx 0.025$ and $R_\lambda \approx 400$ (log-layer), ○ ; $y/\delta \approx 0.5$ and $R_\lambda \approx 600$ (mid-layer).

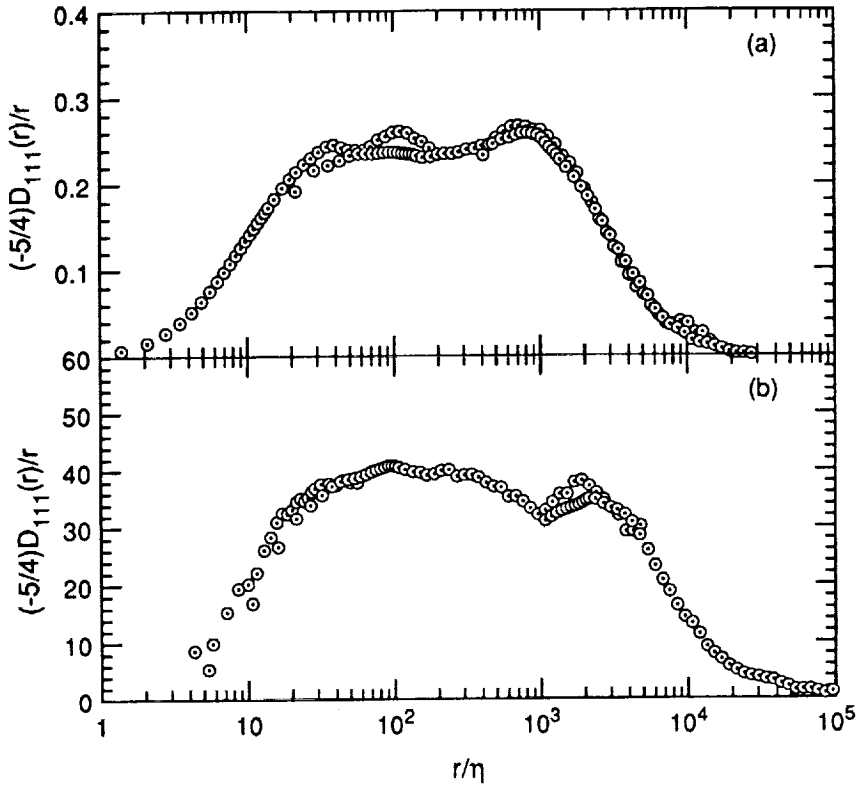

FIGURE 16. Compensated third-order structure functions for longitudinal velocity fluctuations measured around mid-layer. (a) $U_e \approx 10\ m/s$, $R_\lambda \approx 600$; (b) $U_e \approx 50\ m/s$, $R_\lambda \approx 1500$.

log-layer, comparison of the results taken at two freestream velocities gave some support to the conclusion of the above section that for the same y/δ the behavior of spectra for different freestream velocity was apparently determined only by the magnitude of the Reynolds number. The order in which the different components of spectra deviate from the $-5/3$ region, when the Reynolds number is decreased, is v, w, and then u. Referring back to Figure 15, which shows the exponential decay of the three components of spectra, it appears that the data for the near-wall position ($y/\delta \approx 0.025$) agree with the mid-layer measurements in the dissipation region. This perhaps implies some universality of the dissipating scales.

3. Future plans

The immediate task is to analyze all of the data completely. Also, it is important that the concept of local isotropy is examined in a variety of high-Reynolds-number flows with different amount of mean strain. This should enable us to establish a relationship between the degree of anisotropy of the small scales and the magnitude of the mean strain, if such a relation should exist. One possible experiment is the case where an initially two dimensional turbulent boundary layer, which has been developed on a flat plate, is forced to encounter an obstacle placed vertically

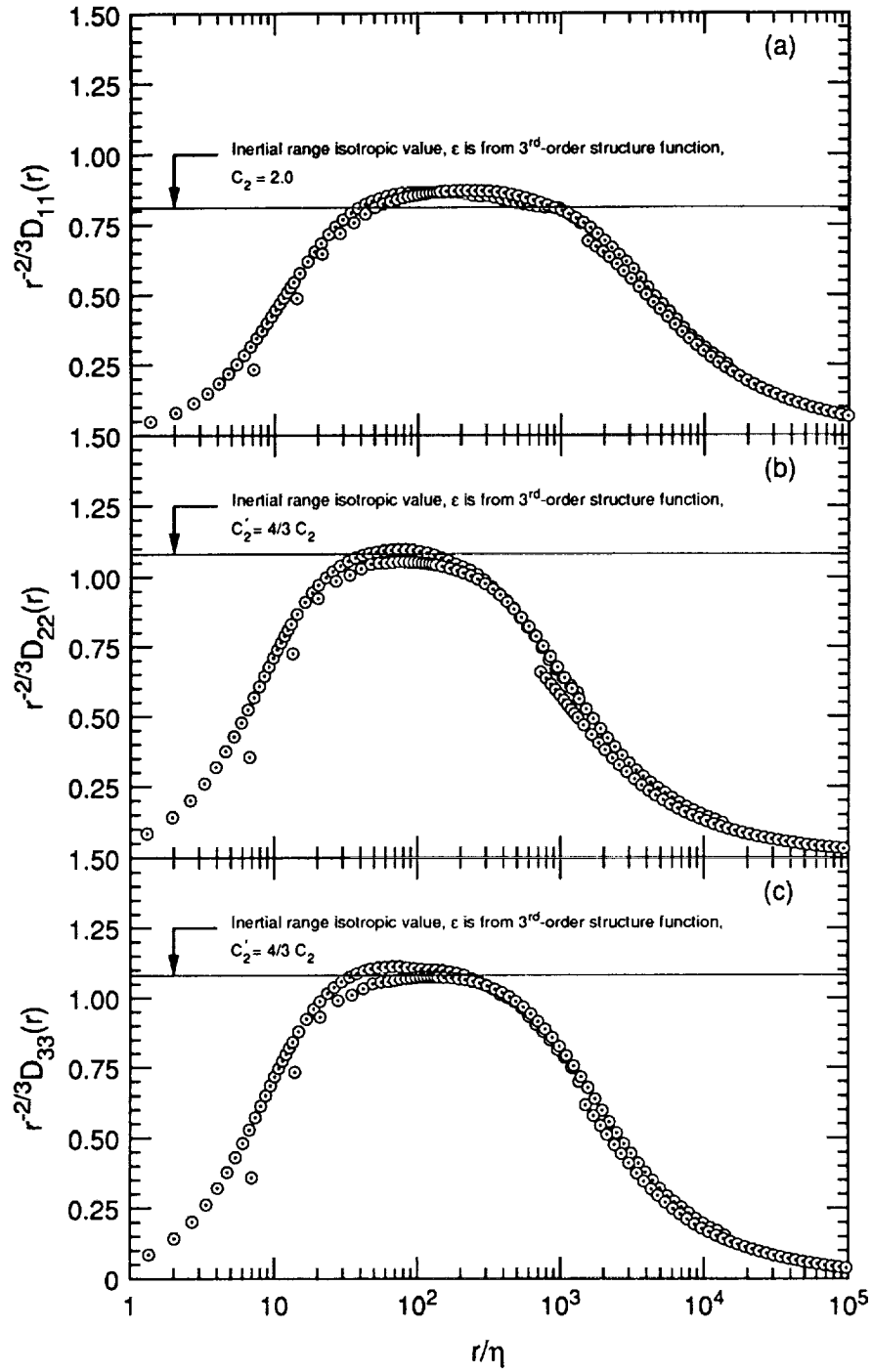

FIGURE 17. Compensated second-order structure functions for longitudinal and transverse velocity fluctuations measured around mid-layer for $U_e \approx 10\ m/s$ and $R_\lambda \approx 600$. (a) u; (b) v; (c) w.

in the boundary layer (e.g. a cylinder placed with its axis perpendicular to the plate). In this type of boundary layer, the pressure rises strongly as the obstacle is approached and in the imaginary plane of symmetry of the flow the boundary layer is also influenced by the effects of lateral straining. The size of this cylinder should be of the order of the thickness of the boundary layer. To conduct such an experiment in the 80′ by 120′ wind tunnel, a cylinder, which its diameter and length are approximately 1 m and 2 m respectively, are to be fixed to the ceiling of the tunnel. This presents an enormous amount of construction difficulties. However, we are investigating the possibilities of conducting such experiments.

Acknowledgements

We wish to thank Dr. Fredric Schmitz, Chief of the Full-Scale Aerodynamics Research Division at NASA Ames for permitting us to use their facility and to thank Dr. James Ross, Group Leader-Basic Experiments, who has been and will be in charge of coordinating our tests in the 80′ by 120′ wind tunnel. Our experiments would have not been possible without their help and efforts. We also wish to thank Drs. Paul Askins, Janet Beegle, and Cahit Kitaplioglu for their help and encouragement during all those "graveyard" shifts.

Through out the course of this work, we have had many valuable discussions with Prof. P. Bradshaw, Prof. P. Moin, Prof. W. C. Reynolds, Dr. J. Kim, Dr. R. S. Rogallo, Dr. P. A. Durbin, and Dr. A. A. Praskovsky. We gratefully thank them for all their help and advice.

We thank Prof. W. K. George for spending one week with us, during the course of which we investigated our hot-wire anemometery problems. We would also like to thank Dr. J. H. Watmuff and Prof. J. K. Eaton, with whom we consulted about these problems.

We wish to thank Prof. A. E. Perry for advising us on different aspects of this project and hot-wire anemometry.

We have greatly benefited from the suggestions made by Prof. R. A. Antonia, Prof. C. W. Van Atta, and Prof. M. Nelkin. We thank them for their advice.

We are grateful to Dr. N. R. Panchapakesan, who helped us during the second phase of these experiments.

REFERENCES

ANTONIA, R. A. & KIM, J. 1992 Isotropy of small-scale turbulence. *Proceedings of the Summer Program of the Center for Turbulence Research.* Stanford Univ./NASA Ames.

ANTONIA, R. A., KIM, J. & BROWNE, R. A. 1991 Some characteristics of small-scale turbulence in a turbulent duct flow. *J. Fluid Mech.* **233,** 369.

BATCHELOR, G. K. 1953 *The Theory of Homogeneous Turbulence. Cambridge University Press.*

CHAMPAGNE, F. H., FRIEHE, C. A., LA RUE, J. C. & WYNGAARD, J. C. 1977 Flux measurements, flux estimation techniques and fine scale turbulent measurements in the surface layer over land. *J. Atmos. Sci.* **34,** 515.

CHAPMAN, D. 1979 Computational aerodynamics development and outlook. *AIAA J.* **17,** 1293.

CORRSIN, S. 1958 On local isotropy in turbulent shear flow. *Report NACA R & M 58B11.*

DURBIN, P. A. & SPEZIALE, C. G. 1991 Local anisotropy in strained turbulence at high Reynolds numbers. *Recent Advances in Mechanics of Structured Continua.* **117,** 29.

EWING, D. W. & GEORGE, W. K. 1992 Spatial resolution of multi-wire probes. 45^{th} *Annual Meeting of the Fluid Dynamics Division of the American Physical Society, Tallahassee.*

GEORGE, W. K. & HUSSEIN, H. J. 1991 Locally axisymmetric turbulence. *J. Fluid Mech.* **233,** 1.

KERR, R. M. 1990 Velocity, scalar and transfer of spectra in numerical turbulence. *J. Fluid Mech.* **211,** 309.

KIDA, S., KRAICHNAN, R. H., ROGALLO, R. S., WALEFFE, F. & ZHOU, Y. 1992 Triad interactions in the dissipation range. *Proceedings of the Summer Program of the Center for Turbulence Research.* Stanford Univ./NASA Ames.

KIDA, S. & MURAKAMI, Y. 1987 Kolmogorov similarity in freely decaying turbulence. *Phys. Fluids A.* **30,** 2030.

KOLMOGOROV, A. N. 1941 The local structure of turbulence in incompressible viscous fluid for very large Reynolds numbers. *C. R. Acad. Sci U.R.S.S.* **30,** 301.

KOLMOGOROV, A. N. 1962 A refinement of previous hypotheses concerning the local structure of turbulence in a viscous incompressible fluid at high Reynolds number. *J. Fluid Mech.* **13,** 82.

KRAICHNAN, R. H. 1959 The structure of isotropic turbulence at very high Reynolds numbers. *J. Fluid Mech.* **5,** 497.

LANDAU, L. D. & LIFSHITZ, E. M. 1987 *Fluid Mechanics. Pergamon Press.*

LEE, M. J., KIM, J. & MOIN, P. 1990 Structure of turbulence at high shear rate. *J. Fluid Mech.* **216,** 561.

LUMLEY, J. L. 1965 Interpretation of time spectra measured in high-intensity shear flows. *Phys. Fluids.* **8,** 1056.

MOIN, P. 1990 Similarity of organized structures in turbulent shear flows. *Near-Wall Turbulence, S. J. Kline and N. H. Afgan (eds.), New York, Hemisphere Publishers, 2.*

MESTAYER, P. 1982 Local isotropy and anisotropy in a high-Reynolds-number turbulent boundary layer. *J. Fluid Mech.* **125,** 475.

MESTAYER, P., CHOLLET, J. P., & LESIEUR, M. 1983 Inertial subrange of velocity and scalar variance spectra in high-Reynolds-number three-dimensional

turbulence. *Turbulence and Chaotic Phenomena in Fluids, T. Tatsumi (ed.), Elsevier Science Publishers, 285.*

NELKIN, M. & NAKANO, T. 1983 How do the small scales become isotropic in Navier-Stokes turbulence?. *Turbulence and Chaotic Phenomena in Fluids, T. Tatsumi (ed.), Elsevier Science Publishers, 319.*

PERRY, A. E. 1982 *Hot-Wire Anemometry. Claredon Press Oxford.*

SADDOUGHI, S. G. & VEERAVALLI, S. V. 1992 Local isotropy in high Reynolds number turbulent shear flows. *CTR Manuscript 140.* Center for Turbulence Research, Stanford Univ./NASA-Ames.

SAFFMAN, P. G. 1992 Vortical states, vortex filaments, and turbulence. *Review Tutorials, Summer Program of the Center for Turbulence Research.* Stanford Univ./NASA Ames.

SANADA, T. 1992 Comment on the dissipation-range spectrum in turbulent flows. *Phys. Fluids A.* **4,** 1086.

SMITH, L. M. & REYNOLDS, W. C. 1991 The dissipation-range spectrum and the velocity-derivative skewness in turbulent flows. *Phys. Fluids A.* **3,** 992.

SREENIVASAN, K. R. 1985 On the fine-scale intermittency of turbulence. *J. Fluid Mech.* **151,** 81.

TAYLOR, G. I. 1935 Statistical theory of turbulence. *Proc. Roy. Soc. Lond. A.* **151,** 421.

VEERAVALLI, S. V., & SADDOUGHI, S. G. 1991 A preliminary experimental investigation of local isotropy in high-Reynolds-number turbulence. *Annual Research Briefs of Center for Turbulence Research.* Stanford Univ./NASA Ames.

WILLIAMS, R. N. & PAULSON, C. A. 1978 Microscale temperature and velocity spectra in the atmospheric boundary layer. *J. Fluid Mech.* **83,** 547.

WYNGAARD, J. C. 1968 Measurements of small-scale turbulence structure with hot wires. *J. Sci. Instrum.* **1,** 1105.

Center for Turbulence Research
Annual Research Briefs 1992

An investigation of small scales of turbulence in a boundary layer at high Reynolds numbers

By J. M. Wallace[1], L. Ong[1] AND J.-L. Balint[1]

The assumption that turbulence at large wave-numbers is isotropic and has universal spectral characteristics which are independent of the flow geometry, at least for high Reynolds numbers, has been a cornerstone of closure theories as well as of the most promising recent development in the effort to predict turbulent flows, viz. large eddy simulations. This hypothesis was first advanced by Kolmogorov (1941, 1962) based on the supposition that turbulent kinetic energy cascades down the scales (up the wave-numbers) of turbulence and that, if the number of these cascade steps is sufficiently large (i.e. the wave-number range is large), then the effects of anisotropies at the large scales are lost in the energy transfer process. Experimental attempts have repeatedly been made to verify this fundamental assumption. However, Van Atta (1991) has recently suggested that an examination of the scalar and velocity *gradient* fields is necessary to definitively verify this hypothesis or prove it to be unfounded. Of course, this must be carried out in a flow with a sufficiently high Reynolds number to provide the necessary separation of scales in order unambiguously to provide the possibility of local isotropy at large wave-numbers. An opportunity to use our 12-sensor hot-wire probe to address this issue directly was made available at the 80'x120' wind tunnel at the NASA Ames Research Center, which is normally used for full-scale aircraft tests. This is an initial report on this high Reynolds number experiment and progress toward its evaluation.

1. Previous studies

Veeravalli and Saddoughi (1991), of the Center for Turbulence Research (CTR), performed experiments with an X-array of two hot-wire sensors in the boundary layer of the upper wall of the NASA Ames 80 ft. x 120 ft. wind-tunnel at a streamwise station with a 50 m fetch. At this location, with a freestream velocity $U_\infty \approx 40\ m/s$, the boundary layer thickness was $\delta \approx 1.0\ m$, the Reynolds number based on momentum thickness was $R_\theta (\equiv U_\infty \theta/\nu) \approx 300{,}000$, and the turbulence Reynolds number at $y/\delta \approx 0.4$ was $R_\lambda (\equiv u_{rms}\lambda/\nu) \approx 1{,}450$, one of the largest ever achieved in a laboratory. Under these conditions and at this location, the Kolmogorov length scale was $\eta \approx 0.1\ mm$. Veeravalli and Saddoughi (1991) obtained one-dimensional velocity component spectra, at $y/\delta = 0.4$, which have a two-decade range of the inertial wave-number subrange. They tested the isotropy of the velocity field where, for isotropic flow,

$$\phi_v(k_x) = \phi_w(k_x) = 1/2[\phi_u(k_x) - k_x d\phi_u(k_x)/dk_x]. \qquad (1)$$

1 Turbulence Research Laboratory, University of Maryland, College Park, MD 20742

They found that the streamwise and spanwise velocity components, u and w, exhibit isotropic spectral properties in the inertial subrange but that the normal component, v, does not. Furthermore, although they obtained more than a decade of spectral data at wave-numbers in the dissipation range, this data was contaminated by electronic noise.

Van Atta *et al.* (1992) have also analyzed our moderately low Reynolds number boundary layer at $Re_\theta \approx 2700$ [Balint *et al.* (1991)], and two-stream mixing layer at $Re_\theta (\equiv \Delta U\theta/\nu) \approx 7200$ [Balint *et al.* (1989)] databases for evidence of local isotropy, utilizing an expression which gives the isotropic relationship between the one-dimensional vorticity spectrum components. This expression is analogous to that for the velocity spectrum components and is given by

$$\phi_{\omega_y}(k_x) = \phi_{\omega_z}(k_x) = 1/2[\phi_{\omega_x}(k_x) - k_x d\phi_{\omega_x}(k_x)/dk_x]. \tag{2}$$

They found that the local isotropy hypothesis is not valid deep in the boundary layer at $y^+ \approx 18$. Only at the highest wave-numbers in the mixing layer on the splitter plate plane is there any indication of its validity. However, the boundary layer flow examined had no extended $k^{-5/3}$ inertial subrange, and the mixing layer flow had only a limited one. A definitive test requires relatively well resolved measurements of the velocity and velocity gradient fields at much higher Reynolds numbers.

2. Objectives

The present experiments have been designed to provide direct measurements of the velocity vector as well as the velocity gradient tensor fields at high Reynolds number, which is necessary for a definitive test of the large wave-number local isotropy hypothesis.

The acquired database will be archived at the Turbulence Research Laboratory of the University of Maryland and at the Center for Turbulence Research of Stanford University/NASA Ames. This database, of course, will not only be useful for the verification of the local isotropy hypothesis. It will be used for investigating the structural characteristics of the turbulent kinetic energy dissipation rate field which can only be examined through an analysis of the turbulent strain-rates. Furthermore, almost all of the statistical and structural characteristics of the velocity and vorticity fields have been obtained only at moderately low Reynolds numbers. Many of these are known only for the quite low Reynolds numbers of the direct numerical simulations of turbulent boundary layer and parallel channel flows. It is an article of faith, but an often questioned one, that these characteristics are Reynolds number independent. This database should make possible the direct experimental test of this article of faith.

3. Experimental facility and instrumentation

These experiments were performed with the freestream velocity of the wind tunnel at $U_e \approx 10\ m/s$, which corresponds to a momentum thickness Reynolds number of $R_\theta \approx 65{,}000$ and a maximum turbulence Reynolds number of $R_\lambda \approx 600$ at

$y/\delta \approx 0.5$ [Saddoughi (1992)], with the boundary layer thickness $\delta \approx 1.0\ m$. Under these conditions, the Kolmogorov length scale is estimated to be $\eta \approx 0.32\ mm$. This is about the spatial resolution we can achieve in our tunnel at the University of Maryland, but in the present flow it is achieved at almost 25 times higher Reynolds number based on momentum thickness. The range of values of the turbulence Reynolds numbers R_λ at the tunnel freestream speed of 10 m/s is still much higher than those which normally can be achieved in the laboratory. For example, in our University of Maryland wind-tunnel, the momentum thickness Reynolds number $R_\theta \approx 2,700$ at $U_\infty = 3.5\ m/s$ [Balint *et al.* (1991)], and $R_\lambda \approx 250$ in the logarithmic layer.

The present experiments were conducted on the ceiling of the wind tunnel at approximately 50 m from the inlet and about 6.6 m from the side wall. This is the location of one of the side viewing ports because the centrally located viewing port was unavailable for the present experiments. It is still to be determined whether secondary corner flow affected the measurements. The Plexiglass window was replaced with a specially designed probe-holder platform. The probe was mounted on a stainless steel rod that was fitted through the platform, and measurements were made with the probe at $y/\delta \approx 0.1$, 0.2, 0.3, 0.4, 0.5, 0.6, 0.7, and 1.6 from the ceiling of the wind tunnel.

3.1 Data acquisition procedure

The hot-wire sensors were operated in the constant temperature mode at an overheat ratio of 1.2 with a A.A. Lab Systems 12-channel hot-wire anemometer. The maximum sustainable throughput of the our Optim 5017A Megadac data acquisition system was approximately 72 kHz, i.e. 6 kHz per channel when sampling twelve channels simultaneously. This relatively low sampling frequency could not sufficiently resolve the expected Kolmogorov frequency range, which was estimated to be approximately 4.5 to 5.5 kHz [Saddoughi (1992)]. In order to overcome this technical limitation, the outputs of the anemometer channels were analog recorded on FM tapes. In this manner, to achieve a high digitization rate, one could either play back the tape at a slower speed than the record speed or digitize each of the channels individually. The second method requires a synchronization signal to be simultaneously recorded on the tape in order to uniquely identify a common trigger time for all the channels. The trigger used was simply a switch connected to a 1.5 V battery. The switch was activated a few seconds into the data recording and kept closed for the duration of the measurement. The 16 channel V-Store FM tape recorder used was provided by RACAL Recorders Inc. through H. Keating Moore and Associates. This FM instrumentation recorder was operated at 40 in/s providing a frequency response of approximately 20 kHz, which is roughly 4 times greater than the expected Kolmogorov frequencies. A total of 13 channels (including the synchronization channel) were recorded at each measurement location for recording durations of 180 s.

3.2 The 12-sensor hot-wire probe

The new 12-sensor probe used in the present study, constructed and tested by P.

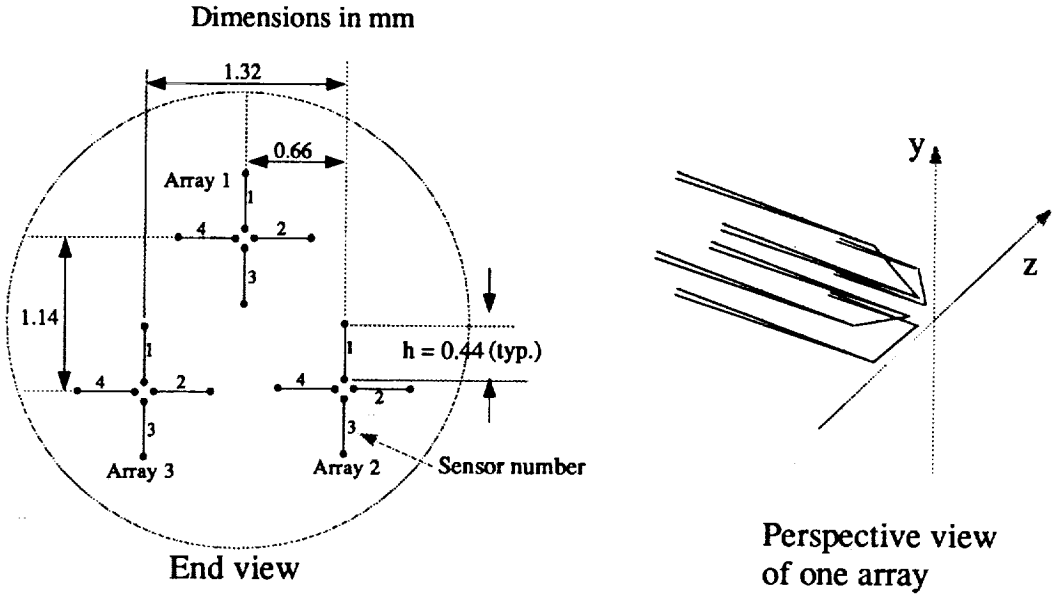

FIGURE 1. Schematic diagrams of the twelve sensor probe

Vukoslavčević, consists of three arrays of 4 hot-wire sensors each, arranged as shown in Figure 1. This probe is able to extend the range of acceptable angles of attack of the velocity vector, which was previously a problem with the 9-sensor design [Vukoslavčević *et al.* (1991)], and to resolve uniqueness problems in the solution of the cooling law equations at these large angles of attack.

During calibration, the probe was placed at the exit of a calibration jet where a uniform velocity profile is generated. The probe was pitched and yawed through $\pm 20^o$ at several fixed flow velocities to simulate the range of angles of attack which the flow in the wind-tunnel is expected to impose on the probe. Following Jorgensen (1971), each sensor's response to the various velocity vectors can be described by defining an effective cooling velocity:

$$U_{eff}^2 = a_1 U^2 + a_2 V^2 + a_3 W^2 + a_4 UV + a_5 UW + a_6 VW. \tag{3}$$

This cooling velocity is also a function of the bridge output voltage which for the present study was fitted with a fourth order polynomial:

$$U_{eff}^2 = P(E) = A_1 + A_2 E + A_3 E^2 + A_4 E^3 + A_5 E^4. \tag{4}$$

The probe response equation is thus a combination of the above two expressions, where the calibration coefficients a and A are obtained by a least squares fit of the calibration data. It is easily seen that when three calibrated hot-wire sensors are subjected to the same flow, one can write a set of three coupled response equations where the only unknowns are the three velocity components. Conceptually, with

three arrays of at least three sensors each, one can simply obtain the velocity components at each array and calculate the gradients by finite differences. However, it is necessary to account for velocity ***gradients*** in the solution of the response equations. This can be done by re-writing the velocity components in a Taylor's series expansion (to first order) about the centroid of the probe and iteratively solving the set of 9 coupled equations, where the unknowns are now the velocity vector and gradient tensor components: $U, V, W, \partial U/\partial y, \partial U/\partial z, \partial V/\partial y, \partial V/\partial z, \partial W/\partial y, \partial W/\partial z$. The streamwise gradients can then be obtained by Taylor's hypothesis [Piomelli *et al.* (1989)] to within the buffer layer of the boundary layer.

With the present 12-sensor probe, there is a total of three extra sources of information resulting from having one spare wire at each array. This built-in redundancy was designed based on previous experience with the nine-sensor probe that some uniqueness and convergence problems can be circumvented by an optimal choice of a three-sensor arrangement, depending on the angle of attack of the velocity vector. This redundancy can also be exploited by solving the twelve coupled response equations for the nine unknowns by an optimization routine such as that developed by Marasli, Nguyen and Wallace (1992). These two methods are being studied for final implementation for the present set of measurements.

4. Preliminary analysis

At this time, for each of the measurement positions, 30 seconds of data from the FM tape have been digitized at 20 kHz, channel by channel, and archived on digital tape. The trigger signal was simultaneously digitized with each of these channels to ensure proper synchronization of the twelve sets of hot-wire voltages. The twelve digitized data files for each position have been combined into a single file consisting of only the twelve hot-wire voltages. The three measurement positions selected for preliminary analysis are at $y/\delta \approx 0.1$, 0.5 and 1.6. The temporally aligned digital data files for these three positions have been reconstructed. An analysis of the calibration files for the experiments indicated that recovery of the induced calibration velocities from the calibration coefficients and calibration voltages are good.

5. Closure

A unique experiment to measure the velocity vector and the velocity gradient tensor in a very high Reynolds number boundary layer flow has been performed. While the analysis of the boundary layer data is still in progress, evaluation of the calibration data and preliminary turbulence data results indicate that the probe performed as expected. Further work is underway to complete the analysis.

Acknowledgements

The authors would like to extend their appreciation to RACAL Inc. and Howard Harvey of H. Keating Moore and Associates for the loan of the FM tape recorder. The help of S. G. Saddoughi and N. R. Panchapakesan throughout this difficult

experiment is greatly appreciated. This research was supported by NSF Grant CTS 9217505 and by the Center for Turbulence Research.

REFERENCES

BALINT, J.-L., WALLACE, J. M. & VUKOSLAVČEVIĆ, P. 1991 The velocity and vorticity vector fields of a turbulent boundary layer: Part 2, Statistical Properties. *J. Fluid Mech.* **228,** 53.

BALINT, J.-L., WALLACE, J. M. & VUKOSLAVČEVIĆ, P. 1989 The statistical properties of the vorticity field of a two-stream turbulent mixing layer. *Advances in Turbulence 2, edited by H.H. Fernholz and H. E. Fiedler.* (Springer-Verlag, Berlin, **74**

JORGENSEN, F. E. 1971 Directional sensitivity of wire and fiber film probes. *DISA Information.* **11,** 31-37.

KOLMOGOROV, A. N. 1941 The local structure of turbulence in incompressible viscous fluid for very large Reynolds numbers. *C.R. Acad. Sci. U.R.S.S.* **30,** 301.

KOLMOGOROV, A.N. 1962 A refinement of previous hypotheses concerning the local structure of turbulence in a viscous incompressible fluid at high Reynolds number. *J. Fluid Mech.* **13,** 82.

MARASLI, B., NGUYEN, P & WALLACE, J.M. 1991 A calibration technique for multiple-sensor hot-wire probes and its application to vorticity measurements in the wake of a circular cylinder. *Submitted to Experiments in Fluids.*

PIOMELLI, U. AND BALINT, J.-L. AND WALLACE, J.M. 1989 On the validity of Taylor's hypothesis for wall-bounded turbulent flows. *Phys. Fluids A.* **1,** 609-611.

SADDOUGHI, S. G. 1992 Local isotropy in high Reynolds number shear flows. *CTR Annual Research Briefs,* Center for Turbulence Research, Stanford Univ./NASA-Ames.

VAN ATTA, C. W. 1991 Local isotropy of the smallest scales of turbulent scalar and velocity fields. *A. N. Kolmogorov commemorative issue of Proc. Roy. Soc. A.* **434,** 139.

VAN ATTA, C. W., BALINT, J.-L. & WALLACE, J. M. 1992 Local isotropy of the vorticity field in turbulent flows. *Submitted to Physics of Fluids A.*

VEERAVALLI, S. V. & SADDOUGHI, S. G. 1991 A preliminary investigation of local isotropy in high Reynolds number turbulence. *CTR Annual Research Briefs,* Center for Turbulence Research, Stanford Univ./NASA-Ames.

VUKOSLAVČEVIĆ, P., WALLACE, J. M. & BALINT, J.-L. 1991 The velocity and vorticity vector fields of a turbulent boundary layer: Part 1. Simultaneous measurements by hot-wire anemometry. *J. Fluid Mech.* **228,** 25-51.

Probability density distribution of velocity differences at high Reynolds numbers

By Alexander A. Praskovsky[1]

1. Motivation and objectives

Recent understanding of fine-scale turbulence structure in high Reynolds number flows is mostly based on Kolmogorov's original (1941) and revised (1962) models. The main finding of these models is that intrinsic characteristics of fine-scale fluctuations are universal ones at high Reynolds numbers, i.e., the functional behavior of any small-scale parameter is the same in all flows if the Reynolds number is high enough. The only large-scale quantity that directly affects small-scale fluctuations is the energy flux through a cascade (see remarks by Kraichnan 1974). In dynamical equilibrium between large- and small-scale motions, this flux is equal to the mean rate of energy dissipation ε.

Kolmogorov obtained some general relations which are the foundation of almost all recent models. In particular, he found that for distances r within the inertial subrange, i.e., if $\eta \ll r \ll L$, the moments of velocity difference $\Delta u(r) = u(x) - u(x+r)$ can be described as (see Monin & Yaglom 1967)

$$< [(\Delta u(r)]^p >= C_p \varepsilon^{p/3} r^{p/3} \left(\frac{r}{L}\right)^{\zeta_p - p/3} . \qquad (1)$$

Hereafter, x and u denote coordinate and velocity component in the mean flow direction, L and η denote the integral scale and Kolmogorov's viscous scale, C_p are constants, and ζ_p is some unknown function.

The main problem in a creation of the theory of fine-scale turbulence structure is clearly seen in Equation (1). Indeed, this equation was derived from general physical considerations and dimensional analysis. However, it is an incomplete result because the function ζ_p cannot be obtained by such a method, nor, at least at the moment, can it be found directly from the Navier-Stokes equations. The same is valid for the probability density distribution (pdd) $P(\Delta u)$ of Δu which is a more general function than ζ_p. As a result, various heuristic models to describe $P(\Delta u)$ have been proposed (for critical review and classification of the models see She 1991).

We believe that further progress in development of more adequate models of $P(\Delta u)$ is hindered by the lack of reliable experimental data. All known measurements were analyzed by Gagne, Hopfinger & Frisch (1988 hereinafter referred to as G,H&F). Two novel results were obtained there: (i) the functional behavior of the

1 Central Aero-Hydrodyamic Institute, Moscow, Russia

tails of the pdd can be represented by $P(\Delta u) \propto \exp(-b(r)|\Delta u/\sigma_{\Delta u}|)$; (ii) the logarithmic decrement $b(r)$ scales as $b(r) \propto r^{0.15}$ when separation r lies in the inertial subrange (symbol σ_φ denotes the rms value of any quantity φ).

The pdd of velocity difference is a very important characteristic for both the basic understanding of fully developed turbulence and engineering problems. Hence, it is important to test the findings (i) and (ii) in high Reynolds number laboratory shear flows.

2. Accomplishments

2.1. Apparatus and measurement techniques

Velocity time series taken in two different high Reynolds number laboratory shear flows were analyzed. The first one was obtained in the large wind tunnel of the Central Aerohydrodynamic Institute (Moscow). The mixing layer between a jet issuing from an elliptical nozzle ($14\times24\text{m}^2$) and ambient air was studied. The wind tunnel had an open 24m long working section. Measurements were performed on the line which continued the nozzle wall at a distance $x = 20$m downstream of the nozzle. The free jet velocity was equal to $U_0 = 11.8$m/s.

The second time series was obtained in the return channel of the same wind tunnel. The channel was 175m long and 22m wide. Its height rose linearly from 20m up to 32m. Measurements were done in the plane of symmetry from a tower 5m above floor level.

In both experiments, standard thermoanemometers were used. X-wire probes with perpendicular wires were operated at an overheat ratio of 1.8. Wires were made of platinum-plated tungsten with diameter of 2.5μm. Both the active length and the distance between the wires were 0.5mm. Signals from both wires were filtered to reduce noise level, digitized, and processed on a computer. The low-pass filter cut-off frequency was equal to $f_c = 1.7$kHz. The sampling frequency f_s and one-channel time series length N were equal to 8kHz and 2000000 respectively. These values were chosen to investigate the inertial subrange. To measure the energy dissipation rate ε, the values of f_c, f_s, and N were doubled.

Description of the experiments and analysis of measurement errors (temporal and spatial resolution, statistical convergence, use of Taylor's hypothesis, non-linearity of the hot-wire response, etc.) can be found in Karyakin, Kuznetsov & Praskovsky (1991).

The main flow characteristics at the measurement points are listed in Table 1 (abbreviations RC and ML stand for return channel and mixing layer). The longitudinal velocity component u was processed at each point. Taylor's hypothesis was used to convert the temporal into the spatial coordinate. The mean energy dissipation rate was estimated using the local-isotropy relation: $\varepsilon = 15\nu < (\partial u/\partial x)^2 >$. The integral length scale L, Taylor's microscale λ, Kolmogorov's scale η, and Reynolds number R_λ were estimated by standard formulas defined by

$$L = \frac{< u >}{\sigma_u^2} \int_0^\infty < [u(t+\tau) - < u >][u(t) - < u >] > d\tau,$$
$$\lambda = \frac{\sigma_u}{\sigma_{\partial u/\partial x}}, \qquad \eta = (\nu^3/\varepsilon)^{1/4}, \qquad R_\lambda = \frac{\sigma_u \lambda}{\nu}, \tag{2}$$

where t is time and τ is a time delay.

TABLE 1.

Apparatus	RC	ML
$< u >, m/s$	10.8	7.87
$\sigma_u, m/s$	1.03	1.67
$\varepsilon, m^2/s^3$	0.11	1.9
λ, mm	46	18
$R_\lambda \cdot 10^{-3}$	3.2	2.0
L, m	4.8	1.3
η, mm	0.41	0.21
$(L/\eta) \cdot 10^{-3}$	12	6.2

Table 1. Main turbulence characteristics at the measurement points.

It is seen from Table 1 that $L/\eta > 6000$. This indicates that in both flows under consideration, fairly large inertial subrange regions should exist.

2.2. Results

It is necessary to determine the inertial subrange bounds for each measurement point since Kolmogorov's definition $\eta \ll r \ll L$ is not exact. It was assumed that the distance r belongs to the inertial subrange if $20\eta \leq r \leq L/5$. The structure functions $< [\Delta u(r)]^p >$ for $p = 2, 3, 4, 6$ are presented in Figure 1, where the bounds are indicated by vertical arrows. The chosen bounds appear plausible: "the two-thirds law" and Kolmogorov's exact equation

$$< [\Delta u(r)]^3 >= -\frac{4}{5}\varepsilon r \tag{3}$$

are in agreement with experimental data within these bounds. (The absolute values of the third-order structure functions are plotted.)

Typical pdd of velocity differences in the two measurement points are presented in Figure 2. Results for three widely different values of r/η within the inertial subrange are presented for every point. All curves in Figure 2 are truncated just before the first point at which $P(\Delta u) = 0$ (no samples in the "bin" of width $\pm 0.2\sigma_{\Delta u}$). Thus, implausible values of $P(\Delta u)$ caused by insufficient samples are ignored. It is seen in Figure 2 that, for sufficiently high amplitudes $|\Delta u/\sigma_{\Delta u}| \geq h$, the obtained pdd may be approximated by the expression proposed by G,H&F

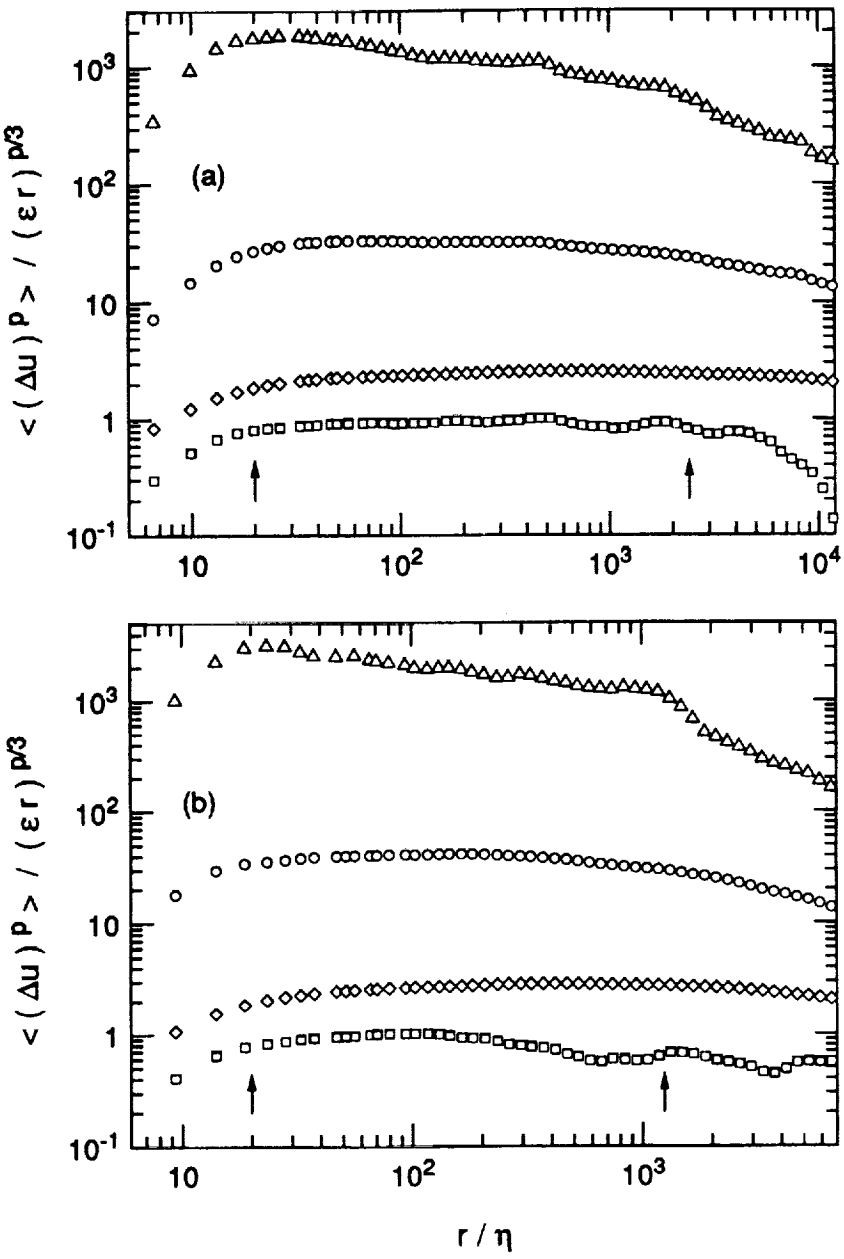

FIGURE 1. Higher-order velocity structure functions (absolute values for $p = 3$). (a), return channel; (b), mixing layer; ◇, $p = 2$; □, 3; ○, 4; △, 6. Vertical arrows correspond to the inertial-range bounds.

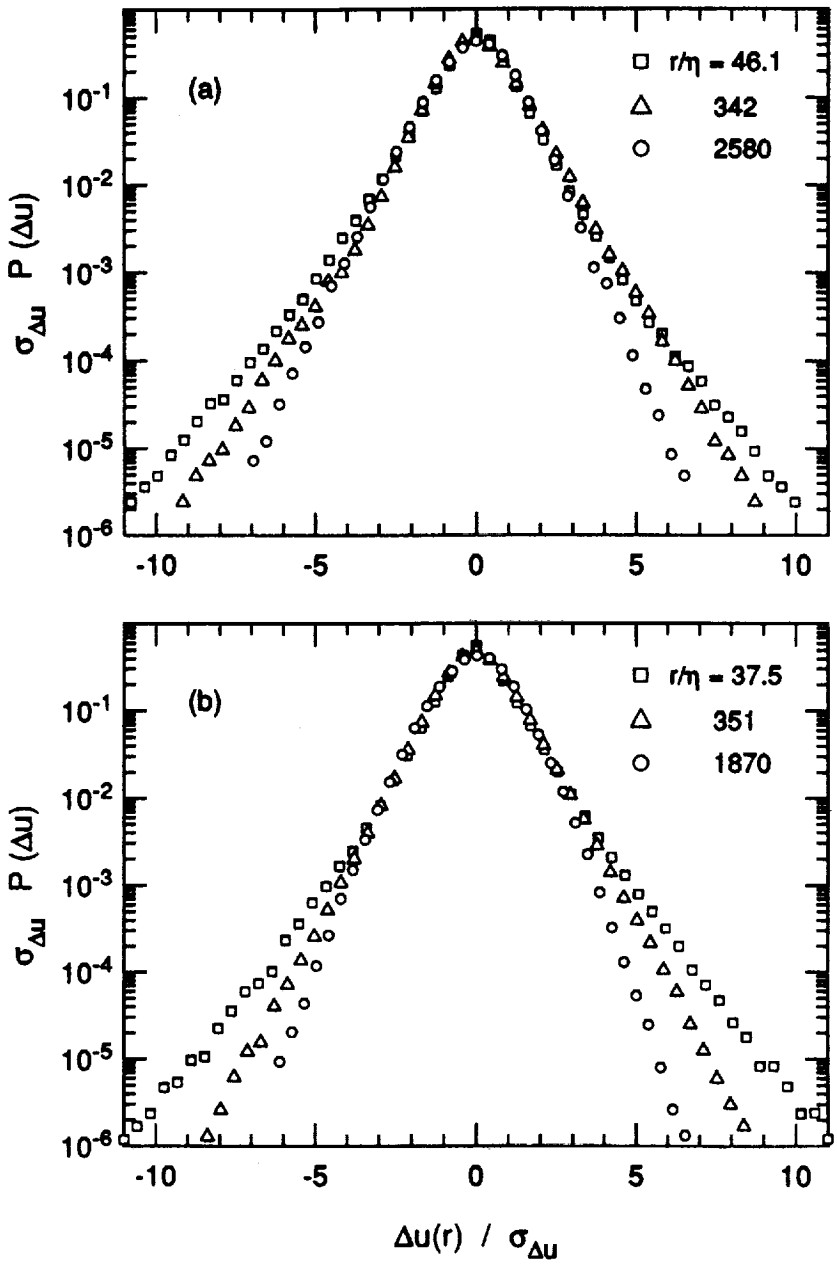

FIGURE 2. The pdd of velocity differences for distances r from the inertial range. (a), return channel; (b), mixing layer.

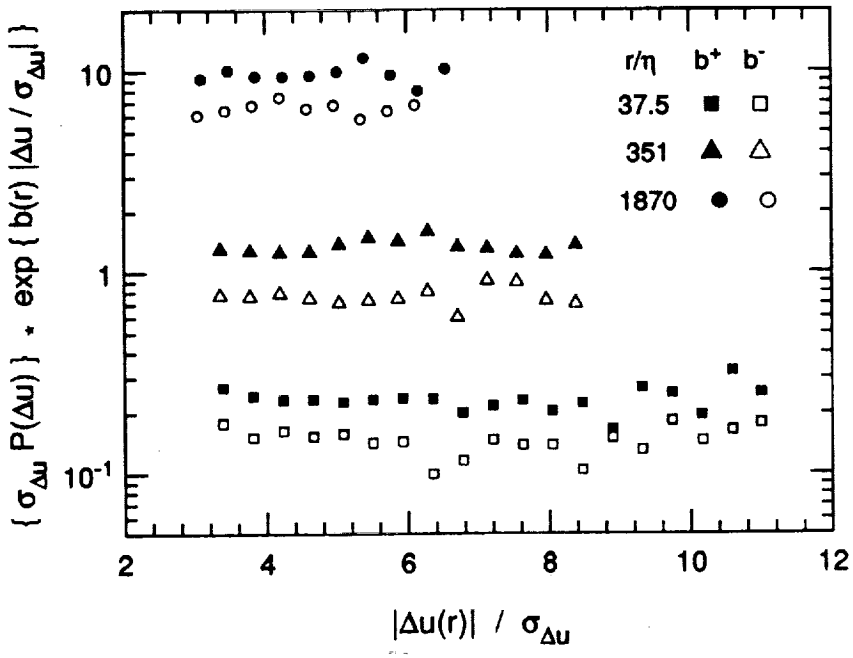

FIGURE 3. The tails of pdd premultiplied by exponentials with appropriate decrements in the mixing layer.

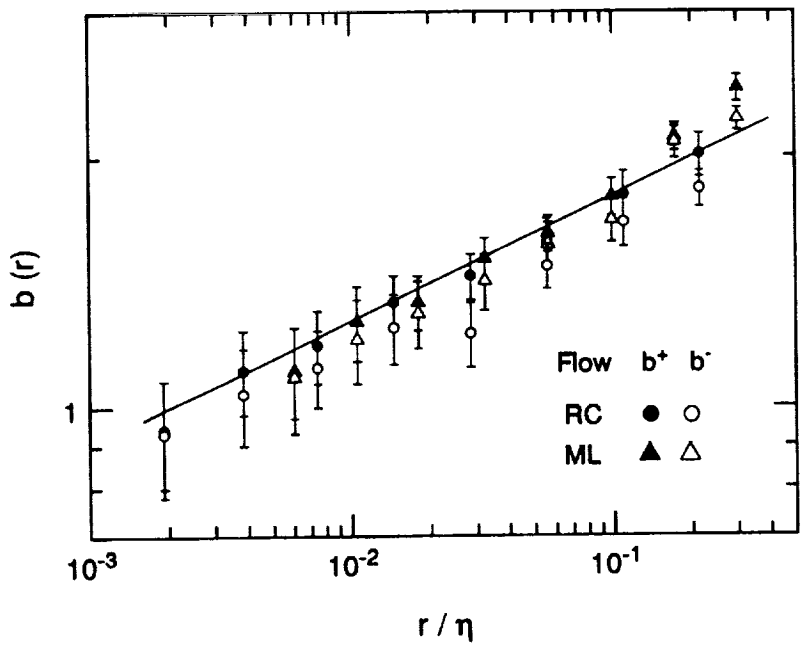

FIGURE 4. Scaling of the logarithmic decrements b^+ and b^-. Solid line corresponds to equation (5) with $\beta = 0.15$.

$$P(\Delta u) \propto \exp\left(-b(r)|\Delta u/\sigma_{\Delta u}|\right). \tag{4}$$

The threshold level h was chosen to be $h = 3$ for all r at all points. Then the values of logarithmic decrements $b(r)$ were estimated for both positive (b^+) and negative (b^-) tails of the pdd by the least-squares method. As an example, the tails of the pdd in the mixing layer premultiplied by exponentials with the decrements so obtained are presented in Figure 3. The scatter of experimental data with respect to the horizontal looks random, i.e. no systematic trends are seen. Thus equation (4) seems to be valid. The rms deviation of the data from the horizontal in Figure 3 (and in plots of $\sigma_{\Delta u} P(\Delta u) \cdot \exp\{b(r)|\Delta u/\sigma_{\Delta u}|\}$ for other r and points) was treated as a measurement error for decrements b^+ and b^-. Such errors are supposed to include both deviations from assumed behavior, equation (4), and statistical scatter. The measured values of these logarithmic decrements with appropriate error bars are presented in Figure 4. In this figure, the solid line corresponds to the power-law scaling

$$b(r) \propto r^{\beta} \tag{5}$$

with scaling exponent $\beta = 0.15$, proposed by G,H&F. It has to be noted that G,H&F verified equation (5) with $\beta = 0.15$ in four different flows: in an atmospheric boundary layer, $R_\lambda = 3000$ (Van Atta & Park 1971); in the return channel of the Modane wind tunnel, $R_\lambda = 2720$ (Gagne 1987); in an axisymmetric jet, $R_\lambda = 852$ and 536, and in a rectangular duct, $R_\lambda = 515$ (Anselmet *et al.* 1984). It is seen in Figure 4 that our experimental results are in agreement with those analyzed by G,H&F. Thus it can be assumed that equations (4) and (5) with $\beta \approx 0.15$ describe some universal behavior in high Reynolds number flows.

It has to be noted that no dependence of $b(r)$ on Reynolds number is seen in Figure 4. This result is opposite to that obtained by G,H&F.

3. Future plans

It is important to investigate two other relevant questions: (1) Within the inertial subrange, is there any "measurable" dependence of $b(r)$ on Reynolds number? and (2) For the viscous subrange, how should equations (4) and (5) be changed?

We believe new experiments in a wide range of Reynolds numbers are desirable to clarify these questions.

Acknowledgements

The author expresses sincere gratitude to M. Yu. Karyakin in collaboration with whom the experimental data were obtained and to Prof. P. Bradshaw and Dr. S. G. Saddoughi for valuable comments on the draft.

REFERENCES

ANSELMET, F., GAGNE, Y., HOPFINGER, E. J. & ANTONIA, R. A. 1984 High-order velocity structure functions in turbulent shear flows. *J. Fluid Mech.* **140**, 63.

GAGNE, Y. 1987 Etude expérimentale de l'intermittence et des singularités dans le plan complexe en turbulence développée. *Thesis* Université de Grenoble, France.

GAGNE, Y., HOPFINGER, E. J. & FRISCH. U. 1988 A new universal scaling for fully developed turbulence: the distribution of velocity increments. In: *New Trends in Nonlinear Dynamics and Pattern-Forming Phenomena: The Geometry of Nonequilibrium*, edited by P. Coullet and P. Huerre. NATO ASI Series, Series B: Physics, **237**, 315, Plenum Press.

KARYAKIN, M. YU., KUZNETSOV, V. R. & PRASKOVSKY, A. A. 1991 Experimental check of isotropy hypothesis for small-scale turbulence. *Izv. AN SSSR, Mekh. Zhidk. i Gaza* **5**, 26.

KOLMOGOROV, A. N. 1941 The local structure of turbulence in incompressible viscous fluid for very large Reynolds numbers. *Dokl. Akad. Nauk SSSR*, **30**, 301.

KOLMOGOROV, A. N. 1962 A refinement of previous hypotheses concerning the local structure of turbulence in a viscous incompressible fluid at high Reynolds number. *J. Fluid Mech.* **13**, 82.

KRAICHNAN, R. H. 1974 On Kolmogorov's inertial-range theories. *J. Fluid Mech.* **62**, 305.

MONIN, A. S. & YAGLOM, A. M. 1967 *Statistical Fluid Mechanics*. Vol. 2. Nauka, Moscow (English Transl.: 1975, MIT Press).

SHE, Z.-S. 1991 Intermittency and non-gaussian statistics in turbulence. *Fluid Dyn. Res.* **8**, 143.

VAN ATTA, C. W. & PARK, J. 1971 Statistical self-similarity and inertial range turbulence. In *Lecture Notes in Physics*, **12**, 402, Springer Verlag.

The 'ideal' Kolmogorov inertial range and constant

By Ye Zhou[1]

The energy transfer statistics measured in numerically simulated flows are found to be nearly self-similar for wavenumbers in the inertial range. Using the measured self-similar form, we were able to deduce an 'ideal' energy transfer function and the corresponding energy flux rate. From this flux rate, we calculate the Kolmogorov constant to be 1.5, in excellent agreement with experiments.

1. Motivation and objectives

Last year, an entire volume of the *Proceedings of the Royal Society* (**434** Compiled and edited by Hunt et al. 1991) was devoted to Kolmogorov's ideas about turbulence. Indeed, Kolmogorov's inertial range theory (Kolmogorov, 1941, Monin and Yaglom, 1975) has formed a foundation for turbulence research for the last fifty years even though the existence of an inertial range requires high Reynolds numbers (Re) normally encountered only in geophysical flows (Monin and Yaglom, 1975, Chapman, 1971).

It is essential to obtain a simulated flow field as close to the Kolmogorov inertial range as possible in order to obtain accurate measurements of the energy transfer process. In this report, the inertial range is represented by statistically stationary flow fields generated using a Fourier spectral code (Rogallo, 1981) in which the $k^{-5/3}$ spectrum is maintained explicitly. The method follows the spirit of Kraichnan's constrained decimation theory (Kraichnan, 1975) and is essentially that of She and Jackson (1992) who reported a simulation at 128^3 resolution. Basically, at each time step, the Fourier modes in each spherical shell are multiplied by the real constant that returns the shell energy to the Kolmogorov $k^{-5/3}$ spectrum. This method can be thought of as a constrained dynamical system. For an N^3 problem, one has placed $N/2$ constraints on the $2N^3$ degrees of freedom. The method is equivalent to the use of forcing at the small wavenumber (via a linear instability) and a spectral eddy viscosity at high wavenumber. To validate the method, we have repeated our analysis using the forced LES dataset of Chasnov (1991)at 128^3 resolution, which was generated using a traditional spectral eddy viscosity (Kraichnan, 1976), and we also performed simulations at 64^3, 128^3, and 256^3 to investigate the effect of mesh size. We analyzed several independent fields at each resolution and found no variation in the statistics. The results reported in this paper were measured in a stationary velocity field on a 256^3 mesh size after 3200 time steps of evolution. The energy spectrum for the inertial range LES is $k^{-5/3}$ over the entire spectral range of the simulation. She and Jackson (1992) found that the measured scaling exponents for flatness factors are in good agreement with experiment (Anselmet et al., 1984).

1 Current address: ICASE, NASA Langley Research Center

As in all numerical simulations, our inertial-range dataset is restricted by the finite computational domain, and separating physics from numerics becomes an important concern. It is necessary to identify and eliminate the numerical artifacts in the measurements. This effort leads to the *construction* of an 'ideal' Kolmogorov inertial range and a determination of the Kolmogorov constant.

2. Self-similarity of the energy transfer in the inertial range

We found that the fractional contributions from interactions between relative scales to the energy flux are essentially independent of k as would be expected in a scale-similar inertial range (Zhou, 1992a,b). This strongly suggests that the transfer process is self-similar, but it is important to confirm this directly.

Kraichnan (1971) pointed out that similarity within a Kolmogorov $k^{-5/3}$ inertial range implies the scaling

$$T(k,p,q) = a^3 T(ak, ap, aq) \tag{1}$$

if all six wave-numbers are in the inertial range. If we take $a = q^{-1}$, (1) reduces to

$$T(k,p,q) = q^{-3} T(k/q, p/q, 1) = q^{-3} F(k/q, p/q), \tag{2}$$

and the number of dependent variables is reduced from three to two. In figure 1, we have plotted $T(k,p,q)$ against k/q for several representative values of p/q. While there is a good collapse of the curves for the various bands, a failure of self-similarity is observed for interactions involving bands near the spectral boundaries of the computation.

The transfer function

$$T(k,p) = \sum_q T(k,p,q) \tag{3}$$

gives the transfer of energy into k resulting from all interactions involving band p. Analogous to (1), the self-similar scaling law for $T(k,p)$ in the inertial range is

$$T(k,p) = a^2 T(ak, ap). \tag{4}$$

We can further reduce (4) to

$$T(k,p) = p^{-2} T(k/p, 1) = p^{-2} H(k/p). \tag{5}$$

This self-similar law is also well satisfied except for p near the computational boundaries, as shown in figure 2.

In both figures 1 and 2, self-similar profiles can be found by averaging over the collapsed curves, and such averaged $T(k,p)$ values have been marked in figure 2.

Note that the question of the locality of dominant interactions can be answered in terms of figure 2. When $s = \max(k,p,q)/\min(k,p,q)$ is large, the three wavenumbers in a triad effectively reduce to two scales. $T(k,p)$ provides a direct measurement of the locality since self-similarity further reduces the variables to one, implying an

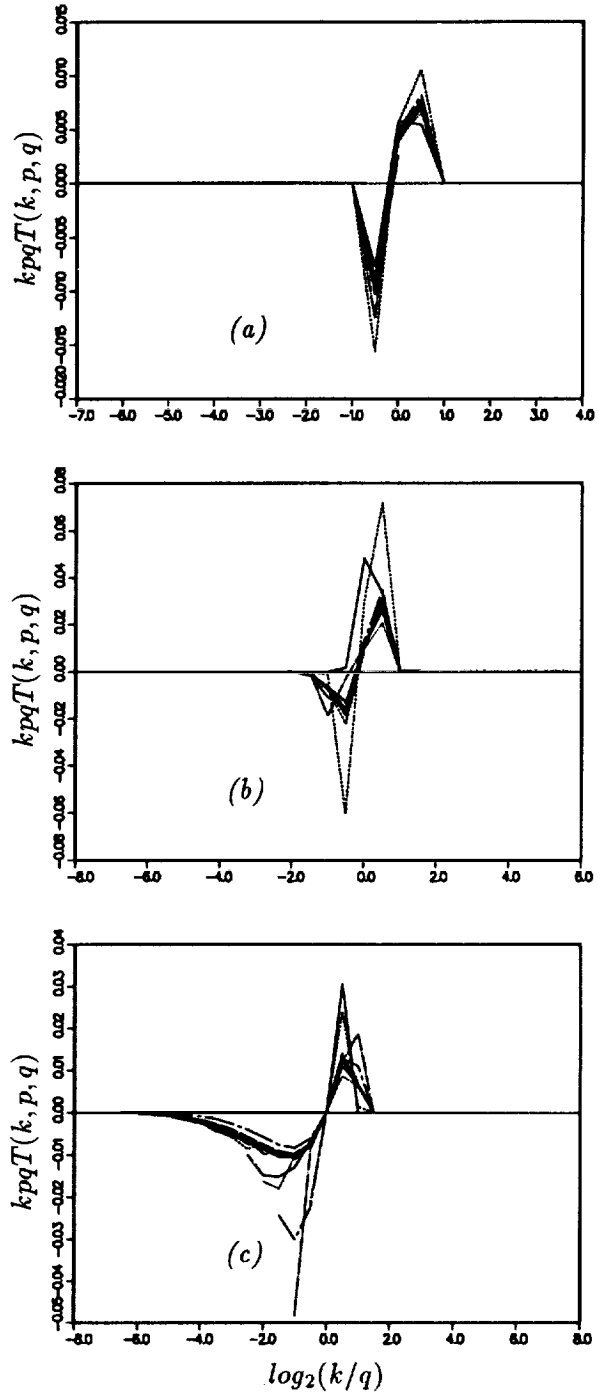

FIGURE 1. Direct verification of self-similarity (1) of the transfer $T(k,p,q)$ in the inertial range. (a) $p/q = 1/8$; (b) $p/q = 1/4$; (c) $p/q = 1$.

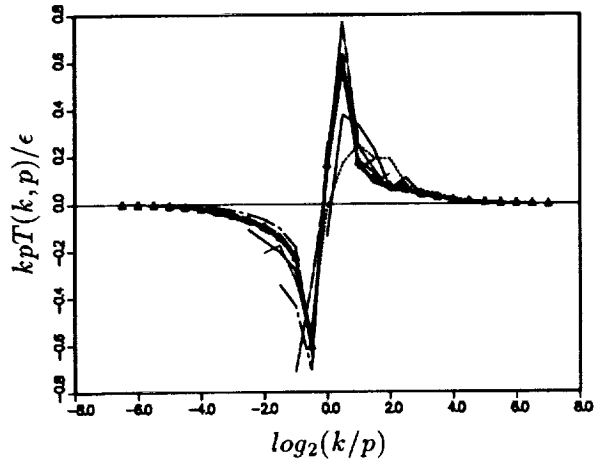

FIGURE 2. Self similarity of the transfer function $T(k,p)$ in an inertial range. The curves are for the various p bands of the inertial range LES. The points $\triangle$ are the average values of $H(k/p)$ used to represent the "ideal" inertial range.

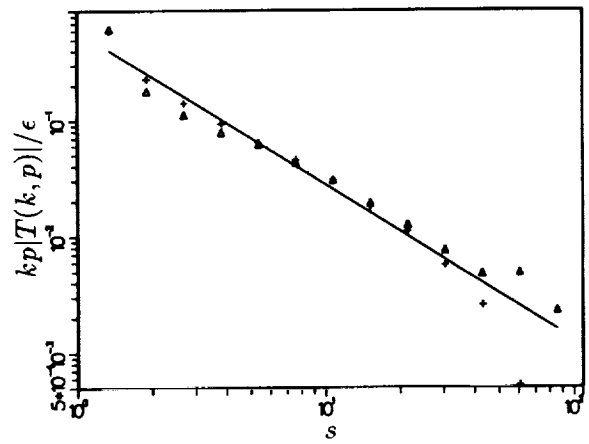

FIGURE 3. The self-similar transfer function $T(k,p)$: $\triangle$, $s = k/p$; $+$, $s = p/k$. The line indicates a $s^{-4/3}$ behavior. The scatter at large s is due to numerical error.

equivalence between s and the ratios k/p or p/k when they are large. While an interaction range of $s = 50$ as seen in figure 2 may seem rather "non-local", the basic question really is whether the interaction range is large enough to contain both the energetic and dissipation scales at large Reynolds number. The rapid $s^{-4/3}$ decay shown in figure 3 would seem to rule that out.

From the detailed balance, one expects that $T(k,p)$ is antisymmetric at large s, that is $H(s) = -H(1/s)$. Figure 3 shows that this is indeed the case. The deviation at very large s is due to numerical error.

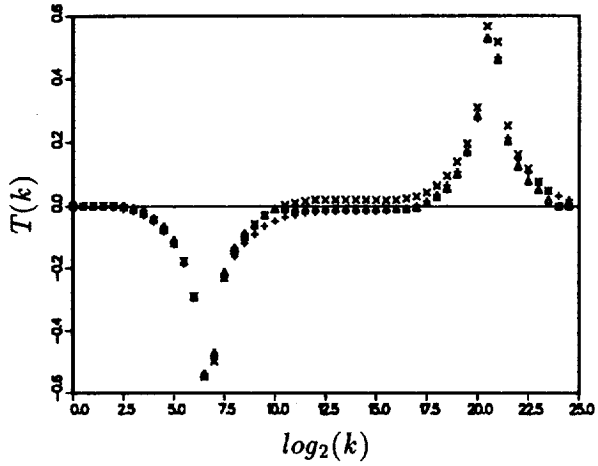

FIGURE 4. The 'ideal' self-similar transfer $T(k)$: $\triangle$, 64^3 mesh; +, 128^3 mesh; $\times$, 256^3 mesh.

3. The 'ideal' Kolmogorov energy transfer and inertial range

The failure of self-similarity near the computational boundaries is a numerical artifact of the forcing and eddy viscosity used in the LES. This suggests that the numerical artifacts can be eliminated, or at least reduced, by using the self-similar scaling to filter the raw data. Essentially, the data redundancy implied by the scaling law's reduction of three variables to two allows us to reduce the error associated with end-effects of the computational domain. To obtain the corrected data, we have simply removed the curves associated with bands near the boundaries that did not collapse and averaged the remaining ones. Such an operation reduces the data to a single curve that can be viewed as the 'ideal' one, that is, the one that would be obtained in an infinitely long inertial range. As a result, we are able to *construct* the 'ideal' energy transfer function $T(k)$ in an infinite inertial range by integrating the self-similar $T(k,p)$ over a finite range of p.

A suitable analogy for such an infinitely long inertial range is an infinitely long 'pipe' without leaks. To illustrate the interaction of scales, we 'cut' a finite section from this 'pipe' and view its inflow and outflow. The finite section of pipe corresponds to the finite range of the integral over p mentioned above. The "ideal" $T(k)$ constructed from simulations of size 64^3, 128^3, and 256^3 are shown in figure 4. The negative and positive peaks correspond to inflow and outflow. Since the flow is statistically steady and $\int dkT(k) = 0$, we have shifted the peaks so that the three mesh sizes overlap. Because the 'ideal' pipe does not leak, its length is not important. This is a direct visualization of the Kolmogorov energy transfer process in a finite section of the 'ideal' inertial range, and the 'ideal' inflow and outflow profiles are quite different from actual measured transfer spectra (figure 5). Indeed, the 'pipe' concept is suggested by the long range of scales in figure 5 in which the net transfer is very small.

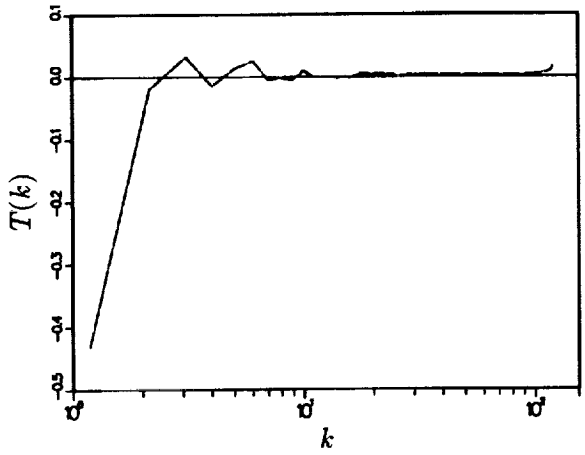

FIGURE 5. Transfer spectrum of the simulations: inertial-range LES at one instant.

4. A determination of the Kolmogorov constant

Experiments at high Reynolds number give values of the Kolmogorov constant in the range of $C_K \sim 1.5$ (Monin and Yaglom, 1975), but values determined directly from spectra in numerical simulations are usually around 2. (Vincent and Meneguzzi,1991; Sanada, 1992; Chasnov, 1991).

For the inertial range LES data, the dissipation rate estimated from the maximum resolved energy flux is .45, giving a value of the Kolmogorov constant of 1.7 (Zhou, 1992b). (Recall that the energy spectrum was held constant at $E(k) = k^{-5/3}$ so that $C_K \epsilon^{2/3} = 1$).

We can also measure the energy flux as the integral of the inflow or outflow of the 'ideal' pipe (figure 4). This gives a flux value of about .64 and a corresponding Kolmogorov constant $C_K \sim 1.5$. This 'ideal' energy dissipation rate, evaluated using the self-similar law, has hopefully eliminated most of the computational artifacts resulting from the limited computational domain. She and Jackson (1992) estimated the Kolmogorov constant using the calculated eddy viscosity, which they showed to be self-similar, and also found $C_K \sim 1.5$.

5. Summary

The measured energy transfer is reasonably self-similar for wavenumbers in the inertial range. Artifacts of the finite computational domain, the LES models, can be identified and to some extent eliminated by constructing an 'ideal' energy transfer function. The energy flux, corrected for the loss due to the finite computation domain, was used to calculate the Kolmogorov constant 1.5, in excellent agreement with experiments (Monin and Yaglom, 1975).

Acknowledgments

The author gratefully acknowledges stimulating discussions with Dr. R. S. Rogallo and Dr. R. H. Kraichnan. The author is also indebted to Dr. R. S. Rogallo for

his assistance with the computations. Time on the Intel Hypercube was furnished by the NAS division at NASA Ames Research Center.

REFERENCES

ANSELMET, F., GAGNE, Y., HOPFINGER, E. J., & ANTONIA, R. A. 1984 High-order velocity structure functions in turbulent shear flows. *J. Fluid Mech.* **140,** 63.

CHAPMAN, D. 1979 Computational aerodynamics development and outlook. *AIAA J.* **17,** 1293.

CHASNOV, J.R. 1991 Simulation of the Kolmogorov inertial subrange using an improved subgrid model. *Phys. Fluids A.* **1,** 945

KRAICHNAN, R.H. 1971 Inertial-range transfer in two- and three- dimensional turbulence. *J. Fluid Mech.* **47,** 525.

KRAICHNAN, R. H. 1976 Eddy viscosity in two and three dimensions. *J. Atmos. Sci.* **33,** 1521.

KRAICHNAN, R. H. 1985 in 'Theoretical approaches to turbulence', edited by D. L. Dwoyer, M. Y. Hussaini and R. G. Voight (Springer)

ROGALLO, R. S 1981 Numerical experiments in homogeneous turbulence. *NASA TM-81315.*

SANADA, T. 1991 Cluster statistics of homogeneous fluid turbulence. *Phys. Rev. A.* **44,** 6480.

SHE, Z.-S. AND JACKSON, E. 1992 A constrained Euler system for Navier-Stokes turbulence (Princeton Univ. preprint).

VINCENT, A. AND MEGEGUZZI, M. 1991 The spatial structure and statistical properties of homogeneous turbulence. *J. Fluid Mech.* **225,** 1.

ZHOU, Y. 1992a Degrees of locality of energy transfer in the inertial range (to be published in *Phys. Fluids A*).

ZHOU, Y. 1992b Interacting scales and energy transfer in isotropic turbulence (submitted for publication).

Center for Turbulence Research
Annual Research Briefs 1992

The helical decomposition and the instability assumption

By Fabian Waleffe

1. Motivations and objectives

Direct numerical simulations (Domaradzki & Rogallo, 1990, Yeung & Brasseur, 1991, Okhitani & Kida, 1992) show that the triadic transfer function $T(k,p,q)$ peaks sharply when q (or p) is much smaller than k. The triadic transfer function $T(k,p,q)$ gives the rate of energy input into wavenumber k from all interactions with modes of wavenumber p and q, where k,p,q form a triangle. This observation was thought to suggest that energy is cascaded downscale through non-local interactions with local transfer and that there was a strong connection between large and small scales. Both suggestions were in contradiction with the classical Kolmogorov picture of the energy cascade.

In fact, the large peaks in $T(k,p,q)$ have no direct physical significance. Their origin lies in the Fourier representation of the differential advection (i.e. distortion) of small scales by large scales. It is only the *difference* between the large peaks which has a physical meaning. That difference represents an advection in Fourier space, i.e. a $\partial/\partial k$ term (Waleffe, 1992). With regard to the energy cascade, the large local transfers in non-local triads are not the primary downscale cascading interactions, their net effect is actually a *reverse* cascade, in the inertial range. A worthy note on this point is that the non-local interactions with large *local downscale* transfer are also present in 2D turbulence, and it is well-known that there the energy cascade is reversed in a $-5/3$ range.

The helical decomposition has been found useful in distinguishing between kinematically independent interactions. That analysis has gone beyond the question of non-local interaction with local transfer. In particular, an assumption about the statistical direction of triadic energy transfer in any kinematically independent interaction was introduced (the *instability assumption*). That assumption is not necessary for the conclusions about non-local interactions with local transfer recalled above. In the case of turbulence under rapid rotation, the instability assumption leads to the prediction that energy is transferred in spectral space from the poles of the rotation axis toward the equator. The instability assumption is thought to be of general validity for any type of triad interactions (e.g. internal waves). The helical decomposition and the instability assumption offer detailed information about the homogeneous statistical dynamics of the Navier-Stokes equations.

The objective of this work was to explore the validity of the instability assumption and to study the contributions of the various types of helical interactions to the energy cascade and the subgrid-scale eddy-viscosity. This was done in the context of spectral closures of the Direct Interaction or Quasi-Normal type.

2. Accomplishments

2.1 Helical decomposition and non-local interactions

The helical decomposition of the velocity field shows that there are two distinct classes of triad interactions. Only one of these classes is such that the energy transfer is mostly between the two longest legs of the triad when the third leg is much smaller than the other two (non-local triad). That class of helical interactions is then wholly responsible for the large local transfers in non-local triads observed in DNS (Domaradzki and Rogallo, 1990, Yeung and Brasseur, 1991, Okhitani and Kida, 1992). Somewhat surprisingly, however, the sum of all such helical interactions gives a *reverse cascade* of energy, from large to small wavenumbers, even though the large local transfers are from the medium to the largest leg of the triad. This is an exact result for an extended inertial range. The meaning of that result is that the peaks in the transfer function $T(k,p,q)$, observed when q, say, is much smaller than k and p, can not be interpreted as representing the downscale transfer of energy.

Interactions between wavevectors in Fourier space are triadic as a result of the quadratic non-linearity of the Navier-Stokes equations. The incompressibility constraint requires that the velocity vector be perpendicular to the wavevector. That leaves only two degrees of freedom per wavevector and eight kinematically independent triad interactions. The helical decomposition is particularly appropriate because the non-linear term and each triad interaction independently conserves both energy and helicity. There are two helical modes per wavevector, a "+" mode of maximum helicity and a "−" mode of minimum helicity. The triadic transfer function is the sum of the eight kinematically independent helical triadic transfers,

$$T(k,p,q) = \sum_{i=1}^{8} T^{(i)}(k,p,q).$$

Normalizing all wavenumbers in the triad by the middle one, let v, 1, w represent the smallest, middle, and largest wavenumbers, respectively, ($v \le 1 \le w \le 1+v$) and s_v, s_1, s_w the signs of the corresponding helical modes. A direct consequence of energy and helicity conservation is the following important relation,

$$\frac{T^{(i)}(v,1,w)}{s_w w - s_1} = \frac{T^{(i)}(1,w,v)}{s_v v - s_w w} = \frac{T^{(i)}(w,v,1)}{s_1 - s_v v}. \qquad (1)$$

One nice advantage of this decomposition is that it distinguishes clearly between *non-local interactions with non-local transfers* and *non-local interactions with local transfers*. Non-local interactions (i.e. $v \ll 1 \sim w$) of the $s_1 = s_w$ type have local energy transfer, while non-local $s_1 = -s_w$ interactions have non-local transfer. This can be deduced from (1). Hence, the *non-local interactions with large local transfers* observed in the DNS are the result of $s_1 = s_w$ interactions.

2.2 The instability assumption

The analysis sketched above highlights some of the characteristics of the triadic transfers but leaves open the question of statistical direction of the energy exchanges.

These directions are determined by the *Instability assumption*: *statistically, the triadic energy transfer is from the mode whose coefficient in the triadic equations (1) is opposite in sign to the other two coefficients.* In other words, $T^{(i)}(v,1,w)$ is negative if $s_1 = -s_w$ (and thus $T^{(i)}(1,w,v)$ and $T^{(i)}(w,v,1)$ are positive), and $T^{(i)}(1,w,v)$ is negative if $s_1 = s_w$ (with $T^{(i)}(v,1,w)$ and $T^{(i)}(w,v,1)$ positive). This assumption was motivated by the stability characteristics of the triadic interactions in (Waleffe, 1992). It amounts to an assumption about the triple correlations.

The instability assumption is in agreement with the numerical observations that energy is transferred statistically *from the medium to the largest wavenumber* in non-local triads. As mentioned above, the large local transfers in non-local triads can only come from $s_1 = s_w$ interactions, and thus the numerical observations imply that the *sum* of all $s_1 = s_w$ interactions must extract energy from the medium wavenumber and feed energy into the longest wavenumber. The instability assumption leads to the same result through the stronger statement that this is so for *each* interaction $s_1 = s_w$.

Analyses of numerical simulation data have focused so far only on the total triadic energy transfer $T(k,p,q) = \sum_i T^{(i)}(k,p,q)$. The total triadic energy transfer is the net result of 8 kinematically independent interactions. In a recent paper, Okhitani and Kida (1992) have classified interactions according to the sign of the total triadic transfer into each leg of the triad. They associate to each interaction a triplet of signs defined as (sign$[T(w,v,1)]$, sign$[T(1,w,v)]$, sign$[T(v,1,w)]$). These triplets can *a priori* take any of 6 different values ($(+,+,+)$ and $(-,-,-)$ are not allowed from energy conservation). Their classification should not be confused with the helical classification used in this and previous papers. They observe that statistically only $(+,+,-)$, $(+,-,+)$ and $(+,-,-)$ appear. The instability assumption is not only consistent with this observation but also predicts it. The total energy transfer is a combination of the two helical classes of transfers determined by the instability assumption. These two helical classes are $(+,+,-)$ when $s_1 = -s_w$ and $(+,-,+)$ when $s_1 = s_w$. The only possible *net sums* of these two classes of helical interactions are $(+,+,-)$, $(+,-,+)$ *and* $(+,-,-)$, exactly as observed by Okhitani and Kida. In other words, it is impossible to observe a net interaction in which the largest wavenumber in a triad loses energy on average.

2.3 Comparison with the closures

The signs of the helical triadic transfers predicted by the instability assumption have been compared to those obtained from the spectral closures (Quasi-Normal or Direct Interaction type). All such closures prescribe the same following form for the shell-averaged triadic transfer function $T^{(i)}(k,p,q)$ due to the i-th interaction (for isotropic flow):

$$T^{(i)}(k,p,q) = \pi^2 kpq\, gg^*\, \theta_{kpq}\, (s_q q - s_p p) \times \\ [(s_q q - s_p p)U(p)U(q) + (s_k k - s_q q)U(k)U(q) + (s_p p - s_k k)U(k)U(p)]$$

where $U(k) = \langle \mathbf{u}(\mathbf{k}) \cdot \mathbf{u}^*(\mathbf{k}) \rangle$, and $gg^* = (s_k k + s_p p + s_q q)^2 Q^2/(16k^2p^2q^2)$, with $Q^2 = 2k^2p^2 + 2p^2q^2 + 2q^2k^2 - k^4 - p^4 - q^4$ (g differs by a factor of 2 from its definition

in (Waleffe, 1992)). The sign coefficients (s_k, s_p, s_q) denote the helical interaction under consideration, i.e. s_k mode for wavenumber k, etc. The parameter θ_{kpq} is a relaxation time scale for the triple moments. The relaxation is due to both viscous and non-linear effects. A simple prescription for θ_{kpq}, is $\theta_{kpq} = C[(k^3E(k))^{1/2} + (p^3E(p))^{1/2} + (q^3E(q))^{1/2}]^{-1}$ where the constant C is chosen to fit the Kolmogorov constant and $E(k)$ is the energy spectrum.

All that is needed for the comparison with the instability assumption is that θ_{kpq} be positive. It can be shown analytically (Waleffe, 1993) for a similarity range $E(k) = 2\pi k^2 U(k) \propto k^n$ that the instability assumption and the closures give the same direction for the triadic transfer if $n < 2$ when $s_1 = -s_w$ and if $n < 1$ when $s_1 = s_w$. These critical values of n correspond to equipartition of energy ($n = 2$) and of helicity ($n = 1$), respectively. Combining both results, the closures agree with the instability assumption whenever $n < 1$. The Kolmogorov spectrum has $n = -5/3$.

The knowledge of the direction for the triadic energy transfer can then be used to determine the cascade direction in a similarity range. The conclusions are that the $s_1 = -s_w$ interactions always forward cascade energy to higher wavenumbers but the $s_1 = s_w$ interactions, which are responsible for the non-local interaction with local transfer character of the total triadic transfer function, reverse cascade whenever $n > -7/3$ (see Waleffe, 1993 for details).

A quantitative analysis with the EDQNM model was made for a -5/3 range. The most interesting result is that 86% of the energy cascade is due to helical interactions of the form $s_v = -s_1 = s_w$. Interactions with $s_1 = s_w$ nearly cancel out, contributing only about -1% to the total cascade.

Decomposition of the subgrid-scale eddy-viscosity into the contributions from the two classes of helical interactions, and also from the forward and reverse cascading triads, shows that the cusp near the cut-off wavenumber arises from non-local reverse cascading $s_1 = s_w$ interactions. The subgrid viscosity due to forward cascading interactions is approximately constant. One noteworthy observation is that the closures also give a mild cusp as $k \to 0$, and thus the eddy-viscosity does not tend to a constant as is usually believed.

3. Future plans

The instability assumption seems to be a solid and general assumption not limited to isotropic turbulence. It could likely be used in other areas, in stratified flows for instance. It would be nice to test the assumption more directly using DNS; only indirect verifications have been made so far (e.g. total triadic transfer but not each helical interaction independently). One would like to have a better theoretical understanding of why the instability assumption works. Why would the stability properties of a single triad determine the statistical dynamics of a large number of interacting triads?

The helical decomposition is a very appropriate way of looking at the fundamental kinematically independent triad interactions. The suggestion from the closures that one type of helical interaction is responsible for 86% of the energy cascade is

puzzling and worthy of further investigation. The physical interpretation of these interactions and the link to some physical mechanism is desired. We still do not have a dynamical mechanism which leads to a $-5/3$ turbulent spectrum. If the cascade is due to a series of successive instabilities, which instability is it? The simplest one, the inflexional Kelvin-Helmholtz instability, reverse cascades. I have suggested before that the $s_1 = -s_\omega$ helical interactions, which forward cascade, have some similarities with the elliptical instability (Waleffe, 1990, 1992), but no work has been done to explore that any further.

Regarding the non-local interactions with local transfer, their importance is far less than a look at $T(k,p,q)$ suggests. This is because of all the subtle cancellations taking place, whether one looks at the total cascade or the effect of large scales on the small scales. The role of non-local interactions in turbulence still needs to be determined. They are responsible for the cusp in the subgrid viscosity. They could be linked to intermittency also. In fact, it is my opinion that the closures do not deal with them correctly. All the closures treat triads as essentially independent (through the Quasi-normal or Direct Interaction assumption) with all the other triads acting as a decorrelating background noise. This seems valid for local interactions. However non-local triads can not be treated as independent because of the near-cancellations between *several* triads needed to represent distortion of small scales by large ones.

REFERENCES

DOMARADZKI, A. J. & ROGALLO, R. S. 1990 Local energy transfer and nonlocal interactions in homogeneous, isotropic turbulence. *Phys. Fluids A.* **2,** 413-426.

OKHITANI, K. & KIDA, S. 1992 Triad interactions in forced turbulence. *Phys. Fluids A.* **4,** 794-802.

WALEFFE, F. 1990 On the three-dimensional instability of strained vortices. *Phys. Fluids A.* **2,** 76-80.

WALEFFE, F. 1992 The nature of triad interactions in homogeneous turbulence. *Phys. Fluids A.* **4,** 350-363.

WALEFFE, F. 1993 Inertial transfers in the helical decomposition. *Phys. Fluids A.* **5,** to appear Feb. 1993.

YEUNG, P. K. & BRASSEUR, J. G. 1991 The response of isotropic turbulence to isotropic and anisotropic forcing at the large scales. *Phys. Fluids A.* **3,** 884-897.

Superfluid turbulence

By D. C. Samuels

1. Motivation and objectives

At low temperatures (below 5 Kelvin), helium is a liquid with a very low kinematic viscosity. It has been proposed (Liepmann and Coles (1979), Donnelly (1991)) that wind tunnels could be built using liquid helium as the test fluid. The primary advantages of such wind tunnels would be a combination of large Reynolds numbers and a relatively small apparatus. It is hoped that this combination will allow the study of high Reynolds number flows in an academic setting.

There are two basic types of liquid helium wind tunnels that can be built, corresponding to the two phases of liquid helium. The high temperature phase (between approximately 2 to 5 Kelvin) is called helium I and is a Navier-Stokes fluid. There are no unanswered scientific questions about the design or operation of a wind tunnel in the helium I phase.

The low temperature phase (below approximately 2 Kelvin) of liquid helium is called helium II. This is a *quantum fluid*, meaning that there are some properties of helium II which are directly due to quantum mechanical effects and which are not observed in Navier-Stokes fluids. The quantum effects that are relevant to this paper are:

(1) Helium II is well described as a superposition of two separate fluids called the *superfluid* and the *normal fluid*. The normal-fluid component is a Navier-Stokes fluid and the superfluid is an irrotational Euler fluid.

(2) Circulation in the superfluid exists only in quantized vortex filaments. All quantized vortex filaments have identical circulations κ and core size a.

One would expect that with these quantum effects the flow of helium II would show departures from Navier-Stokes behavior. Indeed, helium II flows with thermal gradients do not show classical Navier-Stokes behavior. This type of helium II flow has been the most widely studied precisely due to its unusual properties. Recently, isothermal flows have been examined in numerous experiments (see Walstrom *et al.* (1988) and Borner *et al.* (1983) for example). The surprising result of these experiments is that the isothermal flow of helium II appears to behave as a Navier-Stokes fluid. It has been consistently observed in a wide range of flow geometries that the measurable parameters of the flow obey the same laws (empirical and theoretical) as Navier-Stokes fluids. For a description of some of these experiments, see Donnelly (1991).

This apparent Navier-Stokes behavior of isothermal helium II flows could be exploited to study turbulence with a helium II wind tunnel. Some advantages of a

helium II wind tunnel over the helium I wind tunnel are listed by Donnelly (1991) and I will not repeat them here except to say that the technology exists to directly observe vorticity in helium II. This measurement is made possible through the attenuation of *second sound*, a type of sound which only exists in superfluids, by the quantized vortex filaments in the superfluid component. This is a basic technique very commonly used in helium II experiments.

The objective of my research at CTR has been to develop an understanding of the microscopic processes responsible for the observed Navier-Stokes behavior of helium II flows.

2. Accomplishments

The simplest interpretation of the experimental data on helium II flow is that the normal fluid is somehow entraining the superfluid so that both components have the same, Navier-Stokes flow behavior. Since the superfluid can only contain circulation in the form of quantized vortex filaments, it is natural to suspect that the interaction of these quantized vortex filaments with the normal-fluid flow is somehow the cause of the superfluid entrainment. I investigated the vortex filament behavior by simulations of the filament motion in a spatially non-uniform flow field of the normal-fluid. The vortex filaments are represented in the simulations by a series of mesh points placed along the filament. The equation of motion of each mesh point is

$$\frac{d\mathbf{X}}{dt} = \mathbf{v_s} + \mathbf{v_v} + \alpha \mathbf{t} \times (\mathbf{v_n} - (\mathbf{v_s} + \mathbf{v_v})), \tag{1}$$

where $\mathbf{X}$ is the position of the point on the vortex filament, $\mathbf{v_s}$ is the irrotational part of the superfluid velocity field, $\mathbf{v_v}$ is the local velocity due to all the vortex filaments in the fluid, α is a temperature dependent coefficient, $\mathbf{t}$ is the local unit tangent vector of the filament, and $\mathbf{v_n}$ is the local velocity of the normal fluid. The first two terms on the right hand side of equation 1 are simply the total local superfluid velocity. The third term describes the response of the vortex filament to the normal-fluid velocity $\mathbf{v_n}$ due to the scattering of the normal fluid by the vortex filament. This process is called *mutual friction* and is well understood from first principles (Samuels and Donnelly (1990)). The numerical methods used to integrate equation 1 and to form and update the meshing of the vortex filaments are described in Samuels (1991) and Samuels (1992a).

2.1 Laminar flows

Though the final goal is to gain an understanding of the superfluid entrainment process in turbulent flows, I began this project with simulations of Poiseuille flow of helium. There was some indication in the experiments that the superfluid entrainment was not limited to high Reynolds number flows, but may also occur in low speed, laminar flows (Murakami and Ichikawa (1989)). The experimental evidence for this is small simply because there were very few experiments actually done in the low Reynolds number range due to the very low flow speed required for the laminar flow of helium II. If laminar flows did show superfluid entrainment, I expected that some basic understanding of the entrainment process could be more easily gained

in this simple flow. I would then attempt to apply this understanding to the more complex flows characteristic of turbulence.

From the results of my laminar flow simulations, I proposed two necessary conditions for the entrainment of the superfluid in a general flow. These conditions are:

(1) A region of locally matched velocity $\mathbf{v_n} = \mathbf{v_s}$ must initially exist in the flow.

(2) A source of quantized vortex filament must be present.

Through the mutual friction term in the equation of motion (equation 1), vortex filaments will move toward the region of locally matched velocity (called the nodal surface). The effect of the mutual friction is to hold and orient the vortex filaments at the nodal surface so that the circulation of the vortex filament is in the same direction as the local circulation of the normal fluid. As more filaments accrete onto the nodal surface (hence the need for condition 2), the filament density increases until the superfluid circulation, averaged over a region containing many filaments, equals the local normal-fluid circulation. Filaments that are too far apart will be moved closer together by mutual friction and filaments that are too close will be pushed farther apart. The stable point is where the local superfluid and normal-fluid velocity fields are equal, which makes the mutual friction term in the equation of motion equal to zero. The result of this process is that an ordered array of quantized vortex filaments forms around the nodal surface with sufficient density to equal the local circulation density in the normal fluid, thus entraining the superfluid to the normal fluid.

A simple example of the entrainment of the superfluid by the normal fluid is given in figure 1. In this example, I am considering the flow of helium II through a circular pipe. Figure 1a shows the initial velocity profiles of both the superfluid and the normal fluid. The normal fluid has a parabolic profile with zero velocity at the pipe wall. The superfluid, with no initial vortex filaments, has a flat velocity profile that slips completely at the pipe walls. The magnitude of the superfluid velocity is set to be equal to the average normal-fluid velocity. Though the flow rates of the two fluids are equal, the local velocities are only equal at a specific radius inside the pipe. This radius marks the nodal surface (condition 1 above) for this geometry.

As the quantized vortex filaments are generated by the velocity difference at the pipe wall (a process described in detail in Samuels (1992a)), they gather in an ordered manner about the nodal surface. The combined velocity fields of all the vortex filaments produce an approximately parabolic velocity profile in the superfluid that matches the local velocity profile of the normal fluid (figure 1b).

2.2 A simple model of turbulent flows

With the experience gained from the laminar simulations, the problem of superfluid entrainment in turbulent flows is reduced to a question of identifying the nodal surfaces and the process responsible for quantized vortex filament formation in a turbulent flow. For a simple model of turbulence, I chose an isolated, concentrated

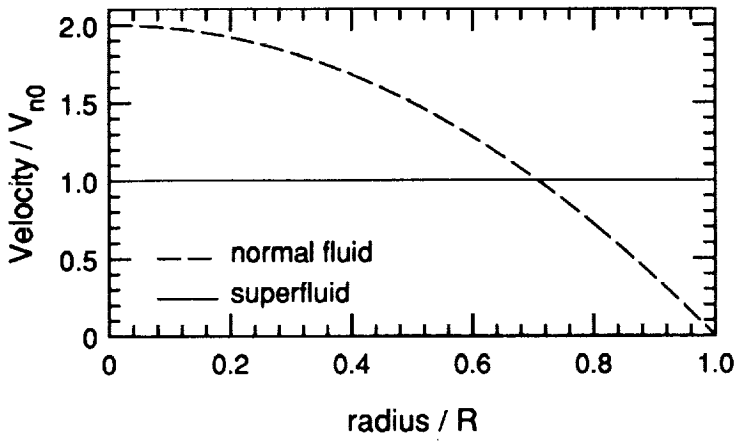

FIGURE 1A. Initial velocity profiles of the normal fluid and superfluid in laminar pipe flow. R denotes the pipe radius. V_{n0} denotes the average normal fluid flow rate. The nodal surface is at a radius of $.707R$.

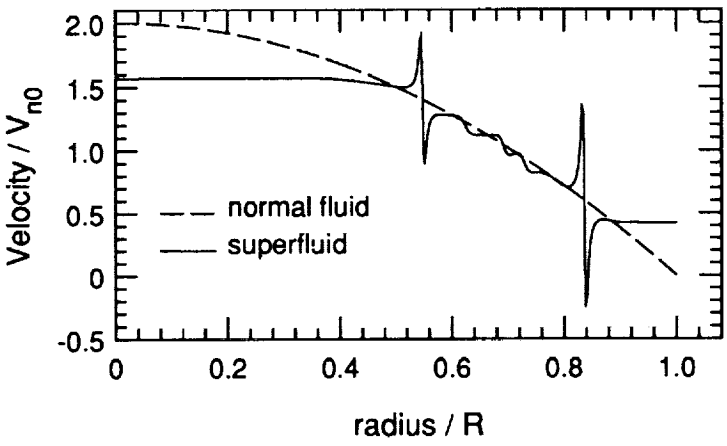

FIGURE 1B. Normal fluid and superfluid velocity profiles after the formation of quantized vortex filaments.

vortex in the normal fluid. This is meant to represent the vortex tubes reported in experiments (Douady *et al.* (1991)) and simulations (Siggia (1981), Kerr (1985), Ruetsch and Maxey (1991)) of Navier-Stokes turbulence. I assume that the superfluid is initially at rest. With these initial conditions, there is a nodal surface on the axis of the normal-fluid vortex tube where both the superfluid and normal-fluid velocities are zero.

With the nodal surface identified, we must now find a process that will form large amounts of quantized vortex filaments. In the simulations reported in this paper, the normal-fluid vortex tube was represented by a gaussian distribution of circulation with the vorticity vector aligned along the Z axis. The core size of the vortex tube is denoted by r_c. In order to make the calculation spatially finite, the vortex tube was limited to a length of $20r_c$. This was accomplished by rapidly expanding the vortex-tube core size beyond this length. The geometry of the vortex-tube core is outlined by the dashed line in figure 2a. None of the results presented here were dependent on the length of the vortex tube as long as the length was greater than approximately $10r_c$. I typically used normal-fluid vortex tubes with circulations much greater than the small circulation of the quantized vortex filaments, so many vortex filaments must be formed to equal the normal-fluid circulation.

Figure 2 illustrates the process responsible for the formation of the vortex filaments. The simulation begins with a small vortex filament ring near the normal-fluid vortex tube (figure 2a). The vortex ring is aimed so that it moves toward the normal-fluid vortex tube under its own self-induced velocity. When the vortex ring reaches the normal-fluid vortex tube, it is captured on the center of the vortex tube (at the nodal surface) by mutual friction (figure 2b). It is then stretched along the vortex tube axis (again by mutual friction). As the vortex filament ring is stretched, it also twists around the vortex tube axis under its self-induced velocity (figure 2c). This three-dimensional twisting motion causes a section of the vortex filament ring to turn towards the azimuthal direction of the normal-fluid vortex core. At this section of the quantized vortex filament, there is now a normal-fluid velocity component (from the vortex tube) along the axis of the vortex filament. A quantized vortex filament with an axial normal-fluid flow is known to be unstable to the growth of a helical wave on the vortex filament (Ostermeier and Glaberson (1975)). Since the unstable length of the vortex filament is small in this situation, the instability to helical wave growth typically leads to the growth of a single loop (figure 2d) on the vortex filament, though I have seen situations where multiple loops are formed simultaneously. This new loop of quantized vortex filament is itself captured by the core of the normal-fluid vortex tube and will follow the same evolution as the initial vortex ring. Meanwhile, the initial vortex ring is still unstable and will continue forming new vortex loops until it eventually moves off the lower end of the vortex tube. This process of loop formation leads to an exponential growth in the length of quantized vortex filament. Figure 2e shows a later stage of this growth. By this time, a dense grouping of highly ordered quantized vortex filaments has formed within the normal-fluid vortex tube. To summarize, a concentration of vorticity in the normal fluid will form a corresponding concentration of

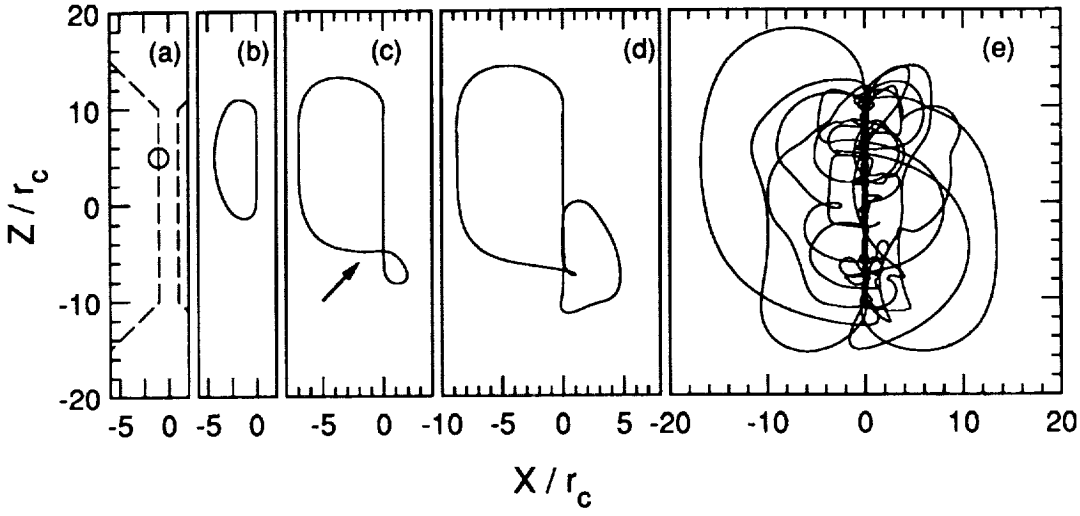

FIGURE 2. Evolution of the quantized vortex filament. Z denotes the direction along the axis of the normal-fluid vortex tube and X denotes the distance along one axis perpendicular to the vortex-tube axis. (a) Initial state. The solid lines denote the quantized vortex filament. Dashed lines outline the core of the normal-fluid vortex tube. (b) The quantized vortex filament is captured by the vortex tube. (c) Instability begins at the section of vortex filament marked by the arrow. (d) A new loop forms. (e) Quantized vortex filaments are concentrated in the core of the normal-fluid vortex tube.

quantized vortex filaments in the superfluid.

Figure 3 shows the velocity profile of the superfluid and the normal fluid along a line in the plane of the normal-fluid vortex tube and through its axis. At this point in the simulation, the quantized vortex filament was still growing (see figure 4), but the computation time per timestep had grown too large to continue the simulation. It is not yet known when this growth will eventually stop. Figure 4 shows the growth of the superfluid circulation within the core of the normal-fluid vortex tube. As expected, the growth is exponential. By the end of the simulation, the superfluid circulation had grown to approximately 35% of the normal-fluid circulation and was still growing exponentially.

From a large number of these simulations, I developed an empirical equation for the time constant τ of the exponential growth of the superfluid circulation Γ_c. This equation is

$$\tau = \frac{C r_c^2}{\sqrt{\alpha}\Gamma_n} \tag{2}$$

where r_c is the core radius of the vortex tube, Γ_n is the circulation of the vortex tube, α is the mutual friction parameter from equation 1, and C is a dimensionless

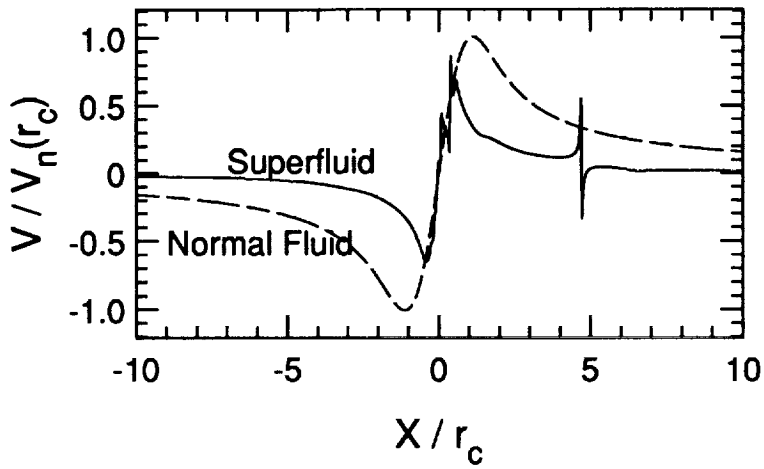

FIGURE 3. Superfluid and normal-fluid velocity profiles in the plane of the vortex tube. Velocities are normalized by the velocity at the core radius $V_n(r_c)$ and position X is normalized by the vortex-tube radius. The position is taken along an axis perpendicular to the vortex-tube axis.

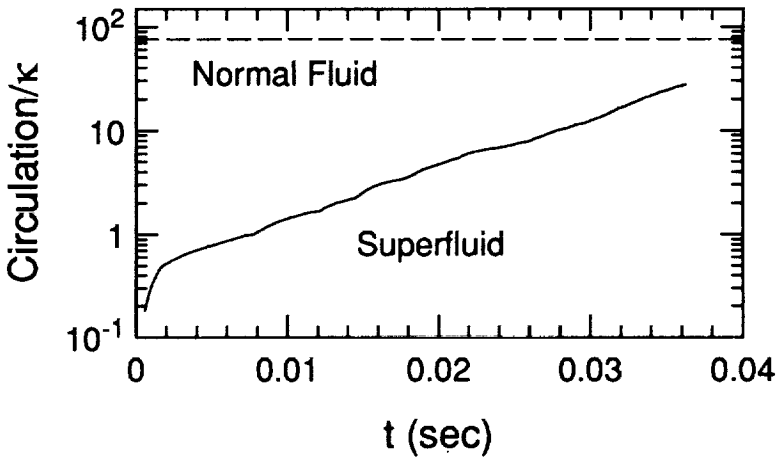

FIGURE 4. Exponential growth of the superfluid circulation inside the core of the normal-fluid vortex tube. The dashed line denotes the circulation of the vortex tube.

constant determined by least squares fit to be $C = 458 \pm 5$.

This process of superfluid filament growth is only useful if the time scale τ is small compared to the lifetime of the concentrated vortex tubes present in the turbulent normal fluid. To make this comparison, we must know the lifetime, core size, and circulation of typical vortex tubes in Navier-Stokes turbulence. These values are not well known at the current time. We take the lifetime to be one large eddy turnover time (Douady *et al.* (1991), the core radius to be $r_c \approx 3\eta$ where η is the Kolmogorov length scale (Ruetsch and Maxey (1991), Vincent and Meneguzzi (1991)), and the circulation to be $\Gamma_n = (300 \pm 100)\nu$ (Jimenez (1992)) where ν is the kinematic viscosity of the normal fluid. All of these values are taken from fairly low Reynolds number experiments or simulations and may very well change with future research. With this caveat, the ratio of the vortex tube lifetime t_{life} to the growth time scale τ is

$$\frac{t_{life}}{\tau} \simeq (.23 \pm .08)\sqrt{\alpha Re}, \tag{3}$$

where I have defined a Reynolds number $Re = U_I L_I/\nu_n$ with the large eddy velocity scale U_I and length scale L_I, and ν_n is the kinematic viscosity of the normal fluid. The mutual friction parameter α has a typical value of $\alpha = .1$, so for Reynolds numbers on the order of 1000 or higher, we expect the vortex tube lifetime to be large compared to the growth time constant τ. Therefore, in high Reynolds number flows the time required for the growth of the superfluid circulation should be small compared to the lifetime of the vortex tubes.

The growth process described above only occurs for normal-fluid vortex tubes with circulations stronger than a minimum value $\Gamma_{n,min}$. From least square fits of many simulations, this minimum value is found to be well described by the empirical formula

$$\frac{\Gamma_{n,min}}{\Gamma_s} = \frac{D}{\alpha} ln(\frac{r_c}{a}) - E, \tag{4}$$

where Γ_s is the circulation of the quantized vortex filaments, α is the temperature dependent mutual-friction parameter, a is the core size of the quantized vortex filaments, and D and E are constants fit from the simulation results. The values found for the constants are $D = 1.30 \pm .05$ and $E = 7.8 \pm .3$. This formula for $\Gamma_{n,min}$ should be compared to the observed circulations of vortex tubes in Navier-Stokes turbulence. From simulation results, Jimenez (1992) gives a value of

$$\Gamma_{tube} = Re_\gamma \nu \tag{5}$$

for the circulation of vortex tubes, where ν is the kinematic viscosity of the fluid and the circulation Reynolds number Re_γ is found to lie in the range $200 < Re_\gamma < 400$. As was stated before, this value for the vortex tube circulation was taken from low Reynolds number simulations and may change with higher Reynolds number. A comparison of $\Gamma_{n,min}$ and the range of vortex tube circulations from equation 5 is given in figure 5. Γ_{tube} has a temperature dependence (and hence an α dependence) through the kinematic viscosity of the normal fluid. For reasonable values of r_c, the minimum circulation $\Gamma_{n,min}$ lies within the range of expected vortex tube

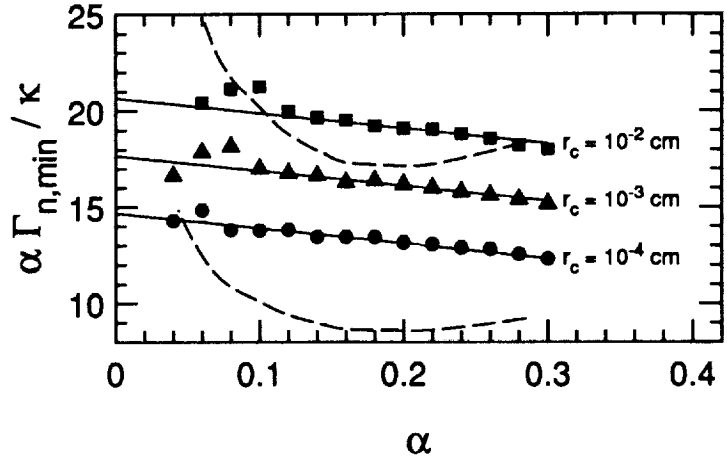

FIGURE 5. Minimum circulation for the vortex filament instability *vs* α. The solid lines are from equation 5. The dashed lines outline the expected range of circulations of the normal-fluid vortex tubes.

circulations. The reader should remember that these simulations were done with a very simplified geometry, using a perfectly straight vortex tube with a uniform cross section. It is reasonable to expect that any nonuniformities in the vortex tube radius or direction would decrease the value of $\Gamma_{n,min}$ since they would act to locally increase the normal-fluid flow along the axis of the quantized vortex filament, which increases the instability of the filament. Thus, the values of $\Gamma_{n,min}$ given by equation 4 should be considered as upper bounds to the actual minimum unstable circulation. More details of these results are given in Samuels (1992b).

In summary, these simulations have identified a process which generates localized superfluid circulation inside the cores of the normal-fluid vortex tubes found in Navier-Stokes turbulence. This growth process is exponential with a time constant small compared to the vortex-tube lifetime taken from current turbulence research. The minimum circulation $\Gamma_{n,min}$ compares well with the vortex-tube circulations taken from Navier-Stokes turbulence simulations. It also should be pointed out that the dense array of quantized vortex filaments formed in the cores of the normal-fluid vortex tubes should allow the detection of these vortex tubes by the attenuation of second sound.

3. Future plans

Though the central objective of the research project has been met, there remain several unresolved issues. Primarily among these is the question of when the growth process shown in figure 4 stops. As stated earlier, the computation time necessary for such a large amount of vortex filament prevented me from running

the simulations to a final steady state. It is possible that simulations in a different parameter range will converge to a steady state within a reasonable computation time. Preliminary work on this approach has been promising.

Once a steady state configuration is available from the simulations, the response of this coupled normal fluid - superfluid state to external perturbations could be examined. This would be an important test of the approximation that the coupled state can be treated as a single component fluid obeying the Navier-Stokes equation.

The most difficult extension of this work would be to include a true interaction between the two fluids. The present simulations are done with an imposed normal-fluid velocity field which is constant in time. In reality, the normal fluid must respond to the motion of the superfluid. To directly include this interaction in the simulations would require an enormous increase in the complexity of the problem. We can say that the use of a non-reacting normal-fluid velocity field is likely to be a good approximation at higher temperatures (near 2 Kelvin) where the normal-fluid density is greater than the superfluid density.

REFERENCES

BORNER, H., SCHMELING, T., & SCHMIDT, D. W. 1983 Experiments on the circulation and propagation of large-scale vortex rings in He II. *Phys. Fluids.* **26,** 1410-1416.

DONNELLY, R. J. 1991 *High Reynolds Number Flows Using Liquid and Gaseous Helium.* Springer Verlag.

DOUADY, S., COUDER, Y., & BRACHET, M. E. 1991 Direct observation of the intermittency of intense vorticity filaments in turbulence. *Phys. Rev. Lett.* **67,** 983-986.

JIMENEZ, J. 1992 Kinematic alignment effects in turbulent flows. *Phys. Fluids A.* **4,** 652-654.

KERR, R. M. 1985 Higher-order derivative correlations and the alignment of small-scale structures in isotropic numerical turbulence. *J. Fluid Mech.* **153,** 31-58.

LIEPMANN, H. W. & COLES, D. 1979 *Proceedings of the Workshop on High-Reynolds-Number Flow.* California Institute of Technology.

MURAKAMI, M. & ICHIKAWA, N. 1989 Flow visualization study of thermal counterflow jet in He II. *Cryogenics.* **29,** 438-443.

OSTERMEIER, R. M. & GLABERSON, W. I. 1975 Instability of vortex lines in the presence of axial normal fluid flow. *J. Low Temp. Phys.* **21,** 191-196.

RUETSCH, G. R. & MAXEY, M. R. 1991 Small-scale features of vorticity and passive scalar fields in homogeneous isotropic turbulence. *Phys. Fluids A.* **3,** 1587-1597.

SAMUELS, D. C. & DONNELLY, R. J. 1990 Dynamics of the interactions of rotons with quantized vortices in helium II. *Phys. Rev. Lett.* **65,** 187-191.

SAMUELS, D. C. 1991 Velocity matching in superfluid helium. *CTR Annual Research Briefs* Stanford Univ./NASA Ames. **93-104.**

SAMUELS, D. C. 1992a Velocity matching and Poiseuille pipe flow of superfluid helium. *Phys. Rev. B.* **46,** 11714-11724.

SAMUELS, D. C. 1992b Response of superfluid Vortex filaments to concentrated normal fluid vorticity. *Phys. Rev. B, Brief Rep.,* to appear.

SIGGIA, E. D. 1981 Numerical study of small-scale intermittency in three-dimensional turbulence. *J. Fluid Mech.* **107,** 375-406.

VINCENT, A. & MENEGUZZI, M. 1991 The spatial structure and statistical properties of homogeneous turbulence. *J. Fluid Mech.* **225,** 1-20.

WALSTROM, P. L., WEISEND II, J. G., MADDOCKS, J. R., & VAN SCIVER, S. W. 1988 Turbulent flow pressure drop in various He II transfer system components. *Cryogenics.* **28,** 101-109.

Regeneration of near-wall turbulence structures

By James M. Hamilton, John Kim AND Fabian Waleffe

1. Motivation and objectives

A remarkable feature of the coherent structures observed in turbulent shear flows is that these structures are self-regenerating. Individual structures may break up or decay, but their presence ensures the creation of subsequent structures. It is through a continuous cycle of generation and regeneration that the turbulence is sustained. In the near-wall region, the principal structures are low- and high-speed streaks and streamwise vortices, and these structures have a characteristic spanwise "wavelength" of about 100 ν/u_τ ($u_\tau = \sqrt{\tau_w/\rho}$ is the friction velocity and τ_w is the shear stress at the wall). The mechanisms involved in the regeneration process, including those which govern the spanwise spacing of the streaks, have, however, been tremendously difficult to determine. Many studies have focused on the kinematics of coherent structures (*e.g.* Kline, *et al.*, 1967, Robinson, 1991), from which the dynamics of regeneration can only be inferred. Direct examination of the flow dynamics in a fully turbulent flow is complicated by the random distribution of the coherent structures in space and time and by the presence of additional structures which may not be essential components of the regeneration process.

Several investigators have avoided these complications by studying simplified flows and, often, by considering only part of the regeneration process. Jiménez and Moin (1991), for example, used direct numerical simulation to study turbulence in a channel flow at Reynolds numbers of 2000 to 5000, simplifying the problem by considering a computational domain in which the streamwise and spanwise dimensions were near the minimum values required to sustain turbulence. The boundary conditions in these directions were periodic, and the flow thus consisted of a doubly periodic array of identical cells. Despite the constraint imposed by the small size of the computational domain, various statistical measures (mean streamwise velocity profile, Reynolds stresses, turbulence intensities) and turbulence structures (sublayer streaks, streamwise vortices, near-wall shear-layers) in the near-wall region closely matched those observed by other investigators.

The origin of the streamwise vortices was addressed by Jang, Benney & Gran (1986) who employed "direct resonance" theory to explain the observed spanwise spacing of the vortices and the accompanying streaks. The direct resonance mechanism produces rapid growth of oblique wall-normal vorticity modes, but applies only to modes which satisfy a resonance condition, and thus provides a scale selectivity. These wall-normal vorticity modes can then interact to form streamwise vortices and streaks of the correct spacing. Subsequently, however, Waleffe & Kim (1991) examined direct resonance and noted that some nonresonant modes were amplified more than the resonant modes, eliminating any scale selection due to the resonance mechanism. Furthermore, they found that the creation of streamwise vortices by

the interactions of oblique modes was dominated by the interactions of the wall-normal velocity modes rather than the wall-normal vorticity modes assumed in the direct resonance theory.

Jiménez and Moin addressed the issue of streak spacing when they noted that turbulence could not be sustained in their plane channel flow simulations if the spanwise dimension of the computational domain was less than the normally observed streak spacing, about 100 wall units, even though the flow Reynolds number, based on half the separation of the channel walls, was 2000 to 5000. This is a fascinating result since reducing the width not only eliminated the streaks, but the turbulence, too. The streaks (or whatever produces them) are not mere artifacts, but essential features of turbulent flow. Waleffe & Kim observed that at 100 wall units, the width of the channel is much less than the wall separation, and that the Reynolds number might more appropriately be based on the spanwise dimension. Indeed, the characteristic spanwise spacing, λ_z, when expressed in wall units, $u_\tau \lambda_z/\nu$, is like a Reynolds number, and the value of 100 may be regarded as the critical Reynolds number for sustained turbulence. This led Waleffe & Kim to conjecture that the preferred spanwise spacing is set by the entire process of self-regeneration rather than by any of the individual mechanisms that constitute the process. They went on to show that the critical Reynolds number obtained from the streak spacing, after conversion to the conventional flow Reynolds number, gives the correct critical values for plane Poiseuille and plane Couette flows.

The present study is an examination of the regeneration mechanisms of near-wall turbulence and an attempt to investigate the critical Reynolds number conjecture of Waleffe & Kim. The basis of this study is an extension of the "minimal channel" approach of Jiménez and Moin which emphasizes the near-wall region and further reduces the complexity of the turbulent flow. Reduction of the flow Reynolds number to the minimum value which will allow turbulence to be sustained has the effect of reducing the ratio of the largest scales to the smallest scales or, equivalently, of causing the near-wall region to fill more of the area between the channel walls. In addition, since each wall may have an active near-wall region, half of the channel is always somewhat redundant. If a plane Couette flow is instead chosen as the base flow, this redundancy is eliminated: the mean shear of a plane Couette flow has a single sign, and at low Reynolds numbers, the two wall regions share a single set of structures. A minimal flow with these modifications possesses, by construction, the strongest constraints which allow sustained turbulence, producing a greatly simplified flow in which we can examine the regeneration process.

2. Accomplishments

2.1 Numerical method and flow geometry

The direct numerical simulation results presented here were obtained using the pseudo-spectral channel flow code of Kim, Moin & Moser (1987) modified to simulate plane Couette flow and using a third-order Runge-Kutta time advancement for the convective terms rather than the original Adams-Bashforth. Dealiased Fourier

expansions are used in the streamwise (x) and spanwise (z) directions, and Chebychev polynomials are used in the wall-normal (y) direction. Boundary conditions are periodic in x and z, and the no-slip condition is imposed at the walls. The mean streamwise pressure gradient is zero, and the flow is driven by the motion of the walls. The flow velocities in the x, y, and z directions are u,v, and w, respectively. The Fourier transforms of the velocities are "hatted" and are functions of the streamwise wavenumber, k_x, the spanwise wavenumber, k_z, and the untransformed y-coordinate, *e.g.* $\hat{u}(k_x, y, k_z)$. The fundamental streamwise and spanwise wavenumbers are $\alpha \equiv 2\pi/L_x$ and $\beta \equiv 2\pi/L_z$. Dimensional quantities are denoted by an asterisk superscript. No superscript is used for quantities non-dimensionalized by outer variables: half the wall separation, h^*, and the wall velocity, U_w^*. A plus superscript is used for quantities non-dimensionalized by wall variables: kinematic viscosity, ν, and friction velocity, $u_\tau = \sqrt{\tau_w/\rho}$. The flow Reynolds number is based on outer variables: Re$= U_w^* h^*/\nu$. The computational grid is $16 \times 33 \times 16$ in x, y, and z. Because of the small computational domain, u_τ varies with time, but the resolution in wall units lies in the range $\Delta x^+ = 10.8$–13.0, $\Delta z^+ = 7.4$–8.9, and $\Delta y^+ = .15$–$.18$ near the wall, and 3.1–3.7 at the center of the channel.

2.2 Regeneration cycle

The first step in the study of the regenerative cycle of near-wall turbulent structures was to determine the minimum Reynolds number and minimum dimensions of the periodic domain of a plane Couette flow. Computations for Reynolds number minimization began with random initial conditions at Re=625, a value known to produce sustained turbulence. The resulting flow was allowed to develop in time, the Reynolds number reduced, and the flow once again allowed to evolve. The Reynolds number was reduced in this manner to Re=500 and 400, with turbulence no longer sustained at Re=300. The domain size was minimized in a similar fashion with reductions first in the spanwise dimension, L_z, then in the streamwise dimension, L_x. Finally, the parameter values selected are $L_x = 1.75\pi$ and $L_z = 1.2\pi$ at Re=400. Turbulence could be sustained at slightly lower L_x and L_z; however, these values were chosen because they produce a flow which is better suited to the present study, as discussed below.

The flow realized in this small domain is ideal for examining the turbulence regeneration mechanisms. Much of the randomness in the location of the turbulence structures is eliminated, and regeneration occurs temporally in a well defined, quasi-cyclic process. The general characteristics of the flow over one complete regeneration cycle can be seen in Figure 1. This is a plot of streamwise (u) velocities in the x-z plane midway between the walls at various times. At the upper left, the flow can be seen to have little x-dependence, and strong streak-like structures dominate the flow. As time increases, the x-dependence increases, with the streak becoming "wavy" and then breaking down. "Break down" means the production of smaller scale features and loss of definition of the streak, particularly near the walls. Finally, at the lower right, a well-defined, nearly x-independent streak has been regenerated, and the cycle is ready to repeat.

Because a spectral method is used in these simulations, Fourier decomposition is

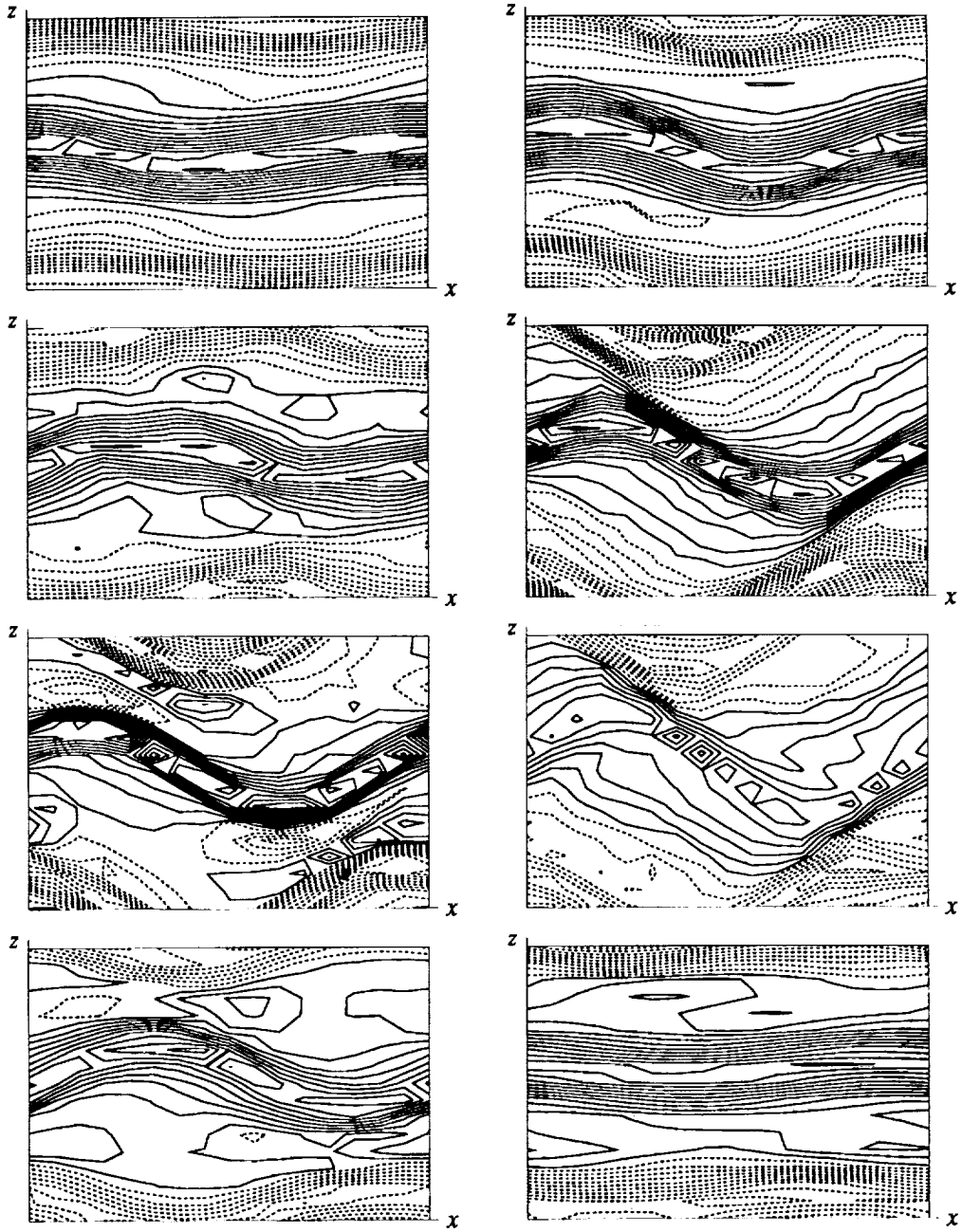

FIGURE 1. Iso-contours of u-velocity in x-z plane centered between walls, solid contours positive, dashed contours negative. Contour interval 0.032. Time increases from left to right, top to bottom. Times are: $t = 757.5$, $t = 764.8$, $t = 772.0$, $t = 777.8$, $t = 783.0$, $t = 794.1$, $t = 808.2$, $t = 830.2$.

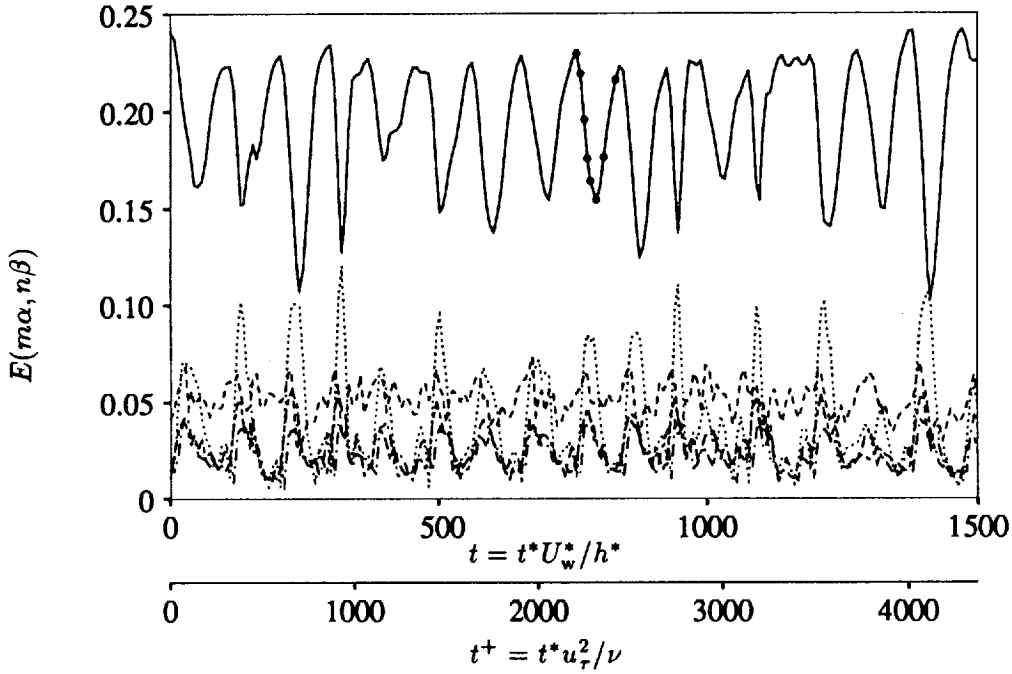

FIGURE 2. Modal energy over many regeneration cycles. Solid circles correspond to times of Figure 1. ——— , $E(0,\beta)$; – – – – , $E(0,2\beta)$; - - - - - - , $E(\alpha,0)$; — – — , $E(\alpha,\beta)$; — · — · — , $E(\alpha,2\beta)$.

a natural means to study the regeneration cycle. The modal kinetic energy is given by

$$E(m\alpha,n\beta) \equiv \int_{-1}^{1} \left[\hat{u}^2(m\alpha,y,n\beta) + \hat{v}^2(m\alpha,y,n\beta) + \hat{w}^2(m\alpha,y,n\beta)\right] dy, \quad (1)$$

and Figure 2 is a plot of this energy in various modes over many cycles. The cyclic nature of the flow particularly apparent in the $(0,\beta)$ and $(\alpha,0)$ modes of Figure 2. Though $E(0,\beta)$ is the energy from all three modal velocity components, the dominant contribution is from $\hat{u}(0,y,\beta)$, the fundamental-in-z, x-independent streamwise velocity mode, *i.e.* the streaks. The flow of Figure 1 is a single cycle of the flow of Figure 2, and the corresponding times are marked. Note the decrease and then increase in $E(0,\beta)$ as the flow passes from small x-dependence to large x-dependence and back again. The period of the regeneration cycle is slightly less than 100, based on 16 cycles in 1500 time units in Figure 2. This is approximately the same period observed by Jiménez and Moin in their minimal channel flow at higher Reynolds number, though their channel flow and the present plane Couette flow have slightly different time normalizations. The regeneration cycle can be divided roughly into two phases, each with a duration of about 50 time units: streak formation, where $dE(0,\beta)/dt > 0$, and streak breakdown, where $dE(0,\beta)/dt < 0$.

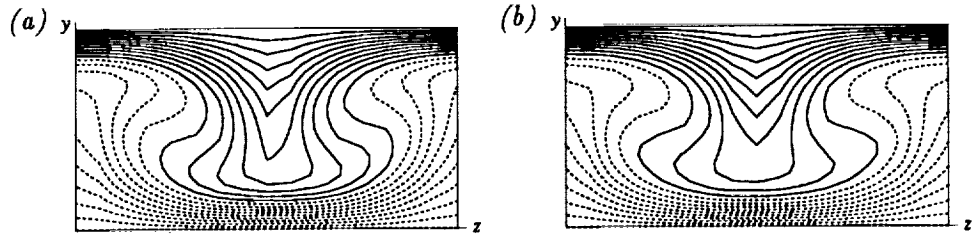

FIGURE 3. Streaks (u-velocity) due to *(a)* streamwise vortices only, at peak of $E(0,\beta)$ response, and *(b)* full simulation. Velocity field in physical space is obtained by inverse Fourier transform in x and z of the $k_x = 0$ modes only. Dashed lines are negative contours. Contour interval, 0.2.

2.3 Streak formation

It is usually argued that streamwise vortices generate the low- and high-speed streaks observed in the near-wall region (*e.g.* Swearingen and Blackwelder, 1987; Waleffe & Kim, 1991). In the present study, various methods of visualization of the flow give clear evidence of the presence of streamwise vortices, and it is desirable to verify that these vortices can not only generate streaks, but generate the observed streaks.

In Figure 1 the streaks remain apparent for most of the regeneration cycle. Nearer the walls, however, the streaks are most clearly defined when the flow is nearly x-independent at times corresponding to peaks in the energy of the $(0,\beta)$ mode. Therefore, in studying streak formation, it is useful to focus on the x-independent ($k_x = 0$) modes. To verify that the vortices produce the streaks, the velocity field at $t = 758$, corresponding to a peak in $E(0,\beta)$, is taken as the initial condition for a model simulation. This initial condition is modified by zeroing all but the $k_x = 0$ modes and zeroing all the $\hat{u}$ modes *except* the mean streamwise velocity mode, $\hat{u}(0,y,0)$. In addition, the $\hat{v}(0,y,n\beta)$ and $\hat{w}(0,y,n\beta)$ modes are held fixed ("frozen") during the model simulation. The energy in the $(0,\beta)$ mode peaks after about 50 time units, the same time scale as in the full simulation, and the resulting streaks are virtually identical to the streaks from the full simulation at $t = 758$, as shown in Figure 3. A similar model simulation with an initially linear $\hat{u}(0,y,0)$ velocity profile indicates that the mean velocity profile is due principally to the streamwise vortices as well.

2.4 Streak breakdown

It is often argued that breakdown occurs due to an instability (*e.g.* Swearingen and Blackwelder, 1987), and the "waviness" that develops in the high- and low-speed streaks in Figure 1 is certainly reminiscent of an instability process. In order to determine whether breakdown is due to an instability in the present case, the growth or decay of small amplitude, spatially random fluctuations in an otherwise x-independent flow was examined. The initial conditions for a model simulation were taken from the flow of Figures 1 and 2 at time $t = 758$, corresponding to a peak in $E(0,\beta)$. The $k_x = 0$ modes of $\hat{u}$, $\hat{v}$, and $\hat{w}$ (*i.e.* the x-independent modes)

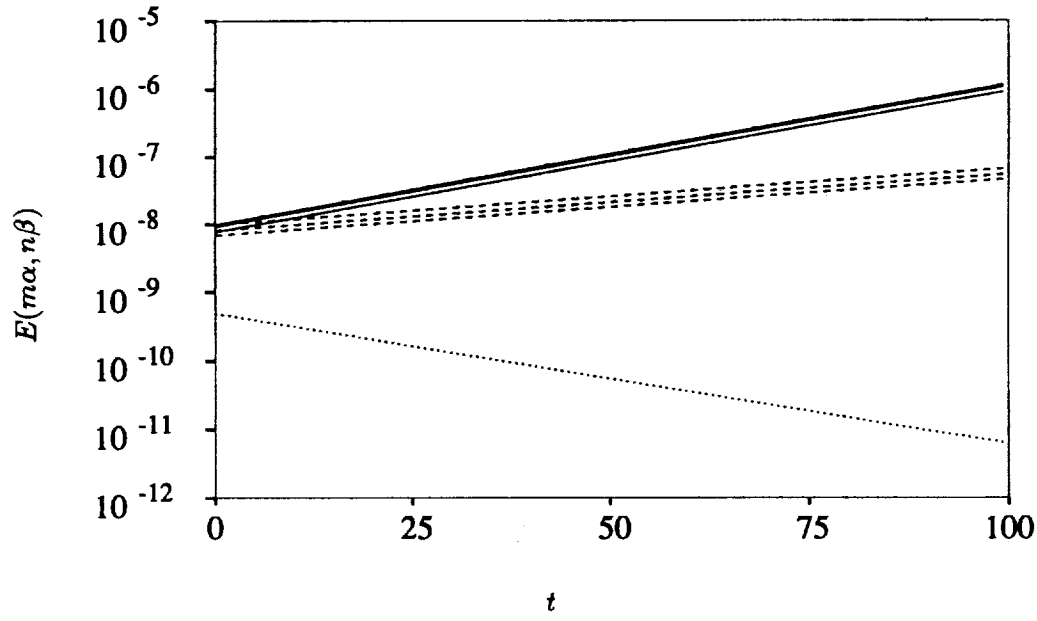

FIGURE 4. Linear stability of $k_x = 0$ modes of flow from full simulation at $t = 757.5$: ——— , $(\alpha, 0)$, (α, β) and $(\alpha, 2\beta)$ modes; – – – – , $(2\alpha, 0)$, $(2\alpha, \beta)$ and $(2\alpha, 2\beta)$ modes; - - - - - - , $(3\alpha, 0)$ modes.

were retained unaltered, and random perturbations, uniformly distributed from zero to 10^{-6}, were placed in all remaining Fourier modes. The $k_x = 0$ modes were "frozen", and the perturbations were allowed to evolve normally. This procedure is much like that used to observe the development of streaks in the previous section, except that here both the cross-flow and the streaks are frozen, and it is the growth of perturbations in the x-dependent modes that are of interest. The small initial perturbation amplitudes were chosen in order to study the linear stability of the flow. If the base flow is unstable, the fastest growing instability mode would be expected to dominate after sufficient time, and in general, this instability mode will consist of many spanwise Fourier modes. The results of this simulation show that the streaks are indeed linearly unstable. The growth in energy of the most unstable modes is shown in Figure 4. For purposes of this plot, the α and 2α instability modes obtained from the simulation were normalized to have approximately the same initial amplitude. Note that the various spanwise Fourier modes that contribute to each instability mode grow in energy at the same rate.

Comparison of the linear stability results to the full simulation shows some differences, but these are to be expected since breakdown is clearly a nonlinear process. The waviness that develops during actual breakdown is not really a "mode"; for instance, $E(\alpha, 0)$, $E(\alpha, \beta)$ and $E(\alpha, 2\beta)$ do not grow together as a single instability mode in Figure 2 as they do in Figure 4. In addition, the time scale of the linear

instability is too long, with $E(\alpha,0)$ in Figure 2 growing by nearly an order of magnitude in less than 20 time units during breakdown, while the α instability mode in the linear simulation of Figure 4 requires nearly 50 time units. The linear approach matches the rapid growth rates of the simulation only during the initial, transient phase. The principal limitation of the linear approach is that the flow we are trying to analyze evolves on the same time scale as the instability. Comparison of the shapes of the linear α-modes to the α-modes obtained in the full simulation (results not shown here) again show some differences but are surprisingly good considering the limitations of the linear approach.

2.5 Streamwise vortex regeneration

The regeneration of turbulence structures as discussed so far consists of a continuous cycle of streak formation and breakdown. Streak formation was shown to be the result of momentum redistribution by streamwise vortices, but this raises the question of the origin of the streamwise vortices.

The streamwise vortices persist throughout the regeneration cycle of Figure 1 and during the many regeneration cycles of Figure 2. It can be shown that streamwise vortices in a strictly x-independent flow will eventually decay: there is no mechanism for the vortices to extract energy directly from the mean flow. Therefore, the x-dependent modes must somehow augment the streamwise vortices if the regeneration cycle is to continue. Though not shown here, plots of the velocity field in the cross-flow (y–z) plane indicate that this augmentation takes place primarily during streak breakdown, when the x-dependence of the flow is greatest. For the cycle of Figure 1, the strength of the streamwise vortices has just begun to increase by the time of the third panel, $t = 772$. The modal interactions which cause this augmentation can be studied by a model simulation using the flow field at $t = 772$ as an initial condition, again with selective alteration of various Fourier modes. In this case, all modes are set to zero except the mean, $\hat{u}(0,y,0)$,and the α-modes: $\hat{u}$, $\hat{v}$, and $\hat{w}$ of $(\alpha,y,n\beta)$ (for all n). In addition, the α-modes are frozen. With this initial condition, streamwise vortices quickly appear, and these vortices then produce streaks, as would be expected. If the α-modes are then "unfrozen", the flow *immediately* begins to follow the regenerative cycle normally observed. This process is shown in Figure 5. Up to $t = 34.9$, the α-modes are frozen, and $E(0,\beta)$ is seen to rapidly increase. After $t = 34.9$ (the heavy vertical line), the α-modes are unfrozen. The energy in the $(0,\beta)$ mode decreases slightly as breakdown due to the α-modes continues, followed by streak regeneration and another cycle. This approach shows that it is the α-modes which regenerate the streamwise vortices but does not reveal the dynamics of the process. The dynamics are most easily studied by an examination of the evolution of streamwise vorticity.

To compare the contributions of the individual nonlinear terms of the vorticity equation over time, it is easiest to consider

$$\frac{\partial|\hat{\omega}_x|^2}{\partial t} = \hat{\omega}_x^\dagger \frac{\partial \hat{\omega}_x}{\partial t} + \hat{\omega}_x \frac{\partial \hat{\omega}_x^\dagger}{\partial t} \tag{2}$$

(where the † superscript represents the complex conjugate), since this quantity is

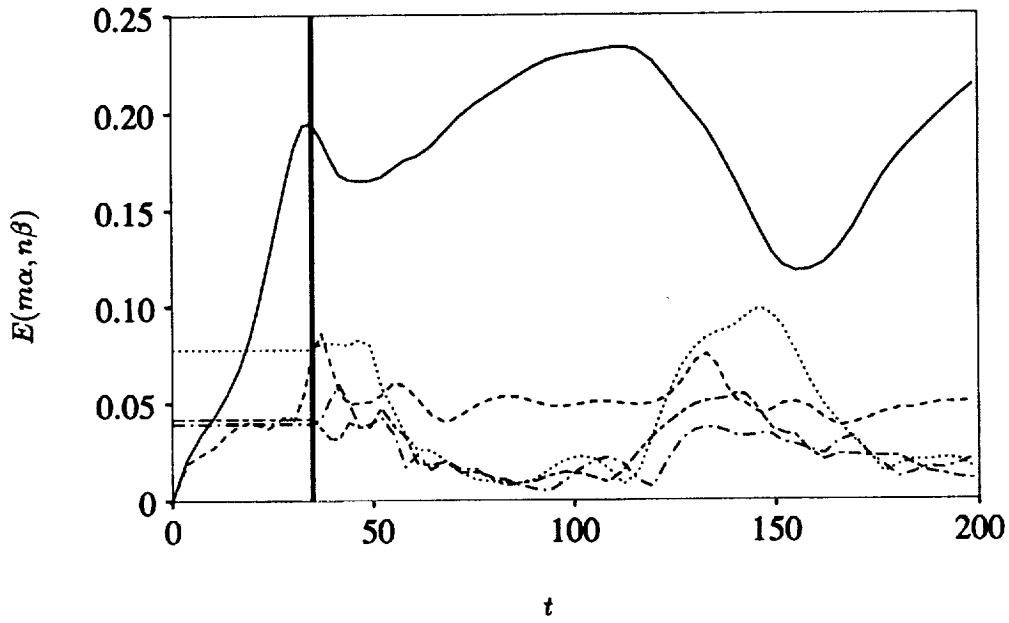

FIGURE 5. Regeneration of streamwise vortices from $k_x = \alpha$ modes, and subsequent reversion to regeneration cycle. Initially conditions: $k_x = \alpha$ modes from full simulation at $t = 772.0$, and all $k_x = 0$ modes zero except $\hat{u}(0, y, 0)$. The $k_x = \alpha$ modes are frozen until $t = 34.9$ (heavy line), and thereafter all modes are free to evolve. Modes plotted same as Figure 2.

positive at y-locations where the existing streamwise vorticity is being augmented and negative where the vorticity is being reduced. The contributions of each term at the y-location of the maximum magnitude of the term are plotted in Figure 6. One might hope, for simplicity, that only a single term in the vorticity equation would be dominant. In fact, one term has about twice the amplitude of any other,

$$-\hat{\omega}_x^\dagger(0,\beta)\left[\hat{v}(\alpha,\beta)\frac{\partial\hat{\omega}_x(-\alpha,0)}{\partial y} + \hat{v}(-\alpha,\beta)\frac{\partial\hat{\omega}_x(\alpha,0)}{\partial y}\right] + C.C., \tag{3a}$$

but four other terms are significant,

$$\hat{\omega}_x^\dagger(0,\beta)\left[\hat{\omega}_y(\alpha,0)\frac{\partial\hat{u}(-\alpha,\beta)}{\partial y} + \hat{\omega}_y(-\alpha,0)\frac{\partial\hat{u}(\alpha,\beta)}{\partial y}\right] + C.C. \tag{3b}$$

$$-\hat{\omega}_x^\dagger(0,\beta)\left[\hat{w}(\alpha,0)\frac{\partial\hat{\omega}_x(-\alpha,\beta)}{\partial z} + \hat{w}(-\alpha,0)\frac{\partial\hat{\omega}_x(\alpha,\beta)}{\partial z}\right] + C.C. \tag{3c}$$

$$-\hat{\omega}_x^\dagger(0,\beta)\left[\hat{u}(\alpha,\beta)\frac{\partial\hat{\omega}_x(-\alpha,0)}{\partial x} + \hat{u}(-\alpha,\beta)\frac{\partial\hat{\omega}_x(\alpha,0)}{\partial x}\right] + C.C. \tag{3d}$$

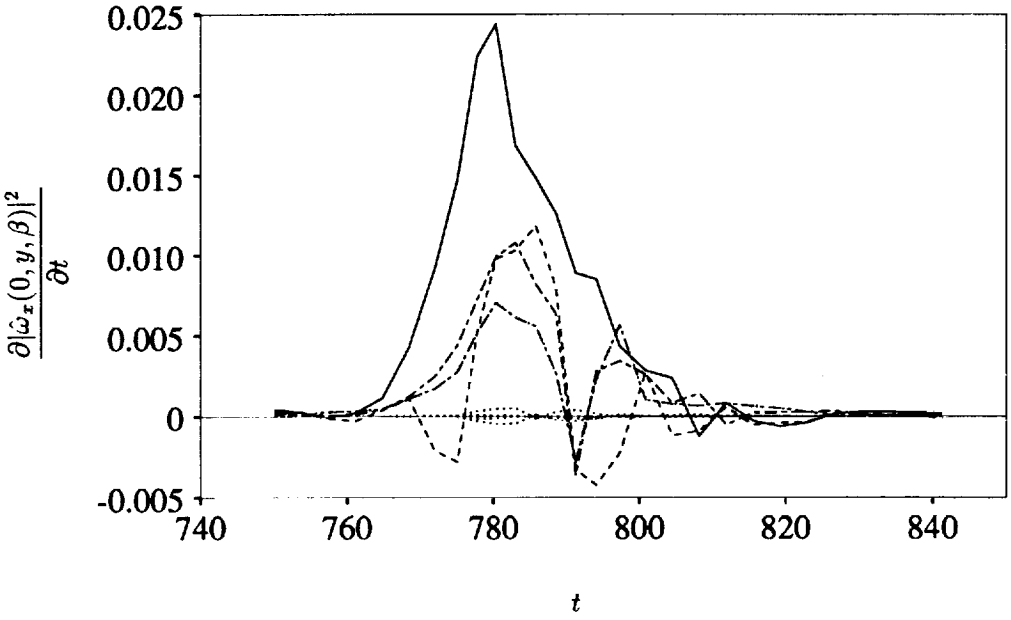

FIGURE 6. Contributions of various terms to $\partial|\hat{\omega}_x(0,y,\beta)|^2/\partial t$ at y-locations corresponding to maximum amplitudes. ———, Expression 3a; – – – –, Expression 3b; — — —, Expression 3c; - - - -, Expressions 3d and 3e; ------, all other interactions.

$$\hat{\omega}_x^\dagger(0,\beta)\left[\hat{\omega}_x(\alpha,0)\frac{\partial\hat{u}(-\alpha,\beta)}{\partial x}+\hat{\omega}_x(-\alpha,0)\frac{\partial\hat{u}(\alpha,\beta)}{\partial x}\right]+C.C. \tag{3e}$$

The y-dependence has been suppressed, and the $C.C.$ are the complex conjugates. Expressions 3d and 3e turn out to be identical for the $(0,\beta)$ mode, thus there are only four dominant curves in Figure 6. This vortex regeneration process is repeated for every breakdown event. The importance of vortex regeneration is particularly evident in the discussion of the next topic, the spanwise spacing of streaks.

2.6 Spanwise spacing of structures

Jiménez and Moin (1991) found that when the spanwise dimension of their computational domain was less than the typically observed spanwise spacing of the streaks, turbulence could not be sustained. As discussed in §1, this led Waleffe & Kim (1991) to conjecture that the streak spacing is determined by the entire self-regeneration process. The regeneration process has been examined in some detail in previous sections, and the techniques used to investigate regeneration can now be used to address the issue of the spanwise spacing of near-wall structures.

The first step is to reduce the dimensions of the computational domain just enough that turbulence is sustained through several regeneration cycles but ultimately decays. Then we can study the details of the flow to determine which part(s)

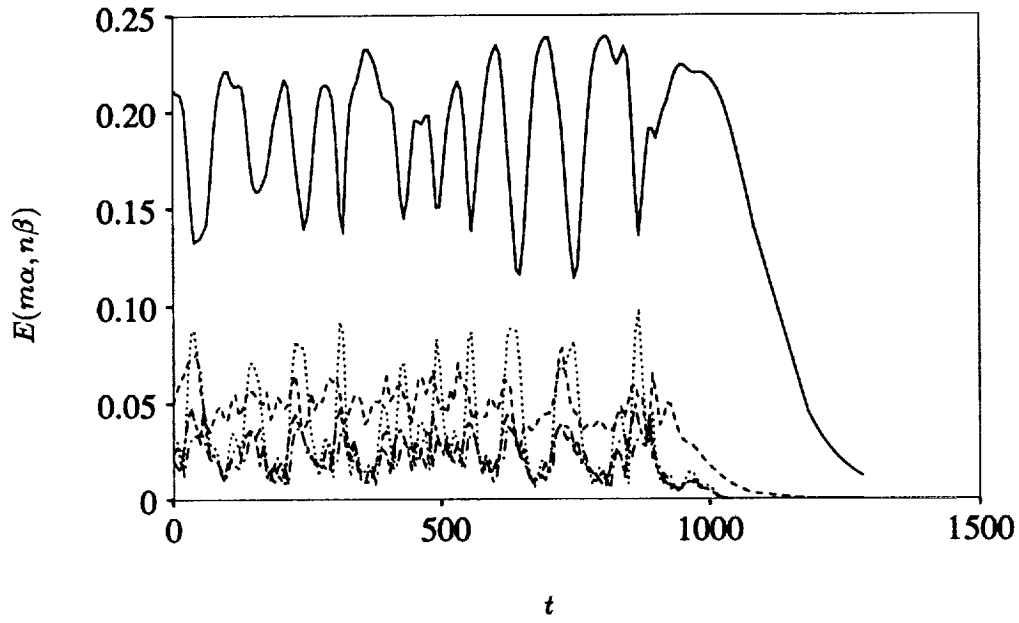

FIGURE 7. Modal energy over many regeneration cycles of an unsustainable turbulent flow: ——— , $E(0,\beta)$; – – – – , $E(0,2\beta)$; - - - - - - , $E(\alpha,0)$; — – — , $E(\alpha,\beta)$; — – — – , $E(\alpha,2\beta)$.

of the regeneration cycle is disrupted. The modal energies for such a flow are plotted in Figure 7. The spanwise dimension of the flow is $L_z = 1.1\pi$, or $L_z^+ = 109.2$ to 126.1 (where L_z^+ is based on u_τ during the early part of the simulation before the turbulence begins to decay). The streamwise dimension is $L_x = 1.6\pi$, and the same Reynolds number, 400, is used. This flow was obtained by first reducing the spanwise dimension of a sustainable turbulent flow and then the streamwise dimension. Turbulence can be sustained in this channel if L_x is increased, but the cycle is very chaotic. Turbulence can also be sustained if L_z is increased.

The regeneration of the streamwise vortices for the unsustainable flow is plotted in Figure 8 for the last few cycles of Figure 7. Vortex regeneration takes place during each streak breakdown event, between $t = 600$ and $t = 900$, but the amount of streamwise vorticity added to the flow decreases with each succeeding cycle. Finally, for $t > 900$, the flow simply decays with no breakdown and no corresponding vortex regeneration.

As the production of streamwise vorticity decreases, the average strength of the streamwise vortices decreases. There is little visible difference in the streaks produced by these weaker vortices, but the instability of the streaks is dramatically reduced as the strength of the streamwise vortices goes down (results not shown here). The flow actually becomes linearly stable by $t = 1000$, and breakdown does not occur.

The computations of this section indicate that the spanwise wavelength of the

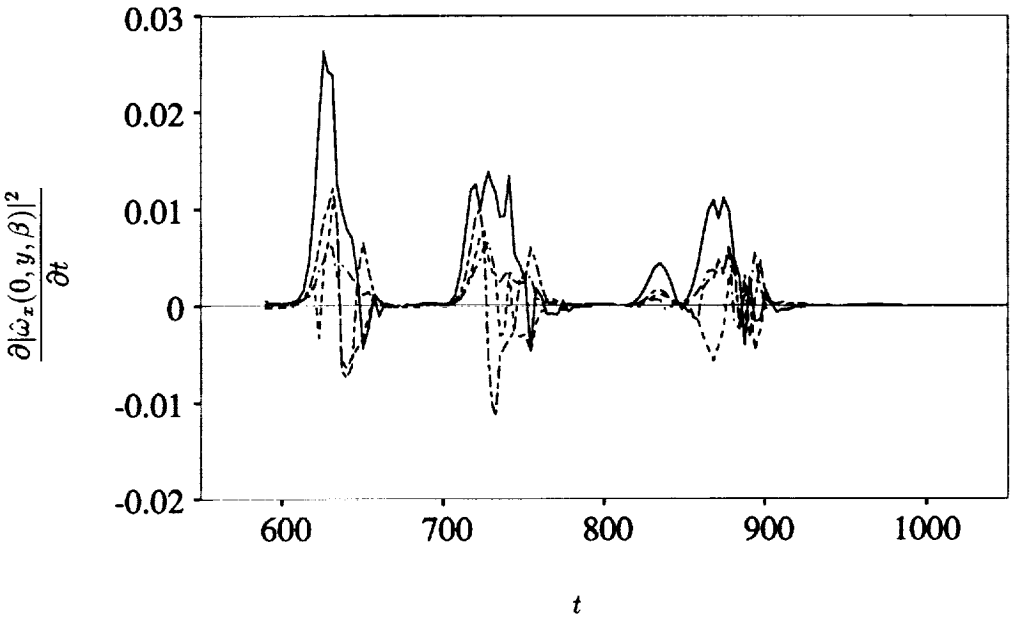

FIGURE 8. Contributions of various terms to $\partial|\hat{\omega}_x(0,y,\beta)|^2/\partial t$ at y-locations corresponding to maximum amplitudes in an unsustainable turbulent flow: ——— , Expression 3a; – – – – , Expression 3b; — — — , Expression 3c; - - - - - , Expressions 3d and 3e; - - - - - - , all other interactions.

near-wall structures is determined by the minimum wavelength required by the regeneration process. This would seem to confirm the conjecture by Waleffe & Kim that this minimum wavelength is set by the entire regeneration process rather than any individual element of regeneration. When the computational domain is too narrow, turbulence decays because the streamwise vortices are inadequately regenerated during each cycle. Vortex regeneration, in turn, depends on the interactions of the α modes produced during breakdown, and breakdown depends on the stability of the streaks produced by the streamwise vortices. This, of course, returns us to the starting point because the streamwise vortices depend on the vortex regeneration of the previous cycle. Ultimately, turbulence decayed in the flow of Figure 7 because breakdown did not occur. But, each step in the regeneration process was progressively weaker for several cycles before the final decay, and thus it was the entire regeneration process that was unsustainable in this flow.

3. Future plans

The results presented here give a fairly complete picture of the regeneration process for near-wall turbulence structures in a minimal domain, but the real objective, of course, is to relate these observations to the near-wall structures in a larger domain at higher Reynolds numbers. Thus, the major element of future work is to examine these processes in full-scale turbulence. Rather than move directly to an

examination of existing databases, however, the robustness of the observed mechanisms will first be checked by a step-by-step increase in the dimensions and Reynolds numbers of the minimal domain.

Some of the details of the present work will also be examined further. For instance, in the work relating to the minimum spanwise spacing of the streaks in §2.6, the length of the domain, L_x, has some effect on whether turbulence is sustained. This dimension will be significantly increased in some future computations so that the streamwise wavenumber of the most unstable modes will be selected by the flow rather than by the choice of box size.

The quasi-cyclic nature of the regeneration cycle also suggests some application of these results to turbulence control. Since breaking the cycle at any point may be sufficient to suppress turbulence, it would be useful to examine regeneration with the aim of implementing possible control schemes.

REFERENCES

JANG, P. S., BENNEY, D. J., & GRAN, R. L. 1986 On the origin of streamwise vortices in a turbulent boundary layer. *J. Fluid Mech.* **169,** 109-123.

JIMENEZ, J. & MOIN, P. 1991 The minimum flow unit in near-wall turbulence. *J. Fluid Mech.* **225,** 213-240.

KIM, J., MOIN, P. & MOSER, R. 1987 Turbulence statistics in fully developed channel flow at low Reynolds number. *J. Fluid Mech.* **177,** 133-166.

KLINE, S. J., REYNOLDS, W. C., SCHRAUB, F. A., & RUNSTADLER, P. W. 1967 The structure of turbulent boundary layers. *J. Fluid Mech.* **30,** 741.

ROBINSON, S. K. 1991 The Kinematics of Turbulent Boundary Layer Structure. *NASA TM-103859.*

SWEARINGEN, J. D. & BLACKWELDER, R. F. 1987 The growth and breakdown of streamwise vortices in the presence of a wall. *J. Fluid Mech.* **182,** 255.

WALEFFE, F. & KIM, J. 1991 On the origin of streaks in turbulent boundary layers. *Proceedings of the Eighth Symposium on Turbulent Shear Flows,* Technical University of Munich, Sept. 9-11.

Center for Turbulence Research
Annual Research Briefs 1992

Experiments on near-wall structure of three-dimensional boundary layers

By K. A. Flack[1] AND J. P. Johnston[1]

1. Motivations

Investigations of three-dimensional turbulent boundary layers have shown basic differences between two- and three-dimensional flows. These differences can significantly impact the modeling of three-dimensional flows since many flow models are based on results from two-dimensional boundary layers. In many cases (Johnston (1976) and Driver & Johnston (1989)) the shear stress vector direction has been shown to lag relative to the direction of the mean velocity gradient as the cross-flow grows downstream. Coincidence of these vectors is necessary for a scalar eddy viscosity modeling assumption. A second effect is a reduction in magnitude of the shear stress and/or the shear stress to turbulence energy ratio, a_1. This reduction has been observed in several experiments, for example Pontikos & Bradshaw (1985) and Anderson & Eaton (1988). Recent numerical simulations (Spalart (1989) and Moin, *et al.* (1990)) also indicate wall-layer structural differences between two- and three-dimensional boundary layers.

The mechanisms by which cross-flow affects the structure of the boundary layer may not be the same in all situations. Anderson and Eaton proposed that streamwise vortices of one sign in the inner layer are overwhelmed by a mean streamwise vorticity of the opposite sign associated with the part of the cross-flow velocity profile near the wall. A net loss of one-sign wall layer structures may reduce the active turbulence in the near-wall region and thereby reduce the Reynolds shear stresses across the boundary layer. Anderson and Eaton's hypothesis was indirectly verified in related experiments by Shizawa & Eaton (1990, 1992). Eaton (1991), in his interpretation of these data, shows that coherent, streamwise vortices of the same sign as the cross-flow vorticity in the wall-layers interact with the cross-flow to form an upwash of low momentum fluid from the wall: a flow similar to a longitudinal low-speed streak. Conversely, a vortex of the opposite sign interacts with the near-wall cross-flow quite differently. The upwash is suppressed so much that the formation of longitudinal low-speed streaks is prevented.

The reduction of shear stress and kinetic energy in the simulation of Sendstad & Moin (1991 a,b) appears to be related to the weakening and breakup of the near-wall high and low speed streaks as the streamwise vortices in the buffer layer, just above the streaks, are first shifted sideways (convected) by the cross-flow and then turned so they cut across the streaks at acute angles. However, the profile of mean streamwise vorticity (due to the cross-flow) for the simulated three-dimensional

1 Stanford University

channel flow has only one sign, and it develops in a favorable pressure gradient, whereas almost all profiles seen in practice have a reversal of sign of streamwise vorticity somewhere in the buffer layer, and in many cases, they develop in adverse pressure gradients.

The differences in structure between two- and three-dimensional boundary layers was also addressed in the experiment of Littell & Eaton (1991). The experiment used two-point correlations to investigate the vortical structures in a three-dimensional boundary layer on a spinning disk. It was found that each sign of longitudinal vortex is equally likely to exist, but one sign of vorticity is associated with a structure which is better at producing ejections.

The goal of the current investigation is to study the structure of the inner layers. Among other questions, the differences between the effects deduced from the three-dimensional flow simulations and the effects seen in experiments can be examined. The research concentrates on the structure of the wall-layer though flow visualization and direct turbulence measurements down to $y^+ = 5$.

2. Accomplishments

2.1 Flow approaching a swept step

A three-dimensional boundary layer was produced by forcing the flow to turn rapidly ahead of a forward facing step which is swept back at 45° to the main flow. Strong boundary layer cross-flows are produced rapidly in response to severe spanwise pressure gradients imposed by the swept step; a case similar to an earlier investigation by Johnston (1970). The experiments are conducted in a low-speed water channel with $Re_\theta = 1400$ for the nominal two-dimensional boundary layer. The two-dimensional characteristics for the facility are already known from previous research (Barlow & Johnston, 1988, Johnson & Johnston, 1989).

2.1.1 Turbulence measurements

Turbulence measurements were obtained using a three-component LDA system at various locations upstream of the step. Profile locations ranged from an upstream station at $x' = 30.5$ cm to a station at $x' = 5.7$ cm, close to but downstream of the three-dimensional detachment line. The experimental configuration and measurement locations are diagrammed in Figure 1. Measurements of the turbulence intensity, shear stress magnitude, and structure parameter, a1, are shown on figures 2, 3, and 4 against y/δ and y^+. These and other results are available in Flack & Johnston (1993).

The turbulence intensity grows downstream outside the wall region, and the location of peak intensity shifts away from the wall. The turbulent shear stress also grows downstream and reaches a maximum value in the neighborhood of $y^+ = 60$. The laminar portion of the total shear stress, shown in Figure 3(b), has the same contribution as the turbulent stress to the total stress at $y^+ = 10$.

The relative growth of the turbulent shear stress with respect to kinetic energy is represented in the structure parameter, a_1, the ratio of the turbulent shear stress to twice the turbulent kinetic energy. a_1 decreased slightly downstream where cross-flows are large, but not as much as might be expected from examination of earlier

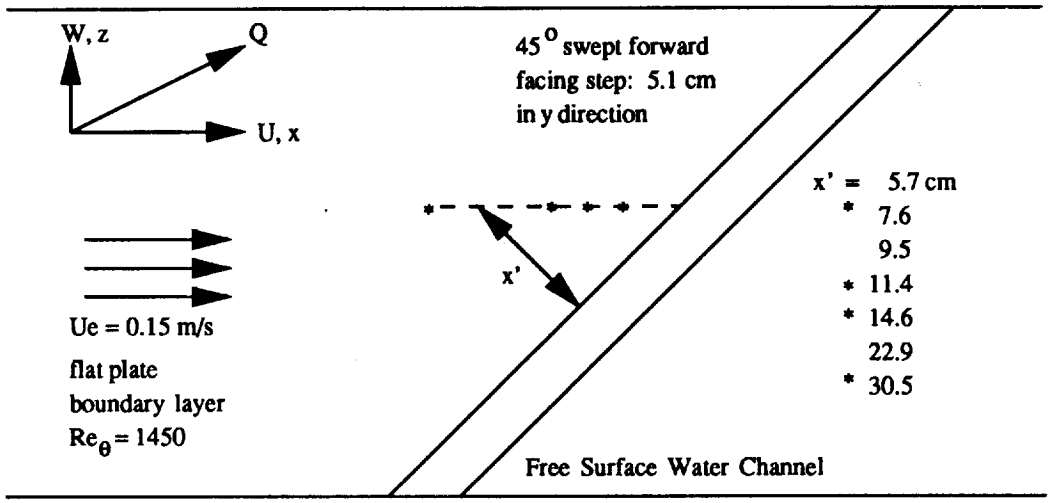

FIGURE 1. Experimental configuration: *, measurement locations presented.

studies such as the closely related flow of Johnston (1970). The effects of strong adverse pressure gradients, which occur in the same region as the strong cross-flows, may mask the effects of three-dimensionality on turbulence stress levels and thus on the a_1 parameter. It is interesting that a_1 seems to scale universally on y^+ up to $y^+ \approx 50$.

The response of the mean flow and turbulent shear stress to the onset of three-dimensionality is represented in the directions of the shear stress vector and the velocity gradient vector. These angles are shown in Figure 5 versus y/δ and y^+. The shear stress is seen to lag the velocity gradient outside the sublayer region for $y^+ > 50$. Below $y^+ = 20$, it is hard to determine the relationship between angles because of high experimental uncertainty, but below y^+ of 30, the isotropic eddy viscosity assumption may be sufficient because the angles are nearly coincident.

2.1.2 Flow visualization

The near-wall flow structure was investigated through a series of flow visualization experiments. Three flow configurations were visualized for comparison: (1) a (base case) two-dimensional turbulent boundary layer, (2) a two-dimensional boundary layer flow approaching a forward facing step set perpendicular to the main flow, and (3) a three-dimensional boundary layer flow approaching the 45° swept, forward facing step. The hydrogen bubble wire technique was used to visualize the flow. Bubbles marked the flow at two locations; within the viscous sublayer at $y^+ \approx 2$ and within the buffer layer at $y^+ \approx 37$. The wall shear stress used in non-dimensionalization is based on the nominal two-dimensional boundary layer flow. The bubbles were illuminated in the cross-sectional view downstream of the wire using a laser light sheet and recorded on video tape for analysis.

The videos were viewed frame-by-frame to obtain "quantitative" results from the visualization. Vortical structures, a mass of hydrogen bubbles which appears

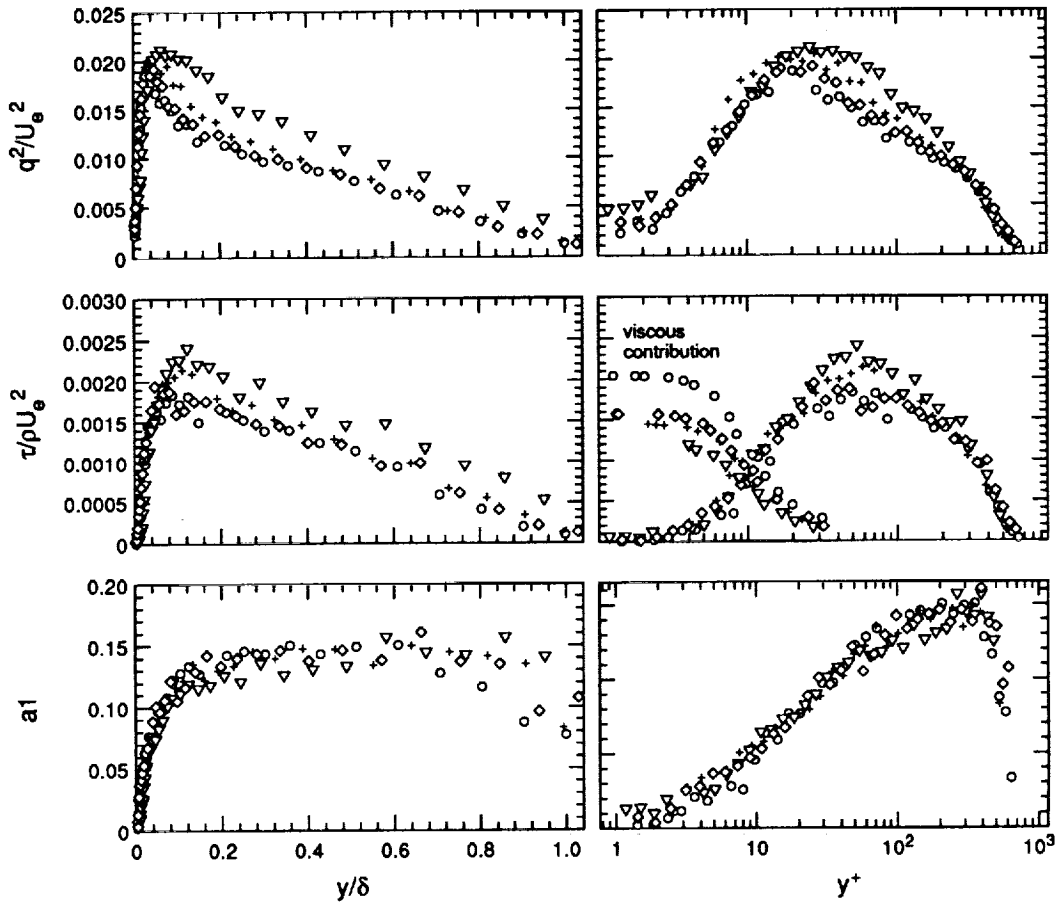

FIGURE 2. (a), (b): q^2/U_e^2 vs. y/δ and y^+; ○, $x' = 30.5$cm; ◇, $x' = 14.6$cm; +, $x' = 11.4$cm; ▽, $x' = 7.6$cm.

FIGURE 3. (a), (b): $\tau/\rho U_e^2$ vs. y/δ and y^+; ○, $x' = 30.5$cm; ◇, $x' = 14.6$cm; +, $x' = 11.4$cm; ▽, $x' = 7.6$cm.

FIGURE 4. (a), (b): a_1 vs. y/δ and y^+; ○, $x' = 30.5$cm; ◇, $x' = 14.6$cm; +, $x' = 11.4$cm; ▽, $x' = 7.6$cm.

to be rotating or moving in a circular direction in the plane of the laser sheet, were identified and given a sign with relationship to the cross-flow. The size of the vortices (indicated by the normal extent of the bubble mass out from the wall beyond which bubbles could not be observed) was also recorded in viscous units. The vortical structures we observed are thought to represent cross-sections of the quasi-streamwise vortices observed by Robinson (1991).

Structural differences between the two- and three-dimensional boundary layers were observed by careful statistical analysis of at least 100 individual vortices for each case. It was found that both types of two-dimensional boundary layers, cases (1) and (2), contained equal numbers of each sign of vortex; however, for case (3), the

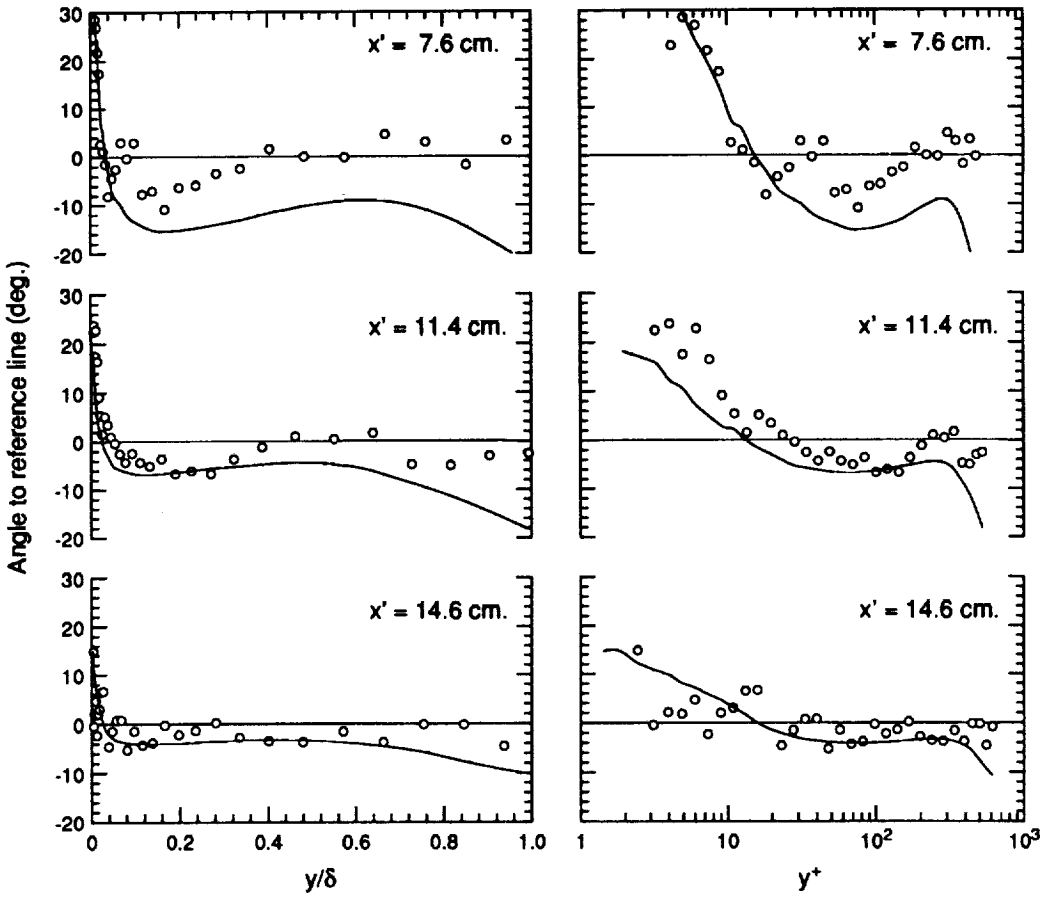

FIGURE 5. (a), (b): o,angles of shear stress; —,mean velocity gradient vs. y/δ and y^+.

three-dimensional boundary layer at $y^+ = 37$ had excess (more than 50 %) vortices that have the same sign as the mean spanwise vorticity near the wall. This result can be interpreted in two ways with respect to previous findings. As hypothesized by Anderson & Eaton, there is a net loss of coherent wall layer structures of one sign which could be caused by the cancellation of vorticity by the mean vorticity near the wall. This preference for one sign of vortical structure could not be determined for the flow pictures marked at $y^+ = 2$, but it appeared in the picture at $y^+ = 37$ as noted.

This result can also be interpreted with respect to the findings of Littell & Eaton. Their research proposed that sweeps and ejections in the boundary layer were influenced by the mean vorticity associated with the cross-flow. Most strong ejections are caused by secondary velocity which augments the cross-flow close to the surface while most strong sweeps are caused by secondary velocity which opposes the cross-flow near the surface. In our visualization, the apparent increase in the number of

vortical structures with the same vorticity as the cross-flow near the surface could be due to a tendency in our visualization to identify the strong ejections as vortical structures.

The strong ejections caused by secondary velocity which augments the cross-flow close to the surface could also explain another finding from the flow visualization. From measurements of the vortex sizes, it was observed that vortices of both sign have the same average height and they reached out to the same maximum distance from the wall as seen in the two-dimensional boundary layers. However, in the three-dimensional case, the vortices with the same sign as the mean spanwise near-wall vorticity have a greater maximum and average height than the opposite signed vortices. Again, this could be the influence of the strong ejections.

2.2 Three-dimensional boundary layer facility

Preliminary turbulence measurements indicate that the abrupt swept-step flow shows some interesting features, but it is not typical of many important practical flows such as the three-dimensional boundary layer on the end wall of a bent duct or the flow over a swept wing. These cases are characterized by weaker streamwise and cross-flow pressure gradients, and, consequently, three-dimensionality in the boundary layer develops more slowly in the streamwise direction than is the case for swept-step flow. In order to study a slowly developing three-dimensional cross-flow on the flat wall of the channel, a new test section was recently constructed. This configuration consists of a 30° curved duct, similar to the flow investigated by Schwartz & Bradshaw (1992), whose experiment studied the outer regions of the boundary layer. The facility and instrumentation allow for measurements of velocity and turbulence profiles at selected streamwise stations along a curved arc representing the approximate path of the free-stream streamline in the region of small streamwise pressure gradients. Velocity measurements are obtained with a three component LDA system which obtains mean velocity vectors deep in the viscous region, $y^+ = 2$, and profiles of the six Reynolds stresses down to $y^+ = 5$. At the beginning of the duct curvature, the boundary layer is two-dimensional, has a $Re_\theta = 1250$, and is about 5.5 cm thick. Preliminary profiles indicate that the freestream turning is approximately 19 ° at the end of curvature and there is 36° of yaw.

3. Future plans

Our ongoing work will concentrate on the three-dimensional boundary layer for the curved duct flow. However, further investigation of the swept step case is also called for. Velocity profiles will be obtained for various stations along the centerline of the duct. Dye slots have been incorporated into the test section design to allow for visualization of the streaky structure in the near-wall region of the skewed flow. Hydrogen bubbles will also be employed to mark flow in the near wall region.

REFERENCES

ANDERSON, S. D. & EATON, J. K. 1989 Reynolds stress development in a pressure

driven three-dimensional turbulent boundary layer. *J. Fluid Mech.* **202,** 263-294.

BARLOW, R. S. & JOHNSTON, J. P. 1988 Structure of a turbulent boundary layer on a concave surface. *J. Fluid Mech.* **191,** 137-176.

BRADSHAW, P. & PONTIKOS, N. S. 1985 Measurements in the turbulent boundary layer on an 'infinite' swept wing. *J. Fluid Mech.* **159,** 105-130.

DRIVER, D. M. & JOHNSTON, J. P. 1990 Experimental study of a shear-driven turbulent boundary layer flow with streamwise adverse pressure gradient. *Thermosciences Division, Stanford University, Stanford, CA, Report MD-57.*

EATON, J. K. 1991 Turbulence structure and heat transfer in three-dimensional boundary layers. *9th Sympo. on Energy Engr, Sci., Argonne Nat. Lab.*

JOHNSON, P. L. & JOHNSTON, J. P. 1989 The effects of grid-generated turbulence on flat and concave turbulent boundary layers. *Thermosciences Division, Stanford University, Stanford, CA, Report MD-53.*

JOHNSTON, J. P. 1970 Measurements in a three-dimensional boundary layer induced by a swept, forward-facing step. *J. Fluid Mech.* **42,** 823-844.

JOHNSTON, J. P. 1976 Experimental studies in three-dimensional turbulent boundary layers. *Thermosciences Division, Stanford University, Stanford, CA, Report MD-34.*

FLACK, K. A. & JOHNSTON, J. P. 1993 Experimental study of a detaching three-dimensional boundary layer. *International Conference on Near-Wall Turbulent Flows, Tempe, AZ.*

LITTELL, H. S. & EATON, J. K. 1991 An experimental investigation of the three-dimensional boundary layer on a rotating disk. *Thermosciences Division, Stanford University, Stanford, CA, Report MD-60.*

MOIN, P., SHIH, T. H., DRIVER, D. M. & MANSOUR, N. N. 1990 Direct numerical simulation of a three-dimensional turbulent boundary layer. *Physics of Fluids.* **2,** 1846-1853.

ROBINSON, S. K. 1991 Coherent motions in the turbulent boundary layer. *Annual Rev. Fluid Mech.* **23,** 601-639.

SCHWARZ, W. R. & BRADSHAW, P. 1993 Measurements on a pressure-driven three-dimensional turbulent boundary layer during development and decay. *AIAA 31st Aerospace Sciences Meeting, Reno, NV, Paper 93-0543.*

SENDSTAD, O. & MOIN, P. 1991 Numerical study of a three-dimensional boundary layer. *Workshop on Turbulence Structure and Control, AFOSR & Ohio State U., Columbus, OH.*

SENDSTAD, O. & MOIN, P. 1991 On the mechanics of three-dimensional turbulent boundary layers. *8th Sympo. on Turbulent Shear Flows, Munich, Germany.*

SHIZAWA, T. & EATON, J. K. 1990 Mean flow development of a longitudinal vortex embedded in an attached, three-dimensional turbulent boundary layer. *Intl. Sympo. on Engineering Turbulence Modelling and Measurements, Dubrovnik.*

SHIZAWA, T. & EATON, J. K. 1992 Turbulence measurements for a longitudinal vortex interacting with a three-dimensional turbulent boundary layer. *AIAA J.* **30,** 1180-1181.

SPALART, P. R. 1989 Theoretical and numerical study of a three-dimensional turbulent boundary layer. *J. Fluid Mech.* **205,** 319-340.

Center for Turbulence Research
Annual Research Briefs 1992

S26-34

325

N94-12310

The three-dimensional evolution of a plane wake

By H. Maekawa,[1] R. D. Moser[2] AND N. N. Mansour[2]

1. Introduction

In the past three decades, linear stability analysis has led to a comprehensive understanding of the linear stages of transition in plane wakes. Our understanding of the nonlinear and turbulent stages is less developed. Nonlinear theory developed by Papageorgiou & Smith (1988) was used to study the long-wavelength regime in wakes. The nonlinear and turbulent stages have been investigated experimentally, and few numerical studies have examined the early nonlinear stages of forced wakes.

Experimental studies of the wake have been carried out extensively by Sato & Kuriki (1961), Sato & Onda (1970), Sato & Saito (1975, 1978), and Gharib & Williams-Stuber (1989). Sato & Onda (1970) reported that the wake responds differently under different kinds of forced disturbances. Gharib & Williams-Stuber (1989) investigated the enhancement and cancellation of perturbations in a plane wake by the strip heater technique. They showed that the mean velocity profile adjusts itself to become more receptive to the forced frequency.

In their numerical study, Maekawa, Mansour & Buell (1992, hereafter referred to as MMB), simulated spatially developing plane wakes with inlet forcing using a single frequency (fundamental mode), a fundamental mode with its subharmonics and random perturbations. They found that phase jitter around the fundamental frequency plays a critical role in generating vortices of random shape and spacing. They also observed pairings and doublets in the wake. These observations were similar to those reported by Comte, Lesieur & Chollet (1989) and by Aref & Siggia (1981) for temporally developing layers. Furthermore, MMB found that infinitesimal random disturbances generate clear alternate-signed vortex streets due to selective amplification of the fundamental mode.

The formation of three-dimensional structures and turbulent breakdown are not as well understood. Chen, Cantwell & Mansour (1990) showed that the phase between a two-dimensional fundamental mode and oblique modes controls the formation of three-dimensional structures in plane wakes. Depending on the phase, loop-like structures were observed. These structures were similar to the flow visualization experiments by Breidenthal (1980), Meiburg & Lasheras (1988), Antonia, Brown & Bisset (1987), and Perry, Lim & Chong(1980). However, a detailed understanding of the underlying mechanism that initiates three-dimensional breakdown in wakes and the resultant structure is still missing.

In what follows, the evolution of three dimensional disturbances in a incompressible wake is investigated using direct numerical simulations. The instantaneous three-dimensional structures and corresponding statistics are presented.

1 University of Electro-Communications, Chofu, Tokyo 182

2 NASA Ames Research Center, 202A-1, Moffett Field, California 94035

2. Preliminaries

The time-developing mixing layer code used by Rogers & Moser (1992) was modified to accommodate wake profiles. The cases described in this study are initialized with controlled initial conditions. We consider temporally evolving layers where the flow is taken to be periodic in x- and z- (streamwise and spanwise) directions. The cross-stream direction, y, is taken to be doubly infinite with boundary conditions applied at $x = \pm\infty$. The length of the computational domain in the streamwise and spanwise directions, L_x and L_z, is set to be integer multiples of the perturbation wavelength, Thus, in general, $L_x = n\lambda_x$ and $L_z = m\lambda_z$. n and m are one or two for all cases reported here. The Reynolds number defined by the half-width and the deficit velocity of the wake is 300. As was done in MMB, the flow structure and various flow statistics were examined for a range of Reynolds numbers, $100 \leq Re \leq 600$. The observed variations with Re indicate that $Re = 300$ is large enough to eliminate low-Reynolds number effects.

2.1 The governing equations and numerical considerations

The simulations reported here were performed by solving the vorticity equation derived from the incompressible Navier-Stokes equations:

$$\frac{\partial \omega}{\partial t} + \nabla \times (\omega \times U) = \frac{1}{Re_0} \nabla^2 \omega, \tag{1}$$

where $Re_0 = U_0 b_{1/2}/\nu$ (ν is the kinematic viscosity) is the Reynolds number, $b_{1/2}$ is the initial half-width of the wake, and U_0 is the centerline deficit velocity. All quantities are non-dimensionalized by the appropriate characteristics scale, U_0 and $b_{1/2}$.

The spectral Galerkin method described by Spalart, Moser & Rogers (1991) was used for spatial discretization. The equations were advanced in time using a compact third-order Runge-Kutta scheme. A typical three-dimensional simulation ($n = 1, m = 1$) required $48 \times 64 \times 48$ Fourier/Jacobi modes.

2.2 Specification of initial conditions

The initial mean velocity used for all the simulations reported here is of the form

$$\overline{U} = \exp\left(-\ln(2)\left(\frac{y}{b_{1/2}}\right)^2\right) \tag{2}$$

which has a half width of $b_{1/2}$. In addition to the mean flow, simple perturbations are included in the initial conditions.

To specify the initial conditions and facilitate discussion through this paper, it is necessary to refer to specific wavenumbers; they will be referred to in ordered pairs

$$(\alpha, \beta) = \left(\frac{k_x \lambda_x}{2\pi}, \frac{k_z \lambda_z}{2\pi}\right) \tag{3}$$

where λ_x and λ_z are the x and z wavelengths from linear stability theory, k_x and k_z are corresponding wavenumbers. The fundamental modes discussed here have α and/or β equal to one. The amplitude $A_{\alpha\beta}$ of a Fourier mode (α, β) is defined to be the square root of the integrated (in y) energy in that mode, as described in Rogers & Moser (1991).

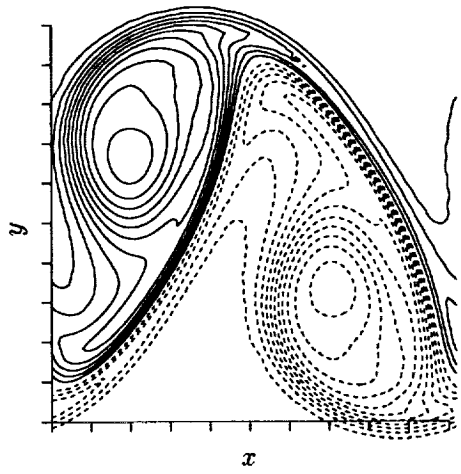

FIGURE 1. Spanwise vorticity structure of the two-dimensional wake (Case 2D-1) at the first maximum of A_{10} ($t = 48$). Contour increments are 0.05 and tic marks are at $b_{1/2}$ intervals.

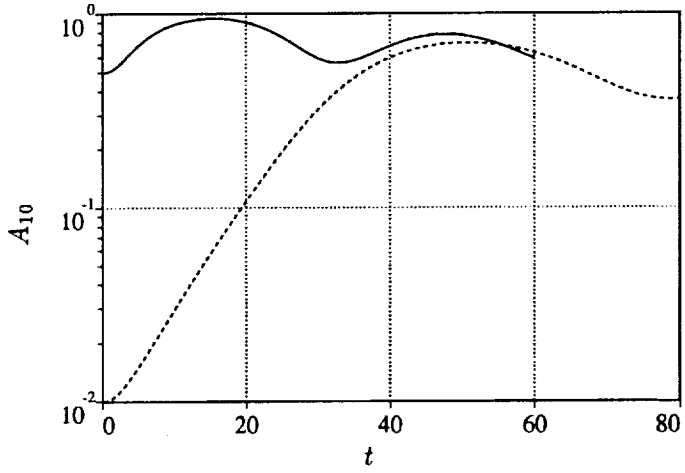

FIGURE 2. Time development of the two-dimensional fundamental mode amplitude for —— Case 2D-2 (high initial amplitude) and ---- 2D-1 (low amplitude).

3. Accomplishments

3.1 Two-dimensional simulations

To facilitate discussion of the three-dimensional evolution of the wake, we start by briefly reexamining the behavior of two-dimensional wakes. The spatially developing simulations of MMB showed that the growth of the fundamental mode is responsible for the formation of the vortex street in wakes. We consider three different initial conditions for the current two-dimensional simulations. Case 2D-1 starts with a

single fundamental mode with small amplitude ($A_{10} = 0.01$), Case 2D-2 starts with a single fundamental mode with large amplitude ($A_{10} = 0.5$), and Case 2D-3 starts with a fundamental mode and its first subharmonic with large amplitudes ($A_{\frac{1}{2}0} = A_{10} = 0.5$).

As in the spatially developing case, the amplitude of the fundamental grows exponentially, then saturates. Contours of spanwise vorticity at the time when the amplitude of the fundamental disturbance, A_{10}, reaches its maximum are shown in Figure 1 for Case 2D-1. The vortices evident in this figure have an oblong or elliptical shape, with the major axis roughly vertical. Successive snapshots show that the structures rotate by 90° so that the major axis is horizontal, consistent with the observations of MMB. If we define the rollup time t_r to be at the first maximum of the fundamental disturbance amplitude, we find for this case, $t_r = 48$.

When a larger initial amplitude is used (Case 2D-2), the fundamental mode saturates sooner ($t_r = 18$). After saturation, the mode loses energy at a much faster rate than in Case 2D-1, then starts growing again, and a second maximum appears (see Figure 2). The orientation of the major axis of the vortical structure at the first maximum of A_{10} ($t_r = 18$) is similar to the low-amplitude case. But as the structure rotates its major axis toward the horizontal, a tail of weak vorticity is formed (see Figure 3 at $t = 32$). Successive snapshots show that the vortices continue to rotate, becoming vertical again when A_{10} reaches a second maximum. This is similar to the observations by MMB of active structures at higher Reynolds number.

In Case 2D-3, we observe (see Figure 4) pairing of negative sign vorticity (in the lower portion of the layer) and shredding of positive sign vorticity (in the upper portion). The development time of the subharmonic is slow relative to the fundamental, and pairing occurs around the time when the amplitude of the subharmonic reaches its maximum.

3.2 Three-dimensional wake

To study the sensitivity of the two-dimensional wake to initial (or inlet) three-dimensional disturbances, five cases were studied: two cases (Case 3D-1, and Case 3D-1-1) where a two-dimensional mode plus background random noise of different amplitudes are used for initial conditions, and three cases with a two-dimensional mode and a pair of oblique modes (Case 3D-2-1, Case 3D-2-2 and Case 3D-2-3) of different amplitudes for initial disturbances. The relative phase between the two-dimensional mode and the oblique modes was kept the same at $\pi/4$ for all cases.

The intent in Case 3D-1 is to mimic the experiment of Sato & Onda (1970) where a fundamental mode is forced, but, as in all experiments, background noise exists. Figure 5(a) shows the evolution of A_{10} for Case 2D-1 and 3D-1. Clearly the weak background noise in this case has little effect on the evolution of the two-dimensional layer. The structure that dominates in this case is the two-dimensional double roller. In this case, the fastest growing three-dimensional modes are those whose wave-numbers are closest to that of the two-dimensional fundamental. Large amplitude disturbances were used in Case 3D-1-1 ($A_{10} = 0.1$, average amplitude of three-dimensional modes of 0.025). In this case, a band of wave numbers around the fundamental are enhanced after the roll-up. But, the energy in the subharmonic

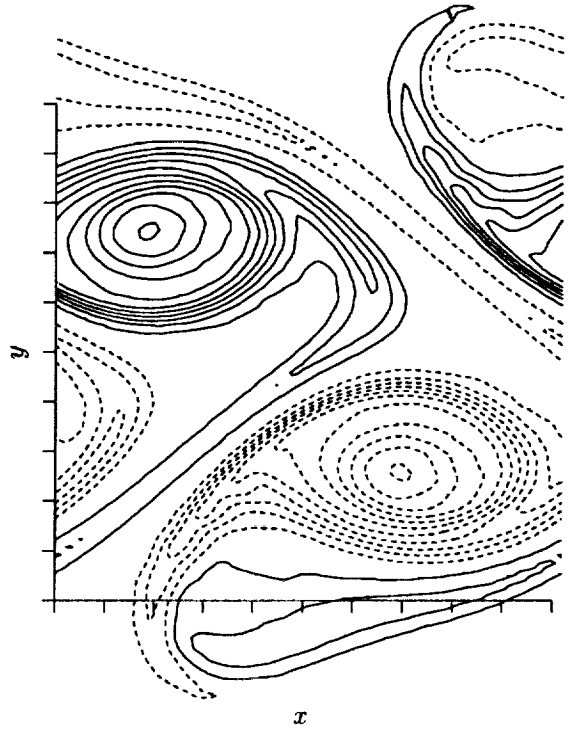

FIGURE 3. Spanwise vorticity in Case 2D-2 at $t = 32$; contour increments are 0.09 and tic marks are at $b_{1/2}$ intervals.

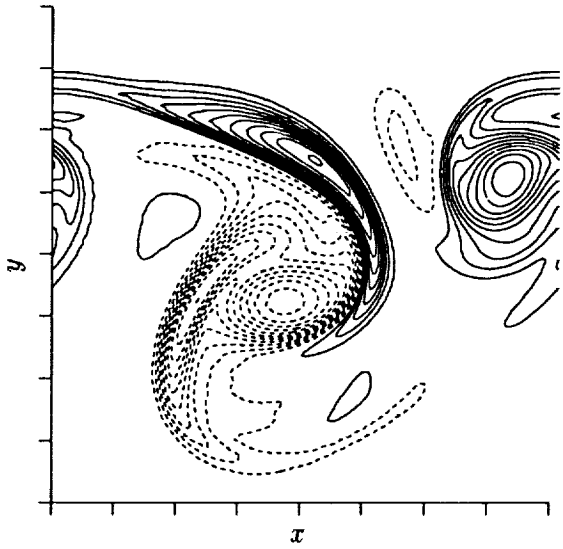

FIGURE 4. Spanwise vorticity in Case 2D-3 during pairing/tearing. Contour increments are 0.05 and tic marks are at $2 \times b_{1/2}$ intervals.

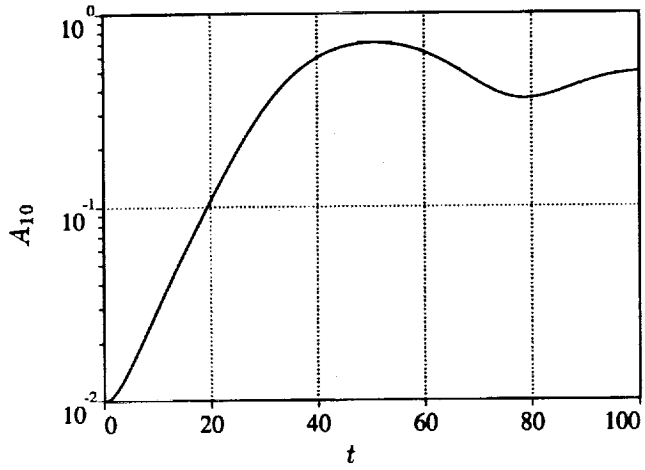

FIGURE 5. Evolution of the two-dimensional fundamental mode amplitude in —— 3D-1 and ---- 2D-1 (plots on top of 3D-1 case).

mode decreases after the rollup, suggesting that pairing in the wake is not as natural as in the mixing layer. But as seen in our two-dimensional simulations, it will occur when forced. The vortex structure in case 3D-1-1 is again dominated by the two-dimensional vortices.

The results of the previous two cases suggest that low-wavenumber oblique modes are not amplified during the rollup of the fundamental structure in the wake. We thus use a relatively small spanwise wavelength ($\lambda_z = 0.6\lambda_x$) for the forced oblique modes as in Rogers & Moser (1992). The three oblique cases; Case 3D-2-1, 3D-2-2 and 3D-2-3 have initial amplitudes such that $A_{10} > A_{11}$, $A_{10} < A_{11}$, and $A_{10} = A_{11}$ respectively.

In Case 3D-2-1, the evolutions of the mode amplitudes indicate that the two-dimensional mode grows, saturates, and decreases while the energy in the oblique modes reaches a first peak at the same time as the fundamental ($t = 14$) but later continues to increase until a second maximum is reached at $t = 30$. At this time, the oblique mode amplitude is at almost the same level as the fundamental. Constant spanwise vorticity surfaces for this case at $t = 14$ and $t = 30$ are shown in Figure 6. In Figure 6(a), the core rolls are apparent but are surrounded by 'wisps' of vorticity that form hoop-like structures. Later ($t = 30$) after the oblique modes grow (at $t = 30$) we find that the strong spanwise vorticity is concentrated in compact regions (Figure 6(b)). At this time, the streamwise and the cross-stream components of the vorticity dominate the large scale structures. The counter-rotating vortices shown in Figure 6(c) become the dominant feature of the flow. Of the three vorticity components, ω_y is largest in magnitude, while ω_z is smallest. The vortex structures are inclined at 40 to 50 degrees with respect to the streamwise direction. These streamwise vortex pairs are reminiscent of the rib vortices in the plane mixing layer.

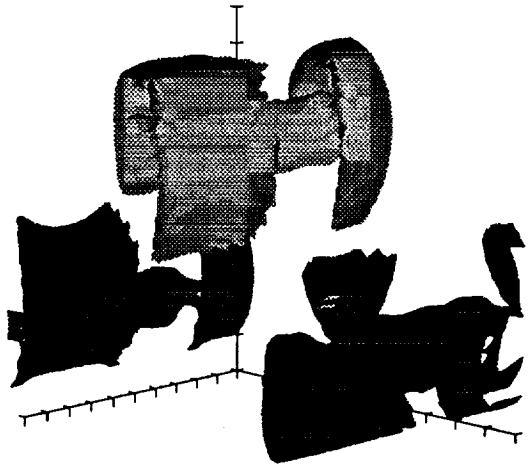

FIGURE 6(a). Three-dimensional structure of spanwise vorticity in Case 3D-2-1 at $t = 14$: Surfaces represent 50% of peak value (± 2.6), and tic marks are $b_{1/2}$ intervals.

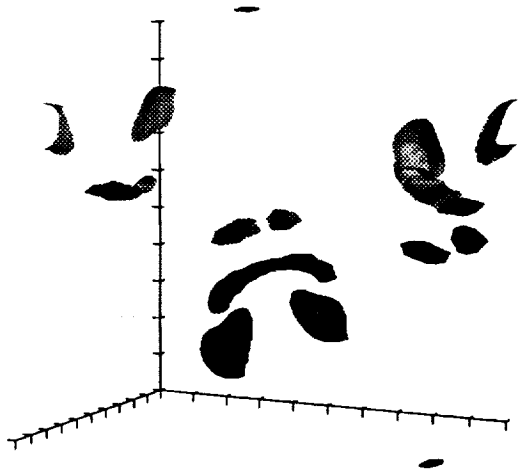

FIGURE 6(b). Three-dimensional structure of spanwise vorticity in Case 3D-2-1 at $t = 30$: Surfaces represent 50% of peak value (± 1.6), and tic marks are $b_{1/2}$ intervals.

When the oblique modes are initially dominant (Case 3D-2-2), it was found that they grow rapidly and suppress the growth of the two-dimensional fundamental mode. Since the oblique modes are larger than the two-dimensional mode, the spanwise vorticity structure is not observed in the wake. When all the modes have the same amplitude (Case 3D-2-3), the energy in the modes indicates that the oblique modes and the fundamental mode grow together and that the oblique mode saturates first, then the fundamental modes saturate.

FIGURE 6(c). Three-dimensional structure of streamwise vorticity in Case 3D-2-1 at $t = 30$: Surfaces represent 50% of peak value (± 1.9), and tic marks are $b_{1/2}$ intervals.

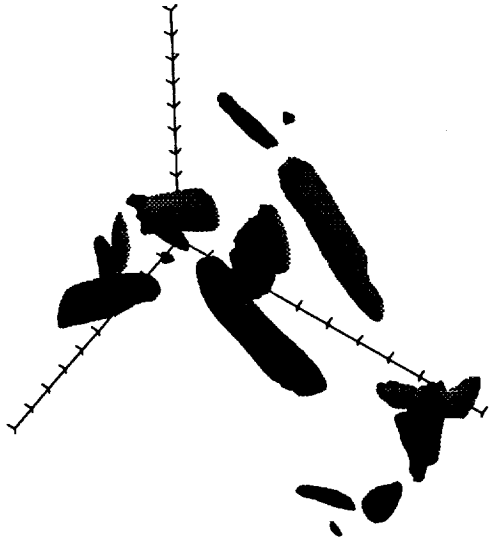

FIGURE 6(d). Three-dimensional structure of ω_y in Case 3D-2-1 at $t = 30$: Surfaces represent 50% of peak value (± 2.6), and tic marks are $b_{1/2}$ intervals.

4. Conclusions

Direct numerical simulations have been used to study the three-dimensional evolution of a plane wake. The flow has been analyzed by visualizing the vortical structures using vorticity contours and by tracking the modal energy in time. The two-dimensional features are similar to the results obtained for a two-dimensional spatially developing wake (MMB).

The growth of fundamental mode generates characteristic alternating sign vortices in the wake. When a two-dimensional fundamental mode is forced with high amplitude, vortical structures with 'wisps' around the roller are generated. When the wake is forced with a fundamental and a subharmonic asymmetric pairing and shredding are observed.

When weak three-dimensional random disturbances are imposed in addition to a two-dimensional fundamental mode, we find that the two-dimensional rollers appear to be the dominant features of the wake. Analysis of the energy contained in each mode reveals that three-dimensional modes with wavenumber close to that of the two-dimensional fundamental mode grow after saturation of the fundamental mode. In contrast, the energy in the low wavenumbers modes decreases.

When the wake is forced with oblique modes of various amplitudes, we find that at large amplitudes the growth of the oblique mode leads to the breakdown of the alternate-sign vortex structures in the wake, and counter-rotating streamwise vortical structures are generated after the breakdown. These streamwise structures are inclined at 40 to 50 degrees with respect to the streamwise direction. When the amplitude of the initial oblique modes is higher than that of the fundamental, the growth of the fundamental mode is suppressed, and no spanwise coherent structures were found in this case.

Acknowledgements

The first author (H. M.) wishes to acknowledge the hospitality of the Center for Turbulence Research during the course of this work.

REFERENCES

ANTONIA, R., BROWNE, W. & BISSET, D. 1987 A description of the organized motion in the turbulent far wake of a cylinder at low Reynolds number. *J. Fluid Mech.* **184,** 423.

AREF, H. & SIGGIA, E. D. 1981 Evolution and breakdown of a vortex street in two dimensions. *J. Fluid Mech.* **109,** 435.

CHEN, J. H., CANTWELL, B. J. & MANSOUR, N. N. 1990 The effect of Mach number on the stability of a plane supersonic wake. *Phys. Fluids, A.* **2,** -(6), 984.

COMTE, P., LESIEUR, M.& CHOLLET, J. P. 1989 Numerical simulations of turbulent plane shear layers. *Turbulent Shear Flows.* **6,** 360-380.

GHARIB, M. & WILLIAMS-STUBER, K. 1989 Experiments on the forced wake of an airfoil. *J. Fluid Mech.* **208,** 225-255.

MAEKAWA, H., MANSOUR, N. N. & BUELL, J. C. 1992 Instability mode interactions in a spatially developing plane wake. *J. Fluid Mech.* **235,** 223-254.

MEIBURG, E .& LASHERAS, J. 1988 Experimental and numerical investigation of the three-dimensional transition in plane wakes. *J. Fluid Mech.* **190,** 1.

MOSER, R. D. & ROGERS, M. M. 1992 The three-dimensional evolution of a plane mixing layer: paring and transition to turbulence. *submitted to J. Fluid Mech.*

PAPAGEORGIOU, D. T. & SMITH, F. T. 1989 Nonlinear instability of the wake behind a flat plate place parallel to a uniform stream. *Proc. R. Soc. Lond. A.* **419,** 1-29.

PERRY, A., LIM, T. & CHONG, J. 1980 The instantaneous velocity fields of coherent structures on coflowing jets and wakes. *J. Fluid Mech.* **101,** 243.

PIERREHUMBERT, R. T. & WIDNALL, S. E. 1982 The two- and three-dimensional instabilities of a spatially periodic shear layer.. *J. Fluid Mech.* **114,** 59-82.

ROGERS, M. M. & MOSER, R. D. 1992 The three-dimensional evolution of a plane mixing layers: the Kelvin-Helmholtz rollup. *J. Fluid Mech.* **243,** 183-226.

SPALART, P. R., MOSER, R. D. & ROGERS, M. M. 1991 Spectral methods for the Navier-Stokes equations with one finite and two periodic directions. *J. Comput. Phys.* **96,** 297-324.

SATO, H. & KURIKI, K. 1961 The mechanism of transition in the wake of a thin flat plate placed parallel to a uniform flow. *J. Fluid Mech.* **11,** 321-352.

SATO, H. & ONDA, Y. 1970 Detailed measurements in the transition region of a two-dimensional wake. *Inst. Space & Aero. Sci., Univ. Tokyo Rep.* **453,** 317-377.

SATO, H. & SAITO, H. 1975 Fine-structure of energy spectra of velocity fluctuations in the transition region of a two-dimensional wake. *J. Fluid Mech.* **67,** 539-559.

SATO, H. & SAITO, H. 1978 Artificial control of the laminar turbulent transition of a two-dimensional wake by external sound. *J. Fluid Mech.* **84,** 657-672.

Mixing in a stratified shear flow: energetics and sampling

By G. N. Ivey[1], J. R. Koseff[2], D. A. Briggs[2] AND J. H. Ferziger[2]

Direct numerical simulations of the time evolution of homogeneous stably stratified shear flows have been performed by Holt (1990), Holt *et al.* (1992), and Itsweire *et al.* (1992) for Richardson numbers from 0 to 1 and for Prandtl numbers between 0.1 and 2. The results indicate that mixing efficiency R_f varies with turbulent Froude number in a manner consistent with laboratory experiments performed with Prandtl numbers of 0.7 and 700. However, unlike the laboratory results, for a particular Froude number, the simulations do not show a clear dependence on the magnitude of R_f on Pr. The observed maximum value of R_f is 0.25. When averaged over vertical length scales of an order of magnitude greater than either the overturning or Ozmidov scales of the flow, the simulations indicate that the dissipation rate ϵ is only weakly lognormally distributed with an intermittency of about 0.01 whereas estimated values in the ocean (Baker and Gibson (1987)) are 3 to 7.

1. Introduction

The specification of the buoyancy flux in a fluid with a stable density gradient and subjected to forcing by either mean shear or a mechanical means of generating turbulent kinetic energy is crucial to the understanding of mixing processes in a wide variety of geophysical applications. Quantifying the rate of vertical mixing in the ocean, for example, is central not only to parameterizing vertical heat and salt fluxes, but also those of passive tracers such as pollutants and chemicals. Thus, predicting the mixing efficiency or flux Richardson number R_f is of central importance in turbulent mixing in density stratified flows. Ivey and Imberger (1991) (hereafter II) introduced a generalized definition of R_f based on the full turbulent kinetic energy equation and demonstrated that available laboratory measurements had peak values of $R_f = 0.20$ for fluids with Prandtl number of 700 and 0.15 for fluids with Prandtl number of 0.7. In the laboratory work, turbulence was generated with grids and, in the case of Rohr *et al.* (1988), by both grids and a mean shear. This work has been extended by the direct numerical simulation work of Holt (1990), Holt *et al.* (1992), and Itsweire *et al.* (1992), who numerically studied the temporal evolution of homogeneous turbulence subjected to a constant mean velocity and density gradients using the pseudo-spectral method of Rogallo (1981). The Boussinesq form of the Navier Stokes equations were solved for the three dimensional velocity and density fields on a $128 \times 128 \times 128$ grid. The velocity fields

1 Centre for Water Research, University of Western Australia, Nedlands, Western Australia
2 Stanford University

were initially isotropic with Reynolds numbers based on the integral scale and the turbulent kinetic energy ranging from 52 to 104, Richardson numbers ranging from 0.058 to 1.0, and Prandtl numbers of either 1 or 2. In the oceanic case, the density stratification is predominantly due to vertical temperature gradients. Therefore, in order to investigate the differences in the behavior of R_f with Pr observed by II, we have extended the earlier work of Holt *et al.* (1992) by performing additional simulations at values of Ri from 0.075 to 1.0 with Prandtl numbers as low as 0.1; these results are described in Section 3 below.

Oceanic turbulence is intermittent in character, and there exists considerable controversy about how to correctly sample the flow to determine the volume averaged dissipation (eg. Baker and Gibson (1987)). We examine this question by averaging over sub-sections of our $128 \times 128 \times 128$ domain and calculating the intermittency, defined as the variance of the logarithm of a quantity: the results are summarized in Section 4. Finally, Section 5 summarizes our conclusions.

2. Dynamics of mixing in stratified flows

The full turbulent kinetic energy equation can be written as:

$$-\frac{\partial}{\partial t}(\frac{\overline{q^2}}{2}) - \frac{\partial}{\partial x_j}(\frac{\overline{u_j q^2}}{2}) - \frac{\partial}{\partial x_j}(\frac{1}{\rho_o}\overline{u_j p}) - \overline{u_i u_j}\frac{\partial \overline{U_i}}{\partial x_j} = \frac{g}{\rho_o}\overline{\rho u_3} + \epsilon = B + \epsilon \quad (1)$$

where $\overline{q^2} = \overline{u_1^2 + u_2^2 + u_3^2}$ is twice the turbulent kinetic energy, ρ_o is the background density, $\epsilon = \nu\overline{\frac{\partial u_i}{\partial x_j}\frac{\partial u_i}{\partial x_j}}$ is the rate of dissipation of turbulent kinetic energy, and velocity component u_3 is in the direction of the gravity vector. For homogeneous turbulence at steady state, (1) can be written as $P = B + \epsilon$ where P is the production of turbulent kinetic energy (the last term on the left hand side of (1)) Then, II defined

$$R_f = \frac{B}{P} = \frac{1}{1 + (\epsilon/B)} \quad (2)$$

and also introduced the concept of a turbulent Froude number associated with the energy bearing eddies defined by

$$Fr_T = \frac{(\overline{q^2})^{1/2}}{NL_c} = (\frac{L_o}{L_c})^{2/3} \quad (3)$$

where L_c is the scale of the most energetic overturns, $L_o = (\epsilon/N^3)^{1/2}$ represents the Ozmidov scale, and N is the buoyancy frequency characterizing the stable background stratification. An alternate form of (2) is

$$R_f = \frac{1}{1 + Fr_T^2/R_{\rho w}} \quad (4)$$

where $R_{\rho w}$ is the correlation coefficient between the density and vertical velocity fluctuations. II found the available laboratory measurements were in accord with

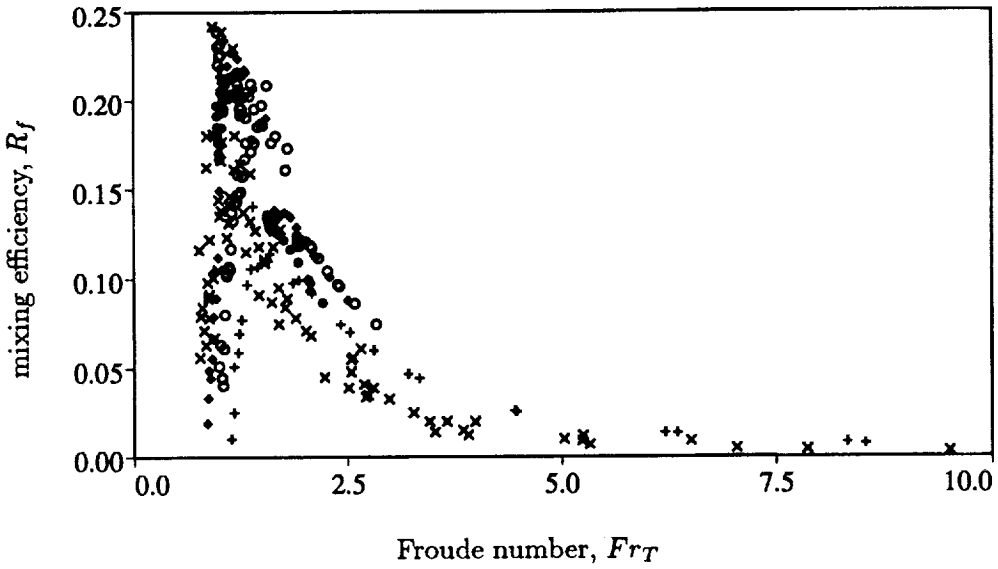

FIGURE 1. R_f as a function of $Fr_T = (L_o/L_e)^{2/3}$ for simulations with $Pr = 0.1$ (○), $Pr = 0.5$ (◇) and $Pr = 2.0$ (•). Experimental data is provided by Stillinger *et al.*, Itsweire *et al.*, and Rohr *et al.* for $Pr = 700$ (×) and Lienhard and Van Atta for $Pr = 0.7$ (+).

the simple predictions in (4). Additionally, II introduced two further dimensionless numbers, the turbulent Reynolds number Re_T and small scale Froude number Fr_γ defined by

$$Re_T = \frac{uL_c}{\nu} = (\frac{L_c}{L_k})^{4/3} \tag{5}$$

and

$$Fr_\gamma = (\frac{\epsilon}{\nu N^2})^{1/2} = (\frac{L_o}{L_k})^{2/3}, \tag{6}$$

where $\epsilon/\nu N^2$ is a measure of the range of overturning scales when buoyancy strongly affects the flow and $L_k = (\nu^3/\epsilon)^{1/4}$ represents the Kolmogorov scale. The dimensionless numbers (3), (5), and (6) are related by

$$Fr_T = (\frac{1}{Re_T})^{1/2} Fr_\gamma. \tag{7}$$

One final length scale is used in discussing the numerical results below. The Ellison scale L_e is defined as

$$L_e = -\frac{(\overline{\rho}^2)^{1/2}}{\frac{\partial \overline{\rho}}{\partial z}} \tag{8}$$

where $\overline{\rho}(z)$ is mean density. As Itsweire *et al.* (1992) show, except at very high Richardson numbers (based on mean shear and density gradient), L_c and L_e are the same scale to within a constant of $O(1)$.

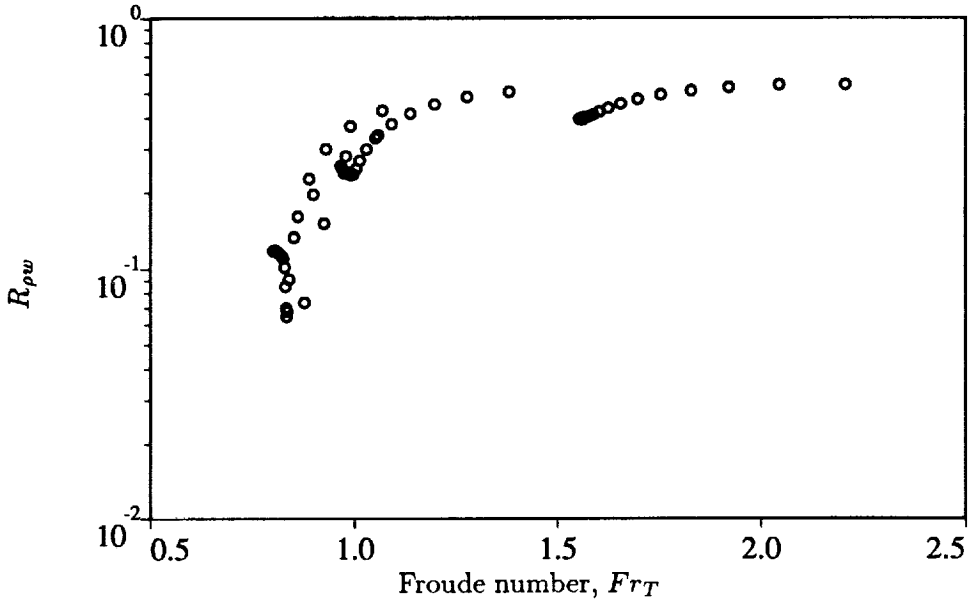

FIGURE 2. $R_{\rho w}$ as a function of Fr_T for $Pr = 2$.

3. Mixing efficiency

All results in this section were computed by ensemble-averaging data over the entire computational domain at each time step. In order to eliminate transient behavior associated with the initial conditions, only the data for $St \geq 2$ are considered, where the shear time, St, is a dimensionless time with $S = \partial\overline{U}/\partial z$. R_f was computed according to the definition in (2), as were the dimensionless numbers Fr_T, Re_T, and Fr_γ from their respective definitions in equations (3), (5), and (6). Figure 1 summarizes the results for the simulations with $Pr = 0.1$, 0.5, and 2. Mixing efficiency, R_f, is plotted against Fr_T to facilitate direct comparison with the laboratory observations (presented by II) which are also shown in Figure 1. The numerical results show the same general distribution as the laboratory measurements. As Fr_T becomes very large, the overturning scale is small compared to the Ozmidov scale, the mixing becomes inefficient because there is much more turbulent kinetic energy than necessary to mix the scalar gradient, and R_f rapidly decreases. Similarly, for very small values of Fr_T when buoyancy effects dominate and reduce the mixing, R_f again sharply decreases. At an intermediate value of Fr_T in the range of 1 to 1.5, the mixing is optimal with peak values of $R_f = 0.25$.

The behavior of $R_{\rho w}$ as a function of Fr_T given in Figure 2 for $Pr = 2$ (as an example) shows a similar trend. For $Fr_T > 1$, the correlation coefficient $R_{\rho w}$ tends to a constant value of about 0.6; hence, from Equation (4), R_f will rapidly decrease with increasing Fr_T. Conversely, for $Fr_T < 1$, $R_{\rho w}$ decreases rapidly as the density and velocity fluctuations become uncorrelated, and R_f tends to zero as a consequence of the denominator in (4) being much greater than unity.

While the overall behavior in the numerical and laboratory results is the same

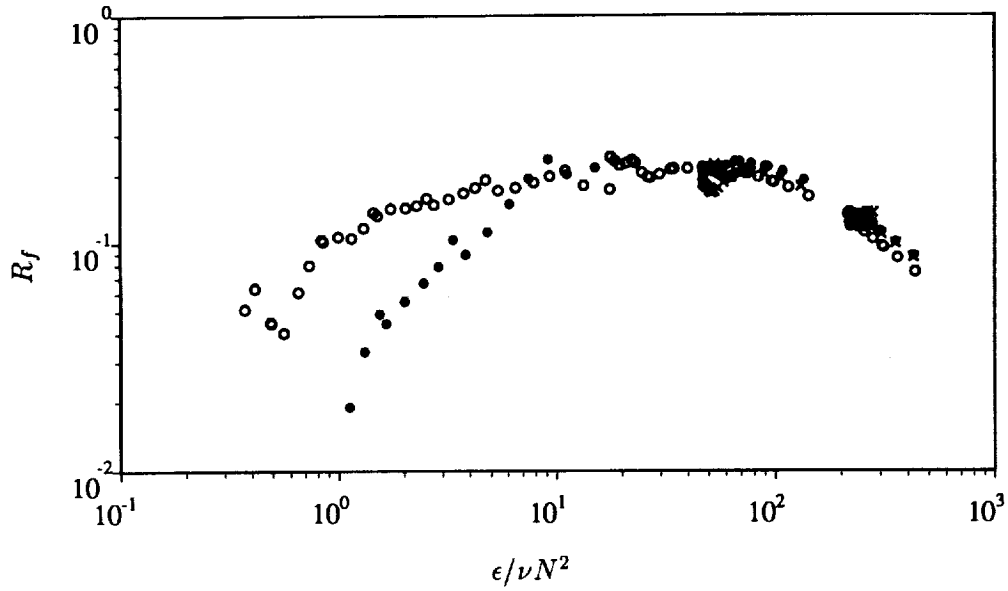

FIGURE 3. R_f as a function of $\epsilon/\nu N^2$ for simulations with $Pr = 0.1$ (○), 0.5 (•), 2.0 (×).

in Figure 1, there are differences in detail. Unlike the laboratory data, for a given Fr_T, the numerically derived values of R_f are independent of Prandtl number and do not show the experimental tendency of R_f to increase with Pr. Nevertheless, recalling that the laboratory data are derived from time-averaged statistics in a steady mean flow whereas the numerical value are ensemble-averaged values in an evolving flow, the differences are remarkably small. The implication is that the peak mixing efficiency is 0.25 for Fr_T 1 to 1.5, irrespective of Prandtl number.

In field measurements of oceanic turbulence, the overturning scales L_ϵ or L_c are not usually measured while ϵ invariably is. Substituting (7) into (4) yields the more practical form

$$R_f = \frac{1}{1 + \beta(\epsilon/\nu N^2)} \tag{9}$$

where $\beta = R_{\rho w}^{-1} Re_T$.

In Figure 3, we re-plot the results from the simulations against $\epsilon/\nu N^2 (= Fr_\gamma^2)$. The minimum dissipation needed to sustain a vertical buoyancy flux, and hence positive R_f, is clearly a strong function of Pr. For $Pr = 0.1$, $\epsilon/\nu N^2$ may be as little as 0.4 and still sustain a positive buoyancy flux ,whereas for $Pr = 2$, the minimum $\epsilon/\nu N^2$ for a positive buoyancy flux is about 20. The other interesting feature of Figure 3 is that R_f becomes independent of Pr for large $\epsilon/\nu N^2$. For $\epsilon/\nu N^2 \gg 10$, a best fit is $\beta = (\epsilon/\nu N^2)^{-0.6}$, hence (9) simplifies to

$$R_f = \frac{1}{1 + (\epsilon/\nu N^2)^{0.4}} \tag{10}$$

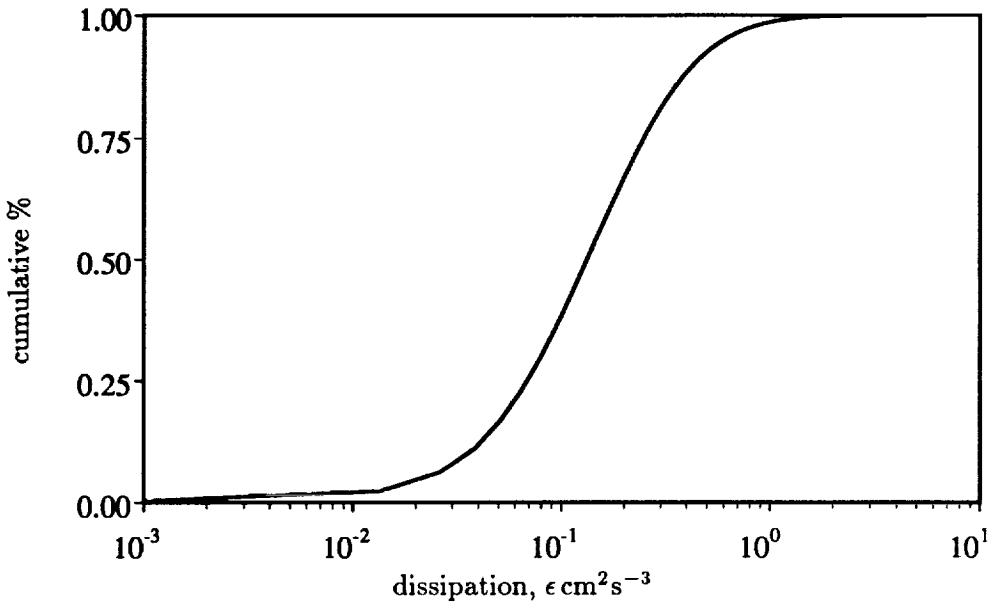

FIGURE 4. Lognormal plot of dissipation estimates with no averaging ($Ri = .075$, $Pr = 2$, $St = 6$).

and using (2)

$$B = \epsilon^{0.6}(\nu N^2)^{0.4} \tag{11}$$

which provides an approximate but simple means of computing buoyancy flux from the dissipation for relatively energetic flows.

4. Sampling turbulence in a stratified fluid

Turbulence measurements are made in the ocean with either vertically falling microstructure instruments or, less commonly, horizontally towed instruments. The buoyancy flux B is not directly measured but, as indicated above, dissipation estimates are made and then B is computed by estimating R_f as outlined in Section 3 (see also Itsweire *et al.* 1992). For falling probes, dissipation estimates are typically made by measuring two turbulent velocity components and computing total dissipation using models (see Itsweire *et al.* 1992). This procedure produces estimates of dissipation averaged over about 2 meters in the vertical, and these estimates are further averaged to characterize the dissipation on much larger scales such as the oceanic thermocline (for example see review of Gregg 1987). Gibson and Baker (1987) and Gibson (1991) have argued that dissipation in oceanic turbulence is lognormally distributed with an intermittency, σ^2, in the range of 3 to 7. Furthermore, they claim that, due to the large scales and the limited sampling, the dissipation is greatly undersampled. Given the large intermittency, Baker and Gibson maintain that to estimate of ϵ to within $\pm 10\%$ one would need to average the dissipation calculated from thousands of independent sampling profiles! Gurvich and Yaglom

(1967) (see also Yamazaki and Lueck (1990)) developed three criteria which must be satisfied in order for dissipation to be a lognormally distributed quantity in the ocean.

(i) The turbulence must be homogeneous,

(ii) the averaging scale, r, must be small compared to the domain scale, L, and

(iii) the averaging scale must be large compared to the Kolmogorov scale L_k.

Yamazaki and Lueck (1990) suggest that (iii) can be satisfied with r as low as $3L_k$, but in all oceanic datasets, there is uncertainty about meeting criterion (i) given the patchy nature of the turbulence away from regions of highly energetic forcing such as the near-surface region. We investigated the sampling question by analyzing the results from one typical simulation. In particular, we examined the numerical results corresponding to $Ri = 0.075$, $Pr = 2$ at $St = 6$. For this data set, $L = 25$ cm, the grid scale, $r = L/128$, is 0.195 cm, the ensemble-averaged dissipation is 0.213 $\mathrm{cm^2 s^{-3}}$, $L_k = 0.0465$ cm, $L_c = 2.68$ cm, and $L_e = 1.37$ cm. For the full data set of 128^3 points without averaging, all three criteria of Yamazaki and Lueck (1990) are met since $r = 4.2L_k$. The corresponding distribution of dissipation should, therefore, be lognormal, and in Figure 4 the strong lognormality of the data with $\sigma^2 \simeq .75$ is evident. However, for comparison with typical oceanic sampling, of greater interest are the consequences of averaging estimates in the vertical. We chose to examine the effect of averaging over the full depth of the computational domain (25 cm), which is equal to 18.2 L_e or 9.3 L_o. Even though we are averaging over the depth, we still have a statistically significant sample of 128^2 points. Note that we do not satisfy criterion (ii) because $r = L$.

Figure 5 shows the distribution of vertically averaged ϵ for four different Richardson numbers. The effect of averaging is quite dramatic and the value of σ^2 is reduced to 0.01 and becomes essentially independent of Ri. Thus, when averaged over vertical scales significantly greater than L_e or L_o, dissipation is only weakly lognormal with σ^2 less than the value of 3 to 7 suggested for the ocean. Using techniques developed in Baker and Gibson, this translates to about 4 to 8 required profiles to obtain an estimate of the mean value of ϵ within $\pm 10\%$.

In order to more fully explore the second criterion of Gurvich and Yaglom, we averaged the data in the vertical but over length scales r which were smaller than L, e.g. 16 points or about $2.5L_e$. The distribution of ϵ averaged over this scale is plotted in Figure 6 which shows that the data is indeed lognormal but with $\sigma^2 \simeq .1$, much smaller than the 3 - 7 obtained by Baker and Gibson (1987). Again, the implication is that, if the data are averaged over length scales comparable to the overturning scale, the intermittency will not be as high as that described by Baker and Gibson (1987). This implies that much fewer sampling profiles are necessary to obtain a reasonable estimate of ϵ. Finally, we should note that since oceanic samples are likely to be drawn from a domain with significant regions of minimal dissipation the homogeneity criteria may be the most difficult restriction to satisfy.

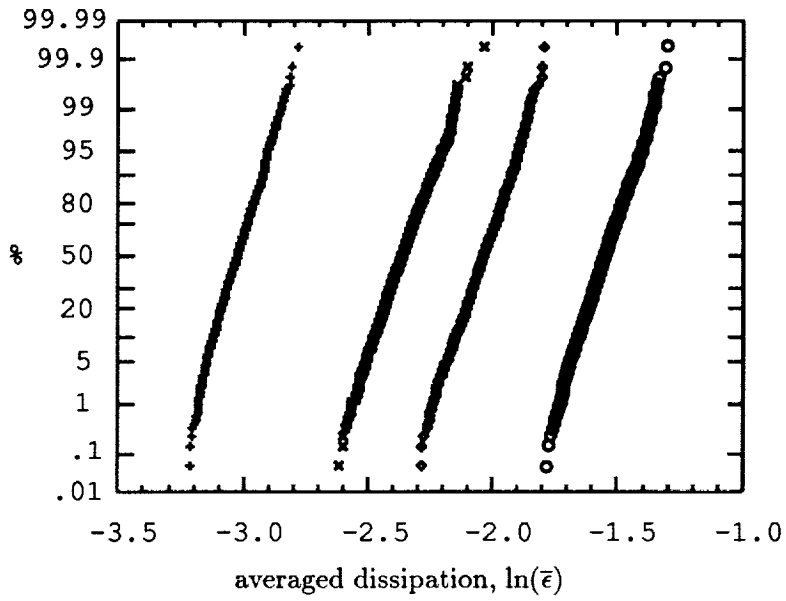

FIGURE 5. Lognormal probability plot of $\bar{\epsilon}$ for $Ri = 0.075$ ($\circ$), 0.21 ($\diamond$), 0.37 ($\times$) and 1.0 ($+$) with $Pr = 2.0, St = 6$.

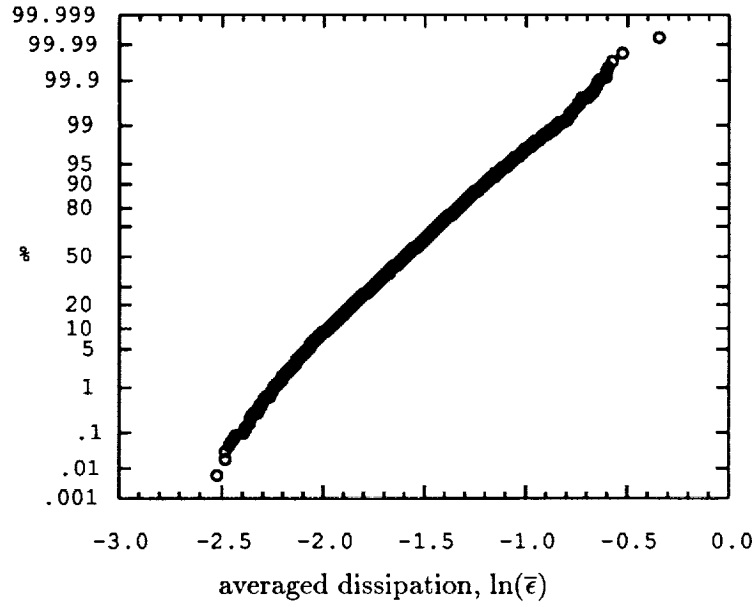

FIGURE 6. Lognormal probability plot of ln($\bar{\epsilon}$) with the averaging scale $r \simeq 2.5L_e$, $Ri = .075$.

5. Conclusions

Direct numerical simulations of homogeneous turbulence in stably stratified shear flows confirm the variation of flux Richardson number R_f with turbulent Froude number Fr_T and $\epsilon/\nu N^2$ observed in laboratory experiments. With R_f defined as the buoyancy flux divided by the production of turbulent kinetic energy, there appears to be no systematic dependence of R_f on Pr in the range of Pr from 0.1 to 2. This result is not consistent with the laboratory observations; however, the differences in R_f between the simulations and the experiments are small, and the data from all sources indicate that R_f has a peak of 0.25, independent of Pr. Subsampling of the computational domain of 128^3 points was investigated to examine the distribution of the dissipation. The results indicate that when dissipation is estimated by averaging over vertical scales of an order of magnitude greater than either the Ellison or Ozmidov scales, the distribution is very weakly lognormal with an intermittency, $\sigma^2 \simeq 0.01$. This value is considerably smaller than some estimates in the oceanic literature and suggests sampling restrictions may not be as severe as previously suggested provided the sampling and averaging are performed over domains where the turbulence is homogeneous.

Acknowledgements

The authors are very grateful to the CTR for making this work possible. JRK, DAB and JHF also wish to acknowledge the Office of Naval Research for their support of this work through grant number N00014-92-J-1611.

REFERENCES

BAKER, M. & GIBSON, C. G. 1987 Sampling turbulence in the stratified ocean: statistical consequences of strong intermittency. *J. Phys. Oceanogr.* **17,** 417-440.

GIBSON, C. H. 1991 *Turbulence and Stochastic Processes: Kolmogorov's ideas 50 years on*, Hunt, J. C., Phillips, O. M. & Williams, D (eds). The Royal Society, London.

GREGG, M. C. 1987 Diapycnal mixing in the thermocline: A review. *J. Geophys. Res.* **92,** 5249-5286.

GURVICH, A. S. & YAGLOM, A. M. 1967 Breakdown of eddies and probability distributions for small scale turbulence. *Phys. Fluids.* **10,** 59-65.

HOLT, S. E., KOSEFF, J. R. & FERZIGER, J. H. 1992 The evolution of turbulence in the presence of mean shear and stable stratification. *J. Fluid Mech.* **237,** 499-539.

LIENHARD, J. H. & VAN ATTA, C. W. 1990 The decay of turbulence in thermally stratified flow. *J. Fluid Mech.* **210,** 57-112.

ITSWEIRE, E. C., HELLAND, K. N. & VAN ATTA, C. W. 1986 The evolution of grid-generated turbulence in a stably stratified flow. *J. Fluid Mech.* **162,** 299-338.

ITSWEIRE, E. C., KOSEFF, J. R., BRIGGS, D. A. & FERZIGER, J. H. 1992 Turbulence in stratified shear flows: Implications for interpreting shear-induced mixing in the ocean. *J. Phys. Oceanogr, (accepted for publication).*

IVEY, G. N. & IMBERGER, J. 1991 On the nature of turbulence in a stratified fluid. Part I: Energetics of mixing. *J. Phys. Oceanogr.* **21,** 650-658.

ROGALLO, R. S. 1981 Numerical experiments in homogeneous turbulence. *NASA Tech. Memo 81315.*

ROHR, J. J., ITSWEIRE, E. C., HELLAND, K. N. & VAN ATTA, C. W. 1988 An investigation of the growth of turbulence in a uniform-mean-shear flow. *J. Fluid Mech.* **187,** 1-33.

STILLINGER, D. C., HELLAND, K. N. & VAN ATTA, C. W. 1983 Experiments on the transition of homogeneous turbulence to internal waves in a stratified fluid. *J. Fluid Mech.* **131,** 91-122.

YAMAZAKI, H. & LUECK, P. 1990 Why oceanic dissipation rates are not lognormal. *J. Phys. Oceanogr.* **20(12),** 1907-1918.

LIF measurements of scalar mixing in turbulent shear layers

By P. S. Karasso[1] AND M. G. Mungal[1]

1. Motivation and objectives

The structure of shear layer flows at high Reynolds numbers remains a very interesting problem. Straight mixing layers have been studied (Brown & Roshko, 1974, Dimotakis & Brown, 1976, Konrad, 1977, Mungal *et al.*, 1985) and yielded information on the probability density function (pdf) of a passive scalar across the layer. Konrad (1977) and Koochesfahani & Dimotakis (1986) measured the pdf of the mixture fraction for mixing layers of moderate Reynolds numbers, each about 25,000 (Re based on velocity difference and visual thickness). Their measurements showed a "non-marching" pdf (central hump which is invariant from edge to edge across the layer), a result which is linked to the visualizations of the spanwise Kelvin-Helmholtz (K-H) instability mode, which is the primary instability for plane shear layer flows. Similar measurements at higher Reynolds numbers remain an open question: a "marching" behavior of a passive scalar pdf at $Re = 70,000$ by Batt (1977) suggests either resolution problems of the measurements or a change in the physical mechanisms of entrainment and mixing.

A secondary instability mode, the Taylor-Görtler (T-G) instability, which is associated with streamwise vortical structures, has also been observed in shear layers (Bernal & Roshko, 1986, Breidenthal, 1981, Konrad, 1977, Lasheras & Choi, 1988). Image reconstruction by Jimenez *et al.* (1985) and volume renderings by Karasso & Mungal (1990) at low Re numbers have demonstrated that the K-H and the T-G instability modes occur simultaneously in a non-mutually destructive way, evidence that supports the quasi two-dimensional aspect of these flows and the non-marching character of the pdf at low Reynolds numbers. At higher Re numbers though, the interaction of these two instability modes is still unclear and may affect the mixing process.

The shear layer is also known to be very sensitive to its initial conditions (Bradshaw, 1966, Browand & Latigo, 1979, Mungal *et al.*, 1985), which eventually determine the transition to turbulence. Furthermore, Huang & Ho (1990) found that the generation and transition to small-scale eddies occurs through vortex pairings. They showed that the transition to the fully developed regime is correlated with the number of large-scale structure pairings which depend on the operating conditions, namely the speed ratio, the first instability wavelength, and the downstream location. Their findings have great implications to the present study since it is the small scales that effect the passive scalar mixing process.

1 Stanford University

In this study, we perform measurements of the concentration pdf of plane mixing layers for different operating conditions. At a speed ratio of $r = U_1/U_2 = 4 : 1$, we examine three Reynolds number cases: $Re = 14,000$, $Re = 31,000$, and $Re = 62,000$. Some other Re number cases' results, not presented in detail, will be invoked to explain the behavior of the pdf of the concentration field. A case of $r = 2.6 : 1$ at $Re = 20,000$ is also considered. The planar laser-induced fluorescence technique is used to yield quantitative measurements. The different Re are obtained by changing the velocity magnitudes of the two streams. The question of resolution of these measurements will be addressed. In order to investigate the effects of the initial conditions on the development and the structure of the mixing layer, the boundary layer on the high-speed side of the splitter plate is tripped. The average concentration and the average mixed fluid concentration are also calculated to further understand the changes in the shear layer for the different cases examined.

2. Accomplishments

2.1. Experimental procedure

2.1.1 Facility

The facility consists of a blow-down water tunnel, the schematic and details of which appear in Karasso & Mungal (1990). The overhead tank is partitioned so that one side can be uniformly seeded with fluorescent dye. The facility can be operated at various speed ratios.

2.1.2 Experimental Technique

The planar laser-induced fluorescence (PLIF) technique (Kychakoff *et al.*, 1984, Pringsheim, 1949) is used to acquire quantitative images of the concentration field across the layer. PLIF is a powerful, non-invasive technique with good temporal and spatial resolution. The low-speed stream is seeded with a fluorescent dye, 5(& 6)-carboxy 2'7'-dichlorofluorescein. The choice of dye will be discussed shortly. A thin laser light sheet (about 400 μm) is generated from a 1.5 W Nd:Yag laser and is oriented in the streamwise direction. A $2-D$ CCD array is used to record the fluorescence signals. The camera collects the light at a right angle with respect to the plane of the laser sheet. Appropriate filters are placed in front of the camera lens (Nikon 50mm, $f = 1.8$) to ensure that only fluorescence signals are recorded on the imaging array. The images are acquired (8 bits) and stored on a computer.

2.1.3 Signal calibrations

The choice of a pulsed laser was made on the basis of improving the temporal resolution of the measurements. Each pulse of the present Nd:Yag laser (532 nm) has a duration of about 10 ns. The fluorescence lifetime is of the same order. The smallest time scale for mixing for all the experimental cases is on the order of microseconds. Our images can then be characterized by superior temporal resolution.

In the past, sodium fluorescein (in combination with CW lasers) was used as a fluorescent dye for quantitative measurements in similar experiments (Dahm, 1985, Koochesfahani *et al.*, 1986, Walker, 1987). The absorptivity of sodium fluorescein,

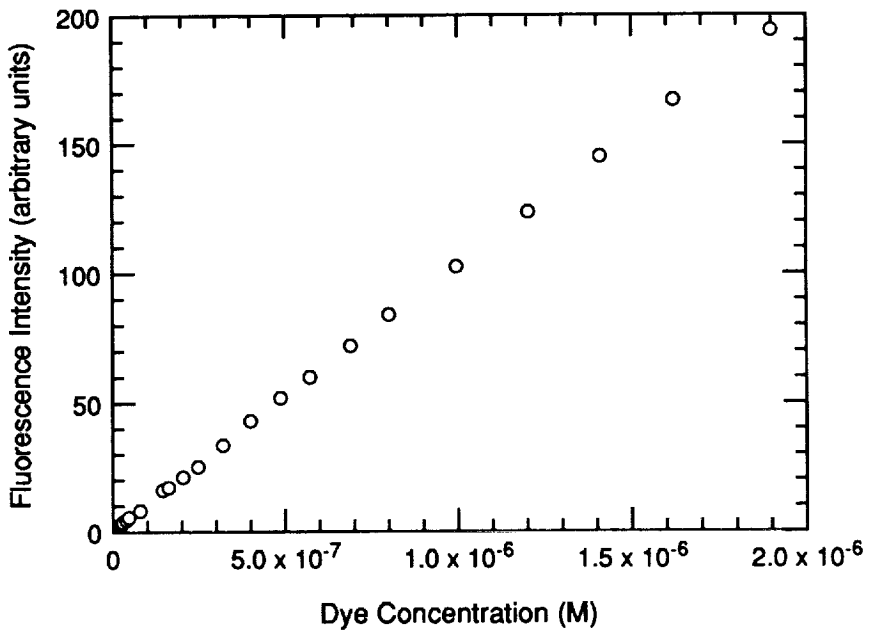

FIGURE 1. Fluorescence intensity vs. dye molar concentration.

though, at 532 nm (Nd:Yag) is significantly decreased (consult absorption spectrum, not shown here). This means that in order to produce, with the Nd:Yag laser, sufficient for imaging fluorescence signals, we would have to either increase the pumping power of the laser or increase the dye concentration. Both suggestions proved not well suited for quantitative imaging since they drove the fluorescence signal into the non-linear regime with dye concentration or with laser energy.

A different dye, 5(& 6)-carboxy2'7'-dichlorofluorescein, was then chosen. Considerations for choosing a dye include solubility in water and avoidance of optical trapping. A linearity check of the fluorescence signal intensity vs. dye concentration (the quantity that is ultimately measured) was performed. The result appears in Figure 1. The response is linear for the range of dye concentrations we used in this experiment. This test also implied that no measurable photobleaching would occur for a flowing system. Furthermore, we ensured that the response of the signal was linear with the laser energy used; although a higher (than that actually used) dye concentration would optimize the fluorescence signal for the input laser energy, a lower signal level was obtained (decreased dynamic range) in order to compensate for the high cost of the dye.

For all runs, a dye concentration of 1.5×10^{-6} M was implemented in seeding the low-speed side. An overall long focal length lens system was used to generate the laser sheet in order to minimize sheet-thickness variations across the imaged region. Also, the sheet was overexpanded in order to minimize the corrections needed to account for the spatial variation of the intensity of the laser light.

2.2. Experimental conditions

For all the acquired images, the actual size of the imaged region is about 7.0 x 5.2 cm. Hence the imaged area on each pixel of a digitized image is 137 μm by 217 μm. These numbers represent nominal values since the actual spatial resolution is determined by the "worst" dimension, which for this case is either the laser sheet thickness (about 400 μm) or the fact that a Nyquist sampling filter should be applied when digitization occurs, thus reducing the pixels' resolution by a factor of two. Additional factors that may limit the spatial resolution of the acquired images include focusing and camera alignment.

A first set of experiments at a speed ratio of $r = 4 : 1$ were performed. Three different cases were examined, corresponding to a high-speed stream velocity magnitude U_1 of 0.34 m/s, 0.90 m/s and 1.80 m/s. The estimated (using Thwaite's method) boundary layer momentum thicknesses θ on the high-speed side at the splitter plate tip are 0.030 cm, 0.020 cm, and 0.015 cm, respectively. The center of each image is located at 25 cm downstream of the splitter plate (the visual thickness of the layer at this location has been used to assign a Reynolds number to each case). A second set of experiments was performed at the same speed ratio and the same three velocity magnitude values by placing a 1.5 mm diameter (trip) rod at the high-speed side of the splitter plate at a location of about 6 cm upstream of the tip. Finally, a case of a speed ratio of $r = 2.6 : 1$ and $U_1 = 0.67$ m/s and another one of $r = 4 : 1$ and $U_1 = 0.75$ m/s were also run.

2.3. Results

About 100 images represent the data used to extract results for the composition field for each case. By averaging all the images for each case, we obtain the visual thickness (δ) of the layer at 25 cm downstream of the splitter plate. Thus, for the untripped boundary layer cases of $r = 4 : 1$ we find:

$$U_1 = 0.34\text{m/s} \quad : \quad \delta = 5.3\text{cm} \quad ; \quad Re \sim 14,000$$

$$U_1 = 0.90\text{m/s} \quad : \quad \delta = 4.7\text{cm} \quad ; \quad Re \sim 31,000$$

$$U_1 = 1.80\text{m/s} \quad : \quad \delta = 4.3\text{cm} \quad ; \quad Re \sim 62,000$$

These Reynolds numbers will be also used to label the tripped cases with similar velocity magnitudes (although the actual Re for the tripped cases is different since the size of the layer changes). When averaging the images for the tripped cases, the following visual thicknesses are obtained ($r = 4 : 1$):

$$U_1 = 0.34\text{m/s} \quad : \quad \delta_{tr} = 5.4\text{cm}$$

$$U_1 = 0.90\text{m/s} \quad : \quad \delta_{tr} = 3.6\text{cm}$$

$$U_1 = 1.80\text{m/s} \quad : \quad \delta_{tr} = 3.6\text{cm}$$

It is seen that the layer shrinks on average by about 20% for the tripped cases for the higher Re (also see Browand & Latigo, 1979).

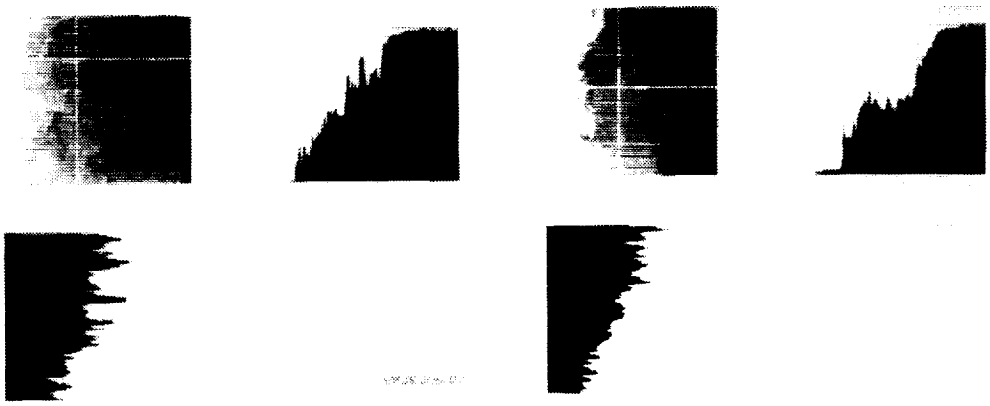

$Re = 31,000$ $Re = 31,000$ tripped

FIGURE 2. Images (7cm x 5 cm) of the mixing layer at speed a ratio of 4:1. Flow is from top to bottom. Streamwise and cross-stream cuts show concentration distributions.

Two examples of (corrected) images are shown in Figure 2. Perpendicular cuts in the streamwise and the cross-stream direction are shown on the right and bottom of each image and represent the distribution of the concentration field. The concentration field across the layer can be uniform or can have strong ramps. The pictures depict organized motion, but loss of organization was also observed, for all the cases. The structures tend to be more uniform in concentration at $Re = 14,000$. The concentration ramps were more frequently encountered at the two higher Re cases (for both tripped and untripped), even when the images displayed strongly organized motion dominated by a K-H roll. For structures of uniform concentration, there was also structure-to-structure variation. This suggests that there is some periodicity or non-uniformity in the amount of entrained fluid in the mixing layer, a result which is not surprising given the fluctuating nature of turbulent flows.

The pdf of the mixture fraction ξ at a given location y across the layer is defined as:

$$\text{Probability} = P(\xi \leq \xi(y) \leq \xi + \Delta\xi)$$

The pdf results for all cases of $r = 4:1$ are shown in Figure 3. The calculated average concentration (mean) and average concentration of mixed fluid (mixed mean) are shown in Figure 4. In defining the mean mixed, concentration values to within 15% of the free streams' values were considered to be pure unmixed fluid. [Note: throughout this work, $\xi = 1$ corresponds to the low-speed side fluid.]

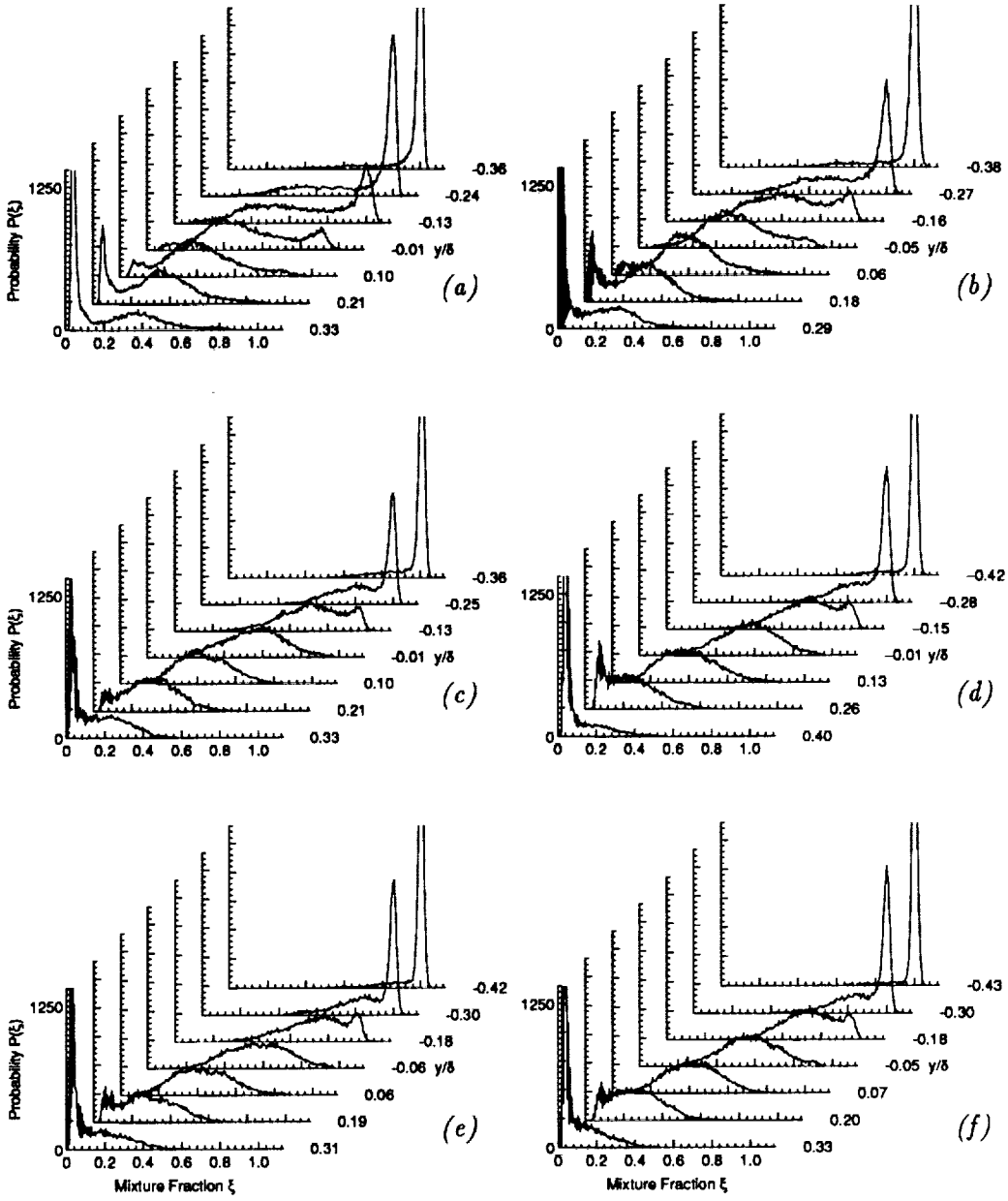

FIGURE 3. Probability distribution function of the mixture fraction ξ across the mixing layer. Speed ratio 4:1. *(a)* Re=14,000. *(b)* Re=14,000 [tripped]. *(c)* Re=31,000. *(d)* Re=31,000 [tripped]. *(e)* Re=62,000. *(f)* Re=62,000 [tripped].

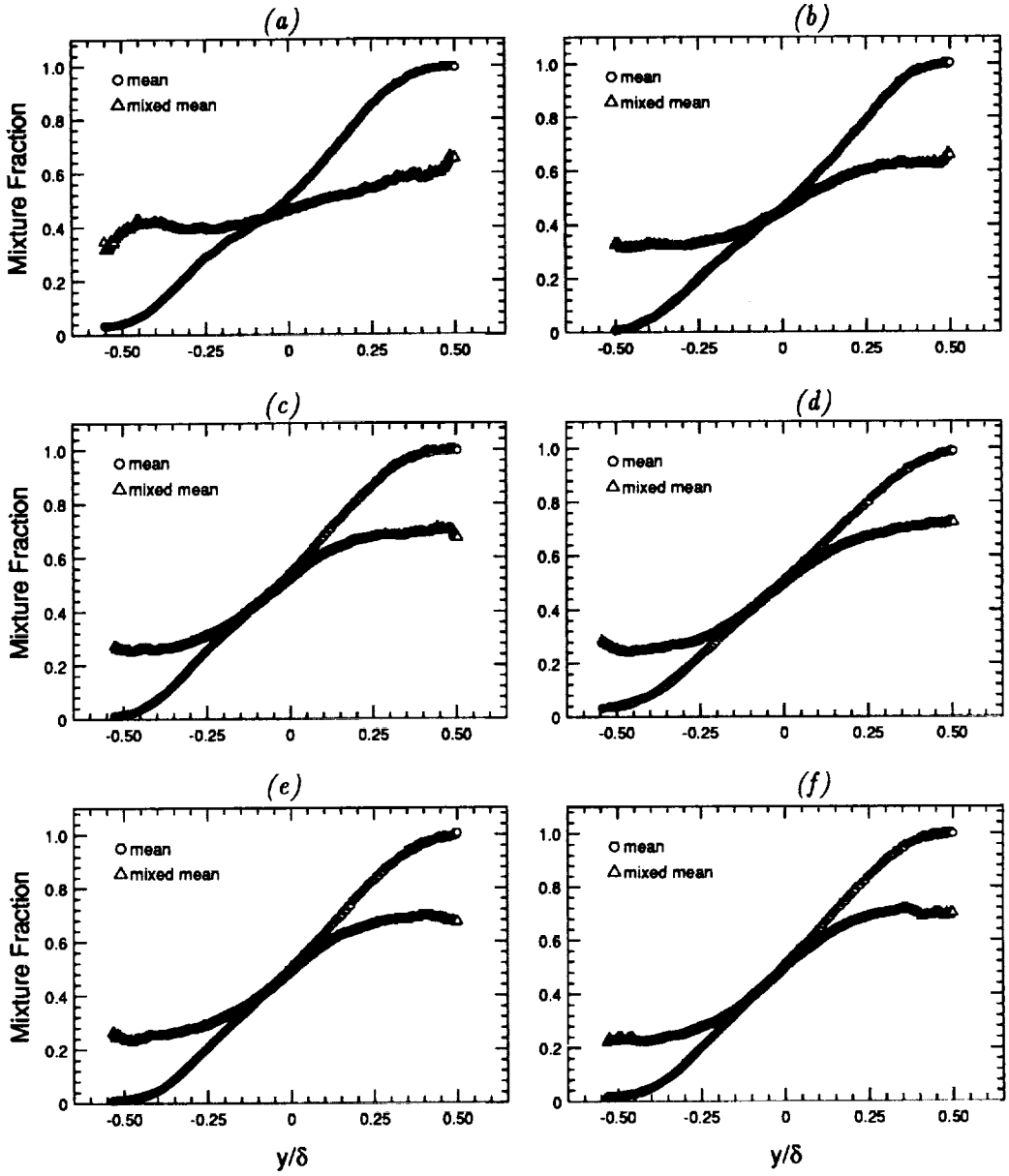

FIGURE 4. Mean and mixed mean fluid concentration across the layer. Speed ratio 4:1. *(a)* Re=14,000. *(b)* Re=14,000 [tripped]. *(c)* Re=31,000. *(d)* Re=31,000 [tripped]. *(e)* Re=62,000. *(f)* Re=62,000 [tripped].

For the $Re = 14,000$ case, the pdf is non-marching (Fig. 3a). A broad range of concentration values is found at each location across the layer. We attribute this phenomenon to both streamwise concentration ramps and to the structure-to-structure variation. In the tripped $Re = 14,000$ case (Fig. 3b), the non-marching feature is essentially preserved, although a small variation of the peak can be observed while moving across the layer. The mean and the mixed mean fluid concentrations are shown in Figure 4a. For the mean concentration, a triple inflection point is evident. This kind of behavior was also noticed by other investigators (Konrad, 1977, Koochesfahani & Dimotakis, 1986), suggesting that the large scale structures affect the way the mixing layer develops. For the mean mixed concentration curve, we notice a much smaller variation across the layer, a result of the fact that large-scale structures dominate the flow. For the tripped case (Fig. 4b), there is little evidence of a triple inflection point, suggesting a shift in the way the large-scale structures influence the growth of the layer.

For the $Re = 31,000$ and the $Re = 62,000$ cases, we notice a broad-marching type pdf of the mixture fraction (Fig. 3c, 3e). The two cases look very similar to each other but very different from the $Re = 14,000$ case. The above is true for both the untripped and the tripped (Fig. 3d, 3f) boundary layer cases. The mean and the mixed mean concentrations (Fig. 4c, 4d, 4e, 4f) still have a much different slope, suggesting that large-scale structures still play an important role in the development of the shear layer. These structures, though, have streamwise concentration ramps which account for the broad-marching behavior of the pdf. It must be noted that K-H rolls were evidenced for all cases up to the highest Re number case examined.

A case of $Re = 27,000$ at the same speed ratio ($r = 4 : 1$) was examined and yielded a broad-marching type pdf similar to the marching type ones that were just presented. This result seems to be in contrast to that of Koochesfahani and Dimotakis if only the Re number is considered to characterize the flows. However, the difference in the speed ratio and hence the difference in the magnitudes of the velocities needed to produce the same Re account for different initial conditions and hence different layers; a more detailed explanation is given at a subsequent section. Furthermore, a case of $r = 2.6 : 1$ at $Re = 20,000$ yielded a non-marching type pdf.

Finally, as one moves to higher Re, the issue of relative resolution could dominate the outcome of the results; we hence address it in the following section.

2.4 Issue of resolution

The smallest spatial fluid mechanical scale characterizing the flow is the diffusive scale λ (Batchelor's scale), which is given by

$$\lambda/\delta = Sc^{-1/2} * Re^{-3/4}$$

For the cases of interest in this experiment, the following λ's are estimated at the location of the measurements (using a constant of proportionality equal to one):

$$U_1 = 0.34\text{m/s} \quad ; \quad \lambda \sim 1.7\mu\text{m}$$

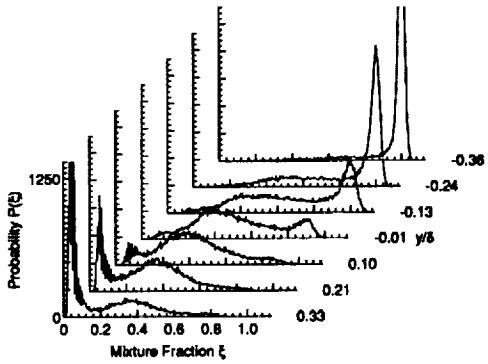

FIGURE 5. Probability distribution function of the $Re = 14,000$ case with decreased spatial resolution.

$$U_1 = 0.90\text{m/s} \quad ; \quad \lambda \sim 0.8\mu\text{m}$$

$$U_1 = 1.80\text{m/s} \quad ; \quad \lambda \sim 0.4\mu\text{m}$$

We notice how these numbers are significantly smaller than the sampled area of our measurements ($\Delta x = 137\mu$m, $\Delta y = 237\mu$m). In order to address the possibility of resolution masking the real mixing field and biasing the pdf results, we artificially worsen the resolution of the untripped $Re = 14,000$ case, via data sample binning, by a factor of two to make it similar to the $Re = 31,000$ case. The result appears in Figure 5. The non-marching character is essentially unchanged (compare with Fig. 3c). We believe that the ramps that are observed at the higher Re number cases, in spite of the decreased resolution of the measurements, are a real phenomenon associated with the evolution of the flow, and that the pdf's reflect this behavior.

2.5. Discussion

According to Huang & Ho (1990), the production of small-scale eddies is associated with the interaction of the K-H with the T-G structures. The vortex pairings, which eventually lead to a transition to the fully developed regime, occur at a location which depends on the operating conditions. They used the non-dimensional parameter Rx/λ to show the evolution of the roll-off exponent of the velocity power spectra, n, to its asymptotic value, and to denote the location of the vortex merging [$R = (1-r)/(1+r)$, x is the downstream from the splitter plate location and λ is the initial instability wavelength; [$\lambda \sim 30\theta$]. Their plot is reproduced in Figure 6. We shall refer to $Rx/30\theta$ as the "pairing parameter".

We then mark on this plot the present experiments as well as the one by Koochesfahani & Dimotakis according to their corresponding value of $Rx/30\theta$. We notice that all cases corresponding to a value of the pairing parameter of less than about 20 have a non-marching type pdf of the mixture fraction, whereas the ones above 20 have a marching type pdf. It is interesting to note that on this plot, experiments of similar Re numbers can differ in their $Rx/30\theta$ value, thus yielding different types of pdf. The mixing transition (Breidenthal, 1981, Konrad, 1977, Koochesfahani

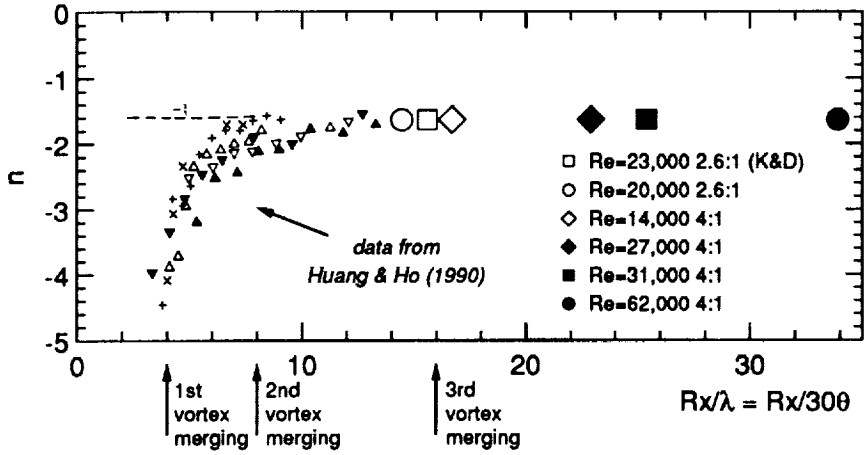

FIGURE 6. Roll-off exponent of velocity power spectra n vs. pairing parameter. (from Huang & Ho).

& Dimotakis, 1986), whereby the amount of molecular mixing is increased, is now logically associated with the second vortex merging. The transition to the fully developed regime is no longer a function of the Re number only, but of the non-dimensionalized distance $Rx/30\theta$ at which sufficient action of vortex merging has led to the generation of small-scale eddies. In particular, our results combined with those of Huang & Ho suggest that the layer yields its asymptotic pdf at locations greater than three vortex mergings. Whereas boundary layer tripping has an effect on the development and growth of the mixing layer for all the cases examined and affects the pdf at a low value of the pairing parameter, it appears to have no effect on the shape of the pdf once the layer is fully developed. It is to be understood that parameters such as the free stream turbulence level or the aspect ratio of the test section, which differ for different facilities, may modify the above pairing parameter value of 20. The important point to be made, though, is that the Re number alone is not a sufficient parameter to characterize shear layers and that fully developed shear layers have, we believe, a broad-marching type pdf.

2.6. Conclusions

Experiments were performed to investigate the dependence of the structure of the shear layer on the operating conditions. We found that the concentration pdf shows a non-marching behavior at an initial stage but eventually develops to a broad-marching type pdf for fully developed layers. The Re number alone is not adequate to characterize whether or not the layer is fully developed: parameters such as the speed ratio and the initial boundary layer momentum thickness are equally important in determining the character of the passive scalar mixing field in shear layers. The value of the pairing parameter, which also correlates with the large-scale structure merging and the transition to small-scale eddies as found by Huang & Ho, seems to offer a criterion in determining the pdf behavior of plane

mixing layers. The second vortex merging appears to be associated with the mixing transition and a non-marching pdf. The third vortex merging defines the fully developed, broad-marching pdf. Well defined, organized large-scale structures were observed for all the cases (tripped and untripped boundary layers, all Re numbers). The structures developed concentration ramps as the layer evolved into the fully developed regime. The broad range of mixture fraction values that were found is associated with structure-to-structure variation. Finally, the mean and the mixed mean concentrations suggest that the large-scale structures affect the overall mixing process.

3. Future work

The interpretation of the structure of the mixing layer through the large-scale structures, and thus through the Kelvin-Helmholtz and the Taylor-Görtler instabilities, lead us to the question: can mixing enhancement be achieved by "adjusting" the strength of either the T-G or the K-H instability mode? To answer this, we intend to measure the pdf of the mixture fraction of longitudinally curved mixing layers. In a curved mixing layer, placing the high-speed stream on the inside of the bend (unstable) enhances the T-G instability mode, whereas placing it on the outside of the bend (stable) suppresses the T-G. Thus, our goal is to measure in detail the pdf of the mixture fraction for stable and unstable mixing layers, with differences in the pdf's reflecting differences in the mechanism of the mixing process as produced by the competition of the two instability modes.

The passive scalar technique has an additional inherent resolution problem in that it cannot distinguish mixed from unmixed (stirred) fluid within the sampling volume but will yield an average intensity (Breidenthal, 1981). A chemical reaction technique will be implemented in the future to address this issue and the changes that can result in the pdf.

Acknowledgements

The authors wish to thank Dr. Jerry M. Seitzman for his help and discussions. Finally, the authors wish to thank Professor R. K. Hanson for the use of the Pixar Imaging System.

REFERENCES

BATT, R. G. 1977 Turbulent Mixing of Passive and Chemically Reacting Species in a Low-Speed Shear Layer. *J. Fluid Mech.* **82,** 53-95.

BERNAL, L. P. & ROSHKO, A. 1986 Streamwise Vortex Structure in Plane Mixing Layers. *J. Fluid Mech.* **170,** 499-525.

BRADSHAW, P. 1966 The Effect of Initial Conditions on the Development of a Free Shear Layer. *J. Fluid Mech.* **26,** 225-236.

BREIDENTHAL, R. 1981 Structure in Turbulent Mixing Layers and Wakes Using a Chemical Reaction. *J. Fluid Mech.* **109,** 1-24.

BROWAND, F. G. & LATIGO, B. O. 1979 Growth of the Two-Dimensional Mixing Layer from a Turbulent and a Non-Turbulent Boundary Layer . *The Physics of Fluids.* **22,no 6,** 1011-1019.

BROWN, G. L. & ROSHKO, A. 1974 On Density Effects and Large Structure in Turbulent Mixing Layers. *J. Fluid Mech.* **64,** 775-816.

DAHM, W. J. A. 1985 *Experiments on Entrainment, Mixing and Chemical Reactions in Turbulent Jets at Large Schmidt Number.* Ph.D. Thesis, Caltech.

DIMOTAKIS, P. E., & BROWN, G. L. 1976 The Mixing Layer at High Reynolds Number: Large-Structure Dynamics and Entrainment. *J. Fluid Mech.* **78,** 535-560.

HUANG, L.-S. & HO C.-M. 1990 Small Scale Transition in a Plane Mixing Layer. *J. Fluid Mech.* **210,** 475-500.

JIMENEZ, J., COGOLLOS, M. & BERNAL, L. P. 1985 A Perspective View of the Plane Mixing Layer. *J. Fluid Mech.* **152,** 125-143.

KARASSO, P. S. & MUNGAL, M. G. 1990 An Experimental Study of Curved Mixing Layers: Flow Visualizations Using Volume Rendering. *CTR Annual Research Briefs*, Stanford Univ./NASA-Ames.

KONRAD, J. H. 1977 *An Experimental Investigation of Mixing in Two-Dimensional Turbulent Shear Flows with Applications to Diffusion-Limited Chemical Reactions.* Ph.D. Thesis, Caltech.

KOOCHESFAHANI, M. M. & DIMOTAKIS, P. E. 1986 Mixing and Chemical Reactions in a Turbulent Mixing Layer. *J. Fluid Mech.* **179,** 83-112.

KYCHAKOFF, G., HOWE, R. D. & HANSON, R. K. 1984 Quantitative Flow Visualization Technique for Measurements in Combustion Gases. *Applied Optics.* **23** (5), 704 -712.

LASHERAS, J. C. & CHOI, H. 1988 3-D Instabilities of a Plane Free Shear Layer: An Experimental Study of the Formation and Evolution of Streamwise Vortices. *J. Fluid Mech.* **189,** 53-86.

MUNGAL, M. G., HERMANSON, J. C. & DIMOTAKIS, P. E. 1985 Reynolds Number Effects on Mixing and Combustion in a Reacting Shear Layer. *AIAA J.* **23** (9), 1418-1423.

PRINGSHEIM, P. 1949 *Fluorescence and Phosphorescence.* Interscience Publishers, Inc.

WALKER, D. A. 1987 A Fluorescence Technique for Measurement of Concentration in Liquids. *J. Phys. E.* **20,** 217-224.

Plane mixing layer vortical structure kinematics

By R. L. LeBoeuf

The objective of the current project was to experimentally investigate the structure and dynamics of the streamwise vorticity in a plane mixing layer. The first part of this research program was intended to clarify whether the observed decrease in mean streamwise vorticity in the far-field of mixing layers (Bell & Mehta 1992) is due primarily to the "smearing" caused by vortex meander or to diffusion. Two-point velocity correlation measurements have been used to show that there is little spanwise meander of the large-scale streamwise vortical structure. The correlation measurements also indicate a large degree of transverse meander of the streamwise vorticity which is not surprising since the streamwise vorticity exists in the inclined braid region between the spanwise vortex core regions. The streamwise convection of the braid region thereby introduces an apparent transverse meander into measurements using stationary probes. These results were corroborated with estimated secondary velocity profiles in which the streamwise vorticity produces a signature which was tracked in time.

1. Motivation and objectives

An extensive data set consisting of single-point mean and turbulence statistics has been obtained for a two-stream mixing layer (Bell & Mehta 1989b, 1992). The plane unforced mixing layer originating from laminar boundary layers was examined in order to quantify the development of streamwise vorticity which previously was identified only through flow visualization studies (e.g. Bernal & Roshko, 1986). The mean streamwise vorticity derived from the mean velocity field shows a continuous decrease in magnitude with streamwise distance from its nearfield occurrence. It is unclear whether the decrease in mean vorticity is a result of diffusion of the streamwise vorticity or due to meander of concentrated vorticity. Based on comparisons with forced streamwise vortex meander in a boundary layer, Bell & Mehta (1992) argued that the observed decrease of the mean vorticity in the far-field mixing layer was more likely a result of diffusion.

Townsend (1976) showed that the governing equations for a free-shear flow admit to self-preserving solutions for sufficiently high Reynolds numbers. The resulting "self-similar" mean and Reynolds stress profiles become functions of single length and velocity scales. Previous measurements (Bell & Mehta 1992) have indicated that the streamwise vorticity persists even in what would normally be considered the "self-similar" region (where a linear mixing layer growth rate and asymptotic peak Reynolds stresses were achieved). The peak streamwise vorticity and the secondary shear stress ($\overline{uw}$), which was strongly correlated with the streamwise vorticity, were found to exhibit significant levels in this region (although they decreased with streamwise distance to levels comparable with the noise threshold). It

is important for the establishment of the criteria for "self-similarity" to investigate whether the measured decay is due to true diffusion of the streamwise vorticity or an artifact of meander. In addition, this assessment will have important implications regarding the ability of the layer to enhance mixing and reaction rates in the far-field.

To resolve the questions regarding the persistence of streamwise vorticity in the far-field, it was proposed to perform two-point cross-wire measurements of the velocity field (Bell 1990). The dependence of the velocity cross-correlation on the fixed probe location is considered a good indicator of the stationarity of the streamwise vortex location. Additional information regarding meander can be obtained from instantaneous velocity profiles. These were estimated using a newly developed technique and the current apparatus (LeBoeuf & Mehta 1992). The facility and flow conditions that were used for the current study are similar to those of Bell & Mehta (1992).

2. Accomplishments

2.1 Experiment and apparatus

The experiments were conducted in a *Mixing Layer Wind Tunnel* specifically designed for free-shear flow experiments (Bell & Mehta 1989b). The wind tunnel consists of two separate legs which are driven independently by centrifugal blowers connected to variable speed motors. The two streams merge at the sharp trailing edge of a slowly tapering splitter plate; the included angle at the splitter plate edge, which extends 15 cm into the test section, is about 1°. The test section is 36 cm in the cross-stream direction, 91 cm in the spanwise direction, and 366 cm in length. One side-wall is adjustable for streamwise pressure gradient control and slotted for probe access.

In the present experiments, the two sides of the mixing layer were set to 15 m/s and 9 m/s for a velocity ratio, $r = U_2/U_1 = 0.6$ [$\lambda = (U_1 - U_2)/(U_1 + U_2) = 0.25$]. For these operating conditions, the measured streamwise turbulence level (u'/U_e) was approximately 0.15% and the transverse levels (v'/U_e and w'/U_e) were approximately 0.05%. The mean core-flow was found to be uniform to within 0.5% and cross-flow angles were less than 0.25° (Bell & Mehta 1989a). The boundary layers on the splitter plate were laminar at these operating conditions.

Measurements were made using two independently traversed cross-wire probes. The probes could be rotated in order to measure flow in two-coordinate planes. The geometry of the instrumentation resulted in a minimum probe spacing of 7 mm. One probe was mounted on a 2-D traverse which was designed and constructed for the current work. The new traverse was manually controlled using an indexing stepper motor controller. The second probe was mounted on a pre-existing computer-controlled 3-D traverse. Both cross-wires were linked to a fully automated data acquisition and reduction system controlled by a *DEC MicroVax II* computer. The software required for multiple-probe measurements was developed for the current study. The *Dantec* cross-wire probes (Model 55P51) consisted of 5 μm platinum-plated tungsten sensing elements approximately 1 mm long with

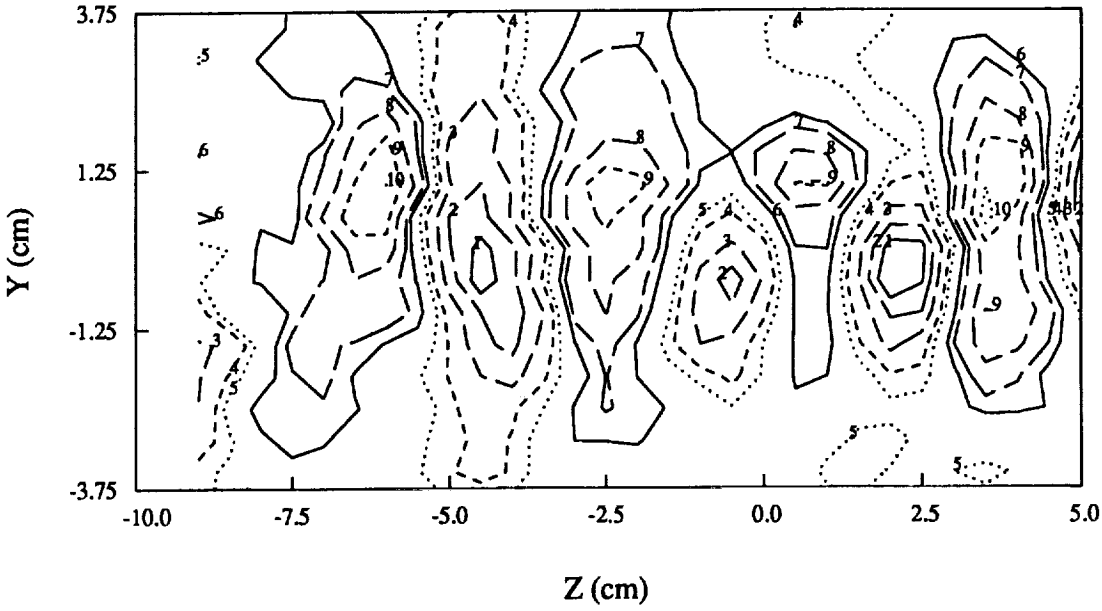

FIGURE 1. Mean streamwise vorticity (Ω_X) at X = 57 cm, starting from -0.08, incremented 0.02.

approximately 1 mm spacing. The probes were calibrated statically in the potential core of the flow assuming a 'cosine-law' response to yaw, with the effective angle determined by calibration. The calibration locations were selected to insure consistent angularity of the measurements of the two probes. The analog signals generated by NASA-built anemometers were DC offset and amplified (x 8) before being fed into a computer interface. The interface contained a fast sample-and-hold A/D converter with 16 bit resolution and a multiplexer for connection to the computer (Bell & Mehta 1992). Individual statistics were averaged over 8192 samples obtained at a rate of 1500 samples per second.

Data were obtained in several Y-Z planes between X = 17 and X = 128 cm with two orientations of the probe (uv and uw) in order to identify mean vortex locations. This method yielded all three components of mean velocity, five independent components of the Reynolds stress tensor, and selected higher order products. Typically, 700-1200 points were measured on a rectangular cross-plane grid at a given streamwise station. The grid spacing (same in both directions, Y and Z) was varied from 0.25-0.5 cm for upstream to downstream stations. The mean spanwise velocity (W) measurements were corrected for mean streamwise velocity gradient ($\partial U/\partial Y$) effects (see Bell and Mehta 1989b for details). The streamwise component of mean vorticity was computed using a central difference numerical differention of the measurements of the velocity components V and W.

An example of the resulting measurement of the mean streamwise vorticity (Ω_X) at X = 57 cm downstream of the splitter plate trailing edge is given in Fig. 1. The

selection of the traverse grid for the correlation measurements is also noted on the figure. Except for the decreasing peak magnitude and increasing size (for increasing streamwise distance), the nominally linear array of counter-rotating vortices was typical of all measurement locations except the first. At the first measurement location, $X = 17$, the streamwise vorticity had not yet organized into a single spanwise row. The correlation locations were nominally selected to cross the location of maximum mean streamwise vorticity.

The two-point cross-correlation measurements required for the estimation of velocity profiles were acquired on grids of equally spaced probe positions. The spacing of measurement locations in the grids was 0.4 cm. The minimum distance between estimation and reference locations was limited by probe geometry to two grid spacings (i.e. 0.8 cm). Therefore, the estimated velocity profile is twice as dense as it could be using probes of the same geometry to measure at all grid locations simultaneously. The grids were positioned 78 cm downstream of the splitter plate trailing edge for the measurements discussed in this paper. It is estimated that this station is located after the third pairing of the spanwise vortex structures.

2.2 Results and discussion

The transverse (v) and spanwise (w) velocity correlations in the spanwise (Z) and transverse (Y) directions, respectively, are shown in Figs. 2a and b for the streamwise location $X = 57$ cm from the splitter plate trailing edge. One noteworthy feature of the sets of curves for each station is the relative phase of each curve. There is generally a shift of the curves from right to left with increasing stationary probe location. There would be a one-to-one correspondence between the change in the probe spacing at the correlation extremes and the change in position of the stationary probe if no meander of the large scale structure is occurring. The transverse velocity correlations on a spanwise measurement grid approximate this no-meander relative phase shift. For example, Figs. 3a and 3b show the probe separation at the first minimum and first maximum (excluding zero spacing) of all of the correlation measurements versus stationary probe location. The slope of the resulting curves for the transverse velocity measurements (Fig. 3a) is very close to -1, indicating that meander in the spanwise (z) direction is negligible at this streamwise location.

The spanwise velocity correlations across the mixing layer have a less consistent phase shift for changing stationary probe location. Typically, the shift of the first minimum is a fraction of the shift of the stationary probe for two sets of correlations (see Fig. 2b). This is reflected in Fig. 3b where the slope of the curve of first minimum versus stationary probe location for the spanwise velocity measurements has a much more gradual slope, which would indicate a large degree of apparent transverse meander. The slope of the curves may be linked to the aspect ratio of the mean streamwise vortices.

A simple, more direct way to identify meander of the large-scale structure is to track them in temporal multi-point velocity records. The presence of streamwise structure should appear clearly in profiles of the secondary velocity. In particular, spanwise meander should produce a jittered signature in spanwise profiles of

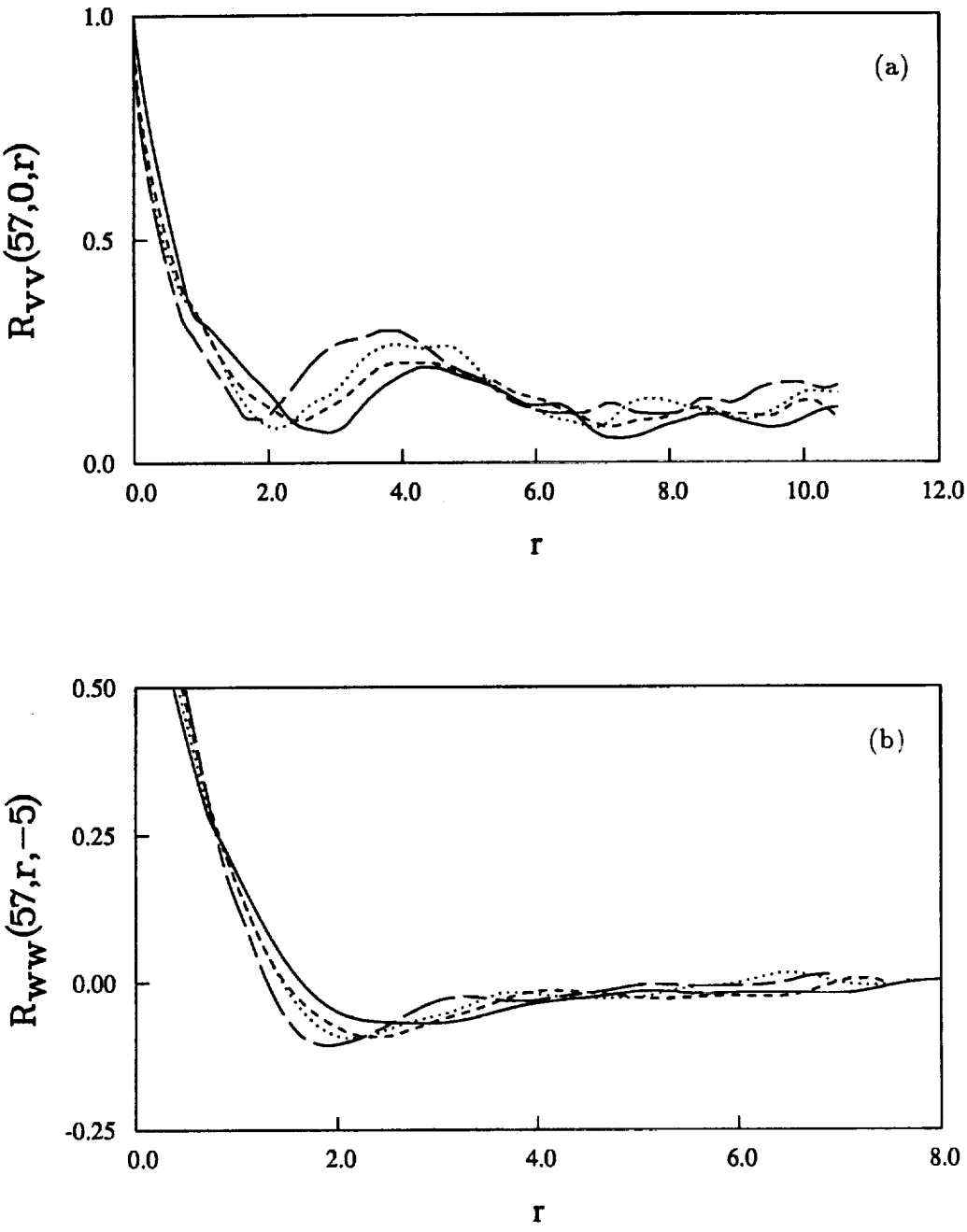

FIGURE 2. Two-point cross-correlation at X = 57 cm. *(a)* Transverse velocity (v) in the spanwise (Z) direction at Y = 0 and Z = -8.5 cm ——— ; -8.15 cm - - - - ; -7.8 cm ····· ; -7.45 cm — — — . *(b)* Spanwise velocity (w) in the transverse (Y) direction at Z = -5 cm and Y = -2.1 cm ——— ; -1.4 cm - - - - ; -0.7 cm ····· , 0.0 cm — — — .

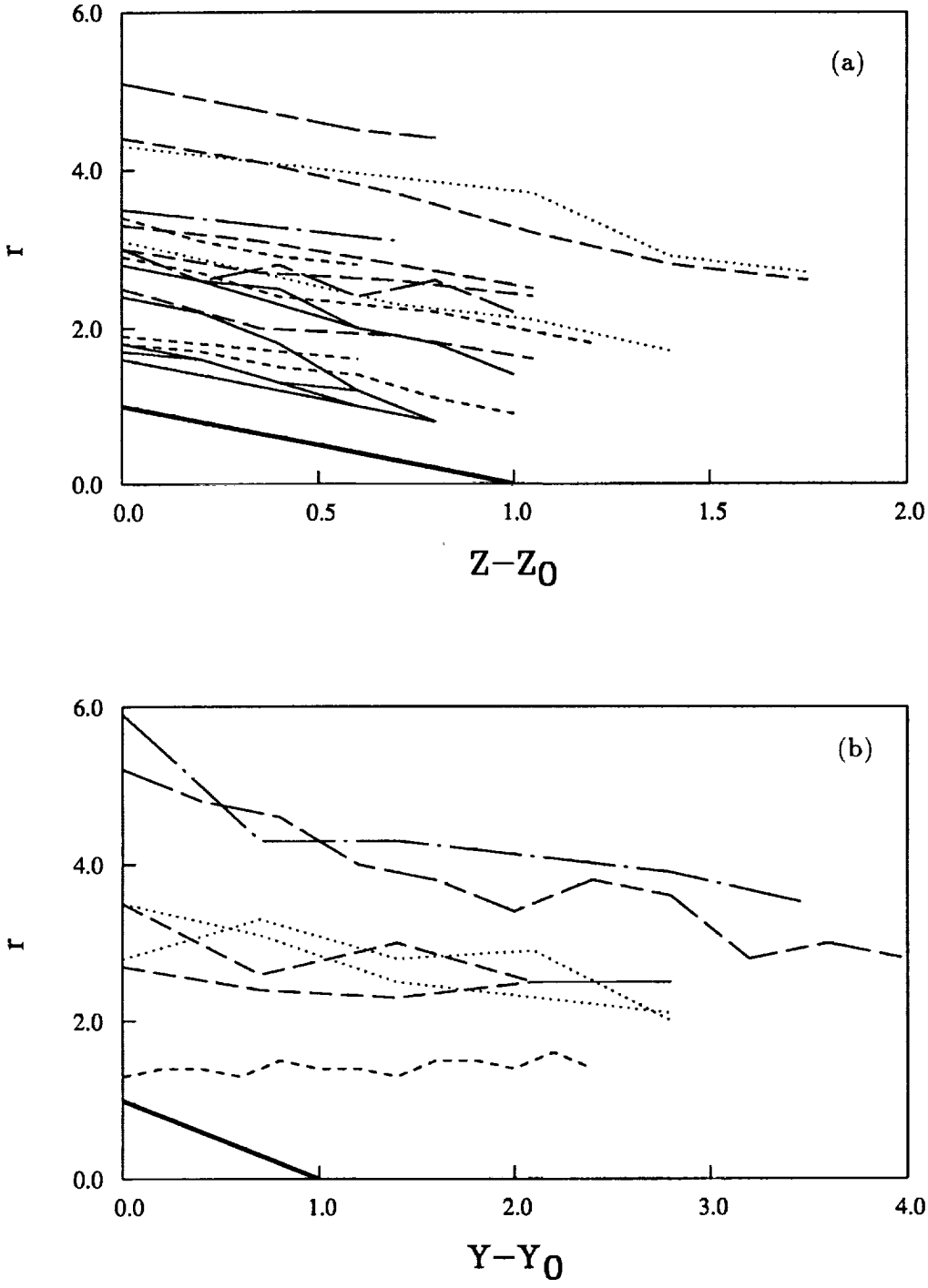

FIGURE 3. Probe separation at extremes of correlations versus relative stationary probe location for X = 27 cm ——— ; 47 cm - - - - ; 57 cm ····· ; 78 cm — — — ; 88 cm ——— ; 128 cm —·— ; Line with slope equal to -1 ———. *(a)* Transverse velocity (v) in the spanwise (Z) direction. *(b)* Spanwise velocity (w) in the transverse (Y) direction.

transverse velocity and transverse meander should produce a jittered signature in transverse profiles of spanwise velocity. Profiles of simultaneous velocity records with sufficient spatial resolution would be very difficult using cross-wire probes and would entail a significant increase in hardware costs. Use of optical techniques such as digital particle image velocimetry would probably be the best suited to this problem, but would also be costly. An alternative approach whereby the velocity profiles were estimated using one or two reference velocities was used to produce simultaneous velocity profiles. This approach required no further investment in hardware.

The linear estimate of the velocity component $\hat{u}_i(x')$ based on m reference (measured) velocity components $u_j(x^{(k)})$ at n locations at the same time can be expressed as:

$$\hat{u}_i(x') = \sum_{k=1}^{n}\sum_{j=1}^{m} A_{ijk} u_j(x^{(k)}). \tag{1}$$

Minimizing the mean-square error, $\overline{[\hat{u}_i(x') - u_i(x')]^2}$, of the estimate yields an equation for the linear estimation coefficients (A_{ijk}):

$$\sum_{k=1}^{n}\sum_{j=1}^{m} A_{ijk}\overline{u_j(x^{(k)})u_l(x^{(p)})} = \overline{u_l(x^{(p)})u_i(x')}. \tag{2}$$

Thus, given the cross-correlation tensors, the linear mean-square (MS) estimation coefficients can be determined. It can be shown [using Eq. (1)] that the left hand side of Eq. (2) is equal to $\overline{u_l(x^{(p)})\hat{u}_i(x')}$. Hence, the estimation-reference cross-correlation tensor is equal to the measurements used to produce the coefficients.

The mean-squared estimation error increases with the distance away from the measurement location (approaching $\overline{u_j^2}$), as the velocity loses correlation with the reference (Adrian & Moin 1988). The estimated signal can be amplified in a rational manner by including the velocity covariance at the estimation locations in the scheme to calculate the estimation coefficients. This optimization which includes the estimation covariance in addition to the two-point cross-correlation tensors forms the basis for the proposed technique.

Consider the error vector,

$$F = \begin{pmatrix} \overline{u_j(x')u_i(x^{(k)})} - \overline{\hat{u}_j(x')u_i(x^{(k)})} \\ \overline{u_j(x')u_i(x')} - \overline{\hat{u}_j(x')\hat{u}_i(x')} \end{pmatrix} \forall i,j,k. \tag{3}$$

Then the estimation coefficients (A_{ijk}) can be optimally determined with respect to both the estimation-reference cross-correlation, $\overline{\hat{u}_j(x')u_i(x^{(k)})}$, and the estimation covariance, $\overline{\hat{u}_j(x')\hat{u}_i(x')}$, by minimizing ($F^TF$), where the superscript T indicates transpose. The statistics of the estimates can be calculated for any value of the coefficients using known reference signals and estimation signals generated using Eq. (1). This optimization can be accelerated, however, by calculating the statistics of the estimates in terms of the reference cross-correlation tensor, $\overline{u_j(x^{(k)})u_l(x^{(p)})}$,

and the estimation-reference cross-correlation tensor, $\overline{u_l(x^{(p)})u_i(x')}$. By operating on Eq. (1), it can easily be shown that the estimation-reference correlation can be expressed as:

$$\overline{\hat{u}_j(x')u_i(x^{(k)})} = \sum_{p=1}^{n}\sum_{q=1}^{m} A_{jqp}\overline{u_q(x^{(p)})u_i(x^{(k)})} \tag{4}$$

and the estimated Reynolds stresses can be expressed as:

$$\overline{\hat{u}_j(x')\hat{u}_i(x')} = \sum_{p=1}^{n}\sum_{q=1}^{m}\sum_{k=1}^{n}\sum_{l=1}^{m} A_{jqp}A_{ilk}\overline{u_q(x^{(p)})u_l(x^{(k)})}. \tag{5}$$

Thus, the new technique requires the same cross-correlation tensor data as the traditional mean-square estimate along with the estimation covariance data. The optimization described above is a non-linear, least-squares optimization which can be solved using standard techniques such as, for example, the modified Levenberg-Marquardt algorithm implemented in the *IMSL* subroutine DUNLSF.

Another alternative to minimizing the mean-squared error is to maximize the correlation coefficient of the estimated signal and the true signal at the estimation location. When this criterion is used to determine the linear estimation coefficients for a two-component one-point estimate, the maximum correlation coefficient is independent of the energy of the estimate:

$$\rho_{ii} = \left(\frac{-\overline{\hat{u}_i^2(x')}a}{(b/2)^2 - \overline{u_1^2(x^{(k)})}\left[\overline{\hat{u}^2(x')}\right]^2 a / \left[\overline{\hat{u}(x')u_1(x^{(k)}}\right]^2} \right)^{1/2} \tag{6}$$

where

$$a = \frac{\left[\overline{\hat{u}(x')u_2(x^{(k)})}\right]^2 \overline{u_1^2(x^{(k)})}}{\left[\overline{\hat{u}(x')u_1(x^{(k)})}\right]^2} + \overline{u_2^2(x^{(k)})} - \frac{2\overline{\hat{u}(x')u_2(x^{(k)})u_1(x^{(k)})u_2(x^{(k)})}}{\overline{\hat{u}(x')u_1(x^{(k)})}} \tag{7}$$

and

$$b = \frac{2\overline{\hat{u}^2(x')}}{\overline{\hat{u}(x')u_1(x^{(k)})}}\overline{u_1(x^{(k)})u_2(x^{(k)})} - \frac{\overline{\hat{u}(x')u_2(x^{(k)})u_1^2(x^{(k)})}}{\overline{\hat{u}(x')u_1(x^{(k)})}}. \tag{8}$$

Hence, once the maximum correlation coefficient has been calculated, the estimation coefficients can then be determined from

$$A_2 = \frac{-\rho_{ii}b}{2a} \tag{9}$$

and

$$A_1 = \frac{\rho_{ii}\overline{\hat{u}^2(x')} - A_2\overline{\hat{u}(x')u_2(x^{(k)})}}{\overline{\hat{u}(x')u_1(x^{(k)})}}, \tag{10}$$

consecutively. This restricts the energy of the estimate to the measured energy at the estimate location.

Verification of the MS estimation and the new estimation schemes outlined above are detailed below. The verifications include comparisons of partial kinetic energy and the estimation-measurement correlation coefficient. Due to the simplicity of the linear estimation, these quantities (and many others) can be calculated using *only* the statistics required for the coefficient calculation (i.e. the time series do not have to be retained). For example, the partial kinetic energy of the estimated velocity signals can be expressed in terms of the Reynolds stresses given by Eq. (5). Similarly, the estimation-measurement correlation coefficient

$$\rho_{ij} = \frac{\overline{\hat{u}_j(x')u_i(x')}}{[\overline{\hat{u}_j^2(x')u_i^2(x')}]^{1/2}} \tag{11}$$

can be expressed in terms of the optimization data, $\overline{u_i^2(x')}$ and $\overline{u_q(x^{(p)})u_i(x^{(k)})}$, since the estimation-measurement correlation is given by:

$$\overline{\hat{u}_j(x')u_i(x')} = \sum_{p=1}^{n}\sum_{q=1}^{m} A_{jqp}\overline{u_q(x^{(p)})u_i(x^{(k)})} \tag{12}$$

and $\overline{\hat{u}_j^2(x')}$ can be obtained from Eq. (5). By not requiring the calculation of such statistics from entire time series, optimum reference locations can quickly be determined without extensive calculation or data storage costs. Furthermore, the appropriate number of references to be used for time-series estimation can be selected using *only* two-point measurements.

Cole *et al.* (1992) suggested comparison of the partial kinetic energy $(\overline{u_1^2} + \overline{u_2^2})$ in order to quantify the effectiveness of the estimation. The results of such a comparison for two sets of reference locations are shown in Figs. 4a and b. Note that in all figures, the results of the estimation schemes have been designated MS for the traditional mean-square estimate, LS for the new technique requiring the non-linear least-squares fit, and OP for the new technique which maximizes the estimation-measurement correlation coefficient. By taking two reference locations near the center of the mixing layer (Fig. 4a), the traditional stochastic estimate appears to recover a large fraction of the measured energy. This result is consistent with the findings for the jet mixing layer (Cole *et al.* 1992). Unfortunately, most of the energy contribution is from the references and little energy is represented by the estimates. It may also be noted in Fig. 4a that including the estimation covariance to the optimization for this choice of reference locations improves the energy recovery of the estimate very little ($\sim 10\%$). The result of taking reference locations near the edges of the mixing layer is shown in Fig. 4b. The traditional stochastic estimate for these choices of reference locations yield a negligible representation of the energy away from those locations. The estimation proposed here gave a very good representation of the energy; even better than that obtained for more centrally located references (as in Fig. 4a). The reason for the large improvement over mean-square

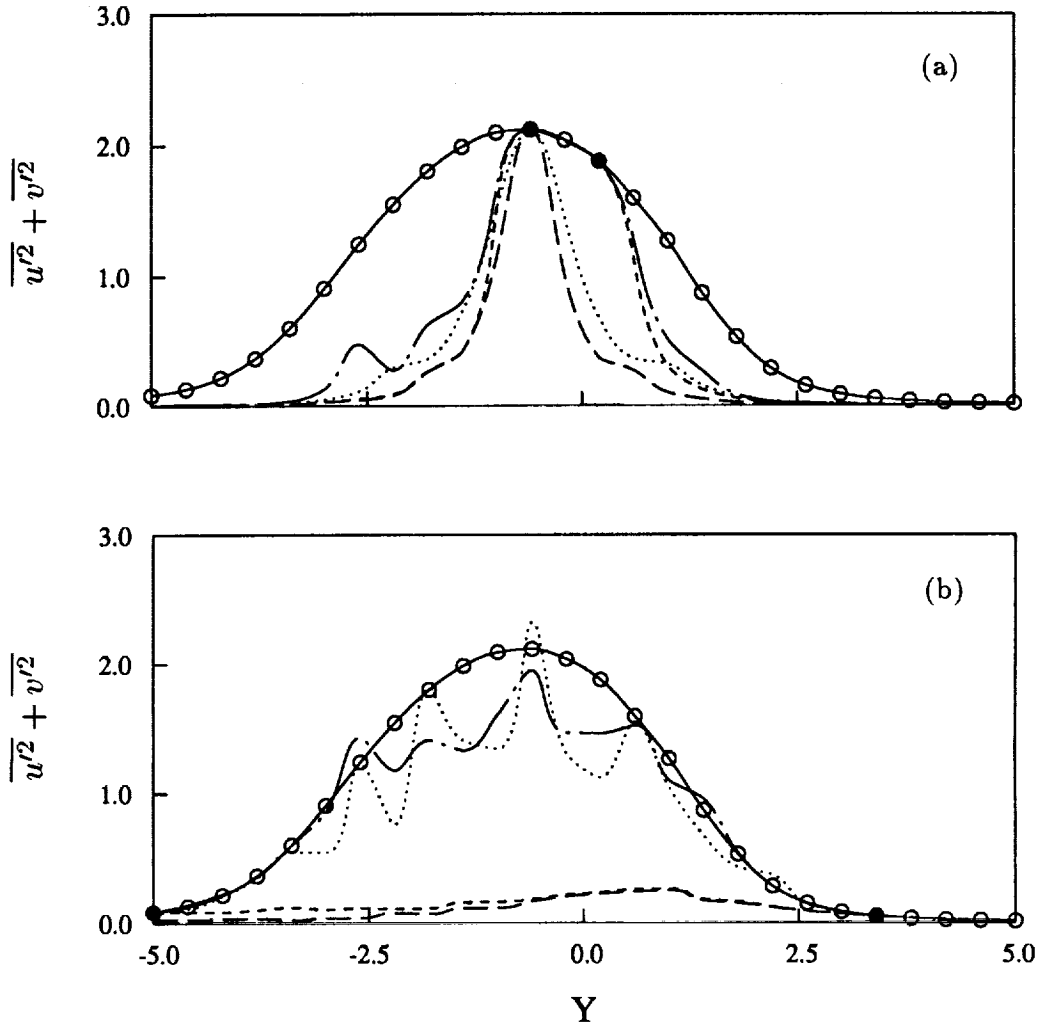

FIGURE 4. Transverse partial kinetic energy comparisons. *(a)* Two-point estimates with references at Y = -0.6 cm and Y = 0.2 cm and one-point estimates with reference at Y = -0.6 cm. *(b)* Two-point estimates with references at Y = -5.0 cm and Y = 3.4 cm and one-point estimates with reference at Y = 3.4 cm, Measured o ; Measured reference • ; Two-point MS ---- ; Two point LS —·— ; One-point MS — — — ; One-point LS ····· ; One-point OP ——— .

estimation for this choice of reference locations is that the estimate-reference cross-correlation is much less than the estimation covariance. Therefore, minimizing the error in both quantities results in a better fit to the estimation covariance (which includes $\overline{u_1^2}$ and $\overline{u_2^2}$). This trade-off does not occur for reference locations near the center of the mixing layer. Consequently, the energy recovery for spanwise profiles

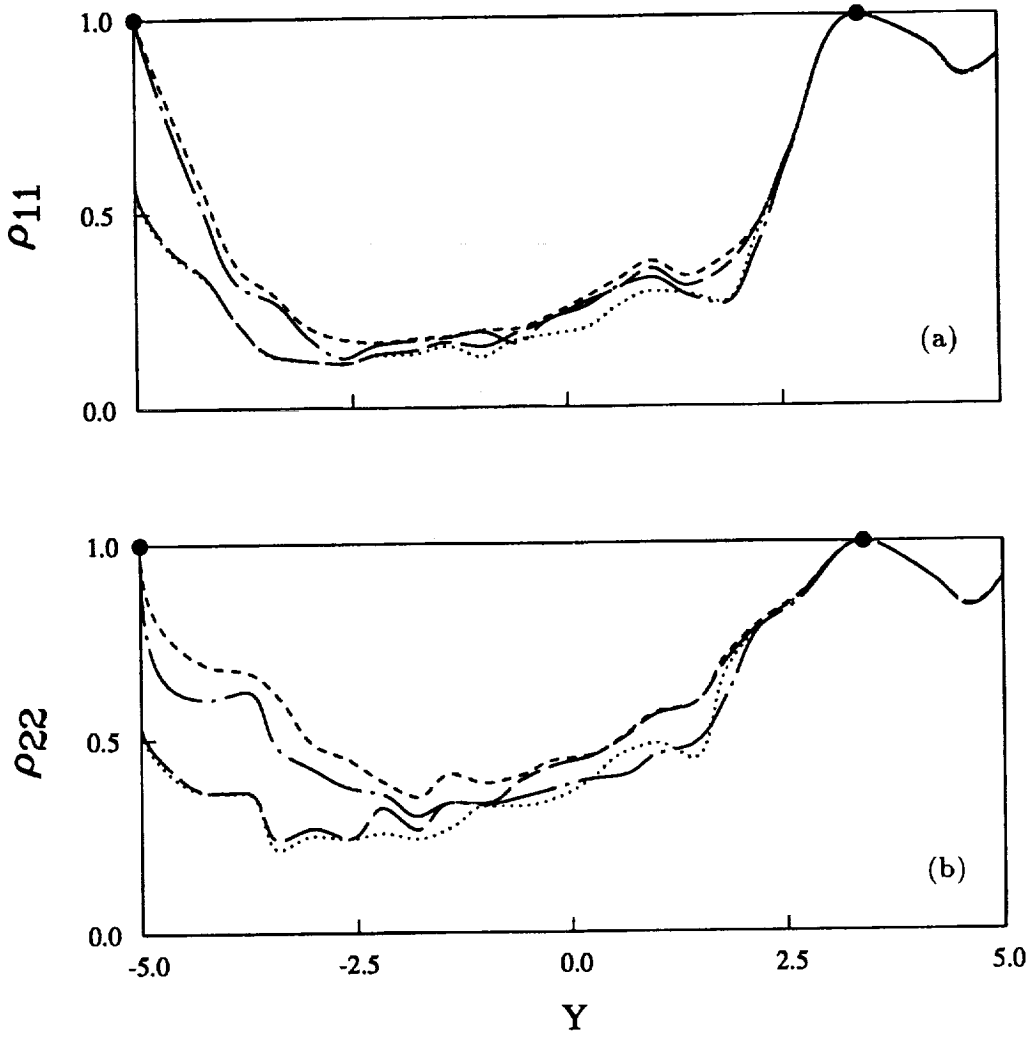

FIGURE 5. Transverse estimation-measurement correlation coefficients. Two-point estimates with references at Y = -5.0 cm and Y = 3.4 cm and one-point estimates with reference at Y = 3.4 cm. *(a)* Streamwise component (u). *(b)* Transverse component (v), Reference • ; Two-point MS ---- ; Two-point LS —·— ; One-point MS ——— ; One-point LS ····· ; One-point OP —— — .

near the center of the mixing layer was very poor for both estimation techniques. By taking spanwise grids near the mixing layer edge, a very good representation of the energy by the new estimation was obtained.

Another measure of the success of an estimation is the correlation coefficient for corresponding estimated and measured velocities at the same location. If an estimated velocity matches the measurement exactly, then the correlation coefficient

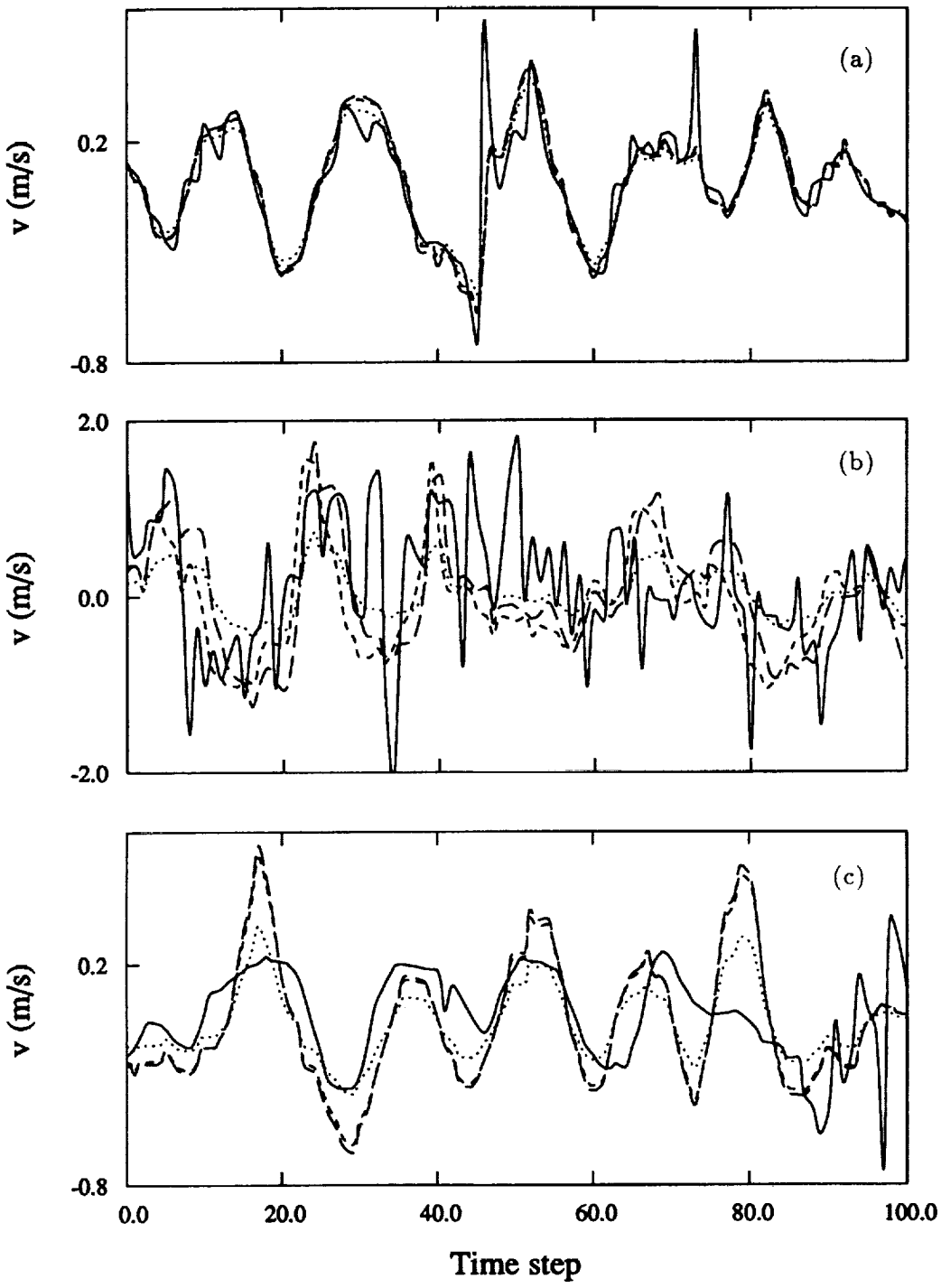

FIGURE 6. Transverse velocity (v) measurement vs. estimate time series comparisons for a reference at Y = 3.4 cm. *(a)* Y = 2.6 cm. *(b)* Y = -0.6 cm. *(c)* Y = -5.0 cm, Measured ——— ; MS ····· ; LS ---- ; OP — — — .

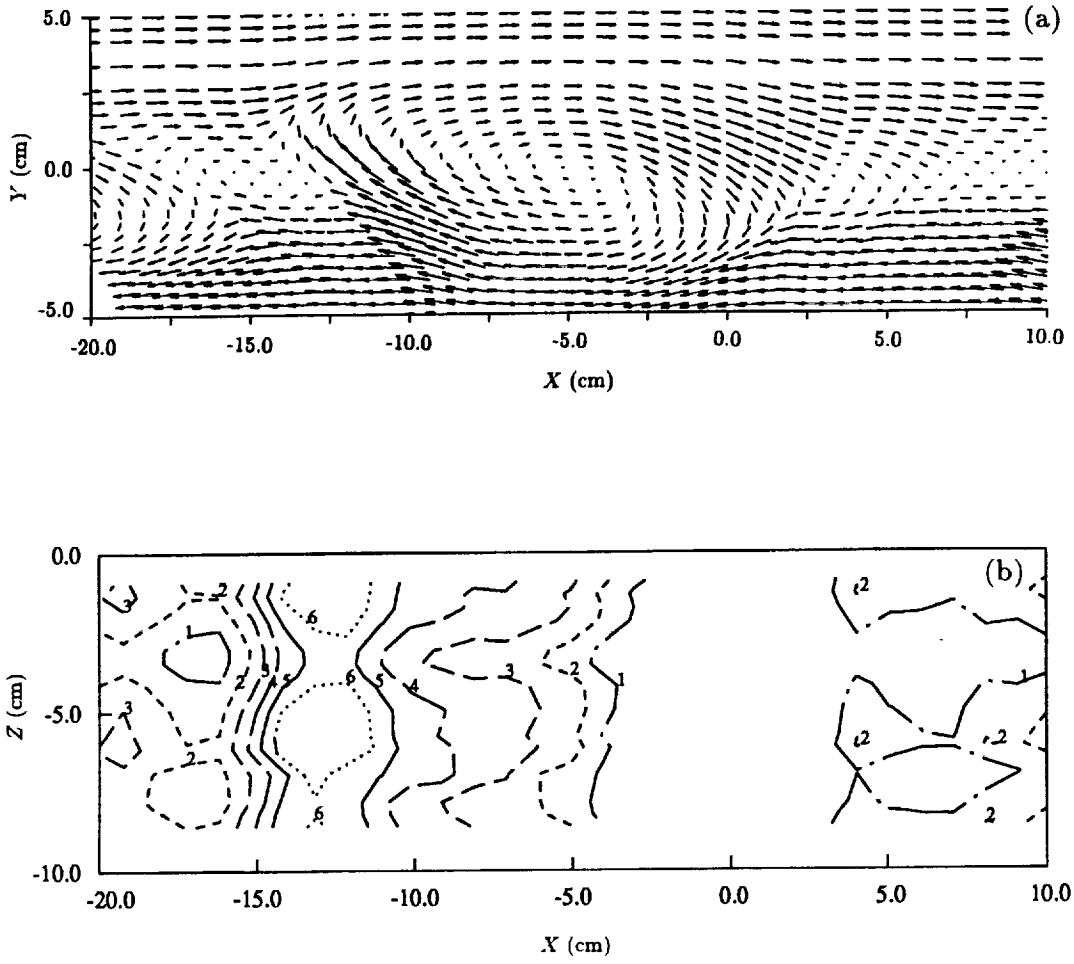

FIGURE 7. Estimated velocity profiles. *(a)* Transverse secondary velocity vectors at Z = -7.0 cm for a reference at Y = -3.4 cm. *(b)* Spanwise profile of transverse velocity at Y = 3.4 cm for references at Z = -5.0 cm and Z = -7.0 cm, starting from -0.1 m/s, incremented 0.08 m/s.

would obviously be equal to one. The results of a calculation of the correlation coefficient for a high speed edge reference are shown in Figs. 5a and b. A high correlation between the estimation and corresponding measurement exists for most of the high-speed side locations. This is reflected in the corresponding time trace comparisons of Fig. 6a. It is no surprise that the low frequency trigger provided by the flow near the mixing layer edge does not yield estimates which are highly correlated with the high frequency signals near the mixing layer center (see Fig. 6b). The low frequency estimate resulting from the technique proposed here is largely an amplified version of the MS estimate. The amplification is a result of an attempt (by the optimization) to match the covariance of the estimate to that of the measured

signal. The estimation of flow on the opposite side of the layer is remarkably good as suggested by the high correlation coefficient for those locations (Figs 5a and b). Presumably, the large-scale structure providing the trigger at the high-speed edge produces similar signatures at the low speed edge, resulting in a good estimation of the flow there (Fig. 6c). The streamwise component time series comparisons were left out for brevity since they were qualitatively similar to the transverse component comparisons of Figs. 6a through 6c.

The results of estimating the one-component simultaneous multi-point velocity profile using the OP method is presented as Fig. 7a. This profile was generated for a transverse grid at Z = -7 cm using a reference at Y = -5 cm. Taylor's hypothesis was used to approximate the spatial development from the temporal signals. This entailed calculating the relative spatial locations of velocity vectors as U_c/fs, where f_s is the sampling frequency and U_c is the mean convection velocity. The secondary velocity vector plot clearly shows the spanwise rollers passing through the measurement station. In spite of the poor representation of the broad-band signals near the center of the mixing layer, the large-scale structure is adequately represented when edge references are selected. In particular, the relationship between the kinematics of the large-scale streamwise and spanwise flow structures can be inferred from simultaneous estimates of velocity profiles on spanwise and transverse grids. For example, using two cross-wire probes makes it possible to estimate three velocity components in one profile (in one direction) and two velocity components in another profile (in another direction) provided the grids have a common reference location. This can be achieved by measuring reference signals u_1 and u_2 (or u_3) at the common grid location and simultaneously measuring u_1 u_3 (or u_2) in the grid for which three velocity components are desired. With the use of such a combination of grid locations, it was possible to estimate the transverse velocity (v) as shown in Fig. 7b. The signature of the streamwise vortices which ride the braid between spanwise vortices appear each time the spanwise vortices carry them through the measurement grid. This gives rise to the juxtaposed spanwise sets of islands in Fig. 7b between time steps -17 and -12. The lack of significant structure to structure spanwise relative motion of this signature observed in longer simultaneous time series profiles is indicative of the low degree of spanwise meander which was also inferred from the correlation measurements.

3. Future plans

During the remainder of the program, phase locked velocity measurements will be obtained by acoustically forcing the mixing layer. The hardware required for this phase of the program has already been prepared. By establishing a periodic sequence of spanwise vortices, it should be possible to examine the detailed structure of the streamwise vortices. By measuring the scale and spacing of the streamwise vorticity in the braid region of the mixing layer vortices, more direct comparisons of the wind tunnel measurements can be made with the direct numerical simulations of the same flow (Rogers, M. M. & Moser, R. D. private communication). In particular, initial conditions (streamwise vortex strength and distribution) will be measured in detail so that they may be used as input to numerical simulations.

During the latter part of the program, some scalar mixing studies using heat to tag one of the streams will also be conducted. An extension of the estimation to include space-time correlations will also be attempted if time permits.

Acknowledgements

This work is being performed in the Fluid Mechanics Laboratory, NASA Ames Research Center in collaboration with Dr. R. D. Mehta.

REFERENCES

ADRIAN R. J. & MOIN, P. 1988 Stochastic estimation of organized turbulent structure: homogeneous shear flow. *J. Fluid Mech.* **190,** 531.

BELL, J. H. 1990 An Experimental Study of Secondary Vortex Structure in Mixing Layers. *Annual Research Briefs.* Center for Turbulence Research, Stanford Univ./NASA Ames, 59-79.

BELL, J. H. & MEHTA, R. D. 1989a Design and Calibration of the Mixing Layer Wind Tunnel. *JIAA TR-84.* Dept. of Aeronautics and Astronautics, Stanford University.

BELL, J. H. & MEHTA, R. D. 1989b Three-Dimensional Structure of Plane Mixing Layers. *JIAA Report TR-90.*

BELL, J. H. & MEHTA, R. D. 1990 Development of a Two-Stream Mixing Layer from Tripped and Untripped Boundary Layers. *AIAA Journal.* **28,** 2034-2042.

BELL, J.H. AND MEHTA, R.D. 1992 Measurements of the Streamwise Vortical Structures in a Plane Mixing Layer. *J. Fluid Mech.* **239,** 213.

BERNAL, L. P. & ROSHKO, A. 1986 Streamwise Vortex Structure in Plane Mixing Layers. *J. Fluid Mech.* **170,** 499-525.

COLE, D. R., GLAUSER, M. N. & GUEZENNEC, Y. G. 1992 An application of the stochastic estimation to the jet mixing layer. *Phys. Fluids A.* **4,** 192.

LEBOEUF, R. L. & MEHTA, R. D. 1992 An Improved Linear Estimation Scheme. *Bulletin of American Physical Society, Division of Fluid Dynamics, 45th Meeting.* also submitted to *Phys. Fluids A.*

TOWNSEND, A. A. 1976 *Structure of Turbulent Shear Flow* (2nd Edition) Cambridge University Press.

Numerical simulation of the non-Newtonian mixing layer

By J. Azaiez [1] AND G. M. Homsy [1]

1. Motivation and objectives

The problem of transition from laminar to turbulent flow in free shear layers is of great practical interest. Many natural and industrial situations involve a free shear flow, and it is very crucial to understand the mechanisms governing the process of transition to turbulence in order to predict and, if possible, control the evolution of the flow. Much past work related to the instability of the mixing layer has dealt exclusively with Newtonian fluids. The interaction between the large scale two-dimensional structures, namely the roll-up and the pairing, and vortex stretching has been explored extensively, leading to a better understanding of the mechanisms of transition to turbulence.

In a wide range of applications, the reduction of hydrodynamic drag is of great importance for reasons of economy and performance. Delaying or accelerating laminar-to-turbulent transition of a free shear layer has many obvious advantages. To delay transition to turbulence as far downstream as possible allows a gain in energy efficiency in some industrial processes. Accelerating the transition, on the other hand, can be of interest in processes where high mixing is desired.

Among the modern techniques for drag reduction are riblets, large-scale eddy breakup devices, and flow suction. Another avenue for drag reduction is the use of polymer additives in the flow. The study of drag reduction obtained by the addition of small amounts of high polymers has been an active area of research for the last three decades (see Sellin and Moses 1989).

This work is a continuing effort to advance our understanding of the effects of polymer additives on the structures of the mixing layer. In anticipation of full non-linear simulations of the non-Newtonian mixing layer, we examined in a first stage the linear stability of the non-Newtonian mixing layer (Azaiez and Homsy 1992). The results of this study show that, for a fluid described by the Oldroyd-B model, viscoelasticity reduces the instability of the inviscid mixing layer in a special limit where the ratio $(\frac{We}{Re})$ is of order 1 where We is the Weissenberg number, a measure of the elasticity of the flow, and Re is the Reynolds number.

In the present study, we will pursue this project with numerical simulations of the non-Newtonian mixing layer. Our primary objective is to determine the effects of viscoelasticity on the roll-up structure. We will also examine the origin of the numerical instabilities usually encountered in the simulations of non-Newtonian fluids.

1 Stanford University

2. Accomplishments

2.1 Problem Definition

We used a vorticity-streamfunction formulation for Cauchy's momentum equation. This equation is closed through evolution equations relating the stress tensor to the shear rate tensor. In all the subsequent analysis, the stress tensor is written as the sum of two stresses:

$$\tau = \tau^s + \tau^p \tag{1}$$

In Eq. (1), the first term corresponds to the contribution of the Newtonian solvent and is proportional to the shear rate tensor:

$$\tau^s \equiv \eta_s \dot{\gamma} \tag{2}$$

where η_s is the solvent viscosity. The second term represents the polymeric contribution:

$$\tau^p \equiv \eta_p a \tag{3}$$

where η_p is the polymeric contribution to the shear viscosity and a is the tensor related to the polymeric stress. Equations for $a(x, y, t)$ define a rheological model and must be given to close the equations. We let $\kappa = \dfrac{\eta_s}{\eta_s + \eta_p} = \dfrac{\eta_s}{\eta}$ be the ratio of viscosities. We fix $\kappa = 0.5$ in all the simulations.

The first step in studying the non-Newtonian behavior of a given flow is the choice of the appropriate constitutive equation required to describe the physics of the non-Newtonian fluid. In the present study, we will focus on two rheological models known to describe dilute polymer solutions: The popular Oldroyd-B model and the FENE model.

We are initially interested in the roll-up of the shear layer into spanwise vortices. The initial base state for the numerical simulations is given by a hyperbolic tangent velocity profile on which we superposed a *cos* perturbation on the stream function with the maximum at the centerline $y = 0$. The most unstable wave number, $\alpha = 0.44$, has been used in all the simulations. The extension of the domain in the streamwise direction is set to $\dfrac{2\pi}{\alpha}\delta$ with δ the momentum thickness of the mixing layer. The vertical extension has been heuristically fixed equal to 8δ. The Reynolds number is defined as $Re = \dfrac{\delta u_0}{\eta}$ where $u_0 = (U_1 - U_2)/2$. U_1 and U_2 are the free-stream velocities.

The vorticity equation and the rheological equations lead to a system of partial differential equations that we solve by a pseudo-spectral method based on the Hartley transform. We use a fourth order Runge-Kutta method to advance the equations for the Hartley coefficients in time.

2.2 The Oldroyd-B model

The Oldroyd-B model describes well the behavior of polymeric liquids composed of a low concentration of high molecular weight polymer in a very viscous Newtonian

solvent at moderate shear rates. These fluids have come to be known as Boger fluids. Data on well-characterized Boger fluids are available (Boger 1977; Mackay & Boger 1987), allowing a comparison of theoretical predictions with experimental results. The Oldroyd-B rheological equations can be derived from a molecular model in which the polymer molecule is idealized as a Hookean spring connecting two Brownian beads (Bird *et al.* 1987).

As above, the stress tensor τ can be written as the sum of two stresses:

$$\tau = \tau^s + \tau^p = \eta[\kappa\dot{\gamma} + (1-\kappa)a]$$

The tensor a satisfies the upper convected Maxwell equation:

$$a_{ij} + \lambda\frac{\delta a_{ij}}{\delta t} = \dot{\gamma}_{ij} \tag{4}$$

where:

$$\frac{\delta a_{ij}}{\delta t} = \frac{\partial a}{\partial t} + \vec{v}\cdot\nabla a - \nabla\vec{v}^{\perp}\cdot a - a\cdot\nabla\vec{v} \tag{5}$$

is the upper-convected derivative of a, and λ is the polymer relaxation time. Using u_o and δ as the reference velocity and the reference length, respectively, Eq. (4) is characterized by one dimensionless group: the Weissenberg number, $We = \frac{\lambda u_o}{\delta}$, a dimensionless measure of the elasticity of the flow. The Oldroyd-B model contains both the upper-convected Maxwell fluid ($\eta_s = 0 \Leftrightarrow \kappa = 0$) and the Newtonian fluid ($\eta_p = 0 \Leftrightarrow \kappa = 1$).

For small values of the Weissenberg number, We, the flow does not show any changes from the Newtonian case. Obviously, viscoelastic terms are not large enough to affect the inertial mechanisms.

As we increase the Weissenberg number, the code starts to develop instabilities and ceases to converge before the completion of the roll-up. Similar problems related to the complexity of the coupling between viscoelastic and inertia effects have been reported by Joseph *et al.* (1985) and Crochet and Delvaux (1990). Numerical instabilities in the simulations of viscoelastic fluids have in fact been the subject of many studies. These studies have in general focused on the Maxwell model, a special case of the Oldroyd-B model, and showed that the absence of the diffusive term in the vorticity equation may be the reason for the blow-up of the numerical schemes. Other studies attribute the breakup of the numerical codes to the reaching of a supercritical regime where the vorticity equation becomes hyperbolic (Joseph (1990)). This regime is reached whenever the viscoelastic Mach number $M = (We\ Re)^{1/2}$ exceeds one. (Crochet and Delvaux (1990))

In the present study, we shall show that the divergence of codes using the Oldroyd-B model is attributed to a relaxation term in the stress equations which plays a major role in the development and growth of the instability. Writing Eq. (5) in component form, we have:

$$\frac{\partial a_{12}}{\partial t} = \underbrace{-\frac{a_{12}}{We}}_{\textit{Damping Term}} \underbrace{-[u\frac{\partial}{\partial x} + v\frac{\partial}{\partial y}]a_{12}}_{\textit{Convective Term}} + \underbrace{\frac{(\partial_{y^2} - \partial_{x^2})\psi}{We} - a_{11}\frac{\partial^2\psi}{\partial x^2} + a_{22}\frac{\partial^2\psi}{\partial x^2}}$$

$$\frac{\partial a_{11}}{\partial t} = \underbrace{\underbrace{[-\frac{1}{We} + 2\frac{\partial^2 \psi}{\partial x \partial y}]}_{1^{st}\ relaxation\ coeff.}}_{Damping\ Term} a_{11} - \underbrace{[u\frac{\partial}{\partial x} + v\frac{\partial}{\partial y}]a_{11}}_{Convective\ Term} + \underbrace{2(\frac{\partial^2{}_{xy}\psi}{We} + a_{12}\frac{\partial^2 \psi}{\partial y^2})}$$

$$\frac{\partial a_{22}}{\partial t} = \underbrace{\underbrace{-[\frac{1}{We} + 2\frac{\partial^2 \psi}{\partial x \partial y}]}_{2^{nd}\ Relaxation\ Coeff.}}_{Damping\ Term} a_{22} - \underbrace{[u\frac{\partial}{\partial x} + v\frac{\partial}{\partial y}]a_{22}}_{Convective\ Term} - \underbrace{2(\frac{\partial^2{}_{xy}\psi}{We} + a_{12}\frac{\partial^2 \psi}{\partial x^2})}$$

We analyzed the evolution of the different terms in the stress equations for various values of the Weissenberg number. We find that the relaxation coefficient behaves differently as we change the Weissenberg number.

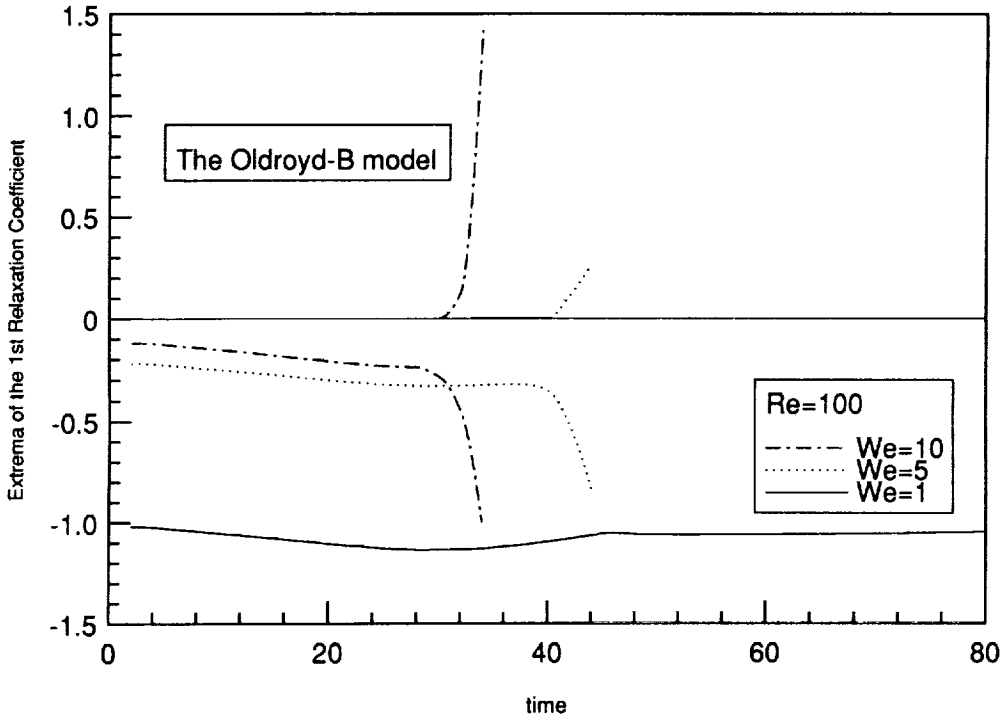

FIGURE 1. Time evolution of the first relaxation coefficient.

The "relaxation coefficients" are spatially dependent and coupled to the vorticity transport equation. Fig. 1 shows the evolution of the minimum and the maximum of the first relaxation coefficient for three different values of We. The blow-up of the code is always associated with positive values of this coefficient. (It is worth mentioning that for another rheological model, the Jeffrey's corotational model, we were able to conduct successful simulations for very large value of We. In fact the relaxation coefficients for this model are all negative and equal to $\frac{-1}{We}$.)

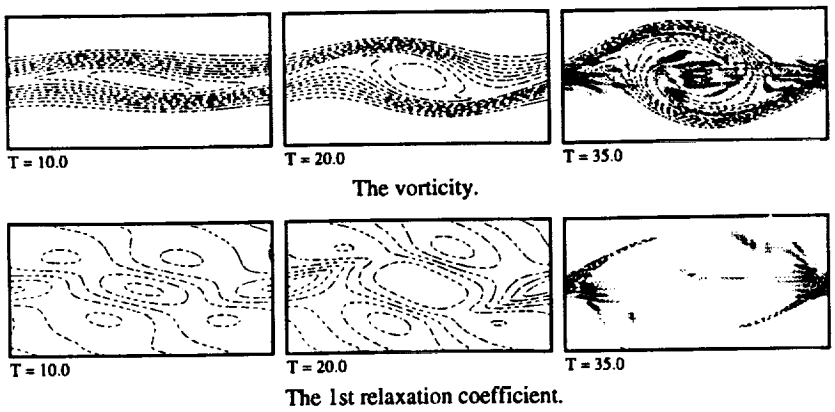

FIGURE 2. Vorticity and 1st Relaxation Coefficient Contours for the Oldroyd-B Model. Re=100,We=5.

The contour plots presented in Fig. 2 show that the regions where the first relaxation coefficient becomes positive correspond to the regions of subsequent numerical instability. In these regions, the a_{11} component of the stress tensor starts to build up, leading to a blow-up of the code. The same results are obtained for the second relaxation coefficient. As a conclusion, it resorts from this analysis that in regions of the flow where the parameter $M = We|(\frac{\partial u}{\partial x} - \frac{\partial v}{\partial y})|$ gets larger than one, the stresses start growing causing the code to blow up. The parameter M involves the elasticity of the polymer and the local normal stress in the flow.

2.3 The F.E.N.E model

The Oldroyd-B model gives a steady state elongational viscosity that goes to infinity at a finite elongational rate. This unlikely behavior results because the Hookean dumbbell model permits infinite extension. In order to avoid this unrealistic behavior, a Warner law is used instead of the Hook law leading to the FENE model. This model is described by Mackay and Petrie (1989) and the rheological equation is:

$$a_{ij}Z + We\frac{\delta a_{ij}}{\delta t} = \dot{\gamma}_{ij} + \frac{DlnZ}{Dt}(\mathbf{I} + a_{ij}We) \tag{6}$$

where $Z = 1 + \frac{n}{b}(1 + \frac{We}{n}a_{ii})$, $n = 2$ for a two dimensional flow. The FENE model is characterized with a third parameter b, related to the nature of the spring used to model the macromolecule. When $b \to \infty$ this rheological model reduces to the Oldroyd-B model. In the numerical solution of Eq. (6), $\frac{DlnZ}{Dt}$ was derived from the transport equation for a_{ii}. The finite extension properties of the FENE model allows full nonlinear simulation of roll-up.

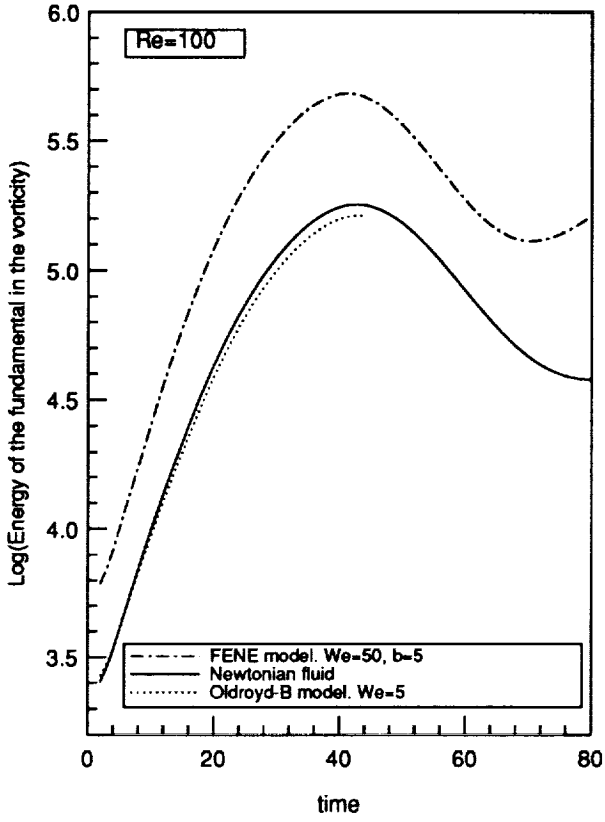

FIGURE 3. Evolution of the energy of the perturbation.

The evolution of the energy in the fundamental is presented in Fig. 3. The region of linear growth shows that the non-Newtonian mixing layer described by the FENE model is more unstable than the Newtonian mixing layer. As we shall see later, the roll-up occurs faster in the non-Newtonian case and the structure of the mixing layer changes from the Newtonian case. This higher instability of the non-Newtonian mixing layer agrees with our linear stability analysis (not discussed here).

Fig. 5 shows contour plots of the vorticity for $Re = 100, We = 50$, and $b = 5$. Notice the changes in the structures of the roll-up as compared to the Newtonian case (Fig. 4). The average value of the vorticity does not differ much from the Newtonian case, but its distribution has clearly changed. Intense accumulation of vorticity tends to occur in the braids and continue into a spiral form within the core of the vortex. The intense gradients of vorticity persist for a longer time in the core, leading to a faster and more intense roll-up.

3. Conclusion and future plans

The simulation of the non-Newtonian mixing layer was very instructive and seems

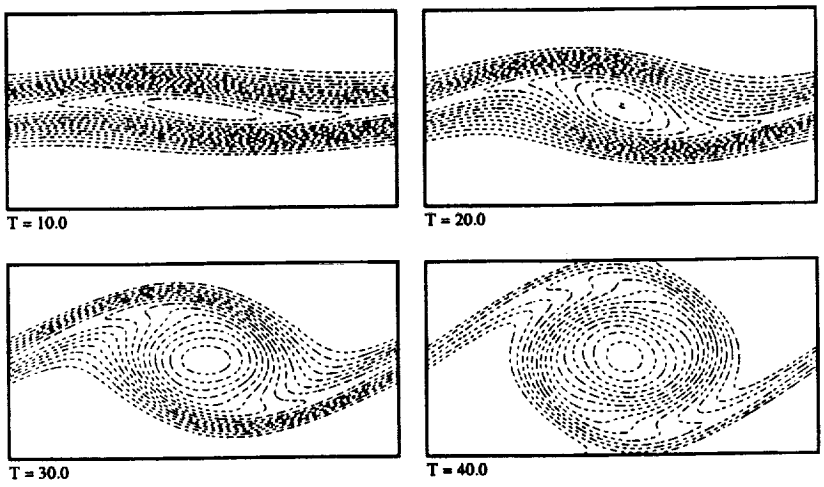

FIGURE 4. Vorticity contours for the Newtonian fluid. Re=100.

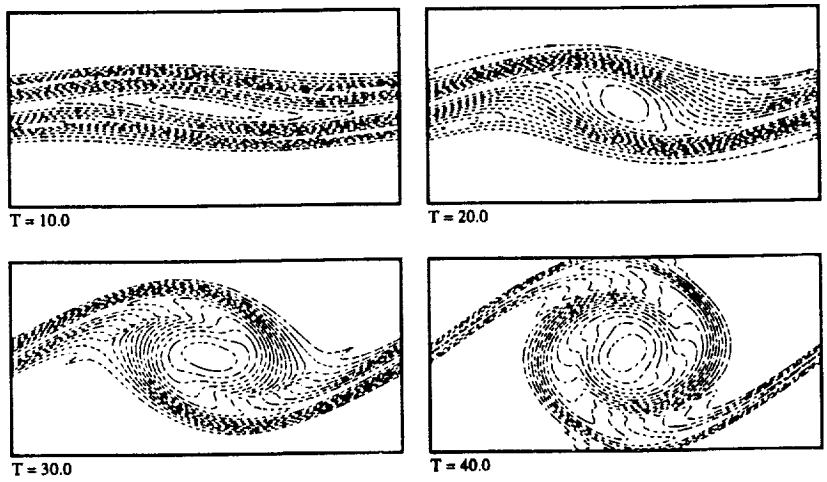

FIGURE 5. Vorticity contours for the FENE model. Re=100, We=50, and b=5.

to be very promising for reaching a better understanding of the mechanisms of instability of the mixing layer and for controlling them through polymer additives. For the Oldroyd-B rheological model, the numerical code ceases to converge whenever one of the relaxation coefficients in the stress equations becomes positive. These coefficients involve the elasticity of the polymer and the extensional stress in the flow. We propose to pursue this analysis in order to understand the physical meaning of these coefficients in terms of the coupling between viscoelastic and inertia effects.

The numerical simulations using the FENE model lead to very interesting results.

For the parameters studied, free shear flows described by this rheological model are more unstable than their Newtonian counterparts and we obtained a fairly good description of the effects of viscoelasticity on the roll-up. The process of roll-up for these flows occurs quickly and induces intense gradients of vorticity in the braids and the core of the flow. The next step of the present study is to study the effects of viscoelasticity on pairing. We will then proceed to examine the effects on vortex stretching and the streamwise vortices of the three dimensional mixing layer.

Acknowledgement

The authors would like to acknowledge useful discussions with Professor Paolo Orlandi.

REFERENCES

AZAIEZ, J., & HOMSY, G. M. 1992 Linear stability of free shear flows of viscoelastic liquids. Submitted to *J. of Fluid Mech.*

BIRD, R. B., CURTISS, C. F., ARMSTRONG, R. C. & HASSAGER, O. 1987 *Dynamics Polymeric Liquids* , vol. 2 2nd edn. Wiley-Intersciences

BOGER, D. V. 1977 A highly elastic constant-viscosity fluid. *J. Non-Newtonian Fluid Mech.* **3,** 87-91.

CROCHET, M. J. & DELVAUX, V. 1990 Numerical simulation of inertial viscoelastic flow with change of type. *I.M.A volumes in Mathematics and its Applications. Vol. 27, p47-66*

JOSEPH, D. D. 1990 *Fluid Dynamics of Viscoelastic Liquids.* Springer-Verlag

JOSEPH, D. D., RENARDY, H. & SAUT., J. C. 1985 Hyperbolicity and change of type in the flow of viscoelastic fluids. *Arch. Rationa. Mech. Anal.* **87,** 213-251

LUMLEY, J. L. 1971 Applicability of the Oldroyd constitutive equations to flow of dilute polymer solutions. *The Physics of Fluids Vol.14, 2282-2284.*

MACKAY, M. E. & BOGER, D. V. 1987 An explanation of the rheological properties of Boger fluids. *J. Non-Newtonian Fluid Mech.* **22,** 235-243.

MACKAY, M. E. & PETRIE, S. J. 1989 Estimates of apparent elongational viscosity using the fibre spinning and pure methods calculations for a FENE-P dumbbell model and comparisons with published data. *Rheological Acta.* **28,** 281-293.

SELLIN, R.H.J. & MOSES, R.T. 1989 *Drag Reduction in Fluid Flows.* Ellis Horwood-Publishers

PDF approach for turbulent scalar field: some recent developments

By Feng Gao

1. Motivation and objectives

The probability density function (PDF) method has been proven a very useful approach in turbulence research. It has been particularly effective in simulating turbulent reacting flows and in studying some detailed statistical properties generated by a turbulent field (see, e.g., Monin & Yaglom 1975, Bilger 1989, Pope 1985 & 1990, Kraichnan 1990, Gao *et al.* 1992).

There are, however, some important questions that have yet to be answered in PDF studies. Our efforts in the past year have been focused on two areas. First, a simple mixing model suitable for Monte Carlo simulations has been developed based on the mapping closure. Secondly, the mechanism of turbulent transport has been analyzed in order to understand the recently observed abnormal PDF's of turbulent temperature fields generated by linear heat sources (Gollub *et al.* 1991, Jayesh & Warhaft 1991).

1.1 Needs for new mixing models in PDF approach

It is well known that the PDF approach provides a closed form representation for the chemical reacting source terms, thus becoming a preferred choice among the available closure models for turbulent reacting flows (O'Brien 1980, Pope 1985). The general argument is that once the PDF of a reacting scalar, ψ, is known, the mean reaction rate, which is the key quantity to be evaluated in reacting flow simulations, can then be readily calculated by

$$\langle S \rangle = \int S(\psi) P(\psi) d\psi.$$

Generally, two approaches have been commonly taken in applying the PDF method, namely, presumed PDF and full PDF methods.

The presumed PDF method assumes a certain form for the PDF with some adjustable parameters, which are supplied by other conventional models (Bray 1980, Borghi 1988, Vervisch 1992). Restricted by the scope of the closure models used (for example $k-\epsilon$ model), the parameters to be adjusted are generally limited to the low order statistics such as mean and variance, thus exposing an important shortcoming of the presumed PDF. In fact, one can construct different PDF's P_1 and P_2 that have the same mean and variance but totally different higher order statistics. If the reaction source term is highly nonlinear (which is true in most cases), the mean reaction rates obtained from P_1 and P_2 may be very different, depending on which PDF form is chosen.

The natural way for obtaining the PDF is the full PDF method which simulates the PDF from its evolution equation. However, a major stumbling block in this approach has been the lack of a proper closure for the diffusion effect (O'Brien 1980, Pope 1985). In order for a model to be accepted in practical simulations, it has to be physically reasonable and numerically easy to implement. Despite the theoretical success the mapping closure enjoys in treating the mixing effect in the PDF approach (Kraichnan 1990, Gao 1991, Pope 1991), it has been shown difficult and computationally intense to implement this closure in simulations (Gao & O'Brien 1991, Valiño & Gao 1992). The most commonly used model for diffusion effect in practical Monte-Carlo simulations remains the LMSE model (Pope 1992) which reads

$$\frac{d\psi_i}{dt} = -\omega(\psi_i - \langle\psi\rangle). \tag{1}$$

It is well known that this model does not relax a PDF. In fact, it can be easily shown that applying this model leads to

$$F_n(t) = \frac{\langle\psi'^n\rangle}{\langle\psi'^2\rangle^{n/2}} = F_n(0),$$

where $\psi' = \psi - \langle\psi\rangle$. Therefore, the PDF so obtained can be very erroneous. This puts us in a rather awkward position. On one hand, we are attempting to use a highly sophisticated approach whose main promise is to provide accurate estimates for mean reaction rates. On the other hand, the PDF could be so contaminated that it does not reflect the true evolution of the fields being considered.

It is, therefore, obvious that in order for the PDF method to live up to its promises, better mixing models which are easy to implement should be developed.

1.2 PDF generated by non-uniform sources

The experiments of Jayesh & Warhaft (1991) and Gollub *et al.*(1991) indicate that the scalar PDF generated by a linear source term exhibits exponential tails. This result is rather surprising because it has generally been believed that the PDF so generated is a Gaussian distribution (Venkataramani & Chevray 1978, Tavoularis & Corrsin 1981). This situation certainly demands a theoretical investigation.

There are three basic processes that determine the distribution of a scalar PDF: the shape of the non-uniform source, the turbulent convection, and the molecular diffusion. A fluid particle leaving the source is convected by the turbulent velocity field to a certain observation point. Because of the chaotic nature of the velocity field, particles from different positions in the source all have certain possibilities of reaching the observation point, thus generating the fluctuations that reflect the characteristics of the source. In the absence of molecular diffusion, the PDF of the scalar is determined by the interaction of the source and the convection.

There are a couple of reasons that justify the neglection of molecular diffusion in search for the mechanism of generating exponential tails. First, it is supported by theoretical arguments and numerical simulations that the molecular diffusion tends to relax a PDF to a Gaussian distribution. Although it has been shown

that the interaction between random turbulent advection and molecular diffusion distorts a Gaussian PDF to generate mild non-Gaussian tails (Gao *et al.* 1992), the clear exponential tails observed in these experiments cannot be explained within the frame of this interaction. Secondly, for high Reynolds (Péclet) number flows, the diffusive effect is very small in comparison with the turbulent transport (Taylor 1935) which is responsible for bring around the fluctuations generated by the non-uniform source.

Based on these arguments, the experiments mentioned earlier can be analyzed explicitly under some idealized conditions. This study suggests a mechanism which seems to provide an explanation for the observed tails.

2. Accomplishments

2.1 A mixing model for PDF simulations

In dealing with turbulent reacting flow problems, it is generally accepted to separate the effects of mixing and reaction by time-splitting schemes. Since the reaction term is closed in PDF formulation, we will concentrate on proper modeling for the mixing effect.

The mapping closure maps a known statistical field ϕ (generally chosen as a multi-variate standard Gaussian field) to a surrogate field $X(\phi,t)$ whose statistics resemble those of the true scalar field ψ (Chen *et al.* 1989). Under homogeneous and non-reacting conditions, the mapping relation is governed by

$$\frac{\partial X}{\partial t} = \omega^*(-\phi\frac{\partial X}{\partial \phi} + \frac{\partial^2 X}{\partial \phi^2}), \tag{2}$$

where ω^* is determined by the time scale of turbulent mixing. It has been shown that this model provides an excellent representation for the mixing effect in the PDF approach (Gao 1991a, Pope 1991).

In spite of its good physics, the mapping closure has posed great difficulties for numerical implementation, as pointed out earlier. The problem stems from the necessity that the fields be re-mapped at each time step, which is computationally intense. This problem worsens drastically as the dimension (number of the scalar quantities) involved increases.

In the model we are proposing, the PDF is represented by a group of representative "particles" which advance in time following certain laws, as is generally used in Monte-Carlo simulations. In case of reaction acting alone, for example, each particle is advanced by

$$\frac{d\psi_i}{dt} = S(\psi_i).$$

The task is, therefore, to develop similar models to describe the mixing effect.

One way to generate such models is to use the mapping solution. It is well known that the general solution for (2) is (Gao 1991a, 1991b)

$$X(\phi,t) = \sum_{n=0}^{\infty} a_n H_n(\frac{\phi}{\sqrt{2}})e^{-n\tau}, \tag{3}$$

where $\tau = \int_0^t \omega^* dt$ and H_n are Hermite functions. The expansion coefficients a_n can be determined as

$$a_n = \frac{1}{\sqrt{2\pi} 2^n n!} \int_{-\infty}^{\infty} X(\phi, 0) H_n(\frac{\phi}{\sqrt{2}}) \exp(-\frac{\phi^2}{2}) d\phi = \frac{1}{2^{n/2} n!} \langle \frac{\partial^{(n)} X}{\partial \phi^{(n)}} \rangle_{t=0}. \quad (4)$$

Clearly, for reasonably well behaved mapping, a_n tends to zero rapidly. Therefore, we expect that a truncation of the right hand side of (3) at a relatively low order

$$X(\phi, t) = \sum_{n=0}^{m} a_n H_n(\frac{\phi}{\sqrt{2}}) e^{-n\tau} \quad (5)$$

can approximate $X(\phi)$ to a satisfactory degree of accuracy.

A group of surrogate particles can be chosen according to (5) to represent the PDF, and each of these particles evolves according to

$$\prod_{i=1}^{m} (\frac{d}{d\tau} + i)(\psi - \langle \psi \rangle) = 0, \quad (6)$$

where $d/d\tau = d/(\omega^* dt)$ and ω^* can be related to the scalar evolution time scale. In fact, if ω in

$$\frac{d\langle \psi'^2 \rangle}{dt} = -\omega \langle \psi'^2 \rangle$$

can be provided by other models, such as the $k - \epsilon$ model, it can be shown that

$$\omega^* = \frac{\omega}{2} \frac{\sum_{n=1}^{\infty} 2^n n! \mu_{n-1}}{\sum_{n=1}^{\infty} n \cdot 2^n n! \mu_{n-1}}, \quad (7)$$

where $\mu_\alpha = (a_{\alpha+1}/a_1)^2 e^{-2\alpha\tau}$. If the truncated form (5) is used, all μ_α where $\alpha \geq m$ should be set to zero.

μ_α can be related to the certain order moments of the field considered. For example, if $m = 3$, it can be shown that

$$\mu_1 = \frac{\sqrt{2}(1 + 4\mu_1^2 + 24\mu_2^2)^{3/2}}{12 + 144\mu_2 + 32\mu_1^2 + 864\mu_2^2} F_3 \quad (8a)$$

and

$$\mu_2 = \frac{F_4(1 + 4\mu_1^2 + 24\mu_2^2)^2 - 3g(\mu_1, \mu_2)}{48(1 + 48\mu_1^2 + 216\mu_2^2)}. \quad (8b)$$

Here F_i are moment coefficients as defined earlier and

$$g(\mu_1, \mu_2) = 1 + 40\mu_1^2 + 336\mu_2^2 + 5952\mu_1^2\mu_2^2 + 80\mu_1^4 + 17856\mu_2^4.$$

These equations can be solved iteratively, and our tests seem to suggest that μ_α are very small and

$$\omega^* \approx \omega/2 \quad (9)$$

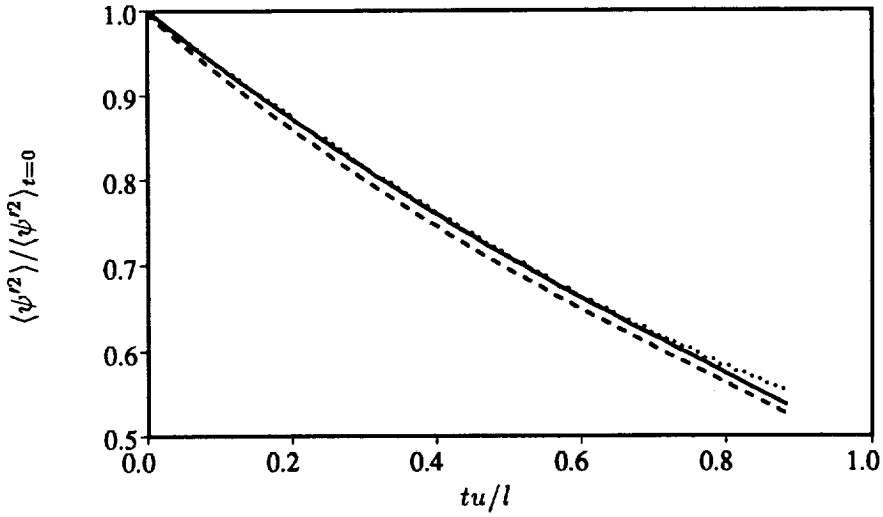

FIGURE 1. Evolution of scalar variance: DNS (dotted line); LMSE (solid line) and current model (dashed line). tu/l is the eddy-turn-over time.

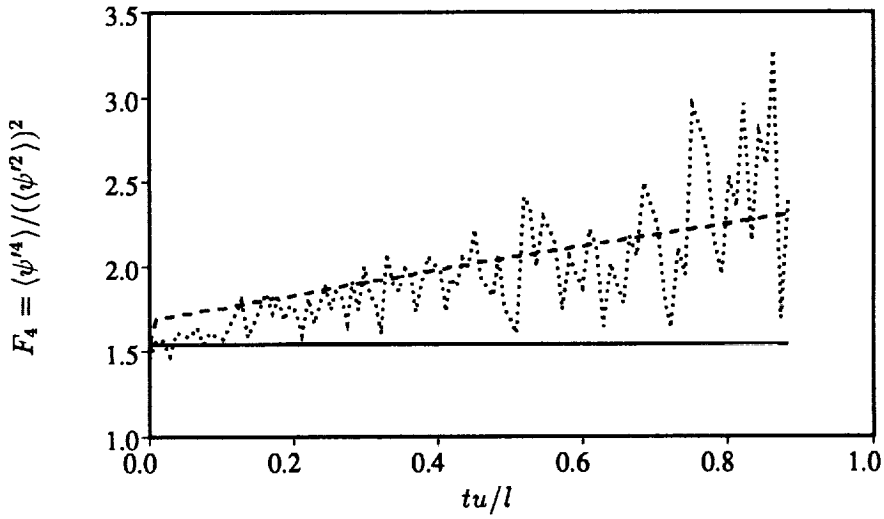

FIGURE 2. Evolution of scalar flatness: DNS (dotted line); LMSE (solid line) and current model (dashed line). tu/l is the eddy-turn-over time.

remains a good approximation. Taking the highly singular double-delta PDF as an example, it can be shown that $\mu_{2\alpha+1} = 0$ (because of symmetry) and $\mu_2 = 1/144$, $\mu_4 = 1/25600$, etc.

It is noticed that if we choose $m = 1$, (6) recovers the equation in the LMSE model (1) and (7) shows that $\omega^* = \omega/2$.

It should be pointed out that in the current model, we are only interested in the

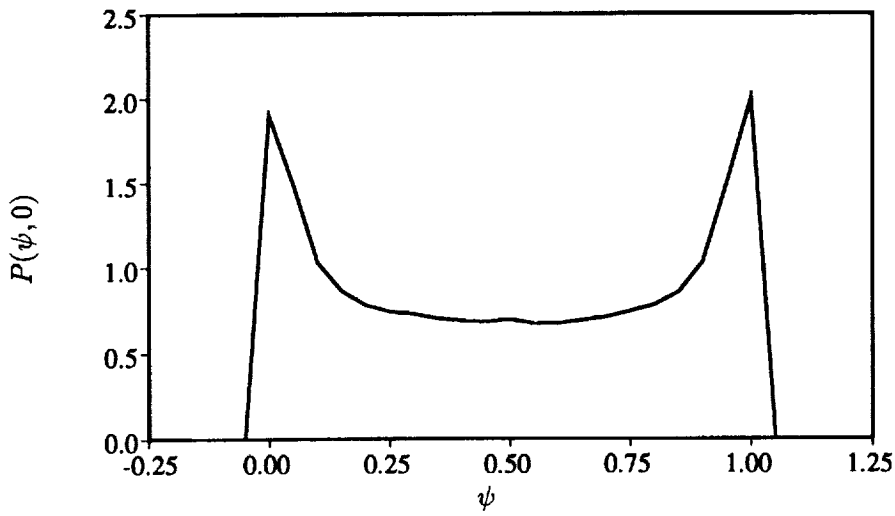

FIGURE 3A. Initial scalar PDF.

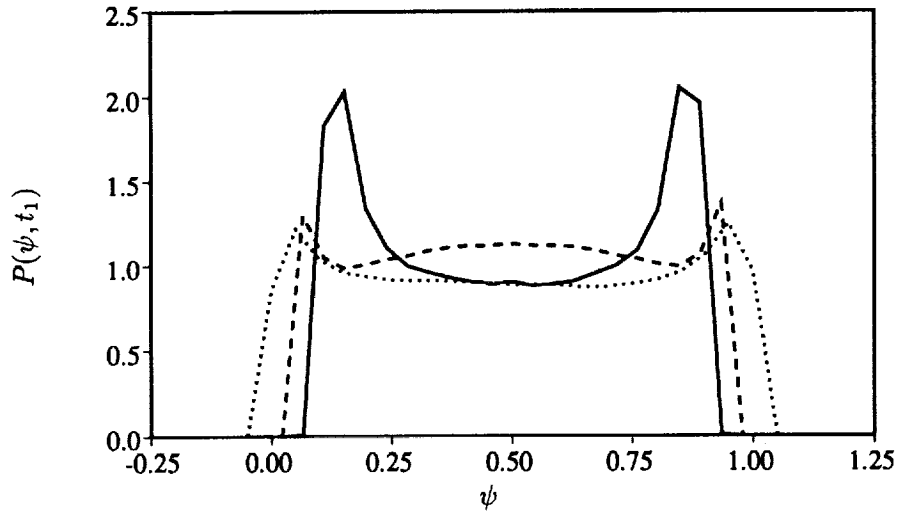

FIGURE 3B. Scalar PDF at $t_1 u/l = 0.178$: DNS (dotted line); LMSE (solid line) and current model (dashed line).

evolution of a group of surrogate particles whose statistics closely resemble those of the true turbulent field. These particles are generally not the fluid particles.

Some tests have been conducted using the model with $m = 3$ and compared with the corresponding cases from DNS and the LMSE model. Figure 1 shows the evolution of scalar variance with ω matched from DNS data. It shows that (8) is indeed a good approximation. Figure 2 exhibits the evolution of the scalar flatness F_4. While the LMSE model clearly does not relax the PDF, the current model catches on the trend of DNS.

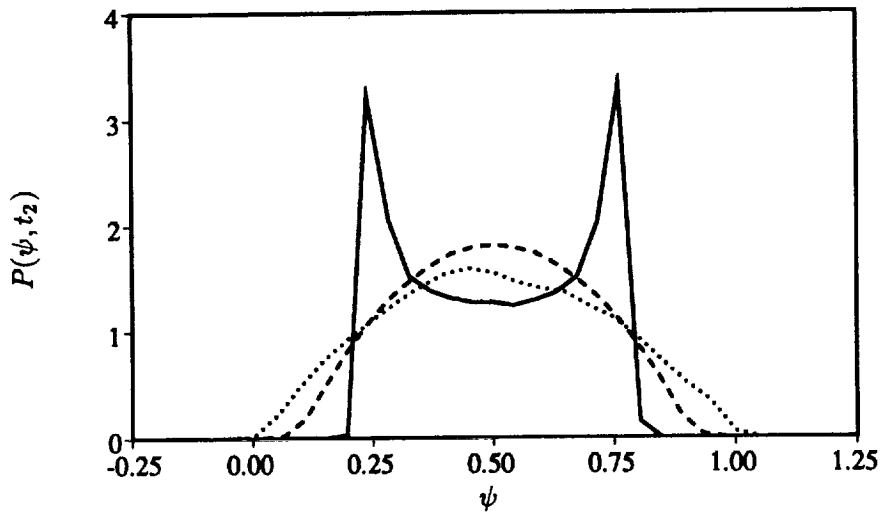

FIGURE 3C. Scalar PDF at $t_2 u/l = 0.685$: DNS (dotted line); LMSE (solid line) and current model (dashed line).

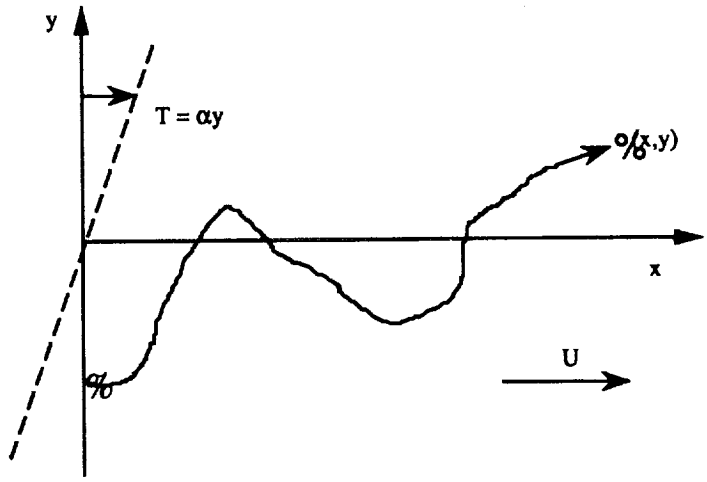

FIGURE 4. Sketch of the system considered.

The plots of PDF evolution perhaps are more revealing. The initial PDF in the model simulations are generated according to that in DNS and normalized in the interval [0,1] (Figure 3(a)). The evolved PDF at two later moments are plotted in Figures 3(b) and 3(c). The improvement achieved by the current model is obvious.

The accuracy of representing the PDF by a collection of surrogate particles depends on the shape of the PDF. Models with better accuracies can be developed along the same line by pushing m higher. However, it is expected that $m = 3$ should suffice for practical simulations.

2.2 PDF of temperature fields generated by a linear heat source

As discussed earlier, the abnormal tails of a scalar PDF are mainly caused by the interaction between the non-uniform source and the random advecting velocity. Let τ_t and τ_d be the time scales of turbulent transport and molecular diffusion, respectively, it is well known that $\tau_d/\tau_t \sim Re$ (Tennekes & Lumley 1973). For high Reynolds number flows, we simply assume that $\tau_d \to \infty$ and $\tau_t \to 0$, namely, neglecting the molecular diffusion and assuming the velocity fluctuation is white in time. The consequences of these simplifications are explained elsewhere (Gao 1992).

Hence, a particle detected at time t at the observation point (x, y) can be traced back to an earlier time τ when it was released from the source at $(0, y_0)$ and acquired the temperature $T(0, y_0; \tau)$ (refer to Figure 4 for a sketch of the system being considered), i.e.

$$x = U(t-\tau) + \int_\tau^t u'dt \qquad \text{and} \qquad y - y_0 = \int_\tau^t u'dt. \tag{10}$$

It can be shown that (Gao 1992)

$$x = U(t-\tau) + \sigma_x\sqrt{t-\tau}r_1 \qquad \text{and} \qquad y - y_0 = \sigma_y\sqrt{t-\tau}r_2, \tag{11}$$

where $\sigma_i^2 = 2u_iL_i$ and r_i are standard independent Gaussian random variables. Here u_i is the variance of velocity and L_i the correlation length in the i direction. The PDF of temperature can be written as

$$P(\hat{T}; x, y, t) = \langle \delta(\hat{T} - T(0, y_0; \tau))_{y_0, \tau \le t}, \tag{12}$$

where the average is taken over all possible particles released from the source prior to t.

Consider the case of linear source, i.e.

$$T(0, y_0; \tau) = \alpha y_0.$$

It can be shown that

$$P(T; x, y, t) = F(T; x, y, t)G(T; x, y, t) \tag{13}$$

where

$$F(T) = \frac{\beta}{2\pi\alpha\sigma}\exp[-\frac{U(\gamma - x)}{\sigma^2}] \tag{14}$$

and

$$G(T) = \frac{1}{2\sigma\gamma^2}\int_{-\infty}^{\infty}\frac{x\xi^2 + 2U\gamma(x+\gamma)}{\sqrt{\xi^2 + 4U\gamma}}\exp(-\xi^2/2\sigma^2)d\xi. \tag{15}$$

Here, $\sigma = \sigma_x$, $\beta = \sigma_x/\sigma_y$ and

$$\gamma^2 = x^2 + \beta^2(\frac{T}{\alpha} - y)^2. \tag{16}$$

It can be demonstrated that

$$\lim_{T\to\infty} \frac{d\ln G}{dT} = 0,$$

hence the main contribution to the tails comes from $F(T)$ which decays exponentially as $T \longrightarrow \infty$.

In linear theory, the fluctuation in x (i.e. r_x) is neglected compare with $U(t-\tau)$. This is equivalent to letting $\sigma \longrightarrow 0$ while keeping $\sigma_y = \sigma/\beta$ finite. In this limit, we have $\beta \longrightarrow 0$. It can be easily shown that

$$F(t) \longrightarrow \frac{1}{2\pi\alpha\sigma_y} \exp[-\frac{U}{2x\sigma_y^2}(\frac{T}{\alpha} - y)^2]$$

and

$$G(T) \longrightarrow \sqrt{\frac{2\pi U}{x}}.$$

Hence,

$$P(T) = \frac{\sqrt{U}}{\sqrt{2x\pi}\alpha\sigma_y} \exp[-\frac{U}{2x\sigma_y^2}(\frac{T}{\alpha} - y)^2],$$

which recovers what would be obtained using the traditional method.

However, this approximation seems to be a rather awkward one because in turbulence, β is generally not small. In fact, in a grid generated turbulence, $u' \sim U$ and $v' \sim 0$ near the grid and $u' \sim v'$ in the later stage. It doesn't seem reasonable to neglect the fluctuation in x direction while keeping the terms of similar or lower order of magnitude in the y direction.

For finite β, we therefore should expect exponential tails under turbulent dispersion at not too distant downstream locations. The exponent can be shown as

$$-\frac{U}{\sigma^2}[\sqrt{x^2 + \beta^2(\frac{T}{\alpha} - y)^2} - x] \sim -\frac{\beta U}{\alpha\sigma^2}T \quad \text{for} \quad T \gg 1.$$

Another limit can be obtained if we look at far downstream locations and finite temperature range. In this limit, $\beta^2(\frac{T}{\alpha} - y)^2/x^2 \ll 1$, hence,

$$-\frac{U}{\sigma^2}[\sqrt{x^2 + \beta^2(\frac{T}{\alpha} - y)^2} - x] \sim -\frac{U}{2x\sigma_y^2}(\frac{T}{\alpha} - y)^2$$

which also recovers the traditional result. This approximation is equally applicable if we have a strong mean scalar gradient. Therefore, if we move the probe to further downstream locations and/or increase the gradient of the scalar source, we will see more Gaussian-like distributions.

Other quantities, such as mean and higher order moments, can be readily calculated. The qualitative features predicted by this idealized model compare favorably with the available experiments. For detailed discussions, please refer to Gao (1992).

3. Future plans

Given the recent exciting developments in large-eddy simulations of turbulent fields (see related reports in this volume), it seems only natural to extend this successful technique to the reacting flow problems. However, despite many attempts, the proper modeling of the reaction source terms remains an unsolved problem. Considering the wide range of different type of reactions encountered in engineering applications, the prospect of developing a suitable sub-grid-scale model for these source terms seems to be grim. The PDF approach can probably be usefully employed to address this problem.

REFERENCES

BILGER, R. W. 1989 Turbulent diffusion flame. *Ann. Rev. Fluid Mech.* **21,** 101-135.

BORGHI, R. 1988 Turbulent combustion modeling. *Prog. Energy Combust. Sci.* **13,** 245-292.

BRAY, K. N. C. 1980 Turbulent flows with premixed reactants. in *Turbulent Reacting Flows.* 115-183, Springer-Verlag.

CHEN, H., CHEN, S. & KRAICHNAN, R. H. 1989 Probability distribution of a stochastically advected scalar field. *Phys. Rev. Lett.* **63,** 2657-2660.

GAO, F. 1991a An analytical solution for the scalar probability density function in homogeneous turbulence. *Phys. Fluids A.* **3,** 511-513.

GAO, F. 1991b Mapping closure and non-Gaussianity of the scalar probability density functions in isotropic turbulence. *Phys. Fluids A.* **3,** 2438-2444.

GAO, F. 1992 Probability distribution of a passive scalar with a mean gradient in homogeneous stationary turbulence (in preparation).

GAO, F., KIMURA, Y. & KRAICHNAN, R. H. 1992 Non-Gaussianity of the scalar probability density function induced by random advection (in preparation).

GAO, F. & O'BRIEN, E. E. 1991 A mapping closure for multi-species Fickian diffusion. *Phys. Fluids A.* **3,** 956-959.

GOLLUB, J. P., CLARKE, J., GHARIB, M., LANE, B. & MESQUITA, O. N. 1991 Fluctuations and transport in a stirred fluid with a mean gradient. *Phys. Rev. Lett.* **67,** 3507-3510.

JAYESH & WARHAFT, Z. 1991 Probability distribution of a passive scalar in grid-generated turbulence. *Phys. Rev. Lett.* **67,** 3503-3506.

KRAICHNAN, R. H. 1990a Intermittent turbulence from closures. *Proc. 6th Beer-Sheva Seminar.* Jerusalem.

KRAICHNAN, R. H. 1990b Models of intermittency in hydrodynamic turbulence. *Phys. Rev. Lett.* **65,** 575-578.

MONIN, A. S. & YAGLOM, A. M. 1975 *Statistical Fluid Mechanics*, MIT press.

O'BRIEN, E. E. 1980 The probability density function (pdf) approach to reacting turbulent flows. in *Turbulent Reacting Flows*. 185-218, Springer-Verlag.

POPE, S. B. 1985 PDF methods for turbulent reactive flows. *Prog. Energy Combust. Sci.* **11**, 119-192.

POPE, S. B. 1990 Computations of turbulent combustion: progress and challenges. *Proc. Int. Symp. Combustion*. 591- , The Combustion Institute, Pittsburgh.

POPE, S. B. 1991 Mapping closures for turbulent mixing and reaction. *Theoret. Comput. Fluid Dynamics*. **2**, 255-270.

POPE, S. B. 1992 PDF method, *Tutorial Lecture*, CTR Summer Program, Stanford Univ./NASA Ames.

TENNEKES, H. & LUMLEY, J. L. 1973 *A First Course in Turbulence*, MIT Press.

TAVOULARIS, S. & CORRSIN, S. 1981 Experiments in nearly homogeneous turbulent shear flow with a uniform mean gradient. Part 1. *J. Fluid Mech.* **104**, 311-347.

VALIÑO, L. & GAO, F. 1992 Monte Carlo implementation of a single-scalar mapping closure for diffusion in the presence of chemical reaction. *Phys. Fluid A.* **4**, 2062-2069.

VENKATARAMANI, K. S. & CHEVRAY, R. 1978 Statistical features of heat transfer in grid-generated turbulence: constant-gradient case. *J. Fluid Mech.* **86**, 513-543.

VERVISCH, L. 1992 see report in this volume.

The evolution equation for the flame surface density in turbulent premixed combustion

By Arnaud Trouvé

1. Motivation and objectives

The mean reaction rate in flamelet models for turbulent premixed combustion depends on two basic quantities: a mean chemical rate, called the flamelet speed, and the flame surface density (Section 1.1). Our previous work had been primarily focused on the problem of the structure and topology of turbulent premixed flames, and it was then determined that the flamelet speed, when space-averaged, is only weakly sensitive to the turbulent flow field (Haworth & Poinsot 1992, Rutland & Trouvé 1991, Trouvé 1991). Consequently, the flame surface density is the key quantity that conveys most of the effects of the turbulence on the rate of energy release. In flamelet models, this quantity is obtained via a modeled transport equation called the Σ-equation. Past theoretical work has produced a rigorous approach that leads to an exact but unclosed formulation for the turbulent Σ-equation (Section 1.2). In the exact Σ-equation, it appears that the dynamical properties of the flame surface density are determined by a single parameter, namely the turbulent flame stretch. Unfortunately, the turbulent flame stretch as well as the flame surface density is not available from experiments, and, in the absence of experimental data, little is known on the validity of the closure assumptions used in current flamelet models.

Direct Numerical Simulation (DNS) is the alternative approach to get basic information on these fundamental quantities. In the present work, three-dimensional DNS of premixed flames in isotropic turbulent flow is used to estimate the different terms appearing in the Σ-equation (Section 1.3). A new methodology is proposed to provide the source and sink terms for the flame surface density, resolved both temporally and spatially throughout the turbulent flame brush (Section 2.1). Using this methodology, our objective is to extract the turbulent flame stretch from the DNS data base and then perform extensive comparisons with flamelet models (Section 2.3). Thanks to the detailed information produced by the DNS-based analysis, it is expected that this type of comparison will not only underscore the shortcomings of current models, but also suggest ways to improve them.

1.1 The flamelet approach for turbulent premixed combustion

Flamelet models constitute one of the most common approaches for turbulent premixed combustion (Bray 1980, Williams 1985, Peters 1986). Such models are very attractive as they conveniently separate the combustion problem from the analysis of the turbulent flow field. These models are based on the "flame sheet" assumption, which requires chemical reaction to occur at fast time scales and short length scales relative to the turbulence. In this situation, the flame is confined to relatively thin layers within the turbulent flow field, and the topology of the

reaction zone corresponds to a surface burning mode. Experimental, theoretical, and numerical evidence suggest that the domain of validity of the flamelet picture is indeed large and that many technologically important reacting flows occur in the flamelet regime.

In the flamelet regime, it is convenient to describe the flame-flow interactions in terms of the following two basic ingredients: a flame speed that characterizes the flame inner structure and the flame front surface area. For instance, the mean reaction rate may be written as a mean integrated chemical rate times the flame surface density:

$$\langle \dot{\omega}_R \rangle = \langle \int \dot{\omega}_R dn \rangle_S \, \langle \Sigma' \rangle, \tag{1}$$

where $\dot{\omega}_R$ is the mass of fuel consumed per unit time and per unit volume; $\int \dot{\omega}_R dn$ is the local integral of the reaction rate along the flame normal direction and characterizes the local combustion intensity; Σ' is the flame surface area per unit volume. The flame surface density is defined as the expected value for Σ': $\Sigma = \langle \Sigma' \rangle$. Note that in Eq.(1), while $\langle\ \rangle$ denotes a standard, unweighted ensemble-average, $\langle\ \rangle_S$ denotes a surface mean, defined as an area-weighted ensemble-average (see Section 1.2).

In Eq.(1), the integral of the reaction rate is simply related to the local fuel consumption speed, S_C, defined as:

$$S_C \equiv \frac{1}{\rho_u Y_{R,u}} \int \dot{\omega}_R dn, \tag{2}$$

where ρ_u and $Y_{R,u}$ are respectively the density and the fuel mass fraction in the unburnt gas. The mean reaction rate may then be expressed as the surface mean of S_C, called the flamelet speed, times the flame surface density:

$$\langle \dot{\omega}_R \rangle = (\rho_u Y_{R,u} \langle S_C \rangle_S) \, \Sigma. \tag{3}$$

Eq.(3) is the classical flamelet expression for the ensemble mean of the reaction rate. In general, this mean reaction rate is a function of both position and time, $\langle \dot{\omega}_R \rangle(\mathbf{x}, t)$. An overall reaction rate can also be obtained by space-averaging Eq.(3) over an arbitrary volume, V, that encloses the reaction zone:

$$\overline{\langle \dot{\omega}_R \rangle}(t) \equiv \frac{1}{V} \int \langle \dot{\omega}_R \rangle(\mathbf{x}, t) dV = (\rho_u Y_{R,u} \overline{S}_C(t)) \, \frac{S_V(t)}{V}, \tag{4}$$

where $S_V(t)$ is the total flame surface area within the volume V, $S_V(t) = \int \Sigma dV$; and $\overline{S}_C(t)$ is a mean fuel consumption speed, $\overline{S}_C(t) = \int \langle S_C \rangle_S \, \Sigma dV / \int \Sigma dV$. $\overline{S}_C$ can also be expressed as the area-weighted, space-averaged value of S_C integrated along the turbulent flame surface: $\overline{S}_C = \int S_C \, \delta A / \int \delta A$, where δA designates the area of an infinitesimal flame element and where integration takes place along the flame surface. $\overline{S}_C$ and S_V are global flame properties and are simply related to the turbulent flame speed (see Section 2.2).

The flamelet speed, $\langle S_C \rangle_S$, in Eq.(3) and the mean fuel consumption speed, $\overline{S}_C$, in Eq.(4) account for local variations of the reaction rate along the flame surface. Laminar flame theory indicates that the local flame structure is modified by flow divergence, usually characterized by the strain rate acting in the flame tangent plane as well as by flame front curvature (Clavin 1985, Williams 1985). Under certain conditions, these variations can become critical and lead to partial or total quenching of the flame. Recent studies using DNS, however, suggest that quenching is a rather unlikely event for turbulent premixed flames (Poinsot *et al.* 1991). In addition, although the local combustion intensity may exhibit large fluctuations along the turbulent flame front, particularly for non-unity Lewis number flames, and although these fluctuations may in turn result in strong spatial variations of the flamelet speed, $\langle S_C \rangle_S$, across the turbulent flame brush, DNS suggest that these departures from the laminar consumption rate always tend to cancel in the mean (Haworth & Poinsot 1992, Rutland & Trouvé 1991, Trouvé 1991). In the simulations, the mean fuel consumption speed, $\overline{S}_C$, remain within 10% to 30% from the one-dimensional, laminar flame speed value, s_L.

Thus, it appears that in the absence of quenching, the mean fuel consumption speed, $\overline{S}_C$, is only weakly sensitive to the flow field, and the principle effect of turbulence is for the fluctuating velocity field to wrinkle the flame and greatly increase its surface area. This phenomenon accounts for most of the increase in the overall burning rate due to the turbulence and is represented in Eq.(3) through the flame surface density, Σ.

1.2 The evolution equation for the flame surface density, Σ

In current flamelet models, the flame surface density, Σ, is obtained via a modeled transport equation. This equation was first postulated by Marble & Broadwell (1977) based on phenomenological grounds. A more rigorous approach was later proposed by Pope (1988) and Candel & Poinsot (1990) who derive an exact balance equation for the flame surface-to-volume ratio, Σ':

$$\frac{\partial \Sigma'}{\partial t} + \nabla.\dot{\mathbf{X}}\Sigma' = (\nabla.\dot{\mathbf{X}} - \mathbf{nn} : \nabla\dot{\mathbf{X}})\ \Sigma', \tag{5}$$

where $\dot{\mathbf{X}}$ is the displacement speed of the flame surface, given by the sum of the fluid velocity and the flame propagation speed in the normal direction: $\dot{\mathbf{X}} = \mathbf{u} + w\mathbf{n}$; $\mathbf{n}$ is the unit vector normal to the flame surface; and where we use tensorial notations: $(\mathbf{nn} : \nabla\dot{\mathbf{X}}) = n_i n_j \frac{\partial \dot{X}_i}{\partial x_j}$.

The right-hand side of Eq.(5) can also be expressed in terms of flame stretch. The flame stretch, k, is defined as the rate of change of a Lagrangian flame surface element, δA:

$$k = \frac{d(\delta A)}{dt} = \frac{\partial(\delta A)}{\partial t} + \dot{\mathbf{X}}.\nabla(\delta A). \tag{6}$$

A more useful expression for k is in terms of strain rate, flame curvature, and flame propagation speed (see for example Candel & Poinsot 1990):

$$k = a_T + 2wk_m, \tag{7}$$

where a_T is the rate of strain acting in the flame tangent plane: $a_T = \nabla.\mathbf{u} - \mathbf{nn} : \nabla\mathbf{u}$; and k_m is the flame surface curvature, as given by the divergence of the flame normal direction: $2k_m = \nabla.\mathbf{n}$. In Eq.(7), positive curvature is chosen convex towards the reactants.

Using Eq.(7), the balance equation for the flame surface-to-volume ratio can be re-written as:

$$\frac{\partial \Sigma'}{\partial t} + \nabla.\dot{\mathbf{X}}\Sigma' = k\ \Sigma'. \tag{8}$$

When ensemble-averaged, this equation yields an exact balance equation for the flame surface density (Pope 1988, Cant *et al.* 1990):

$$\frac{\partial \Sigma}{\partial t} + \nabla.\langle\dot{\mathbf{X}}\rangle_S \Sigma = \langle k\rangle_S\ \Sigma, \tag{9}$$

where the flame surface mean of any quantity Q is given by: $\langle Q\rangle_S = \langle Q\Sigma'\rangle/\langle\Sigma'\rangle = \langle Q\Sigma'\rangle/\Sigma$. Note that surface means are different from standard means. In particular, the surface mean of a quantity Q is different from the ensemble mean of Q conditioned on being at the flame location (see Section 2.1).

Eq.(9) can be cast in various forms. For modeling purposes, it is useful to split the velocity vector into a mean component and a turbulent fluctuation: $\mathbf{u} = \langle\mathbf{U}\rangle + \mathbf{u}'$. We can then re-write Eq.(9) as follows:

$$\frac{\partial \Sigma}{\partial t} + \nabla.\langle\mathbf{U}\rangle\Sigma + \nabla.\langle\mathbf{u}'\rangle_S\Sigma + \nabla.\langle w\mathbf{n}\rangle_S\Sigma = \langle a_T\rangle_S\ \Sigma + \langle A_T\rangle_S\ \Sigma + 2\langle wk_m\rangle_S\ \Sigma, \tag{10}$$

where we use the following notations:

$$\langle a_T\rangle_S = \langle\nabla.\mathbf{u}' - \mathbf{nn} : \nabla\mathbf{u}'\rangle_S,$$

$$\langle A_T\rangle_S = \nabla\langle\mathbf{U}\rangle - \langle\mathbf{nn}\rangle_S : \nabla\langle\mathbf{U}\rangle.$$

The three convective terms on the left-hand side of Eq.(10) are transport terms that correspond respectively to convection by the mean flow, turbulent diffusion, and flame propagation. The terms on the right-hand side of the equation are the source and sink terms for the flame surface density: $\langle a_T\rangle_S$ is the turbulent strain rate acting in the flame tangent plane, $\langle A_T\rangle_S$ is the strain rate due to the mean flow field, and $2\langle wk_m\rangle_S$ is a term that accounts for the combined effects of flame curvature and flame propagation.

Eq.(10) is an exact expression of the evolution equation for the flame surface density, Σ, in a turbulent flow field. Unfortunately, many terms remain unclosed in this exact turbulent Σ-equation. Modeling assumptions are, therefore, required, in particular to calculate the turbulent diffusion term and the turbulent flame stretch. Different formulations of the modeled Σ-equation have been proposed in the literature (Marble & Broadwell 1977, Darabiha *et al.* 1987, Maistret *et al.* 1989, Candel *et al.* 1990, Cant *et al.* 1990, Borghi 1990, Mantel & Borghi 1991). However, since the turbulent flame stretch as well as the flame surface density is not available

from experiments, little is known on the validity of the closure assumptions used in current flamelet models. DNS is an attractive alternate approach to get basic information on these fundamental quantities. In the present work, three-dimensional DNS of premixed flames in isotropic turbulent flow is used to estimate the different terms appearing in the Σ-equation, with particular emphasis on the source and sink terms on its right-hand side that determines production or dissipation of flame surface area.

1.3 Direct Numerical Simulation of turbulent premixed flames

We use DNS to analyze the different terms in the equation for the flame surface density. The simulations are performed using a three-dimensional, compressible Navier-Stokes solver that fully resolves the turbulent flow field. Spatial derivatives are computed with a modified Padé scheme that is sixth-order accurate (Lele 1992). Solutions are advanced in time using a third-order Runge-Kutta method (Wray 1990). Boundary conditions are specified using the NSCBC method (Poinsot & Lele 1992). Because of the otherwise prohibitive computational cost, simulations are limited to simple but finite-rate reaction schemes. In this work, the chemistry model is a single step, irreversible chemical reaction where the reaction rate depends exponentially on temperature (Arrhenius kinetics):

$$\dot{\omega}_R = B\rho Y_R \exp\left(-\frac{T_a}{T}\right), \tag{11}$$

where T_a is the activation temperature and B a constant that depends on the selected flame speed. This formulation corresponds to a binary reaction in which one of the reactants, Y_R, is strongly deficient as, for example, in fuel-lean combustion. Also, it is worth emphasizing that the simulations are not limited by the constant density assumption, and heat release effects are fully accounted for.

Following Williams (1985), we re-write the reaction rate as:

$$\dot{\omega}_R = \Lambda\rho Y_R \exp\left(\frac{-\beta(1-\Theta)}{1-\alpha(1-\Theta)}\right), \tag{12}$$

where Θ is the reduced temperature, $\Theta = (T - T_u)/(T_b - T_u)$; T_u is the temperature of the fresh reactants; T_b is the adiabatic flame temperature; and the coefficients Λ, α, and β are, respectively, the reduced pre-exponential factor, the heat release factor, and the reduced activation energy:

$$\Lambda = B\exp(-\beta/\alpha), \quad \alpha = (T_b - T_u)/T_b, \quad \text{and} \quad \beta = \alpha T_a/T_b. \tag{13}$$

In the following, we use $\alpha = 0.75$ and $\beta = 8$.

Another important feature of the simulations is that the transport coefficients are temperature dependent. These coefficients satisfy the following relations:

$$\mu = \mu_u(T/T_u)^b\ ,\ Le = \lambda/\rho D c_p = \text{constant},\ Pr = \mu c_p/\lambda = \text{constant}, \tag{14}$$

where μ, λ, and D are the molecular diffusivities of, respectively, momentum, internal energy, and species mass, b is a constant, and Le and Pr are, respectively, the Lewis number and the Prandtl number. We use $b = 0.76$, $Pr = 0.75$. Simulations have been performed for different Lewis numbers, $Le = 0.8, 1.0$, and 1.2.

The selected computational configuration corresponds to a premixed flame embedded in a three-dimensional, decaying, isotropic turbulent flow. The left- and right-hand sides of the computational domain are inflow and outflow boundaries, while periodic boundary conditions are applied at lateral walls. The calculations are initialized with fresh reactants on one side of the domain and burnt products on the other side; the two are separated by a plane laminar flame. Isotropic turbulence is initially located in the flow of fresh reactants, its velocity field being specified according to a model spectrum. The turbulence is characterized by a Kolmogorov length scale smaller than the thermal thickness of the laminar flame, $\eta_k/\delta_T = 0.1$ where $\delta_T = (T_b - T_u)/(dT/dx)_{max}$, and a turbulence intensity that is much higher than the laminar flame speed, $u'/s_L = 10$. The initial turbulent Reynolds number, based on the Taylor microscale, is 50. The initial turbulent Reynolds number, based on the integral length scale, is 70. The grid resolution is 129^3.

The simulations describe the wrinkling of the flame zone due to turbulent motions as well as the combustion feedback due to dilatation and temperature-dependent transport properties. Note that the turbulence is decaying in time, and flow conditions are non-stationary.

2. Accomplishments

2.1 Diagnostics

All terms appearing in Eq.(10) can be obtained from the simulations. We now briefly describe how. The velocity vector and the velocity gradient tensor are readily obtained from the resolved flow field. To define flame-based quantities, we make use of concepts based on the thin flame picture. First, a progress variable, c, is introduced to indicate location within the reaction zone, $c = 1 - Y_R$, where Y_R is the normalized fuel mass fraction. The progress variable varies monotonically through the flame from 0 in the reactants to 1 in the products. Constant progress variable surfaces may conveniently be used to define the flame front location: we use the surface $c = c_f = 0.8$. In addition, at any location on this surface, the local gradient of c defines the normal direction to the flame front:

$$\mathbf{n} = -\frac{\nabla c}{|\nabla c|}, \tag{15}$$

where $\mathbf{n}$ points into the fresh reactants.

The propagation speed of the flame surface, w, is obtained from an expression analog to the well-known field equation (also called the G-equation, see for example Kerstein *et al.* 1988). Let us first consider a point on the flame surface, $c = c_f$. The velocity, $\dot{\mathbf{X}}$, at which this point must move to remain on the surface, is given by:

$$\frac{\partial c}{\partial t} + \dot{\mathbf{X}}.\nabla c = 0, \tag{16}$$

which, using Eq.(15), implies that:

$$\dot{\mathbf{X}}.\mathbf{n} = \frac{1}{|\nabla c|}\frac{\partial c}{\partial t}, \tag{17}$$

and yields the following expression for the flame propagation speed:

$$w = \dot{\mathbf{X}}.\mathbf{n} - \mathbf{u}.\mathbf{n} = \frac{1}{|\nabla c|}\frac{Dc}{Dt}, \tag{18}$$

where the quantities are estimated at the surface $c = c_f$. In the simulations, we solve for a conservation equation for the fuel mass fraction, Y_R, and since by definition $c = 1 - Y_R$, the expression above can be readily obtained from the DNS data base.

The flame surface density, Σ, is a more subtle quantity. It includes both geometrical and statistical information. Following Pope (1990), the flame surface density is expressed as the product of the expected value for the magnitude of the gradient of c, conditioned on being on the flame surface, times the probability of being on that surface:

$$\Sigma' = |\nabla c|\ \delta(c - c_f), \quad \text{and} \quad \Sigma = \langle \Sigma' \rangle = \langle |\nabla c| \mid c = c_f \rangle\ p(c_f), \tag{19}$$

where $p(c_f)$ is the probability of $c = c_f$. An equivalent expression for Σ, also proposed by Pope (1990), is in terms of the joint probability of the scalar c and the magnitude of its gradient:

$$\Sigma = \int_0^\infty \gamma p(c_f, \gamma) d\gamma, \tag{20}$$

where $\gamma = |\nabla c|$.

We now turn to the averaging problem. In the simulations, the flame brush propagates along the x direction, and the problem remains homogeneous in the $y - z$ planes. Therefore, averaged quantities depend on x and time t only, and ensemble-averaging can be performed in the $y - z$ planes:

$$\langle Q \rangle(x,t) = \frac{1}{L_y L_z}\int Q(x,y,z,t) dy dz, \tag{21}$$

where L_y and L_z are the y and z dimensions of the computational domain. Since the flow field is non-stationary, time-averaging cannot be used and the present analysis is based exclusively on the slicing of the DNS data base in planes perpendicular to the direction of mean flame propagation.

Let us now consider a particular $y - z$ plane, $x = x_0$. In that plane, the flame contour $c = c_f$ is a set of closed lines. The flame surface density as well as the various surface and conditional means in the analysis can be expressed in terms of line-integrals along this $(c = c_f, x = x_0)$ line-contour. For instance, as suggested by Eq.(20), the flame surface density, Σ, can be obtained via the joint probability

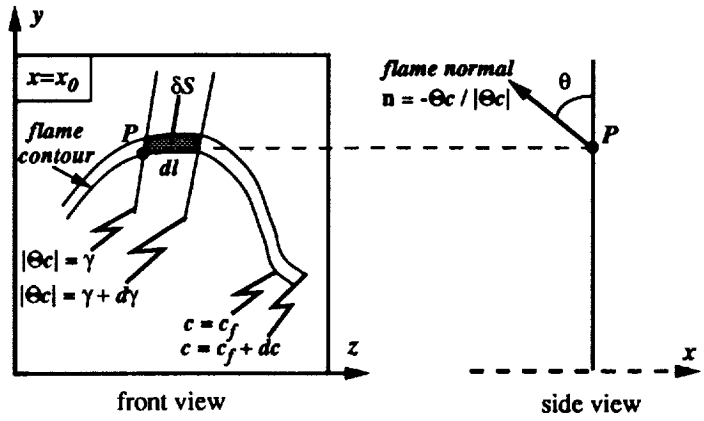

FIGURE 1. A geometrical expression for the joint probability of the progress variable and the magnitude of its gradient in a given $y-z$ plane: $p(c_f,\gamma)\ dc\ d\gamma = prob(c_f \le c \le c_f + dc; \gamma \le |\nabla c| \le \gamma + d\gamma) = \delta S\ /\ L_y L_z$, see Eq.(22).

$p(c_f,\gamma)$. Simple geometrical considerations lead to the following relation (Figure 1):

$$p(c_f,\gamma)d\gamma = \frac{1}{L_y L_z} \sum_{j=1}^{J} \frac{dl}{\gamma\,|cos\theta|}, \tag{22}$$

where dl designates the arc-length of an infinitesimal flame element on the line-contour $c = c_f$ and θ is a measure of the orientation of this flame element with respect to the $x = x_0$ plane. In Eq.(22), summation is over all occurrences of the event $(c, |\nabla c|) = (c_f, \gamma)$. Eqs.(20) and (22) then give the following expression for Σ:

$$\Sigma = \frac{1}{L_y L_z}\int_{c=c_f} \frac{dl}{|cos\theta|} = \frac{1}{L_y L_z}\int_{c=c_f} \frac{|\nabla c|}{\sqrt{(\frac{\partial c}{\partial y})^2 + (\frac{\partial c}{\partial z})^2}} dl, \tag{23}$$

where we use the geometrical relation: $|cos\theta| = \sqrt{(\frac{\partial c}{\partial y})^2 + (\frac{\partial c}{\partial z})^2}/|\nabla c|$.

Eq.(23) differs from the original formulation proposed by Trouvé & Poinsot (1992) due to an error in their original expressions for surface means and conditional means. However, their estimate of the probability $p(c_f)$ remains unchanged:

$$p(c_f) = \int_0^\infty p(c_f,\gamma)d\gamma = \frac{1}{L_y L_z}\int_{c=c_f} \frac{dl}{|cos\theta|\,|\nabla c|} = \frac{1}{L_y L_z}\int_{c=c_f} \frac{dl}{\sqrt{(\frac{\partial c}{\partial y})^2 + (\frac{\partial c}{\partial z})^2}}, \tag{24}$$

and, compared to the new formulation, the results of Trouvé & Poinsot (1992) still hold within a few percents.

Using Eq.(22), the correct expression for conditional means is as follows:

$$\langle Q \mid c = c_f\rangle(x,t) = \frac{\int_{c=c_f} Q\ (|cos\theta|\,|\nabla c|)^{-1}\ dl}{\int_{c=c_f} (|cos\theta|\,|\nabla c|)^{-1}\ dl}. \tag{25}$$

The surface means are then obtained using the following relations:

$$\langle Q \rangle_S(x,t) = \frac{\langle Q\Sigma' \rangle}{\langle \Sigma' \rangle} = \frac{\langle Q|\nabla c| \mid c = c_f \rangle}{\langle |\nabla c| \mid c = c_f \rangle} = \frac{\int_{c=c_f} Q \, |cos\theta|^{-1} \, dl}{\int_{c=c_f} |cos\theta|^{-1} dl}. \tag{26}$$

Clearly, surface means differ from conditional means.

The relations above provide a methodology to estimate the different means needed in our analysis. The accuracy of these expressions depends on the size of the computational domain with respect to the turbulent length scales. In the simulations, the integral length scale of the turbulent flow field grows as the kinetic energy decays; this growth, however, is rather slow, and it has been determined that the integral length scale remains at least 8 times smaller than L_y and L_z. Although we recognize that the statistics are somewhat undersampled, reasonable accuracy is expected when estimating the first moments.

2.2 Global flame properties

As described in the previous section, the analysis takes advantage of the fact that the problem is statistically one-dimensional and provides the various quantities of interest as a function of time t and position x within the turbulent flame brush. We now discuss briefly the relationship between these spatially-resolved quantities and the more familiar, global (space-averaged) flame properties.

By definition, the total flame surface area, S_V, within the computational domain is equal to the volume-integral of the flame surface density, which, in the present case, translates to the following relation:

$$\frac{S_V(t)}{L_y L_z} = \int \Sigma(x,t) dx. \tag{27}$$

Using Eq.(9), it can be shown that the time-derivative of the relative increase in flame surface area is equal to the total flame stretch, $\overline{k}$, space-averaged across the turbulent flame brush:

$$\overline{k}(t) = \frac{d}{dt}\left(\frac{S_V(t)}{L_y L_z}\right) = \int \langle k \rangle_S(x,t) \; \Sigma(x,t) dx. \tag{28}$$

$\overline{k}$ gives the instantaneous rate of change of the total flame surface area in the computational domain. If positive, the flame surface grows; if negative, the flame surface contracts.

The mean fuel consumption speed, $\overline{S}_C$, can also be expressed in terms of space-integrals of the flamelet speed, $\langle S_C \rangle_S$, and the flame surface density, Σ, across the turbulent flame brush:

$$\overline{S}_C(t) = \frac{\int \langle S_C \rangle_S(x,t) \; \Sigma(x,t) dx}{\int \Sigma(x,t) dx}. \tag{29}$$

Finally, using Eq.(4), the turbulent flame speed, S_T, is simply related to the product of S_V and $\overline{S}_C$:

$$S_T(t) = \frac{1}{\rho_u Y_{R,u}} \int \langle \dot{\omega}_R \rangle(x,t) dx = \int \langle S_C \rangle_S(x,t)\ \Sigma(x,t) dx = \overline{S}_C(t)\ \frac{S_V(t)}{L_y L_z}. \quad (30)$$

As described in the previous sections, the present study uses three-dimensional direct numerical simulations of turbulent premixed flames in isotropic flow. Three different cases have been studied that correspond to turbulent flames characterized by the same laminar thermal thickness, δ_T, the same laminar flame speed, s_L, embedded in the same initial turbulent flow field, but with different Lewis number, $Le = 0.8$, 1.0, and 1.2.

The three cases exhibit large differences in the time history of the turbulent flame speed, $S_T(t)$. As suggested by Eq.(30), these differences may be related to a modification of the turbulent flame structure through changes in $\overline{S}_C$, to a modification of the total flame surface area through changes in S_V, or to a combination of both. In fact, irrespective of the value of the Lewis number and in agreement with the findings from previous studies (Ashurst *et al.* 1987, Haworth & Poinsot 1992, Rutland & Trouvé 1991), the mean fuel consumption speed, $\overline{S}_C$, is found to be only a weak function of the turbulence. At all times, departures of $\overline{S}_C$ from the laminar value, s_L, remain within 20%. This result implies that the large effect of the Lewis number on S_T observed in the simulations is primarily a flame surface effect and that the flame surface density is the key quantity that to first order determines the mean reaction rate. For more details, see Trouvé & Poinsot (1992).

2.3 Comparison of DNS results with flamelet models

Using the methodology described in Section 2.1, we now analyze the spatial distribution of flame surface density across the turbulent flame brush. Figure 2 compares several Σ-profiles taken at different instants in the simulations. The Lewis number is 0.8. At $t = 0$, Σ is a delta function located at $x = 0$. As time evolves, the turbulent flame brush gets thicker and propagates deeper into the reactants. Accordingly, the Σ-profile spreads out and shifts towards negative values of x. In the simulations, this shift is rather weak but can clearly be seen at the latest times ($t = 6\tau$ in Figure 2).

Figure 3 compares the Σ-profiles obtained for different Lewis numbers. The comparison is performed at the same instant in the simulations, $t = 4\tau$. The effect of the Lewis number is clearly seen in this plot with a turbulent flame brush that propagates faster and deeper into the reactants for more diffusive mixtures. Note that as shown in Eq.(27), the x-integral of Σ gives the relative increase of total flame surface area and the local differences in the profiles plotted in Figure 3, when integrated, correspond to large global differences in the total amount of flame surface area, S_V.

A different perspective is adopted in Figure 4 where x-location within the turbulent flame brush is indicated by the local mean progress variable, $\langle c \rangle$. Although they are different in physical space, the Σ-profiles obtained for different Lewis numbers collapse when mapped in $\langle c \rangle$-space. This result indicates that the effect of the

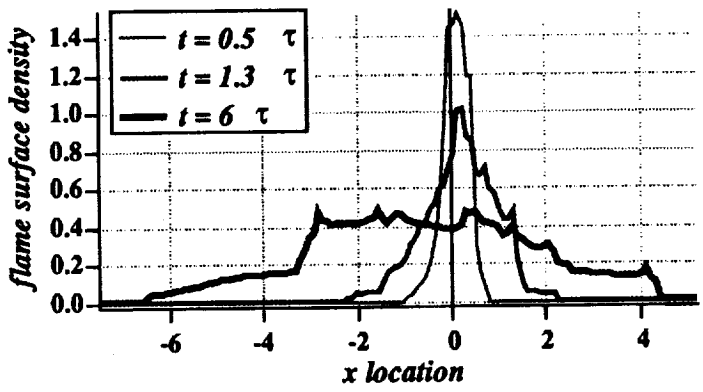

FIGURE 2. Time evolution of the flame surface density, Σ, in the computational domain (reactants on the left; products on the right). $Le = 0.8$. Σ and x are made non-dimensional by the laminar thermal thickness, δ_T. Time is measured in units of the initial turbulent eddy turn-over time, τ.

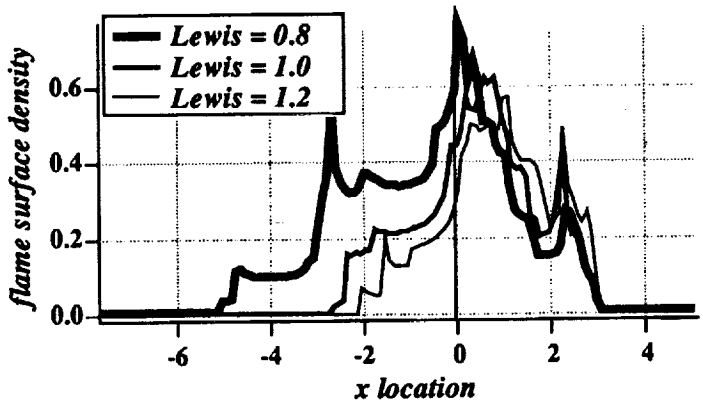

FIGURE 3. Lewis number effects on the spatial distribution of flame surface density, Σ, in the computational domain (reactants on the left; products on the right). $t = 4\tau$. Σ and x are made non-dimensional by the laminar thermal thickness, δ_T.

Lewis number on the spatial distribution of flame surface density is primarily an effect on the turbulent flame thickness.

Also plotted in Figure 4 is the flame surface density predicted by the Bray-Moss-Libby (BML) model. The BML model is a well-documented, second order closure model designed to avoid gradient transport assumptions (see for example Bray 1980, and 1990, Libby & Bray 1980). The model pre-assumes a bimodal shape for the probability density function of the progress variable, an assumption that is consistent with a laminar flamelet description of the reaction zone and represents the intermittent presence of packets of unburnt and fully burnt mixture at any location within the turbulent flame brush. Various degrees of refinement are possible within

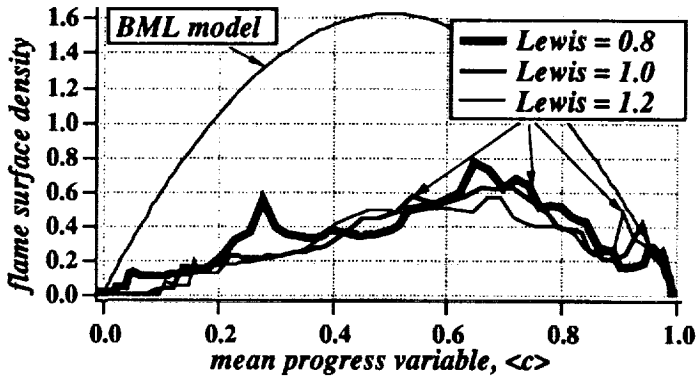

FIGURE 4. The spatial distribution of flame surface density, Σ, across the turbulent flame brush: comparison between DNS and the Bray-Moss-Libby model. $t = 4\tau$. Σ is made non-dimensional by the laminar thermal thickness, δ_T.

the BML framework, in particular with respect to the chemical source terms and the flame surface density. Although a transport equation for Σ could be incorporated easily (Cant *et al.* 1990), current formulations of the model are limited to a simple algebraic closure (Bray *et al.* 1984, 1989). The expression for Σ in a $y - z$ plane, $x = x_0$, where $\langle c \rangle$ = constant, is:

$$\Sigma = \frac{g\langle c \rangle(1 - \langle c \rangle)}{\overline{\sigma}_y \hat{L}_y}, \tag{31}$$

where g is a constant of order unity, $\hat{L}_y$ is a length that characterizes the flame wrinkling, and $\overline{\sigma}_y$ is the mean of a direction cosine defining the flamelet orientation relative to the plane, $x = x_0$. Both $\hat{L}_y$ and $\overline{\sigma}_y$ are assumed to be constant across the turbulent flame brush. $\hat{L}_y$ is specified empirically as follows:

$$\hat{L}_y = C_L \, l \, (\frac{s_L}{u'})^n, \tag{32}$$

where l is the integral length scale of the turbulence,and C_L and n are model constants. Following Bray (1990), we use $n = 1$, $C_L = 1$, $g = 1.5$, $\overline{\sigma}_y = 0.5$.

Figure 4 shows that the structure of the Σ-profile is not well captured by the BML model which predicts a symmetric distribution of Σ in $\langle c \rangle$-space, whereas DNS gives a skewed profile with a maximum close to $\langle c \rangle = 0.7$. Furthermore, although the comparison between DNS and the BML model is rendered difficult by the turbulence decay, some qualitative observations can still be made about the accuracy or inaccuracy of the model. For instance, the BML predictions always overestimate the flame surface densities across the turbulent flame brush by a factor decreasing from more than 5 to approximately 2 in the course of the simulations. Although the exact magnitude of the error might not be meaningful, the fact that it is time-dependent underscores the limits of an algebraic closure that cannot account for memory effects and is, therefore, expected to perform poorly in transient problems.

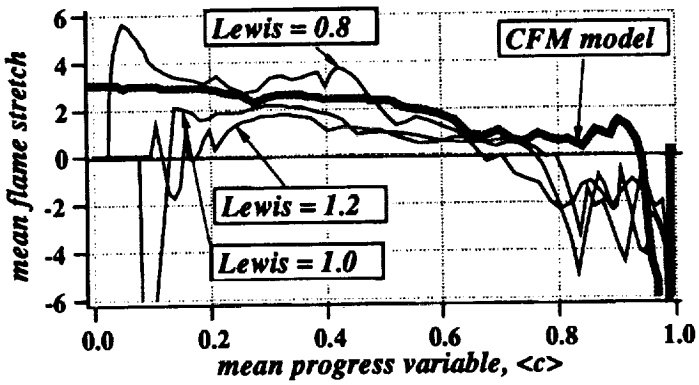

FIGURE 5. The spatial distribution of turbulent flame stretch, $\langle k \rangle_S$, across the turbulent flame brush: comparison between DNS and the Coherent Flame Model. $t = 4\tau$. k is made non-dimensional by the laminar flame time, δ_T / s_L.

We now turn to the more promising approach based on a modeled turbulent Σ-equation. Different formulations of this equation have been proposed in the literature (Marble & Broadwell 1977, Darabiha *et al.* 1987, Maistret *et al.* 1989, Candel *et al.* 1990, Cant *et al.* 1990, Borghi 1990, Mantel & Borghi 1991). These models are based on the exact but unclosed formulation given in Eq.(10). The right-hand side of Eq.(10) is the total flame stretch, which can be decomposed into a strain term and a propagation term. While the strain term, $\langle a_T \rangle_S$, remains approximately constant through the turbulent flame, the propagation term, $2\langle w k_m \rangle_S$, exhibits strong variations and decreases from positive values on the unburnt side, close to $\langle c \rangle = 0$, to negative values on the burnt side, close to $\langle c \rangle = 1$ (Trouvé & Poinsot 1992). Interestingly enough, both contributions to stretch have the same order of magnitude.

Figure 5 presents the mean flame stretch profile, $\langle k \rangle_S$, across the turbulent reaction zone, plotted for different Lewis numbers at $t = 4\tau$. At the leading edge, strain rate and flame propagation effects are locally cumulative, and the overall balance is strongly positive. The leading edge of the turbulent flame is a region of strong production of flame surface area. On the contrary, the propagation term takes large negative values on the burnt side. In that region, strain rate and flame propagation effects are locally opposite, and the overall balance is negative. The rear edge of the turbulent flame thus appears as a region where flame surface area gets strongly dissipated. In addition, while the effect of the Lewis number is not visible on the burnt side of the turbulent flame, there are large differences between the cases $Le = 0.8, 1.0$, and 1.2 close to $\langle c \rangle = 0$. This suggests that the turbulent flame is most sensitive to Lewis number effects on the unburnt side, whereas it remains relatively unaffected on the burnt side.

Using Eq. (28), one can quantify the overall differences due to the Lewis number; we find (in units of the laminar flame time): $\overline{k} = 2.6$ for $Le = 0.8$, and the flame surface area is quickly growing; $\overline{k} \simeq 0.0$ for $Le = 1.0$ and $Le = 1.2$, and the flame

surface area remains roughly constant.

Also plotted in Figure 5 is a comparison with the Coherent Flame Model proposed originally by Marble & Broadwell (1977) and further developed by Candel and his co-workers (Darabiha *et al.* 1987, Maistret *et al.* 1989, Candel *et al.* 1990). In this formulation, the turbulent flame stretch is written as:

$$\langle k \rangle_S = \frac{\epsilon}{k_t} - s_L \frac{\Sigma}{\langle Y_R \rangle}, \tag{33}$$

where k_t is the turbulent kinetic energy and ϵ its dissipation, both measured in the unburnt gas; $\langle Y_R \rangle$ is the ensemble-averaged fuel mass fraction. The first term on the right-hand side of Eq.(33) represents the straining due to the flow motions and is assumed to scale with the integral time scale of the turbulence; the second term is a disparition term associated with flame propagation and is assumed to scale with the laminar flame speed, s_L, and the flame surface density, Σ.

Figure 5 shows that this model is indeed able to reproduce qualitatively the spatial structure of the balance between production and dissipation of Σ, going from production at the leading edge of the turbulent flame to dissipation at the rear edge. However, the $1/\langle Y_R \rangle$ behavior of the disparition term leads to numerical difficulties on the burnt side of the flame. The model, therefore, overpredicts the dissipation of Σ near $\langle c \rangle = 1$ and gives a negative mean flame stretch, $\overline{k} = -3.6$, in strong disagreement with the values reported above. In addition, the disparition term in Eq.(33) is always and everywhere negative and cannot account for the possible transition to unstable thermo-diffusive conditions as observed in the simulations (Trouvé & Poinsot 1992).

3. Conclusion and future plans

In flamelet models, the flame surface density is a central ingredient that conveys most of the effects of the turbulence on the rate of energy release. The flame surface density can be obtained using an algebraic closure, as in current formulations of the Bray-Moss-Libby model, or via a modeled transport equation, called the Σ-equation. The Σ-equation was first postulated by Marble & Broadwell (1977) based on phenomenological grounds. Recent theoretical work has produced a more rigorous approach that leads to an exact but unclosed formulation for the turbulent Σ-equation (Pope 1988, Candel & Poinsot 1990). Since the flame surface density and the different terms of interest in the turbulent Σ-equation are not experimentally accessible, little is known on the validity of the closure assumptions used in current formulations of flamelet models.

Direct Numerical Simulation (DNS) is an attractive alternative approach to get basic information on these fundamental quantities. In the present work, three-dimensional DNS of premixed flames propagating in isotropic turbulent flow have been used to estimate the different terms appearing in the Σ-equation. A new methodology has been proposed to provide the flame surface density, Σ, as well as the source and sink terms for Σ, estimated as a function of time and position within

the turbulent flame brush. Using this methodology, comparisons with flamelet models are possible at a level of detail never reached before.

Principal findings are that: (1) the Bray-Moss-Libby formulation overestimates the flame surface densities; more importantly, the error is a function of time, which underscores the limits of using an algebraic closure; (2) the Coherent Flame Model (CFM), based on a modeled turbulent Σ-equation, is shown capable of reproducing qualitatively the spatial variations in the balance between production and dissipation of flame surface area – the leading edge of the turbulent flame is correctly described as a region of production of flame surface area, whereas the rear edge is a region where flame surface gets strongly dissipated – however, the CFM model tends to overpredict flame surface dissipation and is unable to reproduce variations due to thermo-diffusive phenomena.

Ongoing plans include the development of a new formulation of the Σ-equation that would incorporate thermo-diffusive mechanisms. Also, the effect of the mean flow field as represented by $\langle A_T \rangle_S$ in Eq.(10) is currently studied using three-dimensional DNS of a turbulent flame embedded in homogeneous shear flow.

Finally, it is worth emphasizing that theoretical descriptions of turbulent combustion are aimed at providing tractable expressions for the following two categories of unclosed terms: (1) the mean chemical source term; (2) the double and/or triple correlations representing turbulent transport phenomena. We have focused exclusively so far on the first category of problems, *i.e.* predicting the mean reaction rate. The second category is also a promising field for DNS of turbulent combustion. Indeed, in most current models, turbulent transport terms are treated using conventional, first-order closure assumptions based on the concept of an eddy viscosity. However, since flames of practical interest feature large changes in mass density which affect significantly the turbulent flow field, it is somewhat suspicious, although very common, to directly extend the empirical closures developed in the context of constant density, non-reacting flow problems to the case of turbulent flames. Future work will include studying and modeling of turbulent transport in a combustion environment.

Acknowledgements

Fruitful and friendly interactions with other members of the combustion group at CTR are gratefully acknowledged. In particular, we thank Dr. Feng Gao and Dr. Luc Vervisch.

REFERENCES

ABDEL-GAYED, R. G., BRADLEY, D., HAMID, M. N., & LAWES, M. 1984 Lewis number effects on turbulent burning velocity. *Twentieth Symp. (International) on Combust.* 505-512. The Combustion Institute.

ASHURST, W. T., PETERS, N., & SMOOKE, M. D. 1987 Numerical simulation of turbulent flame structure with non-unity Lewis number. *Combust. Sci. Technol.* **53**, 339-375.

BORGHI, R. 1985 On the structure and morphology of turbulent premixed flames. *in Recent Advances in Aerospace Sciences.* Pergamon.

BORGHI, R. 1990 Turbulent premixed combustion: further discussion on the scales of the fluctuations. *Combust. Flame.* **80,** 304-312.

BRAY, K. N. C. 1980 Turbulent flows with premixed reactants. *in Topics in Applied Physics* **44**. Springer-Verlag.

BRAY, K. N. C., LIBBY, P. A., & MOSS, J. B. 1984 Flamelet crossing frequencies and mean reaction rates in premixed turbulent combustion. *Combust. Sci. Technol.* **41,** 143-172.

BRAY, K. N. C., LIBBY, P. A., & MOSS, J. B. 1984 Scalar length scale variations in premixed turbulent flames. *Twentieth Symp. (International) on Combust.* 421-427. The Combustion Institute.

BRAY, K. N. C., & LIBBY, P. A. 1986 Passage times and flamelet crossing frequencies in premixed turbulent combustion. *Combust. Sci. Technol.* **47,** 253-274.

BRAY, K. N. C., CHAMPION, M., & LIBBY, P. A. 1989 The interaction between turbulence and chemistry in premixed turbulent flames. *in Turbulent Reactive Flows, Lecture Notes in Eng.* **40**. Springer-Verlag.

BRAY, K. N. C. 1990 Studies of the turbulent burning velocity. *Proc. R. Soc. Lond. A.* **431,** 315-335.

CANDEL, S. M., VEYNANTE, D., LACAS, F., MAISTRET, E., DARABIHA, N., & POINSOT, T. 1990 Coherent flame model: applications and recent extensions. *in Series on Advances in Mathematics for Applied Sciences.* World Scientific.

CANDEL, S. M., & POINSOT, T. 1990 Flame stretch and the balance equation for the flame surface area. *Combust. Sci. Technol.* **70,** 1-15.

CANT, R. S., POPE, S. B., & BRAY, K. N. C. 1990 Modelling of flamelet surface-to-volume ratio in turbulent premixed combustion. *Twenty-Third Symp. (International) on Combust.* 809-815. The Combustion Institute.

CLAVIN, P. 1985 Dynamic behavior of premixed flame fronts in laminar and turbulent flows. *Prog. Energy Combust. Sci.* **11,** 1-59.

DARABIHA, N., GIOVANGIGLI, V., TROUVÉ, A., CANDEL, S. M., & ESPOSITO, E. 1987 Coherent flame description of turbulent premixed ducted flames. *in Proc. of the France-USA Joint Workshop on Turbulent Combustion.* Springer Verlag.

HAWORTH, D. C., & POINSOT, T. 1992 Numerical simulations of Lewis number effects in turbulent premixed flames. *J. Fluid Mech.* **244,** 405-436.

KERSTEIN, A. R., ASHURST, W. T., & WILLIAMS, F. A. 1988 Field equation and interface propagation in an unsteady homogeneous flow field. *Phys. Rev. A.* **37,** 2728-2731.

LELE, S. K. 1992 Compact finite difference schemes with spectral-like resolution. *J. Comp. Phys.* **103,** 16-42.

LIBBY, P. A., & BRAY, K. N. C. 1980 Implications of the laminar flamelet model in premixed turbulent combustion. *Combust. Flame.* **39,** 33-41.

MAISTRET, E., DARABIHA, N., POINSOT, T., VEYNANTE, D., LACAS, F., CANDEL, S. M., & ESPOSITO, E. 1989 Recent developments in the coherent flamelet description of turbulent combustion. *in Proc. 3rd Int. SIAM Conf. on Numerical Combustion.*

MANTEL, T., & BORGHI, R. 1991 A new model of premixed wrinkled flame propagation based on a scalar dissipation equation. *in Proc. 13th ICDERS.*

MARBLE, F. E., & BROADWELL, J. E. 1977 The coherent flame model for turbulent chemical reactions. *Project Squid Technical Report.* TRW-9-PU.

PETERS, N. 1986 Laminar flamelet concepts in turbulent combustion. *Twenty-First Symp. (International) on Combust.* 1231-1250. The Combustion Institute.

POINSOT, T., VEYNANTE, D., & CANDEL, S. M. 1991 Quenching processes and premixed turbulent combustion diagrams. *J. Fluid Mech.* **228,** 561-605.

POINSOT, T., ECHEKKI, T., & MUNGAL, M. G. 1992 A study of the laminar flame tip and implications for premixed turbulent combustion. *Combust. Sci. Technol.* **81,** 45-73.

POINSOT, T., & LELE, S.K. 1992 Boundary conditions for direct simulations of compressible viscous flows. *J. Comp. Phys.* **101,** 104-129.

POPE, S. B. 1988 Evolution of surfaces in turbulence. *International J. Engng. Sci.* **26,** 445-469.

POPE, S. B. 1990 Computations of turbulent combustion: progress and challenges. *Twenty-Third Symp. (International) on Combust.* 591-612. The Combustion Institute.

RUTLAND, C. J., & TROUVÉ, A. 1991 Direct simulations of premixed turbulent flames with non-unity Lewis numbers. *Combust. Flame* (submitted for publication).

TROUVÉ, A. 1991 Simulation of flame-turbulence interactions in premixed combustion. *in Annual Research Briefs - 1991,* Center for Turbulence Research, Stanford Univ./NASA Ames.

TROUVÉ, A., & POINSOT, T. 1992 The evolution equation for the flame surface density in turbulent premixed combustion. In *Proc. 1992 Summer Program, Center for Turbulence Research,* Stanford Univ./NASA Ames, 325-343.

WILLIAMS, F. A. 1985 *Combustion theory.* 2nd ed., Benjamin Cummings.

WRAY, A. A. 1990 Minimal storage time-advancement schemes for spectral methods. *Internal Report, NASA-Ames.*

WU, M. S., KWON, S., DRISCOLL, J. F., & FAETH, G. M. 1990 Turbulent premixed hydrogen/air flames at high Reynolds numbers. *Combust. Sci. Technol.* **73,** 327-350.

S33-25

N94-12317

Study and modeling of finite rate chemistry effects in turbulent non-premixed flames

By Luc Vervisch

1. Background and objectives

The development of numerical models that reflect some of the most important features of turbulent reacting flows requires information about the behavior of key quantities in well defined combustion regimes. In turbulent flames, the coupling between turbulent and chemical processes is so strong that it is extremely difficult to isolate the role played by one individual physical phenomenon. Direct numerical simulation (hereafter DNS) allows us to study in detail the turbulence-chemistry interaction in some restricted but completely defined situations. Globally, non-premixed flames are controlled by two limiting regimes: the fast chemistry case, where the turbulent flame can be pictured as a random distribution of local chemical equilibrium problems; and the slow chemistry case, where the chemistry integrates in time the turbulent fluctuations. The Damköhler number, ratio of a mechanical time scale to a chemical time scale, is used to distinguish between these regimes. Today most of the industrial computer codes are able to perform predictions in the hypothesis of local equilibrium chemistry using a presumed shape for the probability density function (hereafter pdf) of the conserved scalar (Couplan *et al.* 1987, Viollet *et al.* 1990). However, the finite rate chemistry situation is of great interest because industrial burners usually generate regimes in which, at some points, the flame is undergoing local extinction or at least non–equilibrium situations. Moreover, this variety of situations strongly influences the production of pollutants (Masri *et al.* 1988).

To quantify finite rate chemistry effect, the interaction between a non-premixed flame and a free decaying turbulence is studied using DNS. The attention is focused on the dynamic of extinction, and an attempt is made to quantify the effect of the reaction on the small scale mixing process (section 2). The unequal diffusivity effect is also addressed (section 3). Finally, a simple turbulent combustion model based on the DNS observations and tractable in real flow configurations is proposed (section 4).

2. Finite rate chemistry effects in turbulent non-premixed flames

Three-dimensional direct numerical simulations of non-premixed flames have been carried out using a high-order finite difference code (Trouvé, 1991). Reacting flows are simulated resolving all of the scales of the turbulent motion, including effects due to variations in density and viscosity (Poinsot 1989, Poinsot *et al.* 1991). The chemistry is represented through a single-step reaction $A + B \rightarrow P$ or a two-step process $A+B \rightarrow I$, $A+I \rightarrow P$. The parameters of the Arrhenius-type reaction rate model chosen for the single-step simulations are close to that of global Methane-Air

combustion. The second mechanism is an attempt to study the effect of radical-like species in turbulent non-premixed flames. The second step ($A + I \rightarrow P$) proceeds with an activation energy four times smaller and an enthalpy of reaction five times larger compared to the first step.

The turbulent simulations are initialized by a well characterized one-dimensional, planar, laminar non-premixed flame which has been previously generated by the code (Chen *et al.* 1992). A prescribed turbulent field interacting with the initially laminar flame is then allowed to decay. The value of the initial Taylor Reynolds number is the order of fifty, a value relevant for some jet flames (Dibble *et al.* 1986; Magre *et al.* 1988), where the Reynolds number based on the velocity profile half-width increases from fifty to eighty along the jet axis.

The Damköhler number, defined as the ratio of the turbulent eddy turnover time to a chemical time based on the heat release of the initial laminar flame, is varied over a range corresponding to fast and slow chemistry in order to study the effect of finite-rate chemistry on flame structure. The flame thickness is such that the flame-flow interactions are limited to a range of reactive and turbulent scales of the same order of magnitude.

2.1 One-step chemistry model

It is observed in the case of intermediate value of the Damköhler number (regime ranging between slow and fast chemistry) that points exist which are influenced by the fully burning and extinguished locations. In the plane (Y_A, Z) defined by species A mass fraction and the mixture fraction (a conserved scalar, Z), these points are located between the lower bound on the species concentration distribution (equilibrium line, stoichiometric value, $Z_{St} = 0.5$) and the upper bound (pure mixing), Figure 1. This is representative of a turbulence-induced mixing influencing both full burning and frozen flow points, and it corresponds to a transient response. Indeed, in the (Y_A, Z) space, the concentration of a fluid particle is governed by (Lagrangian frame) :

$$\frac{dY_A}{dZ} = \frac{\frac{\partial}{\partial x_i}\left(\rho \mathcal{D}_A \frac{\partial Y_A}{\partial x_i}\right) + \dot{w}_A}{\frac{\partial}{\partial x_i}\left(\rho \mathcal{D} \frac{\partial Z}{\partial x_i}\right)}. \tag{1}$$

According to this equation, depending on the time scale involved in the small scale diffusion process (enhanced by the turbulence) and in the reactive phenomenon ($\dot{w}_A$), the concentration of the fluid particle in the plane (Y_A, Z) could reach all the values in the domain that lies between the pure mixing line and the fast chemistry line. The transient response is due to the effect of diffusion at small scale which is affected by the turbulence modifying the instantaneous species profile and, therefore, the reaction rate. This transient response is representative of the finite-rate chemistry effect.

It has been verified (Chen *et al.* 1992) that in the databases, the stoichiometric surface and the location of peak reaction zone coincide, and also that contours of Z are parallel within the reaction zone. The mixture fraction dissipation rate χ

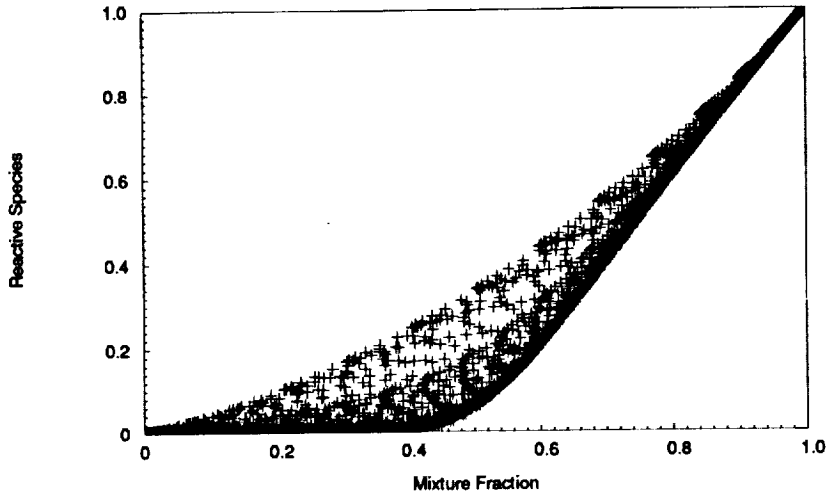

FIGURE 1. Distribution of the reactive species Y_A versus mixture fraction Z.

($\chi = 2\mathcal{D}|\nabla Z|^2$), is found to be well correlated with the tangential strain rate evaluated at the flame surface. Gibson's theory for constant density flows (Gibson 1968) predicts a value of -0.5 for the correlation coefficient between strain rate and scalar dissipation rate. Incompressible DNS (Nomural *et al.* 1992) report values ranging from -0.4 to -0.5. The present simulations provide a value of -0.6. This larger value is likely to be a result of dilatation associated with heat release in our computations. As expected, the scalar gradient is also found to be most probably aligned with the most compressive strain rate direction.

In accord with laminar flamelet theory (Peters 1986), the scalar dissipation rate increases with reaction rate until a critical value is reached at which extinction occurs. Early in the simulation (i.e. within one eddy turnover time), the maximum value of the reaction rate interpolated along the local flame surface normal vector and plotted versus the scalar dissipation rate follows the common laminar flamelet response, Figure 2. However, when the flame is undergoing "full interaction" with turbulence, see Figure 3, a deviation from the bounds indicated by laminar flamelet is observed and is related to the transient effects observed in Figure 1.

The reason for this deviation is due to the reaction rate being influenced by the local temperature but also by the species mass fraction. It appears that turbulent-enhanced mixing convects more species to the reaction zone than in a pure strained laminar flamelet. The vorticity does not penetrate the flame except at locations where extinction is observed. Indeed, within the flame region, the dynamic viscosity increases with temperature, creating a zone of large dissipation which has the effect of damping the turbulence. These observations suggest that even if the fluid mechanics features of the flow are close to the flamelet regime the dynamic information carried by the turbulence introduces some transient effects that certainly need to be included in the modeling to predict the mean burning rate capturing

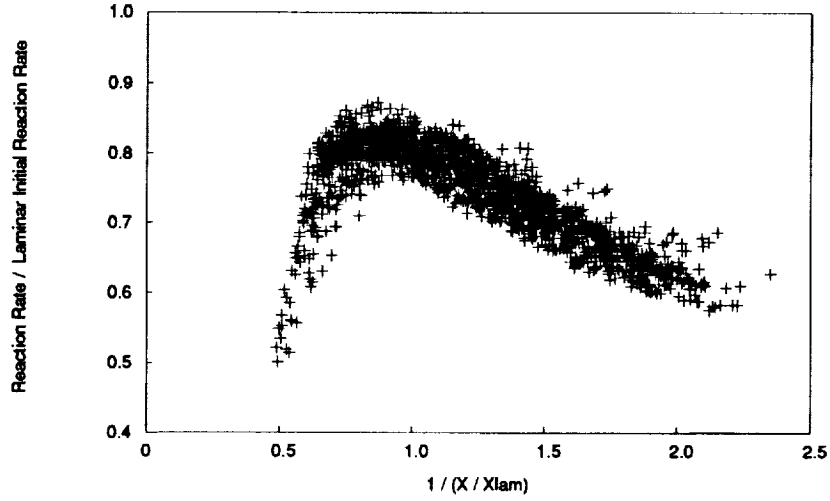

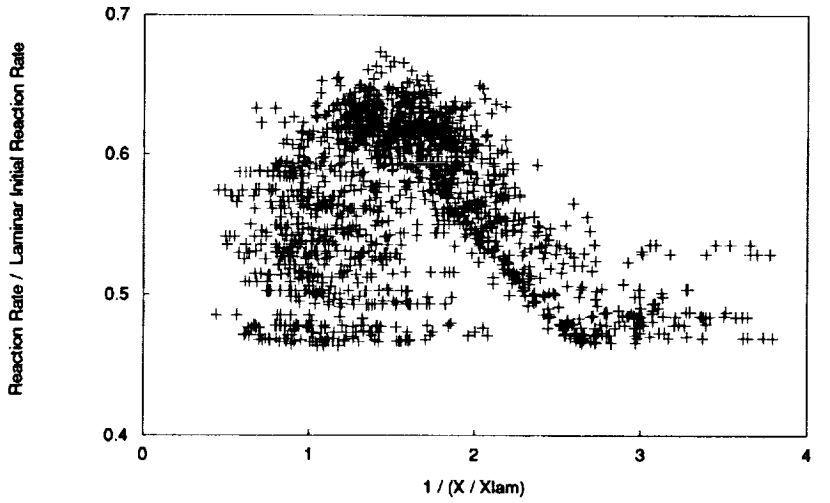

FIGURE 2 AND 3. Distribution of the maximum reaction rate with respect to the inverse scalar dissipation rate $1/(\chi/\chi_{lam})$, for two successive times.

with accuracy finite-rate chemistry effects.

The pdf modeling shifts the problem of the evaluation of the mean burning rate to the estimation of the small scale mixing (Dopazo 1992). Hence, this approach is promising when the mixing process is not too much influenced by the reaction, allowing the chemical kinetics to decouple from the fluid dynamics. The distribution of the reactive species dissipation rate χ_{Y_A} ($\chi_{Y_A} = 2\mathcal{D}_A|\nabla Y_A|^2$) is a quantity representative of the intensity of mixing and is found in the simulations to be

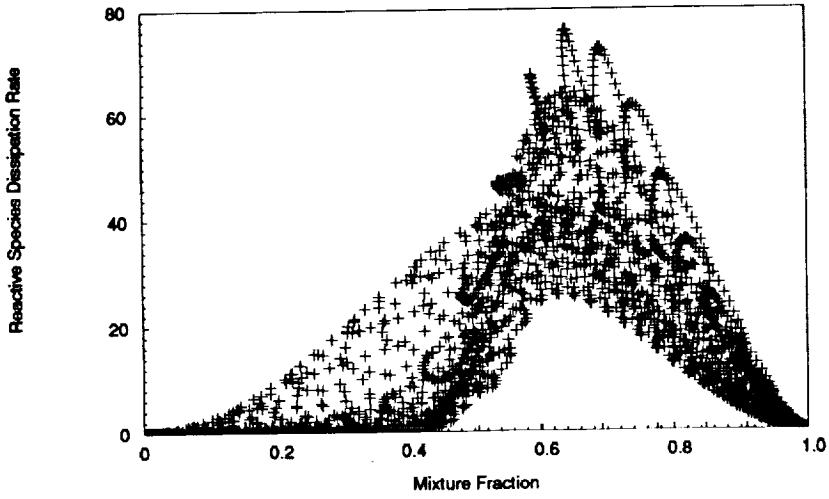

FIGURE 4. Distribution of the reactive species A dissipation rate with respect to the mixture fraction Z, slow chemistry.

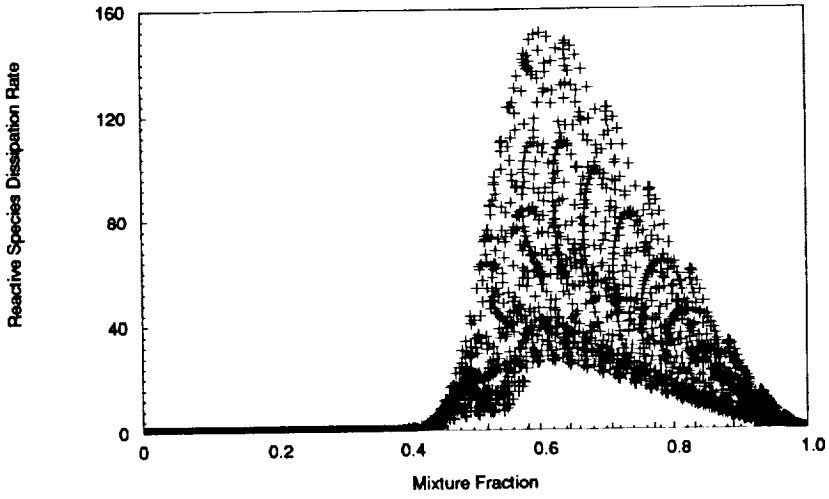

FIGURE 5. Distribution of the reactive species A dissipation rate with respect to the mixture fraction Z, fast chemistry.

sensitive to the Damköhler number. Actually, in the limit of very fast chemistry, the properties of the small scales of the reactives species field are known to be more sensitive to the chemical reaction than to the turbulent cascade energy process (Kuznetsov *et al.* 1990, p61). Thus it is hardly surprising that the reactive effect can still be perceived for intermediate values of the Damköhler number.

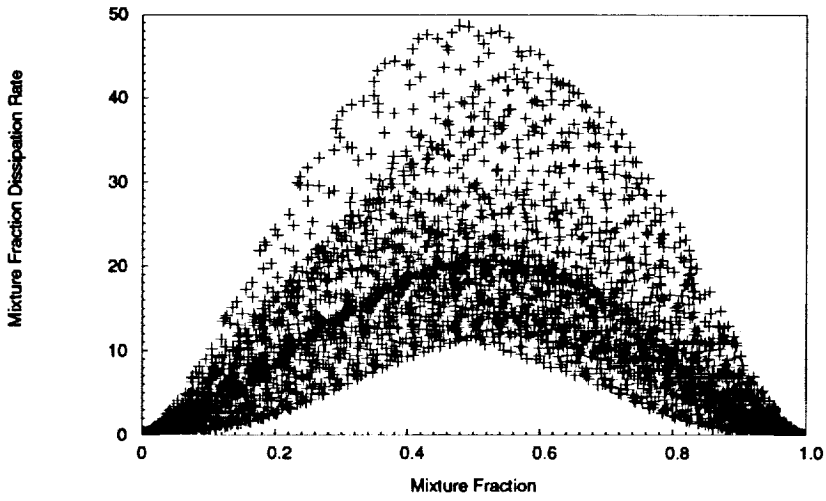

FIGURE 6. Distribution of the mixture fraction dissipation rate χ versus mixture fraction, slow chemistry.

In Figure 4, two zones are observed, corresponding to Figure 1 or Figure 3. When the Damköhler number is large, Figure 5, the dissipation rate is negligible for $Z < 0.4$, whereas for the slower chemistry, Figure 4, a finite bound appears. This figure displays the penetration of the species A in the other side of the flame, creating, at the very least, a partially premixed situation. Here, the same physical turbulent-induced processes are observed than those previously noticed in the investigation of the local flame topology. Locally, the gradient of the reactive species are simultaneously influenced by both reaction rate and turbulent transports. Therefore, even in non-premixed combustion, it is difficult to conclude that small scale mixing is unaffected by the reactive processes.

Consequently, the estimation of a mean mixing time scale (used in any mixing model) without including information related to the reactive activity can lead to large disagreement between numerical predictions and measurements since the fluid dynamics motion is then somewhat disconnected from the kinetics (Chen *et al.* 1990, Borghi *et al.* 1990). A way to overcome this deficiency could be the introduction in the modeling of informations related to the gradient of the species field (Fox 1992a, Mantel *et al.* 1990).

The same approach is used to study the sensitivity of the mixture fraction dissipation rate χ to finite-rate chemistry and turbulence-induced transient effects connected with those mentioned above. A detailed comparison of reactive and non-reactive fields indicates that the distribution of the mixture fraction dissipation rate is sensitive to the chemical processes. This is attributed directly to the modification in density and dynamic viscosity as a result of heat release.

The distribution of the mixture fraction dissipation rate χ appears to lie within an envelope that at first sight follows the response of a typical laminar-like flamelet,

Figure 6. This has also been observed by Fox (Fox 1992b) in the study of the layer-like lamellar system. Usually, it is assumed for modeling purposes that the mixture fraction and its dissipation rate are uncorrelated quantities (Kuznetsov 1990 p60, Peters 1986, Warnartz *et al.* 1986). Figure 6 indicates that the turbulence randomizes the values but that they are not completely uncorrelated.

2.2 Two-step chemistry model

The structure of the reaction zone obtained with the two-step chemistry in the case of slow chemistry is more complex. The intermediate species, I, field is such that a production-recombination zone lies on the oxidizer side of the domain ($Z < 0.5$), and a diffusion zone is observed on the fuel side, Figure 7. If the second reaction was suppressed, the dissipation rate of the intermediate species χ_{Y_I} ($\chi_{Y_I} = 2\mathcal{D}_I \mid \nabla Y_I \mid^2$) would present two symmetric peaks on either side of the value $Z = 0.5$ with a minimum at this point. Since I is consumed by A in the second reaction step, the maximum value of the dissipation rate is enhanced relatively to the peak on the B side, with a minimum shifted to approximately $Z = 0.4$ (location of the generation of I by the first step), Figure 8.

The two reaction zones are not completely segregated in physical and mixture fraction space. However, for the same value of the Damköhler number, the global contribution of the reaction to the energy source term is broader in mixture fraction space than the corresponding contribution in the case of one-step chemistry. This event makes the flame less susceptible to undergoing local extinction compared to a flame modeled with single-step. This suggests that the modeling of extinction is strongly connected to the choice of the chemical scheme in terms of number of steps and species involved.

3. Unequal diffusivity effects in non-premixed flames

Within hydrogen or hydrocarbon flames, mono-atomic hydrogen and diatomic hydrogen atoms are present with heavier species that diffuse more slowly. The laminar flame structure is known to be strongly dependent on the larger diffusivity of radical species, which plays an important role in the ignition processes. One way to determine if, despite the large turbulent-induced transports, unequal diffusivity effects persist in turbulent non–premixed flames is to compare, from experimental results, the value of mixture fraction based on hydrogen atom with those based on carbon atom. Vranos (Vranos *et al.* 1992) investigated Methane-Hydrogen flames at high Reynolds numbers and reported differences between the two different mixture fractions, indicating that unequal diffusivities effects are present.

In most of the turbulent non-premixed combustion models, the hypothesis that all the species diffuse at the same rate is used. Thus the analysis of DNS databases including Schmidt number effects in non–reacting and in reacting flow is relevant.

3.1 Unequal diffusivity effects in non–reacting flows

To investigate the effect of varying the Schmidt number on the small scale mixing, first DNS of non–reacting flows have been carried out.

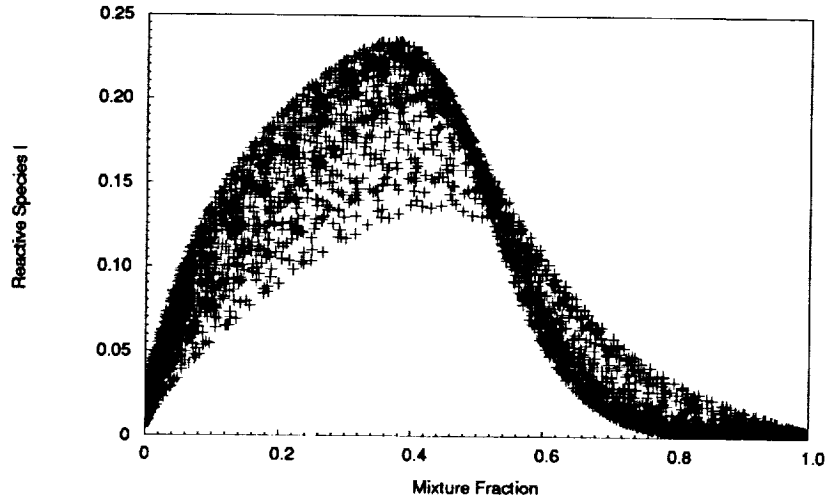

FIGURE 7. Distribution of the intermediate reactive species I versus mixture fraction, slow chemistry.

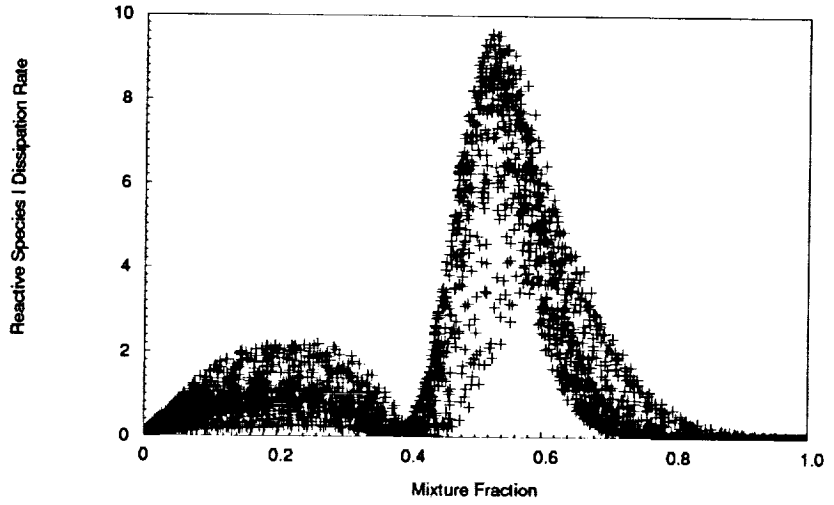

FIGURE 8. Distribution of the dissipation rate of the intermediate reactive species I versus mixture fraction, slow chemistry.

In the free decaying turbulence configuration, a species C is added on the "A-side" with a Schmidt number equal to one-half. The laminar initial pure diffusive zone is then allowed to interact with the turbulence. If the scatter plot of Y_C versus Y_A does not show the evidence of differential diffusion effect as in the experiment of Smith (Smith *et al.* 1992), the distribution of the ratio $r_1 = \frac{Y_A}{Y_C}$, Figure 9, clearly

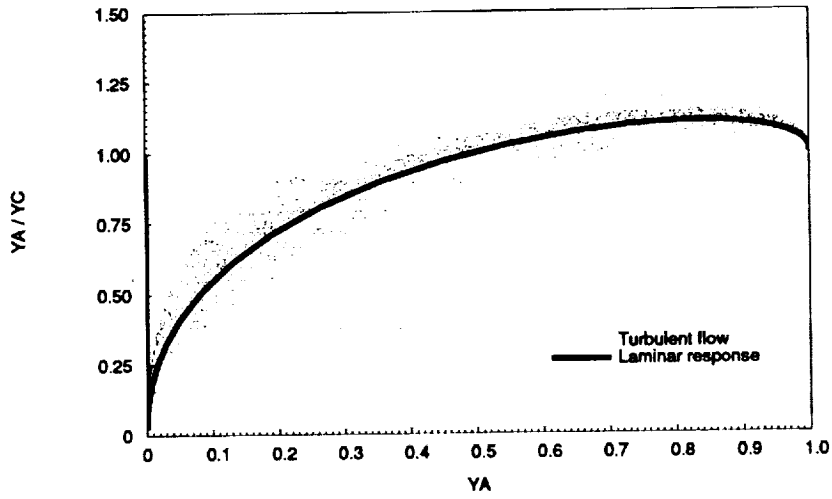

FIGURE 9. Distribution of the ratio $r_1 = \frac{Y_A}{Y_C}$ versus Y_A; pure mixing situation.

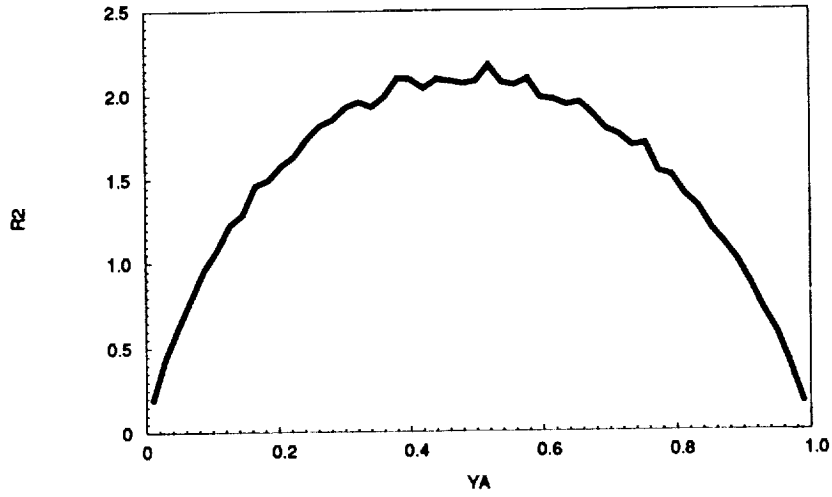

FIGURE 10. Ratio $r_2 = \frac{\langle |\nabla Y_A|^2 | Y_A = \Psi_A \rangle}{\langle |\nabla Y_C|^2 | Y_A = \Psi_A \rangle}$ versus Y_A; pure mixing situation.

demonstrates the presence of this differential diffusion effects. Figure 9 displays for the same time the laminar equivalent evolution (where the exact solution is known) and the scatter plots of r_1 corresponding to the turbulent flow (the equal diffusivity problem would provide $r_1 = 1$). The turbulence induces a spreading of the points around the laminar response, and when Y_A tends to zero, the ratio r_1 also tends to zero. Both of these observations reveal that small scale diffusion is sensitive to the

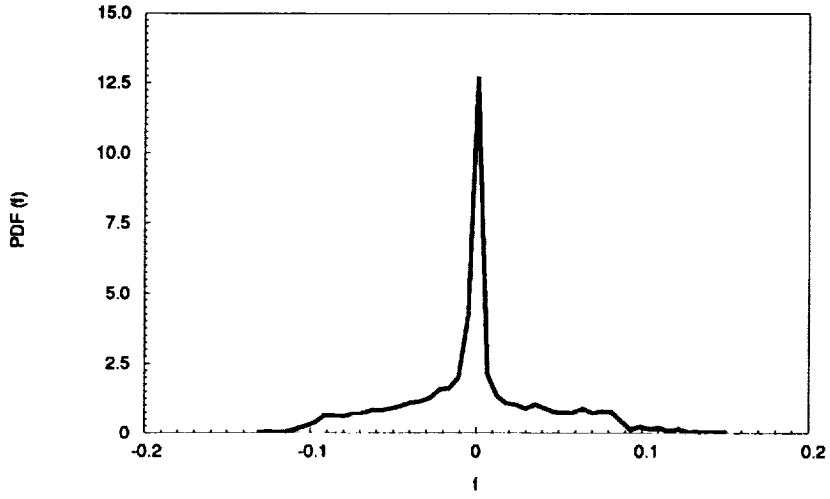

FIGURE 11. pdf of the differential diffusion variable; pure mixing situation.

smaller Schmidt number of the species C. The ratio of the conditional mean values for the magnitude of the gradient of the species A and C, $r_2 = \frac{\langle |\nabla Y_A|^2 | Y_A = \Psi_A \rangle}{\langle |\nabla Y_C|^2 | Y_A = \Psi_A \rangle}$, is presented in Figure 10. This quantity reaches its maximum when $Y_A = 0.5$ and its minimum at the edge of the composition space, with large variations around the value $r_2 = 1$ corresponding to equal diffusivity. Kerstein (Kerstein 1990) proposed to define a differential diffusion variable, f, as: $f = Y_A - Y_C$. The pdf of this quantity is proposed in Figure 11. This pdf is somewhat symmetric around $f = 0$, with unequal zero value tails. The examination of the three previous quantities demonstrates that differential diffusion effects occur in pure mixing simulations. The turbulence induces a deviation from the laminar diffusive motion, but the unequal diffusive effect can still be perceived.

Increasing the Reynolds number will decrease the scales at which the laminar diffusive process is acting. In large Reynolds number reacting flows, because of significant increase in kinematic viscosity with temperature, the differential diffusion effects pointed out above will certainly still be present at the diffusive scales where chemical activities occur, especially for very fast diffusive radical species.

3.2 Unequal diffusivity effects in reacting flows

If the Schmidt number of all the species is assigned a value of unity, the pdf of the curvature of the three dimensional flame is found to be symmetric (the surface exhibits both positive and negative curvature). However, when the Schmidt number of the species A is changed to one half (one-step chemistry) the probability of negative curvature along the stoichiometric surface increases, Figure 12. Negative curvature in this instance corresponds to reaction zones that are curved into the "B-side". This observation is correlated with the broader reaction zone found on

this side in mixture fraction and physical space. The same trend has been found by Trouvé (Trouvé 1991) in the case of premixed combustion.

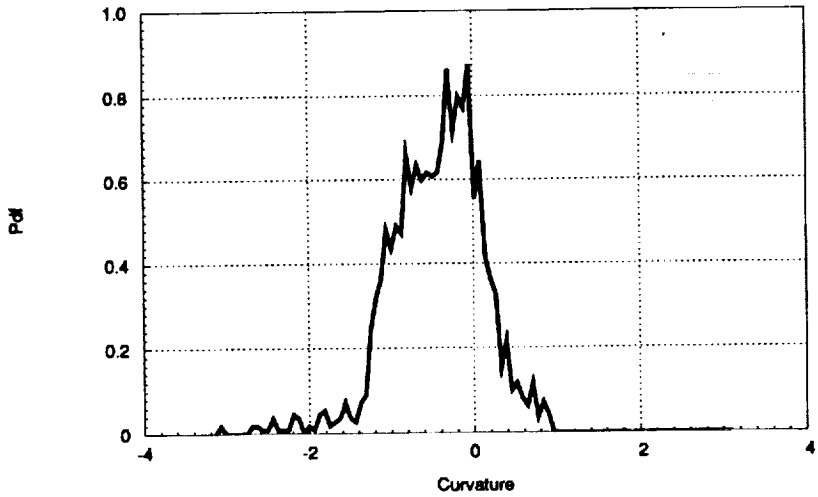

FIGURE 12. Pdf of the curvature along the flame surface; fast chemistry.

In the two-step chemistry case without changing the initial turbulent field but modifying the Schmidt number of the intermediate species, I, DNS allows us to study the impact on the flame of a fast diffusive radical-like species. The contour plots of the intermediate species dissipation rate presents two areas related to the production-consumption and pure diffusion zones of I. For $Sc_{Y_I} = 0.5$, the two zones are wider than for $Sc_{Y_I} = 1$, Figure 13. This observation is related to the penetration of the rapidly diffusing intermediate species into both sides of the flame, which modified the magnitude of the dissipation rate but also the shape of the joint pdf of the dissipation rate and mixture fraction (compare Figure 8 and 14).

These results suggest that globally small scale mixing is sensitive to the fast diffusive intermediate species, even though turbulent diffusion is the more active process in term of mean statistical description of the reactive flow field. Further examination of the non-premixed flame response to the unequal diffusivity effects are in progress.

4. Modeling of non-premixed flames

4.1 Introduction

Usually, in industrial computer codes, transport equations for mean quantities (mean mass fraction, mean velocity and mean energy) are solved with the help of classical turbulence models for the Reynolds stress and the turbulent flux (usually Favre averaging is chosen, $\overline{A} = \frac{\langle A\rho \rangle}{\langle \rho \rangle}$). The validity of these turbulence models in the case of reacting flows with variable density will not be discussed here. The

FIGURE 13. Intermediate species dissipation rate contours, on the left $Sc_I = 1$, on the right $Sc_I = 0.5$.

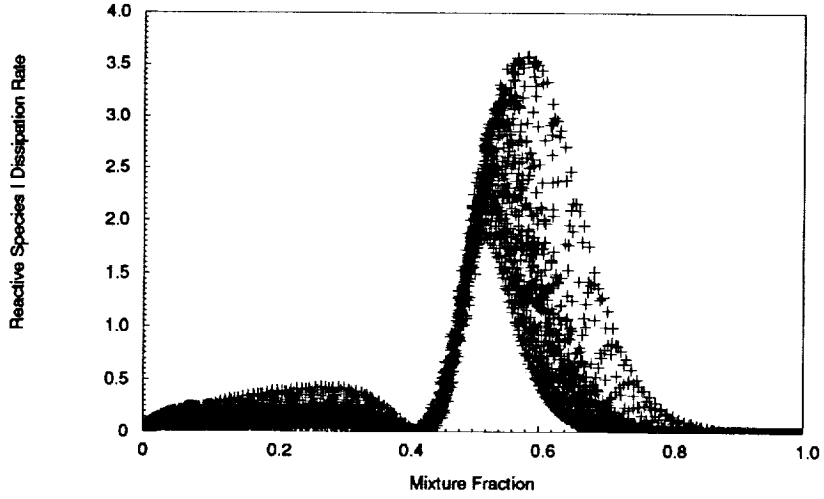

FIGURE 14. Distribution of dissipation rate of intermediate species I versus mixture fraction; $Sc_I = 0.5$.

mean reaction rate that appears in the mean species transport equation needs to be modeled and the aim of the method proposed in the following is to built a kind of "pdf generator" which generates, at a low cost, an approximated pdf of the thermochemical variables. This is with enough accuracy to compute in non-premixed flame in air the mean reaction rate of the oxidizer, $\overline{\dot{\omega}}_{Ox}$.

The chemistry is described through one global reaction step and heat losses by

radiative transfer are neglected; therefore, two variables (mixture fraction and oxidizer mass fraction) only are required for the description of the reactive flow field. This is a very crude approximation, but for engineering purposes, instead of using the local equilibrium hypothesis, it is useful to compute a first approximation of the reactive flow field which accounts for the interaction between the turbulent and chemical processes. This approximation can then be used to study the behavior of global parameters or to initialize more precise and more time consuming computer methods, such as Monte Carlo Methods able to deal with complex chemistry (Jones *et al.* 1985).

The DNS results of turbulent non-premixed flames discussed previously indicate that transient effects have to be included in the modeling. Especially, the scatter plots of the reactive scalar concentration, temperature, and reaction rate show that the pdf of the reactive species exhibits a continuous shape between the frozen flow line and the equilibrium line.

Two curves $y^1_{Ox} = y^1_{Ox}(Z)$ and $y^2_{Ox} = y^2_{Ox}(Z)$ clearly limit the spreading of the pdf in the plane (Y_{Ox}, Z), $(y^1_{Ox} < y^2_{Ox} \quad \forall\ Z)$. The mean burning rate can be computed from an estimated pdf $\overline{P}(Y_{Ox}, Z)$ supported by an area located between y^1_{Ox} and y^2_{Ox}. Three pieces of information are needed to perform this evaluation, the approximated location of the pdf in the concentration space, the extend of spreading, and the local amplitude of the pdf. The location of the pdf and the control on the extend of spreading will be based on the simplified probability density function approach (Borghi *et al.* 1983, Gonzalez *et al.* 1986). A way to evaluate the local amplitude of the pdf is derived from the DNS observations.

4.2 A new formulation for the presumed pdf method

Using information issued from the mean flow field, Borghi (Borghi *et al.* 1983) first proposed to built an approximation of $\overline{P}(Y_{Ox}, Z)$. This approximated pdf was obtained with the help of the Dopazo (Dopazo *et al.* 1976) small scale mixing model (also call *iem* Lagrangian model) and possessed some of the characteristics of the mean reactive scalar field. This model included some properties of the conditional pdf $\overline{P_c}(Y_{Ox}|Z)$, $\left(\overline{P_c}(Y_{Ox}|Z) = \frac{\overline{P}(Y_{Ox},Z)}{\overline{P}(Z)}\right)$, where $\overline{P}(Z)$ was presumed as a Beta function with the two parameters $\overline{Z}$ and $\overline{Z'^2}$.

Inside a two-inlet homogeneous reactor, when the pdf is discretized with two particles (one for each inlet), the evolution of the particles concentration equivalent to the pdf transport equation closed with the *iem* mixing model is (Pope 1979):

$$\frac{dy_{Ox}}{dZ} = \frac{\dot{\omega}_{Ox}\tau_{t_{Ox}} + \overline{Y}_{Ox} - y_{Ox}}{\overline{Z} - Z}. \tag{2}$$

The quantity $\tau_{t_{Ox}}$ is a mixing time scale, and when only mean values are known, the previous equation is a closed form of Eq.(1). According to DNS observations, a transport equation must be solved for the mean dissipation rate of the reactive species $\overline{\varepsilon}_{Y_{Ox}}$ and also for the rms of the reactive species $\overline{Y'^2_{Ox}}$ to get $\tau_{t_{Ox}} = \frac{\overline{Y'^2_{Ox}}}{\overline{\varepsilon}_{Y_{Ox}}}$.

This estimation of $\tau_{t_{Ox}}$ allows the inclusion of information coming from the reactive processes into the mixing model.

The homogeneous situation related pdf, $\overline{P_c}(Y_{Ox}|Z)$, can be written:

$$\overline{P_c}(Y_{Ox}|Z) = \delta\left(y_{Ox}^{iem}(Z) - Y_{ox}\right), \tag{3}$$

where $y_{Ox}^{iem}(Z)$ is composed of two trajectories obtained by solving (2) with the boundary conditions: $(y_{Ox} = 0, Z = 1)$ and $(y_{Ox} = 1, Z = 0)$.

In non homogeneous flows, the shape of the conditional pdf, $\overline{P_c}(Y_{Ox}|Z)$, spreads out, and Borghi (Borghi *et al.* 1983) proposed a way to approximate this pdf in premixed flames. This method has also been extended to non-premixed flame (Vervisch 1992). The pdf, presumed with the help of these previous formulations, reproduced only the mean value of the reactive flow field and was obtained in a discontinuous form, including large holes in the concentration space; moreover, the amplitude of the reactive species pdf was deduced from the amplitude of the mixture fraction pdf. These features are in disagreement with measurements (Masri 1988, Cheng 1991) and previous observations from DNS. An attempt to improve these presumed pdf models is now proposed.

In the DNS field, if the conditional pdf $\overline{P}_c(Y_{Ox}|Z)$ effectively depends on Z, the pdf $\overline{P}_c(\xi|Z)$ where $\xi = \frac{Y_{Ox} - y_{Ox}^1}{y_{Ox}^2 - y_{Ox}^1}$ is only weakly dependent on Z, (Figure 15).

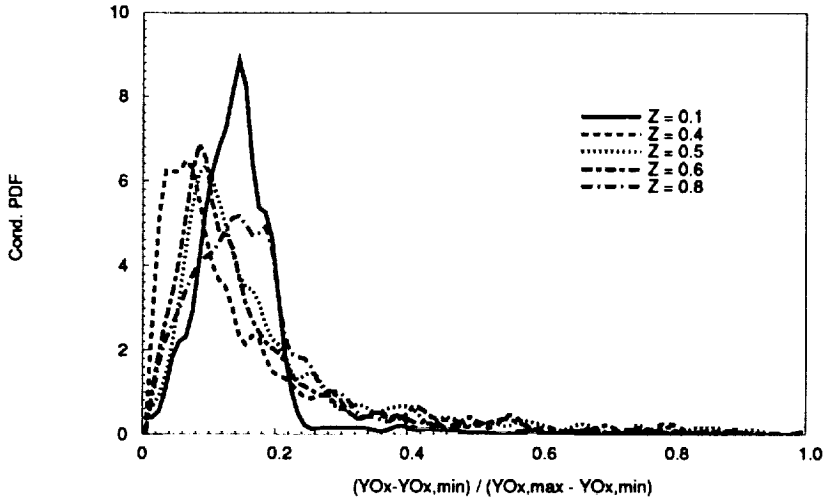

FIGURE 15. Conditional pdf $\overline{P}_c(\xi|Z)$.

Therefore, in the plane (Y_{Ox}, Z), each line between y_{Ox}^1 and y_{Ox}^2, for a fixed value of Z, can be weighted with a reference pdf, $f(\xi)$. The function f, able to mimic situations ranging from low spreading (low oxidizer fluctuations) to the bimodal form (large oxidizer fluctuations), has to be defined as:

$$\begin{gathered}\overline{P}_c(Y_{Ox}|Z) = 0 \quad \text{if } Y_{Ox} < y^1_{Ox}(Z) \text{ or } Y_{Ox} > y^2_{Ox}(Z) \\ \overline{P}_c(Y_{Ox}|Z)\, dY_{ox} = f(\xi)\, d\xi \\ \int_{y^1_{Ox}(Z)}^{y^2_{Ox}(Z)} \overline{P}_c(Y_{Ox}|Z)\, dY_{Ox} = \int_0^1 f(\xi)\, d\xi = 1 \quad \forall Z\ .\end{gathered} \tag{4}$$

The estimation of the position of the pdf in the oxidizer mixture fraction plane is achieved when the curve $y^1_{Ox}(Z)$ and $y^2_{Ox}(Z)$ are known. The *iem* trajectory (which contains information on the joint effect of small-scale mixing and reaction) is taken as a reference. The quantity $\overline{y^{iem}_{Ox}} = \int_0^1 y^{iem}_{Ox}(Z)\overline{P}(Z)\, dZ$ is computed. The following possibilities may be considered to determine the curves $y^1_{Ox}(Z)$ and $y^2_{Ox}(Z)$ (Borghi *et al.* 1983):

	$y^1_{Ox} = y^1_{Ox}(Z)$	$y^2_{Ox} = y^2_{Ox}(Z)$
$\overline{y^{iem}_{Ox}} > \overline{Y}_{Ox}$	Equilibrium Line ($\tau_{t_{Ox}} \to \infty$)	*iem* Line
$\overline{y^{iem}_{Ox}} < \overline{Y}_{Ox}$	*iem* Line	Mixing Line ($\tau_{t_{Ox}} \to 0$)

The estimated boundaries being determined, if $f(\xi)$ is a normalized Beta function, $f(\xi) = \frac{\xi^{m-1}(1-\xi)^{n-1}}{\int_0^1 \phi^{m-1}(1-\phi)^{n-1}\, d\phi}$, then the constraints,

$$\begin{aligned}\overline{Y}_{Ox} &= \int_0^1 \int_0^1 Y_{Ox}\overline{P}(Y_{Ox}, Z)\, dY_{Ox}\, dZ \\ &= \int_0^1 \left(\int_{y^1_{Ox}(Z)}^{y^2_{Ox}(Z)} Y_{Ox}\overline{P}_c(Y_{Ox}|Z)\, dY_{Ox} \right) \overline{P}(Z)\, dZ \\ \overline{Y'^2_{Ox}} &= \int_0^1 \int_0^1 (Y_{Ox} - \overline{Y}_{Ox})^2 \overline{P}(Y_{Ox}, Z)\, dY_{Ox}\, dZ \\ &= \int_0^1 \left(\int_{y^1_{Ox}(Z)}^{y^2_{Ox}(Z)} (Y_{Ox} - \overline{Y}_{Ox})^2 \overline{P}_c(Y_{Ox}|Z)\, dY_{Ox} \right) \overline{P}(Z)\, dZ\ ,\end{aligned} \tag{5}$$

according to the properties of the β function, lead to:

$$\begin{aligned} n &= \frac{(\Omega_1 - 1)(1 - \Omega_2)}{(1 - \Omega_2)\Omega_1 - \Omega_2(1 - \Omega_1)} \\ m &= \frac{\Omega_1(\Omega_2 - 1)}{(1 - \Omega_2)\Omega_1 - \Omega_2(1 - \Omega_1)}\ , \end{aligned} \tag{6}$$

where :

$$\Omega_1 = \frac{\overline{Y}_{Ox} - \overline{y^1}_{Ox}}{\overline{y^2}_{Ox} - \overline{y^1}_{Ox}}$$

$$\Omega_2 = \frac{\overline{Y'^2_{Ox}} - 2\left(\overline{y^1_{Ox}(y^2_{Ox} - y^1_{Ox})} - (\overline{y^2}_{Ox} - \overline{y^1}_{Ox})\overline{Y}_{Ox}\right)\Omega_1}{\overline{(y^2_{Ox} - y^1_{Ox})^2}\Omega_1} \qquad (7)$$

$$- \frac{\left(\overline{(y^1_{Ox})^2} - 2\overline{y^1}_{Ox}\overline{Y}_{Ox} + \overline{Y}^2_{Ox}\right)}{\overline{(y^2_{Ox} - y^1_{Ox})^2}\Omega_1} .$$

(In the equations, the mean values are defined as: $\overline{a} = \int_0^1 a(Z)\overline{P}(Z)\,dZ$.)

The mean reaction rate $\overline{\dot{\omega}}_{Ox}$ can then be computed to advance the equation in time in the Navier Stokes solver,

$$\overline{\dot{\omega}}_{Ox} = \int_0^1 \int_0^1 \dot{\omega}_{Ox}\overline{P}(Y_{Ox}, Z)\,dY_{Ox}\,dZ$$

$$= \int_0^1 \left(\int_{y^1_{Ox}(Z)}^{y^2_{Ox}(Z)} \dot{\omega}_{Ox}\overline{P}_c(Y_{Ox}|Z)\,dY_{Ox} \right) \overline{P}(Z)\,dZ \; . \qquad (8)$$

this is performed until the steady state is reached.

This dynamic "pdf generator" is able to follow different shapes of pdf according to the level of turbulence (through the quantities, $\overline{Z}$, $\overline{Z'^2}$, $\overline{Y}_{Ox}$, $\overline{Y_{Ox}'^2}$, $\tau_{t_{Ox}}$, chemistry model parameters). The finite rate chemistry effect is implicitly included in the mixing model, especially when the time scale includes informations related to the chemistry. Unlike the previous formulation, the pdf is presumed in a continuous form, reproducing the transient effect observed in the DNS simulations. This simple model can be improved using more elaborate mixing model (Gao 1992) and can be of great interest to initialize the Monte Carlo method to reduce the large amount of computer time.

5. Future plans

The study of the turbulent flame structure modeled with two-step chemistry will be completed introducing a third step, $B + I \rightarrow P$, allowing the species I to undergo recombination on both sides of the flame.

The configuration also needs some improvement; a shear will be included in the simulations using the methodology developed by Trouvé (Trouvé 1992). This is to study a model flow problem with properties closer to the non-premixed jet flame situation.

Acknowledgements

Dr. Arnaud Trouvé and Dr. Feng Gao are thanked for their helpful comments and suggestions. The author also acknowledges his fruitful interaction with Dr. Jacqueline Chen, Prof. Shankar Mahalingam, Prof. Ishwar Puri, and Dr. Poinsot.

REFERENCES

BORGHI, R., VERVISCH, L., & GARRETON, D. 1990 The calculation of local fluctuations in non-premixed turbulent flames. *Eurotherm.* **17,** Oct. 8-10, Cascais.

BORGHI, R., & POURBAIX, E. 1983 Lagrangian models for turbulent reacting flows. *Turbulent Shear Flow conferences No 4* Springer-Verlag.

CHEN, J. H., MAHALINGAM, S., PURI, I. K., & VERVISCH, L. 1992 Effect of finite–rate chemistry and unequal schmidt numbers on turbulent non–premixed flames modeled with single–step chemistry. *Paper WSS/CI 92-52, Western States Section of the Combustion Institute Fall meeting, Berkeley.*

CHEN, J. H., MAHALINGAM, S., PURI, I. K., & VERVISCH, L. 1992 Structure of turbulent non-premixed flames modeled with two-step chemistry. *Paper WSS/CI 92-51, Western States Section of the Combustion Institute Fall meeting, Berkeley.*

CHEN, J. Y., & DIBBLE, R. W. 1990 Application of reduced chemical mechanism for prediction of turbulent non-premixed methane jet flames. Sandia report 90-8447.

CHENG, T. S., WEHRMEYER, J. A., & PITZ, R. W. 1991 Simultaneous temperature and multi-species measurement in a lifted hydrogen diffusion flame by a KrF excimer laser. *AIAA 29th Aerospace Sciences Meeting* January 7-10, Reno, Nevada.

COUPLAN, J., & PRIDDIN, C. H. 1987 Modelling the flow and combustion in a production gas turbine combustor. *Turbulent Shear Flow conferences No 5* Springer-Verlag, Heidelber, August 7-9.

DIBBLE, R. W., SCHEFER, R. W., CHEN, J.-Y., HARTMANN, V., & KOLLMAN, W. 1986 Velocity and density measurements in a turbulent non-premixed flame with comparison to numerical model predictions. *Paper WSS/CI 86-65, Western States Section of the Combustion Institute Spring Meeting, Banff, Canada.*

DOPAZO, C. 1992 Recent developments in pdf methods. *To be published.*

DOPAZO, C., & O'BRIEN, R. 1976 An approach to the autoignition of a turbulent mixture. *Department of Mechanics State University of New York, Stony Brook,* N.Y. 11790.

FOX, R. O. 1992a The Fokker-Plank closure for turbulent molecular mixing. *Physics of fluid.* **A4 (6),** 1230-1244.

FOX, R. O. 1992b On the joint scalar, scalar gradient pdf in lamellar system. *To be published.*

GIBSON, C. H. 1968 Fine structure of scalar fields mixed by turbulence: I. Zero gradient points and minimal gradient surfaces. *Phys. Fluids.* **11,** 2305.

GAO, F. 1992 A mixing model for pdf simulations of turbulent reacting flows. *Annual Research Briefs 1992.* CTR, Stanford U./NASA Ames.

GONZALEZ, M., & BORGHI, R. 1986 Application of Lagrangian models to turbulent combustion. *Comb. and Flame.* **63,** 239-250.

JONES, W. P., & KOLLMANN, W. 1985 Multi-scalar pdf transport equations for turbulent diffusion flames. *Turbulent Shear Flow conferences No 5,* Springer-Verlag, Heidelber, August 7-9.

KERSTEIN, A. 1990 Linear-eddy modelling of turbulent transport. Part 3. Mixing and differential molecular diffusion in round jets. *J. Fluid Mech.* **216,** 411-435.

KUZNETSOV, V. R., & SABEL'NIKOV, V. A. 1990 Turbulence and combustion. Ed. P. A. Libby, Hemisphere Publishing Corporation.

MAGRE, P., & DIBBLE, R. W. 1988 Finite chemical kinetic effects in a subsonic turbulent hydrogen flame. *Combust. Flame.* **73,** 195–206.

MANTEL, T., & BORGHI R. 1991 A new model of premixed wrinkled flame propagation based on a scalar dissipation equation. *13th ICDERS Meeting.*

MASRI, A. R., BILGER, R. W., & DIBBLE, R. W. 1988 Turbulent non-premixed flames of methane near extinction . *Comb. and Flame.* **73,** 261–258.

NOMURA, K. K., & ELGHOBASHI 1992 Mixing characteristics of an inhomogeneous scalar in isotropic and homogeneous sheared turbulence. *Phys. Fluids.* **A4 (3),** March.

PETERS, N. 1986 Laminar flamelet concepts in turbulent combustion. *Twenty-First Symposium (International) on Combustion.* 1231–1250. The Combustion Institute.

POPE, S. B. 1979 The relationship between the probability approach and particle models for reaction in homogeneous turbulence. *Comb. and Flame.* **35,** 41–45.

POINSOT, T. 1989 Direct simulation of turbulent combustion. *Annual Research Briefs 1989.* CTR, Stanford U./NASA Ames.

POINSOT, T., & LELE, S. 1991 Boundary conditions for direct simulations of compressible viscous flows. *J. Comput. Phys.* **101,** No 1, July 92.

POINSOT, T., VEYNANTE, D., & CANDEL, S. 1991 Quenching processes and premixed turbulent combustion diagrams. *J. Fluid Mech.* **228,** 561–606.

SMITH, L., DIBBLE, R., TALBOT, L., BARLOW, R., & CARTER, C. 1992 Laser raman scattering measurements of differential molecular diffusion in nonreacting laminar and turbulent jet flows. *Paper WSS/CI 92-74, Western States Section of the Combustion Institute Fall meeting, Berkeley.*

TROUVE, A. 1991 Simulation of flame-turbulence interaction in premixed combustion. *Annual Research Briefs 1991.* CTR, Stanford U./NASA Ames.

TROUVE, A. 1992 The evolution equation for the flame surface density in premixed turbulent combustion. *Annual Research Briefs 1992.* CTR, Stanford U./NASA Ames.

VERVISCH, L. 1992 Applications of pdf turbulent combustion models to non-premixed flame calculations. Von Karman Inst. Modeling of Combustion and Turbulence, March 9-3.

VIOLLET, P.-L., GABILLARD, M., & MECHITOUA, N. 1990 Modélisation de plasma en écoulement. *Revue de Phys. Appl.* **25**, 843–857.

VRANOS, A., KNIGHT, B. A., PROSCIA, W. M., CHIAPPETTA, L., & SMOOKE, M. D. 1992 Nitric oxide formation and differential diffusion in a turbulent methane-hydrogen diffusion flame. *Twenty-Fourth Symposium (International) on Combustion.* The Combustion Institute.

WARNARTZ, J., & ROGG, B. 1986 Turbulent non premixed combustion in partially premixed flamelets detailed chemistry. *Twenty-First Symposium (International) on Combustion.* 1533-1541. The Combustion Institute.

Generation of two-dimensional vortices in a cross-flow

By J.-M. Samaniego

1. Motivations and objectives

The present report is concerned with an experimental study on the generation of plane two-dimensional vortices in a cross-flow. The purpose of this work is to address the problem of the feasibility of a two-dimensional experiment of flame-vortex interactions.

The interaction of a laminar flame with a vortex pair is a model problem in which several questions relevant to turbulent combustion may be addressed such as transient and curvature effects. Based on direct numerical simulation (DNS) of flame-vortex interactions, Poinsot *et al.* (1991) have shown the existence of different types of interaction from the wrinkling of the flame front to local quenching of the reaction zone (Fig. 1). The authors emphasized the importance of heat losses in the quenching process. Studying the interaction of a freely propagating flame with a vortex ring, Roberts & Driscoll (1991) confirmed the existence of the different regimes of flame-vortex interaction. These works have extended the validity of flamelet models for premixed combustion.

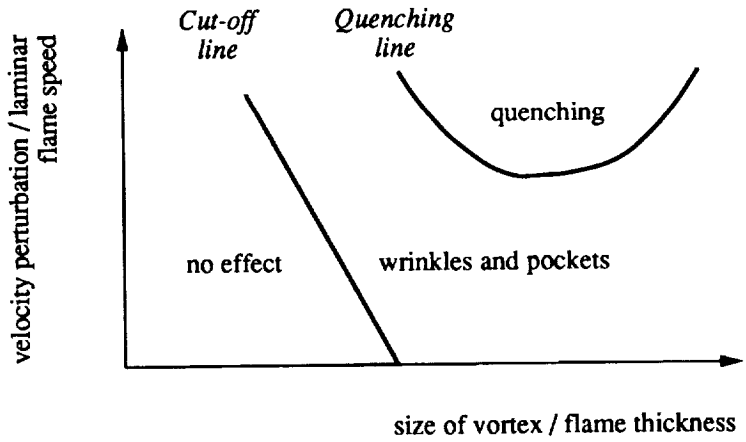

FIGURE 1. The different types of flame-vortex interaction (Poinsot *et al.* 1991).

Recent experimental studies have focused on the quenching of the flame front by a vortex ring: *OH* fluorescence imaging was applied to track the flame front and identify the occurrence of quenching (Roberts *et al.* 1992) and two-color Particle Image Velocimetry to obtain instantaneous planar cuts of the velocity field through

the vortex ring (Driscoll *et al.* 1993). Such studies have allowed a remarkable insight in the quenching process although some problems remain. First, the role of heat losses, which are believed to be one important ingredient, has not been addressed yet. An estimate of the heat losses can be obtained by measurements of the temperature field. Secondly, using OH fluorescence to study flame quenching is questionable since OH molecules persist long after their creation in the flame zone and, hence, do not mark the region of chemical reaction accurately. An alternative approach is the line-of-sight imaging of spontaneous light emission from species such as C_2 or CH that have extremely short lifetimes in the flame and, as such, are very good indicators of the reaction zone. Thirdly, bias of the results due to a misalignment of the vortex trajectory with the laser sheet might occur and introduce significant errors in estimating velocities. In this respect, a planar two-dimensional experiment appears as an attractive solution for the study of flame-vortex interactions.

Computations of two-dimensional and three-dimensional turbulent premixed flames using DNS have investigated the behavior of a flame front submitted to a homogeneous and isotropic turbulent field (Rutland & Trouvé 1990, Trouvé 1991, Haworth & Poinsot 1992). These studies have shown that two parameters play an essential role in the dynamics of the flame sheet: the local curvature of the flame front and the Lewis number. All these numerical studies have a common idealization: they are based on a simplified chemical model (one-step irreversible reaction). Whether or not this assumption is valid is an open question. It clearly depends on the objectives: it is certainly inappropriate for the prediction of pollutant formation, but it could be satisfactory for the study of the dynamics of the flame front. This problem needs to be addressed in order to determine the validity of previous DNS studies. One way of achieving this goal is a project involving an experimental and numerical study of flame-vortex interaction. Comparison of numerical and experimental results would serve as a test for the validity of the chemical model.

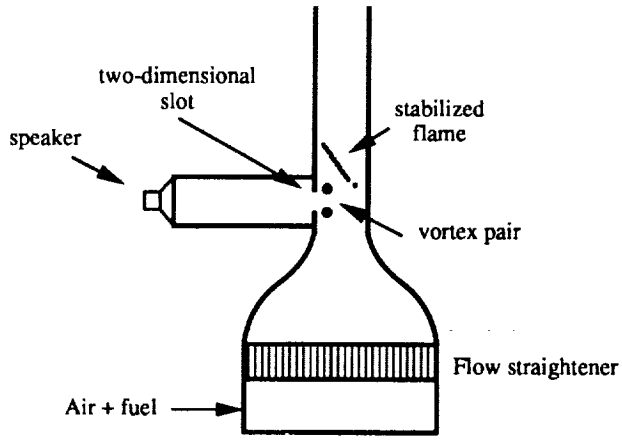

FIGURE 2. Sketch of the proposed two-dimensional geometry.

	r/d	u_{max}/S_l
Poinsot *et al.*	1 to 10	4 to 100
Roberts and Driscoll	6 to 50	0.5 to 20

Table I. Values of r/d and u_{max}/S_l used in the works of Poinsot et al. (1991) and Roberts & Driscoll (1991). r is the size of the vortex pair (size of orifice in Roberts and Driscoll 1991), d the flame thickness, S_l the laminar flame speed and u_{max} the maximum rotational velocity.

The proposed experimental geometry is a two-dimensional tunnel in which the flame is anchored to a stabilizer (for example a heated wire). Since the flame speed of a hydrocarbon flame is of the order of a few tens of centimeters per second ($\sim 40\,cm/s$ for stoichiometric mixtures), the flow speed must be of the order of $1\ m/s$ to achieve flame stabilization. A vortex pair would be generated through a slot located on one lateral wall and would eventually interact with the oblique flame sheet (Fig. 2). While it is possible to stabilize such flames (see for example Boyer & Quinard 1990), the generation of a two-dimensional vortex pair (through a boundary layer) and its propagation is questionable. Various mechanisms may make it difficult: end wall effects (Gerich & Eckelmann 1982, Auerbach 1987), Crow instability (Crow 1970), columnar instability (Leibovich & Stewartson 1983), etc.

The slot width prescribes somehow the size of the vortex pair r. Since the flame thickness d ranges between 1 and 4 millimeters for hydrocarbon flames at ambient conditions (d can be varied by varying the equivalence ratio) and since the ratio r/d must remain small enough ($r/d < 20$) to allow future comparison with DNS, r must remain smaller than a few centimeters and, hence, the slot width. Furthermore, following the values of u_{max}/S_l given in Table 1, u_{max} must range somewhere from a few centimeters per second to a few tens of meters per second in order to address various kinds of interactions (Table I summarizes the values of r/d and u_{max}/S_l in the works of Poinsot *et al.* 1991 and Roberts & Driscoll 1991).

In order to determine whether or not it is possible to generate two-dimensional vortex pairs in these conditions, a preliminary non reacting flow experiment, which is the purpose of the present paper, has been carried out. It involved the construction of a whole set-up: test section, flow controls, smoke generator, timing circuit. The experimental apparatus and the main results are presented and discussed in the following section.

2. Accomplishments

2.1 Experimental apparatus

The test section is a vertical tunnel with an inner square cross-section of 63.5 ×

63.5 mm^2 and a height of 381 mm (Fig. 3). The vortex pair is generated by acoustic forcing through a horizontal nozzle-shaped slot spanning over one lateral wall. The slot width can be adjusted by shifting the upper part of the wall.

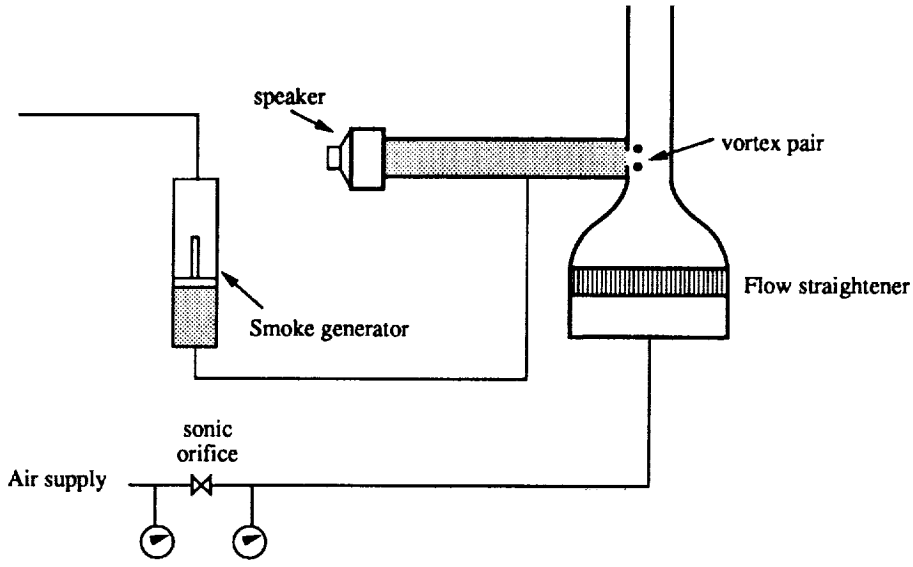

FIGURE 3. Schematic view of the set-up used for visualization of the non-reacting flowfield.

The air flow is metered by a sonic orifice and is supplied to the test section through a plenum chamber. The bulk velocity of the flow in the vertical tunnel can be varied from 0.25 to 1.0 m/s corresponding to Reynolds numbers (based on the tunnel width) ranging from 1060 to 4240.

The vortices are visualized with cigarette smoke. For this purpose, the wave guide is filled with smoke issuing from a smoke generator. When the speaker is actuated, a puff of smoke illuminated by a 100 *Watts* lamp or a strobe lamp is pushed into the tunnel. The smoke pattern, used to trace the vortex pair evolution, is recorded on video tape and photographs and then analyzed.

Velocity measurements were performed using a hot-wire anemometer DISA in order to investigate the flow in the tunnel.

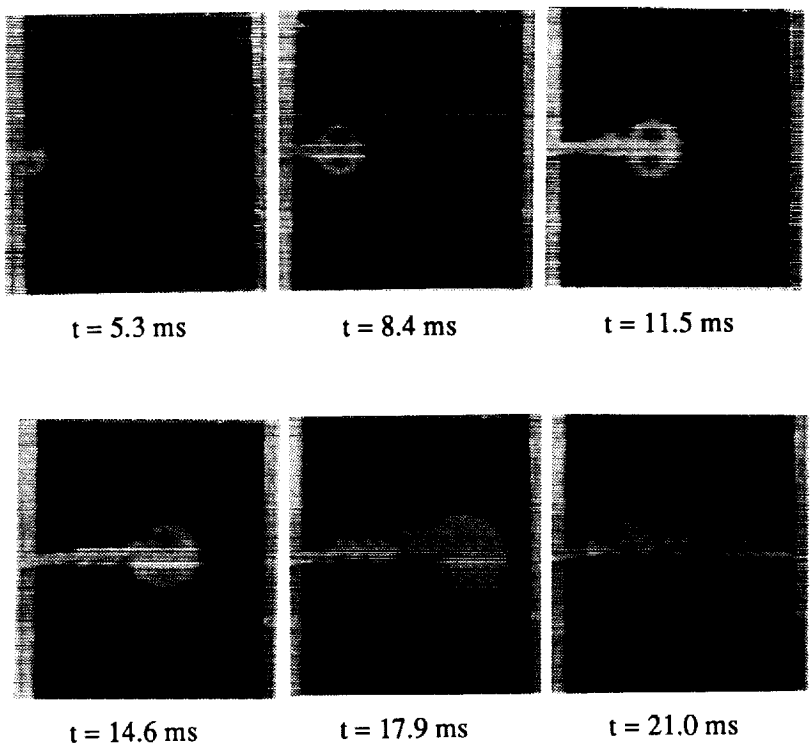

FIGURE 4. Sequence of photographs showing the vortex pair evolution without cross-flow. Slot width = 3 mm. Time $t = 0\,ms$ corresponds to the speaker excitation.

2.2 Results and discussion

2.2.1 Visualization

Figure 4 is a sequence of photographs showing the evolution of a vortex pair in the absence of cross-flow. The time step between the photographs is 3.1 ms. In this case, the slot width is set at 3 mm, and a voltage of 3.2 $Volts$ is suddenly applied through the speaker coils at $t = 0\,s$. The whole smoke puff is illuminated so that the photographs show the smoke pattern integrated over a line of sight. Consequently, a two-dimensional structure would result in a well-defined pattern, and a three-dimensional structure would correspond to a fuzzy pattern.

Although the pictures are slightly blurred, one can easily identify a vortex pair structure propagating rightward at approximately 3 m/s, followed by a "wake". The blur can be attributed to a relatively too long exposure time (1 ms) and to the effect of perspective. In the first instance, as inferred from the smoke pattern, the vortex pair is well-defined and remains self-similar. Two cores, symmetric with respect to

the vortex trajectory, are clearly visible. Later, as small spanwise counter-rotating vortices appear in the "wake", the smoke pattern within the vortex cores becomes non-symmetric and fuzzy.

It can be concluded that the vortex pair is initially two-dimensional and propagates at its self-induced velocity. The smoke trailing the vortex pair (referred previously to as a "wake") may be interpreted as a plane jet resulting from the remainder (or excess) of the fluid pushed out by the speaker membrane. This jet would underlie a Kelvin-Helmholtz instability, resulting in a sinuous mode and giving rise to an alley of counter-rotating vortices. These vortices eventually interact with the vortex pair in a way similar to a pairing process (see time $t = 14.6\,s$). During this process, the vortex pair loses its symmetry and becomes less coherent: this phenomenon can be viewed as a mechanism for transition to three-dimensionality.

Figures 5a and 5b shows a sequence of photographs of a vortex pair generated in a cross-flow of 0.50 m/s. The left column is smoke patterns illuminated by a light sheet of 1 cm thickness centered on the mid-plane of the cavity. The right column shows images of smoke wire visualization taken at same instants after the speaker excitation. The wire was located upstream of the slot at 6 mm from the opposite wall of the tunnel relative to the camera in order to investigate end wall effects. These photographs were taken using a strobe lamp as a light source. The duration of the light pulse (50 μs) is short enough to freeze the flow.

This sequence shows the same trends as Fig. 4: generation of a two-dimensional vortex pair, onset of an instability in the "wake" of the vortex pair, coalescence and rupture of symmetry. Later the smoke pattern becomes fuzzy. Other results indicate that the vortex evolution is repeatable until time $t = 10.5\,ms$ for this particular set of operating conditions (slot width, voltage, cross-flow velocity). After this time, the smoke pattern differs from one run to another. This is attributed to the unsteadiness of the cross-flow in the center of the cavity as revealed by other smoke-wire visualization.

The role of the lateral walls as a source of three-dimensionality is evidenced in Fig. 5. The vortex pair structure appears to be first disrupted near the end walls at time $t = 14.7\,ms$ (see the right column) while it keeps a coherent structure near the mid-plane of the tunnel. Later, the whole vortex pair is affected and degenerates into small-scale structures. Although the Crow instability (or other instabilities such as the columnar instability) may play a role, it seems that the dissipation of the vortex pair is controlled by the coalescence with vortices located in its "wake". This phenomenon is observed both in the cases with and without cross-flow.

One difference between these two cases is the presence of boundary layers along each wall (Fig. 6). Particularly, the presence of a boundary layer along the slot causes the starting vortex pair to be non-symmetric. The boundary layer is characterized by a distributed vorticity of one sign (either positive or negative depending on the reference frame): it has the same sign as the upper vortex vorticity and opposite sign to the lower vortex vorticity. During the roll-up process, fluid from this boundary layer is engulfed in each vortex core, and this results in a strengthening of the upper vortex and in a weakening the lower vortex. As a consequence, the

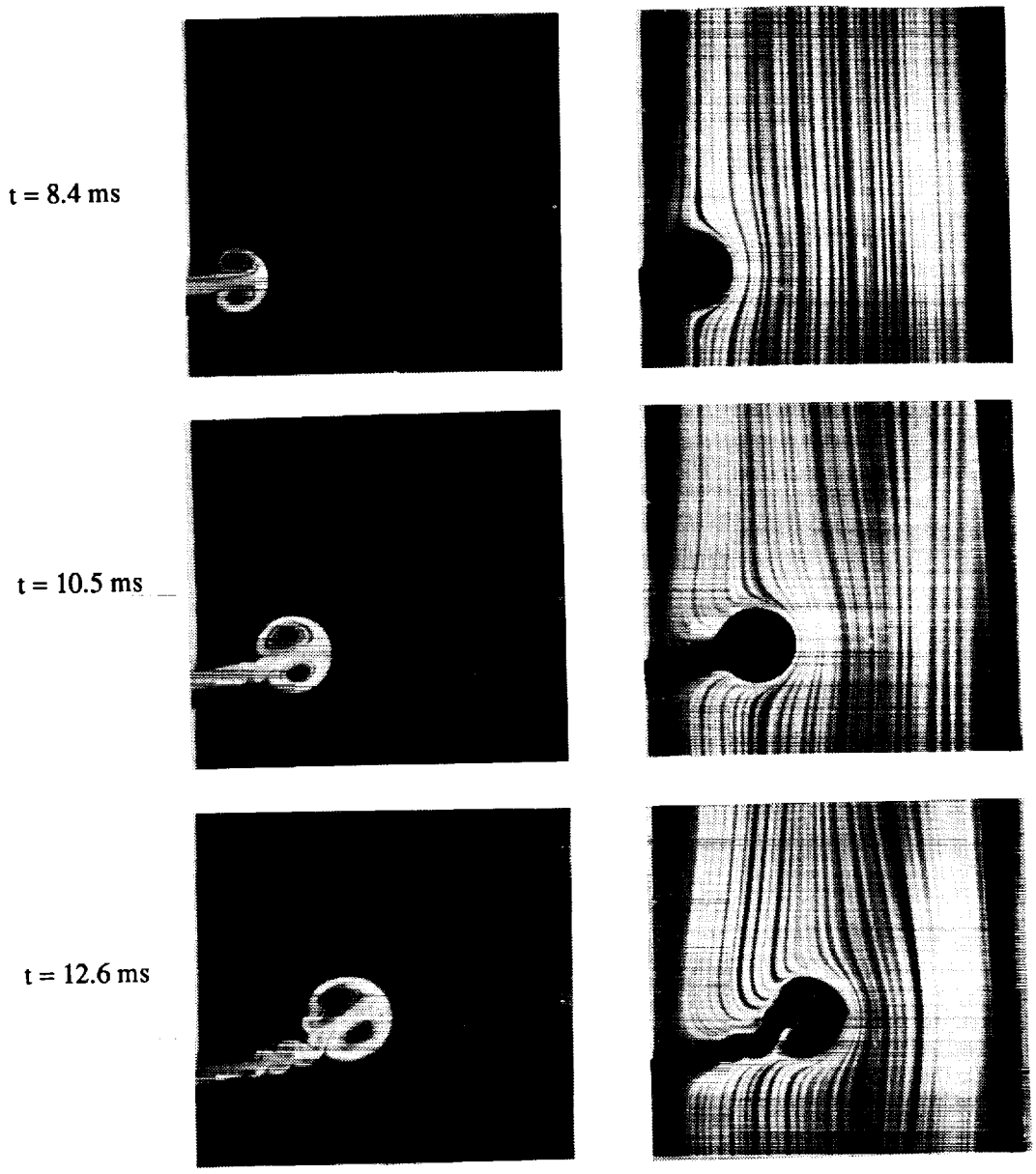

FIGURE 5A. Sequence of photographs showing the vortex pair evolution with a cross-flow of 0.5 m/s. Slot width = 3 mm. Time $t = 0\,ms$ corresponds to the speaker excitation.

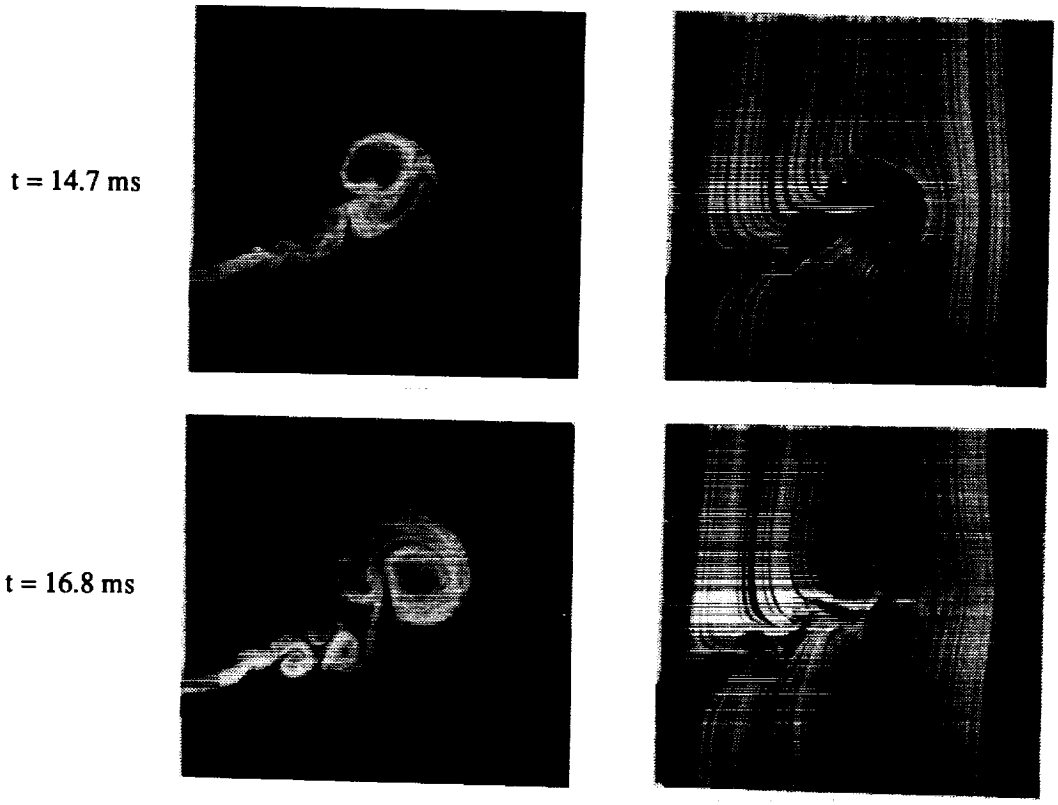

FIGURE 5B. Sequence of photographs showing the vortex pair evolution with a cross-flow of 0.5 m/s. Slot width = 3 mm. Time $t = 0\,ms$ corresponds to the speaker excitation.

vortex pair has an upward circular trajectory as shown by the sequence of Fig. 5 (Batchelor 1967).

2.2.2 parametric study: effect of voltage ΔV and slot width w

These effects have been studied using flow visualization in the absence of cross-flow. The vertical tunnel was replaced by two walls of Plexiglass so that impingement of the vortex pair on the opposite wall was avoided.

For given operating conditions (ΔV and w), a series of vortex sheddings was recorded on video tape. The axial position x and size r of the vortex pair at different moments after the roll-up were measured on the monitor screen. Fig. 7 shows a typical result for the evolution of the axial position and size of a pair vortex obtained from three different vortex sheddings ($\Delta V = 0.65\,Volts$ and $w = 3\,mm$,

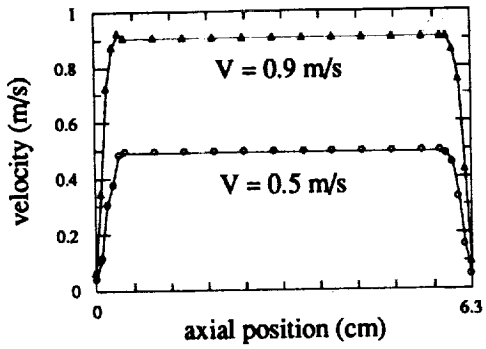

FIGURE 6. Velocity profiles at the exit of the plenum chamber for two different bulk velocities.

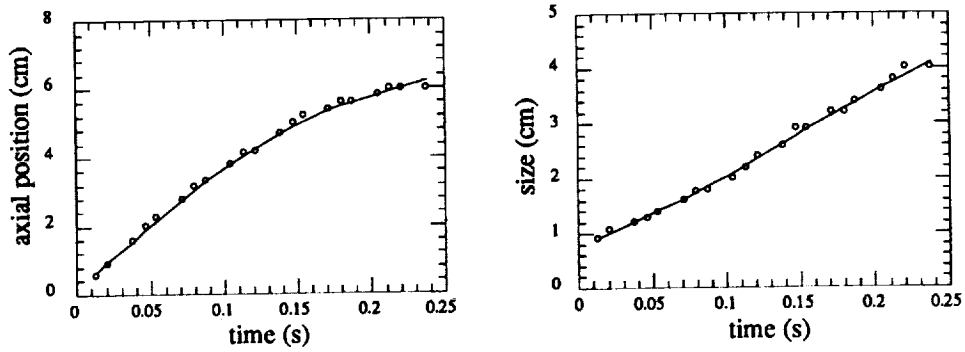

FIGURE 7. Time evolution of the position and size of a vortex pair. Slot width = 3 mm, tension applied to the speaker = 0.65 $Volts$. Time $t = 0\,ms$ is an arbitrary origin. It does not correspond to the speaker excitation.

corresponding to $V_1 = 0.42\,m/s$). Moreover, as it travels on, the vortex pair slows down and grows in size. This evolution can be explained by entrainment due to viscosity of surrounding fluid into the vortex cores and by interdiffusion of vorticity across the symmetry plane (Maxworthy 1972, Cantwell & Rott 1988).

Figure 8 shows the evolution of r/w with x/w for two different slot widths ($w = 3\,mm$ and $5\,mm$) and for various vortex Reynolds numbers ranging from 314 to 7540 ($Re = \Gamma/\nu$ with $\Gamma = 4\pi w V_1$, where ν is the kinematic viscosity and V_1 the initial displacement speed of the vortex pair as estimated from the video sequences). All the data seem to collapse on one quadratic-like curve. This indicates that x/d and r/d are strongly correlated and that a similarity law underlies the behavior of the vortex pairs. It can be deduced that the distance through which the vortex pair remains two-dimensional scales with the slot width (this distance is about ten times the slot width as indicated by the photographs). It can also be noticed that the initial size of the vortex pair is approximately 4 times the slot width.

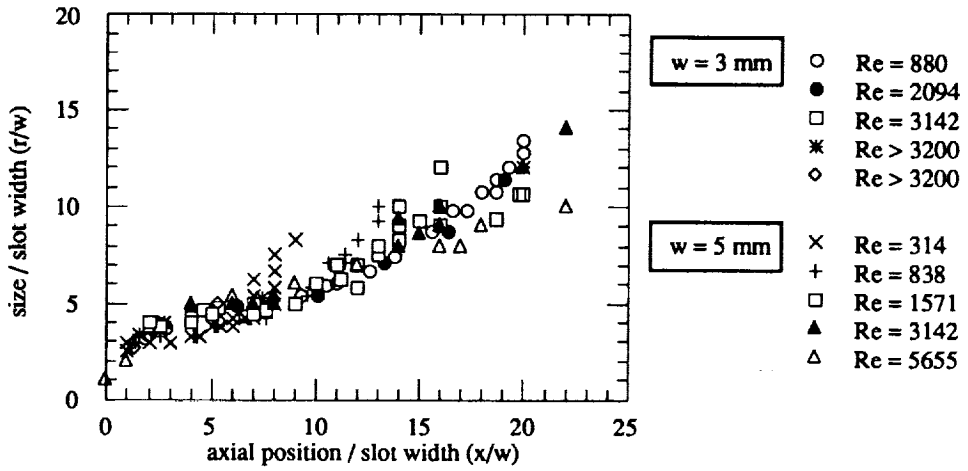

FIGURE 8. Correlation between the non-dimensionalized size and position of vortex pairs for different Reynolds numbers and two slot widths.

2.2.3 On the feasibility of a two-dimensional experiment

The present results indicate that it is possible to generate two-dimensional vortex pairs through a boundary layer. These structures remain two-dimensional over a significant distance (about 10 times the slot width). Since the flame front can be placed as close to the slot as needed by moving the flame stabilizer, it is possible to meet the conditions for a two-dimensional interaction between a flame front and a vortex pair.

3. Future plans

As a consequence of this work, an experimental facility designed for combustion will be set up. Diagnostic tools to monitor the flowfield will be developed. Two-dimensional instantaneous velocity fields will be determined using particle image velocimetry (PIV) or particle tracking velocimetry (PTV). The instantaneous location of the flame front, and possibly the distribution of the reaction rate along the flame front, will be obtained by line-of-sight imaging of radical emission (C_2 or CH). A technique to characterize the heat losses will also be devised.

These data will be used as initial condition for DNS. Comparison between computations and experiments will serve as a test for the quality of the chemical model used in the code.

Acknowledgements

This work is conducted in collaboration with Prof. C. T. Bowman of the High Temperature Gasdynamics Lab. Helpful discussions with Prof. W. C. Reynolds are also gratefully acknowledged. I also wish to thank Dr. A. Trouvé, Dr. T. J.

Poinsot, Dr. F. Gao, and Dr. L. Vervisch for their encouragement and for valuable discussions during the course of this project.

REFERENCES

AUERBACH, D. 1987 Some three-dimensional effects during vortex generation at a straight edge. *Exp. Fluids.* **5,** 385-392.

BATCHELOR, G. K. 1967 *An introduction to Fluid Mechanics.*

BOYER, L. & QUINARD, J. 1990 On the dynamics of anchored flames. *Comb. & Flame.* **82,** 51-65.

CANTWELL, B. & ROTT, N. 1988 The decay of a viscous vortex pair. *Phys. Fluid.* **31,** 3213-3224.

CROW, S. C. 1970 Stability theory for a pair of trailing vortices. *AIAA J.* **8,** 2172-2179.

GERICH, D. & ECKELMANN, H. 1982 Influence of end plates and free ends on the shedding frequency of circular cylinders. *J. Fluid Mech.* **122,** 109-121.

HAWORTH, D. C. & POINSOT, T. J. 1992 Numerical simulations of Lewis number effects in turbulent premixed flames. *Submitted for publication.*

LEIBOVICH, S. & STEWARTSON, K. 1983 A sufficient condition for the instability of columnar vortices. *J. Fluid Mech.* **126,** 335-356.

MAXWORTHY, T. 1972 The structure and stability of vortex rings. *J. Fluid Mech.* **51,** 15-32.

POINSOT, T. J., VEYNANTE, D., & CANDEL S. 1991 Quenching processes and premixed turbulent combustion diagrams. *J. Fluid Mech.* **228,** 561-605.

ROBERTS, W. L. & DRISCOLL, J. F. 1991 A laminar vortex interacting with a premixed flame: measured formation of pockets of reactants. *Comb. & Flame.* **87,** 245-256.

RUTLAND, C. J. & TROUVÉ, A. 1990 Premixed flame simulations for non-unity Lewis numbers. *CTR Proceedings of the 1990 Summer Program.* Stanford Univ./ NASA Ames.

TROUVÉ, A. 1991 Simulations of flame turbulence interactions in turbulent premixed flames. *CTR Annual Research Briefs-1991.* Stanford Univ./NASA Ames.

Center for Turbulence Research
Annual Research Briefs 1992

Why does preferential diffusion strongly affect premixed turbulent combustion?

By V. R. Kuznetsov [1]

1. Introduction

Combustion of premixed reactants in a turbulent flow is a classical but unresolved problem. The key problem is to explain the following data: the maximal turbulent and laminar burning velocities u_t and u_L occur at different equivalence ratios Φ (for a review of experimental data, see Kuznetsov & Sabel'nikov (1990), Chapter 6). Some examples of fuel behavior are: H_2 displays a large shift of the maximum value of u_t towards the lean mixture, CH_4 has a small lean shift, C_2H_6 has no shift, C_3H_8 has a moderate rich shift, and benzene has a large rich shift. The shift can be quite large. For example, the maximum of u_t occurs at $\Phi = 1.0$ for H_2 and at $\Phi = 1.4$ for benzene, while, the maximum of u_L is at $\Phi = 1.7$ for H_2 and $\Phi = 1$ for benzene. This shift is observed over a large range of Damköhler number, but is more pronounced at low Damköhler number. A theory should explain these data.

It can be seen that the fuels in the above-mentioned sequence are arranged according to the ratio of the molecular diffusivities of oxygen (D_o) and fuel (D_f). It can, therefore, be hypothesized that preferential diffusion strongly affects turbulent combustion in all regimes. The correlation between u_t and blow-off velocity, based on this assumption, is very good over a wide range of conditions (Kuznetsov & Sabel'nikov (1990), Chapter 6).

If the reaction zone were distributed, the influence of molecular diffusivity variation should be unimportant since only large-scale fluctuations should affect the reaction and their properties do not depend on Reynolds number. On the other hand, if the flame front were thin (which was verified by direct numerical simulation (Rutland *et al.*, 1989; Trouvé, 1991)), the Reynolds number (based on the flame front thickness) would be small and the influence of preferential diffusion could be significant.

It is known that the equivalence ratio varies along a curved flame if $D_f \neq D_o$. However, the mean flame radius of curvature is much larger than the laminar flame thickness δ_L. Therefore, significant influence of preferential diffusion should occur only if the flame propagation speed varies with flame curvature. This conclusion agrees with Zel'dovich's long-standing idea about the important role of leading points of a flame (the points $L_1, L_2, \ldots$ in Fig. 1 which are deep inside the fresh mixture).

The main objective of this paper is to prove Zel'dovich's hypothesis. An equation for the mean flame surface area density (MFSAD) will be employed for this purpose,

1 Central Institute of Aviation Motors, Moscow, Russia

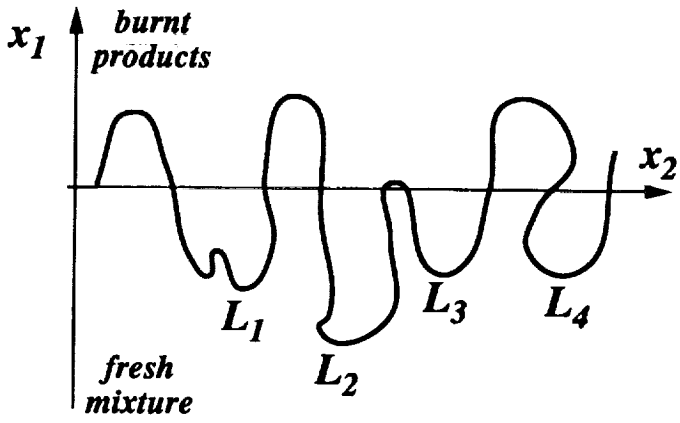

FIGURE 1. A sketch of turbulent flame front. $L_1, L_2, \ldots$ are leading points.

a popular treatment (for a review see Candel, *et al.*, 1990). An equation for MFSAD can be written

$$\left(\frac{\partial \Sigma_f}{\partial t} + < u_k > \frac{\partial \Sigma_f}{\partial x_k}\right) = \frac{\partial}{\partial x_l} D_t \frac{\partial \Sigma_f}{\partial x_l} + H\Sigma_f - G\Sigma_f^2 \tag{1}$$

where D_t is a turbulent diffusivity, H and G are positive functions depending on turbulence properties, and Σ_f is MFSAD.

The second objective of this paper is to suggest a different approach to the derivation of the equation for MFSAD. It is based on the pdf equation for the reaction progress variable C and the relation between the pdf and MFSAD (Kuznetsov & Sabel'nikov (1990)). As will be seen later, this treatment suggests an entirely different closure assumption.

2. Assumptions

We wish to prove the hypothesis about the crucial role of leading points for the case of equal diffusivities, so we consider the case in which the diffusivities of all species and heat are equal.

The main properties of turbulent flames can be correlated using non-dimensional numbers based on two characteristics of the laminar flame, u_L and δ_L (Kuznetsov & Sabel'nikov (1990), Chapter 6). If this is the case, the detailed chemical source term is irrelevant, and it is important only to model u_L and δ_L correctly. This reasoning is widely used (see Rutland, *et al*, 1989). It can then be assumed that the source term in the equation for the reaction progress variable, C, depends only on C itself so that the governing equation is

$$\rho \frac{\partial C}{\partial t} + \rho u_k \frac{\partial C}{\partial x_k} = \nabla D \rho \nabla C + W(C) \tag{2}$$

We shall assume that the dependence of D or ρ on C is known.

If only these two quantities (i.e., u_L and δ_L) are important, it is sufficient to study the high activation energy limit, i.e., it is assumed that

$$W = 0 \quad \text{if} \quad C \leq C_o. \tag{3}$$

$$\int_{C_o}^{1} w dC = const \tag{4}$$

where $C_o \to 1$. It is clear from Eq. (4) that u_L remains constant as $C_o \to 1$.

If $C_o \to 1$, the chemical reaction zone is located on the surface on which $C = 1^-$. This definition is required since a large volume is occupied by fully burnt products in which $C \equiv 1$. If C_o is close to unity, the usual analysis of the solution within the reaction zone proves that

$$\frac{\partial C}{\partial n} = \frac{\rho_o u_L}{\rho_b D_b} \tag{5}$$

Here n is normal to the surface $C = 1^-$, and subscripts 0 and b denote fresh mixture and burnt products. It should be kept in mind that Eq. (5) is exact even when the flamelet model is not valid.

There may be some confusion if the limit $C_o \to 1$ is studied. Indeed, Eq. (4) shows that W tends to $const\ \delta(C-1)$. At the same time, there is a term proportional to $\delta(C-1)$ in the pdf (because there is a non- zero volume where $C = 1$). Since there is a term $\partial(WP)\partial C$ in the equation for the pdf, there can be some confusion. To avoid it, let us choose $W(C) with (C_o \neq 1)$ so that value $C = 1$ occurs far from the flame. For example, we might let $W = const$ if $C_o < C < 1$. For the plane, steady laminar flame, one can prove that $C = 1$ at a finite distance from the flame. The equation for the pdf can be obtained, and only then will the limit $C_o \to 1$ be investigated.

It will also be assumed that δ_L is much smaller than the Kolmogorov scale. From the mathematical point of view, this means that $\delta_L \to 0$ (or equivalently $D \to 0$ since $\delta_L \sim D/u_L$) while other quantities are kept constant.

3. Some geometrical considerations

According to the Zel'dovich model, reaction takes place only on a surface. Hence there are combustion products ($C = 1$) on just one side of this surface, and the volume of products is not zero, i.e. the pdf of C contains a singular term proportional to $\delta(C-1)$, in agreement with the Bray-Moss (1977) model.

There is another singular term in the Bray-Moss model which is proportional to $\delta(C)$ and represents pockets of fresh mixture. However, this term should be absent at any finite Reynolds number (Kuznetsov & Sabel'nikov (1990), Chapter 1) since heat spreads simultaneously throughout the whole volume of fluid due to molecular diffusion. This means that pockets of fresh mixture are diluted by the products. The degree of such a dilution is small at large Reynolds number, i.e. this term arises only at infinite Reynolds number. In this limiting case, the flame front should be treated as infinitely thin and the continuous term in the Bray-Moss model should be absent. It will be assumed in the present treatment that the Reynolds number

is finite and, hence, the second singular term is absent. This means that there is a minimal value $C = C_{min}$ of the reaction progress variable (which depends on distance C_{min} from the flame).

Hence, one has

$$p = \gamma\delta(C-1) + F \tag{6}$$

where F is continuous if $C_{min} < C < 1$ and γ is the probability of observing the value $C = 1$. Clearly, γ can be treated as a combustion efficiency if the flamelet model is valid.

To calculate the continuous term in Eq. (6), one can use the equation (Cant *et al.*, 1990)

$$\frac{d\langle\Sigma|C = const\rangle}{dv} = F\left\langle\frac{dC}{dn}\middle|C = const\right\rangle \tag{7}$$

where Σ is the area of surface on which $C = const$ (so the left-hand side of Eq. (7) is the mean surface area density). Surfaces with different valuts of C have almost the same area since the thickness of the flame is small compared to the Kolmogorov scale. Hence,

$$\frac{d\langle\Sigma|C = const\rangle}{dv} = \Sigma_f(\vec{x}). \tag{8}$$

To calculate the conditionally averaged gradient of the reaction progress variable, let us choose some point on the surface $C = 1^-$ and the frame moving with the velocity of this point. Then, at a distance much smaller than the Kolmogorov scale and much larger than δ_L, one sees an almost plane, steady laminar flame, so that Eq. (2) reduces to

$$\rho_o u_L \frac{dC}{dn} = \frac{d}{dn} D\rho \frac{dC}{dn} + W$$

which is familiar from laminar flame theory. If $C_o \to 1$, the chemical source term can be neglected. Hence, after the integration one has

$$\rho_o u_L C = D\rho \frac{dC}{dn} \tag{9}$$

There are no random parameters, thus

$$\left\langle\frac{dC}{dn}\middle|C = const\right\rangle = \frac{\rho_o u_L}{D\rho} C \tag{10}$$

Combining Eqs. (7), (8), and (10), one has

$$F = \frac{D\rho}{\rho_o u_L C}\Sigma_f \tag{11}$$

It should be kept in mind that Eq. (11) is exact for $C = 1^-$ since Eq. (5) is exact if $C_o \to 1$. Eq. (11) is approximate for $C < 1$ since any influence of turbulence on

flame structure was neglected in Eq. (9). This influence is not necessarily small for small C since surfaces $C = const \sim C_{min}$ are located far from the flame where the structure of the scalar field is heavily affected by the turbulence. This conclusion agrees with direct numerical simulations (Rutland *et al.*, 1989) performed at large Damköhler number.

This is not a serious deficiency of Eq. (11) since the mean value of any function $\varphi(C)$ can be easily calculated using identities

$$< \varphi >=< \varphi(C)-\varphi(0) > +\varphi(0) = \gamma\varphi(1)+(1-\gamma)\varphi(0)+\frac{\Sigma_f}{\rho_o u_L}\int_o^1 D\rho\frac{\varphi(C)-\varphi(0)}{C}dC$$

The integrand has no singular points, i.e. the domain $C \sim 0$ where Eq. (11) is not valid does not play a significant role.

One can see that the pdf of reaction progress variable depends only on two functions of coordinates, the mean flame surface area density Σ_f and the combustion efficiency γ.

4. Exact equations for Σ_f and γ

It is natural to try to obtain equations for Σ_f and γ using an exact (but unclosed) equation for the pdf. Using methods developed by Kuznetsov & Sabel'nikov (1990), one can obtain two equivalent forms of the pdf equation:

$$\frac{\partial}{\partial x_k}[\rho v_k(\vec{x},C)F + \rho v_k(\vec{x},1)\gamma\delta(C-1)] = -\frac{\partial^2}{\partial C^2}N(\vec{x},C)\rho F - \frac{\partial}{\partial C}WF \qquad (12)$$

$$\frac{\partial}{\partial x_k}[\rho v_k(\vec{x},C)F + \rho v_k(\vec{x},1)\gamma\delta(C-1)] = -\frac{\partial}{\partial C}F\Delta(\vec{x},C) - \frac{\partial}{\partial C}WF \qquad (13)$$

where v_k is a flow velocity averaged at the condition $C = const$, N and Δ are quantities $D(\partial C/\partial x_k)^2$ and $\nabla D\rho\nabla C$ averaged at the same condition. These equations are valid only for the chemistry model adopted in Section 2. The presence of a δ-function on the left-hand side can lead to some confusion. To clarify it, let us note the $F \equiv 0$ if $C > 1$ and $F \neq 0$ if $C < 1$. It can be guessed that another δ-function will appear on the right-hand side on differentiation of the function F.

Quantities N and Δ can be calculated to first approximation using the flamelet model. For example, using Eq. (9), one has

$$N = \frac{\rho_o^2 u_L^2}{\rho^2 D}C^2. \qquad (14)$$

Note that this equation is exact if $C = 1$ and $C_o \to 1$ since Eq. (5) is exact. Similarly, one has

$$\Delta = \frac{\rho_o^2 u_L^2}{D\rho}C. \qquad (15)$$

The flamelet model is valid if $D \to 0$ and other quantities are kept constant. It is seen from Eq. (15) that $\Delta \to \infty$ if $D \to 0$. Therefore, Eq. (13) reduces to

$$\frac{\partial}{\partial c} F\Delta = 0 \quad \text{if} \quad C < C_o.$$

This equation is easily integrated. After the use of Eq. (15), one again has Eq. (11), which was obtained previously using purely geometrical considerations.

Thus Eq. (11) is the first term of the asymptotic expansion of the solution of the pdf equation. The difficulty is that to calculate MFSAD (which appears as a constant of integration), other terms must be investigated, i.e. small, previously neglected terms in Eq. (14) or (15) should be taken into account. This means that the small influence of turbulence on the inner structure of the flame front, flame stretch, and flame curvature should be included. Clearly, in the general case, it will also include effects of preferential diffusion.

There is a simpler approach based on integral relations which can be deduced from the exact Eqs. (12) and (13) without use of the approximate relations (14) and (15). In performing the calculations, one should keep in mind that the pdf is defined for all values of $C(-\infty < C < \infty)$ and

$$F \equiv 0 \quad \text{if} \quad C < 0 \quad \text{or} \quad C > 1. \tag{16}$$

To obtain the first equation, let us integrate Eq. (13) from C_o to $C = \infty$. Using Eqs. (3) and (16) and assuming that $C_o \to 0$, one has

$$\frac{\partial}{\partial x_i} \rho_b v_i(\vec{x}, 1)\gamma = F(\vec{x}, 1^-)\Delta(\vec{x}, 1).$$

Small corrections to Eq. (15) do not play a significant role here. Hence, using Eqs. (11) and (15), one has

$$\frac{\partial}{\partial x_i} \rho_b v_i(\vec{x}, 1)\gamma = \rho_o u_L \Sigma_f. \tag{17}$$

To obtain the second equation, one should multiply Eq. (12) by C and integrate from $C = -\infty$ to $C = C_o$. Using Eqs. (3) and (16), one has

$$\frac{\partial}{\partial x_i} \int_o^{C_o} \rho v_i F dC = [NF\rho - C\frac{\partial}{\partial C} NF\rho]_{C=C_o}.$$

Assuming $C_o \to 1$ and using Eq. (14), which is exact for $C = 1$, one has

$$\frac{\partial}{\partial x_i} \int_o^1 \rho v_i C F dC = \left[\frac{\rho_o^2 u_L^2}{D_b \rho_b} F - \frac{\partial N\rho F}{\partial C}\right]_{C=1}. \tag{18}$$

Note that the second term on the right-hand side of Eq. (18) can not be calculated exactly using Eqs. (11) and (14). To calculate it, let us compare Eqs. (12) and (13). One has

$$\frac{\partial^2}{\partial C^2} N\rho F = \frac{\partial}{\partial C} F\Delta$$

Integrating, one has

$$\frac{\partial}{\partial C} N\rho F = F\Delta. \tag{19}$$

The term $F\Delta$ can not be calculated exactly from Eqs. (11) and (15). However, the use of Eq. (19) has some advantages since Δ is related to a mean velocity of chemical reaction zone which has a clear physical meaning. Since the reaction zone is located where $C = 1^-$, its velocity in a laboratory frame u_k^{ch} is given by

$$u_k^{ch} = -\frac{\partial C}{\partial t}\frac{\partial C}{\partial x_k}\Big/\left(\frac{\partial C}{\partial x_i}\right)^2 \quad \text{if} \quad C = C_o. \tag{20}$$

Using Eqs. (2) and (20), one has

$$u_k^{ch} = \frac{\Delta}{\rho_b}\frac{\partial C}{\partial x_k}\Big/\left(\frac{\partial C}{\partial x_i}\right)^2 - u_k \quad \text{if} \quad C = C_o. \tag{21}$$

Evidently, Eq. (21) is valid if $C_o \to 1$. So the normal component of chemical reaction zone velocity relative to the local velocity of burnt products is

$$\omega = (u_k^{ch} - u_k)\frac{\partial C}{\partial x_k}\Big/\sqrt{\left(\frac{\partial C}{\partial x_k}\right)^2} = -\frac{\Delta}{\rho_b}\Big/\sqrt{\left(\frac{\partial C}{\partial x_i}\right)^2}. \tag{22}$$

It should be kept in mind that ω is negative (if the normal to the flame is directed toward the fresh mixture). To avoid confusion, it is convenient to change the sign in Eq. (22) so that ω is positive. Using Eq. (15), one has

$$\omega = \frac{D_b}{\rho_o u_L}\Delta. \tag{23}$$

This equation is valid on the surface $C = 1^-$ for instantaneous values of ω and Δ. At the same time, one needs to calculate the conditionally averaged value of Δ. This means that in the homogeneous case, quantity Δ should be averaged over a volume between surfaces $C = 1^-$ and $C = 1 - dC$. Generally speaking, the averages over this volume and over the surface $C = 1^-$ are different due to the random fluctuation of the distance between the surfaces $C = 1^-$ and $C = 1 - dC$. However, in the studied case, such fluctuations are absent since this distance is

$$dn = \frac{dC}{(\partial C/\partial u)}$$

where $\partial C/\partial u$ is constant according to Eq. (5). Hence, Eq. (22) can be averaged over surface $C = 1^-$ to calculate the conditionally averaged value of Δ.

Using Eqs. (18), (19), and (23), one has

$$\frac{\partial}{\partial x_i}\int_o^1 \rho v_i C F dC = \frac{\rho_o u_L}{D_b \rho_b}(\rho_o u_L - \rho_b \omega)F|_{C=1}.$$

The approximate Eq. (11) can now be used to obtain

$$\frac{\partial}{\partial x_i}\int_o^1 D\rho^2 v_i dC\Sigma_f = \rho_o^2 u_L(\Theta u_L - \omega)\Sigma_f \tag{24}$$

where $\Theta = \rho_o/\rho_b$.

This equation is exact if the flamelet model is used. It is seen that two quantities should be modeled: the conditionally averaged gas velocity and the difference $\Theta u_L - \omega$. It is clear that Θu_L is the velocity of a plane steady laminar flame relative to the burnt products. Hence, ω would equal to Θu_L if the properties of a flame front in a turbulent flow were exactly the same as those of a laminar flame. Of course, this is not true. In fact, a small difference between Θu_L and ω is caused by the flame curvature and strain, which can not be neglected since the left-hand side of Eq. (23) is also small (note that $D \to 0$).

5. Turbulent diffusion in a flame

Consider now the quantity v_k. It is convenient to begin with the constant density case. Since the flame front is very thin, there is no appreciable velocity difference across it, i.e. v_k does not depend on C. In a variable density case, the variation of gas velocity across the flame front can be calculated from the continuity equation. Since the flame front is almost planar, in a frame moving with the front

$$u_k = \frac{\rho}{\rho_o} u_L n_k$$

where n_k is a unit vector normal to a flame front. Hence, in the laboratory frame,

$$u_k = u_k(\vec{x}, 1^-) + \frac{\rho - \rho_b}{\rho_o} u_L n_k$$

where $u_k(\vec{x}, 1^-)$ is the gas velocity on the surface $C = 1^-$. After averaging at the condition $C = 1^-$, one has

$$v_k = v_k(\vec{x}, 1^-) + \frac{\rho - \rho_b}{\rho_o} u_L < n_k | C = 1^- > . \tag{25}$$

Consider now the case $u' >> u_L$ where u' is the rms flow velocity. Then the second term on the right-hand side of Eq. (25) can be neglected. Also, the flame moves with almost the same velocity as the gas. Hence, the theory of turbulent diffusion can be applied. This means that the quantity v_k should be treated as differential operator

$$v_k(\vec{x}, 1^-) = < u_k > - D_t \frac{\partial}{\partial x_k} \tag{26}$$

where D_t is a turbulent diffusivity. Using Eqs. (24) and (26), one has

$$\frac{\partial < u_k > \Sigma_f}{\partial x_k} = \frac{\partial}{\partial x_k} D \frac{\partial \Sigma_f}{\partial x_k} + \frac{\rho_o^2(\Theta u_L - \omega)u_L}{\int_o^1 D\rho^2 dC}\Sigma_f . \tag{27}$$

It is worth noting that the validity of Eq. (27) is questionable when $u' \sim u_L$ because the surface $C = 1^-$ is moving rapidly relative to the gas. At the same time, the surface on which a non-reactive scalar is constant moves with the Kolmogorov velocity relative to the gas. This is easily seen from Eq. (22) which is also valid for a non-reacting scalar if u_k^{ch} is the velocity of an isoscalar surface. Obviously, the quantities Δ and $(\partial C/\partial x_i)^2$ have Kolmogorov scaling. Hence, the left-hand side of Eq. (22) also has Kolmogorov scaling, i.e. $\omega << u'$.

Therefore, it could be expected that if $u' \sim u_L$, the quantity D_t in Eq. (27) is not the turbulent diffusivity of non-reactive scalar. Even counter-gradient diffusion can be expected.

The same approach can be used to close Eq. (17), i.e.

$$\frac{\partial}{\partial x_k} < u_k > \gamma = \frac{\partial}{\partial x_k} D_t \frac{\partial \gamma}{\partial x_k} + \Theta u_L \Sigma_f. \tag{28}$$

6. Effects of flame curvature

As was mentioned earlier, one can not neglect the difference between Θu_L and ω. It is easily seen that if one assumes $\Theta u_L - \omega = const - const\ \Sigma_f$, then Eq. (27) reduces to Eq. (1). However, we do not intend to develop a model for this difference since, as will be seen later, we can reach important conclusions by analyzing only the sign of difference $\Theta u_L - \omega$ in various parts of a flame.

We shall consider only the effects of flame curvature. Obviously, flame curvature in low and high mean temperature regions have opposite predominant signs. This becomes clear from examination of Fig. 1 where a flame homogeneous in x_2 direction is shown. In a low mean temperature region ($x_2 < 0$), the flame front $x_1(x_2)$ has more minima than maxima. In a high mean temperature region ($x_2 > 0$), the flame front has more maxima than minima. One more example is the Gaussian curve $x_1(x_2)$. In this case, one has

$$\left\langle \frac{d^2 x_1}{dx_2^2} \middle| x_1 = const \right\rangle = -\left\langle \left(\frac{dx_1}{dx_2}\right)^2 \right\rangle \frac{x_1}{< x_1^2 >},$$

i.e. the flame curvature is positive in a low mean temperature region and is negative in a high mean temperature region.

It was shown long ago (Markstein, 1964) that $\Theta u_L > \omega$ if the curvature is negative and $\Theta u_L < \omega$ if the curvature is positive. So $\Theta u_L < \omega$ in a high mean temperature part of a flame and $\Theta u_L > \omega$ in a low mean temperature part of a flame. For the plane turbulent flame shown in Fig. 1, one has

$$\Theta u_L - \omega > 0 \quad \text{if} \quad x_1 \to -\infty \tag{28}$$

$$\Theta u_L - \omega < 0 \quad \text{if} \quad x_1 \to +\infty. \tag{29}$$

7. Plane turbulent flame

Consider now a steady plane turbulent flame such as the one shown in Fig. 1. One has

$$< u_1 > = u_t \quad \text{if} \quad x_1 \to -\infty$$
$$< u_1 > = \Theta u_t \quad \text{if} \quad x_1 \to +\infty.$$

Let us analyze solutions of Eq. (27) in the regions $x_1 \to +\infty$ and $x_1 \to -\infty$, assuming that all coefficients in this equation tend to constants in these limits.

One has

$$\Sigma_f = const \ \exp\left\{\frac{x_1}{2D_t}\left(\Theta u_t \pm \sqrt{\Theta^2 u_t^2 - w}\right)\right\} \quad \text{if} \quad x_1 \to +\infty$$

where

$$w = \frac{4D_t\rho_o^2(\Theta u_L - \omega)u_L}{\int_o^1 D\rho^2 dC}.$$

One can see from Eq. (29) that $w < 0$; hence, one solution increases without bound and the other tends to zero as $x_1 \to \infty$.

One has also

$$\Sigma_f = const \ exp\left\{\frac{x_1}{2D_2}\left(u_t \pm \sqrt{u_t^2 - w}\right)\right\}.$$

One can see from Eq. (28) that $w > 0$. So there are two cases. The first one is $u_t < \sqrt{w}$, in which case each solution changes sign and is meaningless. The second case is $u_t \geq \sqrt{w}$, and both solutions tend to zero as $x_1 \to -\infty$. Therefore, the spectrum of eigenvalues is continuous. Such spectra are often met in the combustion theory and other areas (Barenblatt, *et al.*, 1985). It was proven that the physical meaningful velocity is the minimal value of flame velocity (the other values are due to the initial disturbances). Hence, one has

$$u_t = \sqrt{\frac{4Du_L\rho_o^2(\Theta u_L - w)}{\int_o^1 D\rho^2 dC}}.$$

Since u_t depends only on value w deep in the fresh mixture, this proves Zel'dovich's assumption about the crucial role of leading points.

As was said above, the difference $\Theta u_L - \omega$ depends on flame curvature. In the general case, the value of this difference depends on effects caused by the preferential diffusion. This means that $\Theta u_L - \omega$ and u_L should be calculated at an equivalence ratio different from the overall equivalence ratio. This is the cause of a shift between maximal values of u_t and u_L.

The sign of this shift can be established by studying simple configuration (say, a spherical flame). It was found that $\Phi_f < \Phi$ if $D_t > D_o$ and $\Phi_f > \Phi$ if $D_f < D_o$ (Kuznetsov & Sabel'nikov, 1990). Here, Φ_f is the equivalence ratio in the reaction zone and Φ is the overall equivalence ratio. Therefore, a lean shift should be observed in H_2-air flame and a rich shift should be observed in C_3H_8-air flame. This conclusion is fully consistent with experimental data (see Introduction).

8. Conclusion

This investigation led to three important conclusions:

i) The influence of turbulence on the inner structure of a flame front is quite important even when the laminar flame thickness is much smaller than the Kolmogorov scale.

ii) Turbulent flame propagation depends on conditions within the low temperature part of a flame. Preferential diffusion plays an important role here because flame curvature in this part of the flame has a predominant sign.

iii) To develop a correct equation for the mean flame surface area density, one should properly model the difference between laminar flame velocity and the actual velocity of a flame front.

REFERENCES

BARENBLATT, G. I., ZEL'DOVICH, YA.B., LIBROVICH, V. B., & MAKHVILADSE, G. M. 1985 *The Mathematical Theory of Combustion and Explosions*, Plenum, NY.

BRAY, K. N. C., & MOSS, J. B. 1977 *Acta Astronautica* **4**, 291-319.

CANDEL, S., VEYNANTE, D., LACAS, F., MAISTRET, E., DARABIHA, N., & POINSOT, T. 1990 *Rec. Adv. in Comb. Model*, B. Larrouturou, ed., Series on Adv. in Math. for App. Sci., World Scientific, Singapore.

CANT, R. S., POPE, S. B., & BRAY, K. N. C. 1990 *Twenty-third Symp. (Int.) on Combustion*, The Combustion Inst., 809-815.

KUZNETSOV, V. R., & SABEL'NIKOV, V. A. 1990 *Turbulence and Combustion*, Hemisphere.

MARKSTEIN, G. H. 1964 *Nonsteady Flame Propagation*, Pergamon Press, MacMillan Corp., New York.

RUTLAND, C. J., FERZIGER, J. H., & CANTWELL, B. J. 1989 Rept. No. TF-44, Thermosciences Div., Dept. Mech. Engr., Stanford Univ.

TROUVÉ, A. 1991 *Annual Research Briefs*, Center for Turbulence Research, Stanford Univ./NASA Ames, 237-286.

ZEL'DOVICH, YA.B. 1979 Private communication.

Tensoral: a system for post-processing turbulence simulation data

By Eliot Dresselhaus

1. Motivations and objectives

1.1 General motivations

Many computer simulations in engineering and science — and especially in computational fluid dynamics (CFD) — produce huge quantities of numerical data. These data are often so large (consider the roughly 1 Gbyte needed for a single scalar variable in 512^3 isotropic turbulence simulations) as to make even relatively simple post-processing of this data unwieldy. The data, once computed and quality-assured, is most likely analyzed by only a few people (usually only the simulation's authors) and from at most a few perspectives (usually only those at which the authors are most concerned and knowledgeable). As a result, much useful numerical data is under-utilized. Since future state-of-the-art simulations will produce even larger datasets, will use more complex flow geometries, and will be performed on more complex super-computers (for example, super-computers with many loosely coupled processors), data management issues will become increasingly cumbersome.

My goal is to provide software which will automate the present and future task of managing and post-processing large turbulence datasets. My research has focused on the development of these software tools — specifically, through the development of a very high-level language called "*Tensoral*". The ultimate goal of *Tensoral* is to convert high-level mathematical expressions (tensor algebra, calculus, and statistics) into efficient low-level programs which numerically calculate these expressions given simulation datasets. For example, a user's program to calculate vorticity would be coded in *Tensoral* as something akin to $\vec{\omega} = \nabla \times \vec{u}$. *Tensoral* would process this "program" — at least for the case of homogeneous turbulence on the Cray Y-MP — into a roughly 200-line *Vectoral* program to calculate vorticity.

This approach to the database and post-processing problem has several advantages. Using *Tensoral* the numerical and data management details of a simulation are shielded from the concerns of the end user. This shielding is carried out without sacrificing post-processor efficiency and robustness. Another advantage of *Tensoral* is that its very high-level nature lends itself to portability across a wide variety of computing (and super-computing) platforms. This is especially important considering the rapidity of changes in supercomputing hardware.

1.2 Specific motivations and objectives

The fundamental scientific goal of fluids research is to reach an understanding of the correlation between the Navier–Stokes equations

$$\partial_t \vec{u} + (\vec{u} \cdot \nabla)\vec{u} = -\nabla p/\rho + \nu \nabla^2 \vec{u}$$

(whether incompressible or compressible) and the observed and theoretically predicted features of the velocity field $\vec{u}(\vec{x},t)$, the pressure field $p(\vec{x},t)$, and other related quantities. $\vec{u}(\vec{x},t)$ is the fundamental hydrodynamic quantity: all other quantities, both dynamic and statistical, are derived from it (at least for incompressible flows). Turbulence theory, modeling, and experiments are all phrased in terms of quantities derived from the velocity field $\vec{u}(\vec{x},t)$. The quantities arising in this theory, modeling, and experiments are precisely the ones we desire to compute; they include:

- the vorticity vector field, $\vec{\omega}(\vec{x},t) = \nabla \times \vec{u}(\vec{x},t)$,
- the strain rate tensor, $S_{ij} = (\partial_i u_j + \partial_j u_i)/2$,
- the pressure scalar, $p(\vec{x},t) = -\nabla^{-2}\, \nabla \cdot (\vec{u} \cdot \nabla)\vec{u}$ (for incompressible flows),
- the kinetic energy dissipation density $\epsilon(\vec{x},t) = \nu \sum_{ij} S_{ij} S_{ij}$ (incompressible),
- the wave-space velocity field $\vec{u}(\vec{k},t)$ and associated energy spectrum $E(k) = |\vec{u}(\vec{k},t)|^2$,
- the density scalar $\rho(\vec{x},t)$ (for compressible flows),
- the stream function $\vec{\psi}$, $\nabla \times \vec{\psi} = \vec{u}$,
- the helicity density, $\vec{u} \cdot \vec{\omega}$.

Statistical quantities of interest include:

- mean velocity profiles and other averaged velocity components,
- the Reynolds stress tensor $R_{ij} = \langle u_i u_j \rangle$,
- the correlation tensor $\langle u_i(\vec{x}) u_j(\vec{x} + \vec{x}') \rangle$,
- the total energy dissipation $\epsilon \propto \sum_{ij} \langle S_{ij} S_{ij} \rangle$,
- the enstrophy (mean square vorticity) $\langle \vec{\omega}^2 \rangle$,
- the pressure strain correlation $\langle p S_{ij} \rangle$.

We desire to compute quantities such as the above using data from several families of turbulence simulations. These datasets solve either the incompressible or compressible Navier–Stokes equations for a variety of geometries and boundary conditions. Different geometries and boundary conditions imply that the velocity field is represented by different grids or with various different orthogonal function expansions (for spectral methods). Even though these datasets simulate roughly the same underlying equations, such dissimilarities in geometry and boundary conditions require dissimilar numerical methods and data management schemes. Some simulations use orthogonal functions (e.g. Fourier, Chebyshev, Jacobi eigenfunctions) to satisfy the boundary conditions; derivatives are calculated spectrally. Other simulations use finite-difference methods to calculate derivatives and are likely set in complex geometries (relative to the spectral simulations). Certain simulations use curvilinear grids. Some simulations evolve the evolution equation for $\vec{u}$; others evolve its curl, $\vec{\omega}$. Thus, some databases contain the velocity field $\vec{u}$ itself while others contain its curl. On a more mundane level, the simulations are performed on several different super-computers (Cray Y-MP, Intel Hypercube, Thinking Machines CM-2) and retain some degree of machine specificity even at the database level (e.g. machine byte-order, floating point format, machine-specific optimized Fourier transform routines, etc.).

2.2 Current post-processing

Currently all post-processing of turbulence data is done "by hand." That is, for each simulation and for each desired quantity, someone must either add the required code to an existing post-processor or develop a specific new post-processor, perhaps with an existing one as a model. If the databases in question were small and simple, either of these options would be straightforward. Since the databases are very large and have numerical quirks to them, both options involve significant effort.

A simple example will illustrate this. Suppose we desire to calculate the physical-space pressure $p(\vec{x})$ given a wave-space space velocity field snapshot $\vec{u}(\vec{k})$ from an isotropic turbulence database (the simplest to post-process in the above table). Here is an outline of what must be done to calculate $p(\vec{x}) = -\nabla^{-2} \sum_{ij} \frac{\partial u_i}{\partial x_j} \frac{\partial u_j}{\partial x_i}$

- Read in $\vec{u}(\vec{k})$ in k_x-k_y planes and calculate necessary y derivatives in wave space (multiplying by ik_y).
- Fourier transform these derivatives from wave y space to physical y space. This is the first of three sub-transform steps that make up a full three-dimensional Fourier transform.
- Read in data in x-z planes, still in wave space, and calculate necessary x and z derivatives (multiplying by ik_x and ik_z).
- Fourier transform both x and z axes into physical space. At this point, all of the required velocity derivatives are in physical space.
- Form the source term $\sum_{ij} \frac{\partial u_i}{\partial x_j} \frac{\partial u_j}{\partial x_i}$ in physical space.
- Transform source term, now fully calculated, back into full wave space and invert ∇^2 (divide by $-\vec{k}^2$).
- Transform result back to full physical space.

Much of the complexity of this example stems from the fact that the complete velocity field is too large to fit into even a super-computer's central memory. Thus, the data must be split into "pencils" or "planes" of one or two dimensional data. For more complex databases, even more steps must be taken to perform a similar computation: for example, for certain simulations the physical space product must be dealiased on a 3/2 size grid; for others the derivatives involve Chebyshev and Fourier transforms rather than just Fourier transforms as above.

Considering the above example, one can see that a post-processor which computes many quantities can become significantly complex and inscrutable to the uninitiated. In fact, for certain simulations the post-processing software is a more complex code than the simulation code itself. This is particularly true when time and space optimization issues are important. It is important to realize, however, that these complexities can all be understood and are fairly algorithmic. In particular, it is plausible that an expert system (such as the *Tensoral* language) can be taught to *generate* code to perform the above and similar post-processing tasks.

To summarize, the post-processing of turbulence data involves performing tensor calculus and statistics on a number of dissimilar numerical dataset types. Numerical operations must be performed in a manner consistent with the simulation which generated the database. Currently post-processors are written entirely by hand and are specific not only to the simulation in question but also to one or more

particular quantities of interest. Moreover, these post-processors are quite complex codes in their own rights and provide significant barriers to the uninitiated who desire to distill scientific understanding from the myriad computational details. It is entirely plausible that this task — the creation of database post-processors — can be automated.

2. Accomplishments: tensoral design and μtensoral implementation.

2.1 Tensoral by example

The best way to introduce a new computer language is by example: suppose we desire to study the role of the pressure strain term $\langle pS_{ij} \rangle$ in the mean Reynolds stress $\langle u_i u_j \rangle$ evolution

$$\frac{\partial}{\partial t} \langle R_{ij} \rangle = 2 \langle pS_{ij} \rangle + \nu \left\langle u_j \nabla^2 u_i + u_i \nabla^2 u_j \right\rangle .$$

This hypothetical study would calculate $\langle pS_{ij} \rangle$ for various turbulence databases. To calculate $\langle pS_{ij} \rangle$ given a database file `db`, one would code the following *Tensoral* program in a file `ps.tl`:

```
Line 1   A_ij = db:u_i,j
Line 2   S_ij = (A_ij + A_ji)/2
Line 3   w_k = 1/2 epsilon_ijk A_ij
Line 4   p = -unlaplacian(S_ij*S_ji - w_k*w_k)
Line 5   print "Mean pressure strain", <p S_ij>
```

Line 1 defines the velocity gradient tensor `A_ij`. Lines 2 and 3 form the strain `S_ij` tensor and vorticity `w_k`. Line 4 inverts the Poisson equation for the pressure `p`. Line 5 averages the pressure strain and writes the result to the console. To complete our study, we would run this program for several database files from several different simulations.

2.2 Tensoral design: from top to bottom

Exactly *how* is the program `ps.tl` turned into an efficient post-processor to perform the indented task? The overall answer to this question is illustrated in figure 1 and is described in what follows. The *Tensoral* compiler takes the program supplied by the end database user (e.g. `ps.tl`), determines the appropriate numerical methods and data management techniques for the database file `db` (found in a "database description"), and uses this information to output a post-processor in a lower-level language (relative to *Tensoral*). This low-level post-processor is automatically generated and may in principal be any sufficiently powerful language such as *Vectoral*, *Fortran*, or *C*; we use the *Vectoral* language in our prototype because of several of its unique features. Finally, this low-level post-processor is compiled and combined with the requisite library routines (e.g. Fourier, Chebyshev, Jacobi transforms, Poisson solvers) to make an executable post-processor which can then be used to visualize data, to make graphs, or to transport post-processed data to other sites.

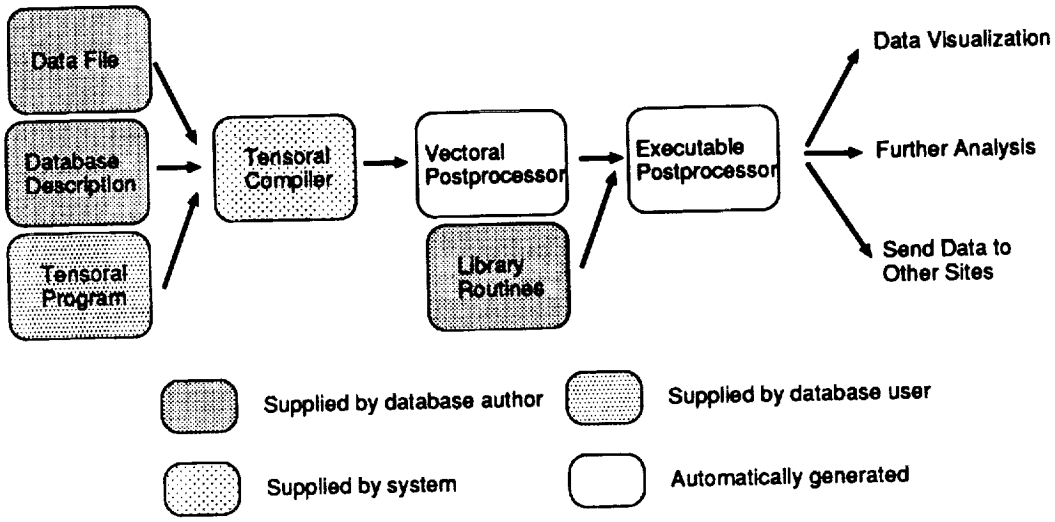

Figure 1

Clearly, the most involved step of this automated system is the generation of a low-level *Vectoral* post-processor given a high-level *Tensoral* program. This step is performed by the *Tensoral* compiler, which compiles very high-level tensor operations into a low-level "machine code" (called μ*Tensoral*). μ*Tensoral* machine code consists of the primitive database operations such as reading a pencil or plane of data into main memory, Fourier transforming that pencil or plane, etc. These primitive operations are defined in the database description. Seen this way, the *Tensoral* compiler is an expert system which figures out how to generate and order primitive μ*Tensoral* database operations to accomplish a given task. If the database description is properly coded, the compiler should be able to generate code which is nearly as efficient as that generated by hand.

2.3 Tensoral implementation: from the bottom up

Implementation of the *Tensoral* proceeds from the bottom up. That is, my goal is to develop a fully functional and robust low-level μ*Tensoral* machine code before launching into the *Tensoral* compiler development which will eventually generate this low-level code. Using this approach, the design outlined above can be proved and tuned from its foundations up. In particular, database descriptions and μ*Tensoral* codes can be written and refined as experience is gained.

Currently a functional μ*Tensoral* system has been implemented. This system is built atop a small Lisp interpreter. The description of numerical methods and data management schemes provided to μ*Tensoral* by database descriptions drive Lisp code which sets up an environment in which μ*Tensoral* code is then executed. Thus, slight differences between simulations can be conditionalized in Lisp (using `if` statements, for example) so that one database description file can actually handle

multiple related simulations. Also, using such conditionals one can write *μTensoral* programs which are common between closely related simulations. The Lisp system is only seen by those programming in *μTensoral* and writing database descriptions, and only then in the remote background. In particular, Lisp will never be seen by *Tensoral* programmers and almost never by *μTensoral* programmers.

A *μTensoral* program to calculate vorticity $\vec{\omega}(\vec{x},t) = \nabla \times \vec{u}(\vec{x},t)$, given spectral $\vec{u}(\vec{k},t)$, is coded as follows:

```
(define-tensor w 1)

; Read u in xy planes; calculate y derivatives;
; transform to physical y.
(loop-memxy
(bs->memxy u_1 u_3)
(->memxy w_3 w_1)
(= w_1 (diff_2 u_3))
(= w_3 (diff_2 u_1))
(wavey->physy- w_1 w_3)
(memxy->bs w_1 w_3))

; Read u in xz planes; calculate other derivatives;
; form vorticity.
(loop-memxz
(bs->memxz u)
(bs->memxz w)
(= w_1 (- w_1 (diff_3 u_2)))
(= w_2 (- (diff_3 u_1) (diff_1 u_3)))
(= w_3 (- (diff_1 u_2) w_3))
(wavez->physz- w)
(wavex->physx- w)
(memxz->bs w))
```

This program is essentially a high-level "shorthand" for the two passes through the database needed to calculate vorticity. It is particularly noteworthy that the roughly 20 line *μTensoral* shorthand shown here generates an approximately 180-line *Vectoral* program. This large code expansion indicates that even the embryonic *μTensoral* system can be used as a useful post-processing tool, even though it assumes a programmer be familiar with the precise numerics of a simulation (as represented by its database description).

Current work focuses on extending *μTensoral*. Currently *μTensoral* only "knows" about tensor algebra and calculus but not statistics. General statistical functions are now being added to average over combinations of x, y, and z coordinates to form correlations and probability density functions (PDFs). Thus far only one database description has been completed; others will follow.

Appendix

NAME/TERM		AREA OF RESEARCH
POSTDOCTORAL FELLOWS		
BELCHER, Dr. Stephen E. 10/30-3/92	(Ph.D. Fluid Mechanics, 1990, DAMTP-Cambridge)	Turbulence modeling
CHASNOV, Dr. Jeffrey 9/91-present	(Ph.D. Physics, 1990, Columbia University)	Turbulence theory and simulation
COLEMAN, Dr. Gary 5/92-present	(Ph.D. Mechanical Engineering, 1990, Stanford University)	Compressible turbulence
GAO, Dr. Feng 9/90-present	(Ph.D. Mechanical Engineering, 1990, SUNY at Stony Brook)	PDF approach for turbulent scalar fields
GHOSAL, Dr. Sandip 2/92-present	(Ph.D. Physics, 1992, Columbia University	Subgrid scale modeling
HAMILTON, Dr. James M. 6/91-present	(Ph.D. Engineering Science, 1991, Harvard University)	Structure of turbulent boundary layers
JACOB, Dr. Marc C. 6/91-7/92	(Ph.D. Acoustics, 1991, Ecole Centrale de Lyon)	Aerodynamic noise
JONES, Dr. Donald A. 9/92-present	(Ph.D. Mathematics, 1992, UC-Irvine)	Approximate inertial manifold theory
KALTENBACH, Dr. Hans-Jakob 9/92-present	(Ph.D. Atmospheric Physics, 1992, TU Munchen, Germany	Large eddy simulation of complex flows
KO, Dr. Sung Ho 7/91-present	(Ph.D. Mechanical Engineering, 1991, Texas A&M University)	Application of turbulence models in the wall region

LEBOEUF, Dr. Richard L. 9/91-present	(Ph.D. Mechanical Engineering, 1991, SUNY at Buffalo)	Experimental study of turbulent mixing layer
LEE, Dr. Sangsan 4/92-present	(Ph.D. Mechanical Engineering 1992, Stanford University)	Shock waves
SADDOUGI, Dr. Seyed G. 6/91-present	(Ph.D. Mechanical Engineering, 1989, the University of Melbourne)	Experimental investigation of local isotropy in high-Reynolds-number turbulence
SAMANIEGO, Dr. Jean-Michel 4/92-present	(Ph.D. Combustion, 1992, Ecole Centrale Paris)	Flame/vortex interaction
SAMUELS, Dr. David C. 10/90-9/92	(Ph.D. Physics, 1990, University of Oregon)	Superfluid turbulence
SHEN, Dr. Hubert 1/90-12/91	(Ph.D. Physics, 1988, University of Illinois)	Turbulence theory
TROUVE, Dr. Arnaud 4/90-present	(Ph.D. Mechanical Engineering, 1989, Ecole Centrale de Paris)	Flame-turbulence interactions in premixed combustion
VERVISCH, Luc 1/92-12/92	(Ph.D. Physics, 1991, Univ. Rouen, France)	Finite rate chemistry effects in turbulent non-premixed flames
WALEFFE, Dr. Fabian A. 9/89-8/92	(Ph.D. Applied Mathematics, 1989, MIT)	Non-linear interactions in homogeneous turbulence
WANG, Dr. Meng 9/92-present	(Ph.D. Mechanical Engineering, 1989, University of Colorado)	Aerodynamic noise and transition
ZHOU, Dr. Ye 10/90-9/92	(Ph.D. Physics, 1987, College of William & Mary)	Turbulence theory

RESEARCH ASSOCIATES

CABOT, Dr. William H. 3/88-present	(Ph.D. Physics, 1983, University of Rochester)	Large eddy simulation and convection
DRESSELHAUS, Dr. Eliot 9/91-present	(Ph.D. Applied Mathematics, 1991, Columbia University	Post-processing facility
LUND, Dr. Thomas S. 11/90-present	(Ph.D. Aero-Astro, 1987, Stanford Univ.)	Large eddy simulation

SENIOR VISITING FELLOWS

CAMBON, Prof. Claude 7/92-8/92	Professor, Fluid Mechanics, Ecole Centrale de Lyon	RDT analyses of compressing compressible flows
GEORGE, Prof. William K. 6/92	Professor, Mech. & Aero. Engr., SUNY-Buffalo	Consultant on the 80X120 experiment
KRAICHNAN, Robert H. 12/91-9/92	Santa Fe, New Mexico	Turbulence theory
KUZNETSOV, Dr. Vadim R. 9/92-11/92	Sr. Scientist, Central Inst. of Aviation Motors, Moscow	Turbulent reacting flows
PRASKOVSKY, Dr. Alexander 12/91-5/92	Head Researcher, Central Aero-Hydrodynamic Inst., Moscow	Local isotropy in high Reynolds number turbulence
TEMAM, Prof. Roger 8/92	Professor, University of Paris - SUD and University of Indiana	Feedback procedures for flow control
TOKUNAGA, Prof. Hiroshi 4/92-4/93	Professor, Kyoto Institute of Technology	Numerical methods
WALLACE, Prof. James M. 8/92	Professor, University of Maryland	Vorticity measurements in the 80X120 tunnel
ZASLAVSKY, Prof. George M. 8/92	Professor, Courant Inst., New York Univ.	Dynamical systems

SR. RESEARCH FELLOWS

DURBIN, Dr. Paul 1/90-present	DAMTP, Cambridge University	Reynolds stress closure modeling
HILL, Dr. D. Christopher 5/92-present	Cambridge University	Analytical methods in active and passive flow control
JIMENEZ, Prof. Javier 7/92-11/92	Professor of Fluid Mechanics, School of Aeronautics, University of Madrid	Small scale vortices in turbulent flows
ZEMAN, Dr. Otto 3/89-present	Pennsylvania State University	Compressible turbulence

GRADUATE STUDENTS

AZAIEZ, Jalel 10/91-9/92		Viscoelastic mixing layers
FLACK, Karen 4/92-6/92		Wall-layer structure of 3-D turbulent boundary layers
KARASSO, Paris 7/89-12/92		Curved shear layer
LE, Hung 4/88-present		Simulation of turbulent flow over a backward-facing step

1992 ADVISORY COMMITTEE

Prof. Ronald J. Adrian
University of Illinois

Prof. Garry Brown
Princeton University

Dr. Dennis M. Bushnell
NASA Langley Research Center

Prof. Robert Dibble
Univ. of California at Berkeley

Dr. Marvin E. Goldstein (Chairman)
NASA Lewis Research Center

Dr. Robert H. Kraichnan
Santa Fe, New Mexico

Dr. Spiro Lekoudis
Office of Naval Research

Prof. Hans W. Liepmann
California Institute of Technology

Dr. James M. McMichael
Air Force Office of Scientific Research

Dr. Robert Melnik
Grumman Corporation

Prof. Mark V. Morkovin
Illinois Institute of Technology

Prof. Stephen B. Pope
Cornell University

Mr. A. D. (Bert) Welliver
Boeing Airplane Company

Dr. Ron Bailey (Ex-officio)
NASA Ames Research Center

Dr. Kristen Hessenius (Ex-officio)
NASA Headquarters

1992 STEERING COMMITTEE

Prof. Dean R. Chapman
Dept of Aeronautics & Astronautics
& Mechanical Engineering, Stanford

Dr. Terry L. Holst
Chief, Applied Computational Fluids Branch
NASA Ames Research Center

Prof. Javier Jimenez
Senior Research Fellow, 7/92-11/92
Center for Turbulence Research,
Professor, Fluid Mechanics,
University of Madrid

Dr. John J. Kim
Ames Coordinator,
Center for Turbulence Research,
Head, Turbulence Physics Section,
NASA Ames Research Center

Mr. Joseph G. Marvin
Chief, Experimental Fluid Dynamics Branch
NASA Ames Research Center

Prof. Parviz Moin
Director, Center for Turbulence Research,
Professor, Mech. Eng., Stanford,
Sr. Staff Scientist, NASA Ames Res. Center

Prof. William C. Reynolds
Program Coordinator, Center for Turbulence Research, Professor & Chairman,
Mechanical Engr., Stanford University,
Sr. Staff Scientist, NASA Ames Res. Center